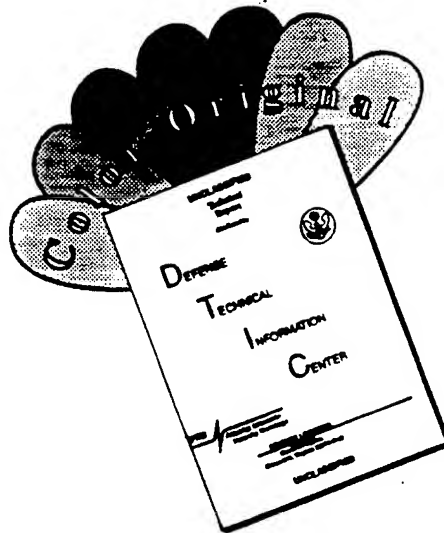


REPORT DOCUMENTATION PAGE			Form Approved OMB No. 0704-0188	
Public reporting burden for this collection of information is estimated to average 1 hour per response, including the time for reviewing instructions, searching existing data sources, gathering and maintaining the data needed, and completing and reviewing the collection of information. Send comments regarding this burden estimate or any other aspect of this collection of information, including suggestions for reducing this burden, to Washington Headquarters Services, Directorate for Information Operations and Reports, 1215 Jefferson Davis Highway, Suite 1204, Arlington, VA 22202-4302, and to the Office of Management and Budget, Paperwork Reduction Project (0704-0188), Washington, DC 20503.				
1. AGENCY USE ONLY (Leave blank)		2. REPORT DATE 4/96		3. REPORT TYPE AND DATES COVERED Technical, 5/92-5/96
4. TITLE AND SUBTITLE Unsteady Flow Over a 6:1 Prolate Spheroid			5. FUNDING NUMBERS N00014-87-K-0816 N00014-91-J-1732 N00014-95-I-0101	
6. AUTHOR(S) Todd G. Wetzel and Roger L. Simpson				
7. PERFORMING ORGANIZATION NAME(S) AND ADDRESS(ES) Advanced Research Projects Agency, 3701 Fairfax Dr. Suite 100, Arlington, VA 22203-1714 through the Office of Naval Research, Applied Hydrodynamics, 800 N. Quincy St., Arlington, VA 22217			8. PERFORMING ORGANIZATION REPORT NUMBER  VPI-AOE-232	
9. SPONSORING/MONITORING AGENCY NAME(S) AND ADDRESS(ES)			10. SPONSORING/MONITORING AGENCY REPORT NUMBER	
11. SUPPLEMENTARY NOTES				
12a. DISTRIBUTION/AVAILABILITY STATEMENT Approved for public release, distribution unlimited			12b. DISTRIBUTION CODE	
13. ABSTRACT (Maximum 200 words) The flow over a 6:1 prolate spheroid undergoing time dependent maneuvers is studied. The model is mounted on the Dynamic Plunge-Pitch-Roll (DyPPiR) model mount in the Virginia Tech Stability Wind Tunnel. The model undergoes 30° pitchup ramps in 0.33s and a 13.5° submarine maneuver in 0.25s. All tests are done at a Reynolds number of 4.2 million. Unsteady surface pressures, skin friction, and force and moment measurements are documented for these two maneuvers. In particular, time dependent separation locations are documented for the first time.				
14. SUBJECT TERMS Three-Dimensional Separation Unsteady Aerodynamics Maneuvering			15. NUMBER OF PAGES 524	
			16. PRICE CODE	
17. SECURITY CLASSIFICATION OF REPORT UNCLASSIFIED	18. SECURITY CLASSIFICATION OF THIS PAGE UNCLASSIFIED	19. SECURITY CLASSIFICATION OF ABSTRACT UNCLASSIFIED	20. LIMITATION OF ABSTRACT	

19960422 134

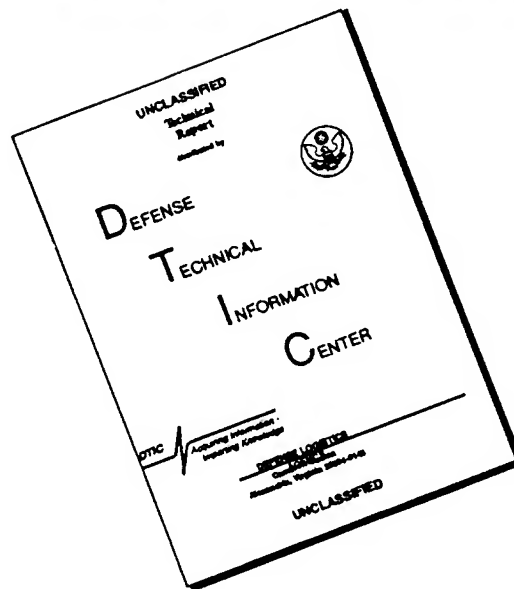
# DISCLAIMER NOTICE



THIS DOCUMENT IS BEST QUALITY AVAILABLE. THE COPY FURNISHED TO DTIC CONTAINED A SIGNIFICANT NUMBER OF COLOR PAGES WHICH DO NOT REPRODUCE LEGIBLY ON BLACK AND WHITE MICROFICHE.



# DISCLAIMER NOTICE



THIS DOCUMENT IS BEST QUALITY AVAILABLE. THE COPY FURNISHED TO DTIC CONTAINED A SIGNIFICANT NUMBER OF PAGES WHICH DO NOT REPRODUCE LEGIBLY.

# UNSTEADY FLOW OVER A 6:1 PROLATE SPHEROID

by

Todd G. Wetzel

Roger L. Simpson, Chairman  
Aerospace and Ocean Engineering Department

## ABSTRACT

The flow over a 6:1 prolate spheroid undergoing transient maneuvers is studied. The Dynamic Plunge-Pitch-Roll (DyPPiR) model mount provides the unique capability to simulate truly unsteady maneuvers in a wind tunnel. The DyPPiR is presented along with several transducer systems used to study specific aspects of the spheroid flow field. The types of unsteady measurements performed include hot-film surface skin friction measurements, surface pressure measurements, and force and moment measurements. Unsteady measurements are much more difficult to perform than steady ones and require many special considerations. In light of this fact, each transducer system is examined in detail for its appropriateness in detecting unsteady phenomena and the associated uncertainties. Recommendations are made for each of these systems for the improvement of their accuracy and relevance in studying unsteady phenomena. In particular, time dependent separation locations are measured successfully for the first time, as are time dependent force and moment measurements. Steady and unsteady data are presented for each of these systems for two maneuvers: a  $0^\circ$  to  $30^\circ$ , 0.33 second pure ramp pitchup about the model center, and thus referred to as the Pitchup Maneuver; and a  $0^\circ$  to  $13.5^\circ$  pure pitchup about the model center that simulates the time dependent sideslip angle of a submarine entering a turning maneuver, thus referred to as the Submarine Maneuver. These data are coupled with steady oil flow visualizations and data sets from other researchers to describe the spheroid flow field in detail in both steady and unsteady cases. This flow field is characterized by complex, three-dimensional cross-flow separations that are highly non-linear and are expected to have very complex time dependencies in unsteady flows. It is shown that, especially at higher angles of attack, significant lags occur in the flow field during the maneuvers compared to the steady cases. In particular, separation is delayed at all locations of the model by up to  $10^\circ$  higher angle of attack in the unsteady maneuvers compared to the steady data. Equivalently, the separation structure during the unsteady maneuvers lag the steady data by from 1.5 to 4.5 non-dimensional time units ( $t'$ ). The range of these time constants and the fact they are constant for neither the entire model or a given sensors shows for the first time the complex nature of the time dependency of three-dimensional crossflow separation. In addition, normal force and pitch moment lags on the order of 1 time unit are demonstrated.

## Acknowledgments

---

The author would like to acknowledge the many people without whom this work would not exist.

This work is not performed in complete isolation, and the many discussions with the author's colleagues have contributed greatly toward the solution of many problems. Notable among these people are Semih Olcmen, Chris Chesnakas, Kevin Shinpaugh, Ngoc Hoang, Jon Fleming, and Eric Roback. Ngoc Hoang is particularly noted for his work in making the DyPPiR operational and in acquiring the unsteady pressure data. Eric Roback is acknowledged for his help in developing the lightweight carbon fiber models. Finally, Jon Fleming is acknowledged in particular for his many hours of arduous assistance in the wind tunnel and DyPPiR operation.

The author wishes to acknowledge Kent Morris, Bruce Stanger, and Greg Dudding for construction of most of the mechanical hardware used in these tests. Their craftsmanship is only exceeded by their willingness to help improve design concepts and their cooperation in meeting important deadlines.

This work is the culmination of a program of *education*, and in that regard the author must recognize the important guidance provided by his advisor, Dr. Roger L. Simpson. The author is indebted to him and the entire Aerospace and Ocean Engineering Department for imparting on him the skills and knowledge necessary for a future in this field. The entire Committee is also acknowledged for their detailed reading of this work and their numerous constructive suggestions.

Of course, this author must also thank his parents for providing the opportunities and the work ethic necessary for pursuing higher education all the way through the Doctorate program. And finally, the author must thank the Lord for all of the blessings he has bestowed on the author, through both the opportunities and people He has provided.

This work was sponsored by the National Science Foundation through a Graduate Fellowship, and by the Applied Hydrodynamics Program through the Office of Naval Research Grants N00014-91-J-1732-3-4, N00014-94-J-1732-3-4, and N00014-95-1-0101, James A. Fein, Program Manager.

## Table of Contents

---

ABSTRACT	II
ACKNOWLEDGMENTS	III
TABLE OF CONTENTS	IV
LIST OF TABLES	IX
LIST OF FIGURES	X
NOMENCLATURE	XXVII
GLOSSARY OF TERMS	XXX
CHAPTER 1: INTRODUCTION	1
1.1 Unsteady Aerodynamics	1
1.2 6:1 Prolate Spheroid	2
1.3 Overview of Present Research Program	6
1.4 Present Work	7
CHAPTER 2: DYNAMIC PLUNGE-PITCH-ROLL MODEL MOUNT (DYPPiR)	10
2.1 Stability and Control Wind Tunnel	10
2.2 DyPPiR Hardware Overview	10
2.3 Maneuvers Tested	10

2.3.1 The 0.33s, 30° Ramp Pitchup	10
2.3.2 The 0.25s Submarine Maneuver	11
2.3.3 The 0.33s Plunge Down Maneuver	12
2.4 Model Geometry	12
<b>CHAPTER 3: CONSTANT CURRENT HOT-FILM MEASUREMENTS</b>	<b>13</b>
3.1 Theory of Operation	13
3.2 The Sensors	14
3.3 Experimental Apparatus	15
3.4 Frequency Response	16
3.5 Data Reduction and Uncertainties	16
3.5.1 Fundamental Quantities	16
3.5.2 Sensor Temperature and Heat Transfer	18
3.5.3 Film Coefficient	19
3.5.4 Wall Shear	22
3.5.5 Uncertainty Calculations	22
3.5.6 Non-Ideal Sensor Operation Uncertainties	23
3.6 Separation Location	24
3.7 Calibration	25
3.8 Steady Results	27
<b>CHAPTER 4: CONSTANT TEMPERATURE HOT-FILM MEASUREMENTS</b>	<b>30</b>
4.1 Theory of Operation	30
4.2 Experimental Apparatus	30
4.3 Frequency Response	32
4.4 Spatial Averaging	32
4.5 Data Reduction and Uncertainties: Steady Data	33
4.5.1 Wall Shear	33
4.5.2 Sensor Voltage	34
4.5.3 Sensor Temperature and Resistance	34
4.5.4 Nonlinear Averaging Uncertainties	36
4.6 Steady Calibration	37
4.7 Unsteady Data Reduction and Calibration	37

4.8 Steady Results	40
4.9 Unsteady Results	41
4.9.1 Pitchup Maneuver	41
4.9.2 Submarine Maneuver	42
4.10 Future Improvements	43
<b>CHAPTER 5: OIL FLOW VISUALIZATION</b>	<b>47</b>
5.1 Introduction	47
5.2 Experimental Apparatus	47
5.3 Basic Separation Locations	48
5.4 Some Selected Detail Flow Topologies	48
5.4.1 Nose Flow Separations at 30° Angle of Attack	48
5.4.2 Crossflow Separation Topology	49
<b>CHAPTER 6: PRESSURE MEASUREMENTS</b>	<b>50</b>
6.1 Experimental Apparatus	50
6.2 Data Reduction and Uncertainties	51
6.2.1 Pressure Coefficient	51
6.2.2 Circumferential Pressure Gradient	52
6.2.3 Pressure Fluctuations (RMS)	52
6.2.4 Sectional Lift Coefficients	52
6.2.5 Normal Force and Pitch Moment	55
6.3 Steady Results	57
6.3.1 Pressure Coefficient	57
6.3.2 Circumferential Pressure Gradient	58
6.3.3 Pressure Fluctuations (RMS)	59
6.3.4 Forces and Moments	59
6.4 Unsteady Results	60
6.4.1 Pitchup Maneuver	60
6.4.2 Submarine Maneuver	60
6.5 Future Improvements	61
<b>CHAPTER 7: FORCE AND MOMENT MEASUREMENTS</b>	<b>62</b>
7.1 Introduction	62

<b>7.2 Previous Work</b>	<b>62</b>
7.2.1 Curved Flow Methods	63
7.2.2 Rotary Balances	63
7.2.3 Forced Oscillation Mechanisms	63
<b>7.3 Iteration 1: The Balance and Model of Ahn (1990)</b>	<b>66</b>
<b>7.4 Iteration 2: "Fly-weight" Balance and Light-weight Model</b>	<b>68</b>
<b>7.5 Iteration 3: Two-point balance and Light-weight Model</b>	<b>69</b>
<b>7.6 Data Reduction and Uncertainties</b>	<b>71</b>
<b>7.7 Steady Results</b>	<b>72</b>
<b>7.8 Unsteady Results</b>	<b>73</b>
<b>7.9 Future Iterations</b>	<b>78</b>
 <b>CHAPTER 8: DISCUSSION</b>	 <b>81</b>
8.1 Flow Separation: Definitions and Measurement Techniques	81
8.2 Quasi-Steady Flow-Field Description for a Pitching Prolate Spheroid	85
8.3 Unsteady Aerodynamics on the Prolate Spheroid	90
 <b>CHAPTER 9: CONCLUSIONS</b>	 <b>92</b>
 <b>CHAPTER 10: SUGGESTIONS FOR FUTURE WORK</b>	 <b>93</b>
10.1 Overview	93
10.2 Future Unsteady Experiments	93
10.3 Measurement System Improvements	94
10.3.1 Constant Temperature Hot-Film Sensor Measurements	94
10.3.2 Surface Pressure Measurements	95
10.3.3 Force and Moment Measurements	95
10.3.4 DyPPiR Improvements	96
10.3.5 Other Possible Measurements	97
 <b>REFERENCES</b>	 <b>98</b>

<b>TABLES</b>	<b>107</b>
<b>FIGURES</b>	<b>111</b>
<b>APPENDIX A: INTEGRAL MOMENTUM BOUNDARY LAYER SOLUTION FOR A LINE OF SYMMETRY ON A BODY OF REVOLUTION</b>	<b>478</b>
A.1 Method Derivation	478
A.2 The Code	484
<b>VITA</b>	<b>492</b>



## List of Tables

---

<i>Table 1. Maneuver conditions.</i>	<i>107</i>
<i>Table 2. Constant current calibration factors.</i>	<i>107</i>
<i>Table 3. Constant temperature sensor temperatures.</i>	<i>108</i>
<i>Table 4. Steady Constant temperature calibration factors.</i>	<i>108</i>
<i>Table 5. Unsteady constant-temperature calibration factors.</i>	<i>109</i>
<i>Table 6. Pressure Transducer sensitivities.</i>	<i>109</i>
<i>Table 7. Estimated force and moment loads for old and new model. Assumes a representative maximum linear acceleration of 5 g's and a representative angular acceleration of 130 rad/s<sup>2</sup>. Added mass forces and moments from section 7.7.</i>	<i>110</i>

## List of Figures

- Figure 1. Different types of crossflow separation: a) separation horseshoe-type, closed separation; b) Werle type, closed separation; c) open crossflow separation. From Yates and Chapman (1992). 111
- Figure 2. Simplified Flow Separation Topology for the secondary streamlines in a plane normal to the major axis of an axisymmetric body. S1 and S2 refer to primary and secondary separation locations, respectively, and R1 and R2 refer to primary and secondary reattachment locations. 112
- Figure 3. Laminar/turbulent separation interaction on a body of revolution (Poll, 1985). 113
- Figure 4. Wall shear vector data on a 6:1 prolate spheroid at  $x/L=0.139$ ,  $\alpha=30^\circ$ , and Reynolds number of 6.5 million. From Meier and Kreplin (1985). 114
- Figure 5. Virginia Tech Stability and Control Wind Tunnel. 115
- Figure 6. Dynamic Plunge-Pitch-Roll (DyPPiR) Model Mount installed in wind tunnel. 116
- Figure 7. Coordinate Nomenclature.  $x$  is measured from the nose;  $\phi$  is the circumferential location measured from the windward line of symmetry;  $z$  is the plunge ordinate; and  $\alpha$  is the pitch angle and equivalently the model center angle of attack. 117
- Figure 8. Pitch-up maneuver pitch angle position feedback. Dotted lines represent 20:1 odds positional repeatability. The regions (a), (b), and (c) indicate the extent of individual time series plots of hot-film data presented in Chapter 4. 118
- Figure 9. Pitch-up maneuver plunge position feedback. Dotted lines represent 20:1 odds positional repeatability. The regions (a), (b), and (c) indicate the extent of individual time series plots of hot-film data presented in Chapter 4. 119
- Figure 10. Model center of gravity motion during pitch-up maneuver. Dotted lines represent 20:1 odds positional repeatability. 120
- Figure 11. Model center of gravity acceleration during pitch-up maneuver. 121
- Figure 12. Submarine maneuver pitch angle command signal compared to data from DTMB sideslip data. 122
- Figure 13. Submarine maneuver pitch angle position feedback. Dotted lines represent 20:1 odds positional repeatability. The regions (a), (b), and (c) indicate the extent of individual time series plots of hot-film data presented in Chapter 4. 123
- Figure 14. Submarine maneuver plunge position feedback. Dotted lines represent 20:1 odds positional repeatability. The regions (a), (b), and (c) indicate the extent of individual time series plots of hot-film data presented in Chapter 4. 124

Figure 15. Model center of gravity motion during submarine maneuver. Dotted lines represent 20:1 odds positional repeatability. _____	125
Figure 16. Model center of gravity acceleration during submarine maneuver. _____	126
Figure 17. Hot-film sensor geometry. _____	127
Figure 18. Hot-film sensor orientation on model. At angles of attack up to around $30^\circ$ , most of the local wall shear angles are bounded in the range of $40^\circ$ below $10^\circ$ above longitudinal. The sensors were oriented with their centerlines $65^\circ$ off longitudinal to minimize directional sensitivity. _____	128
Figure 19. Hot-film sensor directional sensitivity, calculated as an effective length relative to the mean effective length. Dotted lines show bounded flow directions. _____	129
Figure 20. Locations of sensor on model for constant current tests. _____	130
Figure 21. Constant current anemometer block diagram. _____	131
Figure 22. Line-of-symmetry $C_f$ calculations. Calculations are for a 6:1 prolate spheroid at $Re=4.2$ million with trip posts at $x/L=0.20$ and the model at various angles of attack. Meier and Kreplin data from $5^\circ$ and $10^\circ$ shown for comparison. _____	132
Figure 23. Comparison of present skin friction magnitudes, $Re=4.2$ million (both constant temperature and constant current), with hot-film data from Meier and Kreplin (1984), $Re=6.4$ million, at $x/L=0.48$ and $\alpha=10^\circ$ . Closest sensors from present data set are shown. _____	133
Figure 24. Comparison of present skin friction magnitudes (both constant temperature and constant current) with LDV data from Chesnakas and Simpson (1996) at $x/L=0.77$ , $\alpha=10^\circ$ , and $Re=4.2$ million. Closest sensors from present data set are shown. _____	134
Figure 25. Comparison of present skin friction magnitudes (both constant temperature and constant current) with LDV data from Chesnakas and Simpson (1996) at $x/L=0.60$ , $\alpha=20^\circ$ , and $Re=4.2$ million. Closest sensors from present data set are shown. _____	135
Figure 26. Comparison of present skin friction magnitudes (both constant temperature and constant current) with LDV data from Chesnakas and Simpson (1996) at $x/L=0.77$ , $\alpha=20^\circ$ , and $Re=4.2$ million. Closest sensors from present data set are shown. _____	136
Figure 27. Skin friction values superimposed on secondary streamlines from Chesnakas and Simpson (1996) at $x/L=0.40$ and $\alpha=10^\circ$ . _____	137
Figure 28. Skin friction values superimposed on secondary streamlines from Chesnakas and Simpson (1996) at $x/L=0.60$ and $\alpha=10^\circ$ . _____	138
Figure 29. Skin friction values superimposed on secondary streamlines from Chesnakas and Simpson (1996) at $x/L=0.77$ and $\alpha=10^\circ$ . _____	139

Figure 30. Skin friction values superimposed on secondary streamlines from Chesnakas and Simpson (1996) at $x/L=0.60$ and $\alpha=20^\circ$ .	140
Figure 31. Skin friction values superimposed on secondary streamlines from Chesnakas and Simpson (1996) at $x/L=0.77$ and $\alpha=20^\circ$ .	141
Figure 32. Constant current $C_f$ vs. $\phi$ for all $x/L$ , $\alpha=5^\circ$ .	142
Figure 33. Constant current $C_f$ vs. $\phi$ for all $x/L$ , $\alpha=10^\circ$ .	143
Figure 34. Constant current $C_f$ vs. $\phi$ for all $x/L$ , $\alpha=15^\circ$ .	144
Figure 35. Constant current $C_f$ vs. $\phi$ for all $x/L$ , $\alpha=20^\circ$ .	145
Figure 36. Constant current $C_f$ vs. $\phi$ for all $x/L$ , $\alpha=25^\circ$ .	146
Figure 37. Constant current $C_f$ vs. $\phi$ for all $x/L$ , $\alpha=30^\circ$ .	147
Figure 38. Constant current $C_f$ vs. $\phi$ for all $\alpha$ , $x/L=0.118$ .	148
Figure 39. Constant current $C_f$ vs. $\phi$ for all $\alpha$ , $x/L=0.143$ .	149
Figure 40. Constant current $C_f$ vs. $\phi$ for all $\alpha$ , $x/L=0.169$ .	150
Figure 41. Constant current $C_f$ vs. $\phi$ for all $\alpha$ , $x/L=0.194$ .	151
Figure 42. Constant current $C_f$ vs. $\phi$ for all $\alpha$ , $x/L=0.220$ .	152
Figure 43. Constant current $C_f$ vs. $\phi$ for all $\alpha$ , $x/L=0.245$ .	153
Figure 44. Constant current $C_f$ vs. $\phi$ for all $\alpha$ , $x/L=0.271$ .	154
Figure 45. Constant current $C_f$ vs. $\phi$ for all $\alpha$ , $x/L=0.296$ .	155
Figure 46. Constant current $C_f$ vs. $\phi$ for all $\alpha$ , $x/L=0.322$ .	156
Figure 47. Constant current $C_f$ vs. $\phi$ for all $\alpha$ , $x/L=0.347$ .	157
Figure 48. Constant current $C_f$ vs. $\phi$ for all $\alpha$ , $x/L=0.373$ .	158
Figure 49. Constant current $C_f$ vs. $\phi$ for all $\alpha$ , $x/L=0.398$ .	159
Figure 50. Constant current $C_f$ vs. $\phi$ for all $\alpha$ , $x/L=0.424$ .	160
Figure 51. Constant current $C_f$ vs. $\phi$ for all $\alpha$ , $x/L=0.449$ .	161
Figure 52. Constant current $C_f$ vs. $\phi$ for all $\alpha$ , $x/L=0.474$ .	162
Figure 53. Constant current $C_f$ vs. $\phi$ for all $\alpha$ , $x/L=0.500$ .	163
Figure 54. Constant current $C_f$ vs. $\phi$ for all $\alpha$ , $x/L=0.525$ .	164
Figure 55. Constant current $C_f$ vs. $\phi$ for all $\alpha$ , $x/L=0.551$ .	165
Figure 56. Constant current $C_f$ vs. $\phi$ for all $\alpha$ , $x/L=0.576$ .	166
Figure 57. Constant current $C_f$ vs. $\phi$ for all $\alpha$ , $x/L=0.602$ .	167
Figure 58. Constant current $C_f$ vs. $\phi$ for all $\alpha$ , $x/L=0.627$ .	168

Figure 59. Constant current $C_f$ vs. $\phi$ for all $\alpha$ , $x/L=0.653$ .	169
Figure 60. Constant current $C_f$ vs. $\phi$ for all $\alpha$ , $x/L=0.678$ .	170
Figure 61. Constant current $C_f$ vs. $\phi$ for all $\alpha$ , $x/L=0.704$ .	171
Figure 62. Constant current $C_f$ vs. $\phi$ for all $\alpha$ , $x/L=0.729$ .	172
Figure 63. Constant current $C_f$ vs. $\phi$ for all $\alpha$ , $x/L=0.754$ .	173
Figure 64. Constant current $C_f$ vs. $\phi$ for all $\alpha$ , $x/L=0.780$ .	174
Figure 65. Constant current $C_f$ vs. $\phi$ for all $\alpha$ , $x/L=0.805$ .	175
Figure 66. Constant current $C_f$ vs. $\phi$ for all $\alpha$ , $x/L=0.831$ .	176
Figure 67. Constant current $C_f$ vs. $\phi$ for all $\alpha$ , $x/L=0.856$ .	177
Figure 68. Constant current $C_f$ vs. $\phi$ for all $\alpha$ , $x/L=0.882$ .	178
Figure 69. Constant current $C_f$ vs. $\phi$ for all $\alpha$ , $x/L=0.907$ .	179
Figure 70. Constant current separation line topology for $\alpha=10^\circ$ .	180
Figure 71. Constant current separation line topology for $\alpha=15^\circ$ .	181
Figure 72. Constant current separation line topology for $\alpha=20^\circ$ .	182
Figure 73. Constant current separation line topology for $\alpha=25^\circ$ .	183
Figure 74. Constant current separation line topology for $\alpha=30^\circ$ .	184
Figure 75. Primary separation location as a function of $\alpha$ for various $x/L$ .	185
Figure 76. Constant temperature anemometer/data acquisition interface box.	186
Figure 77. Typical frequency response for the Miller anemometers with the present hot-film sensors.	187
Figure 78. Constant temperature $C_f$ vs. $\phi$ for all $x/L$ , $\alpha=4.8^\circ$ .	188
Figure 79. Constant temperature $C_f$ vs. $\phi$ for all $x/L$ , $\alpha=7.3^\circ$ .	189
Figure 80. Constant temperature $C_f$ vs. $\phi$ for all $x/L$ , $\alpha=12.2^\circ$ .	190
Figure 81. Constant temperature $C_f$ vs. $\phi$ for all $x/L$ , $\alpha=15.2^\circ$ .	191
Figure 82. Constant temperature $C_f$ vs. $\phi$ for all $x/L$ , $\alpha=17.6^\circ$ .	192
Figure 83. Constant temperature $C_f$ vs. $\phi$ for all $x/L$ , $\alpha=20.2^\circ$ .	193
Figure 84. Constant temperature $C_f$ vs. $\phi$ for all $x/L$ , $\alpha=22.4^\circ$ .	194
Figure 85. Constant temperature $C_f$ vs. $\phi$ for all $x/L$ , $\alpha=24.8^\circ$ .	195
Figure 86. Constant temperature $C_f$ vs. $\phi$ for all $x/L$ , $\alpha=27.5^\circ$ .	196
Figure 87. Constant temperature $C_f$ vs. $\phi$ for all $x/L$ , $\alpha=29.9^\circ$ .	197
Figure 88. Constant temperature $C_f$ vs. $\phi$ for all $x/L$ , $\alpha=32.4^\circ$ .	198
Figure 89. Constant temperature $C_f$ vs. $\phi$ for all $x/L$ , $\alpha=34.8^\circ$ .	199

Figure 90. Constant temperature $C_f$ vs. $\phi$ for all $\alpha$ , $x/L=0.118$ .	200
Figure 91. Constant temperature $C_f$ vs. $\phi$ for all $\alpha$ , $x/L=0.194$ .	201
Figure 92. Constant temperature $C_f$ vs. $\phi$ for all $\alpha$ , $x/L=0.220$ .	202
Figure 93. Constant temperature $C_f$ vs. $\phi$ for all $\alpha$ , $x/L=0.271$ .	203
Figure 94. Constant temperature $C_f$ vs. $\phi$ for all $\alpha$ , $x/L=0.347$ .	204
Figure 95. Constant temperature $C_f$ vs. $\phi$ for all $\alpha$ , $x/L=0.424$ .	205
Figure 96. Constant temperature $C_f$ vs. $\phi$ for all $\alpha$ , $x/L=0.500$ .	206
Figure 97. Constant temperature $C_f$ vs. $\phi$ for all $\alpha$ , $x/L=0.576$ .	207
Figure 98. Constant temperature $C_f$ vs. $\phi$ for all $\alpha$ , $x/L=0.653$ .	208
Figure 99. Constant temperature $C_f$ vs. $\phi$ for all $\alpha$ , $x/L=0.729$ .	209
Figure 100. Constant temperature $C_f$ vs. $\phi$ for all $\alpha$ , $x/L=0.831$ .	210
Figure 101. Constant temperature $C_f$ vs. $\phi$ for all $\alpha$ , $x/L=0.882$ .	211
Figure 102. Constant temperature separation line topology for $\alpha=7.3^\circ$ .	212
Figure 103. Constant temperature separation line topology for $\alpha=12.2^\circ$ .	213
Figure 104. Constant temperature separation line topology for $\alpha=15.2^\circ$ .	214
Figure 105. Constant temperature separation line topology for $\alpha=17.6^\circ$ .	215
Figure 106. Constant temperature separation line topology for $\alpha=20.2^\circ$ .	216
Figure 107. Constant temperature separation line topology for $\alpha=22.4^\circ$ .	217
Figure 108. Constant temperature separation line topology for $\alpha=24.8^\circ$ .	218
Figure 109. Constant temperature separation line topology for $\alpha=27.5^\circ$ .	219
Figure 110. Constant temperature separation line topology for $\alpha=29.9^\circ$ .	220
Figure 111. Constant temperature separation line topology for $\alpha=32.4^\circ$ .	221
Figure 112. Constant temperature separation line topology for $\alpha=34.8^\circ$ .	222
Figure 113. Comparison of constant current and constant temperature separation topology for $\alpha=15^\circ$ . Solid lines are constant current data. Dashed lines are constant temperature data.	223
Figure 114. Comparison of constant current and constant temperature separation topology for $\alpha=20^\circ$ . Solid lines are constant current data. Dashed lines are constant temperature data.	224
Figure 115. Comparison of constant current and constant temperature separation topology for $\alpha=25^\circ$ . Solid lines are constant current data. Dashed lines are constant temperature data.	225
Figure 116. Comparison of constant current and constant temperature separation topology for $\alpha=30^\circ$ . Solid lines are constant current data. Dashed lines are constant temperature data.	226

Figure 117. Constant temperature separation locations for various $x/L$ stations sensors as a function of angle of attack. _____	227
Figure 118.(a) Pitch-up maneuver time development of $C_f$ vs. $\phi$ for $x/L=0.118$ . _____	228
Figure 119.(a) Pitch-up maneuver time development of $C_f$ vs. $\phi$ for $x/L=0.194$ . _____	231
Figure 120.(a) Pitch-up maneuver time development of $C_f$ vs. $\phi$ for $x/L=0.220$ . _____	234
Figure 121.(a) Pitch-up maneuver time development of $C_f$ vs. $\phi$ for $x/L=0.271$ . _____	237
Figure 122.(a) Pitch-up maneuver time development of $C_f$ vs. $\phi$ for $x/L=0.347$ . _____	240
Figure 123.(a) Pitch-up maneuver time development of $C_f$ vs. $\phi$ for $x/L=0.424$ . _____	243
Figure 124.(a) Pitch-up maneuver time development of $C_f$ vs. $\phi$ for $x/L=0.500$ . _____	246
Figure 125.(a) Pitch-up maneuver time development of $C_f$ vs. $\phi$ for $x/L=0.576$ . _____	249
Figure 126.(a) Pitch-up maneuver time development of $C_f$ vs. $\phi$ for $x/L=0.653$ . _____	252
Figure 127.(a) Pitch-up maneuver time development of $C_f$ vs. $\phi$ for $x/L=0.729$ . _____	255
Figure 128.(a) Pitch-up maneuver time development of $C_f$ vs. $\phi$ for $x/L=0.831$ . _____	258
Figure 129.(a) Pitch-up maneuver time development of $C_f$ vs. $\phi$ for $x/L=0.882$ . _____	261
Figure 130. Separation position versus time for pitch-up maneuver at $x/L=0.118$ compared with quasi-steady separation positions. _____	264
Figure 131. Separation position versus time for pitch-up maneuver at $x/L=0.194$ compared with quasi-steady separation positions. _____	265
Figure 132. Separation position versus time for pitch-up maneuver at $x/L=0.220$ compared with quasi-steady separation positions. _____	266
Figure 133. Separation position versus time for pitch-up maneuver at $x/L=0.271$ compared with quasi-steady separation positions. _____	267
Figure 134. Separation position versus time for pitch-up maneuver at $x/L=0.347$ compared with quasi-steady separation positions. _____	268
Figure 135. Separation position versus time for pitch-up maneuver at $x/L=0.424$ compared with quasi-steady separation positions. _____	269
Figure 136. Separation position versus time for pitch-up maneuver at $x/L=0.500$ compared with quasi-steady separation positions. _____	270
Figure 137. Separation position versus time for pitch-up maneuver at $x/L=0.576$ compared with quasi-steady separation positions. _____	271
Figure 138. Separation position versus time for pitch-up maneuver at $x/L=0.653$ compared with quasi-steady separation positions. _____	272

Figure 139. Separation position versus time for pitch-up maneuver at $x/L=0.729$ compared with quasi-steady separation positions. _____	273
Figure 140. Separation position versus time for pitch-up maneuver at $x/L=0.831$ compared with quasi-steady separation positions. _____	274
Figure 141. Separation position versus time for pitch-up maneuver at $x/L=0.882$ compared with quasi-steady separation positions. _____	275
Figure 142. Separation position versus $\alpha$ for pitch-up maneuver at $x/L=0.118$ compared with quasi-steady separation positions. _____	276
Figure 143. Separation position versus $\alpha$ for pitch-up maneuver at $x/L=0.194$ compared with quasi-steady separation positions. _____	277
Figure 144. Separation position versus $\alpha$ for pitch-up maneuver at $x/L=0.220$ compared with quasi-steady separation positions. _____	278
Figure 145. Separation position versus $\alpha$ for pitch-up maneuver at $x/L=0.271$ compared with quasi-steady separation positions. _____	279
Figure 146. Separation position versus $\alpha$ for pitch-up maneuver at $x/L=0.347$ compared with quasi-steady separation positions. _____	280
Figure 147. Separation position versus $\alpha$ for pitch-up maneuver at $x/L=0.424$ compared with quasi-steady separation positions. _____	281
Figure 148. Separation position versus $\alpha$ for pitch-up maneuver at $x/L=0.500$ compared with quasi-steady separation positions. _____	282
Figure 149. Separation position versus $\alpha$ for pitch-up maneuver at $x/L=0.576$ compared with quasi-steady separation positions. _____	283
Figure 150. Separation position versus $\alpha$ for pitch-up maneuver at $x/L=0.653$ compared with quasi-steady separation positions. _____	284
Figure 151. Separation position versus $\alpha$ for pitch-up maneuver at $x/L=0.729$ compared with quasi-steady separation positions. _____	285
Figure 152. Separation position versus $\alpha$ for pitch-up maneuver at $x/L=0.831$ compared with quasi-steady separation positions. _____	286
Figure 153. Separation position versus $\alpha$ for pitch-up maneuver at $x/L=0.882$ compared with quasi-steady separation positions. _____	287
Figure 154. Comparison of steady and unsteady separation lines at $\alpha=12.2^\circ$ . Dashed lines are equivalent steady separation lines, solid lines are instantaneous separation lines. _____	288



Figure 155. Comparison of steady and unsteady separation lines at $\alpha=15.2^\circ$ . Dashed lines are equivalent steady separation lines, solid lines are instantaneous separation lines. _____	289
Figure 156. Comparison of steady and unsteady separation lines at $\alpha=17.6^\circ$ . Dashed lines are equivalent steady separation lines, solid lines are instantaneous separation lines. _____	290
Figure 157. Comparison of steady and unsteady separation lines at $\alpha=20.2^\circ$ . Dashed lines are equivalent steady separation lines, solid lines are instantaneous separation lines. _____	291
Figure 158. Comparison of steady and unsteady separation lines at $\alpha=22.4^\circ$ . Dashed lines are equivalent steady separation lines, solid lines are instantaneous separation lines. _____	292
Figure 159. Comparison of steady and unsteady separation lines at $\alpha=24.8^\circ$ . Dashed lines are equivalent steady separation lines, solid lines are instantaneous separation lines. _____	293
Figure 160. Comparison of steady and unsteady separation lines at $\alpha=27.5^\circ$ . Dashed lines are equivalent steady separation lines, solid lines are instantaneous separation lines. _____	294
Figure 161. Comparison of steady and unsteady separation lines at $\alpha=29.9^\circ$ . Dashed lines are equivalent steady separation lines, solid lines are instantaneous separation lines. _____	295
Figure 162. Comparison of steady and unsteady separation lines at $\alpha=29.9^\circ$ at the end of the time record. Dashed lines are equivalent steady separation lines, solid lines are instantaneous separation lines. _____	296
Figure 163.(a) Submarine maneuver time development of $C_f$ vs. $\phi$ for $x/L=0.424$ . _____	297
Figure 164.(a) Submarine maneuver time development of $C_f$ vs. $\phi$ for $x/L=0.500$ . _____	300
Figure 165.(a) Submarine maneuver time development of $C_f$ vs. $\phi$ for $x/L=0.576$ . _____	303
Figure 166.(a) Submarine maneuver time development of $C_f$ vs. $\phi$ for $x/L=0.653$ . _____	306
Figure 167.(a) Submarine maneuver time development of $C_f$ vs. $\phi$ for $x/L=0.729$ . _____	309
Figure 168.(a) Submarine maneuver time development of $C_f$ vs. $\phi$ for $x/L=0.831$ . _____	312
Figure 169.(a) Submarine maneuver time development of $C_f$ vs. $\phi$ for $x/L=0.882$ . _____	315
Figure 170. Separation position versus time for submarine maneuver at $x/L=0.500$ compared with quasi-steady separation positions. _____	318
Figure 171. Separation position versus time for submarine maneuver at $x/L=0.576$ compared with quasi-steady separation positions. _____	319
Figure 172. Separation position versus time for submarine maneuver at $x/L=0.653$ compared with quasi-steady separation positions. _____	320
Figure 173. Separation position versus time for submarine maneuver at $x/L=0.729$ compared with quasi-steady separation positions. _____	321
Figure 174. Separation position versus time for submarine maneuver at $x/L=0.831$ compared with quasi-steady separation positions. _____	322

Figure 175. Separation position versus time for submarine maneuver at $x/L=0.882$ compared with quasi-steady separation positions. _____	323
Figure 176. Comparison of pitch angle schedules for pitchup and submarine maneuvers. _____	324
Figure 177. Comparison of wall shear distribution at $x/L=0.118$ for steady data, pitchup maneuver, and submarine maneuver at $\alpha=4.8^\circ$ . _____	325
Figure 178. Comparison of wall shear distribution at $x/L=0.194$ for steady data, pitchup maneuver, and submarine maneuver at $\alpha=4.8^\circ$ . _____	326
Figure 179. Comparison of wall shear distribution at $x/L=0.220$ for steady data, pitchup maneuver, and submarine maneuver at $\alpha=4.8^\circ$ . _____	327
Figure 180. Comparison of wall shear distribution at $x/L=0.271$ for steady data, pitchup maneuver, and submarine maneuver at $\alpha=4.8^\circ$ . _____	328
Figure 181. Comparison of wall shear distribution at $x/L=0.347$ for steady data, pitchup maneuver, and submarine maneuver at $\alpha=4.8^\circ$ . _____	329
Figure 182. Comparison of wall shear distribution at $x/L=0.424$ for steady data, pitchup maneuver, and submarine maneuver at $\alpha=4.8^\circ$ . _____	330
Figure 183. Comparison of wall shear distribution at $x/L=0.500$ for steady data, pitchup maneuver, and submarine maneuver at $\alpha=4.8^\circ$ . _____	331
Figure 184. Comparison of wall shear distribution at $x/L=0.576$ for steady data, pitchup maneuver, and submarine maneuver at $\alpha=4.8^\circ$ . _____	332
Figure 185. Comparison of wall shear distribution at $x/L=0.653$ for steady data, pitchup maneuver, and submarine maneuver at $\alpha=4.8^\circ$ . _____	333
Figure 186. Comparison of wall shear distribution at $x/L=0.729$ for steady data, pitchup maneuver, and submarine maneuver at $\alpha=4.8^\circ$ . _____	334
Figure 187. Comparison of wall shear distribution at $x/L=0.831$ for steady data, pitchup maneuver, and submarine maneuver at $\alpha=4.8^\circ$ . _____	335
Figure 188. Comparison of wall shear distribution at $x/L=0.882$ for steady data, pitchup maneuver, and submarine maneuver at $\alpha=4.8^\circ$ . _____	336
Figure 189. Comparison of wall shear distribution at $x/L=0.118$ for steady data, pitchup maneuver, and submarine maneuver at $\alpha=12.2^\circ$ . _____	337
Figure 190. Comparison of wall shear distribution at $x/L=0.194$ for steady data, pitchup maneuver, and submarine maneuver at $\alpha=12.2^\circ$ . _____	338
Figure 191. Comparison of wall shear distribution at $x/L=0.220$ for steady data, pitchup maneuver, and submarine maneuver at $\alpha=12.2^\circ$ . _____	339

Figure 192. Comparison of wall shear distribution at $x/L=0.271$ for steady data, pitchup maneuver, and submarine maneuver at $\alpha=12.2^\circ$ .	340
Figure 193. Comparison of wall shear distribution at $x/L=0.347$ for steady data, pitchup maneuver, and submarine maneuver at $\alpha=12.2^\circ$ .	341
Figure 194. Comparison of wall shear distribution at $x/L=0.424$ for steady data, pitchup maneuver, and submarine maneuver at $\alpha=12.2^\circ$ .	342
Figure 195. Comparison of wall shear distribution at $x/L=0.500$ for steady data, pitchup maneuver, and submarine maneuver at $\alpha=12.2^\circ$ .	343
Figure 196. Comparison of wall shear distribution at $x/L=0.576$ for steady data, pitchup maneuver, and submarine maneuver at $\alpha=12.2^\circ$ .	344
Figure 197. Comparison of wall shear distribution at $x/L=0.653$ for steady data, pitchup maneuver, and submarine maneuver at $\alpha=12.2^\circ$ .	345
Figure 198. Comparison of wall shear distribution at $x/L=0.729$ for steady data, pitchup maneuver, and submarine maneuver at $\alpha=12.2^\circ$ .	346
Figure 199. Comparison of wall shear distribution at $x/L=0.831$ for steady data, pitchup maneuver, and submarine maneuver at $\alpha=12.2^\circ$ .	347
Figure 200. Comparison of wall shear distribution at $x/L=0.882$ for steady data, pitchup maneuver, and submarine maneuver at $\alpha=12.2^\circ$ .	348
Figure 201. Comparison of wall shear distribution at $x/L=0.118$ for steady data and pitchup maneuver at $\alpha=20.2^\circ$ .	349
Figure 202. Comparison of wall shear distribution at $x/L=0.194$ for steady data and pitchup maneuver at $\alpha=20.2^\circ$ .	350
Figure 203. Comparison of wall shear distribution at $x/L=0.220$ for steady data and pitchup maneuver at $\alpha=20.2^\circ$ .	351
Figure 204. Comparison of wall shear distribution at $x/L=0.271$ for steady data and pitchup maneuver at $\alpha=20.2^\circ$ .	352
Figure 205. Comparison of wall shear distribution at $x/L=0.347$ for steady data and pitchup maneuver at $\alpha=20.2^\circ$ .	353
Figure 206. Comparison of wall shear distribution at $x/L=0.424$ for steady data and pitchup maneuver at $\alpha=20.2^\circ$ .	354
Figure 207. Comparison of wall shear distribution at $x/L=0.500$ for steady data and pitchup maneuver at $\alpha=20.2^\circ$ .	355

Figure 208. Comparison of wall shear distribution at $x/L=0.576$ for steady data and pitchup maneuver at $\alpha=20.2^\circ$ .	356
Figure 209. Comparison of wall shear distribution at $x/L=0.653$ for steady data and pitchup maneuver at $\alpha=20.2^\circ$ .	357
Figure 210. Comparison of wall shear distribution at $x/L=0.729$ for steady data and pitchup maneuver at $\alpha=20.2^\circ$ .	358
Figure 211. Comparison of wall shear distribution at $x/L=0.831$ for steady data and pitchup maneuver at $\alpha=20.2^\circ$ .	359
Figure 212. Comparison of wall shear distribution at $x/L=0.882$ for steady data and pitchup maneuver at $\alpha=20.2^\circ$ .	360
Figure 213. Comparison of wall shear distribution at $x/L=0.118$ for steady data and pitchup maneuver at $\alpha=29.9^\circ$ .	361
Figure 214. Comparison of wall shear distribution at $x/L=0.194$ for steady data and pitchup maneuver at $\alpha=29.9^\circ$ .	362
Figure 215. Comparison of wall shear distribution at $x/L=0.220$ for steady data and pitchup maneuver at $\alpha=29.9^\circ$ .	363
Figure 216. Comparison of wall shear distribution at $x/L=0.271$ for steady data and pitchup maneuver at $\alpha=29.9^\circ$ .	364
Figure 217. Comparison of wall shear distribution at $x/L=0.347$ for steady data and pitchup maneuver at $\alpha=29.9^\circ$ .	365
Figure 218. Comparison of wall shear distribution at $x/L=0.424$ for steady data and pitchup maneuver at $\alpha=29.9^\circ$ .	366
Figure 219. Comparison of wall shear distribution at $x/L=0.500$ for steady data and pitchup maneuver at $\alpha=29.9^\circ$ .	367
Figure 220. Comparison of wall shear distribution at $x/L=0.576$ for steady data and pitchup maneuver at $\alpha=29.9^\circ$ .	368
Figure 221. Comparison of wall shear distribution at $x/L=0.653$ for steady data and pitchup maneuver at $\alpha=29.9^\circ$ .	369
Figure 222. Comparison of wall shear distribution at $x/L=0.729$ for steady data and pitchup maneuver at $\alpha=29.9^\circ$ .	370
Figure 223. Comparison of wall shear distribution at $x/L=0.831$ for steady data and pitchup maneuver at $\alpha=29.9^\circ$ .	371

Figure 224. Comparison of wall shear distribution at $x/L=0.882$ for steady data and pitchup maneuver at $\alpha=29.9^\circ$ .	372
Figure 225. Oil flow visualization for $\alpha = 10^\circ$ , $Re = 4.2$ million.	373
Figure 226. Oil flow visualization for $\alpha = 15^\circ$ , $Re = 4.2$ million.	374
Figure 227. Oil flow visualization for $\alpha = 20^\circ$ , $Re = 4.2$ million.	375
Figure 228. Oil flow visualization for $\alpha = 25^\circ$ , $Re = 4.2$ million.	376
Figure 229. Oil flow visualization for $\alpha = 30^\circ$ , $Re = 4.2$ million.	377
Figure 230. Primary and secondary separation lines for $\alpha = 10^\circ$ , $Re = 4.2$ million.	378
Figure 231. Primary and secondary separation lines for $\alpha = 15^\circ$ , $Re = 4.2$ million.	379
Figure 232. Primary and secondary separation lines for $\alpha = 20^\circ$ , $Re = 4.2$ million.	380
Figure 233. Primary and secondary separation lines for $\alpha = 25^\circ$ , $Re = 4.2$ million.	381
Figure 234. Primary and secondary separation lines for $\alpha = 30^\circ$ , $Re = 4.2$ million.	382
Figure 235. Asymmetry of secondary separation lines, $\alpha=30^\circ$ .	383
Figure 236. Laminar nose separation topology.	384
Figure 237. Turbulent nose separation topology.	385
Figure 238. Crossflow separation/low-velocity trough topology.	386
Figure 239. Steady $C_p$ vs. $\phi$ for all $x/L$ , $\alpha=2.2^\circ$ . "Real" refers to the measured data while "Ideal" refers to potential flow solution.	387
Figure 240. Steady $C_p$ vs. $\phi$ for all $x/L$ , $\alpha=4.8^\circ$ . "Real" refers to the measured data while "Ideal" refers to potential flow solution.	388
Figure 241. Steady $C_p$ vs. $\phi$ for all $x/L$ , $\alpha=7.6^\circ$ . "Real" refers to the measured data while "Ideal" refers to potential flow solution.	389
Figure 242. Steady $C_p$ vs. $\phi$ for all $x/L$ , $\alpha=9.8^\circ$ . "Real" refers to the measured data while "Ideal" refers to potential flow solution.	390
Figure 243. Steady $C_p$ vs. $\phi$ for all $x/L$ , $\alpha=12.7^\circ$ . "Real" refers to the measured data while "Ideal" refers to potential flow solution.	391
Figure 244. Steady $C_p$ vs. $\phi$ for all $x/L$ , $\alpha=14.9^\circ$ . "Real" refers to the measured data while "Ideal" refers to potential flow solution.	392
Figure 245. Steady $C_p$ vs. $\phi$ for all $x/L$ , $\alpha=17.8^\circ$ . "Real" refers to the measured data while "Ideal" refers to potential flow solution.	393
Figure 246. Steady $C_p$ vs. $\phi$ for all $x/L$ , $\alpha=19.9^\circ$ . "Real" refers to the measured data while "Ideal" refers to potential flow solution.	394

Figure 247. Steady $C_p$ vs. $\phi$ for all $x/L$ , $\alpha=22.8^\circ$ . "Real" refers to the measured data while "Ideal" refers to potential flow solution.	395
Figure 248. Steady $C_p$ vs. $\phi$ for all $x/L$ , $\alpha=24.9^\circ$ . "Real" refers to the measured data while "Ideal" refers to potential flow solution.	396
Figure 249. Steady $C_p$ vs. $\phi$ for all $x/L$ , $\alpha=27.8^\circ$ . "Real" refers to the measured data while "Ideal" refers to potential flow solution.	397
Figure 250. Steady $C_p$ vs. $\phi$ for all $x/L$ , $\alpha=30.0^\circ$ . "Real" refers to the measured data while "Ideal" refers to potential flow solution.	398
Figure 251. Steady $C_p$ vs. $\phi$ for all $x/L$ , $\alpha=32.5^\circ$ . "Real" refers to the measured data while "Ideal" refers to potential flow solution.	399
Figure 252. Steady $C_p$ vs. $\phi$ for all $x/L$ , $\alpha=35.0^\circ$ . "Real" refers to the measured data while "Ideal" refers to potential flow solution.	400
Figure 253. Steady $C_p$ vs. $\phi$ for all $\alpha$ , $x/L=0.11$ . "Real" refers to the measured data while "Ideal" refers to potential flow solution.	401
Figure 254. Steady $C_p$ vs. $\phi$ for all $\alpha$ , $x/L=0.23$ . "Real" refers to the measured data while "Ideal" refers to potential flow solution.	402
Figure 255. Steady $C_p$ vs. $\phi$ for all $\alpha$ , $x/L=0.31$ . "Real" refers to the measured data while "Ideal" refers to potential flow solution.	403
Figure 256. Steady $C_p$ vs. $\phi$ for all $\alpha$ , $x/L=0.44$ . "Real" refers to the measured data while "Ideal" refers to potential flow solution.	404
Figure 257. Steady $C_p$ vs. $\phi$ for all $\alpha$ , $x/L=0.56$ . "Real" refers to the measured data while "Ideal" refers to potential flow solution.	405
Figure 258. Steady $C_p$ vs. $\phi$ for all $\alpha$ , $x/L=0.69$ . "Real" refers to the measured data while "Ideal" refers to potential flow solution.	406
Figure 259. Steady $C_p$ vs. $\phi$ for all $\alpha$ , $x/L=0.77$ . "Real" refers to the measured data while "Ideal" refers to potential flow solution.	407
Figure 260. Steady $C_p$ vs. $\phi$ for all $\alpha$ , $x/L=0.83$ . "Real" refers to the measured data while "Ideal" refers to potential flow solution.	408
Figure 261. Steady $C_p$ vs. $\phi$ for all $\alpha$ , $x/L=0.90$ . "Real" refers to the measured data while "Ideal" refers to potential flow solution.	409
Figure 262. Steady $\partial C_p / \partial \phi$ vs. $\phi$ for all $x/L$ , $\alpha=2.2^\circ$ . "Real" refers to the measured data while "Ideal" refers to potential flow solution.	410

Figure 263. Steady $\partial C_p / \partial \phi$ vs. $\phi$ for all $x/L$ , $\alpha=4.8^\circ$ . "Real" refers to the measured data while "Ideal" refers to potential flow solution.	411
Figure 264. Steady $\partial C_p / \partial \phi$ vs. $\phi$ for all $x/L$ , $\alpha=7.6^\circ$ . "Real" refers to the measured data while "Ideal" refers to potential flow solution.	412
Figure 265. Steady $\partial C_p / \partial \phi$ vs. $\phi$ for all $x/L$ , $\alpha=9.8^\circ$ . "Real" refers to the measured data while "Ideal" refers to potential flow solution.	413
Figure 266. Steady $\partial C_p / \partial \phi$ vs. $\phi$ for all $x/L$ , $\alpha=12.7^\circ$ . "Real" refers to the measured data while "Ideal" refers to potential flow solution.	414
Figure 267. Steady $\partial C_p / \partial \phi$ vs. $\phi$ for all $x/L$ , $\alpha=14.9^\circ$ . "Real" refers to the measured data while "Ideal" refers to potential flow solution.	415
Figure 268. Steady $\partial C_p / \partial \phi$ vs. $\phi$ for all $x/L$ , $\alpha=17.8^\circ$ . "Real" refers to the measured data while "Ideal" refers to potential flow solution.	416
Figure 269. Steady $\partial C_p / \partial \phi$ vs. $\phi$ for all $x/L$ , $\alpha=19.9^\circ$ . "Real" refers to the measured data while "Ideal" refers to potential flow solution.	417
Figure 270. Steady $\partial C_p / \partial \phi$ vs. $\phi$ for all $x/L$ , $\alpha=22.8^\circ$ . "Real" refers to the measured data while "Ideal" refers to potential flow solution.	418
Figure 271. Steady $\partial C_p / \partial \phi$ vs. $\phi$ for all $x/L$ , $\alpha=24.9^\circ$ . "Real" refers to the measured data while "Ideal" refers to potential flow solution.	419
Figure 272. Steady $\partial C_p / \partial \phi$ vs. $\phi$ for all $x/L$ , $\alpha=27.8^\circ$ . "Real" refers to the measured data while "Ideal" refers to potential flow solution.	420
Figure 273. Steady $\partial C_p / \partial \phi$ vs. $\phi$ for all $x/L$ , $\alpha=30.0^\circ$ . "Real" refers to the measured data while "Ideal" refers to potential flow solution.	421
Figure 274. Steady $\partial C_p / \partial \phi$ vs. $\phi$ for all $x/L$ , $\alpha=32.5^\circ$ . "Real" refers to the measured data while "Ideal" refers to potential flow solution.	422
Figure 275. Steady $\partial C_p / \partial \phi$ vs. $\phi$ for all $x/L$ , $\alpha=35.0^\circ$ . "Real" refers to the measured data while "Ideal" refers to potential flow solution.	423
Figure 276. Steady $\partial C_p / \partial \phi$ vs. $\phi$ for all $\alpha$ , $x/L=0.11$ . "Real" refers to the measured data while "Ideal" refers to potential flow solution.	424
Figure 277. Steady $\partial C_p / \partial \phi$ vs. $\phi$ for all $\alpha$ , $x/L=0.23$ . "Real" refers to the measured data while "Ideal" refers to potential flow solution.	425
Figure 278. Steady $\partial C_p / \partial \phi$ vs. $\phi$ for all $\alpha$ , $x/L=0.31$ . "Real" refers to the measured data while "Ideal" refers to potential flow solution.	426

Figure 279. Steady $\partial C_p / \partial \phi$ vs. $\phi$ for all $\alpha$ , $x/L=0.44$ . "Real" refers to the measured data while "Ideal" refers to potential flow solution.	427
Figure 280. Steady $\partial C_p / \partial \phi$ vs. $\phi$ for all $\alpha$ , $x/L=0.56$ . "Real" refers to the measured data while "Ideal" refers to potential flow solution.	428
Figure 281. Steady $\partial C_p / \partial \phi$ vs. $\phi$ for all $\alpha$ , $x/L=0.69$ . "Real" refers to the measured data while "Ideal" refers to potential flow solution.	429
Figure 282. Steady $\partial C_p / \partial \phi$ vs. $\phi$ for all $\alpha$ , $x/L=0.77$ . "Real" refers to the measured data while "Ideal" refers to potential flow solution.	430
Figure 283. Steady $\partial C_p / \partial \phi$ vs. $\phi$ for all $\alpha$ , $x/L=0.83$ . "Real" refers to the measured data while "Ideal" refers to potential flow solution.	431
Figure 284. Steady $\partial C_p / \partial \phi$ vs. $\phi$ for all $\alpha$ , $x/L=0.90$ . "Real" refers to the measured data while "Ideal" refers to potential flow solution.	432
Figure 285. Steady $C_{p_{RMS}}$ vs. $\phi$ for all $\alpha$ , $x/L=0.11$ .	433
Figure 286. Steady $C_{p_{RMS}}$ vs. $\phi$ for all $\alpha$ , $x/L=0.23$ .	434
Figure 287. Steady $C_{p_{RMS}}$ vs. $\phi$ for all $\alpha$ , $x/L=0.31$ .	435
Figure 288. Steady $C_{p_{RMS}}$ vs. $\phi$ for all $\alpha$ , $x/L=0.44$ .	436
Figure 289. Steady $C_{p_{RMS}}$ vs. $\phi$ for all $\alpha$ , $x/L=0.56$ .	437
Figure 290. Steady $C_{p_{RMS}}$ vs. $\phi$ for all $\alpha$ , $x/L=0.69$ .	438
Figure 291. Steady $C_{p_{RMS}}$ vs. $\phi$ for all $\alpha$ , $x/L=0.77$ .	439
Figure 292. Steady $C_{p_{RMS}}$ vs. $\phi$ for all $\alpha$ , $x/L=0.83$ .	440
Figure 293. Steady $C_{p_{RMS}}$ vs. $\phi$ for all $\alpha$ , $x/L=0.90$ .	441
Figure 294. Steady sectional lift coefficients versus angle of attack for all $x/l$ .	442
Figure 295. Steady normal force coefficient and pitch moment versus angle of attack computed from surface pressure data.	443
Figure 296. Pitchup Maneuver $C_p$ vs. $\phi$ for all $x/L$ , $\alpha=9.8^\circ$ .	444
Figure 297. Pitchup Maneuver $C_p$ vs. $\phi$ for all $x/L$ , $\alpha=14.9^\circ$ .	445
Figure 298. Pitchup Maneuver $C_p$ vs. $\phi$ for all $x/L$ , $\alpha=19.9^\circ$ .	446
Figure 299. Pitchup Maneuver $C_p$ vs. $\phi$ for all $x/L$ , $\alpha=24.9^\circ$ .	447
Figure 300. Pitchup Maneuver $C_p$ vs. $\phi$ for all $x/L$ , $\alpha=30.0^\circ$ .	448
Figure 301. Pitchup Maneuver $C_p$ vs. time for all $x/L$ , $\phi=0^\circ$ .	449
Figure 302. Pitchup Maneuver $C_p$ vs. time for all $x/L$ , $\phi=50^\circ$ .	450
Figure 303. Pitchup Maneuver $C_p$ vs. time for all $x/L$ , $\phi=90^\circ$ .	451



Figure 304. Pitchup Maneuver $C_p$ vs. time for all $x/L$ , $\phi=135^\circ$ .	452
Figure 305. Pitchup Maneuver $C_p$ vs. time for all $x/L$ , $\phi=180^\circ$ .	453
Figure 306. Submarine Maneuver $C_p$ vs. $\phi$ for all $x/L$ , $\alpha=12.7^\circ$ .	454
Figure 307. Original five-component balance (Ahn, 1992).	455
Figure 308. Typical dynamic response on original five-component balance.	456
Figure 309. Dynamic calibration frame.	457
Figure 310. Typical second order transfer function.	458
Figure 311. Light-weight model.	459
Figure 312. Lightweight model construction.	460
Figure 313(a). "Fly-weight" balance strain gage layout. NF = normal force, PM = pitch moment, SF = side force, YM = yaw moment, RM = roll moment, and AF = Axial force.	461
Figure 314. Typical dynamic response of "fly-weight" balance.	463
Figure 315. Two point balance.	464
Figure 316. Steady normal force and pitch moment on prolate spheroid at $Re = 4.2$ million for various angles of attack from balance data. Compared with data from Ahn (1992).	465
Figure 317. Unsteady normal force and pitch moment for pitchup maneuver.	466
Figure 318. Repeatability for load cell 1 and 2 during pitchup maneuver. The " $2\sigma$ " level on the y-axis of each plot represents the 20:1 odds repeatability for each instant in time.	467
Figure 319. Unsteady normal force and pitch moment for submarine maneuver.	468
Figure 320. Repeatability for load cell 1 and 2 during the submarine maneuver. The " $2\sigma$ " level on the y-axis of each plot represents the 20:1 odds repeatability for each instant in time.	469
Figure 321. Typical skin friction streamline pattern obtained from directional hot-film skin friction gages (Kreplin et. al., 1985).	470
Figure 322. Circumferential distributions of crossflow velocity at fixed distances from model surface. $\alpha=20^\circ$ , $x/L=0.77$ . Crossflow velocity in body coordinates (Chesnakas, 1996).	471
Figure 323. Circumferential distributions of crossflow velocity at fixed distances from model surface. $\alpha=20^\circ$ , $x/L=0.77$ . Crossflow velocity in coordinate system perpendicular to local separation line. (Chesnakas, 1996).	472
Figure 324. Various separation line comparisons for $\alpha=10^\circ$ .	473
Figure 325. Various separation line comparisons for $\alpha=15^\circ$ .	474
Figure 326. Various primary and secondary separation line comparisons for $\alpha=20^\circ$ .	475
Figure 327. Various separation line comparisons for $\alpha=25^\circ$ .	476
Figure 328. Various separation line comparisons for $\alpha=30^\circ$ .	477



# Nomenclature

---

$a_z$	model acceleration in normal force direction
$A$	constant temperature gain; OR total trip post frontal area
$A_s$	sensor area
$A_i$	force and moment amplifier gain
$B$	constant temperature offset
$C_D$	trip post drag coefficient
$C_f$	skin friction coefficient, $\tau_w/q_\infty$
$C_l$	sectional lift coefficient, $(L/b)/2 q_\infty R$
$C_M$	pitch moment coefficient, $M/q_\infty \pi R^2 L$
$c_p$	specific heat
$C_p$	pressure coefficient, $(p-p_s)/q_\infty$
$C_{p\ RMS}$	root-mean-square of pressure coefficient
$C_Z$	normal force coefficient, $Z/q_\infty \pi R^2$
$d$	sensor diameter
$D$	trip post drag
$f(y)$	generic boundary layer profile shape
$h$	heat transfer film coefficient; OR trip post height
$H$	shape factor, $\delta^*/\theta$ ; OR some arbitrary height from the model surface
$I$	current
$I_{air}$	moment of inertia of air displaced by model
$k$	system stiffness; or thermal conductivity
$k'$	added mass coefficient for pitching direction
$k_2$	added mass coefficient for normal force direction
$K_i$	load cell calibration factor
$l$	sensor length
$L$	model length
$L_i$	load cell force
$m$	exponent for skin friction law
$M$	pitch moment

$n$	number of currents used; OR exponent relating length Reynolds number to boundary layer thickness Reynolds number
$N$	constant
$p$	model surface pressure
$p_0$	total pressure
$p_s$	free-stream static pressure, $p_0 - q_\infty$
$\dot{q}$	heat transfer
$q_\infty$	dynamic pressure, $\frac{1}{2} \rho U_\infty^2$
$r$	correlation coefficient; OR local radial distance in flow from model axis
$r_0, R$	body radius
$R_{cold}$	reference (cold) resistance at free-stream temperature
$R_{curr}$	current-sensing resistance
$Re$	Reynolds number, $U_\infty L / \nu$
$R_L$	total lead resistance
$R_{L1}, R_{L2}$	component lead resistances
$R_o$	cold resistance at the reference temperature; OR model nose radius of curvature
$R_s$	sensor resistance
$S$	model frontal area
$St$	Stanton number
$t$	time
$t'$	non-dimensional time, $t U_\infty / L$
$T$	temperature
$T_{cold}$	cold resistance reference temperature
$T_f$	foil temperature
$T_w$	wall temperature
$T_\infty, T_o$	free-stream temperature
$U$	local streamwise velocity
$U_\infty$	free-stream velocity
$v'$	fluctuating voltage
$V$	wall normal velocity
$V_1, V_2$	constant temperature measured voltages
$V_s$	sensor voltage
$V_{model}$	model volume

$w$	sensor width
$W$	crossflow velocity
$W_e$	crossflow velocity at boundary layer edge
$x$	model longitudinal position from nose; OR longitudinal surface tangent direction coordinate
$y$	wall normal coordinate
$z$	DyPPiR plunge ordinate; OR crossflow direction coordinate
$\alpha$	angle of attack; OR thermal coefficient of resistivity; OR thermal diffusivity
$\alpha''$	angular acceleration of model
$\beta$	skin friction law coefficient
$\beta_w$	wall skin-friction direction
$\delta$	uncertainty
$\gamma$	unsteady constant temperature offset calibration
$\eta$	constant current anemometer calibration factor
$\kappa$	unsteady constant temperature gain calibration
$\mu$	viscosity
$\theta$	DyPPiR pitch angle; OR momentum thickness
$\theta_1$	momentum thickness immediately upstream of trip posts
$\theta_2$	momentum thickness immediately downstream of trip posts
$\Theta$	sensor temperature difference, $T_f T_\infty$
$\sigma_q^2$	heat transfer variance
$\sigma_\theta^2$	temperature difference variance
$\rho$	air density
$\tau$	shear force
$\tau_w$	wall shear force
$\tau_w'$	wall shear fluctuations
$\omega_n$	force and moment system natural frequency
$\zeta$	force and moment system damping coefficient

## Glossary of Terms

---

- closed separation*: a separation which emanates from a saddle point, or equivalently one in which the separation line has no starting point on the body (Tobak and Peake, 1982).
- constant current anemometer*: circuitry for hot-film or hot-wire sensors that supplies the sensor(s) with a constant current as a means of heating the sensor (Blackwelder, 1981).
- constant temperature anemometer*: circuitry for hot-film or hot-wire sensors that uses feedback circuitry to supply individual sensors with an instantaneous current that heats the sensor such that its temperature stays constant regardless of the amount of heat being transferred; this results in much higher frequency response than a constant current anemometer (Blackwelder, 1981).
- crossflow separation*: the separation characteristic of bodies of revolution, named so because the separation is caused by dominant adverse crossflow pressure gradients (Simpson, 1995).
- crossflow velocity*: velocity in a direction perpendicular to the wall-normal direction and perpendicular to either the free-stream velocity or some localized velocity (Simpson, 1995).
- gradient transport of momentum and scalars*: many fluid properties, including skin friction (momentum transport) and heat transfer, are proportional to local velocity gradients (Schlichting, 1979).
- laser Doppler velocimetry (LDV)*: a measurement technique that uses the interference pattern caused by the intersection of two coherent laser beams as a means for accurately measuring the velocity of particles passing through the interference pattern; this technique provides the capability for measuring velocities in very small effective control volumes and thus in extreme detail (Chesnakas and Simpson, 1996).
- Loess smoothing*: a data smoothing technique that fits a local data set of points surrounding a target point with a least squares polynomial that is weighted to place more emphasis on the points nearest the target point and less emphasis on the outlying points; this localized fit then provides a "smoothed" value for the target point and can be used to provide estimates for the derivative at the target point as well. (Jandel, 1995)
- low velocity trough*: a term coined by Chesnakas and Simpson (1996) to describe the region of fluid locally leeward of a crossflow separation that is characterized by very low velocities.
- modal analysis*: a technique used to characterize any dynamical system (but usually a structure) as being made up of multiple second order systems (Ewins, 1984).
- open separation*: a separation which does not emanate from a saddle point, or equivalently one in which the separation line has a starting point on the body (Tobak and Peake, 1982).

*prolate spheroid*: an ellipsoidal body of revolution, where the two equal axes are smaller than the third, longitudinal axis.

*primary separation*: the most windward, and thus strongest, crossflow separation on a body of revolution.

*quasi-steady*: a time-varying phenomenon is termed quasi-steady if it exhibits no history effects; that is, if the equivalent steady phenomenon  $f$  is a function of some parameter  $x$ , then if  $x$  varies with time and  $f$  is quasi-steady  $f$  is a function of  $x(t)$  only, and not a function of  $t$  in any other way.

*secondary separation*: any separation in addition to a primary separation on a body of revolution.

*second order system*: a dynamical system that can be described by a second-order differential equation; equivalently, a dynamical system that can be described with a mass-spring-dashpot analogy (Doebelin, 1990).

*separation bubble*: in crossflow separations, a topology that can result if a laminar crossflow separation forms at a high enough Reynolds number for the separated fluid to undergo transition and reattach to the body surface (Poll, 1985).

*stability and control derivatives*: values computed for a vehicle that describe how the forces and moments depend on specific variables and various orders of rates of those variables, such as angle of attack and rate of angle of attack; such analysis results in linear governing equations for the motion of such a vehicle, but results in no direct time-dependence of the forces and moments of the vehicle except through the time dependence of the specified variables and their rates (Etkin, 1972).

*transfer function*: a frequency-domain function that characterizes the dynamics of a dynamical system and provides a mathematical function for transforming between system inputs and outputs (Doebelin, 1990).

*wall-normal velocity*: velocity in a direction perpendicular to the local body surface (Simpson, 1996).

# Chapter 1: Introduction

---

## ***1.1 Unsteady Aerodynamics***

With recent efforts to expand submarine, aircraft, and ordinance dynamic performance beyond conventional regimes, the need for studying the truly unsteady, high excursion, and high Reynolds number flows thus encountered has increased. Standard stability and control derivative techniques fail to capture the non-linearities in such flows and CFD techniques cannot accurately compute the highly complex, separated flow fields of full vehicle geometries in steady conditions, let alone unsteady ones. Such methods are deficient because they lack physical models on which to base their computations that accurately describe the complexities of a time-dependent, turbulent, separated flow field. These models can only be developed with suitable experimental flow field data from sufficiently realistic flows. A new apparatus at Virginia Tech, the Dynamic Plunge-Pitch-Roll (DyPPiR) model mount, provides for the first time the capability to model truly time-dependent, high-excursion, high Reynolds number flows in a laboratory setting (Ahn, 1989;1992).

“Dynamic” testing has been an important part of design and validation of various types of craft for decades. Typically these techniques are only “quasi-steady”, relying on very small amplitude sinusoidal oscillations that can describe small-excursion maneuvers reasonably well (McCroskey, 1977). Even in these tests however, the measurements are usually limited to forces and moments. Seldom are flow field data taken in dynamic tests.

The DyPPiR is installed in Virginia Tech’s 1.8m square Stability Wind Tunnel. The DyPPiR combines three 20.6 MPa hydraulic actuators to plunge a model through a 1.5m range vertically, pitch the model through a  $\pm 45^\circ$  range, and roll the model through a  $\pm 140^\circ$  range. Typical models are on the order of up to 2m long, and typical maneuvers last several tenths of a second. Even at Reynolds numbers of over 4 million the maneuvers are fast enough to exhibit significant unsteadiness. All degrees of freedom are digitally controlled by a personal computer, which allows the researcher to program not only sinusoidal trajectories, but more importantly, user-defined trajectories. Thus, the DyPPiR successfully fills the need of forcing a model to perform general, rapid, truly unsteady, high excursion, high Reynolds number maneuvers.

The DyPPiR has been used primarily to study submarine-like configurations. While a force and moment measurement capability has been developed for use with these configurations on the DyPPiR, the primary measurements made during DyPPiR tests are time-dependent surface pressure measurements and time-dependent, constant temperature surface hot-film measurements. The pressure measurements are useful



in determining how unsteadiness affects the forces and moments and the structure of the vortical separation that forms on the leeward side. The hot-film sensors are used to measure wall shear. Minima in the wall shear are interpreted as near separation locations. Thus, hot-film measurements provide the capability to study separation formation and migration during transient maneuvers.

To relate unsteady wind tunnel tests to real-time maneuvers, the time is non-dimensionalized by the time for flow to pass over a model,  $L/U_\infty$  (Etkin, 1972):

$$t' = \frac{tU_\infty}{L}$$

First, this non-dimensionalization asserts that time-dependent phenomena, and therefore time lags or other such effects, scale inviscidly since there is no viscosity term in the nondimensionalization. This inviscid non-dimensionalization follows from non-dimensionalizing the equations of motion typically used to study aircraft dynamics (Etkin, 1972). For the flows studied in this report, the major flow physics are caused by viscous phenomena, that being three-dimensional, turbulent separation. To counter that, the vortices that are formed in the model wake behave largely inviscidly.

Another repercussion of this scaling is that since the tunnel temperature is not controlled at all, it is impossible to control both the Reynolds number *and* the non-dimensional time for a given maneuver. Since the trip strips provide relative insensitivity to the Reynolds number, as a convention the tunnel speed was set to 45 m/s for each run. During typical conditions, that resulted in Reynolds number fluctuations of no more than +/-5%. However, this is only because all of the data presented here just happened to be taken during the warm months of March through September. The temperature swings in Southwest Virginia could easily lead to +/-10% changes in Reynolds number for a given time non-dimensionalization from January to July.

Most parameters studied are related to the angle of attack. The DyPPiR specifically sets a pitch actuator position during a maneuver. Since for all of the maneuvers studied the model is rotated about the model center, it can be stated that the DyPPiR pitch angle is equal to the instantaneous angle of attack of the model, referenced at the model center. Of course, the model motion will lead to local deviations in angle of attack as a function of rotational speed and distance from model center. In all cases studied here, however, these angle of attack deviations are less than 1.4°.

### **1.2 6:1 Prolate Spheroid**

The prolate spheroid is an interesting geometry because, although the body shape is very simple, the flowfield is very complicated. In addition, the prolate spheroid flow field carries over qualitatively to submarines, missiles, torpedoes, and to a certain extent aircraft fuselages. The prolate spheroid is a fairly

well-documented flow. Other simple bodies that have been studied that are of interest are ellipsoid-cylinders and ogive cylinders. Until the present, all data taken on prolate spheroids has been steady.

Perhaps the most detailed measurements made on the 6:1 prolate spheroid were the series of measurements made by Meier et. al. (1980a;1980b;1983;1984;1986;1987) and Kreplin et. al. (1982,1985,1986,1993). These included wall shear measurements, surface pressure measurements, and some flow field measurements, and were taken at a variety of angles of attack and Reynolds numbers. Ahn (1992) has supplemented these data with extensive oil flow visualizations. The most interesting phenomenon in the prolate spheroid flow field at incidence is the separation topology. by Meier et. al. (1980a;1980b;1983;1984;1986;1987) and Kreplin et. al. (1982,1985,1986,1993) interpreted their data to only a limited extent, and Ahn's separation studies were limited to the rear 60% of the model.

The flowfield has been studied extensively as well. This includes some hot-wire boundary layer measurements by Meier, Kreplin, and Vollmers (1983); hot wire measurements of the external flowfield by Barber and Simpson (1990;1991); Particle Displacement Velocimetry (PDV) measurements of the external flowfield by Fu et. al (1993); the Reynolds stress measurements via crosswires of Kreplin and Stäger (1993); and more recently, the Laser Doppler Velocimetry (LDV) measurements of the near-wall and external flow-fields by Chesnakas and Simpson (1994;1995). Barberis and Molton (1993) have performed LDV and three-hole pressure probe measurements on a half prolate spheroid (4:1)/cylinder configuration.

Before summarizing the results of Ahn and Meier and Kreplin, it is important to discuss separation definitions. Simpson (1995) treats three-dimensional turbulent separation in detail, while Tobak and Peak (1982) have written a fairly thorough description of three-dimensional flow separation topology. The separations that typically form on a shape such as a prolate spheroid are called "crossflow separations" due to the dominance of the circumferential pressure gradients in the separation process (see Figure 1c). These separations typically develop from the rear of the model at very low angles of attack and stretch forward at increasing angles of attack. In the simplest case, the crossflow separation is delineated by a line, called the "primary separation", that starts from some point on the model leeward side and extends all the way to the model tail (see Figure 1, part c). For weak separations or the beginning of separations, these lines form out of a significant thickening of the leeward shear layer and the formation of a "sheet" of fluid that exhibits relatively large wall-normal velocities (Simpson, 1995). This separation sheet has one edge coincident with the separation line. In two-dimensional separation, the separation location is the point where the streamwise velocity is zero, or equivalently, where it changes sign. In a three-dimensional crossflow separation, there is a real velocity component tangent to the separation line. However, it is the large wall-normal velocities that characterize a region of flow as separated (Simpson, 1995). For the purpose of analyzing data, it is convenient to make the simplifying assumption that separation is located by a local maximum in a circumferential distribution of normal velocity, and it is shown later that this corresponds to wall shear

minima (Simpson, 1995). Simpson (1995) points out that the minima does not precisely identify the location of flow separation but it does in practice give a very good approximation.

The crossflow separations typically found on bodies of revolution at high incidence and high Reynolds numbers are also characterized as “open” separations because the separation line has a free endpoint on the model surface. Defining where the separation starts is very difficult. In practice it is impossible to pin down the start of separation to within better than 10% of the model length. This is because there is typically no easily located, distinct location where the wall shear lines “first” intersect at a finite angle. Rather, the angle between adjacent wall shear vectors along a separation streamline gradually, near the start of separation, vary from  $0^\circ$  to finite values. Typically, oil flows or directional wall shear data do not have the resolution to make such a location distinctly clear.

All of the surface data presented in this report are magnitude only. No surface directional information, for wall shear vectors or pressure gradients, was measured. Therefore, it is impossible to apply any criteria that depends on directional information as in the detection of the start of separation. But using a detection of large normal velocity is even less robust in detecting separation initiation. It is possible to have a maxima in a normal velocity and yet not have separation. Separations require the normal velocity to be “large”. How “large” is large enough to identify separation is arbitrary and leads to even more fundamental questions about how one defines the start of separation. Simpson (1995) asserts that the wall-normal velocities must be large enough to cause “breakaway” or “departure” of flow from the shear layer. The fundamental effect that differentiates true separation from mere thickening of the shear layer is a substantial interaction between the fluid leaving the model via the separation and the inviscid external flow (Simpson, 1995).

A further complication is that near even “strong” separations (ones involving significant interaction with the free stream), the normal velocities are not very large in an infinitely thin sheet but instead are large over a region and smoothly, if not gradually, taper down to “unseparated” normal velocity values. In “ideal” descriptions of separation, it is usually assumed that there is a distinct separation surface or sheet that delineates the separated flow from the inviscid outer flow. There are distinct streamlines, and one could argue that there is possibly one distinct streamline, that could in theory represent an infinitesimally thin, distinct boundary of flow and could therefore be defined as “the” separation location. But the local steadiness of 3-D, turbulent, “steady” separated flows has not been established *per se*. There is nothing to suggest that in a real flow the separation location is stable and distinct. It is very possible that temporally the separation line fluctuates over a region, or even has a probabilistic spacial and time distribution. Therefore, separation is most precisely a small *region* in real flows. These regions are typically smaller than typical measurement resolutions, which are usually on the order of a degree circumferentially, and so are usually

not a huge factor in measurement interpretation. However, interpreting separation locations and topologies in general is a somewhat subjective matter in practice.

For the prolate spheroid at zero incidence, the separation is relegated to the tail and is "closed"; that is, the separation line is a fully connected axisymmetric ring around the tail. The majority of the circulation is contained in separated vortices that have their axes in a circumferential direction and are thus "spanwise" vortices. At angles of attack of even  $5^\circ$  the separation seems to exhibit "open" crossflow separation characteristics in that the separation is characterized by two distinct and symmetric separation lines that lie in the tail region (Kreplin *et. al.*, 1985). This will eventually result in weak, but stream-wise oriented, separation vortices. The mechanisms for going from the closed separation to open separation are not well understood and are very difficult to measure due to the relatively weak nature of these separations.

At increasing angles of attack, the flow topology gets more complicated. The separation sheet rolls up and eventually forms a coherent vortex somewhere downstream of the model (Figure 2). At higher angles of attack, that vortex gets stronger and forms farther upstream. At some angle of attack coherent vortices formed from the two primary separations (one on either side of the body) are actually above the model itself. As these vortices move forward on the model at even higher angles of attack, they facilitate flow reattachment. A reattachment line is then similarly defined as the location in a circumferential distribution of a local maximum, *inward* wall-normal velocity. At still higher angles of attack the flow can then generate secondary separation lines and reattachments.

At higher angles of attack, the separation lines start more noseward on the model and move towards the windward side. As the separation reaches farther forward on the nose, Reynolds number effects become important as boundary layer transition plays a role in separation formation. The flow on the nose is very important and also very difficult to interpret. Poll (1985), however, addresses these nose effects in detail for an ogive cylinder (Figure 3). For very low Reynolds numbers, the boundary layer is laminar and the flow will separate early. If the Reynolds number is low enough, this laminar separation will be stable, and the flow will remain separated. However, at high Reynolds numbers, such as in the flows studied here, the laminar separation is not very stable, undergoes transition to turbulent flow, and quickly reattaches, thus forming only a small longitudinal laminar separation bubble. The reattached flow has fully transitioned to turbulent flow, and continues around the model nose until the circumferential pressure gradient forces it to separate again.

The existence of this effect in the prolate spheroid flow field is proved in the data of Meier and Kreplin (1985) (Figure 4). This figure contains directional wall shear data taken at  $x/L=0.139$  for a 6:1 prolate spheroid at  $30^\circ$  angle of attack and a Reynolds number of 6.5 million. The top plot shows the wall shear magnitude plotted with its circumferential and longitudinal components. This is a typical wall shear distribution for the nose of such a body. The large and sudden jump in skin friction suggests transition. The

true flow picture is made more clear by the bottom plot, which shows the wall shear vector angle relative to longitudinal. Over the first half of the nose the flow curves leeward, away from longitudinal, and carries fluid more and more circumferentially around the nose. As the circumferential adverse pressure gradient becomes stronger, the pressure gradient forces the wall shear vectors back towards longitudinal. The point where the wall shear vector direction changes sign is near (but not precisely at) separation. At this location, flow is coming in from either side, and by continuity it must be relieved normal to the wall. But just as quickly as the shear directions become negative they become positive again. At this intersection with zero shear direction, the limiting streamlines are diverging, indicating a normal inrush of fluid, or a reattachment. This is evidence of the separation bubble discussed by Poll, and it can be seen in oil flow visualizations. This separation bubble is coincident with the jump in skin friction magnitude, thus indicating flow transition. The flow eventually separates again further around the leeward side.

Thus, at high angles of attack, the nose can have two separation lines. However, the second separation line is not to be confused with what is normally referred to as a “secondary” separation line. Typically secondary separation lines in such a flow pair with an earlier, turbulent, primary separation. The reattachment that eventually leads to such a conventional secondary separation is formed only because the primary separation is strong enough to form a relatively strong vortex. In the nose region, the additional separation is more analogous to a “second” primary separation or could be more precisely termed the “turbulent primary separation”. It is dependent on the formation first of the laminar separation bubble. There must also be a range of angles of attack where the pressure gradient is strong enough to cause the laminar separation bubble, but not strong enough to separate the leeward, turbulent nose flow.

This flow pattern is due to the presence of laminar flow on the nose. On a naturally tripped model at a high enough Reynolds number, the flow can not stay laminar indefinitely. In particular, all of the data presented in this report is for a tripped model, so there is definitely a finite extent for the laminar flow. When the flow on the windward side of the nose undergoes transition, what tends to happen is the separation bubble rapidly moves leeward until it joins with the turbulent primary separation. Thus, the separation line on the nose exhibits a two-pronged fork shape at high angles of attack.

### ***1.3 Overview of Present Research Program***

The present work represents the first unsteady data taken on the DyPPiR at Virginia Tech. The focus up through this report has been placed on making the DyPPiR fully operational and developing the measurement systems necessary to support DyPPiR experiments. These measurement systems include surface hot-film measurements, surface pressure measurements, and force and moment measurements.

With this present work as a basis, the DyPPiR is intended to provide a platform to study truly unsteady aerodynamics on a wide range of vehicles. The emphasis will be placed on high Reynolds number,

high speed, high excursion maneuvers that are characterized by massive flow separations. The data obtained by DyPPiR experiments will provide data sets upon which to base unsteady models of the separation process in these flows. For example, by having the capability to measure separation location as a function of time, one can potentially develop a model describing that time dependency as a function of non-dimensional maneuver pitch rate. In addition to developing new models, the DyPPiR will be used to test existing models, particularly those for stability and control parameters, and determine their applicability. As an example of this type of test, the DyPPiR can be used to determine all lateral and longitudinal stability and control derivatives for a given model. The DyPPiR can then be used to perform several general maneuvers, measuring the forces and moments during those maneuvers, and compare the measured forces and moments to those obtained from the stability derivative test. The DyPPiR represents a truly unique capability in its ability to perform these general time-dependent maneuvers.

The generality of the DyPPiR makes it capable to perform all of the standard stability and control derivative tests, with the exception of rotary balance tests. Therefore, despite the fact that the DyPPiR was designed to be more capable than standard rigs, the DyPPiR can be used to perform these standard tests.

The DyPPiR will be used in the near future for a variety of models. In addition to future prolate spheroid work, a submarine configuration and an F-18 configuration are planned models for the DyPPiR for the coming year. Automobile configurations and spacecraft configurations are also being explored as potential candidates for DyPPiR work.

## **1.4 Present Work**

This work focuses on two aspects of unsteady aerodynamics. While the obvious focus is on new unsteady data and its comparison to steady cases, a parallel and equally important focus is on unsteady wind tunnel testing measurement methodologies, transducer systems, and uncertainties. The DyPPiR provides unique capabilities to make measurements of quantities that have well established methodologies for steady tests but little similar development for unsteady cases. In all cases, the specific transducer systems employed for measuring a given quantity are examined very thoroughly along with their uncertainties. Data are presented for each of these quantities, but guidelines are also provided for the steps necessary to further reduce uncertainties.

Chapter 2 starts by introducing the DyPPiR, giving a brief description of its construction and capabilities. The maneuvers are then described and documented, with a focus on repeatability.

Chapter 3 describes the constant current hot-film data set. The constant current anemometers were used only to take steady measurements as the frequency response is too low. The theory behind the determination of separation location with hot film sensors is described, leading to the conclusion that wall shear minima is an indication of separation. A detailed discussion is included for the calibrations and

uncertainties. It is shown that the calibrations used to convert the measured voltages to skin friction values have very high uncertainties, but that these uncertainties are not representative of the uncertainties that govern the ability to determine skin friction minima and thus to characterize separation locations.

Chapter 4 discusses the constant temperature hot film data. The theory of operation discussed in Chapter 3 still applies, but the constant temperature anemometers provide the increased frequency response necessary to measure the time-varying surface skin frictions. The use of different anemometers necessitates significantly different calibration techniques. These are outlined along with the uncertainties, which are again very large for the absolute skin friction magnitudes. Again, however, the relative skin friction uncertainties are significantly smaller, thus permitting the determination of time-dependent wall shear minima.

Chapter 5 details oil flow visualization measurements that are primarily used as an independent method of determining separation locations. These are used later in the dissertation to qualify the hot-film results of Chapters 3 and 4.

Chapter 6 presents surface pressure measurements. Again, a detailed uncertainty analysis is performed which indicates the uncertainties are small enough to make accurate steady measurements, but not small enough to resolve unsteady effects with precision. An *ad hoc* calibration routine is described and used to decrease these errors. Unsteady phenomena are shown, but only at the highest angles of attack at the end of the pitchup maneuver. Even these trends are only qualitative.

Chapter 7 describes unsteady force and moment measurements. Because there has been significant work in dynamic force and moment measurements, if only on rotary balances and forced-motion mechanisms, an overview of typical force and moment techniques used in dynamic tests is included. However, the DyPPiR requirements are so unique that the previous work for the most part did not adequately guide DyPPiR balance design. Therefore, a chronological description of the different phases of DyPPiR balance development are included in detail, with particular emphasis on the dynamic effects that make DyPPiR balance design so different from standard wind tunnel balance design. Data are included for the most recent iteration which does show unsteady phenomena for the pitchup maneuver, but even more significantly shows that DyPPiR balance design has progressed greatly. These data are followed by a detailed description and analysis for the next iteration in DyPPiR balance evolution.

Finally, Chapter 8 ties all of the data together into a general discussion of the flowfield and its measurement. First, the fundamental description and measurement of 3-D flow separation is discussed. Several different techniques for locating separation locations are compared and contrasted to serve as an aid in interpreting particularly the hot-film data sets, but also as a guide for future similar measurements. This is followed by a detailed description of the flowfield as it develops during the unsteady maneuvers, with

particular emphasis on the aspects of the flowfield that differ in the unsteady flow from the equivalent quasi-steady flowfield.



# Chapter 2: Dynamic Plunge-Pitch-Roll

## Model Mount (DyPPiR)

---

### 2.1 Stability and Control Wind Tunnel

The DyPPiR is installed in the Virginia Tech 1.8mx1.8m Stability and Control Wind Tunnel (Figure 5). The Stability Tunnel is a closed return, closed test section, subsonic facility with a speed range of over 60 m/s. Turning vanes, screens, and a 9:1 contraction ratio inlet nozzle reduce the free-stream turbulence to less than 0.05% (Choi and Simpson, 1987). An air exchange tower continually entrains atmospheric air which thus stabilizes the wind tunnel temperature. The fan is powered by a 450 kW DC motor.

### 2.2 DyPPiR Hardware Overview

The Dynamic Plunge-Pitch-Roll (DyPPiR) Model Mount (Figure 6) was designed to provide the unique capability of performing general, high-excursion, large-scale, high Reynolds number, truly unsteady maneuvers (Ahn *et. al.*, 1989; Ahn, 1992). The DyPPiR has three degrees of freedom. It can plunge a model 1.5m vertically; it can pitch the model  $\pm 45^\circ$ ; and it can roll the model over a  $280^\circ$  range. The DyPPiR is designed to carry models up to 2m or more in length and up to 45 kg of mass. Three 20.6 MPa actuators give the DyPPiR the tremendous amount of power required to force 45 kg of model and over 250 kg of DyPPiR hardware at rates approaching 9 m/s in plunge and over  $90^\circ/\text{s}$  in pitch. Most importantly, however, the DyPPiR is digitally controlled by a personal computer, so it is capable of performing *general*, pre-programmed maneuvers. It is not limited to sinusoids or fixed rate ramps. The nomenclature used for the three degrees of freedom, along with body nomenclature, are shown in Figure 7.

### 2.3 Maneuvers Tested

Data are presented in this report for the two maneuvers presented below. The maneuvers are summarized in Table 1.

#### 2.3.1 The 0.33s, $30^\circ$ Ramp Pitchup

The Pitchup Maneuver, as it is referred to throughout this report, is a simple linear ramp from  $0^\circ$  to  $30^\circ$  in 0.33s. No specific acceleration or deceleration curves were programmed in. The objective is to get as

abrupt a start and a stop as possible. The DyPPiR does, in any case, have a finite acceleration and deceleration capability. Figure 8 shows actual pitch angle position feedback taken during several hundred maneuver executions. The solid line is the mean over the ensemble, and the dotted lines delineate two standard deviation boundaries. The model is pitched about the model center, so the carriage has to be plunged roughly 70 cm during the maneuver to prevent the model center from moving. Figure 9 shows the plunge position feedback data for the same maneuvers. While it is possible to keep the model center from moving vertically during a maneuver, it is inevitable that the model center will translate downstream during a maneuver. This downstream movement is deemed insignificant compared to the tunnel speed (typically 45 m/s). Figure 10 shows the motion of the model center during the pitchup maneuvers. The vertical displacement, which should be zero, is probably non-zero due to different lags between the pitch and plunge actuators. Figure 11 shows the linear and angular accelerations of the model center measured with Schaevitz LSGP-50 50g accelerometers. The uncertainties on the accelerations are  $\pm 0.05$  g's for the linear acceleration and  $\pm 100$   $^\circ/\text{s}^2$  for the angular accelerations.

### 2.3.2 The 0.25s Submarine Maneuver

The Submarine Maneuver is modeled after data taken on a real submarine during the transient, initial portion of a turning maneuver by researchers at the David Taylor Model Basin. It is impossible for the DyPPiR to match both the angle of sideslip of the model and its yawing rate, so for the DyPPiR tests, the Submarine Maneuver models the time history of the sideslip angle from the actual submarine tests (Figure 12). This is characterized by a ramp up to  $13.5^\circ$  with a slight overshoot. Also, the motion simulated on the DyPPiR is roughly half the speed in non-dimensional time units than the DTRC data set. Figure 13 shows actual pitch position feedback measurements, and Figure 14 shows actual plunge position feedback measurements. In Figure 13 it is clear that the DyPPiR control system was not properly adjusted, as the "overshoot" was actually realized as an undershoot. The strong non-linearities inherent in the DyPPiR hydraulics makes control system tuning extremely difficult. This is particularly amplified by the fact that hydraulic actuators such as the ones used on the DyPPiR are intended for either high-force/low-speed/low position-precision applications or low-force/low-speed/high-position-precision. The DyPPiR performance requirements of high-force/high-speed/high-precision make designing and tuning of the control system difficult, but the general repeatability is typically excellent. Future control system work will focus on improved fidelity. Figure 15 shows the motion of the model cg during this maneuver. Figure 16 shows the linear and angular accelerations of the model center measured with Schaevitz LSGP-50 50g accelerometers. The uncertainties on the accelerations are  $\pm 0.05$  g's for the linear acceleration and  $\pm 100$   $^\circ/\text{s}^2$  for the angular accelerations.

### **2.3.3 The 0.33s Plunge Down Maneuver**

Data were taken for a 0.33s, pure plunge maneuver. The model was held at  $0^\circ$  angle of attack, and the model was plunged vertically 30.5 cm in 0.33s in a simple ramp. Absolutely no significant separation or unsteadiness was observed because the model was essentially at zero angle of attack for the entire maneuver. Therefore, no data are reported for this maneuver.

### **2.4 Model Geometry**

All models tested were 1.372 m long 6:1 ellipsoids with circular cross section (see Figure 7). The maximum radius was 114 mm. The rearmost 38 mm was removed to allow for sting entry. Model construction is discussed in each relevant chapter.

# Chapter 3: Constant Current Hot-Film Measurements

## 3.1 Theory of Operation

The surface skin-friction was measured with the hot film sensors designed and documented by Simpson et. al.(1991). The sensors work by heating the near-wall fluid through forced convection. Due to the similarity between gradient transport of momentum and scalars (heat), the amount of heat transfer into the fluid gives a measure of the wall shear. Simpson et. al.(1991) provide an analysis for the operation of the sensor by assuming forced convection into a high Prandtl number fluid. The high Prandtl number requirement stems from the need for the thermal boundary layer developed on the sensor to be within the viscous sublayer. Simpson et. al.(1991) show that the mean film coefficient  $\bar{h}$  is proportional to the cube root of the near-wall velocity gradient, which is thus proportional to the wall shear:

$$\bar{h} = \frac{\bar{\dot{q}}}{lw(T_w - T_\infty)} = \frac{3}{2} Nk \frac{(\partial U / \partial y)_w^{1/3}}{(3\alpha l)^{1/3}}$$

$$\tau_w = \mu \frac{\partial U}{\partial y} \propto \bar{h}^3$$

In this relation,  $\bar{\dot{q}}$  is the time-mean heat transfer into the fluid,  $T_w$  is the wall (sensor) temperature,  $T_{cold}$  is the free-stream temperature,  $N$  is a constant (1.12),  $k$  is the thermal conductivity,  $l$  and  $w$  describe the sensor size,  $\alpha$  is the thermal diffusivity and  $\mu$  is the viscosity. The main purpose of the sensors is not necessarily to measure the absolute magnitude of the wall shear or the skin friction coefficient, but to more importantly measure the relative shear distributions, through measurements of the film coefficient, to allow the researcher the ability to locate shear minima and thus separation locations. However, wall shear magnitudes are possible with adequate calibration. In the same work, Simpson et. al.(1991) show that the wall shear provides higher order information about the separation location than pressure by arguing that three-dimensional separations are characterized by high wall-normal velocity ( $V$ ) components. By analyzing the continuity and momentum equations near the wall, Simpson et. al.(1991) showed that

$$V = -\frac{1}{2\mu} (\nabla \cdot \bar{\tau}_w) y^2 + \frac{1}{6\mu} (\nabla^2 p) y^3 + \dots$$

To use this equation rigorously, the entire wall shear direction and magnitude fields would need to be known in order to perform the divergence operation to compute the wall-normal velocity at all points on the

body and determine separation location. The sensors used in the present experiment are only magnitude sensitive, eliminating the possibility of using the above equation verbatim. Instead, it is found in practice that separations occur near wall shear minima. Bellhouse and Schultz (1966) show this phenomenon quite clearly in several circular cylinder flows.

Constant current anemometers were used in some steady tests to operate the hot-film sensors. A voltage-controlled current is supplied to a string of sensors that are connected in series. The voltage drop across the sensor is sampled as a measurement of the change in resistance of the sensor foil. The heat transfer is then obtained by assuming that all of the Joule heating in the sensor is transferred to the fluid (no heat transfer to the substrate):

$$\dot{q} = I^2 R_s = h A_s (T_f - T_{cold})$$

where  $I$  is the sensor current,  $R_s$  is the sensor resistance,  $T_f$  is the foil temperature, and  $T_{cold}$  is the free-stream temperature. The foil temperature is determined from the change in resistance relative to a known "cold" resistance at a known temperature:

$$(T_f - T_{cold}) = \frac{1}{\alpha} \left( \frac{R_s}{R_{cold}} - 1 \right)$$

where  $\alpha$  is the temperature coefficient of resistivity, and  $R_{cold}$  is the sensor resistance at  $T_{cold}$ .

### 3.2 The Sensors

The sensors used are shown in Figure 17. They consist primarily of a spiral 5.1 mm in diameter. This corresponds to  $d/L=0.004$  longitudinally,  $2.5^\circ$  wide at the model center, and  $3.9^\circ$  wide at the extreme sensor locations. The spiral shape results in a directional sensitivity of as much as 10% (see Figure 19). This design of hot film sensor is intended for measuring shear magnitude only, and not shear direction. To minimize the directional sensitivity, oil flow photos of this flow were studied. It was determined that up to angles of attack of  $30^\circ$  the wall shear angle ( $\beta_w$ ) varies from  $40^\circ$  below to  $10^\circ$  above longitudinal. Therefore, the sensors were mounted at  $65^\circ$  off the longitudinal line to reduce directional sensitivity effects to less than 3% (see Figure 18).

The sensors are made of Balco foil (70% nickel, 30% iron) with a nominal temperature coefficient of resistivity of  $0.0051/^\circ\text{C}$ . The foil sensor is bonded to a Kapton substrate. The total sensor thickness is 0.0635 mm. These particular sensors were manufactured by MINCO, Inc., and can be placed in any array or configuration. The sensors were glued to the fiberglass model using Micro Measurements M-BOND 200 strain gage adhesive. Before placing each sensor, a 0.635 cm diameter, 0.69 cm deep hole was drilled where the active sensor area was to be located. Then, this hole was filled with an insulating foam (thermal conductivity of  $0.029 \text{ W/m}^\circ\text{K}$ , or 1.25 times that of air) to minimize the amount of heat transfer into the model skin. 32 sensors were placed along a longitudinal line spaced every 3.49 cm (see Figure 20). The first

sensor was located at  $x/L = 0.118$ . The last sensor was placed at  $x/L = 0.907$ . The sensors are connected in series with 0.0254 mm thick copper foil that is soldered to the contact pads on the sensors. Combining the copper foil and the sensor thickness and the thickness of any solder between the copper and the sensor, the maximum disturbance introduced on the body by the sensor installation was 0.10 mm. Any such disturbances were smoothed with fillets of polyester resin. All power and data lines are attached to portions of the copper foil buried beneath the model surface. The data lines run from inside the model, out the tail, along the sting, and into the control room. The data lines are 50' long shielded ribbon cable.

### **3.3 Experimental Apparatus**

The constant current hot-film anemometers are diagrammed in Figure 21. Each anemometer board can handle up to 128 sensors. Up to 32 sensors are connected in series with one of four voltage-controlled current sources that are hooked up to a D/A line from the Analogic HSDAS-16 data acquisition board. Leads from each sensor are connected to the inputs of a differential amplifier with a gain set by interchanging resistor chips on the anemometer board. The output of the amplifiers, in groups of 16, are fed into one of eight 16-channel multiplexers. Digital lines for the data acquisition board are connected to the multiplexer in order to select the proper sensor address. Finally, the output of each multiplexer is fed to an A/D line on the data acquisition board, which is installed inside a PC computer. A CTRTM-5 counter-timer board installed in the PC is hooked up to the multiplexers and the data acquisition card to automatically sequence the multiplexers and synchronize data acquisition. The timer card is triggered by the DyPPiR computer.

The anemometers are identical to those designed and described in Simpson et. al. (1991) and used by Wetzel and Simpson (1996). The boards were modified for these tests as follows. In the standard board arrangement, a small but finite amount of current leaks into the resistors that set the gain on the amplifier circuits due to their finite impedance. The resistors can be increased while keeping the gain constant, but if the resistors are too high the small but finite input current will create stray voltages in the inputs that corrupt the amplifier output. Normally, this current leakage is analytically accounted for, but this adds additional uncertainty and complexity to both the data reduction and the board calibration. Therefore, the amplifier resistors were changed to carefully selected values that reduced the current leakage below the accepted current uncertainty while keeping stray input voltage errors below the accepted voltage uncertainty.

The current sources were modified to increase their robustness. It was found that the current sources on the anemometer boards are very linear if a quick calibration is performed, but if the anemometers are left on for long periods of time (20 seconds or more) at high currents, the output current tends to drift by as much as several milliamps. Several cooling schemes were tried, and the power transistors that make up the bulk of the current sources were replaced with higher power ones. These

changes all resulted in more predictable output currents, but the drift was still higher than the desired uncertainty. Therefore, a precision ( $\pm 0.05\%$ ) resistor was hard-wired in series with the sensor string. This current-monitoring resistor was connected to a dedicated amplifier that measured the voltage drop across the resistor as a measure of the current going through the resistor and thus the sensor string. The amplifier was very carefully calibrated, and its output was sampled by an extra A/D channel on the HSDAS-16. This provided a direct measurement of the sensor current.

It was also recognized that the flow temperature uncertainty was going to be dominant. Therefore, an Omega ON-905 thermistor probe was used to measure tunnel temperature. The manufacturer claims the accuracy to be  $\pm 0.2^\circ\text{C}$ .

### **3.4 Frequency Response**

The frequency response of the constant current system was found to be very slow. Due to the large thermal mass of the sensors, the system was found to have a time constant on the order of several seconds. Therefore, the sensors were powered to a desired current and allowed to warm-up for at least 10 seconds in the desired free-stream velocity and at the desired angle of attack before acquiring data. Therefore, the constant current system is only applicable to steady skin-friction data.

### **3.5 Data Reduction and Uncertainties**

#### **3.5.1 Fundamental Quantities**

Several fundamental quantities are measured that are used to compute the film coefficient and ultimately the wall shear. The current is set with a 12 bit DAC that has an output range of  $\pm 10\text{V}$ . The current source has a calibrated gain of  $40.8\text{ mA/V}$ . The current sources drift at high currents as they overheat, so the current source output is monitored with a very high precision resistor ( $2.5\Omega \pm 0.05\%$ ) and one of the 16-bit A/D lines. This results in an effective current source resolution of  $0.1\text{ mA}$ , or  $0.03\%$  full scale.

The sensor voltage is amplified with a differential amplifier that is set to a nominal gain of 10. Each amplifier is calibrated against precision resistors ( $2.5\Omega \pm 0.05\%$ ) and the current source monitor calibration ( $\pm 0.03\%$ ) to determine each amplifier offset and gain. The 16-bit ADC (analog/digital converter) is set with a  $0\text{--}10\text{V}$  range, resulting in  $0.15\text{ mV}$  bit noise. The electronic noise has been found to be roughly  $0.5$  to  $1.0\text{ mV}$ . Due to the extremely good linearity and repeatability of the amplifier calibrations ( $R^2$  typically  $0.99999$  for a given least-squares calibration), the sensor voltage uncertainty is assumed to be due only to electronic noise. Therefore, the sensor voltage uncertainty is  $(1.0\text{ mV})/(\text{gain of } 10)$  or  $100\text{ }\mu\text{V}$ , or  $0.01\%$  full scale.

The other fundamental quantities that are measured are the sensor coefficient of resistivity,  $\alpha$ , and the cold resistance of each sensor. The coefficient of resistivity was not determined experimentally. This uncertainty is much less critical since the same value of  $\alpha$  is used for all calculations. Thus, this uncertainty will affect all measurements equally, which may increase the absolute wall shear uncertainty but will have no effect on the relative wall shear uncertainty between any two sensors. A value of  $0.0051 \text{ }^\circ\text{K}^{-1}$  is used, which is the supplied value for BALCO foil.

The cold resistance of each sensor is first measured at some known temperature. The cold resistance is calculated from:

$$R_{cold} = R_0 [1 - \alpha(T_{cold} - T_0)]$$

The cold resistance uncertainty relation is:

$$\delta R_{cold}^2 = [1 + \alpha(T_{cold} - T_0)]^2 \delta R_0^2 + R_0^2 (T_{cold} - T_0)^2 \delta \alpha^2 + R_0^2 \alpha^2 (\delta T_{cold}^2 + \delta T_0^2)$$

The uncertainty of primary concern here is the temperature measurement uncertainty, since the resistance can be measured to within 0.2% and thermal coefficient of resistivity uncertainty is unimportant. To establish the relative uncertainty required on the temperature, it is desired to force the temperature uncertainty contribution of the cold resistance uncertainty to the same order of magnitude as the other uncertainty terms ("balance of uncertainties"). The first uncertainty term is the dominating one. Also, it is assumed that the two temperature uncertainties are identical, since they are measured with the same transducer. Then, these two uncertainty terms can be equated to determine the required temperature uncertainty:

$$\begin{aligned} [1 + \alpha(T_{cold} - T_0)]^2 \delta R_0^2 &= 2 R_0^2 \alpha^2 \delta T^2 \\ \delta T^2 &= \frac{\delta R_0^2 [1 + \alpha(T_{cold} - T_0)]^2}{R_0^2 2 \alpha^2} \\ &= \frac{1}{2} \frac{\delta R_0^2}{R_0^2} \left[ \frac{1}{\alpha^2} + 2 \frac{T_{cold} - T_0}{\alpha} + (T_{cold} - T_0)^2 \right] \end{aligned}$$

Using the estimate that the relative resistance uncertainty is 0.2% and the thermal coefficient of resistivity is  $0.0051/^\circ\text{K}$ , this uncertainty becomes:

$$\begin{aligned} \delta T^2 &= \frac{1}{2} (0.002)^2 \left[ \frac{1}{0.0051^2} + 2 \frac{T_{cold} - T_0}{0.0051} + (T_{cold} - T_0)^2 \right] \\ &= 0.076 + 8 \times 10^{-4} (T_{cold} - T_0) + 5 \times 10^{-7} (T_{cold} - T_0)^2 \\ &\approx 0.076 \\ \text{so } \delta T &\approx 0.28 \text{ }^\circ\text{C} \end{aligned}$$



In this approximation, it was assumed that the temperature difference would be less than 50°C. Therefore, the temperature measurement must be accurate to within roughly 0.1°C. The temperature is measured with an Omega ON-905-44005 Thermistor, with a claimed accuracy of 0.2°C. The thermistor was found, however, to be repeatable only to about 0.3°C.

Measuring the cold resistance can be very difficult. It was found that the sensor resistance can drift significantly just due to breezes in the room or even the body temperature of a person holding probes on a sensor. To maximize the accuracy of the cold resistance readings, blocks of foam rubber were taped over the sensors in order to damp out any local temperature fluctuations imposed by the environment. A calibrated, high precision HP 3478A Multimeter was used in four-wire resistance mode to measure the cold resistances down to 0.005 Ω, or roughly 0.2% full scale.

### 3.5.2 Sensor Temperature and Heat Transfer

Heat transfer is computed from the sensor voltage and sensor current, thus:

$$\dot{q} = V_s I$$

In relative terms, this uncertainty can be expressed as

$$\frac{\delta \dot{q}}{\dot{q}} = \sqrt{\left(\frac{\delta V_s}{V_s}\right)^2 + \left(\frac{\delta I}{I}\right)^2}$$

which indicates that the heat transfer uncertainty will be dominated by the lower resolution of the current sources, or 0.15% full scale.

The temperature difference  $\Theta$  is computed from:

$$\Theta = \frac{1}{\alpha} \left( \frac{V_s}{IR_{cold}} - 1 \right)$$

Its uncertainty is

$$\delta \Theta = \sqrt{\Theta^2 \left(\frac{\delta \alpha}{\alpha}\right)^2 + \left(\frac{\delta V_s}{\alpha I R_{cold}}\right)^2 + \left(\frac{\delta I}{\alpha I^2 R_{cold}}\right)^2 + \left(\frac{\delta R_{cold}}{\alpha I R_{cold}^2}\right)^2}$$

or in relative terms:

$$\frac{\delta\Theta}{\Theta} = \sqrt{\left(\frac{\delta\alpha}{\alpha}\right)^2 + \frac{\left[\left(\frac{\delta V_s}{V_s}\right)^2 + \left(\frac{\delta I}{I}\right)^2 + \left(\frac{\delta R_{cold}}{R_{cold}}\right)^2\right]}{\left(1 - \frac{R_{cold}}{R_s}\right)^2}}$$

$$R_s = \frac{V_s}{I}$$

where the sensor resistance has been substituted in order to help relate the relative uncertainties. This expression is disturbing, since the uncertainty is very high unless there is a large change in the sensor resistance from the cold resistance. If the sensor resistance is close to the cold resistance, the denominator in the balance of the uncertainty expression can get extremely small. Practice has shown that the resistance ratio can in fact be close to unity, resulting in potentially large foil temperature uncertainties.

### 3.5.3 Film Coefficient

The film coefficient uncertainty is significantly more difficult to analyze, since the film coefficient is computed using a least-squares linear regression on several uncertain data point pairs. Assuming that runs are made at  $n$  currents, resulting in  $n (\Theta_i, q_i)$  pairs, the film coefficient is calculated from:

$$h = \frac{1}{A_s} \frac{n \sum_{i=1}^n \dot{q}_i \Theta_i - \sum_{i=1}^n \dot{q}_i \sum_{i=1}^n \Theta_i}{n \sum_{i=1}^n \Theta_i^2 - \left(\sum_{i=1}^n \Theta_i\right)^2}$$

The uncertainty on  $h$  is rather complicated:

$$\delta h = \sqrt{\sum_{j=1}^n \left(\frac{\partial h}{\partial \Theta_j} \delta \Theta_j\right)^2 + \sum_{j=1}^n \left(\frac{\partial h}{\partial \dot{q}_j} \delta \dot{q}_j\right)^2}$$

$$\frac{\partial h}{\partial \Theta_j} = \frac{1}{A_s} \frac{n \dot{q}_j - \sum_{i=1}^n \dot{q}_i}{n \sum_{i=1}^n \Theta_i^2 - \left(\sum_{i=1}^n \Theta_i\right)^2}$$

$$- \frac{1}{A_s} \frac{n \sum_{i=1}^n \dot{q}_i \Theta_i - \sum_{i=1}^n \dot{q}_i \sum_{i=1}^n \Theta_i}{\left(n \sum_{i=1}^n \Theta_i^2 - \left(\sum_{i=1}^n \Theta_i\right)^2\right)^2} \left(2n \Theta_j - 2 \sum_{i=1}^n \Theta_i\right)$$

$$\frac{\partial h}{\partial \dot{q}_j} = \frac{1}{A_s} \frac{n\Theta_j - \sum_{i=1}^n \Theta_i}{n \sum_{i=1}^n \Theta_i^2 - \left( \sum_{i=1}^n \Theta_i \right)^2}$$

It is important to distinguish between the indices  $i$  and  $j$  in the partial derivatives, since  $i$  is used for complete summations while  $j$  points to the data pair corresponding to the  $j$ th partial derivative. To take these huge expressions and multiply them by individual uncertainties, and then square them, and then sum them, and finally square root them would be not only tedious but also uninformative. Therefore, a conservative approximation is made by replacing the individual  $\delta q_i$ 's and  $\delta \Theta_i$ 's (uncertainties) with their *maximum* respective uncertainties over all  $j$ , the expression becomes:

$$\delta h \leq \sqrt{(\delta \Theta_j)_{MAX}^2 \sum_{j=1}^n \left( \frac{\partial h}{\partial \Theta_j} \right)^2 + (\delta \dot{q}_j)_{MAX}^2 \sum_{j=1}^n \left( \frac{\partial h}{\partial \dot{q}_j} \right)^2}$$

Of course, this is hardly an overwhelming mathematical simplification, but it does make the math tractable.

Now the partial derivatives must be squared and summed. Invoking the definition of the correlation coefficient, the two partial derivative summations become:

$$\begin{aligned} \sum_{j=1}^n \left( \frac{\partial h}{\partial \Theta_j} \right)^2 &= h \frac{n}{r^2} \frac{1}{n \sum_{i=1}^n \Theta_i^2 - \left( \sum_{i=1}^n \Theta_i \right)^2} \\ \sum_{j=1}^n \left( \frac{\partial h}{\partial \dot{q}_j} \right)^2 &= h \frac{n}{r^2} \frac{1}{n \sum_{i=1}^n \dot{q}_i^2 - \left( \sum_{i=1}^n \dot{q}_i \right)^2} \\ r^2 &\equiv \frac{\left( n \sum_{i=1}^n \Theta_i \dot{q}_i - \sum_{i=1}^n \Theta_i \sum_{i=1}^n \dot{q}_i \right)^2}{\left( n \sum_{i=1}^n \Theta_i^2 - \left( \sum_{i=1}^n \Theta_i \right)^2 \right) \left( n \sum_{i=1}^n \dot{q}_i^2 - \left( \sum_{i=1}^n \dot{q}_i \right)^2 \right)} \end{aligned}$$

The denominator in each of the partial derivative expressions can be recognized as variances:

$$\begin{aligned}
\sigma_q^2 &= \frac{\sum_{i=1}^n (\dot{q}_i - \bar{\dot{q}})^2}{n-1}, \quad \bar{\dot{q}} = \frac{1}{n} \sum_{i=1}^n \dot{q}_i \\
\text{so } \sigma_q^2 &= \frac{\sum_{i=1}^n \left( \dot{q}_i - \frac{1}{n} \sum_{j=1}^n \dot{q}_j \right)^2}{n-1} = \frac{\sum_{i=1}^n \left( \dot{q}_i^2 - \frac{2}{n} \dot{q}_i \sum_{j=1}^n \dot{q}_j + \frac{1}{n^2} \left( \sum_{j=1}^n \dot{q}_j \right)^2 \right)}{n-1} \\
&= \frac{\sum_{i=1}^n \dot{q}_i^2 - \frac{1}{n} \left( \sum_{j=1}^n \dot{q}_j \right)^2}{n-1} = \frac{n \sum_{i=1}^n \dot{q}_i^2 - \left( \sum_{j=1}^n \dot{q}_j \right)^2}{n(n-1)} \\
\text{similarly } \sigma_\Theta^2 &= \frac{n \sum_{i=1}^n \Theta_i^2 - \left( \sum_{j=1}^n \Theta_j \right)^2}{n(n-1)}
\end{aligned}$$

Finally, the film coefficient uncertainty is estimated by:

$$\frac{\delta h}{h} = \frac{1}{r\sqrt{n-1}} \sqrt{\left( \frac{\delta \Theta_{MAX}}{\sigma_\Theta} \right)^2 + \left( \frac{\delta q_{MAX}}{\sigma_q} \right)^2}$$

This is a very important uncertainty relation, but it must be interpreted properly. First, as expected, the uncertainty is lowest for a perfect linear curve fit, or  $r$  close to unity. In actual experiments, this is achieved as  $r^2$  is typically on the order of 0.995 or higher. The uncertainty relation also points out the familiar trend that the uncertainty goes down with the square root of the number of points used in the regression ( $n$ ), or equivalently the number of currents used during the data acquisition.

The final thing to note is that the relative uncertainty contributions of the heat transfers and sensor temperatures is scaled not on some mean value, but rather on the variance of the data used for the regression. These variances are not the same as the variance on a given value at one current (i.e., the root-mean-square noise fluctuations on the signals, which are desired to be small); instead, these variances are a measure of the spread of currents run. The uncertainty is lowest when these variances are *highest*. This expression simply states that the slope of the  $q$ - $\Theta$  line is easier to determine accurately when a wide *range* of  $q$ 's and  $\Theta$ 's are used. This is equivalent to running as large a range of currents as possible. The highest current set is determined by the burnout current of the sensors or the maximum voltage potential of the

current source. The lowest current is zero, but at very low currents the basic quantity uncertainties become huge.

### 3.5.4 Wall Shear

The final uncertainty relation is for the calculation of the wall shear. The wall shear is given by:

$$\tau_w \propto h^3$$

so the shear uncertainty is trivially

$$\frac{\delta\tau_w}{\tau_w} = 3 \frac{\delta h}{h}$$

It is important to note that the calibration uncertainties are not included here. This analysis is for determining the relative uncertainties between measurements made by one sensor at different locations of the model in different flow conditions. This relative uncertainty determines the precision with which one can determine the location of flow separation, which is the most important piece of information sought after. The uncertainty due to the calibration is huge, on the order of 20%, and is a bias uncertainty, not a random one. This uncertainty, while much larger, is also secondary in importance due to the fact that it does not inhibit one from determining the location of separation.

### 3.5.5 Uncertainty Calculations

While these uncertainty relations are thorough, it is very difficult to analytically take the shear uncertainty and write it exclusively in terms of meaningful relations of fundamental measured quantities and their uncertainties. Instead, a computer program was written to compute the shear uncertainties as a way to assess the relative uncertainty importance of the many fundamental parameters.

The code is supplied an approximate Stanton number, along with the run speed, specific heat, and air density in order to compute an assumed film coefficient from

$$h = St\rho U_\infty c_p$$

Various fluid parameters and uncertainty constants are input.

The program was used to determine the relative effect of these parameters and to tweak the system with the goal of getting the shear uncertainty below 5% while minimizing the number of currents needed

and thus the amount of run-time required. Of course, increasing the maximum current decreases the shear uncertainty. It was determined experimentally that, with a tunnel speed of 150 ft/s, the sensors could be run at a current as high as 340 mA without risking burnout. With this upper current limit and the number of currents fixed at 5, the optimum lower current was found to be 120 mA. The uncertainty in the current source was found to play a significant role. This led to a modification of the current source circuitry to cut the current source uncertainty by a factor of 4 to its present value of 0.15%. Finally, it was determined that the cold resistance needed to be measured as accurately as possible, perhaps even as accurately as 0.2%.

The most important parameter to be determined is the number of currents necessary to be run. For the set-up used, it was determined that  $n = 5$  currents were necessary to get the shear uncertainty down to 5%.

### 3.5.6 Non-Ideal Sensor Operation Uncertainties

There are several other sources of uncertainty that result from non-ideal operation of the sensor system. The most significant is current leakage into the differential amplifiers. If the resistors that set the amplifier gain are not set high enough, a small but important amount of current can leak into the amplifiers. The current source used is a sinking current source, so the desired current is accurately set at the exit lead of the last sensor in a chain of sensors. At each input to each differential amplifier, as high as several tenths of a milliamp of current can leak into the differential amplifier. While this is much smaller than the 0.1 mA resolution of the DAC setting the current sources, the effect is summed to each previous sensor in the chain. Therefore, the first sensor will have the highest current of all of the sensors, and the difference can easily be several milliamps. More importantly, this uncertainty quickly becomes amplified, as that current error results in a heat transfer error and sensor temperature error, which results in an even larger film coefficient error and a yet larger wall shear error. This can be corrected for by simply analyzing the differential amplifier circuit and computing the current leakage, and thus the true sensor current, for each sensor. However, this results in more necessary measurements, uncertainty analyses, and computation complexity and expense, so current leakage is avoided as much as possible by using megohm-sized resistors for all differential amplifiers. However, if the resistors are too large, the natural input bias current of the op-amps passing through the resistors will result in a huge no-load voltage offset. The resistors used in these tests,  $R1 = 100 \text{ k}\Omega$  and  $R2 = 1.0 \text{ M}\Omega$ , adequately minimize current leakage effects below the resolution of the hardware while keeping post-amplified voltage offsets on the order of millivolts.

Finally, several phenomena are responsible for other sources of uncertainty that do not directly affect the measurement or computation of the wall shear, but instead change the actual wall shear value from run to run. The film coefficient is sensitive to tunnel velocity to the first order. This means that either the tunnel velocity must be maintained very accurately or must be explicitly measured for each run in order

to allow all film coefficients for a given run to be re-referenced back to some common flow velocity. This emphasizes the need to take an entire data set's worth of data in as short a time as possible. Also, the shear is definitely dependent on the position and motion of the model, so DyPPiR maneuver uncertainties are an issue. As with all DyPPiR measurements, at least 50 ensemble averages will be taken for any given sensor orientation for any given maneuver. With 19 periphery sensor orientations at 50 ensembles per orientation, that results in 950 individual DyPPiR maneuvers, which takes several hours of DyPPiR and tunnel run time. During this time, the free-stream temperature will undoubtedly change by several degrees and assuming the tunnel speed is left alone, so will the free stream velocity.

### **3.6 Separation Location**

Determining separation location by identifying wall shear minima proved to be a very difficult and potentially subjective process. The process was hindered by noise in the data and a finite ( $2^\circ$ ) data point spacing near minima. In addition, an easy, largely automated technique was necessary in order to determine separation locations for the literally hundreds of wall-shear profiles taken during the time-dependent maneuvers (see Chapter 4). A least squares curve fitting algorithm would have been most desirable, but the minima tended to be asymmetrical. For a realistic fit, this would require a model equation with too many degrees of freedom to get a usable fit. Instead, Loess smoothing was used (Jandel, 1995). Loess smoothing is a technique whereby data is locally interpolated using a bi-cubic weighted least squares technique. The user specifies the percentage of data points considered to be "local" (that is, the percentage of the total data set; the closest data points to the point of interest which are also "local" are used), and the order of the least squares regression. The higher the percentage of data points considered to be "local", the higher the smoothing. For all data sets, the "locality" was specified to be 12% of the data points and a parabolic least squares fitting routine was used. A program was written with a graphical interface that would plot a specified wall shear distribution on the computer screen. The user outlines a range delineating a minima, and the computer interpolates data on a very fine grid over that range using Loess smoothing. It then searches for the minima of that smoothed data. It was found that this technique faithfully reproduced the shapes of the minima and did a very reasonable job at locating the true minima with minimal user input. However, it is still sensitive to spurious data points, thus often resulting in "jumps" of separation location in adjacent time steps of as much as  $2^\circ$ . This is assumed to not be real. Therefore, the unsteady time variations of separation location discussed below were smoothed further to eliminate such jumps. It is assumed that the uncertainty in wall-shear minima location is  $\pm 2^\circ$  in all cases.

### 3.7 Calibration

Originally there was no intention to calibrate the sensors to actual skin friction values. However, it was believed after taking the data that calibration was possible. The constant current data requires only a proportionality factor between film coefficient and wall shear:

$$\tau_w = \eta h^3$$

To come up with a rough estimate of this proportionality constant, boundary layer solutions were computed on the windward line of symmetry of the prolate spheroid at several angles of attack (Figure 22). For details of this computation technique, refer to Appendix A. The computed skin friction values are for a Reynolds number of 4.2 million. The results are compared with the data of Meier and Kreplin (1985), which were taken at a Reynolds number of 6.4 million. It is first noted that the calculations agree well within the magnitude uncertainties of the Meier and Kreplin data set. It is also important to quantify the effect of the Reynolds number discrepancy on the skin friction values. A simplified form of a skin friction law, identical to that used in the code presented in Appendix A, is useful towards this end:

$$C_f = \beta Re_\delta^m$$

where  $C_f$  is the skin friction,  $\beta$  is some multiplicative factor,  $Re_\delta$  is the Reynolds number based on boundary layer thickness, and  $m$  is some exponent, dependent on whether the flow is laminar (-1.0) or turbulent (-0.25) (Schetz, 1993). The boundary-layer-thickness Reynolds number is similarly related to the  $x$  or length based Reynolds number, and thus the skin friction coefficient, via:

$$\begin{aligned} Re_\delta &\propto Re_x^n \\ C_f &\propto Re_x^{mn} \end{aligned}$$

where  $n$  is also an exponent dependent on whether the flow is laminar (0.5) or turbulent (0.8) (Schetz, 1993). So given identical geometries with identical fixed transition, the skin friction scales according to the power  $mn$ :

$$\frac{C_{f1}}{C_{f2}} = \left( \frac{Re_{x1}}{Re_{x2}} \right)^{mn}$$

This exponent  $mn$  is -0.5 for laminar flow and -0.2 for turbulent flow, so a higher Reynolds number should in all cases result in a lower skin friction value, given the restrictions listed above. In comparing data between a Reynolds number of 6.4 million (Meier and Kreplin) and 4.2 million (the present data), the laminar skin friction values should be roughly 20% lower for the 6.4 million Reynolds number case compared to the present data, while the turbulent skin friction values should be roughly 10% lower in the present data compared to the 6.4 million data. In Figure 22, the Meier and Kreplin (1985) data is



consistently lower in the turbulent region ( $x/L > 0.20$ ), but is not so consistent in the laminar region. However, these trends are easily smaller than the uncertainties of either the data or the calibrations.

These calculated data were used along with constant current data extrapolated to the windward side of the model to come up with proportionality factors. This was done for all 7 angles of attack ( $0^\circ$  to  $30^\circ$  every  $5^\circ$ ), and the seven resultant factors were averaged to obtain the factors used. Table 2 shows these factors and their standard deviations.

It is important to note that this calibration by its very nature places a very high (at least 20%) uncertainty on the skin friction magnitudes. It can only be expected that a simple boundary layer code will provide "ballpark" skin friction values with at least a 10% or 20% uncertainty compared to the real flow. Calibrating against such uncertain numbers can provide a calibration no more certain. Therefore, the uncertainty on the final *skin friction* values presented is estimated to be  $\pm 20\%$ . It is important to distinguish this uncertainty, which only characterizes the magnitude calibration, from the *relative* uncertainty between two measurements made by the same sensor, which stands at 5% as obtained section 3.5.5. Every skin friction plot within this report compares skin friction against circumferential location. Because the model was rolled to statically locate individual sensors at specific roll angles, all such circumferential distributions represent data taken by a single individual sensor. Therefore, for all of these plots, while the magnitude may be off by  $\pm 20\%$ , all points in a given curve are affected *identically*, so the trends, and most importantly, the minima location, are governed by the 5% relative uncertainty obtained earlier.

In general, calibration of hot-film sensors used for skin friction measurements is so difficult to do with certainty that many researchers do not bother attempting it. The papers by Bellhouse and Schultz (1966), Solomon and Walker (1995), Mangalam et. al. (1990), Feyzi et. al. (1989); Agarwal et. al. (1992); and van Dam et. al. (1995) are examples of papers where the relative skin friction measurements were far more meaningful than the actual skin friction magnitudes. In each of these cases, the hot-film sensor data were presented un-calibrated. Even in the present experiment, the actual skin friction magnitude is far less important than the location of separation. The forces directly caused by wall shear (those obtained by integrating the wall shear force over the model surface) are orders of magnitude smaller than the pressure forces due to separation.

An exception to presenting uncalibrated hot-film data is the work performed by Kreplin et. al. (1982;1985). In these works, a boundary layer code was used to calculate skin friction values that were used to calibrate the hot-film sensors much like done here. In their case, a  $\pm 20\%$  uncertainty is the result, even though the relative uncertainty of measurements performed by individual sensors is probably much lower. McCroskey and Durbin (1972) scaled hot-film measurements against a calculation, but the calculation was fine-tuned with a floating-gage skin-friction balance. Rubesin et. al. (1975) calibrated directly against a

floating-gage skin-friction balance. Feyzi et. al. (1989), while presenting all of their data uncalibrated, did present calibrations obtained by comparison against a Preston Tube and a dual-laser-beam interferometer. In all of these cases, the hot-film sensors were removable, allowing them to be placed in a calibration flow, usually in a two-dimensional-flow wind tunnel. The calibrations of Kreplin et. al. were performed with the sensors installed on the prolate spheroid model.

### **3.8 Steady Results**

The constant current system was used to measure the wall shear on the prolate spheroid at roll angles nominally from  $0^\circ$  to  $180^\circ$  with a spacing of  $5^\circ$  on the windward side and  $2^\circ$  on the leeward side. Data were taken at angles of attack from  $0^\circ$  to  $30^\circ$  every  $5^\circ$ . All positioning was done by the roll actuator of the DyPPiR.

Figure 23 through Figure 26 show comparisons between the present data sets (including constant temperature data presented in the next chapter) and selected data from Meier and Kreplin (1985) and Chesnakas and Simpson (1996). Meier and Kreplin performed similar hot-film tests on a larger scale 6:1 prolate spheroid with directionally sensitive hot-film sensors. The data shown are for a similarly tripped flow condition, but the body Reynolds number was 6.4 million, which is substantially higher. Chesnakas and Simpson have performed near-wall LDV measurements on an identical prolate spheroid to the one being used in the present tests, with identical trip and free-stream conditions. Agreement is moderate between the different data sets. In general, the present data seems to be biased high, but any differences are well within the uncertainties for each of the data sets (Meier and Kreplin  $\pm 20\%$ ; Chesnakas and Simpson:  $\pm 10\%$ ). In comparing the present data against the data of Meier and Kreplin it is important to recall, as shown in section 3.7, that the discrepancy in Reynolds number between the present data set and the Meier and Kreplin data set should result in the Meier and Kreplin skin friction values being roughly 10% lower in the turbulent region ( $x/L > 0.20$ ), which can possibly explain a lot of the discrepancy. The Chesnakas and Simpson data was taken at the same Reynolds number as the present data set (4.2 million), and therefore should not have the magnitude bias.

More important than the agreement of the magnitudes between these data sets is the agreement between the locations of the minima and maxima, which in general is very good. The exception is Figure 24, which is a comparison between this data set and the data of Chesnakas and Simpson at  $20^\circ$  angle of attack and at  $x/L = 0.60$ . The positional discrepancy is roughly  $5^\circ$ . It is important to note that the discrepancies shown in these plots are an indication of the difficult nature of calibrating heat transfer measurements to skin friction. The discrepancies only indicate poor calibrations. The trends still show excellent qualitative agreement as a result of the lower (5%) relative uncertainty between different measurements made by the same sensor.

Figure 27 through Figure 31 show the present constant current skin friction coefficients superimposed on top of secondary streamlines measured by Chesnakas and Simpson (1996). It is important to note that the skin friction values are not in scale, but the streamline plots are in scale. In fact, the secondary streamline plots represent data taken up to approximately 3 cm away from the wall and thus represents the near-wall flow field in these separated zones. The radial grid lines represent locations where the LDV data were actually taken, therefore separation uncertainties in this data set are limited by the  $5^\circ$  spacing of the profile locations. Each profile contains 17 points spaced logarithmically down to 0.007 cm from the wall, corresponding to  $y^+$  values on the order of 7. In all cases, it is seen that the wall shear minima qualitatively corresponds to the separation location. In fact, the wall shear minima seems to consistently lag the wall shear minima by around  $5^\circ$ , although considering the positional uncertainties in both data sets, the true size of this lag is difficult to measure. Exactly where the separation is located in the streamline plots is subject to a certain amount of subjectivity. In any case, the flow minima seems to consistently lag the visible flow separation streamline, and this fact is consistent with the findings of Chesnakas and Simpson (1996). It is important to be careful about one's definition of "lag" in this case, however. If one considers the main secondary flow direction to be in a circumferential fashion from windward to leeward, then by the virtue that the wall shear minima tend to be further leeward in all cases tends to fit with a conventional lag definition. However, when one examines the *secondary* separations, as in Figure 30 and Figure 31, it is seen that the secondary separation occurs more windward than the corresponding wall shear minima. However, the main source of fluid feeding this separation is flow backwards - from leeward to windward - and so in this case, from the point of reference of the secondary flow feeding the secondary separation, the wall shear minima *lags* the secondary separation.

The full constant current data set is plotted in Figure 32 through Figure 69. Figure 32 through Figure 37 show the data plotted for all sensors at individual angles of attack. At  $5^\circ$  (Figure 32), the data variations are small and any separation is difficult to discern. It is easy to see the jump in the skin friction values at sensor #5 ( $x/L=0.220$ ), the first sensor downstream of the trip posts. This jump is of course due to the transition to turbulent flow caused by the trip strips. However, at  $5^\circ$  there does seem to be a small separation on the nose. The laminar flow on the nose experiences an adequate adverse pressure gradient to separate from the prolate spheroid. However, there doesn't seem to be any significant separation downstream of the trips. Therefore, it is expected that at  $5^\circ$  to flow is possibly reattaching downstream of the trips. There is evidence only of the weakest of separations near the rearward sensors.

By  $10^\circ$  (Figure 33), minima are clearly present in the last 3 or 4 sensors indicating possible separation on the tail. This separation seems to extend all the way to the nose, but the minima in the middle half of the model are weak at best. A rise in the wall shear for the first four sensors around  $160^\circ$  is again due to laminar separation on the nose upstream of the trip. By  $15^\circ$  the tail separation is more clear, forming

around  $x/L=0.500$ , and a secondary separation forms at sensor 24 ( $x/L=0.704$ ). The separation on the nose is increasing in strength. By  $20^\circ$  (Figure 35) the nose seems to have a second minima. Also at  $20^\circ$ , the secondary separation is well formed and covers nearly the entire rear half of the model. It is also curious to note that the secondary separation seems fixed at a constant circumferential location. The primary separation, on the other hand, of course moves windward as it moves rearward. These trends continue increasing in magnitude and clarity at  $25^\circ$  and  $30^\circ$  (Figure 36 and Figure 37).

Figure 38 through Figure 69 show the same constant current data. However, each of these 32 plots shows data for only one sensor, with data plotted at each angle of attack. By examining sensor #1 (Figure 38,  $x/L=0.118$ ), it seems on this expanded scale that separation forms even at  $5^\circ$  angle of attack. At higher angles of attack the separation moves toward the windward side. By  $30^\circ$  a second separation is clearly formed. Examining sensor #4 (Figure 41,  $x/L=0.194$ ), which is the last sensor before the trip strips, the second separation seems to have formed by  $20^\circ$  angle of attack already. Even more interesting is the fact that the primary separation seems to have moved rather abruptly between  $15^\circ$  and  $20^\circ$  angle of attack, which may be a result of the formation of the second separation.

Figure 70 through Figure 74 shows separation line topologies for each angle of attack obtained by locating the wall shear minima for each sensor. The separation lines at  $5^\circ$  are difficult to determine with a high precision due to the very gentle nature of the wall shear minima, so this case is not included. These figures show more clearly that the separation starts on the tail, moves forward at higher angles of attack, and eventually splits into two separations in the nose region by  $20^\circ$  angle of attack.

Figure 75 shows the primary separation lines for individual sensors as functions of angle of attack. Data is only plotted for the same sensors for which constant temperature data was taken (see Chapter 4). At increasing angles of attack, the separation line of course moves windward. Near the tail, the separation locations seem to level out at some minimum separation location at high angles of attack.

## Chapter 4: Constant Temperature Hot-Film Measurements

---

### **4.1 Theory of Operation**

The general description of the operation of the hot film sensors provided in the previous chapter applies, of course, regardless of the type of anemometer circuitry used. It was shown that the time response of the constant current anemometers was too slow (on the order of seconds) to take time-dependent data. Therefore, constant temperature anemometers were used to take the unsteady data and to retake the steady data. Constant temperature anemometers basically consist of a sensor in a bridge, with the bridge voltage fed back to an open-gain amplifier which controls the amount of current going into the bridge. The feedback circuit tries within its limits to keep the sensor resistance constant, and thus the sensor temperature constant. The primary physical phenomenon that prevents the constant current anemometers from having a higher frequency response is the time constant associated with heating up and cooling down the sensor, which in this case is a sensor with a relatively high thermal mass and therefore a relatively long time constant. The constant temperature anemometer electronics, by keeping the sensor temperature constant, prevent the thermal mass from playing a role in the frequency response of the system, thus significantly increasing the system time response (Blackwelder, 1981).

### **4.2 Experimental Apparatus**

For these constant temperature tests, a fresh set of 32 hot film sensors were installed on the model and rewired individually (not in series, as in the constant current tests). The signals were carried from the sensors to the anemometers first by 8 m of shielded, round-to-flat 28 AWG ribbon cable. This relatively thin cable was selected as the best way to get a huge bundle of wires into the model through only a 5 mm gap between the model and the sting. However, the 28 AWG wire was forced to carry up to 300 mA or more, which is a large current for such wire. Therefore, the lead resistance was definitely a significant factor. The ribbon cable was then spliced into 2 m of 32, individual BNC cables. These BNC cables were fed into a data acquisition interface box (Figure 76). This box can handle 16 sensors at one time. Inside the box, the sensor current is fed through a 1 W, nominally 2.2  $\Omega$ , calibrated resistor to give a measure of the sensor current. Also in the box, voltages are tapped off and fed to two HSDAS-16 boards. The combined 32 signals provide essentially a measurement of the sensor voltage and current for each of 16 sensors. The

original intent was to take data on 16 sensors at a time, and to do each test twice. This limitation was imposed both by the number of anemometers available and the number of data acquisition channels available.

The anemometer circuits used were non-linearized Miller-type anemometers (Miller, 1976) as modified by Simpson et. al. (1979). Twelve anemometers were available, so four more were constructed for these tests. The anemometers proved to be very difficult to operate for these tests. First, hot-film sensors in general, and these sensors in particular, require much more current than hot wires for a given operating temperature. While the currents being drawn were within the capacity of the power transistor on board, it still seemed to tax the system as a whole. The data acquisition boards were operated in a single ended mode, not a differential mode, due to the lack of available channels. Originally the anemometers were in three groups in individual housings. The huge amount of current being drawn by groups of these anemometers operating together meant huge voltage drops across the anemometer power cords, and thus the anemometer grounds were different. To solve this problem, all 16 anemometers were hooked to the same power supply. Even then, it was found that very short and extremely thick power cables were needed, and even then the grounds were different by at least a few millivolts. Also, the local grounds were about 1 volt higher than the computer ground, so the HSDAS-16 boards were operated in pseudo-differential mode, whereby a wire was run from the local ground to a pin on the HSDAS-16 boards, which then referenced all measurements to that local ground. It is expected, though, that this setup reduced the effective precision of the 16-bit ADC's by at least a couple of bits.

The anemometers were modified for these tests to maximize the available current by increasing the bridge ratio to 60. Increasing the bridge ratio increases the amount of current available to the sensor leg of the bridge, but this also decreases frequency response. In addition, many of the anemometers were not operational and needed to be repaired, which in most cases required replacing the op-amps. When a first batch of op-amps was ordered, that these "replacement" op-amps made the anemometer circuits become unstable. This was the beginning of a lot of electronic stability problems. A second manufacturer's op amps were tried, and these resulted in stable operation. Then it was found that the anemometers worked fine when hooked up to a sensor on a short cable, but when hooked up to the sensors on the model with 9 m of cable, the circuits were unstable. This, it was found, was due to the natural inductance in the long cables. To solve this problem, both of the feedback capacitors, which essentially filter high frequency disturbances in the op amp to prevent unstable oscillations, were increased by a factor of 10 (Jung, 1986). This seemed to solve the problem. However, during the wind tunnel entry, it was found that with all 16 of the anemometers running, the anemometers would become unstable after running for about 10 minutes. Cooling didn't help, so eventually the solution was to run only 12 anemometers at one time. Therefore, this data set includes

measurements made on only 12 sensors which are listed in Table 3. The sensors were run at a nominal, but imprecisely set, overheat ratio of 1.07.

### 4.3 Frequency Response

Frequency response was measured following Wood (1975). Figure 77 shows the frequency response of one of the anemometers using this technique. The response of the anemometer is considered "flat" up along the increasing slope to the peak in this plot, which occurs at around 200 Hz. This is rather low frequency response for constant temperature anemometry. This low response is due to the fact that these sensors have a very high thermal mass compared to a standard hot-wire probe. Doebelin(1990) shows that the time lag of either a constant temperature or constant current anemometer is proportional to the mass of the heated element. A typical hot wire that is 0.0008 mm in diameter and 1 mm long contains only  $5 \times 10^{-7} \text{ mm}^3$  of material. The sensors used in these tests contain a volume of almost  $0.1 \text{ mm}^3$ . This shows that the current sensors contain far more element mass than standard hot wires and thus should be expected to have a much lower frequency response. While this frequency response is too low to measure turbulence quantities, it is adequately high to capture the time variations of the mean wall shear during maneuvers that are several tenths of a second long.

### 4.4 Spatial Averaging

A separate but equally important measure of the response of the hot-film sensor is its ability or inability to resolve turbulence scales in the flow field. To this end, it is necessary to estimate the range of turbulence scales present in the measured flow field. The smallest scales present are the Kolmogorov scales, and these tend to be on the order of 12 viscous units in size (Simpson, 1976):

$$z^+ \equiv \frac{zu_\tau}{\nu} = 12$$

$$u_\tau = \sqrt{\frac{\tau_w}{\rho}} = U_\infty \sqrt{\frac{C_f}{2}}$$

Recall that in this report the skin friction coefficient  $C_f$  is normalized in terms of the free-stream velocity and not some edge velocity. It is known from the measurements that the skin friction coefficient thus defined ranges up to roughly 0.015, which provides a conservative estimate for the largest  $u_\tau$ . Using this as a conservative estimate, the smallest scales can be no smaller than 0.05 mm, or 1% the size of the sensor. Even the cross-wise spacing of the longitudinal vortices in the near-wall region of the boundary layer, which is on the order of  $z^+ = 100$  (Robinson, 1992), are only 10% of the sensor size. The largest scales are typically the order of the boundary layer thickness (Tennekes and Lumley, 1972), which for this flow is typically no more than 3 cm (Chesnakas and Simpson, 1996). This represents a size barely six times larger than the

sensor size. Therefore, the only structures the sensors are capable of resolving spatially are the absolute largest, lowest-energy structures. This essentially leads to the conclusion that the sensors are not capable of resolving any turbulence quantities and are only capable of measuring the time-mean-varying skin frictions (Corcos, 1963). This was seen in practice as the signal fluctuations were at least three orders of magnitude smaller than the mean voltages.

#### 4.5 Data Reduction and Uncertainties: Steady Data

As in the constant current analysis, there are two levels of uncertainty analysis that must be examined. The first, and most important, is the relative uncertainty between measurements made by one sensor at different circumferential locations on the model in different flow conditions. This is the uncertainty that determines how accurately one can measure the flow separation location. The second and less important uncertainty is the bias uncertainty of the calibration, which is quite high, but does not impact the ability to locate separation.

##### 4.5.1 Wall Shear

The same equations used in the constant temperature model apply, but in a different form. First, since this analysis is only for the uncertainty of the pre-calibrated data, the following model is assumed:

$$\tau_w \sim \left( \frac{\dot{q}}{\Theta} \right)^3$$

where again  $\dot{q}$  is the sensor heat transfer and  $\Theta$  is the sensor temperature difference  $T_f - T_\infty$ . The heat transfer is again due to Joule heating, but the difference is that the sensor resistance is held constant, thus:

$$\begin{aligned} \tau_w &\sim \left( \frac{V_s^2 / R_s}{\Theta} \right)^3 \\ &\sim \left( \frac{V_s^2}{\Theta} \right)^3 \end{aligned}$$

Therefore the wall shear uncertainty is dependent on the sensor voltage uncertainty and foil temperature uncertainty as:

$$\frac{\delta \tau_w}{\tau_w} = \sqrt{\left( \frac{\delta V_s}{V_s} \right)^2 + \left( \frac{\delta \Theta}{\Theta} \right)^2}$$



### 4.5.2 Sensor Voltage

The sensor voltage is computed from  $V_1$  and  $V_2$  and the lead resistances as indicated in Figure 76:

$$I_s = \frac{V_1 - V_2}{R_{curr}}$$

$$V_s = V_2 - (V_1 - V_2) \frac{R_{L1} + R_{L2}}{R_{curr}}$$

$$= V_2 - (V_1 - V_2) \frac{R_L}{R_{curr}}$$

where the individual lead resistances have been summed into one lead resistance,  $R_L$ . Assuming both of the voltage measurements have the same uncertainty and both of the resistance measurements have the same uncertainty, the sensor voltage uncertainty is then

$$\delta V_s = \sqrt{\left[ \left( 1 + \frac{R_L}{R_{curr}} \right)^2 + \left( \frac{R_L}{R_{curr}} \right)^2 \right] \delta V^2 + \left( 1 + \frac{R_L}{R_{curr}} \right)^2 \left( \frac{V_1 - V_2}{R_{curr}} \right)^2 \delta R^2}$$

Assuming a typical lead resistance of 4  $\Omega$ , a current-monitoring resistance of 2.2  $\Omega$ , a typical run current of 300 mA, a voltage uncertainty of 1 mV and a resistance uncertainty of 0.005  $\Omega$ , the sensor voltage uncertainty is about 5 mV.

### 4.5.3 Sensor Temperature and Resistance

The temperature difference  $\Theta$  mainly depends on the sensor resistance:

$$\Theta = T_f - T_\infty = \frac{1}{\alpha} \left( \frac{R_s}{R_\infty} - 1 \right)$$

It is again assumed that the coefficient of resistivity  $\alpha$  uncertainty is non-important due to the fact that it is very constant for all measurements. The sensor resistance is computed from:

$$R_s = \frac{V_s}{I_s} = \frac{V_2}{V_1 - V_2} R_{curr} - R_L$$

and its uncertainty is given by:

$$\delta R_s = \sqrt{\left( \frac{R_{curr}}{V_1 - V_2} \right)^2 \left( 1 + \frac{2V_s^2}{(V_1 - V_2)^2} \right) \delta V^2 + \left( 1 + \frac{V_s^2}{(V_1 - V_2)^2} \right) \delta R^2}$$

Using the same values as above, the sensor resistance uncertainty is about 0.025  $\Omega$ . The uncertainty for the temperature difference is:

$$\delta\Theta = \frac{1}{\alpha} \sqrt{\left(\frac{\delta R_s}{R_\infty}\right)^2 + \left(\frac{R_s}{R_\infty}\right)^2 \left(\frac{\delta R_\infty}{R_\infty}\right)^2}$$

Again using values from above, along with an overheat ratio of 1.07, the temperature difference uncertainty calculated this way is about 2.3°C. This is quite large, especially considering the temperature difference for these tests is on the order of 20°C. The temperature difference in fact becomes the dominant uncertainty, pushing the relative wall shear uncertainty above 10%, which is unacceptable.

This was seen clearly in the data when first reduced. It becomes particularly evident when the sensor outputs follow the temperature changes better than the wall shear changes. If the ambient temperature did not fluctuate, this would not be an issue because the temperature difference would be a constant. However, the flow temperature varied by as much as 10°C. The cause of the uncertainty was the sensor resistance uncertainty of over 1%. It is important to note, however, that the sensor resistance should not change at all due to the constant temperature anemometers. So several different techniques were tried to deduce either the sensor resistance or equivalently the sensor temperature for each sensor, and leave it as a constant. Then the temperature difference uncertainty would merely be the uncertainty of the flow temperature measurement, or 0.3°C. This would result in a relative wall shear uncertainty of less than 2%.

The data set used to perform this level of calibration was the unsteady pitchup data set. The anemometers were set up at the very beginning of the wind tunnel entry and were not changed from the time the steady data were taken until all of the unsteady data were obtained. Therefore, it was assumed that the sensor temperature was constant during all of the tests. When taking the unsteady pitchup data, there was always 0.33s worth of data taken at the beginning of the maneuver during which the model sat motionless at 0° angle of attack. This same 0° data was taken at 66 different roll angles, 10 ensembles each, 85 time-series data points during which the model was at 0° angle attack. It took about 6 hours from about 8:00 AM to 2:00 PM to take that data set during which time the temperature changed by over 10°C. Assuming the wall shear was constant during each of those runs, then so should the following be constant:

$$\frac{V_s^2}{\Theta} = \frac{V_s^2}{T_f - T_\infty} = \text{constant}$$

This data set had over 50,000 data points per sensor described by the above relation, so its statistics were excellent. Therefore, the sensor voltage was calculated for all of these data runs, and the square of the sensor voltage was plotted against the ambient temperature as measured by the thermistor. These plots proved to be linear as expected. The point where the curve intersects the temperature axis then corresponds to the sensor temperature. Those sensor temperatures and the correlation coefficients for the line fit to the  $V_s^2 \cdot T_\infty$  data are given in Table 3.

Therefore, the constant temperature data were reduced assuming a constant sensor temperature as given in the table. This reduces the temperature difference uncertainty by almost an order of magnitude and puts the wall shear relative uncertainty at 5%.

#### 4.5.4 Nonlinear Averaging Uncertainties

The raw voltages measured were averaged at each location before applying the nonlinear model equations outlined above for the data reduction. This can introduce an error, since the mean wall shear does not correspond identically to the mean voltages measured due to the nonlinear relationship between the two quantities. It can be shown that this error is small. Rather than examining the full set of model equations for this particular setup, it can be recognized that the above equations are really a modified form of the King's Law used in most constant temperature anemometry. Such a King's law might take the following form (Bellhouse and Schultz, 1966):

$$V^2 = A\tau_w^{\frac{1}{3}} + B$$

where  $V$  is the instantaneous measured voltage,  $\tau_w$  is the instantaneous wall shear, and  $A$  and  $B$  are calibration constants. Replacing the voltage and wall shear with mean quantities and fluctuating quantities results in:

$$V = \bar{V} + v'$$

$$\tau_w = \bar{\tau}_w + \tau'_w$$

$$(\bar{V} + v')^2 = A(\bar{\tau}_w + \tau'_w)^{\frac{1}{3}} + B$$

This equation can be linearized to provide the following approximation:

$$(\bar{V})^2 \left( 1 + 2 \frac{v'}{\bar{V}} \right) = A(\bar{\tau}_w)^{\frac{1}{3}} \left( 1 + \frac{\tau'_w}{3\bar{\tau}_w} \right) + B$$

$$\text{thus } (\bar{V})^2 \neq A(\bar{\tau}_w)^{\frac{1}{3}} + B$$

This equation shows that using the mean voltage levels to determine a mean wall shear is not rigorously accurate. It also shows, however, that the errors due to using the mean voltages to compute the mean wall shear is proportional to the ratio of the fluctuating voltage and the mean voltage. In all cases, the fluctuating voltages were found to be at least three orders of magnitude smaller than the mean voltages due to spatial averaging. Thus the error due to nonlinear averaging is negligible.

## 4.6 Steady Calibration

It is more difficult to calibrate the constant temperature data because both a gain and an offset are needed from any calibration, so a few points from the windward side do not give adequate statistics for a calibration. The model equation used is:

$$\left( \frac{V_s^2}{\Theta} \right) = A \tau_w^{\frac{1}{3}} + B$$

where  $A$  and  $B$  are the calibration coefficients. These coefficients are dependent on sensor design and construction, and Bellhouse and Schultz (1966) show that these coefficients are largely independent of temperature. The only difference between this model equation and the simplified version used in the previous section is the effect of free-stream temperature via  $\Theta$ , which is usually ignored in temperature-controlled experiments where the changes in free-stream temperature are insignificant. It is shown subsequently that in the present tests the free-stream temperature effects were very significant and are handled individually in each data set as described below.

The calibrated constant current data were used to calibrate the constant temperature data. This technique used several hundred point-pairs for the calibration, resulting in relatively good statistics. However, the calibrations thus fit showed a significant amount of scatter. The uncertainties are augmented by the fact that the constant current data being used as a standard already has a 20% calibration uncertainty on it. The gains, offsets, and correlation coefficients for the constant temperature calibration are listed in Table 4. It is noted that the correlation coefficients are fairly low, indicating the significant amount of scatter involved. However, the linear regressions do faithfully represent the calibrated trend, and this calibration does succeed in getting the wall shear data scaled in the proper range. Figure 23 through Figure 26 show comparative plots between the constant current and constant temperature data sets, and the data of Meier and Kreplin (1985) and of Chesnakas and Simpson (1996) at several  $x/L$  stations at  $10^\circ$  and  $20^\circ$  angle of attack. These comparisons are discussed in the preceding chapters. The important thing to note is that in general the constant current and constant temperature data match up well, thus validating the calibration. It is also important to stress that the same caveats detailed in the constant current calibration section (Section 3.7) apply to all calibrations performed on the constant temperature data.

## 4.7 Unsteady Data Reduction and Calibration

It was pointed out in the steady data reduction section that the driving uncertainty in the uncertainty analysis is the foil temperature uncertainty. A mean, calibrated foil temperature was determined as a "best fit" to the model equation. In the case of the steady data, a given run for a given angle of attack only takes 15 to 20 minutes, during which time the tunnel temperature typically does not vary by more than

1°C. For a given unsteady maneuver, it typically takes 6 hours to take the entire data set. Compound this with the fact that the pitchup maneuver data was taken during a morning session, the temperature changes were much larger, in fact on the order of 15°C. The sensor temperature was only on the order of 35° C, so the temperature difference between the sensor and the free stream results in an overwhelming uncertainty. When reducing the unsteady data with the scheme used for the steady data, temperature effects were an order of magnitude even more important, so again some “data massaging” was necessary to extract meaningful information from the raw data.

These temperature effects are of course primarily due to the temperature sensitivity of the film material, that is, the property of the BALCO foil that makes its resistivity change predictably with temperature. It is also true that fluid properties change with temperature, which would effect the amount of heat transfer into the fluid and consequently the calibration of the sensor. However, Bellhouse and Schultz (1966) show that for free-stream temperature changes of even 100°C, the impact of the change in fluid properties is negligible. Therefore, fluid property temperature dependencies were ruled out as a means for correcting the data.

The following solution was found for reducing the data while eliminating the temperature effects. During a given single execution of a DyPPiR maneuver, all data taken (256 data points in 1 second) essentially are taken at the same flow temperature. Also, all maneuvers start with the model at 0° angle of attack, so the sensors should be measuring the same starting wall shear regardless of the roll position of the sensor. Recall the model equation for the sensor operation, including calibration coefficients, is:

$$\left( \frac{V_s^2}{\Theta} \right) = A \tau_w^{\frac{1}{3}} + B$$

The temperature effects are solely limited to  $\Theta$  and are thus algebraic in their effect on the model equation. This suggests the following non-dimensionalization:

$$\eta \equiv \frac{\left( \frac{V_s^2}{T_f - T_\infty} \right) \Big|_t}{\left( \frac{V_s^2}{T_f - T_\infty} \right) \Big|_{t=0}} = \left( \frac{V_s|_t}{V_s|_{t=0}} \right)^2 = \frac{A \tau_w^{\frac{1}{3}} \Big|_t + B}{A \tau_w^{\frac{1}{3}} \Big|_{t=0} + B}$$

In this relationship,  $\eta$  represents a strategically non-dimensionalized anemometer voltage ( $\eta$  in this context should not be confused with the calibration constant used in Chapter 3). Since both the foil temperature and the free-stream temperature are constant during a given maneuver (which only lasts 1 second), the temperature effects can be eliminated by non-dimensionalizing any time-step's data point (at time “ $t$ ”) with the first data point (time “ $t=0$ ”, or equivalently “ $C_f=C_{f,\alpha=0^\circ}$ ”). This technique cleans up the data very well,

eliminating any visible sign of a temperature dependence. The final manipulation to wall skin friction at time  $t$  results in:

$$\begin{aligned}\eta\left(A\tau_w^{\frac{1}{3}}\Big|_{t=0} + B\right) &= A\tau_w^{\frac{1}{3}}\Big|_t + B \\ \eta\left(AC_f^{\frac{1}{3}}\Big|_{t=0} + \frac{B}{q_\infty}\right) &= AC_f^{\frac{1}{3}}\Big|_t + \frac{B}{q_\infty} \\ C_f\Big|_t &= \left[\eta C_f^{\frac{1}{3}}\Big|_{t=0} + \frac{(\eta-1)B}{q_\infty^{\frac{1}{3}}A}\right]^3\end{aligned}$$

This equation shows the dependence of the unsteady skin friction calculation on the steady constant temperature hot-film calibration coefficients  $A$  and  $B$ . Also, the calculation requires the skin friction coefficient for this sensor at  $\alpha=0^\circ$  (or time  $t=0$ ). For consistency, this should be supplied by the constant temperature  $\alpha=0^\circ$  measurements.

When this equation was originally implemented, the end data from the pitchup maneuver were compared to the steady  $30^\circ$  angle of attack data to check the validity of the calibration. It was assumed that the flow had reached steady state by the end of the maneuver (0.33s after motion stopped), and this assumption was verified by comparing primary and secondary separation locations between the steady and unsteady constant temperature data. However, the unsteady skin friction coefficients did not agree with the steady  $30^\circ$  data in *magnitude*. While the qualitative shape of the data curves was correct, the unsteady skin friction values tended to be low by an order of magnitude.

The cause of this significant discrepancy is unknown, but the following technique does work in correcting the data and a possible explanation for the errors is offered. To investigate and eventually cure this disparity, it was recognized that the unsteady data reduction equation depends only on two parameters ( $\gamma$  and  $\kappa$ , defined below), not three ( $A$ ,  $B$ , and  $C_{f,t=0}$ ):

$$\begin{aligned}C_f\Big|_t &= \left[\eta\gamma + \frac{(\eta-1)}{q_\infty^{\frac{1}{3}}}\kappa\right]^3 \\ \gamma &= C_f^{\frac{1}{3}}\Big|_{t=0} \\ \kappa &= \frac{B}{A}\end{aligned}$$

This can equation can be put in the following form:

$$\frac{C_f^{\frac{1}{3}}\Big|_t}{\eta} = \gamma + \frac{(\eta-1)}{\eta q_\infty^{\frac{1}{3}}}\kappa$$

This equation was used to calibrate the unsteady hot-film data to match the steady hot-film data at the end of the pitchup maneuver, or  $\alpha=30^\circ$ . Therefore, using any of the last several time data points from the pitchup constant-temperature hot-film data to compute  $\eta$ , and the steady  $30^\circ$  data to supply the skin friction coefficient  $C_f$ , the values for  $\gamma$  and  $\kappa$  can be determined for each sensor using a linear regression analysis. The results of this analysis are contained in Table 5. It is important to note that the values for  $\gamma$  match very closely with their expected values, namely the  $\alpha=0^\circ$  skin friction coefficient. However, the value of  $\kappa$  is not consistent with the values of  $A$  and  $B$  determined in the steady data calibration. This is probably due to the fact that  $A$  and  $B$  each already have a very high uncertainty (at least 25%), and that their ratio, the factor  $\kappa$ , would then have an even higher uncertainty. By performing this additional level of calibration, the steady and unsteady data are made consistent with each other. It is important to note that this cannot indicate that either calibration was invalid because both calibrations assumed the same model equation. In addition, this calibration casts no doubt on the relative values of the wall shear and the ability to locate separation locations with either the steady or unsteady data.

#### 4.8 Steady Results

Figure 78 through Figure 89 show the wall shear distributions for all sensors at each angle of attack. This data shows the same trends displayed by the constant current data, so a thorough description will not be rehashed. A huge discrepancy though does exist in the data before the trips. The constant current data set shows possible separation on the nose at  $5^\circ$  angle of attack (see Figure 38). The constant temperature measurements predict separation at the same location to begin at around  $20^\circ$  angle of attack. This discrepancy is maybe due to the fact that the flow separation on the nose is laminar, where the separation is very sensitive to free-stream flow conditions and surface imperfections.

Again, the sensor immediately downstream of the trips shows very peculiar trends. A strong minima is seen on the *windward* side starting at  $\phi=50^\circ$  at  $12.2^\circ$  angle of attack and moving windward to around  $\phi=20^\circ$  by  $34.8^\circ$  angle of attack. It is unclear what this minima truly represents.

The constant temperature data set includes more angles of attack than the constant current data set and goes up to  $35^\circ$  angle of attack, providing even more detail into the behavior of the flow separation at various  $\alpha$ . This is in fact more helpful in Figure 90 through Figure 101, where all data for one sensor at various angles of attack are plotted on the same plot. This makes it easier to track the development of the nose and tail separations and their interactions. For example, by examining the sensor immediately before the trip (Figure 92) it is clear that separation begins at between  $12.2^\circ$  and  $15.2^\circ$  angle of attack. In the next figure (Figure 93), which is for the next sensor immediately downstream of the trips, a minima seems to exist even at  $12.2^\circ$  angle of attack and certainly exists at  $15.2^\circ$  angle of attack. The distinction is that the

nose separation formed at a higher angle of attack for the constant temperature case than it did for the constant current case.

Figure 102 through Figure 112 shows the separation line topologies at all angles of attack for the constant temperature data set. Figure 117 shows the same data plotted against angle of attack. Figure 113 through Figure 116 show comparisons between the constant current and constant temperature separation topologies for four angles of attack. The nose separation locations differ substantially, as pointed out above. Otherwise, separation location agreement on the rear 75% of the model is well within the position uncertainties for all cases except at  $\alpha=15^\circ$ . At  $15^\circ$  angle of attack (Figure 113) there is a significant discrepancy between the separation lines immediately downstream of the trips. The irregular wall shear distributions at these sensors make separation location fairly uncertain in these isolated cases.

## **4.9 Unsteady Results**

### **4.9.1 Pitchup Maneuver**

In Figure 118 through Figure 129, wall shear distributions are plotted for each sensor at every time step during the Pitchup Maneuver as shown in Figure 8. In Figure 8, the regions delineated as “a”, “b”, and “c” indicate the times correlating to the subfigures “a”, “b”, and “c” in Figure 118 through Figure 129. The dotted lines separate each of these three regions into two subregions, relating to the two plots in each sub-figure in Figure 118 through Figure 129. In each subplot, the lowest plot corresponds to the initial time step, and the highest plot corresponds to the final time step. The time range for each sub-plot is given at the top of each sub-plot. For the pitchup maneuver, section “a” corresponds to roughly the first half of the pitchup; section “b” corresponds to the second half of the pitchup; and section “c” corresponds to the deceleration of the model and the model holding a steady final position, where the flow is expected to reach steady state. In all cases, the very last plot in the second half of section “c” is the very last time step where data were taken.

It is interesting to note from these plots that separation on the nose does not begin until after  $t'=10$ , when the model is at around  $25^\circ$  angle of attack. (see Figure 118b). The variations on Figure 118a are assumed to be noise and not due to some flow phenomena. As expected, the separation at the second sensor (Figure 119) forms a little earlier at roughly  $t'=8$ . However, the next three sensors downstream of the trips (Figure 120 through Figure 122) don't seem to form a separation until around  $t'=10$ . It is very possible that this means the flow separated on the nose separate from a separation on the tail and these two separations eventually “hooked up”.

As would be expected, the flow on the tail separates earliest (Figure 129), at around  $t'=6$ . Even on this plot, it is clear that flow separation doesn't form until section “b”, or the second half of the pitchup. The



tail reaches almost  $15^\circ$  angle of attack before getting any flow separation. In a steady flow, separation begins at angles of attack of  $5^\circ$ . It is clear that the separation process is delayed by the motion of the model.

Figure 130 through Figure 141 shows the time dependent separation location plotted versus time for each maneuver. This is plotted against the expected quasi-steady result, which corresponds to the instantaneous separation locations obtained from the steady data. In all cases the separation is delayed in time by around 2 non-dimensional time units. Another way of looking at these data is that at all times the separation is delayed by roughly  $10^\circ$  circumferential location. In all cases, the separation does eventually reach the final steady separation location, so no flow hysteresis is observed within the uncertainties. Figure 142 through Figure 153 show the same data plotted against instantaneous angle of attack.

#### 4.9.2 Submarine Maneuver

Figure 163 through Figure 169 shows the wall shear distributions for all time steps for the submarine maneuver as shown in Figure 13. The section and sub-section nomenclature is similar to that used in the pitchup maneuver. For the submarine maneuver, section "a" corresponds to the pitch -up, section "b" is the deceleration to steady state, and section "c" is steady state.

The one main difference between the pitchup and submarine maneuvers is range: the pitchup maneuver goes from  $0^\circ$  to  $30^\circ$ , while the submarine maneuver only goes from  $0^\circ$  to roughly  $13^\circ$ . Both do so at essentially the same rate (about  $90^\circ$  per second). For the submarine maneuver, no separation ever forms on the nose. In fact, at the very end of the time record there is just barely the hint of separation at  $x/L=0.424$  (see Figure 163). So for this maneuver, separation is essentially limited to the rear half of the model. The last sensor exhibits no separation during section "a", but quickly forms a strong separation during section "b". The flow has not reached steady state at the end of section "b" and continues to develop in section "c", even forming a weak secondary separation. Figure 170 through Figure 175 shows the instantaneous time-dependent separation locations for each sensor.

Figure 176 through Figure 200 show comparisons of steady, pitchup, and submarine maneuver wall shear distributions at discrete angles of attack, while Figure 201 to Figure 224 show comparisons of just pitchup and steady wall shear distributions at higher angles of attack. The individual time steps selected for comparison are shown as dots in Figure 176. Figure 177 through Figure 188 show all three cases at  $5^\circ$  instantaneous angle of attack. Both unsteady maneuvers result in essentially flat wall shear distributions at this point in the maneuvers. Thus the flow field, despite the model being at incidence, is behaving as if the model is not at incidence.

At  $12.2^\circ$  (Figure 189 through Figure 200) significant differences are visible. The nose sensors are less interesting as the differences appear to be mainly in magnitude, which is an imprecise measurement anyway considering the magnitude calibration uncertainties. It is interesting that sensor 6 (Figure 194)

shows the first separation at this angle of attack. The separation seems to be present in the pitchup maneuver and the end of the submarine maneuver, but it hadn't formed yet when the model first reached  $12.2^\circ$  in the submarine maneuver. In all cases, the unsteady minima lag the steady minima, including the submarine maneuver at the end of the maneuver. It is important to point out that the comparison with the end on the submarine maneuver is a crude one as it ends up  $1.5^\circ$  higher than the  $12.2^\circ$  angle of attack for which the other curves are plotted. In sensors 7 and 8 (Figure 195 through Figure 196) the submarine maneuver has still not separated, and only hints to separate at sensor 10 (Figure 198). For all cases on sensors 7 through 12, the submarine maneuver ends the time record by approaching the steady data, and even hints at a secondary separation at the rearmost sensor. The pitchup data lags the steady data more strongly closer to the tail, where it barely resembles the steady data (Figure 200).

At  $20.2^\circ$  (Figure 201 through Figure 212) still no separation has just formed on sensor 2 in the pitchup maneuver (Figure 202), though the steady data shows the separation should be strong and extend to the first sensor. Again, this isn't a direct comparison because the repeatability of the nose laminar separation is questionable. The tail separation still seems to be separate from the nose separation as the tail separation only barely extends to sensor 5 (Figure 205). The tail sensor (Figure 212) still exhibits a significant lag, but the hint of a secondary separation forming is present. At  $29.9^\circ$  (Figure 213 through Figure 224), the separation has reached the first sensor, but it is still significantly weaker than the steady data. By the end of the time record, the pitchup data flow field on the nose seems to be close to steady state, and the separations are within  $5^\circ$  of each other. There is strong separation on the prolate spheroid at the end of the maneuver and a significant secondary separation is clear in the last sensor (Figure 224). By the end of the time record, all sensors seem very close to steady state.

#### **4.10 Future Improvements**

While constant temperature anemometry in general is a fairly common procedure, the implementation in this case was very difficult. Certainly lower uncertainties can be achieved. The constant temperature anemometers must take the bulk of all hot-film work on the DyPPiR due to frequency response restraints. While it is possible to run the constant temperature anemometers at multiple currents (implemented as multiple overheats) like the constant current anemometers, this is not practical due to the increased number of runs required on the DyPPiR. Therefore, the constant temperature anemometers will always have to be run at single overheat ratios.

The first improvement that must be made is to reduce the uncertainty on the voltage measurements. The 16-bit resolution A/D board was handicapped in accuracy by using the off-board reference ground. This coupled with the high anemometer currents and the resultant floating grounds made it all the more difficult to achieve low uncertainties on the measured voltages. The voltage uncertainties can be reduced by

1 or 2 orders of magnitude in the future by using the A/D board in a differential mode instead of a single ended mode. This reduces the number of channels available for use, but this problem can be circumvented with a multiplexer. There is more than enough data acquisition rate available to go to differential mode and still use 16 or more sensors at a given time.

The next largest uncertainty was in the flow temperature measurement. Measuring temperature to better than  $0.5^{\circ}\text{C}$  requires moderately expensive equipment. Ideally, a system with several electronic thermometers with accuracy to  $0.01^{\circ}$  or better would help reduce the true free-stream temperature effects, particularly in the unsteady tests. Although this may be moderately expensive, it is very cheap compared to adding temperature control to the wind tunnel. Another alternative is to run the sensors at an overheat ratio, thus increasing the sensor temperature and decreasing the importance of temperature effects. This would require different sensors and/or different anemometers.

The final source of uncertainty in the measurement system was the measurement of several small resistances: the current measuring resistance, the sensor cold resistance, even the lead resistances. These can be dealt with in several ways in the future. First, it would make sense to switch to a four-wire sensor system, which involves two wires going to the sensor and two wires returning from the sensor (Omega Engineering, 1995). Two wires would be used to carry the current to and from the sensor, and two wires would be used to measure voltage drop across the sensor. This way, no lead resistance corrections need to be made. However, this significantly increases the number of wires leaving the model, although the voltage wires could be 30 AWG or even smaller. To reduce the uncertainty on the current measuring resistances, instead of measuring these resistances in house, very-high-precision (0.01%) resistances could be special ordered. And to decrease the uncertainty on the cold resistance measurements, in the future sensors may be submerged in oil to stabilize the sensor temperature while the measurements are being made. A further refinement would be to measure the temperature coefficient of resistivity explicitly, instead of assuming the manufacturer's value, and one could presumably measure this constant for each individual sensor.

All of these improvements would substantially decrease the uncertainty of the relative measurements, which would make separation location determination less difficult. However, all of these uncertainties are very small compared to the calibration uncertainties. In order to get reliable skin friction magnitudes, a better calibration technique is required. For the purpose of these tests, skin friction magnitude was deemed second in importance to relative magnitude, and wasn't even considered until after the data were taken. To improve the calibration, first more calibration-specific data must be taken in the wind tunnel, and these must be taken at a very wide range of wall shear magnitudes. All sensors should be calibrated in laminar and turbulent flows. But even given all of these run conditions, it is still difficult to come up with the actual wall shear values. The calculation methods used represent the most simple-minded approach

possible. More sophisticated techniques could be used, as in Meier and Kreplin (1985), where the model was placed at zero incidence and run at a wide range of Reynolds numbers; these results were then calibrated against a boundary layer computer program developed by J.C. Rotta. However, even these results had a  $\pm 20\%$  uncertainty attached to the final calibration. In addition, there is something philosophically wrong with using calculations to calibrate experimental results. This is only done when it seems that almost nothing else will work.

This all stems from the fact that wall shear is one of the hardest magnitudes to measure accurately. Preston tubes, floating balances, and direct velocity measurements all result in wall shear uncertainties of at least 5% and usually more like 10% in real, three dimensional flows. One possibility is to package the sensors in a housing or a plug that makes them removable, much like typical pressure transducers, from the model. Then the sensors could individually be calibrated in some calibrated flow in a smaller tunnel against some other calibrated instrument. This would have the advantage of calibrating all sensors against the same flow conditions. It would also allow a more direct study of calibration effects on these sensors. In the end, however, the biggest challenge is in building or obtaining another transducer of suitable accuracy to calibrate the hot-film sensors against.

Finally, different sensors could be considered. For one, the sensors presently used were designed for a model 4 times larger. The sensors installed on the present model span  $2.5^\circ$  circumferentially at the widest point of the model, and almost  $4^\circ$  at the forward- and rear-most sensors. Smaller sensors would improve the positional resolution of the system. Also, smaller sensors would mean less thermal mass and a higher frequency response. Presently, the frequency response is so low that not even RMS fluctuations are meaningful. A smaller, higher frequency response sensor would yield at least RMS data and could be used for turbulent spectrum data in steady flows. Finally, it would be very interesting to use the directionally sensitive sensors, similar to those used in Meier and Kreplin (1985). Of course, this would require twice as many anemometers, but would yield much more flow detail, particularly about the separation line locations. Conceivably, one could use the technique of Meier and Kreplin and take such directional wall shear data and construct limiting skin friction plots *at all time steps during a maneuver*. This would result in unsteady data of unprecedented detail.

To facilitate any of these improvements, the anemometers themselves must be further examined. The intermittent oscillations made operation very difficult and eventually limited the measurements to only 12 sensors. The anemometers were stressed by demanding such high currents, and the impedances from the very long signal lines were devastating from a stability point of view. In addition, the anemometers were built with components that are now largely outdated. Especially if the current sensors continue to be used, new anemometers should be considered. Due to the low frequency response requirements of these measurements, only "bare-bones" anemometers are required. It is even conceivable that a compact, many-

anemometer system could be developed to be placed inside the model to minimize cable runs, although this would be admittedly an ambitious undertaking.

# Chapter 5: Oil Flow Visualization

---

## 5.1 Introduction

Oil flow visualization is a technique which indicates the wall shear direction. Ahn (1992) has documented the oil flow patterns on a 6:1 prolate spheroid for various angles of attack and Reynolds numbers, but most of his cases were for an untripped model. The visualizations presented in this chapter are all for the 6:1 prolate spheroid, with trip posts at  $x/L=20\%$  and a Reynolds number of 4.2 million. Angles of attack from  $10^\circ$  to  $30^\circ$  every  $5^\circ$  are included.

## 5.2 Experimental Apparatus

A mixture of 40 parts Titanium Dioxide, 80 parts of Kerosene, and 5 parts Oleic Acid are mixed into a very thin, white paint mixture. The same black fiberglass prolate spheroid model used for the hot-film and pressure measurements was used for the oil flow tests. The mixture is painted on the model, after which the wind tunnel is set to the desired speed. The mixture tends to streak in the direction of the wall shear stress. After several minutes, the kerosene completely evaporates, leaving the pigment affixed to the model surface in a frozen skin friction pattern. The tunnel is shut off, and the visualization is photographed and measured. Convergent skin friction lines indicate flow separation.

The black model is covered with a white grid spaced every 5% of the length longitudinally and every  $45^\circ$  circumferentially. The grid lines were located with a precision of  $\pm 0.2\%$  longitudinally and  $\pm 1^\circ$  circumferentially. The grid was then painted over with several coats of Parks Satin Finish Clear Lacquer to protect the grid from the oil flow mixture. The model was mounted to the Stability Tunnel NACA Strut, with  $11^\circ$  offset arms. The NACA Strut allows static angle of attack adjustment from  $-22.5^\circ$  to  $22.5^\circ$ ; with the  $11^\circ$  offset, the range is shifted to  $-11.5^\circ$  to  $33.5^\circ$ . The DyPPiR was not used because the oil flow mixture would harm the delicate DyPPiR hardware. The model mount allowed static roll positioning. Model roll alignment was set using a combination square and center head to within an accuracy of better than  $1^\circ$ . Angle of attack accuracy was  $\pm 0.2^\circ$ , and the model was at zero sideslip to within  $0.2^\circ$ .

Thirty two hot-film sensors were left on the model to study the impact of their roughness on the separation. The sensing area themselves were covered with scotch tape to prevent sensor area corrosion, and everything was covered with the clear coat, but the sensors were otherwise unmodified. For all but the last run, the sensors were located at  $\phi=60^\circ$  (from the windward side). The pressure taps also remained in the

model, but the pressure sensors were removed. The pressure taps were located at  $\phi=250^\circ$  from the windward side.

Separation lines were measured by using a flexible plastic ruler at each longitudinal grid station. The measurements were accurate to  $\pm 2$  mm or  $\pm 1^\circ$ , but there were many times when it was difficult to visually pick off the separations to better than  $\pm 6$  mm or  $\pm 4^\circ$ .

### **5.3 Basic Separation Locations**

Figure 225 through Figure 229 show the oil flows for the model at angles of attack from  $10^\circ$  to  $30^\circ$  in increments of  $5^\circ$ . Figure 230 through Figure 234 show the primary and secondary separation locations for each of these cases. At  $10^\circ$  (Figure 225 and Figure 230), the separation is fairly weak and seems to begin aft of the model mid section. At  $15^\circ$  (Figure 226 and Figure 231), the primary separation line has moved windward and starts much farther up on the nose. Also, a strong secondary separation has formed on the tail. Note in the separation line plot (Figure 231) that there is a significant discrepancy between the separation locations on the side with the hot-film sensors at  $\phi=60^\circ$  ("Sensor Side") and the opposite side of the model ("Clean Side"). It is assumed that this is due to the roughness effect of the sensors. The difference in separation locations is as much as  $5^\circ$ .

At  $20^\circ$  and  $25^\circ$  (Figure 227 and Figure 232; Figure 228 and Figure 233) these same trends continue. At  $30^\circ$  (Figure 229 and Figure 234) a very interesting phenomena was observed. The  $30^\circ$  case was the very first one done. On the clean side, a laminar and turbulent separation were observed ahead of the trips; these two separations merged into one just downstream of the trips. This topology is discussed in more detail below. On the sensor side, only a turbulent separation was found. It was assumed that the sensors were tripping the flow on that side of the model, and preventing a laminar nose separation from forming. However, in subsequent attempts to repeat the flow, the laminar separation was never observed again. It is assumed that the oil flow itself at that point was tripping the flow on both sides of the model. This would definitely result in an artificially asymmetric flow condition. An example of the extent of the flow asymmetry in the first  $30^\circ$  angle of attack oil flow is shown in Figure 235 which shows the starting locations of the secondary separation lines. The secondary separation on the right is on the sensor side. It starts almost 10% of the model length earlier than the similar separation location on the clean (left) side.

### **5.4 Some Selected Detail Flow Topologies**

#### **5.4.1 Nose Flow Separations at $30^\circ$ Angle of Attack**

Figure 236 and Figure 237 show a detailed comparison of the nose flow separation topologies for the clean side and sensor side of the model at  $30^\circ$  angle of attack for the very first oil flow. It has been

identified in earlier chapters that the nose flow seems to play a large role in the overall separated flow development of the rest of the model, and thus warrants detailed examination. For the sensor side (Figure 237), the flow is already turbulent, so only one separation forms. This separation has a very indistinct beginning, and the skin friction lines converge on it at very shallow angles. This makes it very difficult to pick out not only the separation initiation, but also which streamline is actually the separation line.

On the clean side (Figure 236), the laminar separation is characterized by a much larger intersection between approaching skin friction lines and the separation line. Behind this separation line is a reattachment line and then a turbulent separation. It is very interesting to follow the development of the laminar separation downstream of the trips. It looks as if the laminar separation suddenly deflects leeward and merges with the turbulent separation at roughly  $x/L=27\%$ . However, the local streamlines surrounding this separation branch do not clearly intersect the "separation line" at discrete angles, but instead seem to be parallel to it. This feature is very similar to the description of the start of the turbulent separation on either side, that is, that the approaching skin friction lines intersect the "separation line" at very shallow angles. In the last two sentences, separation line has been in quotes because there has to be speculation as to whether a true separation line exists at these locations.

#### 5.4.2 Crossflow Separation Topology

Crossflow separation is often described as a skin friction line approached from either side by converging skin friction lines (Simpson, 1996). As an extension of this definition, the start of separation is often described as the first location where the streamlines intersect at a finite angle. Figure 238 shows the start of the secondary separation. The vertical grid line in the center of each of the photos is the model center, and the nose is to the left of the photos. It is clear from these photos that secondary separation begins at roughly  $x/L=48\%$ . These photos are from the  $30^\circ$  angle-of-attack case, where the separations are fairly strong. In practice, separation initiation is not so easily discernible at lower angles of attack.

In all cases, the oil flows show converging skin friction lines clearly on the approach-side of the separation lines. By the conventional description of a crossflow separation line (Figure 238), skin friction lines should also converge on the separation line from the separation-side. In the photos (Figure 238) one can see that there is typically a wide (on the order of  $5^\circ$ ) band of skin friction lines that appear to be parallel to the separation line, but in any case are very mottled and indistinct. Chesnakas and Simpson (1996) have described this region as a "low-velocity trough" on the separation-side of a separation line. In the case of primary separation, the separation-side is leeward of the separation line, and such a feature is clearly evident in the photos of Figure 238. For the secondary separation, since the flow is feeding from the  $\phi=180^\circ$  reattachment line, the separation side is *windward* of the secondary separation line. This again is consistent with the photos.



## Chapter 6: Pressure Measurements

---

### 6.1 Experimental Apparatus

Model wall pressure taps were installed in the prolate spheroid model in a longitudinal row at 10 locations:  $x/L=0.00, 0.11, 0.23, 0.31, 0.44, 0.56, 0.69, 0.77, 0.83,$  and  $0.90$ . Since the first transducer was located so close to the stagnation point, no data are presented from this transducer. A brass plug with a  $0.74$  mm diameter pinhole was mounted at each location flush to the model surface. Endevco 8510B-2 miniature pressure transducers were mounted in these plugs. The close proximity of the transducers to the model surface coupled with the tiny pinhole results in negligible signal attenuation; the sensor/pinhole combination then has a frequency response well above  $1$  kHz (Ahn, 1992). The transducers have a nominal range of  $0$  to  $13.8$  kPa with a sensitivity of  $21.75$  mV/kPa and a non-repeatability of  $1.5\%$  of transducer full scale at  $20:1$  odds. The maximum contribution from accelerations to the measured pressures during any DyPPiR maneuvers is  $0.0026$  kPa ( $C_p=0.002$ ) (Hoang et. al., 1994). The transducers are referenced to the static pressure port of a pitot tube upstream of the model via roughly  $15$  m of Tygon tubing. While this results in a poor frequency response by the transducers in the presence of changes in the static pressure, it has been found that the static pressure changes by no more than  $1\%$  during the most extreme DyPPiR maneuvers, with most of this change occurring after the pressure data record is done being taken (Hoang et. al., 1994). Therefore, it is assumed that this long length of tubing is not inhibiting the measurement response.

The transducers are connected to Measurement Group 2310 Strain Gage Amplifiers with an excitation voltage of  $10$  V. For the steady tests, the signals were amplified  $100$  times and sampled with a HSDAS-16  $16$ -bit data acquisition board in a PC.  $512$  samples were taken at a  $2048$  Hz sampling rate. No filtering was applied to the signal. The model was rolled to various orientations in order to sweep the transducers from the windward to the leeward sides to map out the pressure distribution over the model surface. The flow was assumed to be symmetric in the ensemble mean, so data were only taken on one half of the model. Data was taken at every  $2.5^\circ$  angle of attack, and the transducers were rolled to every  $5^\circ$  on the windward side and every  $2^\circ$  on the leeward side.

For the unsteady data, the signals were amplified  $300$  times and sampled with a RC-Electronics ISC-16  $12$ -bit data acquisition board.  $2000$  samples were taken over a total time of  $1$  second (thus sampled at  $2000$  Hz) during which time the steady-state before the model was sampled, the maneuver was sampled (which typically lasted from  $0.25$  to  $0.33$  seconds), and data was taken after the end of the maneuver while the flow reached steady state. The pressure signal was filtered with a  $10$  kHz low pass filter. Data were

taken at every 10° roll on the windward side and every 5° on the leeward side. Fifty ensembles were taken at each roll angle.

The pressure differences measured by the transducers were non-dimensionalized by the free-stream dynamic pressure forming the standard definition of the pressure coefficient:

$$C_p = \frac{p - p_s}{q_\infty}$$

The dynamic pressure was measured with the same pitot tube used for the static pressure reference. A Datametrics Barocel precision pressure transducer was used to measure the dynamic pressure.

## 6.2 Data Reduction and Uncertainties

### 6.2.1 Pressure Coefficient

The full pressure coefficient reduction equation used is:

$$C_p = \frac{\Delta p}{q_\infty}$$

$$\Delta p = \frac{V_p}{G} \cdot S$$

where  $V_p$  is the measured voltage from the amplifiers,  $G$  is the amplifier gain, and  $S$  is the transducer sensitivity (see Table 6). The amplifier gains were found to be accurate to better than 0.05% and were thus found to be the least uncertain part of the data reduction. Also, the voltages were measured to better than 1 mV accuracy, so the pressure uncertainty is mainly due to calibration uncertainties. The transducer calibration is reported to be accurate to within 1.5% full scale, with full scale being 13.8 kPa. This non-repeatability is due mostly to hysteresis effects and secondarily to temperature effects. Therefore, the calibration uncertainty is on the order of 200 Pa. The full range of measurements actually made, on the other hand, is on the order of 1.6 kPa, so the actual uncertainty of the pressure measurement is roughly 13%.

The Datametrics Barocel precision transducer used to measure the dynamic pressure has a stated nonrepeatability of 0.15% full scale which is also 13.8 kPa. The dynamic pressure in these test were on the order of 1.6 kPa, so the actual dynamic pressure uncertainty for these tests is 13%. The pressure coefficient uncertainty is then dominated by the pressure measurement uncertainty, or 13%. Over a  $C_p$  range of +/-1, this corresponds to an uncertainty of +/-0.13  $C_p$ .

This uncertainty is very large, and tends to overwhelm any differences between steady and unsteady data. Therefore, an *in situ* calibration of the unsteady pressure data was performed by forcing the pressure at the beginning and end of the maneuvers to match the equivalent steady case. This in essence is

equivalent to modeling the hysteresis and temperature errors as gain and offset errors on a run-by-run basis. Therefore, while the true uncertainty on all of the pressure data is still 13%, the comparative uncertainty between the steady and unsteady data is lower by an amount that is hard to predict. It is assumed that the uncertainty of the difference between the steady and unsteady data is on the order of  $0.05 C_p$ .

### **6.2.2 Circumferential Pressure Gradient**

The circumferential pressure gradient,  $\partial C_p / \partial \phi$ , was calculated with a Loess smoothing technique (Jandel Scientific, 1995). A window size was defined (for this data the window was chosen to include 30% of the data points), and a parabola was least-squares fitted to the data in that window. Then the slope of the parabola at the point in question was taken to be the slope of the data at that point. It is difficult, considering the complexity of the gradient calculation, to analytically estimate the pressure gradient uncertainty. Therefore, the uncertainty of the pressure gradient data is assumed to be 25%. The pressure gradient information is presented in  $C_p$  units/radians.

### **6.2.3 Pressure Fluctuations (RMS)**

The pressure data at each location was also used to compute an RMS representative of the pressure fluctuations. High pressure fluctuations usually accompany strong separations. The RMS distribution was smoothed with a Loess smoothing routine using a smoothing factor of 10%. The uncertainty of an RMS computation is proportional to the inverse of the square root of the number of samples (Bendat and Piersol, 1986). In the steady data, the number of samples at a given location is 512. A conservative estimate on the RMS uncertainty is +/-5% full scale, where RMS full scale is roughly  $0.05 C_p$ .

### **6.2.4 Sectional Lift Coefficients**

The pressure data were integrated to obtain both sectional and total lift coefficients. The sectional lift coefficient is computed using:

$$\begin{aligned}
C_l &\equiv \frac{L/b}{2q_\infty R} \\
&= \frac{1}{2q_\infty R} \oint_C p \hat{n} \cdot \hat{j} ds \\
&= \frac{1}{2q_\infty R} \int_{\phi=0}^{\phi=2\pi} p (\hat{n} \cdot \hat{j}) r(x) d\phi \\
&= \frac{1}{2q_\infty R} \int_{\phi=0}^{\phi=2\pi} p \cos \phi \cos \varphi r(x) d\phi \\
&= \frac{r(x) \cos \varphi}{q_\infty R} \int_{\phi=0}^{\phi=\pi} p \cos \phi d\phi \\
&= \frac{r(x)}{R} \cos \varphi \int_0^\pi C_p \cos \phi d\phi
\end{aligned}$$

In this case,  $b$  refers to the “span”, which in the present geometry is really the length. Thus the sectional lift coefficient represents a “lift per unit span” as in a classical two-dimensional cylinder. The equation differs significantly from the “classical” definition of a sectional lift coefficient, which usually comprises only the integral and not the other multiplicative factors (for example, see Kays and Crawford, 1980). The multiplicative factors account for the change in cross section size and slope at different cross sections on the model. The cosine term outside of the integral accounts for the slope of the body in a longitudinal-section plane, which is based on the elliptical geometry and can be written as:

$$\begin{aligned}
y(x) &= b \sqrt{1 - \left(\frac{x}{a}\right)^2} \\
m = y'(x) &= -\left(\frac{x/a}{y/b}\right) \left(\frac{b}{a}\right) \\
\text{then } \cos \varphi &= \frac{1}{\sqrt{1 + m^2}}
\end{aligned}$$

This is a minor term, as it's maximum contribution is about a 2.5% reduction for the sectional lift coefficient at the extreme nose and tail sensors. The integral was computed using a trapezoidal rule. It is important to distinguish that “lift” is a partial misnomer in this case. From the standpoint of looking at a given cross section as a cylindrical analogy, sectional “lift” coefficient is a proper terminology. However, the direction of this “lift” is not oriented with the lift vector on the model; it is instead oriented with the normal force vector, the distinction being the normal force is perpendicular to the model centerline while the lift force is perpendicular to the free-stream velocity. Both are located in the flow plane of symmetry.

To estimate the uncertainty imposed by this computation, consider the numerical version of the above integration as actually implemented in the reduction code, which has to account for unevenly spaced data:

$$C_l = \frac{r(x)}{R} \cos \varphi \sum_{i=1}^n \left( \frac{C_{p_i} + C_{p_{i-1}}}{2} \right) (\phi_i - \phi_{i-1}) \cos \left( \frac{\phi_i + \phi_{i-1}}{2} \right)$$

The partial derivative of the sectional lift coefficient with respect to the  $i$ th pressure coefficient is:

$$\frac{\partial C_l}{\partial C_{p_i}} = \frac{r(x)}{R} \cos \varphi \left[ \frac{1}{2} (\phi_i - \phi_{i-1}) \cos \left( \frac{\phi_i + \phi_{i-1}}{2} \right) + \frac{1}{2} (\phi_{i+1} - \phi_i) \cos \left( \frac{\phi_{i+1} + \phi_i}{2} \right) \right]$$

The uncertainty on the sectional lift coefficient is then:

$$\delta C_l = \sqrt{\sum_{i=1}^n \left( \frac{\partial C_l}{\partial C_{p_i}} \delta C_{p_i} \right)^2}$$

Since the individual pressure coefficients being summed were measured using one transducer, the pressure coefficient uncertainties are all equal (in a statistical sense), thus:

$$\begin{aligned} \delta C_l &= \delta C_p \frac{r(x)}{R} \cos \varphi \sqrt{\sum_{i=1}^n \left( \frac{\partial C_l}{\partial C_{p_i}} \right)^2} \\ &= \delta C_p \frac{r(x)}{R} \cos \varphi \sqrt{\sum_{i=1}^n \left( \frac{1}{2} (\phi_i - \phi_{i-1}) \cos \left( \frac{\phi_i + \phi_{i-1}}{2} \right) + \frac{1}{2} (\phi_{i+1} - \phi_i) \cos \left( \frac{\phi_{i+1} + \phi_i}{2} \right) \right)^2} \\ &\approx \delta C_p \frac{r(x)}{R} \cos \varphi \sqrt{\sum_{i=1}^n \left( (\phi_{i+1} - \phi_i) \cos \left( \frac{\phi_{i+1} + \phi_i}{2} \right) \right)^2} \end{aligned}$$

One more simplifying assumption that can be made is to state that the roll angles ( $\phi_i$ ) are uniformly spaced. They aren't; however, for the purposes of computing a statistical uncertainty, a "representative" spacing can be used. In the present data, sometimes the roll angles were spaced every 10°, 5°, or 2°. A conservative approximation is to use the 10° spacing (radians are required for the actual computation). This leads to:

$$\begin{aligned} \overline{d\phi} &\approx \overline{\phi_{i+1} - \phi_i} \\ \delta C_l &\approx \delta C_p \sqrt{\overline{d\phi}} \frac{r(x)}{R} \cos \varphi \sqrt{\sum_{i=1}^n \left( \cos \left( \frac{\phi_{i+1} + \phi_i}{2} \right) \right)^2 (\phi_{i+1} - \phi_i)} \\ &\approx \delta C_p \sqrt{\overline{d\phi}} \frac{r(x)}{R} \cos \varphi \sqrt{\int_0^\pi \cos^2 \phi d\phi} \\ &\approx \delta C_p \sqrt{\overline{d\phi}} \frac{r(x)}{R} \cos \varphi \sqrt{\frac{\pi}{2}} \end{aligned}$$

This relation shows several trends. First, as would be expected, the numerical integration introduces an uncertainty that is proportional to the square root of the spacing size. So the tighter the  $\phi$  grid the lower the integration uncertainty. Besides that trend, the sectional lift coefficient uncertainty is directly proportional to the pressure coefficient uncertainty. Finally, because the uncertainty is proportionally smaller for smaller grid spacings, the sectional lift coefficient uncertainty can actually be lower than the pressure coefficient uncertainty. This is a result of the smoothing characteristic of the integrating operation whereby the effects of random errors at different locations tend to zero as they are integrated, effectively canceling themselves out. Using conservative estimates for all of the necessary quantities, the magnitude uncertainty for the sectional lift coefficient is 0.07; given a maximum sectional lift coefficient of roughly 0.5, this results in a full scale uncertainty of 14%.

These trends only apply to randomly distributed uncertainties; biases will have a separate affect. A simple offset error in the pressure coefficient data will not affect the lift calculation at all due to the presence of the cosine function in the integral. A gain error on the pressure coefficient data will result in a gain error for the sectional lift coefficient. Considering the potential hysteresis errors, which often behave with a "gain" effect, and temperature gain sensitivities of 4%, these errors could be substantial. For these reasons, sectional lift coefficients were not calculated for the unsteady cases.

## 6.2.5 Normal Force and Pitch Moment

These sectional lift coefficients can then be used to compute the normal force and pitching moment acting on the body. By carrying out the surface integration of the pressures, it can be shown that:

$$\begin{aligned}
 C_z &\equiv \frac{Z}{q_\infty \pi R^2} \\
 &= \frac{2}{\pi} \int_{x=0}^{x=L} C_l \frac{dx}{R} \\
 &= \frac{2}{\pi} \sum_{j=1}^m C_{l_j} \frac{dx_j}{R} \\
 C_M &\equiv \frac{M}{q_\infty \pi R^2 L} \\
 &= \frac{2}{\pi} \int_{x=0}^{x=L} C_l \frac{x}{L} \frac{dx}{R} \\
 &= \frac{2}{\pi} \sum_{j=1}^m C_{l_j} \frac{x_j}{L} \frac{dx_j}{R}
 \end{aligned}$$

Assuming the uncertainties for these quantities are dominated by the sectional lift uncertainties, the normal force uncertainty relation becomes:

$$\begin{aligned}
\frac{\partial C_z}{\partial C_{l_j}} &= \frac{2}{\pi} \frac{dx_j}{R} \\
\delta C_z &= \sqrt{\sum_{j=1}^m \left( \frac{2}{\pi} \frac{dx_j}{R} \delta C_{l_j} \right)^2} \\
&= \frac{2}{\pi} \frac{\delta C_l dx}{R} \sqrt{m} \\
&= \frac{2}{\pi} \delta C_l \frac{\sqrt{dx} \sqrt{L}}{R}
\end{aligned}$$

The last step was done because  $m$  and  $dx$  are co-dependent ( $dx=L/m$ ); therefore, the last line has only one dependence on the data grid. The pitch moment uncertainty is:

$$\begin{aligned}
\frac{\partial C_M}{\partial C_{l_j}} &= \frac{2}{\pi} \frac{x_j dx_j}{RL} \\
\delta C_M &= \sqrt{\sum_{j=1}^m \left( \frac{2}{\pi} \frac{x_j dx_j}{RL} \delta C_{l_j} \right)^2} \\
&= \frac{2}{\pi} \frac{\delta C_l \sqrt{dx}}{RL} \sqrt{\sum_{j=1}^m x_j^2 dx_j} \\
&= \frac{2}{\pi} \frac{\delta C_l \sqrt{dx}}{RL} \sqrt{\int_{x=0}^{x=L} x^2 dx} \\
&= \frac{2}{\pi} \frac{\delta C_l \sqrt{dx}}{RL} \sqrt{\frac{1}{3} L^3} \\
&= \frac{2}{\pi \sqrt{3}} \delta C_l \frac{\sqrt{dx} \sqrt{L}}{R}
\end{aligned}$$

Again, the uncertainties are proportional to the square root of the grid spacing; in this case, the grid spacing is longitudinal and represented by  $dx$ . From that standpoint, the longitudinal grid spacing is coarse, so the uncertainties can be expected to be higher. An important assumption in the implementation of the numerical integration is that the section lift coefficient goes to zero at the nose and tail. Using the above relations, the normal force uncertainty is on the order of 0.17; the pitch moment coefficient uncertainty is roughly 0.10. Assuming full scale values of roughly 1 for  $C_z$  and 0.25 for  $C_M$ , the relative uncertainties are on the order of 17% for the normal force coefficient and 40% for the pitch moment coefficient.

This uncertainty analysis does not account for the errors introduced by the numerical integration. In the case where an integration is being performed over the length of the model with only 9 data stations, these errors can be significant. Also, the pitch moment as calculated above results in a nose-down positive

moment about the nose. The pitch moment is presented as a nose-up moment about the model center after a simple moment translation.

## **6.3 Steady Results**

### **6.3.1 Pressure Coefficient**

Figure 239 through Figure 252 show the steady pressure measurements presented for all sensors at each angle of attack. These results are compared to the potential flow solution. At  $2.5^\circ$  (Figure 239) the distributions are very flat. The data agrees with the potential solution to well within the uncertainties except at the tail, where separation results in a pressure increase. At  $5^\circ$ ,  $7.5^\circ$ , and  $10^\circ$  (Figure 240 through Figure 242) the distributions are exhibiting increased deviations from the potential solution, particularly on the leeward side, where separation is preventing full pressure recovery. At  $10^\circ$ , for example, it is quite clear that the last 2 sensors are showing decreased suction over the last  $30^\circ$  peripherally. By  $17.5^\circ$  (Figure 245), pressure valleys are becoming pronounced. These are a result of the flow separation and probably coincide beneath the coherent vortices that form in such an open separation. At higher and higher angles of attack, the pressure distribution on the tail deviates more towards the windward side. The pressure valleys seem to get strongest in the 5th and 6th sensor, while flattening out over the last 3 sensors. At higher and higher angles of attack, the separation gets stronger, resulting in vortices with higher circulation. The higher circulation induces higher local velocities, which leads to a decrease in the pressure coefficient immediately beneath the vortical core. However, at higher and higher angles of attack, the primary vortices also move farther away from the model surface. Thus, the direct influence of the vortices on the local pressure distribution decreases. Therefore, because the rear sensors show little indication of the pressure valleys, this does not mean that there are no separation vortices above the model; instead, it means that the vortices are displaced away from the model surface. Indeed it is clear at the highest angle of attack ( $35^\circ$ , Figure 252), the pressure valley is strongest at the 4th sensor.

Figure 253 through Figure 261 show the same data, this time plotted for single sensors at all angles of attack. At  $x/L=0.11$  (Figure 253) the measured data agree reasonably well with the potential solution, and only start deviating significantly at around  $25^\circ$  angle of attack, probably due to flow separation. The sensor at  $x/L=0.23$ , just downstream of the trip posts, agrees over a much larger range of angles attack. At  $x/L=0.44$  (Figure 256), a valley starts forming at  $20^\circ$  and increases dramatically in strength at higher angles of attack. This is indicating a highly coherent vortex bound close to the model wall. The next station (Figure 257) shows a similar valley forming even earlier, but never reaching the same strength. In Figure 258 these valleys are much less noticeable. Instead, now the pressure distribution is flat, much like the leeside of a two-dimensional cylinder. The extent of this separated zone increases as one moves farther back on the tail.



It is interesting to note in many of these plots that the measured pressures sometimes deviate from the potential solution even on the windward side, where one would expect the potential solution to be accurate. These deviations sometimes can be larger than the uncertainties. As an example, Figure 250, for a  $30^\circ$  angle of attack, shows a significant deviation (more than the stated uncertainties) even on the forward-most sensor. Meier and Kreplin (1983) saw a similar effect in their data, as did Ahn (1992). Meier and Kreplin tried to account for it in a number of ways, including an "inverse blockage effect" as the result of taking data in an open throat tunnel. None of their explanations accounted for the magnitude of the deviation, and in a later paper the authors were referenced as describing the deviation as an "unexplained error." (Lien and Leschziner, 1995). In the Meier and Kreplin data set, Ahn's data set, and the present data set, the pressure measurements are *higher* than expected on the windward side, although by differing amounts. In the present case, wind tunnel wall blockage affects would result in a deviation *opposite* in direction as observed; that is, blockage would have caused lower pressure measurements. It is assumed that the deviation is the result of some form of strut interference or blockage effect, although the specific cause is not presently known.

### 6.3.2 Circumferential Pressure Gradient

Regardless of any offset that might be impressed on the pressure data, the pressure gradient distribution should otherwise remain unchanged. Figure 262 through Figure 275 show the pressure gradient distribution for all sensors at each angle of attack, while Figure 276 through Figure 284 show the pressure gradient distribution for each sensor at all angles of attack. In all of these plots, the negative of the pressure gradient is plotted, so a positive value indicates a favorable pressure gradient and a negative value indicates an adverse pressure gradient.

Even at the low angles of attack of  $2.5^\circ$  and  $5^\circ$  (Figure 262 and Figure 263), there is a small but significant deviation between the potential solution and the data on the tail. The data indicate a more favorable pressure gradient on the tail. This is the result of flow separation on the tail, caused initially by a more adverse pressure gradient, but resulting in a more favorable one after the onset of separation. This effect grows stronger at higher angles of attack. At higher angles of attack, the leeward deviations grow stronger; however, it is more important to recognize the increasing deviation in the windward-side pressure gradient, as the less favorable (and then more adverse) pressure gradients on the windward side are what lead to eventual flow separation. Again, peaks are clearly visible as indications of separated vortices, and at the highest angles of attack, 2 peaks can be seen on some of the middle sensors, perhaps indicating the presence of a second separation.

### 6.3.3 Pressure Fluctuations (RMS)

Figure 285 through Figure 293 show the RMS pressure fluctuation distributions for each sensor at all angles of attack. High RMS pressure fluctuations are usually found near a strong separation. Certainly, the growing peak at around  $130^\circ$  in Figure 285 is indicative of the laminar nose separation. This peak begins at around  $15^\circ$  angle of attack. What is interesting is that these fluctuations are very small for the second sensor, which is just downstream of the trips (Figure 286). The exception is at  $12.5^\circ$  and maybe even  $10.0^\circ$  angle of attack, where peaks are visible. This probably corresponds to flow conditions where the separation starts very near this sensor location ( $x/L=0.23$ ), but not farther noseward. The middle sensors (Figure 287 and Figure 288) show no noticeable trends, but sensor 5 (Figure 289,  $x/L=0.56$ ) shows strong double peaks at the highest angles of attack ( $27.5^\circ$  and up). These peaks are displayed in lessening degrees in Figure 290 and Figure 291. On the remaining two sensors (Figure 292 and Figure 293), only the first peak is visible, and it is much weaker at that. The first peak is likely due to the primary separation. It is not clear what the second peak corresponds to, but it has been conjectured that this accompanies a strong reattachment (Ahn, 1992).

### 6.3.4 Forces and Moments

Figure 294 shows the sectional lift coefficients (as calculated using pressure data) for each of the nine stations as a function of angle of attack. It is interesting to note that most of the lift is generated by the nose and not the separated tail. In fact, the tail section actually has a small but significant downforce. The highly accelerated fluid on the windward side near the tail is providing a large amount of windward suction, while the separation region is stagnant enough as to produce no noticeable suction at all.

Overall, however, the lift acting on the nose will outweigh the downforce on the tail. This is borne out in Figure 295, which shows the total body normal force and pitch moment coefficients (as calculated with pressure data) versus angle of attack. This data is plotted against the force and moment data of Ahn (1992). It is very interesting to note that the pressure data grossly underpredicts the lift magnitude, particularly at low angles of attack. This is due to the lack of longitudinal resolution. However, the force and moment data of Ahn (1992) does the same qualitative trends as the pressure data, including a shallow normal-force-curve slope below  $15^\circ$  and a much steeper one above  $15^\circ$ . The pitch moment in this figure is referenced about the model center. A nose-up pitch moment is generated about this point. Its slope steadily decreases at higher angles of attack and again the pressure data underpredicts the moment compared to the data of Ahn (1992).

## **6.4 Unsteady Results**

### **6.4.1 Pitchup Maneuver**

Figure 296 through Figure 300 show a comparison between the data taken during the pitchup maneuver and the steady data for all sensors at discrete angles of attack. At  $10^\circ$  and  $15^\circ$  (Figure 296 and Figure 297) any differences between the steady and unsteady data are the same order of magnitude as the uncertainties. By  $20^\circ$  (Figure 298) the differences are still marginal, with the exception of the pressure minima on the middle sensors. The peak position is further leeward for the pitchup data compared to the steady data, indicating the separated vortices are farther leeward and thus that separation has been delayed. At both  $20^\circ$  and  $25^\circ$ , it is interesting that the largest impact on the pressures occurs on the model sides ( $\phi = 60^\circ$  to  $120^\circ$ ). Of course, pressure changes in this surface region do not significantly impact normal force or pitch moments.

Figure 301 through Figure 305 show the time-varying nature of the pressure at fixed locations on the model. At the windward side of the model ( $\phi=0^\circ$ , Figure 301), as seen before, the deviations are small but tend towards slightly increased suction. Also, there are no significant deviations between the steady and unsteady cases until the higher angles of attack during the last third of the maneuver. Further around the model ( $\phi=50^\circ$ , Figure 302) the deviations again only occur during the last half of the ramp, and these deviations tend to indicate higher pressures during the maneuver compared to the steady data. Large differences are seen at  $90^\circ$  roll (Figure 303), particularly on the nose, but these do not contribute to the normal force. The deviations at  $135^\circ$  (Figure 304) are smaller except on the nose, where there is significantly more pressure at the end of the maneuver and consequently less lift. The leeward side (Figure 305) shows practically no differences that are significant compared to the uncertainties.

### **6.4.2 Submarine Maneuver**

Since the submarine maneuver only encompasses low angles of attack (less than  $14^\circ$  at all time), the deviations between the steady and unsteady data are not significant compared to the uncertainties. As an example of this, Figure 306 shows the submarine maneuver pressure distributions for steady and unsteady cases at  $12.5^\circ$  where the differences should be largest. While there appears to be more suction on the leeward side of the model during the pitchup maneuver, these trends are less than the uncertainties.

## 6.5 Future Improvements

Just because the differences between the steady and unsteady pressure fields are usually smaller than the uncertainties in this report, this doesn't mean these differences are not important. Subtle changes in the model surface pressures can have a large effect on the model forces and moments when integrated. When faced with the task of measuring the surface pressures on the model for either a steady flow or an unsteady maneuver, doing so with a low enough uncertainty is plausible if only looking at that one case in isolation. However, when comparing the steady and unsteady cases, the differences, while significant, are going to be small. Thus, the goal for such experiments should be to have uncertainties one order of magnitude lower than what would normally be tolerable. From that standpoint, the present uncertainties are barely adequate to point some important trends, but to better quantify these trends and to allow for the study of much more subtle, lower excursion maneuvers, uncertainties should be reduced from their present levels.

The primary uncertainty that needs to be reduced is the pressure measurement itself. The most important change is to find pressure transducers that have lower full scales and lower uncertainties. Special *in situ* calibration procedures may also need to be developed in order to minimize uncertainties further.

Also, it would probably be better to use a shorter length of tubing for the reference static pressure. Another option is to eliminate the static reference and instead measure absolute pressures. This would require very accurate total and dynamic pressure measurements, but this is the case anyway

Another issue that needs to be addressed is the correct reference dynamic pressure to use when computing the pressure coefficient. Steady blockage corrections are crude enough, and closed form simple unsteady corrections are just not achievable. Important information to obtain to address this issue might be dynamic pressure measurements in the model region during a maneuver or tunnel wall pressure measurements during a maneuver. Again, the differences between steady and unsteady wall pressures will be very low and will require very precise transducers. An absolute minimum precision required to qualitatively represent the unsteady pressure differences for the pitchup maneuver is  $0.01 q$ , where  $q$  is the dynamic pressure. For less drastic maneuvers like the submarine maneuver, even more precision may be required.

# Chapter 7: Force and Moment Measurements

---

## **7.1 Introduction**

Unsteady forces and moments will eventually become the staple measurement made on the DyPPiR, much as it is in steady wind tunnel testing, because the data describe a global effect of the aerodynamics on the model and as such provides much information in a small number of runs. This is contrasted to surface parameters, such as pressure and skin friction, which require one or more orders of magnitude more runs in order to get enough data to map out the data over the entire surface, or flow field measurements that require another order of magnitude in order to piece together the topology of a three-dimensional space. Steady force and moment data are difficult enough to acquire with precision. Unsteady force and moment measurements are more difficult to make, especially compared to pressure and skin friction. Below is a description of the various techniques used for quasi-steady force and moment measurements. Then a chronology is presented of the several iterations of force and moment transducers used on the DyPPiR. Finally, force and moment data are presented, and directions for future iterations are described.

## **7.2 Previous Work**

Force and moment measurement by strain gage balances is a staple tool for the aerodynamicist. Methods for designing, constructing, and implementing the strain gage balance are well-established for static measurements (see Ahn (1992) for a brief overview). The same is not true for dynamic force and moment measurements. As in any transducer used for measuring dynamic phenomena, the dynamic response of the transducer must be known and modeled in order to reconstruct the phenomena from the transducer response signal, or the frequency response must be properly tailored to eliminate dynamic distortion of the force signal. What follows is a description of force and moment measurement and reduction techniques for quasi-steady aerodynamics. This brief review only describes the reduction from an instrumentation and computation standpoint. Because the premise of linear dynamic aerodynamic analysis is not applicable for the types of DyPPiR maneuvers being performed, no information about stability derivative computation is presented.

### **7.2.1 Curved Flow Methods**

The simplest (from a force and moment measurement standpoint) implementation of force and moment measurements of dynamic phenomena is the curved flow technique as described by Marchman et. al. (1975). The model is held still and the air is made to curve around the model, thus simulating steady dynamic maneuvers. Another similar technique involves the straight flow of air over a mapped, curved model (Chang and Purtell, 1986). Of course, the forces acting on the balance in these cases are static, so standard static force and moment reduction methodologies can be used.

### **7.2.2 Rotary Balances**

For rotary-balance operators, force and moment data reduction can be dealt with in the time domain in different ways. Since a rotary balance provides dynamic motion in a circular trajectory, the forces and moments are sinusoidal. Malcolm and Schiff (1985) describe the techniques used at NASA Ames Research Center. First, the data are corrected for first order interactions. For their rotary rigs, the force and moment output signal contains an unsteady term, composed of sinusoidal gravitational oscillations and any unsteady aerodynamics affects, and the steady, desired aerodynamic term. The oscillatory portion is then removed with a low pass filter. Wind-off tares are used to eliminate steady inertial contributions.

O'Leary and Rowthorn (1985) describe a similar technique for the rotary balance at RAE. Instead of filtering out the gravitational sinusoidal contributions, the signal is averaged over one revolution, thus effectively eliminating such a component.

Jansson and Torngren (1985) describe the force and moment measurement techniques used at FFA for their low-amplitude rotary balance capable of speeds up to 300 rpm. All force and moment signals are low-pass filtered with a 20 Hz cut-off frequency. An in-phase/out-of-phase procedure is implemented. In the transonic rotary rig at FFA, forces and moments are sampled for a complete revolution in order to cancel out gravitational forces, and tare forces are taken to account for inertia. No dynamic corrections are made.

Bihrlé and Bowman (1980) describe a rotary balance installed in a vertical spin tunnel at NASA Langley. Due to the fact that the rotary motion is in a horizontal plane, there are no time-varying gravitational effects.

### **7.2.3 Forced Oscillation Mechanisms**

Forced oscillation operators use similar techniques. Once again, the maneuvers performed at these facilities are usually forced sinusoidal oscillations, so the force and moment output are also sinusoidal in nature. Goodman (1987) describes the set-up for the HSMB Large-Amplitude Horizontal Planar Motion Mechanism (LAHPMM). For these analyses, the output signal is broken up into in-phase and out-of-phase (or quadrature) components. These signals are then integrated over one period, and the resulting in-phase

and out-of-phase values yield stability derivatives for the model. Corrections are made for interactions between different balance components. A basic assumption here is that the dynamic response of the balance is perfectly flat. This is probably a good assumption, since the maximum frequency of the facility is only 0.20 Hz. Goodman (1960) outlines similar procedures in use at DTMB for their Planar Motion Mechanism (PMM), while O'Leary (1991) briefly describes the similar capability at Langley.

Schmidt, on the other hand, describes a forced oscillation mechanism for a transonic wind tunnel. This facility is capable of oscillations up to 20 Hz. An Integrating Digital Volt Meter (IDVM) is used on the unfiltered strain gage data to obtain the steady output magnitude. The dynamic signals are also each input to Vector Component Resolvers (VCR) that determine in-phase and out-of-phase components of each signal, each of which is measured by subsequent IDVMs. Each of these components yield different stability derivative information. Data are measured over roughly 20 seconds with wind on in order to get stable readings on the IDVMs. No corrections are made for the dynamics of the balance, including magnification and phase translation. This may become significant at such high frequencies.

Jansson and Torngren (1985) describe the force and moment measurement techniques used at FFA for their low-amplitude subsonic forced oscillation rig (pitch or yaw) capable of speeds up to 5 Hz. All force and moment signals are low-pass filtered with a 20 Hz cut-off frequency. An in-phase/out-of-phase procedure is implemented similar to the ones presented above. For the transonic forced oscillation rig, the signals are first broken up into DC and AC parts with filters, and then the AC part is amplified up to an additional 100 times. A dynamic calibrator was then used on the balance and the entire system to account for phase shifts and gain discrepancies in the system. From here, a cross-correlation technique was implemented to extract appropriate in-phase and out-of-phase components. (Forster and Hanff, 1979).

Jones et. al. (1978) describe a unique experiment that involved the forced oscillation of a cylinder and the measurement of the resultant dynamic drag. Jones et. al. analyzed the forces and moments in terms of time series, mean square value, power spectral density, autocorrelation functions, and probability densities of the lift data, in addition to in-phase and out-of-phase components of the lift force (Jones et. al., 1978).

Hanff (1977) correctly identified that balances designed for measuring dynamic phenomena need to be calibrated dynamically. As a result, Hanff has designed and implemented a dynamic calibrator capable of impressing accurately known, sinusoidal loads on the balances used in several forced oscillation apparatus at the National Research Council of Canada. The response can be measured and appropriate dynamical equations and parameters relating the balance input and output can be obtained. Hanff assumed that interactions between the different components (i.e., a yaw or roll moment output when a pitch moment is supplied) had to be negligible in order for the data reduction methodology to work; he found such interactions to be acceptably low. With all of this calibration information, Hanff could take the strain gage

outputs and reconstruct the dynamic forces and moments that caused them. He found this technique to work acceptably, with uncertainties on the order of a few percent in phase and amplitude. Hanff (1979) presents a similar rig for roll measurements. In addition, Hanff (1979) presents an analytical description of the dynamics of the balance/model system in one plane assuming a single mode, second order, lumped parameter model of the balance. Forster and Hanff (1979) describe the implementation of a cross-correlation technique for the extraction of these sinusoidal signals from noisy strain gage outputs.

Hanff (1983) notes that in most contemporary forced oscillation tests, the oscillation amplitude is small so that the aerodynamic forces are assumed to be linearly related to the model motion. This is hardly a valid assumption for large excursion maneuvers. Hanff (1983) recommends reducing the force and moment data in the frequency domain by using transfer functions to relate the strain gage output to the input forces and moments. Hanff (1983) assumes that the aerodynamic reactions can only contain frequency components equal to or related to the primary motion frequency. Inertial affects are eliminated (in the time domain) with a tare run. Finally, he assumes that the model-balance subsystem can be modeled in three independent planes with a suitable second order equation of motion. Johnson (1983) describes the similar utilization of a second order model equation for determining dynamic characteristics of balances in the design phase at FFA. In later tests, Hanff (1985) extends this technique to high excursion, non-linear aerodynamic regimes.

Kimura and Nomiya (1975) performed a dynamic calibration for a single component forced oscillation system. An analytical analysis was performed, but the researchers opted to use experimentally determined transfer functions instead. Treines (1975) models aerodynamic force and moment output with a *non-linear* second order equation to extract aerodynamic derivatives from high amplitude, free-oscillations in a transonic wind tunnel.

Luk (1981) describes a modal analysis technique that can utilize dynamic-calibration constants to predict response of a system with multiple modes of vibration. This technique is capable of modeling inter-component interactions and can be used to analytically and accurately account for the dynamic effects of additional mass, i.e. the addition of a wind tunnel model.

Drevet and Robert (1988) describe preliminary results from an experiment involving the forces and moments imparted on a missile with pulsating jets. The input force is typically sinusoidal, but results are presented for a trapezoidal-oscillation excitation. A three mode, second order model is used, along with accelerometer data and strain gage data, to extract the dynamic aerodynamic forces.

In all of these techniques, an underlying *aerodynamic* assumption is that the maneuvers studied are linear in nature and can thus be superimposed on top of each other to formulate general maneuvers (Etkin, 1972). However, in large excursion maneuvers, this assumption is entirely invalid (McCroskey, 1977). Therefore, the capability to simulate general maneuvers in the wind tunnel, as provided by the DyPPiR, is essential for this regime of truly unsteady aerodynamics.



### **7.3 Iteration 1: The Balance and Model of Ahn (1990)**

The first iteration was a balance and model system described by Ahn (1992). The model was designed to be very robust in order to prevent model distortion due to the dynamic loads incurred during projected maneuvers. The design boundaries of the original model were outlined without the benefit of an operational DyPPiR, and as a result the model was designed too conservatively. The original model design would have resulted in a 55 kg model. Before construction, the model weight was cut down to about 27 kg, and the present researcher cut it down even further by eliminating some of the structure, reducing the weight to 23 kg. The model consisted of a 6 mm thick chopped-strand fiberglass skin over a very stout aluminum frame. It is the same model used in the pressure and hot-film measurements presented in earlier chapters.

It was very difficult for the original designers of the DyPPiR to predict the maximum model accelerations. To allow for several g's of acceleration on a heavy model and adequate factors of safety, a balance had to be designed with a maximum normal force of 6200 N, and a maximum pitching moment of 340 N-m. Actual estimated loads for the pitchup maneuver are listed in Table 7, which lists a maximum normal inertial force of 1320 N and a maximum inertial pitch moment of 400 N-m. The 5-component balance (no drag flexures) is shown in Figure 307. This balance was designed using standard sting-mounted, bending-element strain gage techniques as used in most *steady* wind tunnel testing. The first problem that was identified was that the maximum aerodynamic force is on the order of 45 N and the maximum pitching moment 23 N-m. Therefore, during any dynamic maneuver, the inertial loads overwhelm the aerodynamic loads. This is because a tare run must be made with the wind off, and this data must be subtracted from data taken with the wind on. The desired aerodynamic loads are a small signal riding on a very large inertial offset, so two large signals must be subtracted to obtain the small desired signal. This is in general poor data acquisition practice. Assuming the full-scale uncertainties for this balance as stated by Ahn (1992) (NF +/- 7.5%; PM +/- 15%), the magnitude uncertainties on the normal force and pitch moment (using Ahn's designed full scale) are 460 N and 50 N-m. These uncertainties are larger than the full-scale aerodynamic loads being measured. However, Ahn did succeed in obtaining steady forces and moments because of the lack of inertial loads in those tests. (1992).

Before the magnitude of the inertial force problem was fully realized, the balance was used to take unsteady forces and moments. Data was taken with both the wind off, as a tare, and the wind on. Fifty ensembles of each the wind-on and wind-off cases were obtained and averaged for each maneuver. Figure 308 shows the response of one of the normal force gages during a pitchup maneuver. It was found that not only were the inertial forces very large, but the balance dynamics were such that the balance and model acted like a lightly damped mass-spring-dashpot system. The balance oscillations, excited by the inertial inputs, were huge, and made resolution of the aerodynamic forces and moments impossible

It was felt that the balance dynamics should be capable of being either modeled or measured. Initially, the raw data were manipulated very extensively to infer a simple second-order system transfer function (essentially using a mass-spring-dashpot-analogy), which is one characterized by a single resonant frequency (Cannon, 1967; Doeblin, 1990). Transfer function techniques, impulse-function techniques, and piece-wise ramps were all used, (Cannon, 1967; Doeblin, 1990), but it was found that all of these techniques performed equally poorly because they relied on the exact same model equation and were just different mathematical operations applied to the same ends. Other problems that occurred included the fact that a single mode, second order system was too restrictive to describe the system with precision and that the signal was transient in nature and not ergodic. The primary reason the reductions failed though was the huge uncertainties on the desired signal: the aerodynamic signal just did not exist in the data because the real uncertainties were larger than the aerodynamic loads. Attempts were then made to measure the transfer function of the model-balance system, which would allow for multiple modes to be measured and would relax the second order model restriction (Ewins, 1984; Luk, 1981; Cobb and Mitchell, 1990). A rigid frame was built, upon which the sting, balance, and model were mounted (Figure 309). A shaker excited the system with random noise, and a load cell on the model measured the input force. The random noise, input force, and all strain gage outputs were measured, and multi-modal transfer functions were obtained. However, it was found that the uncertainties inherent in measuring a transfer function made it impossible to extract the aerodynamic forces at all. Even if these transfer functions could be measured with adequate precision (and it is very difficult to analytically determine what this analytical precision is), they would be difficult to use in general practice because they depend on the model mass and moments of inertia which can be difficult to obtain with precision. Finally, the transfer function techniques still did not solve the problem of the huge uncertainties on the data itself.

In general, it was found that frequency domain techniques work best on ergodic signals. DyPPiR maneuvers tend to be transient, which presents problems when applying transfer functions, filters, and other frequency domain concepts. In this first iteration, second order model equations and filtering techniques were used in numerous ways to try to convert the oscillations from the balance output into the true, time-dependent forces and moments that had brought the oscillations about. All failed because of the truly transient nature of the signals being measured and because of the additional uncertainties brought in by the models and calibration processes. Based on all of these reasons and experiences, one of the primary conclusions from this set of tests is that *model/balance dynamics (distortion) should not be measured and compensated for; they should instead be eliminated entirely.*

## 7.4 Iteration 2: "Fly-weight" Balance and Light-weight Model

From the original iteration, several important points were noted. The first was that model mass, and even balance mass supported by the flexures, had to be absolutely minimized in order to bring the inertial forces down to the same order of magnitude as the aerodynamic forces. The second point realized was that the balance dynamics needed to be minimized. This requires essentially that the natural frequency of the model-balance system be very high, so that most of the force and moment signal is in a bandwidth where the balance response is essentially zero-order. Figure 310 shows a typical single-mode second order transfer function. The goal is to keep most of the signal dynamics in frequencies below the resonant frequency,  $\omega$ , or conversely to raise the natural frequency of the system to well above the range of the force and moment dynamics. The natural frequency is

$$\omega = \sqrt{k/m}$$

where  $k$  is some characteristic system stiffness and  $m$  is some characteristic system mass (Cannon, 1967). Therefore, to raise the natural frequency of the system, one must decrease the system mass or increase its stiffness. The natural frequency of the original balance-model system was roughly 20 Hz. It is assumed, since the fastest DyPPiR maneuvers take place in tenths of seconds, that the force and moment information is roughly in the tens of Hz range.

The first change made was to replace the heavy fiberglass and aluminum model with a much lighter composite one (Figure 311). A composite sandwich construction was used consisting of a 8 mm thick, 2 lb./ft<sup>3</sup> polyurethane foam core surrounded by single layers of 10 oz. eight harness satin carbon fiber cloth (Figure 312). The model was left completely hollow except for the sting mounting hardware. The model was made in two symmetric top and bottom halves. The final weight was roughly 2.3 kg, a savings of an order of magnitude over the previous iteration. Many of the design details for the model structure can be found in Roback (1995).

In addition, a new balance was designed and constructed (Figure 313). This was mandated by the fact that the inertial loads, and thus the balance full-scale range, would be at least an order of magnitude lower. The new balance was designed with 6 full components, and was set up to minimize the actual weight of the balance carried by the flexures. To achieve this end, several new features were incorporated. All flexures were designed to maximize their sensitivity-to-weight ratio. Therefore, instead of the bending flexures typically being solid beams, hollow structures were designed that provided the same stiffness (and thus the same strain under load) for several orders of magnitude less mass than a standard solid beam. The normal force/side force/pitch moment/yaw moment gage cluster was condensed into one small (2.5 cm long) set of flexures instead of the standard two flexures separated by a long moment arm, as in the balance of Ahn (1990). This decreased significantly the amount of mass carried by the rearward gages, but also

increased the balance's sensitivity to gage alignment errors. The roll gages and axial gages were heavier, so they were put aft of the main flexures. They too were optimized for minimum weight. Aluminum was chosen instead of steel because the flexure geometries resulted in very thin structures. The aluminum allowed thicker structures than the steel, thus making fabrication easier. Higher resistance ( $1500\Omega$ ) gages were used in order to allow a higher excitation voltage (15V), which increased gage sensitivity and allowed for stiffer flexures. Finally, the 12-bit data acquisition system used by Ahn (1992) was replaced by the 16-bit system described in the hot-film and pressure chapters of this report, thus increasing system resolution and again allowing for stiffer flexures. The balance was fabricated in the Aerospace machine shop, and all gaging was done by the author.

The system was tested on the DyPPiR. Data was again taken with both the wind off, as a tare, and the wind on. 50 ensembles of each the wind-on and wind-off cases were obtained and averaged for each maneuver. A typical result for the normal force gage with the wind on is shown in Figure 314. It is clear that the oscillations are still present, but this time the aerodynamic trend is evident beneath the oscillations. This proves that the light weight model played a key role in reducing the inertial loads to roughly the same order of magnitude as the aerodynamic loads. However, the presence of the oscillations still prohibits accurate determination of the true time dependency of the aerodynamic forces. It is noted that the frequency of oscillation is still roughly 20 Hz. This is because the balance stiffness  $k$  scales on the inertial loads, which scales on the model mass. Therefore, the model mass was decreased, but so was the stiffness by roughly the same amount, so the oscillation problem still remained.

It is important to point out the pitch vibrations in this case were of large enough a magnitude to be visible to the eye. The model would "shake" at the end of the maneuver, and sometimes the model tail would even hit the sting. This results in a real change in angle of attack with time that would have a serious impact on the aerodynamics if this system fully succeeded in measuring the forces and moments. It is important to note that the vibrations in the previous iteration were very small and were *not* visible by eye. While the natural frequencies of the two systems were similar, the stiffness magnitude was much higher on the balance of Ahn, so these vibrations were negligible. Also, this does not impact the hot-film or pressure measurements. Those measurements were made with a substitute "balance", which is even stiffer than the actual balance, in place for attaching the model to the sting. For further rigidity, set screws in the tail cone were tightened to the sting for the hot-film and pressure measurements, making motion of the model relative to the sting essentially impossible.

### ***7.5 Iteration 3: Two-point balance and Light-weight Model***

The solution to the balance problem rests on greatly increasing balance stiffness without decreasing sensitivity. The bending-beam type of balance system is completely incapable of meeting these

requirements. A similar need exists in the hypersonic community, where force and moment measurements take place during runs that are only milliseconds long, thus necessitating much higher stiffness model-balance-sting systems than can be afforded in most steady, subsonic wind tunnel testing (Jessen and Gronig, 1989). A configuration more suitable is the type used at the David Taylor Research Center for very large scale, static and quasi-steady, sting-mount submarine hydrodynamic testing (Goodman, 1960; Bedel, 1995). In these tests, the models are mounted to the sting by two sets of load cells that are separated by a large distance, with one set of load cells in the forward half of the model and the second set in the aft model half. Strain-based load transducers in general have small deflections of displacements when under load. However, while bending beam sting mounted balances used in many wind tunnel tests may bend by only a fraction of a degree, this translates into many millimeters at the model tips. If the transducers are placed at each model end, as they are in tests at DTRC, then each end can only move by a fraction of a millimeter, and overall system stiffness is greatly enhanced.

To test this concept on the DyPPiR, a two component system was constructed using off-the-shelf load cells (Figure 315). The load cells used were Transducer Techniques MLP-50 200 N single component load cells with tension and compression calibrations performed by Transducer Techniques. The load cells were connected to two of the same Measurements Groups 2310 Strain Gage Amplifiers used for all of the pressure measurements. The load cells were excited with 10 V, and the resultant signal was amplified 100 times. A key to the success of this system is that the load cells be mounted to the sting or model with low-friction pivots instead of rigid mounts. This prevents the sting or model structures from absorbing any of the moments acting on the model. These pinned mounts were provided by using hardened steel dowel rods fitted very closely in brass inserts. The pivots were mounted on a robust aluminum channel that was attached to the sting using the "fly-weight" balance as one mount, and two clamping blocks on the sting as other mounts. Solid carbon fiber inserts 10 mm thick were molded into the model skin to provide a very stiff, light weight, and precise mounting surface for the load cells. This system proved to be very stiff in normal force and pitch moment.

However, the system was much less stiff in roll because the load cells were not designed to take moments. The model could vibrate slightly in roll, and the load cell is sensitive to such an out-of-plane load. Thus, while results are not free from corrupting oscillations, they provide insight into the fluid dynamics of the unsteady maneuvers, as well as point toward the next iteration. Data was again taken with both the wind off, as a tare, and the wind on. 50 ensembles of each the wind-on and wind-off cases were obtained and averaged for each maneuver. The results from these tests are presented below.

## 7.6 Data Reduction and Uncertainties

The voltage read from each load cell was divided by the amplifier gain and multiplied by the calibrated stiffness as supplied by the load cell manufacturer; thus,

$$L_i = \frac{V_i K_i}{A_i}$$

where  $L_i$  is the load in N,  $A_i$  is the amplifier gain,  $K_i$  is the load cell stiffness in N/volt, and  $i$  indicates either the first (nose-mounted) or second (tail-mounted) load cell. The amplifier gain was calibrated with a HP-3478A multimeter. Input and output voltages were read and fitted with a least squares regression to obtain the amplifier slope. The square of the correlation coefficients on these calibrations were found to be higher than 0.9999999, thus assuring a very high accuracy on the amplifier gain calibration. It is therefore assumed that the uncertainty of the amplifier calibration does not contribute significantly to the force calibration. The load cell calibration supplied by the manufacture is accurate to within 0.5%.

For all cases, tares were performed with the wind off, and subtracted out as voltages. Therefore, the tares introduce uncertainties only in the accuracy and repeatability of the voltages. The voltages were measured with the 16-bit HSDAS-16 data acquisition card in a PC, and are thus accurate and repeatable to better than 1 mV. The full scale steady voltage in practice was 700 mV for load cell 1 and 140 mV for load cell 2. Therefore the full-scale voltage uncertainty is better than 1%. The force uncertainty is thus given by

$$\delta L = L \sqrt{\left(\frac{\delta V}{V}\right)^2 + \left(\frac{\delta K}{K}\right)^2}$$

which in a worst case results in a force uncertainty of 0.36 N for load cell 1 and 0.18 N for load cell 2. These occur at maximum loads of 76 N for load cell 1 and 18 N for load cell 2, or 0.5% and 1% respectively.

The aerodynamic forces acting on the model during the wind off tares are ignored. With the wind on, the inertial forces are roughly the same order of magnitude as the aerodynamic forces (see Table 7 for an estimate of all forces and moments acting on the model). In the wind-on conditions, the wind velocity is roughly 45 m/s. With the wind off, the maximum aerodynamic velocity of the model, being imparted by the model motion during a maneuver, is on the order of 1 m/s, or roughly 2% of the wind-on free-stream velocity. Since the aerodynamic forces on the body are roughly proportional to the square of the model velocity, the aerodynamic forces on the model with the wind off are less than 0.1% of the wind-on aerodynamic forces and are thus negligible. The maximum local Reynolds number, which will occur at both the nose and tail, is 2% of 4.2 million or 84,000. This is subcritical, resulting in a higher local "drag" coefficient (perpendicular to the model axis) that will be no more than double that at 4.2 million

(Schlichting, 1979), suggesting that even including subcritical Reynolds number effects the wind-off aerodynamic force can be no more than 0.2% of the wind-on aerodynamic force.

The normal force is calculated as the sum of the two load cells, so its uncertainty is better than 1% full scale. The pitch moment is computed from

$$M = L_1 d_1 - L_2 d_2$$

where  $d_1$  and  $d_2$  are the distances of the load cells from the model center. These values are 392 mm and 369 mm, respectively, and are each accurate to within 2 mm or roughly 0.5%. The pitch moment uncertainty is then

$$\delta M \approx \sqrt{(L_1^2 + L_2^2) \delta d^2 + d^2 (\delta L_1^2 + \delta L_2^2)}$$

Again, at full scale ( $M=23$  N-m), the uncertainty is less than 0.2 N-m, or better than 1% full scale.

The normal force coefficient is defined as

$$C_z = \frac{L_1 + L_2}{qS}$$

where  $q$  is the dynamic pressure, and  $S$  is the model frontal area. It is again assumed that the frontal area uncertainty does not contribute to the coefficient uncertainty. The dynamic pressure is found accurately to within 1%. The resultant full-scale uncertainty of the normal force coefficient is better than 1.5%, or  $\delta C_z=0.015$ .

The pitch moment coefficient is defined as

$$C_M = \frac{M}{qSL}$$

where  $L$  is the model length, which is again assumed to not contribute to the coefficient uncertainty. The pitch moment coefficient is accurate to better than 1.5% full scale, or  $\delta C_M=0.0035$ .

These uncertainties apply to the steady data exactly, but do not include uncertainties due to the dynamics of the model/balance system. Many attempts were made to model these dynamics or to even just filter out any oscillations, but all such efforts fail for the reasons mentioned above. It is impossible to assign an uncertainty level to the distortion caused by system dynamics in transient signals such as those generated by the maneuvers presented in this report. Therefore, while a true uncertainty level for the unsteady forces and moments is difficult to compute, the trends must be examined for system dynamics effects, and these effects must be differentiated from the true aerodynamic forces and moments.

## 7.7 Steady Results

Figure 316 shows the steady normal force and pitch moment coefficients for the prolate spheroid at various angles of attack up to 35°. The Reynolds number is 4.2 million, and trip strips were mounted at

$x/L=0.200$ . The data are compared with the data of Ahn, which are stated to have a 7.5% uncertainty on the normal force and 15% uncertainty on the pitch moment. It is clear that the two data sets easily agree to within the stated uncertainties on Ahn's data. The data were primarily taken with increasing angles of attack. However, several data points were repeated going back down (these are on the plot), and these were found to be repeatable to within the stated uncertainty of 1.5% full scale. While the normal force coefficient increases at greater rates at the higher angles of attack, the pitch moment settles in at a relatively constant slope at around  $\alpha=10^\circ$ .

## **7.8 Unsteady Results**

The normal force and pitch moments for the pitchup maneuver are shown in Figure 317. The oscillations, while small, do make it difficult to discern the trends in the lower angles of attack of the ramp. However, there is a definite lag in both the unsteady normal force and pitch moment. These dynamic distortions seem to be due mainly to a low frequency (roughly 6 Hz) signal component that exists in the wind on and wind off data. This is most easily seen in both the normal force and pitch moment plots as the damped sine waves that start at the beginning and ends of the maneuver. These damped oscillations are caused by the inertial impulse imparted on the model-balance system by the DyPPiR as it accelerates the model from rest into a steady ramp, and again as the DyPPiR decelerates the model back to rest at the end of the maneuver. The natural frequency of the load cell in a normal load mode is 2500 Hz, which is well above this observed frequency. During the maneuvers the model exhibited roll oscillations. It was soon determined that the model-load cell system was much less stiff in roll than in normal force/pitch moment. This is due to the fact that the load cells are not designed to withstand bending moments and the fact that the mounting area provided by the load cell consisted of only one bolt, which is adequate for a normal load but not adequate for a bending moment. Therefore, the low frequency oscillations are due to secondary roll oscillations of the model relative to the sting. The load cells are not designed to cancel out bending moments, so such loads imparted on the load cell corrupt the voltage output of the load cells.

There is another oscillatory component (roughly 15 Hz) visible in the wind-off and wind-on data that is slightly higher than the very low 6 Hz component but much less than the 2500 Hz natural frequency of the load cell. This oscillation is most easily seen at the end of the maneuver, while the model is at rest at  $30^\circ$  angle of attack. This oscillation is most likely due to the DyPPiR itself, as evident in Figure 11. this figure contains accelerometer data from the model taken during the pitchup maneuver. Despite the fact that the model is "at rest" at a constant  $30^\circ$  angle of attack, some vibratory load does occur, either due to the sting vibrating from the sudden stop or due to actual pressure inputs from the DyPPiR itself as it corrects and re-corrects the load required to suddenly hold the model at rest. These loads show up on the force and moment output.



In computing the aerodynamic loads, the wind-off force and moment time series is subtracted from the wind-on time series. The intent is that the undesired inertial loads will be identical for both the wind-off and wind-on cases and thus subtract out exactly. Since these loads are the same order of magnitude as the aerodynamic loads, it can be expected that small errors in the repeatability of the inertial loads will corrupt the computed aerodynamic loads. This is in fact the case. The residual oscillations in the aerodynamic force and moment time series correspond directly with oscillations in the inertial components of the wind-on and wind-off time series. There are several potential explanations for these effects. The primary argument is that the undesired loads, which includes mostly inertial loads imparted by the DyPPiR on the model but can also include the very small aerodynamic loads experienced during the wind-off tare runs, are actually slightly different from the wind-off case to the wind-on case. This is probably due to the loading effect of the aerodynamic forces and moments on the performance of the DyPPiR. It is important to stress that overall this effect should be small, at least as seen by the DyPPiR, since the DyPPiR force capacity is much larger than the aerodynamic forces generated by the prolate spheroid model. However small these inertial loads are, it is important to remember that they are *inputs* to a dynamical system, and that these small changes in the system inputs can have a more visible effect on the time series of the system output. As such, the low frequency oscillations that do corrupt the aerodynamic force and moment signals are relatively small. It is shown in the next section that the way to eliminate these distortions altogether is to design load cells that are very stiff in all modes of vibration (including roll), thus increasing the natural frequency of all modes to the point that damped sine oscillations no longer exist, and all that remains are actual measured loads, be they inertial or aerodynamic.

However, several attempts were made to eliminate these distortions from the aerodynamic signals. The response of the load cells was again modeled with second-order dynamic system impulse responses, but it was found that these did not come close to adequately modeling the oscillations for the precision required. The distortions in the final signals themselves were modeled as damped sin waves (outputs from a second order system given an impulsive input). These two did not faithfully eliminate the distortion, and required arbitrarily-selected parameters to come even close to matching the distortions. Finally, the wind-on and wind-off data were time-shifted relative to each other, but this also did not eliminate the distortions. The distortions can only be eliminated with properly designed hardware and *not* with any data post-processing.

In addition it is important to establish the nature of the lags that are shown in Figure 317. In examining the response of the balance to the aerodynamic loads, these pitchup-maneuver aerodynamic loads can be examined essentially as a ramp input to a second-order system, where the balance-model system in whatever vibrational mode studied behaves as the second-order system and as such exhibits a natural frequency and a certain amount of damping. For such a ramp input to a second-order system, the output lags the input in time by the following amount (Doeblin, 1990):

$$\Delta t = \frac{2\zeta}{\omega_n}$$

In this equation,  $\zeta$  is the non-dimensional damping coefficient ( $\zeta > 1$  is overdamped;  $\zeta = 1$  is critically damped;  $\zeta < 1$  is underdamped),  $\omega_n$  is the natural frequency in rad/s, and  $\Delta t$  is the amount of time that the output lags the input. In the case of the model-load cell system, in any mode the system is significantly underdamped, thus  $\zeta < 1$ . The wind-off pitchup force and moment data was used to roughly establish a conservative estimate of the natural frequency and non-dimensional damping coefficient for the lowest frequency component (the 6 Hz component). The damping coefficient was found to be less than  $\zeta = 0.01$ , and the natural frequency was found to be roughly 6 Hz. These values yield less than a millisecond lag between the input and output. In terms of the non-dimensional time units used in Figure 317, the maximum model-balance dynamics lag is less than 0.03 non-dimensional time units. The lags in the plots are on the order of one time unit. Therefore, these lags cannot be due to system dynamics and must be due to actual lags in the flow field. This analysis is very important, as it establishes for the first time a force and moment capability on the DyPPiR that adequately resolves flow-field lags from balance-induced dynamical effects.

It is important to establish the level of repeatability of the balance response. The 50 ensembles were examined to determine the standard deviation of the response over the 50 ensembles at each time step. Figure 318 shows the repeatability, measured as twice the standard deviation of the data over all 50 ensembles at each time step, for load cells 1 (nose) and 2 (tail) for both wind-on and wind-off conditions. The standard deviation is higher for load cell 1 because this is the nose load cell, and the forces on the nose are larger in magnitude than the forces on the tail typically. It is clear that the worst repeatability corresponds exactly with the portions of the force and moment time-series that exhibit the highest degree of distortion. In these regions, the maximum two-sigma repeatability (20:1 odds) for the wind-on case is 0.06  $C_Z$  units for the normal force. The corresponding value for the pitch moment, found by multiplying the normal force coefficient repeatability by the moment arm of the load cells (0.381 m) and dividing by the model length (1.37 m) results in 0.017  $C_M$  units for the pitch moment. This corresponds to roughly 4 times the normal force uncertainty and less than half the pitch moment uncertainty. In regions of the time series where distortion is low, the repeatability was an order-of-magnitude lower (better), or therefore less than the uncertainties.

It is also desirable to assess the potential impact of added mass forces and moments on the unsteady forces and moments during this maneuver. The force due to added mass is the product of any model acceleration relative to the free stream and some proportion of the mass (or inertia for rotational degrees of freedom) of the air displaced by the model (Lamb, 1945). First one must calculate the mass and inertia of the air displaced by the model. The volume of the spheroid is needed as it represents the amount of mass displaced by the model:

$$V_{model} = \frac{4}{3} \pi a b^2$$

$$m_{air} = \rho V_{model}$$

For  $a=0.656$  and  $b=0.114$ , and an air density of  $1 \text{ kg/m}^3$ , the mass of the displaced air is thus  $0.04 \text{ kg}$ . For the moment of inertia (in the pitching direction) of the displaced air, the following integration is performed:

$$dm = \rho \pi r(x)^2 dx$$

$$I_{air} = \int_{Volume} x^2 dm$$

$$= \int_{-a}^a \rho \pi r(x)^2 x^2 dx$$

$$= 2\pi\rho \int_0^a r(x)^2 x^2 dx$$

$$= 2\pi\rho \frac{2a^3 b^2}{15}$$

which results in the inertia of the displaced air being  $0.00036 \text{ kg-m}^2$ .

The force due to added mass in the normal force direction is then:

$$Z_{added\ mass} = k_2 m_{air} a_z$$

where  $a_z$  is the acceleration in the normal force direction and  $k_2$  is the added mass coefficient in the normal force direction. Similarly the pitch moment due to added mass is:

$$M_{added\ mass} = k' I_{air} \alpha''$$

where  $\alpha''$  is the angular acceleration and  $k'$  is the added mass coefficient in the pitch rotational direction (Lamb, 1945). The added mass constants are  $k_2=0.918$  in the normal force direction and  $k'=0.764$  in the pitching direction (Lamb, 1945).

It remains to determine the accelerations. Forces due to added masses only exist in flows with accelerations, or thus unsteady flows. In the pitchup maneuver as an example, there are two such accelerations. The first is an inertial acceleration, which is prevalent in both the wind-off and wind-on cases. There is an intended angular inertial acceleration required to start the pitching motion. There is also an unintended normal inertial acceleration. There should be no normal inertial acceleration because the model center is supposed to remain stationary. Due to slightly different lags in the plunge and pitch actuators, there is a slight motion of the model center of gravity (see section 2.3.1 or Figure 10) in the vertical direction; therefore there must also be vertical accelerations. These are the inertial accelerations measured on the model via the accelerometers and shown in Figure 11. For the sake of order-of-magnitude calculations, one can use  $\pm 6 \text{ g}$ 's as a representative maximum inertial acceleration and  $130 \text{ rad/s}^2$  as a representative angular inertial acceleration.

The second type of acceleration, that is only present in the wind-on case, is the acceleration due to the fact that the model is changing its orientation in time with respect to the free stream, or equivalently the free stream changing its orientation with respect to the model. This is born in a crossflow acceleration, thus:

$$V(t) = U_{\infty} \sin(\alpha(t))$$

$$V'(t) = \frac{d\alpha}{dt} U_{\infty} \cos(\alpha(t))$$

This is due to a rotation of the free stream relative to the model and is thus present during the entire ramp portion of the maneuver. There would be a similar longitudinal *deceleration*, resulting in an added mass thrust, but this analysis is only concerned with normal force and pitch moment. Also, since the ramp is at a constant angular rate, there is no similar angular flow acceleration during the maneuver. Assuming the pitch rate is constant at  $\pi/2$  rad/s and a free-stream velocity of 45 m/s this crossflow acceleration is:

$$V'(t) = 7.2 \cos(\alpha(t)) \text{ g's}$$

So this crossflow acceleration will range from 7.2 g's at  $\alpha=0^\circ$  to 6.2 g's at  $\alpha=30^\circ$ . The average crossflow acceleration is roughly 6.7 g's during the entire maneuver.

It is also important to note the direction that these forces are in. The added mass force is always in a direction opposite the acceleration. For the inertial normal acceleration, the added mass force is negative (downforce) at the start of the motion and positive (normal force) at the end of the maneuver. The crossflow acceleration added mass force is always in a positive (normal force) direction. The total acceleration of the model relative to the flow is the sum of the inertial acceleration and the crossflow acceleration. This results in almost no added mass effect at the maneuver start, since the negative inertial acceleration and the positive crossflow acceleration roughly cancel out. There is a positive acceleration during most of the maneuver due to the crossflow acceleration, and this results in an added mass force in the direction of positive normal force. The magnitude of this force, assuming a mean crossflow acceleration of 6.7 g's, is 2.4 N, or in terms of non-dimensional normal force coefficients,  $\delta C_{Z, \text{ added mass}} = 0.047$ . This is three times the stated uncertainty of 0.015. At the end of the maneuver, the crossflow acceleration *adds* to the inertial acceleration associated with stopping the model for a sum acceleration of roughly 12 g's, resulting in a normal added mass force of 4.3 N or  $\delta C_{Z, \text{ added mass}} = 0.085$ , fully five times larger than the stated uncertainties. Therefore, for the pitchup maneuver, the added mass normal force is at least detectable in that it reaches levels larger than the uncertainties. Also note that the added mass force should be such that it yields a net force *larger* than the equivalent steady state force. These estimates are for the wind-on case. The wind-off case will result in added mass force generated only at the beginning and end of the maneuver.

The added mass effect perhaps explains why the lags in the force and moment data are smaller than the lags in the separation location data. The added mass effect is such that a larger, not smaller, normal

force should be generated. This is equivalent to the unsteady data leading the steady data, or the added mass resulting in a leading time constant. Using an estimated  $\partial C_z / \partial t'$  of 0.11 from Figure 317, a 0.047 positive shift in the normal force is equivalent to a 0.4 non-dimensional time lead. This may mean the effective force and moment lag of the flow field, minus added mass effects, is higher than the 1 time unit shown and may be as high as 1.4 non-dimensional time units.

For the pitch moment, the only accelerations are at the beginning and end of the maneuver. Using  $130 \text{ rad/s}^2$  as a representative angular acceleration,  $0.00036 \text{ kg-m}^2$  as the inertia of the displaced air, and  $k'=0.764$ , the moment due to added mass effects is  $0.036 \text{ N-m}$ , or  $\delta C_{M, \text{ added mass}}=0.0005$ . That represents a moment much smaller than the pitch uncertainty and is thus negligible. So there do not appear to be added mass effects in the pitch moment measurements.

Figure 319 shows the normal force and pitch moment, respectively, for the submarine maneuver, while Figure 320 shows the repeatability as a function of time for each load cell for the submarine maneuver. The trends are much less clear in this maneuver than in the pitchup maneuver due to the lower relative aerodynamic forces and moments for this lower-excursion maneuver. It is clear in Figure 320 that the standard deviations are considerably higher during most of the maneuver for the nose load cell (load cell 1) compared to the data from the pitchup maneuver (Figure 318). Dynamic distortion is much lower at the start of this maneuver due to the lower accelerations imparted at the gentle initiation of this maneuver. However, the accelerations at the end of the maneuver are large and result in a significant stopping oscillation. The lags in the pitch moment are actually larger in this maneuver compared to the pitchup maneuver, but the normal force lags are smaller. However, such distinction in lag magnitude is hampered by the relative level of the force and moment uncertainties (see section 7.6).

## 7.9 Future Iterations

Two main goals remain to be reached before a viable, robust force and moment system is in place on the DyPPiR. The first is to improve signal fidelity. As demonstrated in section 7.4 this can be further improved by reducing the model weight, but will be most improved by increasing the balance stiffness. It was learned in the last balance iteration that system stiffness is required in all possible degrees of freedom. In the case of the two-point balance system, a limiting condition was the fact that the load cells were not very stiff in roll. The MLP-50 load cells used in the final force and moment iteration are foil-strain-gage based. As shown below, semiconductor strain gages offer much higher sensitivity than foil gages, and thus could be used to increase balance stiffness. This sensitivity is expressed as a "gage factor" ( $GF$ ), and is related to the force voltage signal through

$$V_{out} = V_{in} AGF\epsilon$$

where  $V_{out}$  is the output voltage signal,  $V_{in}$  is the excitation voltage,  $A$  is the amplifier gain, and  $\varepsilon$  is the sensor strain (Doebelin, 1990). A load cell is usually designed for a maximum strain, so this equation shows that the maximum strain is inversely proportional to the gage factor, all other things held constant. The desired force is usually translated into a strain via some form of a bending beam, usually a beam restrained such that its end slopes are zero. The bending beam element's mechanical properties are such that, considering a nominal mounting location for the strain gage and a cross section of given aspect ratio, the beam's strain is inversely proportional to the cube of the beam thickness; using simple beam theory, it can be shown that the gage factor is then directly proportional to the cube of the thickness:

$$\begin{aligned}\varepsilon\left(\frac{x}{L}\right) &= \frac{PLt}{2EI}\left(\frac{x}{L} - \frac{1}{2}\right) \\ w &= \gamma t \\ I &= \frac{1}{12}wt^3 = \frac{1}{12}\gamma t^4 \\ \varepsilon &\propto \frac{1}{t^3} \\ \therefore GF &\propto t^3 \text{ or } t \propto \sqrt[3]{GF}\end{aligned}$$

where  $x/L$  is some station along the beam (or the strain gage location),  $L$  is the beam length,  $t$  is the beam thickness,  $w$  is the beam width,  $\gamma$  is the cross-sectional aspect ratio,  $I$  is the cross sectional moment of inertia,  $P$  is the load, and  $E$  is the modulus of elasticity (Riley and Zachary, 1989). The beam stiffness is the load divided by the deflection, and is thus proportional to the fourth power of the thickness:

$$\begin{aligned}k &= \frac{P}{y} \\ &= \frac{12EI}{L^3} \\ &\propto t^4\end{aligned}$$

It follows that the stiffness is proportional to the 4/3rd power of the gage factor in a properly designed, strain gage based load cell. When one considers that a typical foil gage factor is on the order of 2, while a semiconductor gage factor can typically be 140, a stiffness gain of well over 200 times can be realized with no loss in balance sensitivity.

The second major goal that still needs to be achieved is to obtain all six force and moment components instead of just two. To measure side force and yaw moment in addition to normal force and pitch moment requires twice as many gages, and, more importantly, a two-degree-of-freedom gimbaled mount for each load cell pair. These are challenging to design on such a small scale, but are achievable. What is more difficult is measuring axial force and roll moment without compromising balance stiffness. The load cells are oriented longitudinally relative to the model, so all forces and moments measured

perpendicular to the longitudinal axis are inherently stiff as shown in the DTRC system (Bedel, 1995). The two components parallel to such an axis can not similarly benefit from the two-point configuration. In addition, even in a four component system, the load cells must be designed to be very stiff in all six components. Axial gages can actually be incorporated quite easily at each load cell cluster without compromising balance stiffness. It is clear that the roll moment provides the most serious stiffness constraint on a longitudinally-oriented two point balance system. The DTRC system incorporates a special roll moment gage block that is designed very similar to the roll moment flexures in the original DyPPiR balance (see Figure 307). However, the DTRC system does not require the stiffness in roll that the DyPPiR system will due to the quasi-steady nature of their tests.

## Chapter 8: Discussion

---

### **8.1 Flow Separation: Definitions and Measurement Techniques**

Flow separation plays a dominating role in the aerodynamic performance of many systems. In most experimental settings, there has truthfully not been a need to identify separation location rigorously to better than  $5^\circ$  or  $10^\circ$  of circumferential position. When comparing flow conditions with more subtle differences, such as when comparing steady and unsteady cases, more precision is needed, both in the measurement capabilities used and in the rigor of the definitions and indicators used to interpret the data.

Topologically, general three-dimensional separation off a body exists as a line of intersection between the body surface and a "separation sheet" that acts as a fluid boundary (Simpson, 1995). Since this separation, both as a sheet in the free stream and as a line on the model surface, is a real boundary, no fluid can pass through it, and thus streamlines on either side of a separation converge asymptotically to the separation sheet/line. The important side effect of separation, and thus its defining trait, is the breakdown of "normal" boundary layer flow, resulting in the significant departure of fluid away from the body surface, and creating regions of relative backflow on opposite sides of separation (Simpson, 1995). This separation "event" can ideally be traced to a single defining stream surface and line in the flow field.

Several different measurement techniques are used as indicators of separation. It is instructional to examine these different techniques from the standpoint of their respective implications on what is meant by separation. Each of these indicators are based either directly or indirectly on the definition of separation, or are based on some other observation about the flow in a separation region. Some of these indicators and their descriptions of separations are listed thus:

**Description: Separation occurs at a limiting surface skin friction line formed by neighboring skin friction lines that converge on the separation line.**

*Indicator: Oil flow visualization.*

Pigment streaks in the oil flow pattern indicate surface skin friction directions. In strongly separated flows, separation lines are easy to pick out, as are other flow features. Separation initiation is difficult to pinpoint in practice, and separation lines in weakly separated flows are also difficult to discern. In general, Simpson et. al. (1991) have shown that the oil flow itself tends to predict separation early, but this observation was based upon a comparison with skin friction



magnitudes obtained from hot film measurements. Oil flows can also influence transition and thus transition-sensitive separations.

*Indicator: Surface skin friction direction and magnitude via directionally sensitive hot-film sensor measurements.*

Measurements of the surface skin friction magnitude and direction, such as those performed by Kreplin et. al (1985), provide perhaps the most direct way of measuring separation location, with perhaps the exception being near-wall flow field measurements. The sensors only rely on a relationship between heat transfer and skin friction, which tends to be at least monotonic and in practice can be accurate to better than 5% in relative magnitude and theoretically exact in direction. Errors are only introduced by either roughness effects, which can be eliminated by making the sensors flush with the model, or errors due to heating the fluid, which are much more difficult to quantify, but are assumed to be negligible due to the rapid mixing associated with both turbulent boundary layers and separated flows. Measurements in one cross section, however, are not adequate for precisely locating separation. This would only be possible if the local direction of the separation line is known *apriori* (which is not generally the case). Instead, the entire field of measured skin friction magnitudes and directions needs to be integrated to obtain the wall bounded streamlines. An example of this is presented in Figure 321. In this case the definition used is rigorous, but limitations are placed on this technique based upon the carryover of measurement uncertainties and spatial resolution into the numerical uncertainties of the integrations and interpolations required to obtain the skin friction patterns. A further advantage of this technique is no magnitude calibration is required of the sensors. Only directional calibration is necessary in order to recreate the model surface skin friction lines and thus the separation lines.

**Definition: Local crossflow velocity (W) is zero.**

This definition stems from the fact the separation line bounds one edge of a separation sheet, which feeds into the flow and is a stream surface. As such, no flow can pass through it. Therefore, the flow velocity perpendicular to this sheet must be zero. This is in fact similar to examining a cross-flow streamline pattern in a separated region and searching for the one streamline that leaves perpendicular to model surface. However, this streamline is *not* a rigorous descriptor, as the crossflow velocity is dependent on the coordinate system used to present the velocity data and thus the streamlines. The velocity must be

transformed to a coordinate system that is locally perpendicular to the separation line. As will be shown, the exact velocity coordinate system used only plays a significant role in weak separations.

*Indicator: Near wall three-component LDV measurements.*

Laser Doppler Velocimetry, such as used in the study by Chesnakas and Simpson (1994; 1995) is presently the only practical technology for making accurate, near wall measurements of all velocities, specifically the cross-flow velocity. The measurements must be made very close to the wall because the separation sheet is only normal to the model surface very close to the wall and skews leeward very rapidly as one traverses through the boundary layer. Thus, hot wires are completely unsuited towards accurately identifying separation. However, since the crossflow velocity is identically zero *on* the wall at all locations, measurements must be made far enough away from the wall in order to obtain velocities high enough to not be dominated by uncertainties.

An example of this type of data is shown in Figure 322. Here, the data of Chesnakas (1995) at  $x/L=0.77$  and  $20^\circ$  angle of attack have been interpolated to obtain circumferential crossflow-velocity distributions at various fixed radii away from the model. The crossflow velocity  $W$  is in a body referenced coordinate system. The point where  $W$  is zero closest to the wall is the separation location. At the farthest radii, the crossflow velocity changes sign at around  $150^\circ$ , but as one moves towards the wall (decreasing  $W$ ), that crossing point moves windward until it seems to converge at around  $123^\circ$ .

However, this crossflow velocity is *not* exactly perpendicular to the separation line location. Using the oil flows to obtain the approximate local separation line direction, the velocities of Chesnakas and Simpson (1996) were rotated to a coordinate system perpendicular to the separation line. Figure 323 shows the resultant crossflow velocity distributions. The separation line, now more accurately defined, has moved leeward by about  $6^\circ$  to  $117^\circ$ .

**Definition: Wall-normal velocities are maximum very near separation.**

This argument is based on a more fundamental description of separation as a process, specifically the significant departure of fluid away from the model. Tobak and Peake (1982) show that converging streamlines on each side of a separation by necessity result in large wall-normal velocities at separation. However, there is no requirement for the *largest* wall-normal velocity to correspond *exactly* to the separation location. In the limit, the separation sheet is perpendicular to the model surface, but again, it quickly skews leeward away from the model surface. However, perpendicularity of the separation sheet

does not require a maximum wall-normal velocity; instead, it requires a change in the sign of a properly oriented crossflow velocity. Therefore, while large wall-normal velocity represents a necessary condition for separation, it does not serve as an exact separation indicator.

*Indicator: Near wall three-component LDV measurements.*

Again, LDV gives a direct measure of these velocities. The advantages and disadvantages as listed above still apply. The only further advantage is that this technique is valid independent of coordinate system so long as the coordinate system chosen is normal to the model surface. No information about the separation line direction is needed. Still, such an LDV capability would be much better served measuring crossflow velocities as a means of separation detection.

*Indicator: Surface skin friction magnitude via directionally insensitive hot-film sensors.*

This is perhaps the easiest technique of all, as it requires the least amount of measurements. It is also the most indirect. This measurement technique not only relies on the wall-normal velocity as an indication of separation, it also relies on the wall shear as the best indicator of the wall-normal velocity. In light of this latter indicator, a minimum in wall shear magnitude is assumed to be an indication of maximum wall normal velocity, which is in turn interpreted to be the separation location. In practice this is actually a good set of assumptions in strongly separated flows, but becomes less robust in weakly separated flows. The discrepancy between the wall shear minima and the true separation location stems from the "low-velocity trough" described by Chesnakas and Simpson (1996) that exists in such crossflow separations. This low-velocity trough refers to the region of fluid on the downstream-side of a separation line. This fluid exhibits very low momentum compared to the fluid impinging on the upstream-side of separation. Therefore, wall shear minima will be biased towards this low velocity trough, and as such will be located downstream of the true separation line.

Figure 324 through Figure 328 shows a comparison of the separation lines from the oil flow data and hot-film data from this report and the LDV data of Chesnakas and Simpson (1994;1995) for angles of attack from  $10^\circ$  to  $30^\circ$ . In all cases, the oil flows show the separation forming windward of the skin friction minima. There is more than a  $10^\circ$  discrepancy at  $10^\circ$  angle of attack, but also the constant current minima line is traced all the way to the nose. The hot-film data indicate laminar separation on the nose, but this was not seen in the oil flows. The two shaded diamonds show the separation locations determined from the crossflow velocity data of Chesnakas and Simpson presented above. The higher shaded diamond, at around  $127^\circ$ , is the separation location determined using the zero crossflow velocity in body coordinates. The lower

diamond, at around  $123^\circ$ , shows the location determined using the transformed crossflow velocity in a plane normal to the separation line. It is clear in this case that this correction can move the determined separation by as much as  $5^\circ$  circumferentially closer to the oil flow. At each of the higher angles of attack, the hot-film data consistently lags both the primary and secondary separation lines (more leeward than the oil flow primary separation lines, more windward than the oil flow secondary lines). An identical effect was seen in the separations on a normal cylinder studied by Bellhouse and Schultz (1966). The possible exception is at  $25^\circ$ , where the constant temperature skin friction minima agrees with the oil flows in some regions better than the constant current data. These plots also show the precision difficulty in locating either oil flow separations or skin friction minima. Both are difficult to do because they require a certain amount of subjectivity.

Of all of the techniques presented, the LDV data are the most detailed and most direct, but also represent by far the most complicated, time consuming, and expensive. The hot film data present the easiest technique, but do not pin down the exact location. Perhaps the best compromise is the directional skin friction gage, which requires twice the effort of the non-directional gage for the same number of measurement locations, but also provides the capability of deducing the exact surface skin friction pattern. This still does not solve the problem of locating the separation line given directional skin friction data. While this data would make possible plots like those of Kreplin et. al. (Figure 321), there would still remain the problem of algorithmically extracting the separation lines from all of the other skin friction lines. While this is superficially easy to do by eye, getting a computer to extract such lines accurately, and coming up with specific rules for determining separation initiation locations, would still be challenging.

## ***8.2 Quasi-Steady Flow-Field Description for a Pitching Prolate Spheroid***

Based on the data presented in this report, one can piece together significantly detailed descriptions of the flow field at various angles of attack. One can use this to postulate how a quasi-steady flow field would develop. By "quasi-steady" it is meant that the flow field is dependent on time only through other variables' time-dependence. For the present description, it will be assumed that the flow field is instantaneously dependent only on angle of attack. Once this quasi-steady flow field is fully described, it can be contrasted to the actual unsteady data to determine what pure time dependencies exist that cause the unsteady data to depart from the quasi-steady model.

In the two maneuvers tested, the model starts at  $0^\circ$  angle of attack at rest. The flow is attached over most of the length of the model, and only separates somewhere on the extreme tail. The flow field is essentially axisymmetric. The pressure field behaves inviscidly with the exception of slightly increased pressures near the tail due to the thickening and eventual separation of the rearward boundary layer. The flow field is essentially two-dimensional, if examined in any model plane of symmetry, and thus the

separation line behaves like a two-dimensional separation in that it is normal to the model surface, is characterized by zero velocity and thus zero wall shear, and extends in a closed ring around the model tail. The present data make it difficult to pick out how far rearward this separation occurs, but for fully turbulent separations like the ones simulated in these tests, the separation location can be as far back as  $x/L=0.95$  (Meier et. al., 1987). Considering the rear 3.8 cm (or 3% of the total model length) of the model was removed for the sting, no measurements were made anywhere within the probable separated zone at zero incidence.

As the model starts to move, the windward flow decelerates while the leeward flow accelerates. This necessitates that the separation will start to skew, moving upstream on the leeward side in response to the lower pressures, while moving downstream on the windward side against higher pressures (for example, see Figure 240). For very small angles of attack it is probable that the separation line still exists as a closed ring, just skewed so it isn't perpendicular to the model center line. But considering how far back the separation is at low incidence, it isn't long before the separation "runs out of tail" and actually leaves the model surface. In this case, the separation line then forms a streamline that leaves the model and convects downstream from the model through the model wake. The separation is now a crossflow separation instead of a normal separation. It takes the form of either Figure 1a or Figure 1b. On a full prolate spheroid (one without the tail removed), this event probably happens at a higher angle of attack than for the model with the severed tail. Regardless, the actual process of switching from the normal separation of the zero incidence flow field to the closed crossflow separation at very low angles of attack is probably highly complex and nonlinear. None of the present data documents these changes, but it is arguable that these changes are not of practical interest due to the fact that the tail of most real bodies is obstructed by surfaces and propulsors. In addition, any non-linearities in the forces generated will have minimal effect on the body (since the force is still oriented almost entirely parallel to the model) compared to the forces generated at higher angles of attack.

A similar process must also occur fairly shortly after the normal separation becomes a crossflow separation. The crossflow separation at this point is termed "closed", or alternatively "global", because it emanates from a saddle point singularity that occurs downstream of the separation (Tobak and Peake, 1982). This results in one separation line spanning both model sides and crossing through the leeward plane of symmetry. In turbulent crossflow separations, this type of separation is atypical. This closed, crossflow separation quickly evolves into two distinct, open crossflow separations (one on each the left and right sides of the model, see Figure 1c). Again, the data do not provide insight into this process, but the data of Kreplin et. al. (1985) seem to support the idea that open crossflow separation has fully occurred by  $5^\circ$  angle of attack. For the same reasons listed in the preceding paragraph, this process of changing from closed separation to an open one, while highly complex, is of little engineering interest.

By 5° angle of attack, the flow is exhibiting open crossflow separation on the tail. This is limited to a very small region of the tail. The constant current hot-film data, which does extend back to  $x/L=0.907$ , does indicate wall shear minima (Figure 32). These minima are very weak, however. In flows with weak separations, the separations are very difficult to detect. In this case, a wall shear minima is a necessary but insufficient criteria for separation. A fully attached flow will exhibit a wall shear minima anywhere where the flow is decelerating or where the shear layer is thickening. Such is certainly the case upstream of separation. As has been discussed earlier, this phenomenon makes pinpointing the spatial initiation of a crossflow separation impractical.

Regardless of the nature or location of this separation, it is very limited in its extent and therefore does not contribute significantly to the forces and moments acting on the body. Since the flow is mostly attached, the body can act as a reasonably efficient lift generator (efficient compared to how it behaves at large angles of attack). The nose in particular sees significant lift generation (Figure 294). This also results in a nose-up pitch moment (Figure 316).

As the model goes through higher and higher angles of attack, the crossflow separation becomes more pronounced, extends more noseward, and moves more towards the windward side (see Figure 70, Figure 71, and Figure 102 through Figure 104). The separation tends to be located significantly more windward on the tail than on the nose. The skin friction minima become increasingly pronounced at increasing angles of attack as the separations increase in strength (Figure 38 through Figure 69, and Figure 90 through Figure 101). The pressure distributions on the tail of the model reflect the increasing separation through less and less pressure recovery (Figure 253 through Figure 261). This results in the tail of the model not contributing to the overall lift of the model, and even in many cases contributing a downforce (Figure 294). The separated flow reattaches at  $\phi=180^\circ$ . This results in momentum transfer towards the windward side, circumferentially a “backflow”, that converges on the separation line from the leeward side (Figure 2). This fluid has significantly less momentum than the fluid on the windward side of the separation. So low is the separation that a “trough” of low-momentum fluid exists just leeward of the separation (Figure 238). This trough is observed in the velocity measurements of Chesnakas and Simpson (1996) and the oil flows detailed in this report. This low-velocity trough is responsible for the true skin friction minima being leeward of the true separation location (Figure 324 through Figure 328).

As the separation grows stronger, the fluid in the separated zone rolls up into a vortical structure. By 17° the separated flow has formed a truly coherent vortex that is also close enough to the model surface to cause localized pressure peaks from at least  $x/L=0.56$  to  $x/L=0.69$  and maybe even extending slightly farther in both upstream and downstream directions (Figure 245). Typically, pressure distributions in a crossflow separation are “flat” regardless of the structure of the separation. Pressure data often can’t provide detailed insight into the flow-field structure due to the influence of the entire flow field on the

pressure of every point of the model surface (Townsend, 1976). The exception is when a vortex is strong enough and close enough to the model surface to form a pressure peak. Upstream of  $x/L=0.56$  the vortex is not strong enough to actually result in a real pressure peak, while downstream of  $x/L=0.69$  the vortex is far enough off the model surface to minimize its direct effect in the model surface pressures. At this point, however, the adverse pressure gradient (Figure 268) on the model leeward side is strong enough to force a secondary separation, smaller in strength than the primary separation, and opposite in sense (Figure 71 and Figure 105). The evolution of this secondary separation mimics that of the primary separation in that it starts at the extreme tail, probably at around  $15^\circ$  angle of attack, and slowly moves nose-ward at increasing angles of attack. Unlike the primary separation, however, the secondary separation seems to reside at a fixed circumferential location over its extent.

By  $20^\circ$  angle of attack, the separation has extended to the forwardmost 20% of the model, ahead of the trip strip (Figure 72 and Figure 106). At this point, transitional effects play an important role in the separation fluid dynamics. The laminar flow on the nose results in a laminar separation forming at roughly  $\phi=120^\circ$ . After the laminar boundary layer separates, it quickly undergoes transition and reattaches to the model, forming a localized separation bubble like the one described by Poll (1985) (Figure 3). The newly attached turbulent boundary layer then proceeds farther around the model until it re-separates. Therefore, the nose exhibits two separations much like the tail, but the structure is significantly different. The "second" separation on the nose is not a "secondary" separation and is not topologically joined to the secondary separation formed on the tail. Instead, the separation on the nose is most precisely a "second primary separation", formed as a result of transition effects only. Immediately downstream of the trip strip the laminar flow undergoes transition very quickly. This forces the separation, which was laminar in nature immediately upstream of the trip strip, to turn sharply leeward and join up with the turbulent separation within 10% to 20% of the body length. The movement of the separation line leeward also necessitates increased leeward momentum, so the nose turbulent separation also diverts leeward, but much more slightly than the nose laminar separation. Therefore, the two nose primary separations join shortly downstream of the trip strip, forming a "forked" separation pattern on the nose. It is important to note that without flowfield measurements it is very difficult to thoroughly characterize the true nature of this separation structure, particularly the laminar nose separation and how it is affected by the strips. It is possible that this separation actually reattaches before joining up with the turbulent nose separation. The skin friction measurements made immediately downstream of the trip strip were highly irregular, making it difficult to pick out minima with certainty (see Figure 42 and Figure 92). The oil flows were only capable of reproducing the forked separation flow once, presumable because the oil flow mixture was forcing premature transition (Figure 236 and Figure 237). But even in the one case where a forked separation was observed in the oil flows, there was some speculation as to the nature of the nose laminar separation downstream of the trip strip.

The flow has basically reached its final form, at least for angles of attack up to  $35^\circ$ . As the model completes the quasi-steady maneuver and reaches  $30^\circ$  angle of attack, the separations grow strong (Figure 73, Figure 74, and Figure 107 through Figure 112). The primary separation does not move much farther up on the nose than  $x/L=0.1$ . Both of the nose separations also surprisingly do not change their circumferential location much from formation at  $20^\circ$  angle of attack until  $30^\circ$  angle of attack. The turbulent separation downstream of the trip strip does tend to continue to move more windward at increasing angles of attack. The exception is that the separation at  $x/L=0.882$  stops moving windward at basically  $20^\circ$  angle of attack, while the separation at  $x/L=0.831$  stops migrating windward at roughly  $25^\circ$  angle of attack. This suggests that the separations move windward quickly at lower, increasing angles of attack until at some angle of attack the separation movement slows down considerably. This angle of attack at which the separation movement stops is different at different model locations, generally increasing as one moves noseward. Considering a cylindrical analogy, the separation lines should all converge at roughly  $\phi=120^\circ$  at  $90^\circ$  angle of attack (Bertin and Smith, 1989). The skin friction minima at  $x/L=0.882$  (Figure 68 and Figure 101) is at around  $102^\circ$ , and separation is several degrees windward of that. Therefore, this would suggest that if the maneuver were carried out to  $90^\circ$  angle of attack the separation would actually have to reverse direction and move leeward slightly to reach the correct final position.

The movement of the separation plays a huge role in the generation of forces and moments. The sectional lift coefficients computed from the pressure data indicate that the tail creates a downforce that increases in magnitude with angle of attack but levels out at around  $10^\circ$  angle of attack for the sensor at  $x/L=0.90$  (Figure 294). A similar trend is also seen on the rest of the tail sensors, and the middle sensors indicate a sectional lift coefficient that initially drops but later starts increasing. The sectional lift coefficients on the nose continually increase positively. Because the tail downforce increases and then decreases in magnitude at increasing angles of attack, the overall normal force increases at a greater rate at the higher angles of attack than it does at the lower angles of attack (Figure 316). Equivalently, the prolate spheroid has a higher lift curve slope at  $30^\circ$  angle of attack than it does at  $0^\circ$  angle of attack. Smith and Nunn (1976) show a similar trend for an ogive-cylinder configuration. For similar reasons, the pitch-moment slope is steeper at  $0^\circ$  angle of attack than it is at  $30^\circ$  angle of attack.

Meanwhile, as the maneuver is finished and the primary separation moves windward, the secondary separation tends to extend farther towards the nose (Figure 73, Figure 74, and Figure 107 through Figure 112). It is even probable that a tertiary separation has formed on the rear of the tail by  $30^\circ$ , but such a separation, if it exists, is too weak to detect with either oil flows or hot-film measurements.



### ***8.3 Unsteady Aerodynamics on the Prolate Spheroid***

The two maneuvers presented here represent non-dimensionally slow maneuvers, and thus the unsteadiness is subtle. In all cases, with the possible exception of some isolated and highly uncertain pressure measurements, the unsteady data lags the steady data. This is clearest in the separation data. The separation locations on the nose form much later in the pitchup maneuver, but also do not migrate very much during the maneuver (Figure 118(a) through Figure 119(c), Figure 130, and Figure 131). Downstream of the trips (Figure 120(a) through Figure 129(c); Figure 132 through Figure 141; Figure 154 through Figure 161), the separations lag both in formation and migration but quickly converge to the steady state case after the end of the maneuver (Figure 162). During the maneuver, the separations can lag the steady separations by as much as  $15^\circ$ . Perhaps more important is the associated time lag, which can range from 1.5 to 4.5 time units. These time lags are neither identical nor constant for each model location, thus pointing to the overwhelming complexity not only of a three dimensional separation but also of its time-dependent formation. Pending the development of a more robust, next-generation separation location system based on these findings, one could study in great detail the parametric effects of pitch rate, pitch range, pitch direction (up or down), Reynolds number, center of rotation, and even pitch maneuver shape (such as using the submarine maneuver or any imaginable maneuver) on the separation formation and migration. Such data could lead to dynamical models of unsteady separation on axisymmetric bodies.

The lagging separation locations implies lagging normal force and pitch moment. For the most part, the force and moment data obtained with the two point balance supports these trends (Figure 317), and the pressure data do to a lesser degree (Figure 301 through Figure 305). The force and moment lags are much smaller than the separation location lags in general. This may be due to the fact that the majority of the normal force and pitch moment is generated by the attached nose flow, which also exhibited the least amount of flow unsteadiness. So while the crossflow separation on the rear two-thirds of the model is significantly affected by the model motion, the delay in separation at the tail plays less of a role in lagging the forces and moments. Again, more robust systems will allow one to determine not only whether the unsteady aerodynamics lead or lag the steady data, but will also bring out more specific details about the processes involved and point to improved dynamical models. The lags shown here do not eliminate the possibility for unsteady aerodynamics leading in some cases. In fact, one of the few other pitching axisymmetric-body data sets in the literature, that of Smith and Nunn (1976), shows the normal force is higher than, and thus leading, the steady data. This is referred to as "dynamic lift" and is a phenomenon more often associated with the vortical separations occurring on delta wings at high angle of attack. In the case of Smith and Nunn, the largest dynamic lift occurs at very high ( $>50^\circ$ ) angles of attack. Below  $50^\circ$  angle of attack, the unsteady data do not vary beyond the uncertainties for the unsteady case from the steady data. In addition, this case was assumed fully laminar, whereas the present case is mostly turbulent.

The original publications reporting the pressure data (Hoang et. al., 1994a,b) interpreted the pressure data as supporting dynamic lift. This was without due consideration for the true uncertainties on the data and the scaling necessary to make the data meaningful. Those publications did conclude correctly, however, that the unsteady data results in a shift of the vortex suction peaks leeward, thus indicating delayed separation and less, not more, lift. Interestingly, the unsteady Navier-Stokes calculations of Taylor et. al. (1995) for these same maneuvers support the trend that the suction peaks are more leeward during the maneuvers compared to the steady case. Taylor et. al. did not report the computed forces and moments, however.

## Chapter 9: Conclusions

---

Some features of steady and unsteady flow over a 6:1 prolate spheroid were measured experimentally. All tests were conducted at  $Re = 4.2$  million. Trip strips were located on the model at  $x/L=0.20$ . The steady flowfield was established with surface pressure measurements, constant-current and constant-temperature hot-film surface skin-friction measurements, oil flow visualization, and force and moment measurements. The hot-film data showed the location of the crossflow separation on the leeward side of the model, and indicated its formation at the tail at low angles of attack, its migration forward and windward at increasing angles of attack, and its eventual split into two nose separations, one laminar and one turbulent. The oil flow data corroborated these trends, but also showed that the hot film data tends to lag the oil flow data by as much as  $10^\circ$ . Also, the oil flows were much less successful at retaining the "forked" nose separation, which is probably due to some interference from the oil flow mixture itself resulting in premature transition. The oil flows also indicated that for such bodies of revolution, the trip strips located at 20% are only fully effective at low (less than  $15^\circ$ ) angle of attack. At higher angles of attack, the laminar flow on the nose can separate before the trips, resulting in a flow field not typical of the high Reynolds number flows trying to be simulated. Future axisymmetric models should have trip strips much farther forward on the nose, perhaps even as far as  $x/L=0.05$ .

Surface pressure, constant-temperature hot-film, and force and moment measurements were made on the model in two maneuvers. Each of the transducers required special attention for them to work for unsteady measurements and for the uncertainties to be low enough for the data to be meaningful. For the use of these transducers to become routine, all of the transducers still require further refinement and uncertainty reduction. The surface pressure measurements could only resolve differences between steady and unsteady data at angles of attack great than  $15^\circ$ ; thus, no differences were seen for the submarine maneuver, but small differences were seen for the pitchup maneuver. This lack of differences does not mean that significant differences do not exist; it only means that the differences were less than the uncertainty on the pressure measurements. The hot-film data showed definite lags in the formation and migration of the separation line for the pitchup maneuver, but showed much weaker trends for the submarine maneuver due to the much weaker separations at the lower angles of attack. The force and moment development proved to be the most difficult, but an ultra-stiff, two point balance was successfully implemented along with a very light-weight composite model. The force and moment data again shows definite lags at the higher angles of attack of the pitchup maneuver in both normal force and pitch moment, but shows only pitch moment lags during the submarine maneuver.

## Chapter 10: Suggestions For Future Work

---

### **10.1 Overview**

The work presented herein provides a basis upon which to design and conduct future experiments in unsteady aerodynamics. As in the report, the suggestions are broken up into those for future unsteady experiments and future unsteady measurement system development.

### **10.2 Future Unsteady Experiments**

The next logical step from an experiment design standpoint is to try to relate the unsteady lags of the various data sets to maneuver parameters. The types of parameters that should be studied are non-dimensional pitch rate, pitch direction (compare pitch-down to pitch-up), model pitch center, and model pitch range. Lags in separation location, pressure fields, and force and moment generation between steady and unsteady data sets can then be parameterized based upon these parameters for each model position studied (for surface flow parameters like skin friction and surface pressure). This will provide data for a wider range of flows for developing flow models and testing CFD codes. Focus should initially be placed on force and moment data because it requires fewer runs to obtain results for these different maneuver parameters, but eventually surface skin friction and pressure data will be very valuable for explaining the force and moment lags and freeing up models to allow lags to be different at different model locations.

Future work is planned for full submarine configurations instead of simple prolate spheroid bodies. This will allow the effects of sails and appendages and their lags on the flowfield to be studied in detail. This will make surface parameter measurements more difficult since the body will no longer be fully axisymmetric, so rolling the model to locate sensors at different circumferential locations will not be as easy or even possible. Either full rings of sensors will need to be installed or all mounted appendages will need to be remotely movable on the model surface. In addition, maneuvers with time dependent roll trajectories are planned for this model.

One possible force and moment experiment that would be very beneficial and informative would be to perform standard small-amplitude, forced-sinusoidal-oscillation maneuvers as a means to determine the model's stability and control derivatives. The results from these tests could then be used to try to simulate the truly unsteady trajectories, such as the pitchup and submarine maneuvers, in order to outline specific flow regimes where these stability and control derivatives do and do not work.

Experiments are currently also planned for an F-18 configuration and an automobile configuration.

## **10.3 Measurement System Improvements**

### **10.3.1 Constant Temperature Hot-Film Sensor Measurements**

Further reductions in hot-film measurement uncertainty are possible. First, the 16-bit HSDAS A/D board was handicapped due to the requirement to run it in single ended mode. Particularly due to the ground problems found in the anemometers, this increased the effective voltage measurement uncertainty significantly. Single-ended mode was used because more than 8 channels (the maximum number of differential-mode measurements) were required. A multiplexer can be purchased that would allow up to 32 differential-mode voltage measurements. For the HSDAS data acquisition board, this would reduce the maximum per-channel sampling rate to 6250 Hz, but this sampling rate is much higher than the one actually used for the data in this report (512 Hz). Additional multiplexers could be daisy-chained to provide up to 128 differential-mode voltage measurements at a per-channel sampling rate of 1562 Hz, again plenty high for all envisioned experiments.

Another major source of uncertainty was flow temperature fluctuations. There is no feasible way to control the wind tunnel temperature presently. Therefore, the flow temperature must be measured accurately some way. Methods are used and presented in detail in this report for cases when these flow temperature measurements are not accurate enough (better than  $0.1^{\circ}\text{C}$ ), but are not recommended if a more direct and robust method can be found. Measurement systems exist to measure air temperature to within  $0.01^{\circ}\text{C}$ , although these can cost more than \$1000. Another technique is to repeat sensor measurements at some fixed angle of attack, most easily  $0^{\circ}$  angle of attack, every 15 minutes or so (which is essentially what was used to calibrate the sensors in this work). This is still limited if accurate flow temperatures are not known. Also, the impact of flow temperature uncertainty can be reduced by running the anemometers at a higher overheat ratio.

Finally, too many resistances were required for accurate data reduction for the data in this report. This includes current-monitoring resistances and lead resistances. Lead resistances can be eliminated entirely by using a four-wire method, which essentially uses two leads to supply the current to the sensor and two to measure its voltage drop (Omega Engineering, 1995). This would double the number of wires required per sensor, but would eliminate all lead-resistance effects. Any current monitoring resistors, rather than being measured in the lab, could be replaced with ultra-high-precision resistors (0.01%). Also, sensor cold-resistance measurement could be made more stable by submerging the sensor in an oil bath to stabilize temperature fluctuations. Finally, the temperature coefficient of resistivity for the BALCO foil could be measured explicitly instead of relying on the supplied value of  $0.0051/^{\circ}\text{C}$ .

New anemometers should be constructed for any future tests. The existing anemometers were very hard to stabilize and had a hard time running at the high currents necessary. Using contemporary

components, new, very simple anemometers could be designed and constructed in house. A "bare-bones" anemometer is all that is needed as the frequency response of the sensor/anemometer system does not need to be any higher than a few hundred Hertz and therefore would require no impedance-matching variable inductors, variable bridge ratios or even calibrated overheat-ratio-setting potentiometers. The anemometers would need to be designed purposefully to minimize circuit instabilities and be able to supply at least 500 mA of current.

New sensors could be designed. The present sensors were designed for a much larger model and a constant-current anemometer system. New sensors could be designed with a higher sensor resistance, smaller effective area, smaller thermal mass, and thus higher frequency response, although this would also make the sensor less robust. Plug-mounted sensors, instead of sensors glued to the model surface, could be considered to make sensor interchangeability and replacement easier. Also, directional sensors could be incorporated, which would provide the information necessary to determine exact separation locations at the expense of more leads running from the models and more anemometers required.

### **10.3.2 Surface Pressure Measurements**

The surface pressure measurement system will require higher precision transducers to reach its full potential. New sensors need to be selected with a range of less than 3.5 kPa differential. Most vendors do not make miniature transducers with ranges smaller than 14 kPa, such as the ones used in this work. Therefore it is possible that a custom transducer might need to be commissioned for this capability to be feasible. Also, larger (in size) low-range pressure transducers exist, however they will take up more room in the model and will require longer tubing runs to the model surface. It is important that any such tubes do not reduce the transducer frequency response to below several hundred Hertz for temporal accuracy.

If possible, more pressure transducers should be used in future work. It is especially true that more transducers should be placed on the nose since this is where the largest pressure changes occur and this is also where most of the useful lift is generated. No pressure transducer should be placed on the nose tip since it is so close to the stagnation point that the pressure changes with angle of attack are very small.

### **10.3.3 Force and Moment Measurements**

More improvements can be made in the force and moment measurement methodology. First, custom load cells should be designed and constructed that are very stiff (natural frequency greater than 500 Hz in all possible modes of vibration) and reject undesired loads well. Semiconductor strain gages can be used to this end. Model mounting points need to be more stable and use at least four mounting bolts while keeping weight low. These mounting points should probably be aluminum instead of carbon fiber, but should be molded integral with the model skin. New pivots should be incorporated that decrease friction

and play. All of these requirements need to be made in a package that is compact and sturdy to make it durable and usable in many different models.

Attempts should be made to reduce model weight even further. A newly designed model will use thinner carbon fiber and thicker foam to achieve 50% less weight per unit area while at the same time slightly increasing model stiffness. Instead of making the model in two complete halves, the nose from one half should be permanently attached to the other half to make a solid, seam-free nose for at least 20% of the model length. The rest can serve as a removable "lid", allowing ample access to the inside of the model.

Trip strip placement should be re-considered. The nose trips should be placed farther forward than 20%, perhaps as far forward as 5%. The tail flow must be examined very closely at high angles of attack to verify that the flow is fully turbulent. Longitudinal trips similar to those used in Wetzel and Simpson (1993) might be considered.

#### **10.3.4 DyPPiR Improvements**

Some possibilities do still exist for improvement in the capability and usability of the DyPPiR. While the plunge control system works extremely well, the pitch and roll control systems have yet to achieve the same level of fidelity. Most improvements will be made by cleaning up any remaining electrical noise in the system with the goal of making the control system more accurate than the resolution of the 12-bit D/A converters.

The present version of the control program essentially limits maneuvers to one second in length. This limitation is a computer memory limitation. A new version of the control program is completed (but still requires thorough testing) that allows the user to program the DyPPiR D/A updating rate, which was previously hardwired at 4000 Hz. For most maneuvers performed, updating frequencies an order of magnitude lower (in the hundreds of Hertz) are all that are required. This capability increases the maneuver length capability of the control program to several minutes, which is much longer than any "maneuver" will ever be on the DyPPiR. It remains to be seen how long of a maneuver the DyPPiR hydraulics can perform, although there are two reserve hydraulic pumps installed in parallel to the pump presently used that would triple the available flow rate and thus increase the maximum length of a maneuver significantly.

The DyPPiR has presently been run fairly conservatively. Future work will document upper practical speed bounds, providing for the possibility of faster, and thus more unsteady, maneuvers. For example, the submarine maneuver for which data was taken is characterized by a 0.25s dimensional ramp time. This maneuver has been successfully run as fast as 0.15s, although no data was taken at this rate. While higher rate maneuvers will provide more dramatic unsteadiness, it is also possible to program maneuvers with tailored acceleration profiles that aren't so drastic and don't impose the high (5g or high)

loads on the model characterizing the present maneuvers. Such smaller accelerations will result in lower inertial loads for the force and moment measurements and lower wear and tear on the DyPPiR itself.

### **10.3.5 Other Possible Measurements**

To aid in unsteady blockage correction development, wall surface pressures could be measured. The same resolution and uncertainty limitations of the model surface pressure measurement system apply.

One common assumption made is that the model and sting are stiff, and therefore the pitch actuator position accurately reflects the model angle of attack. However, verifying this being "visual" proof is difficult. It is possible to consider building a system that, at least in limited cases, can measure the true model orientation (angle of attack, plunge position, roll position) independent of the pitch actuator position to account for sting or model mount deflections. Such techniques could not be gravity-based due to the inertial loads applied to the model by the DyPPiR. Optical methods have been considered in the past (Hoang et. al., 1994).



## References

---

Ahn, S., Choi, K. Y., and Simpson, R. L. (1989), "The Design and Development of a Dynamic Plunge-Pitch-Roll Model Mount", AIAA-89-0048, AIAA 27th Aerospace Sciences Meeting, Reno, NV.

Ahn, S. (1992), *An Experimental Study of Flow Over a 6 to 1 Prolate Spheroid at Incidence*, Dissertation, Virginia Polytechnic Institute and State University Aerospace Engineering Department.

Agarwal, N. K., Maddalon, D. V., Mangalam, S. M., and Collier Jr., F. S. (1992), "Crossflow Vortex and Transition Measurements by Use of Multielement Hot Films", *AIAA Journal*, Vol 30., no. 9, pp. 2212-2218.

Band, E. G. U., and Payne, P. R. (1980), "The Pressure Distribution on the Surface of an Ellipsoid in Inviscid Flow", *Aeronautical Quarterly*, February, 1980, pp. 70-84.

Barber, K. M., and Simpson, R. L. (1990), *Mean Velocity and Turbulence Measurements of Flow Around a 6:1 Prolate Spheroid*, Aerospace and Ocean Engineering Report, VPI-AOE-174, Blacksburg, VA.

Barber, K. M., and Simpson, R. L. (1991), "Mean Velocity and Turbulence Measurements of Flow Around a 6:1 Prolate Spheroid", AIAA-91-0255, 29th AIAA Aerospace Sciences Meeting, Reno, NV.

Barberis, D., and Molton, P. (1993), "Experimental Study of 3-D Separation on a Large Scale Model", AIAA-93-3007, 24th AIAA Fluid Dynamics Conference.

Bedel, J. (1995), David Taylor Research Center, Bethesda, MD, Private Discussion.

Bellhouse, B. J., and Schultz, D. L. (1966), "Determination of Mean and Dynamic Skin Friction Separation and Transition in Low-Speed Flow with a Thin-Film Heated Element", *Journal of Fluid Mechanics*, vol. 24, part 2, pp. 379-400.

Bendat, J. S., and Piersol, A. G. (1986), *Random Data*, John Wiley & Sons, New York, N.Y.

Bertin, J. J., and Smith, M. L. (1989), *Aerodynamics for Engineers*, Simon & Schuster, Englewood Cliffs, NJ, pp. 86-88.

Bihrlé, W. Jr., and Bowman, J. S. Jr. (1980) "Influence of Wing, Fuselage, and Tail Design on Rotational Flow Aerodynamics Beyond Maximum Lift", *Journal of Aircraft*, vol. 18, no. 11, AIAA-80-0455R.

Blackwelder, R.F. (1981): "Hot-Wire and Hot-Film Anemometers", *Methods of Experimental Physics: Fluid Dynamics*, vol. 18, part A, pp. 259-314.

Cannon, Robert H. (1967), *Dynamics of Physical Systems*, McGraw-Hill Publishing, New York, NY.

Chang, M. S., and Purtell, L. P. (1986), "Three Dimensional Flow Separation and the Effect of Appendages", *16th Symposium on Naval Hydrodynamics*, Berkeley, CA, pp. 352-370.

Chesnakas, C. J., Simpson, R. L., and Madden, M. M. (1994), *Three-Dimensional Velocity Measurements on a 6:1 Prolate Spheroid at 10° Angle of Attack*, Virginia Polytechnic Institute and State University, VPI-AOE-202.

Chesnakas, C. J., and Simpson, R. L. (1994), "An Investigation of the Three-Dimensional Turbulent Flow in the Cross-Flow Separation Region of a 6:1 Prolate Spheroid," *Experiments in Fluids*, Vol. 17, pp. 68-74.

Chesnakas, C. J., and Simpson, R. L. (1996), "A Detailed Investigation of the 3-D Separation about a 6:1 Prolate Spheroid at Angle of Attack", AIAA-96-0320, 34th Aerospace Sciences Meeting and Exhibit, Reno, NV.

Christophe, J. (1980), "A New Rig for Flight Mechanics Studies in the ONERA Aerothermodynamic Test Center of Modane", AIAA 80-0464.

Choi, K. and Simpson, R. L. (1987), *Some Mean Velocity, Turbulence, and Unsteadiness Characteristics of the VPI&SU Stability Wind Tunnel*, Virginia Polytechnic Institute and State University, Aerospace and Ocean Engineering Dept. Report VPI-AOE-161

Cobb, R. E., and Mitchell, L. D. (1990), "Estimation of Uncorrelated Content in Experimentally Measured Frequency Response Functions Using Three Measurement Channels", *Mechanical Systems and Signal Processing*, pp. 449-461.

Corcos, G. M. (1963), "Resolution of Pressure in Turbulence", *Journal of Acoustical Society of America*, Vol. 35, no. 2, February 1963, pp. 192-199.

Coulter, S. M., and Buchanan, T. D. (1980), "Description of a New High-Alpha, High-Load, Pitch-Yaw Dynamic Stability Test Mechanism at AEDC", AIAA 80-0451.

Doebelin, Ernest O. (1990), *Measurement Systems: Application and Design*, McGraw-Hill Publishing Company, New York, N.Y.

Drevet, J. P., and Robert, M. (1988), "Mesures des Efforts Instantanes Sur une Maquette Soumise a des Variations Rapides de Commande", AGARD-CP-429, no. 26.

Etkin, B. (1972), *Dynamics of Atmospheric Flight*, John Wiley & Sons, New York, NY.

Ewins, D. J. (1984), *Modal Testing*, John Wiley & Sons, New York, NY.

Feyzi, F., Kornberger, M., Bachor, N., and Ilk, B. (1989), "Development of Two Multi-Sensor Hot-Film Measuring Techniques for Free-Flight Experiments", ICIASF 1989, Goettingen.

Forster, L. R., and Hanff, E. S. (1979), "A Second Generation Instrumentation System for Measuring Cross Coupling Derivatives", ICIASF 1979.

Fu, T. C., Shekariz, A., Katz, J., and Huang, T. T. (1994), "The Flow Structure in the Lee of an Inclined 6:1 Prolate Spheroid", *Journal of Fluid Mechanics*, Vol. 269, pp. 79-106.

Goodman, A. (1960), "Experimental Techniques and Methods of Analysis Used in Submerged Body Research", *Third Symposium on Naval Hydrodynamics; High Performance Ships*, Report No. ACR-65, Office of Naval Research, Department of the Navy, David Taylor Model Basin.

Haldeman, C. W., Coffin, J. B., Birtwell, E., and Vlajinac, M. (1973), "Improvements in Magnetic Balance Systems Required for Magnus Testing", ICIASF 1973.

Haldeman, C. W., and Covert, E. E. (1979), "New Techniques for Production of Combined Spinning and Coning Motion with Magnetically-Suspended Wind Tunnel Models", ICIASF 1979.

Hanff, E. S. (1977), "A Dynamic Calibrating Apparatus for Cross Derivative Experiments", ICIASF, 1977.

Hanff, E. S. (1979), "Measurement of Direct and Cross-Coupling Derivatives due to Oscillatory Roll", ICIASF 1979.

Hanff, E. S. (1983), "Determination of Non-Linear Loads on Oscillating Models in Wind Tunnels", ICIASF 1983.

Hanff, E. S., Jenkins, S., and Prini, A. (1985), "Instrumentation and Other Issues in Non-linear Dynamic Testing in Wind Tunnels", ICIASF 1985.

Hoang, N. T., Barber, K. M., Walker, D., Simpson, R. L., and Wetzel, T. G. (1994), "Design and Development of an Optical Pitch Sensor Utilizing Polarized Infrared Light", AIAA-94-0734, 32nd Aerospace Sciences Meeting and Exhibit, Reno, NV.

Hoang, N. T., Wetzel, T. G., and Simpson, R. L. (1994), "Unsteady Pressure Measurements over a 6:1 Prolate Spheroid Undergoing a Pitch-up Maneuver", AIAA-94-0197, 32nd Aerospace Sciences Meeting and Exhibit, Reno, NV.

Hoang, N. T., Wetzel, T. G., and Simpson, R. L. (1994), "Surface Pressure Measurements Over a 6:1 Prolate Spheroid Undergoing Time-Dependent Maneuvers", AIAA-94-1908, 12th AIAA Applied Aerodynamics Conference, Colorado Springs, CO.

Jandel Scientific. (1995), "Loess Smoothing Algorithms", *Jandel Scientific World Wide Web Home Page*, [www.jandel.com](http://www.jandel.com).

Jannson, T., and Torngren, L. (1985), "New Dynamic Testing Techniques and Related Results at FFA", AGARD-CP-386, no. 20.

Jessen, C. and Gronig, H. (1989), "A New Principle for a Short-Duration Six Component Balance", *Experiments in Fluids*, Volume 8, pp. 231-233.

Johnson, G. I. (1983), "Some Design Considerations Regarding Multicomponent Transducers for Static and Dynamic Load Measurements", ICIASF 1983.

Jones, G. W. Jr., Cincotta, J. J., and Walker, R. W. (1978), "Aerodynamic Forces on a Stationary and Oscillating Circular Cylinder at High Reynolds Numbers", NASA TR R-300.

Jung, Walter G. (1986), *IC Op-Amp Cookbook*, Prentice Hall Computer Publishing, Carmel, Indiana.

Kays, W. M., and Crawford, M. E. (1980), *Convective Heat and Mass Transfer*, McGraw-Hill Book Company, New York, NY.

Kimura, H., and Nomiyama, A. (1975), "Stabilized Resonance Method for Measuring the Oscillatory Aerodynamic Derivatives at Subsonic and Transonic Speeds", ICIASF 1975.

Kreplin, H. P., Meier, H. U., Mercker, E., and Landhauber, A. (1986), "Wall Shear Stress Measurements on a Prolate Spheroid at Zero Incidence in the DNW Wind Tunnel", DFVLR Report Mitt. 86-06.

Kreplin, H. P., and Stäger, R. (1993), "Measurements of the Reynolds-Stress Tensor in the Three-Dimensional Boundary Layer of an Inclined Body of Revolution", *Ninth Symposium on Turbulent Shear Flows*, Kyoto, Japan, paper no. 2-4, 1993.

Kreplin, H. P., Vollmers, H., and Meier, H. U. (1982), "Measurements of the Wall Shear Stress on an Inclined Prolate Spheroid", *Z. Flugwiss. Weltraumforsch.*, Heft 4, pp. 248-252.

Kreplin, H. P., Vollmers, H., and Meier, H. U. (1985), *Shear Stress Measurements on an Inclined Prolate Spheroid in the DFVLR 3m x 3m Low Speed Wind Tunnel, Göttingen - Data Report*, DFVLR Report IB 222-84 A 33.

Lamb, H. (1945), *Hydrodynamics*, Dover Publications, New York, N.Y., p. 155.

Lien, F. S., and Leschziner, M. A. (1995), "Computational Modeling of Multiple Vortical Separation from Streamlined Body at High Incidence", *Tenth Symposium on Turbulent Shear Flow*, Pennsylvania State University, PA, pp. 4-19 to 4-24.

Luk, Y. W. (1981), *System Modeling and Modification via Modal Analysis*, Dissertation, Virginia Polytechnic Institute and State University.

Malcolm, Gerald N. and Schiff, Lewis B. (1985), "Recent Developments in Rotary Balance Testing of Fighter Aircraft Configurations at NASA Ames Research Center", AGARD-CP-386, no. 18.

Mangalam, S. M., Maddalon, D. V., Saric, W. S., and Agarwal, N. K. (1990) "Measurement of Crossflow Vortices, Attachment-Line Flow, and Transition Using Microthin Hot Films", AIAA-90-1636, AIAA 21st Fluid Dynamics, Plasma Dynamics, and Lasers Conference.

Marchman, J. F. III, Lutze, F. E. Jr, and Cliff, E. M. (1975), "A Facility for the Measurement of Individual Rotary Motion Aerodynamic Stability Derivatives", ICIASF 1975.

McCroskey, W. J. (1977), "Some Current Research in Unsteady Fluid Dynamics", *Journal of Fluids Engineering*, Vol. 99, pp. 8-39.

McCroskey, W. J., and Durbin, E. J. (1972), "Flow Angle and Shear Stress Measurements Using Heated Films and Wires", *Journal of Basic Engineering*, vol. D94, no. 1.

Meier, H. U., and Cebeci, T. (1984), "Flow Characteristics of a Body of Revolution at Incidence", DFVLR Report IB 222-84 A 44.

Meier, H. U., and Kreplin, H. P. (1980a), "Experimental Study of Boundary Layer Velocity Profiles on a Prolate Spheroid at Low Incidence in the Cross Section  $x_0/L = 0.64$ ", Viscous and Interacting Flow Field Effects Meeting, US Naval Academy, Annapolis, MD, Technical Report AFFDL-TR-78.

Meier, H. U., and Kreplin, H. P. (1980b), "Experimental Investigation of the Boundary Layer Transition and Separation on a Body of Revolution", *Z.Flugwiss. Weltraumforsch.* 4, Heft 2.

Meier, H. U., Kreplin, H. P., and Vollmers, H. (1983), "Development of Boundary Layers and Separation Patterns on a Body of Revolution at Incidence", *Second Symposium on Numerical and Physical Aspects of Aerodynamic Flows*.

Meier, H. U., Kreplin, H. P., and Landhauber, A. (1986), *Wall Pressure Measurements on a 1:6 Prolate Spheroid in the DFVLR 3m x 3m Low Speed Wind Tunnel ( $\alpha = 10^\circ$ ,  $U = 55$  m/s, artificial transition) - Data Report*, DFVLR Report IB 222-86 A 04.

Meier, H. U., Michel, U., and Kreplin, H. P. (1987). "The Influence of Wind Tunnel Turbulence on the Boundary Layer Transition", *Perspectives in Turbulence Studies*, Edited by H. U. Meier and P. Bradshaw, Springer-Verlag, New York, NY, pp. 26-46.

Miller, James A. (1976), "A Simple Linearized Hot-Wire Anemometer", *Journal of Fluids Engineering*, December, 1976.

O'Leary, C.O. (1991), "Oscillatory Data for Typical Configurations", AGARD-R-776, no. 5

O'Leary, C. O., and Rowthorn, E. N. (1985), "New Rotary Rig at RAE and Experiments on HIRM", AGARD-CP-386, no. 19.

Omega Engineering. (1995), "Practical Strain Gage Measurement", *The Pressure Strain and Force Handbook*, Vol. 29, pp. E-55 to E-56.

Poll, D. I. A. (1985), "On the Effects of Boundary Layer Transition on a Cylindrical Afterbody at Incidence in Low-Speed Flow", *Aeronautical Journal*, paper no. 1307, October, 1985, pp. 315-327.

Riley, W. F., and Zachary, L. (1989), *Introduction to Mechanics of Materials*, John Wiley & Sons, New York, NY.

Roback, V. E. (1995), "Design and Development of a Graphite/Epoxy 6:1 Prolate Spheroid Wind Tunnel Model for Use in Time-Dependent Force and Moment Tests", 1995 Mid-Atlantic Student Conference, submitted to DTIC for distribution.

Robinson, S. K. (1992), "The Kinematics of Turbulent Boundary Layer Structure", NASA TM 103859.

Rubsin, M. W., Okuno, A. F., Mateer, G. G., and Brosh, A. (1975), "A Hot-Wire Surface Gage for Skin Friction and Separation Detection Measurements", NASA TM X-62,465.

Schetz, J. (1993), *Boundary Layer Analysis*, Prentice-Hall, Englewood Cliffs, NJ.

Schlichting, H. (1979), *Boundary Layer Theory*, McGraw-Hill Book Co., New York, NY.

Schmidt, E. (1985), "Standard Dynamics Model Experiments with the DFVLR/AVA Transonic Derivative Balance", AGARD-CP-386, no. 21.

Simpson, R. L. (1976), "An Investigation of the Spatial Structure of the Viscous Sublayer", Report no. 188, MPI Strömungs forschung, Göttingen.

Simpson, R. L., Walker, D. A., and Shinpaugh, K. A. (1991), *Description of a 1000 Sensor Constant Current Anemometer System for Locating Three-Dimensional Turbulent Boundary Layer Separations*, Report no. VPI-AOE-185.

Simpson, R. L. (1995), "Three-Dimensional Turbulent Boundary Layers and Separation", AIAA-95-0226, 33rd Aerospace Sciences Meeting and Exhibit, Reno, NV.

Simpson, R. L. (1996), "Aspects of Turbulent Boundary Layer Separation", in press, *Progress in Aerospace Sciences*.

Smith, L. H., and Nunn, R. H. (1976), "Aerodynamic Characteristics of an Axisymmetric Body Undergoing a Uniform Pitching Motion", *Journal of Spacecraft*, Vol. 13., No. 1, pp. 8-14.

Solomon, W. J., and Walker, G. J. (1995) "Intermittency Detection from Surface Film Arrays on Aerofoils in Unsteady Flow", *Twelfth Australian Fluid Mechanics Conference*, The University of Sydney, Australia, pp. 85-88.

Taylor, L. K., Arabshahi, A., and Whitfield, D. L. (1995), "Unsteady Three-Dimensional Incompressible Navier-Stokes Computations for a Prolate Spheroid Undergoing Time-Dependent Maneuvers", AIAA-95-0313, 33rd Aerospace Sciences Meeting and Exhibit, Reno, NV.



Tennekes, H., and Lumley, J. L. (1972), *A First Course in Turbulence*, MIT Press, Cambridge, MA.

Tobak, M. and Peake, D. J. (1982), "Topology of Three-Dimensional Separated Flows", *Annual Review of Fluid Mechanics*, 14, pp. 61-85.

Townsend, A. A. (1976), *Structure of Turbulent Shear Flow*, 2nd. Edition, Cambridge University Press, p. 43.

Treines, N. (1975), "The Determination of Coefficients of Nonlinear Equations by Discrete Fourier-Transformation Oscillations and Application on the Measurement of Aerodynamic Derivatives", ICIASF 1975.

van Dam, C. P., Los, S. M., Miley, S. J., Yip, L. P., Banks, D. W., Roback, V. E., and Bertelrud, A. (1995), "Analysis of In-flight Boundary Layer State Measurements on a Subsonic Transport Wind in High-Lift Configuration", *1st AIAA Aircraft Engineering, Technology, and Operations Congress*, Los Angeles, CA.

Wetzel, T. G., and Simpson, R. L. (1993) *The Effect of Vortex Generators on the Crossflow Separation of a Submarine in a Turning Maneuver*, Virginia Polytechnic Institute and State University, Aerospace and Ocean Engineering, Report no. VPI-AOE-195.

Wetzel, T. G., and Simpson, R. L. (1996), *1024 Constant current Hot-film System*, Virginia Polytechnic Institute and State University, Aerospace and Ocean Engineering, Report no. VPI-AOE-226.

Wood, N. B. (1975), "A Method for Determination and Control of the Frequency Response of the Constant-Temperature Hot-Wire Anemometer", *Journal of Fluid Mechanics*, vol. 67, part 4, pp. 769-786.

Yates, L. A., and Chapman, G. T. (1992), "Streamlines, Vorticity Lines, and Vortices Around Three-Dimensional Bodies", *AIAA Journal*, Vol. 30, no. 7, pp. 1819-1826.

## Tables

Table 1. Maneuver conditions.

Maneuver Name	Pitch Range	Plunge Range	Time
Pitchup Maneuver	0° to 30°	0 cm to -70.1 cm	0.33 s
Submarine Maneuver	0° to 13.6°	0 cm to -32.2 cm	0.25 s
Plunge Down Maneuver	0°	+15.2 cm to -15.2 cm	0.33 s

Table 2. Constant current calibration factors.

<i>Sensor</i>	<i>x/L</i>	$\eta \times 10^{-7}$	<i>Std. Dev.</i>	<i>Sensor</i>	<i>x/L</i>	$\eta \times 10^{-7}$	<i>Std. Dev.</i>
1	0.118	2.34	5.7%	17	0.525	4.27	4.6%
2	0.143	2.18	7.6%	18	0.551	4.19	3.9%
3	0.169	2.07	3.2%	19	0.576	4.38	4.9%
4	0.194	1.89	5.6%	20	0.602	4.09	5.4%
5	0.220	4.79	8.2%	21	0.627	4.05	5.3%
6	0.245	3.88	4.6%	22	0.653	3.79	6.1%
7	0.271	3.62	5.7%	23	0.678	4.16	4.9%
8	0.296	3.75	7.9%	24	0.704	4.33	4.3%
9	0.322	3.61	8.3%	25	0.729	3.67	5.3%
10	0.347	3.63	7.2%	26	0.754	4.30	6.0%
11	0.373	4.29	7.7%	27	0.780	3.74	5.7%
12	0.398	3.32	9.2%	28	0.805	3.99	5.1%
13	0.424	3.41	7.6%	29	0.831	3.99	5.0%
14	0.449	3.27	9.2%	30	0.856	4.55	3.8%
15	0.474	4.69	4.0%	31	0.882	5.51	2.6%
16	0.500	3.98	8.5%	32	0.907	5.50	2.2%

Table 3. Constant temperature sensor temperatures.

<i>Sensor</i>	$T_p$ °C	$r^2$
1	36.12	0.997
4	34.00	0.987
5	32.02	0.987
7	32.48	0.989
10	33.04	0.994
13	35.27	0.998
16	33.28	0.995
19	34.11	0.997
22	35.57	0.998
25	36.82	0.998
29	45.88	0.998
31	35.61	0.998

Table 4. Steady Constant temperature calibration factors.

<i>Sensor</i>	$x/L$	$A, V^2/^\circ K/Pa$	$B, V^2/^\circ K$	$r^2$
1	0.118	0.01013	0.00659	0.534
4	0.194	0.0120	0.00554	0.602
5	0.220	0.00773	0.00575	0.624
7	0.271	0.00861	0.00425	0.775
10	0.347	0.00881	0.00564	0.939
13	0.424	0.0114	0.00398	0.847
16	0.500	0.00818	0.00599	0.845
19	0.576	0.00841	0.00688	0.840
22	0.653	0.00962	0.00532	0.841
25	0.729	0.00950	0.00488	0.873
29	0.831	0.00713	0.00427	0.904
31	0.882	0.00748	0.00549	0.893

Table 5. Unsteady constant-temperature calibration factors.

<i>Sensor</i>	$\gamma$	$\kappa, Pa^{1/3}$
1	0.113	2.13
4	0.170	2.05
5	0.198	1.93
7	0.173	2.18
10	0.180	2.88
13	0.172	1.59
16	0.179	2.53
19	0.173	1.78
22	0.178	2.09
25	0.169	1.28
29	0.166	1.58
31	0.163	2.16

Table 6. Pressure Transducer sensitivities.

Pressure Port	x/L	S/N	Sensitivity, mV/psi
0	0.00	B30M	129.9
1	0.11	B15M	104.9
2	0.23	B38M	140.6
3	0.31	B42M	135.3
4	0.44	B19M	122.0
5	0.56	B22L	121.6
6	0.69	B45M	124.6
7	0.77	C13B	127.6
8	0.83	B08L	133.6
9	0.90	B36M	139.2

Table 7. Estimated force and moment loads for old and new model. Assumes a representative maximum linear acceleration of 5 g's and a representative angular acceleration of 130 rad/s<sup>2</sup>. Added mass forces and moments from section 7.7.

	Old Model	New Model
model mass, kg	27	2.3
inertial force at 5 g's, N	1320	113
model inertia, kg-m <sup>2</sup>	3.17	0.27
inertial moment at 130 rad/s <sup>2</sup> , N-m	412	35
mass of displaced air, kg	0.04	0.04
maximum estimated added mass normal force, N	4.3	4.3
inertia of displaced air, kg-m <sup>2</sup>	0.0038	0.0038
maximum estimated added mass pitch moment, N-m	0.036	0.036
aerodynamic normal force, N	45	45
aerodynamic pitch moment, N-m	23	23

## Figures

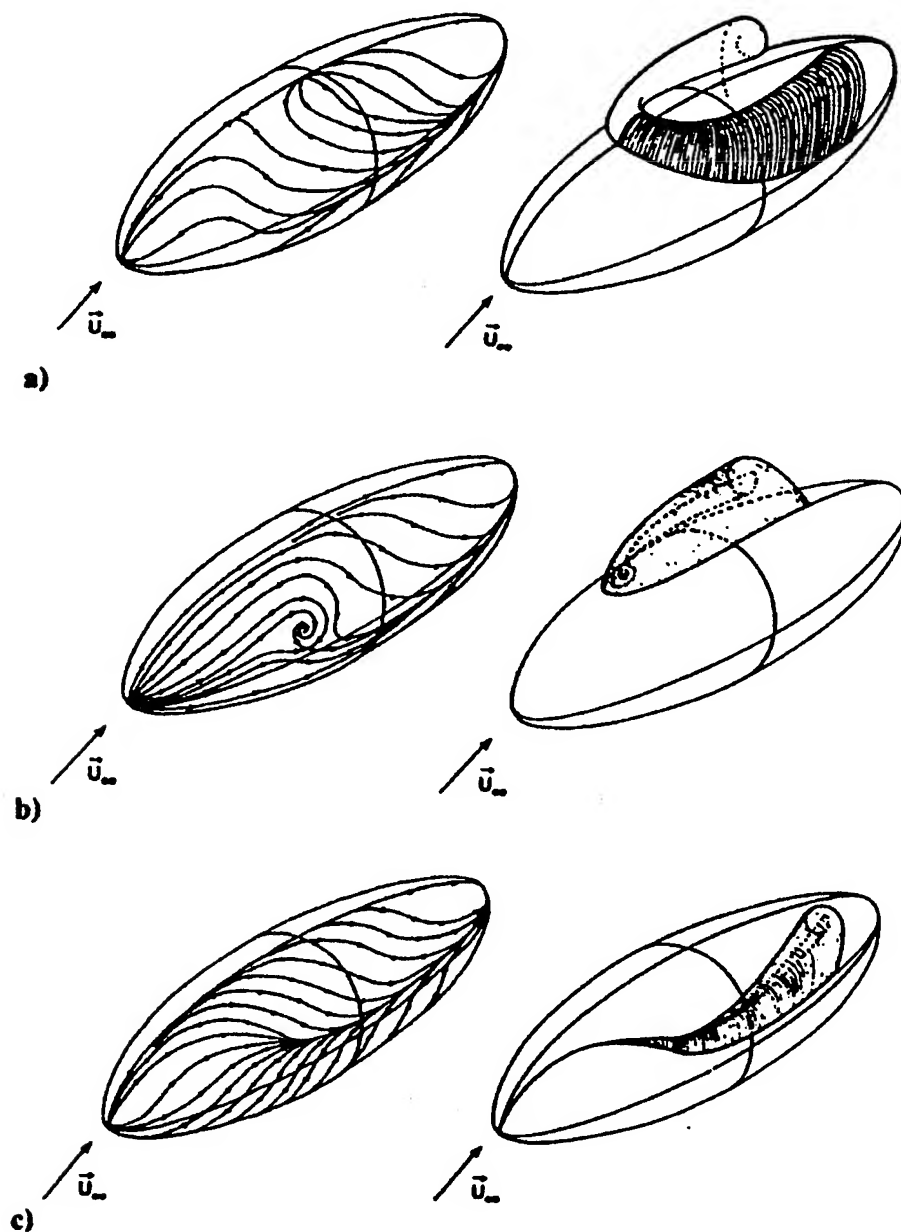


Figure 1. Different types of crossflow separation: a) separation horseshoe-type, closed separation; b) Werle type, closed separation; c) open crossflow separation. From Yates and Chapman (1992).

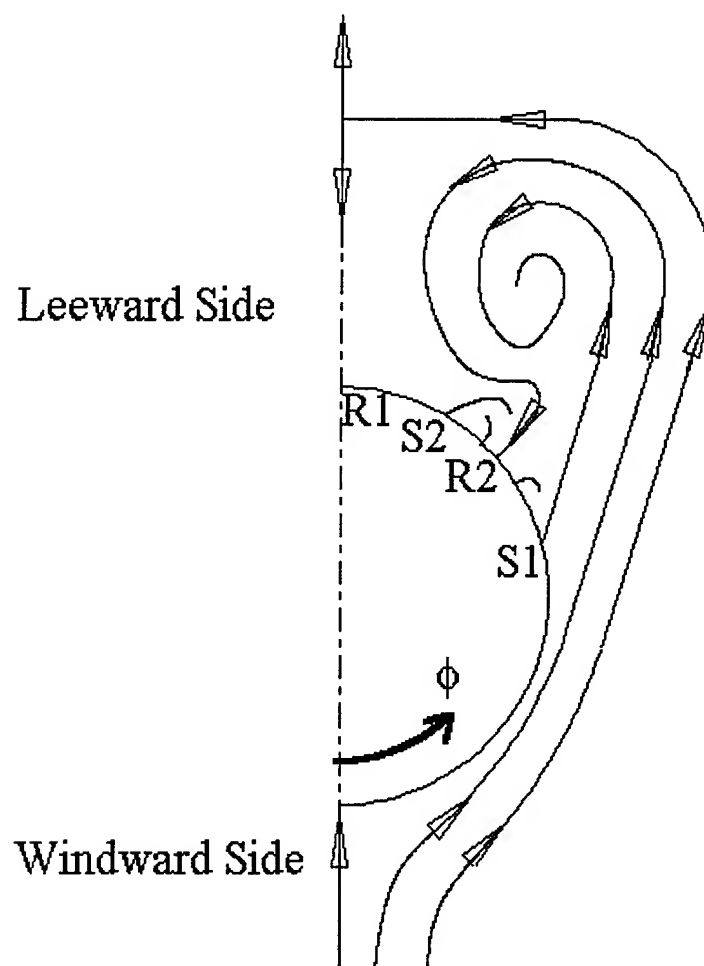


Figure 2. Simplified Flow Separation Topology for the secondary streamlines in a plane normal to the major axis of an axisymmetric body. S1 and S2 refer to primary and secondary separation locations, respectively, and R1 and R2 refer to primary and secondary reattachment locations.

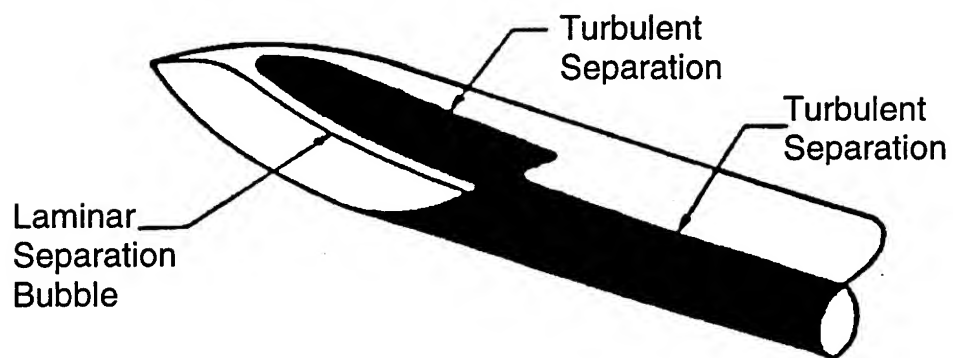


Figure 3. Laminar/turbulent separation interaction on a body of revolution (Poll, 1985).



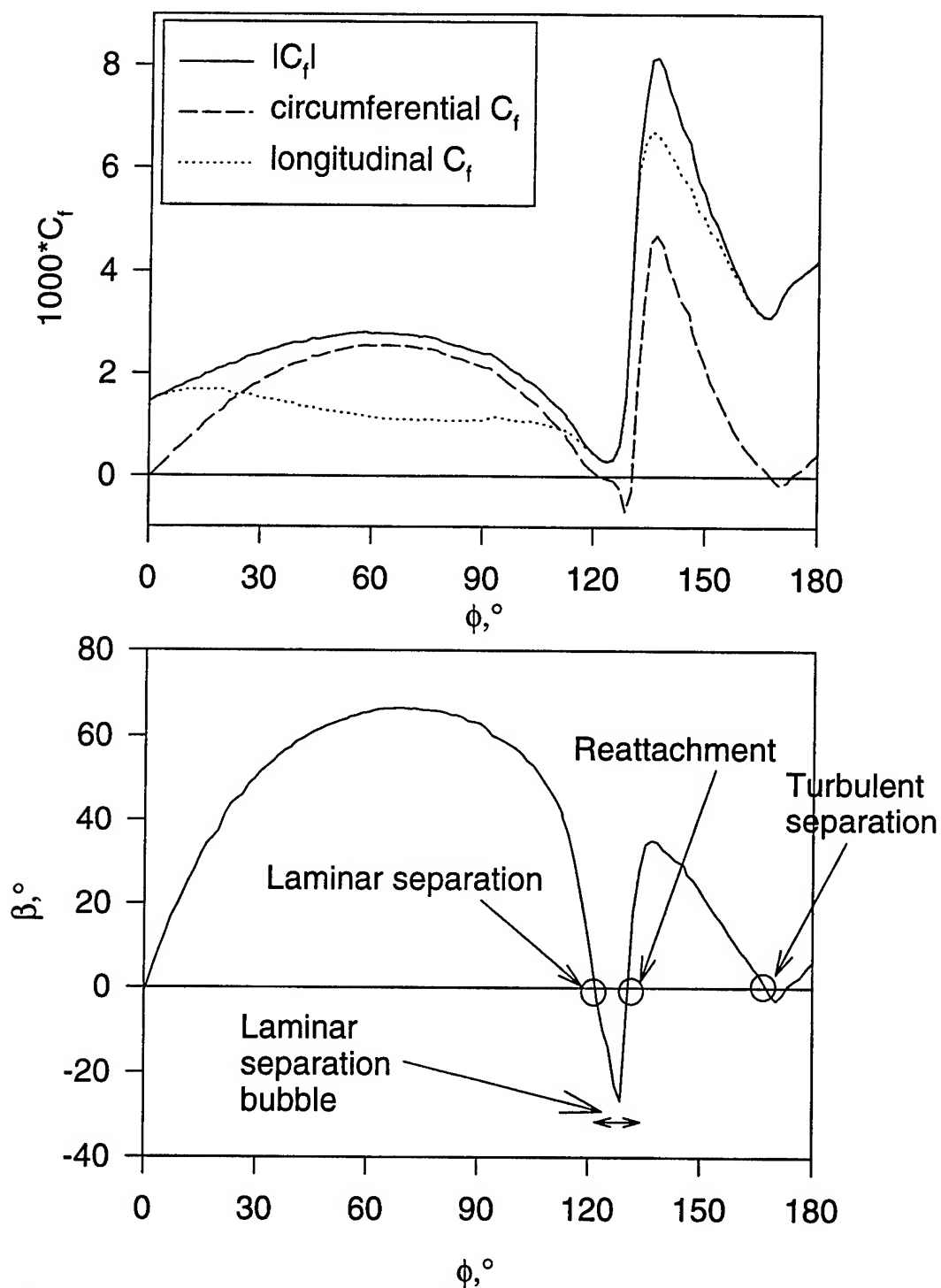


Figure 4. Wall shear vector data on a 6:1 prolate spheroid at  $x/L=0.139$ ,  $\alpha=30^\circ$ , and Reynolds number of 6.5 million. From Meier and Kreplin (1985).

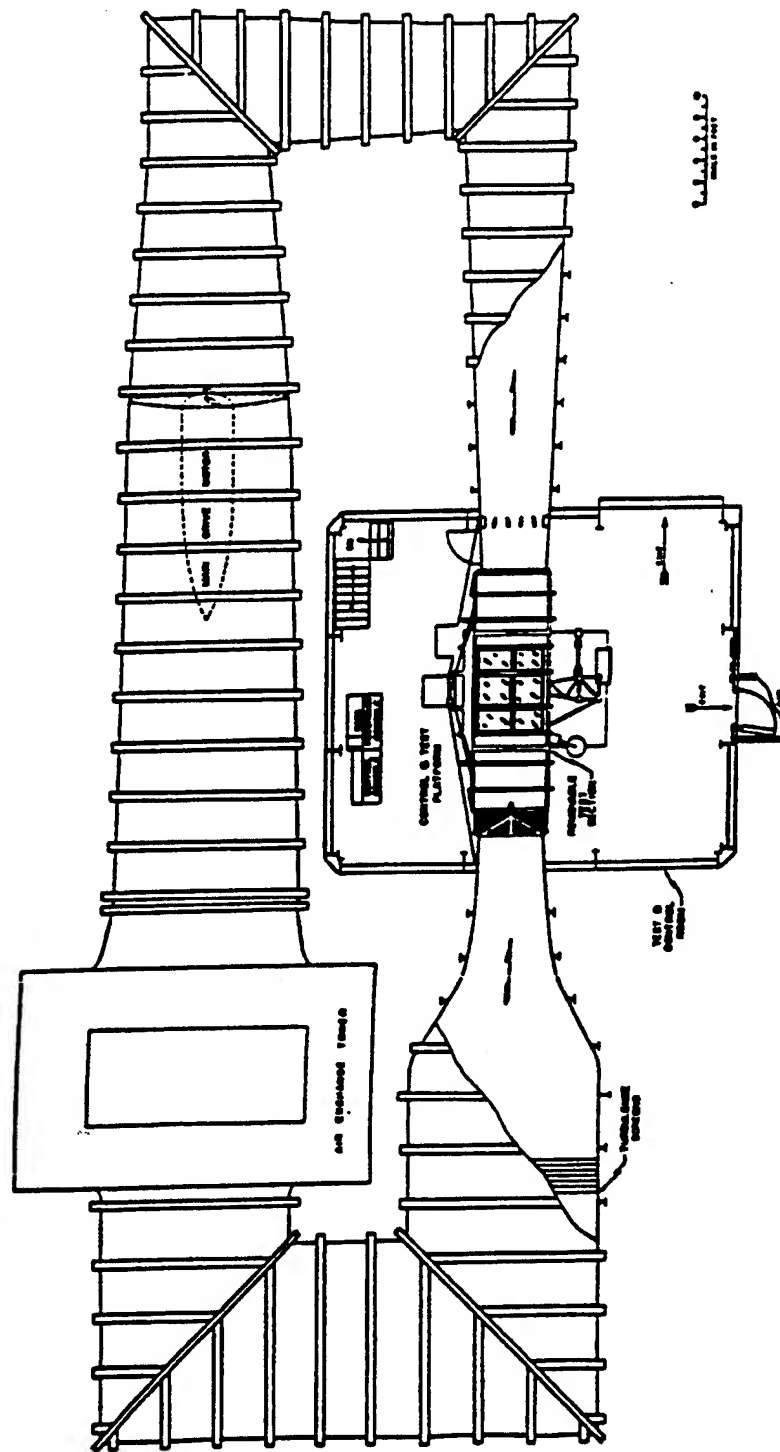


Figure 5. Virginia Tech Stability and Control Wind Tunnel.

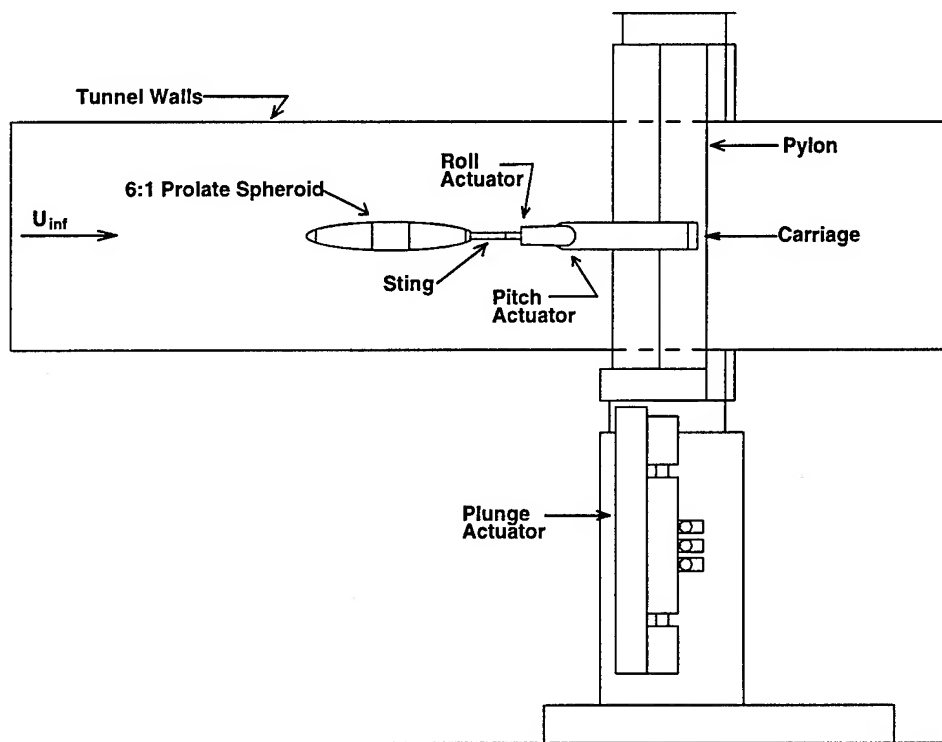


Figure 6. Dynamic Plunge-Pitch-Roll (DyPPiR) Model Mount installed in wind tunnel.

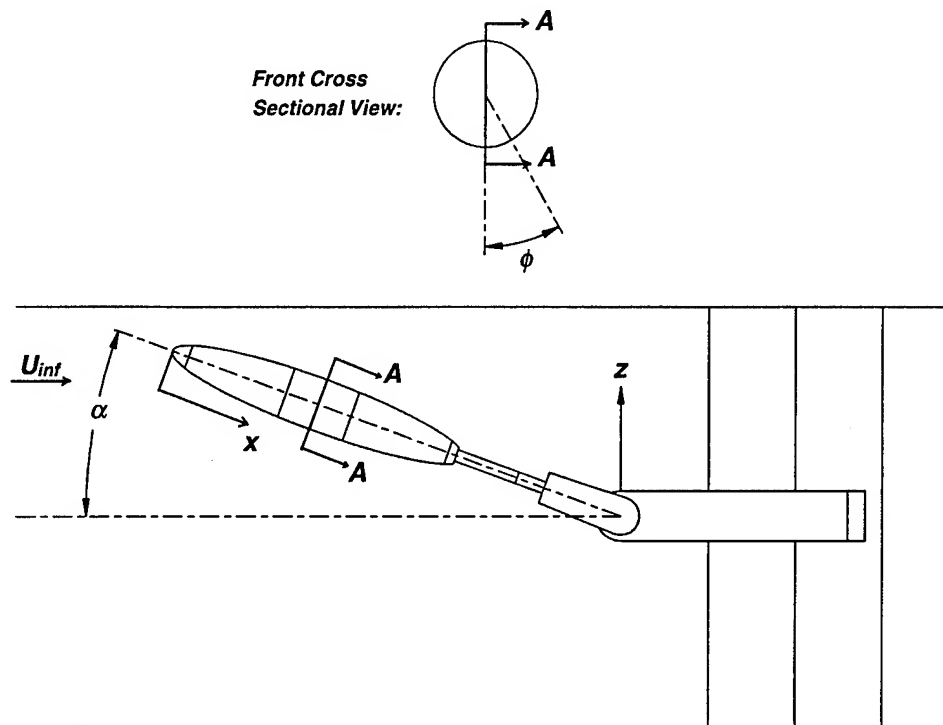


Figure 7. Coordinate Nomenclature.  $x$  is measured from the nose;  $\phi$  is the circumferential location measured from the windward line of symmetry;  $z$  is the plunge ordinate; and  $\alpha$  is the pitch angle and equivalently the model center angle of attack.

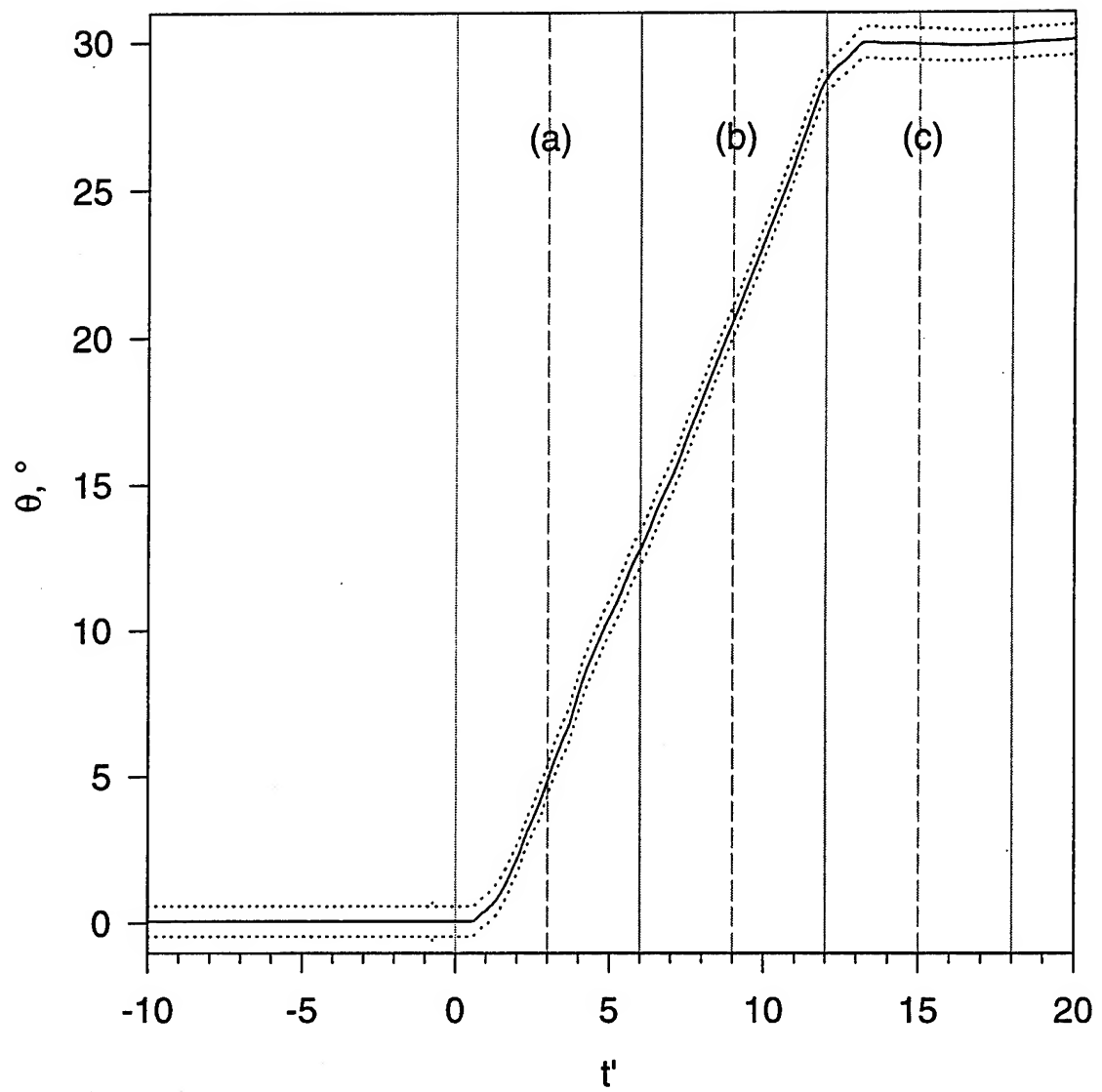


Figure 8. Pitch-up maneuver pitch angle position feedback. Dotted lines represent 20:1 odds positional repeatability. The regions (a), (b), and (c) indicate the extent of individual time series plots of hot-film data presented in Chapter 4.

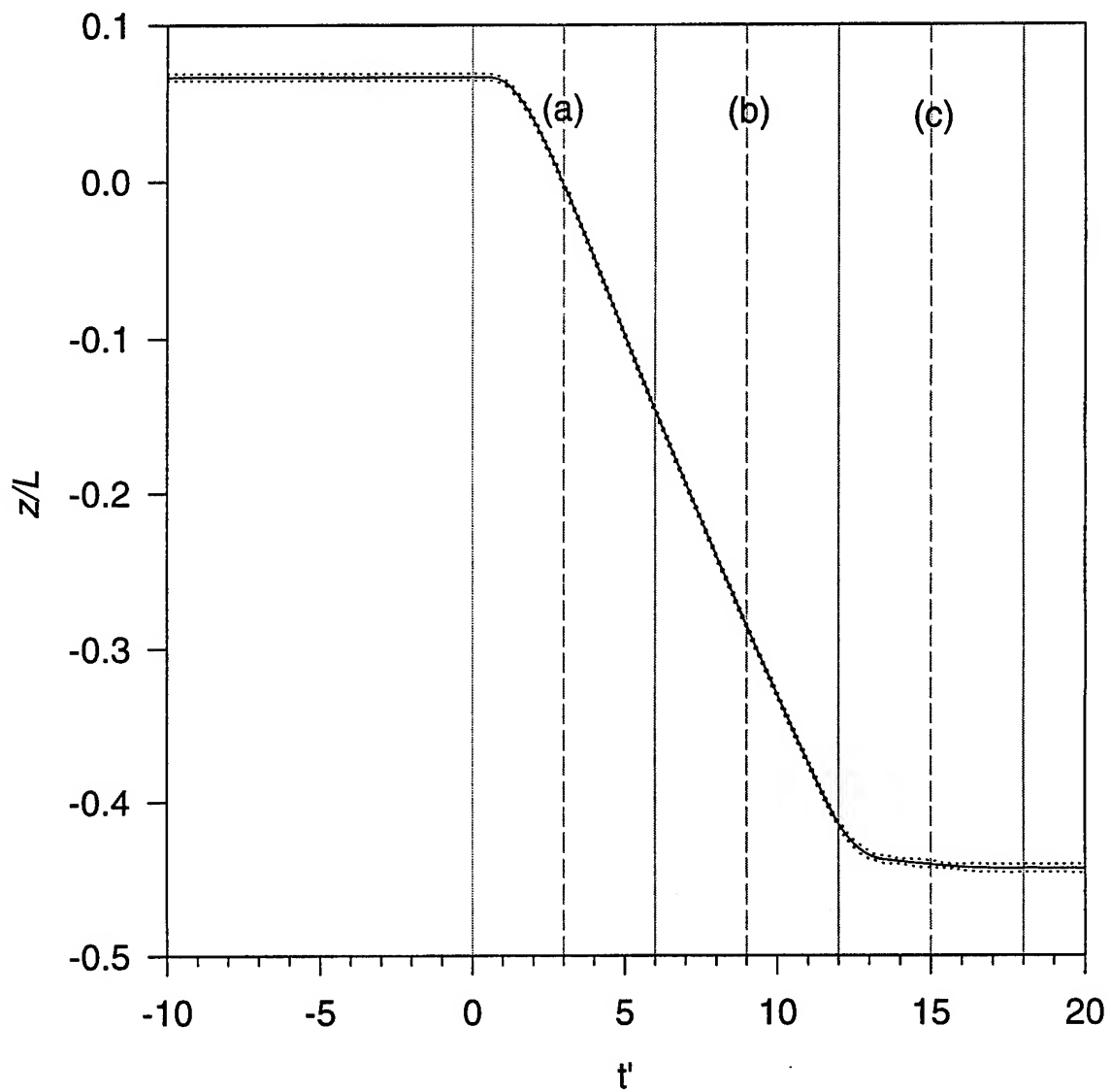


Figure 9. Pitch-up maneuver plunge position feedback. Dotted lines represent 20:1 odds positional repeatability. The regions (a), (b), and (c) indicate the extent of individual time series plots of hot-film data presented in Chapter 4.

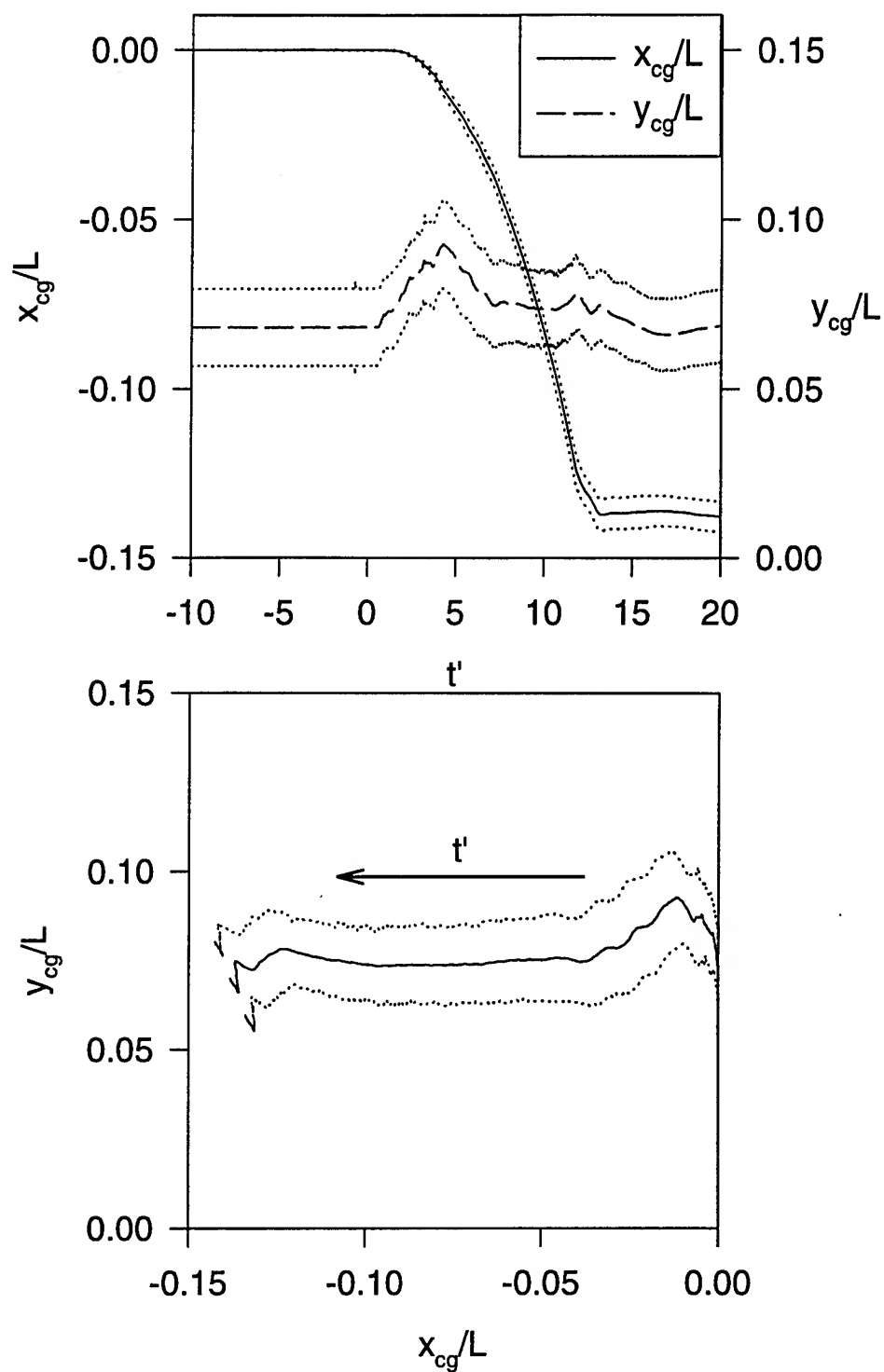


Figure 10. Model center of gravity motion during pitch-up maneuver. Dotted lines represent 20:1 odds positional repeatability.

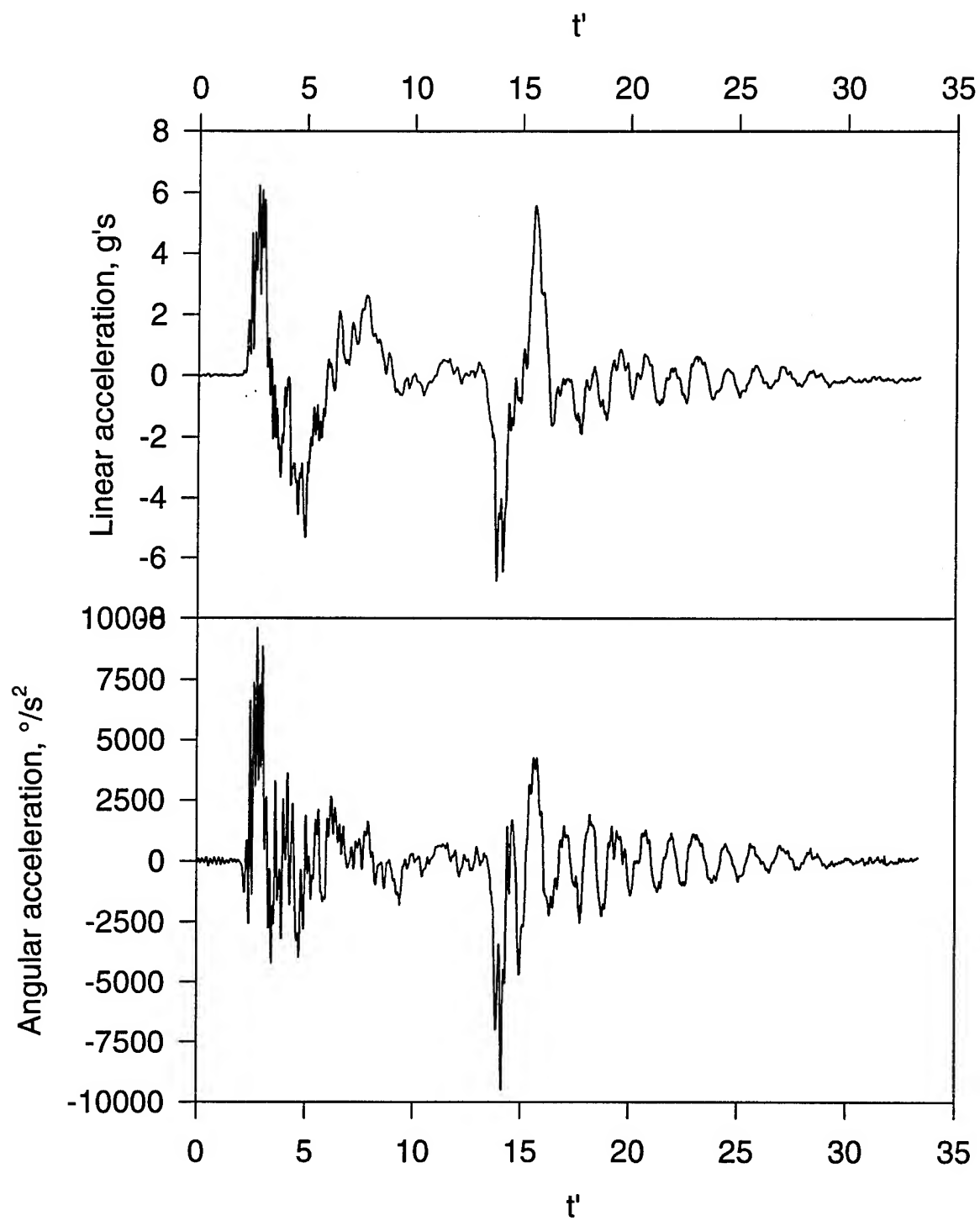


Figure 11. Model center of gravity acceleration during pitch-up maneuver.



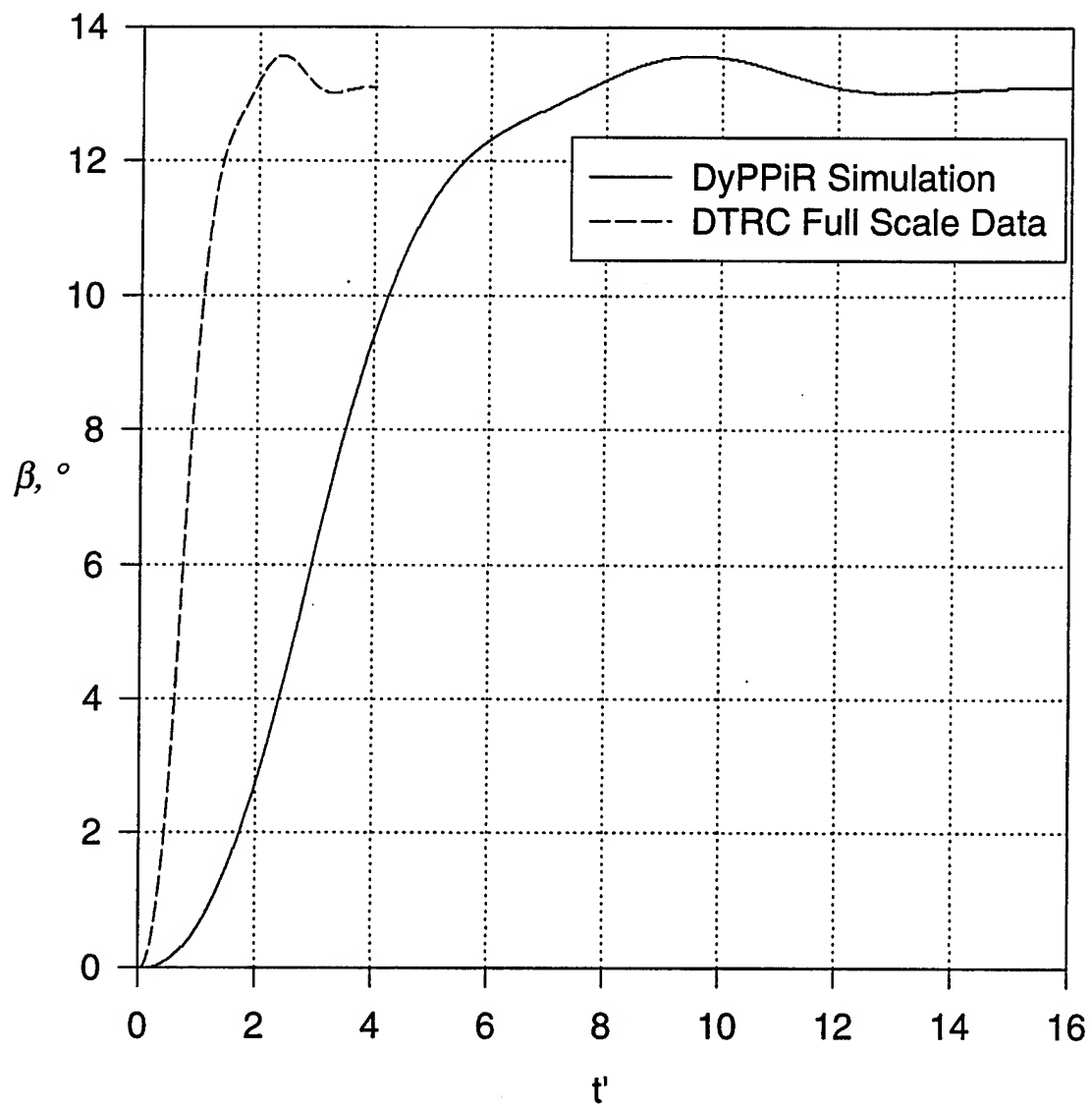


Figure 12. Submarine maneuver pitch angle command signal compared to data from DTMB sideslip data.

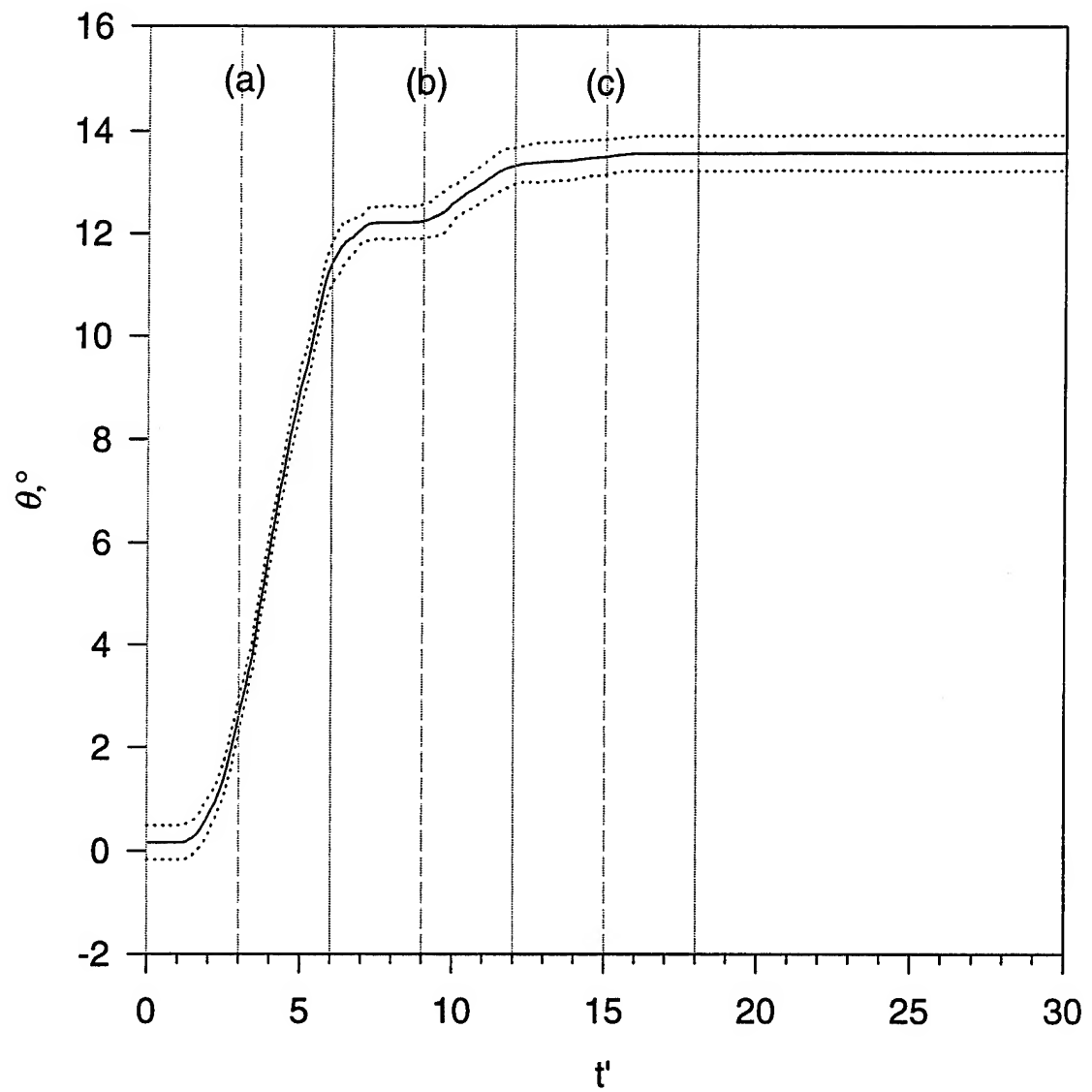


Figure 13. Submarine maneuver pitch angle position feedback. Dotted lines represent 20:1 odds positional repeatability. The regions (a), (b), and (c) indicate the extent of individual time series plots of hot-film data presented in Chapter 4.

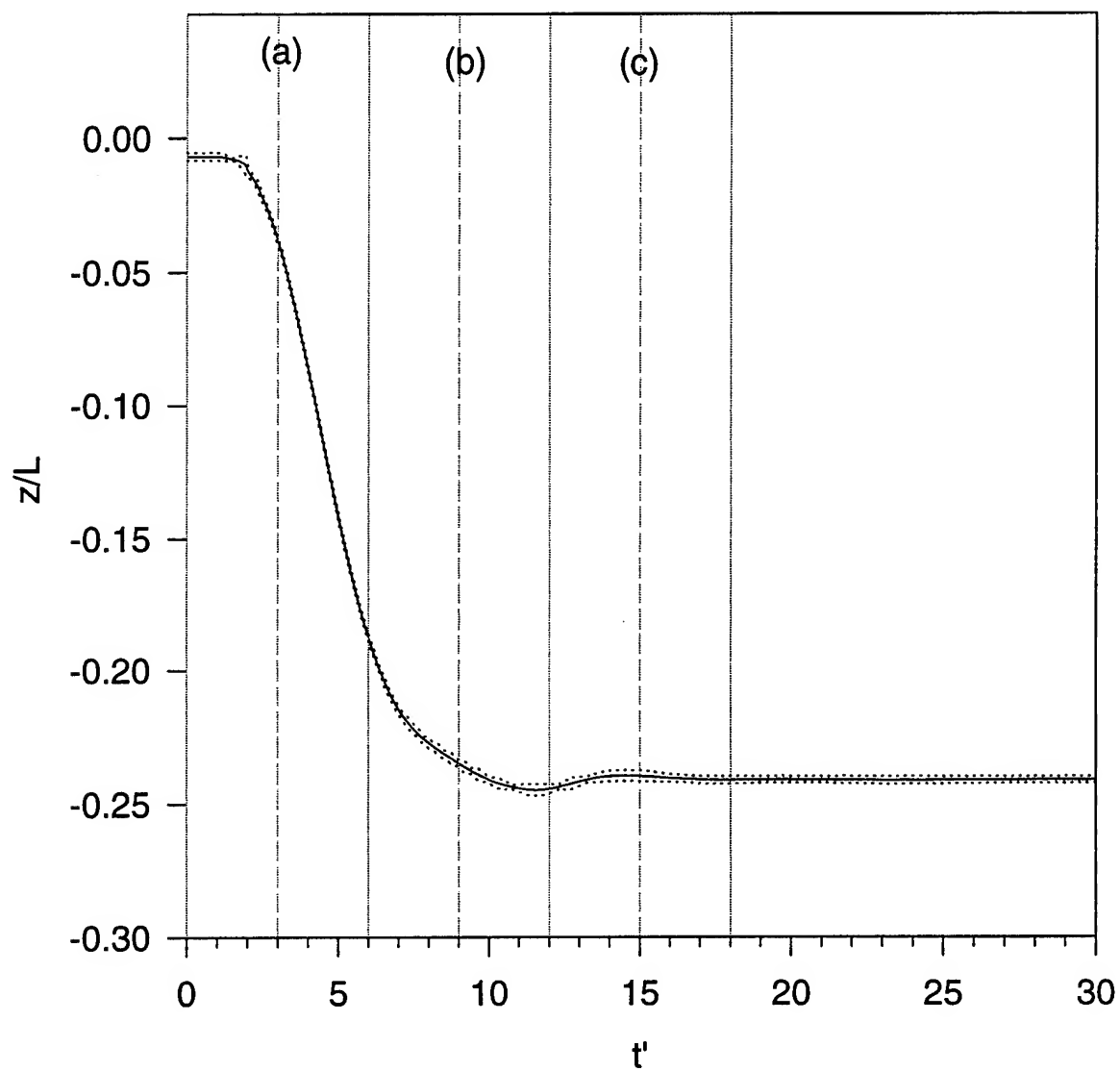


Figure 14. Submarine maneuver plunge position feedback. Dotted lines represent 20:1 odds positional repeatability. The regions (a), (b), and (c) indicate the extent of individual time series plots of hot-film data presented in Chapter 4.

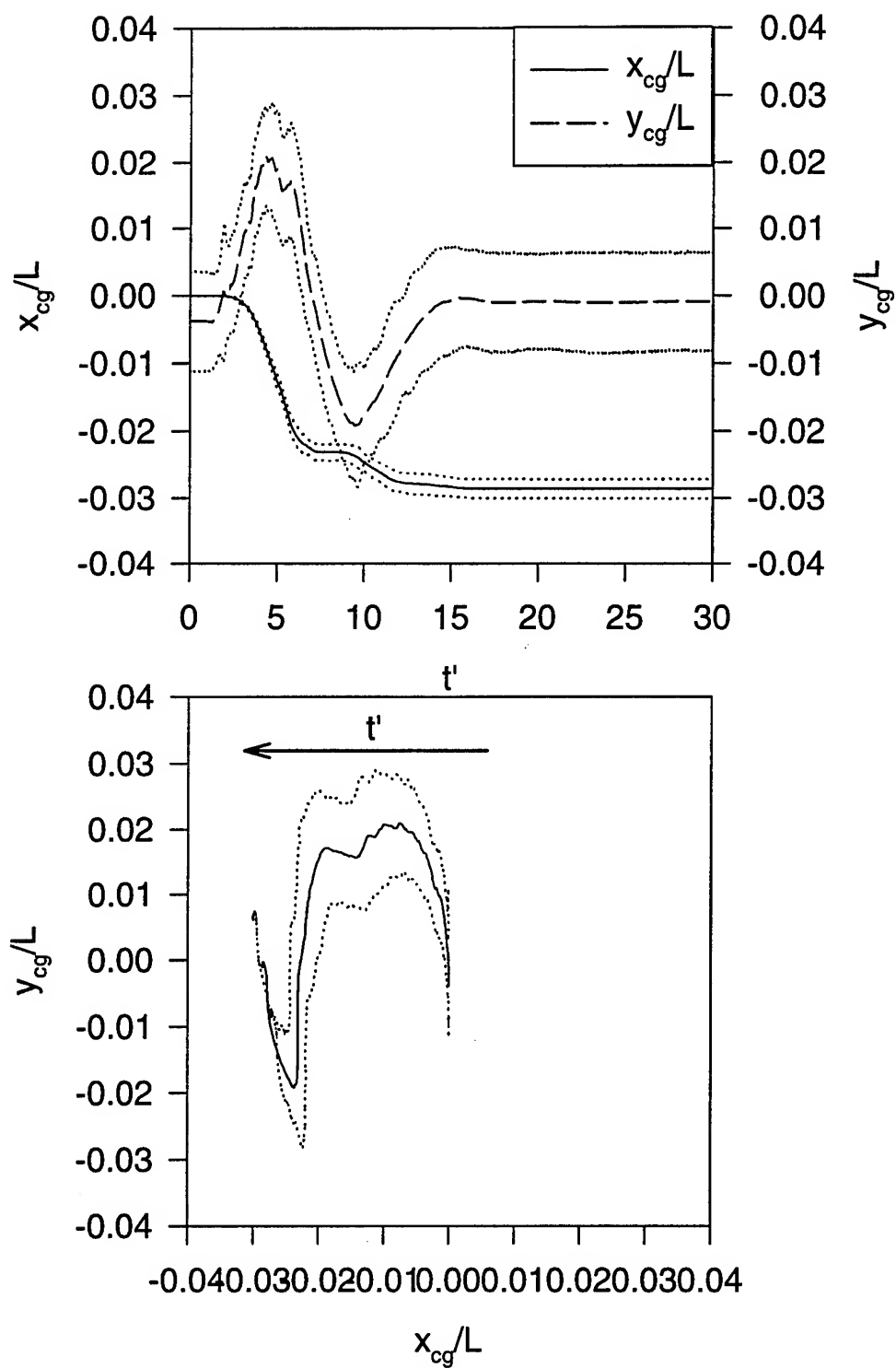


Figure 15. Model center of gravity motion during submarine maneuver. Dotted lines represent 20:1 odds positional repeatability.

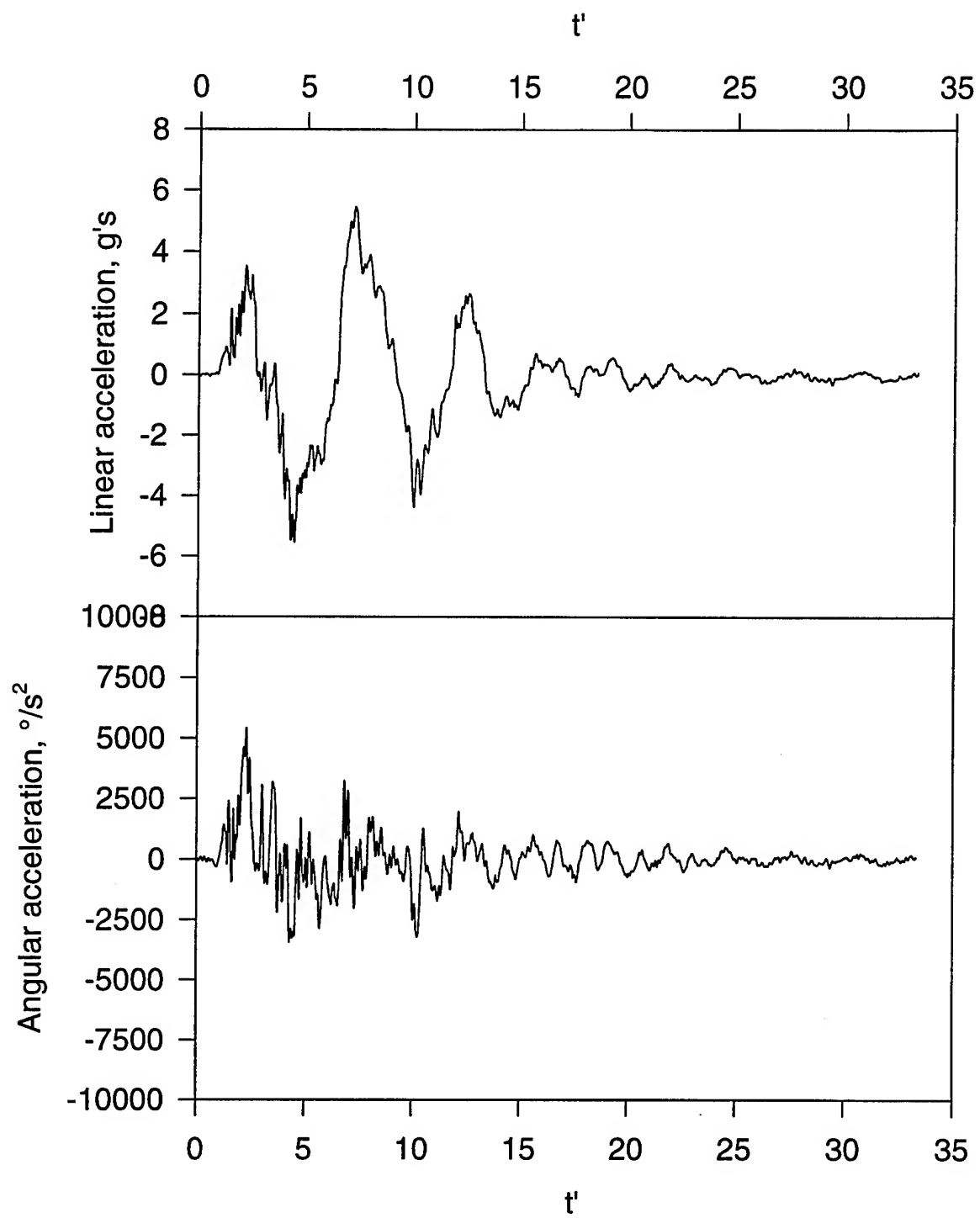


Figure 16. Model center of gravity acceleration during submarine maneuver.

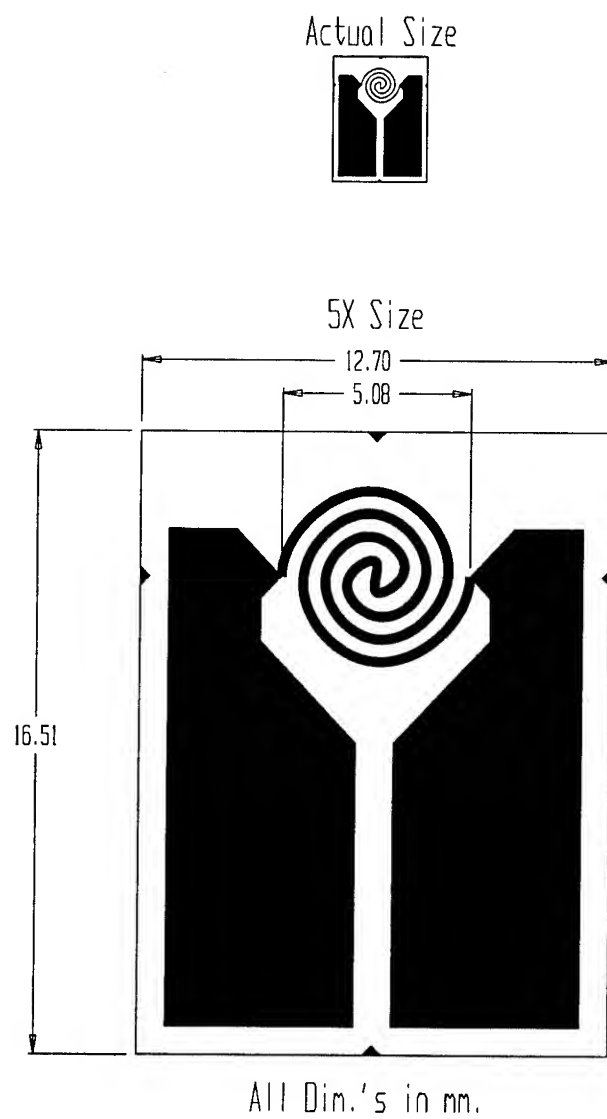


Figure 17. Hot-film sensor geometry.

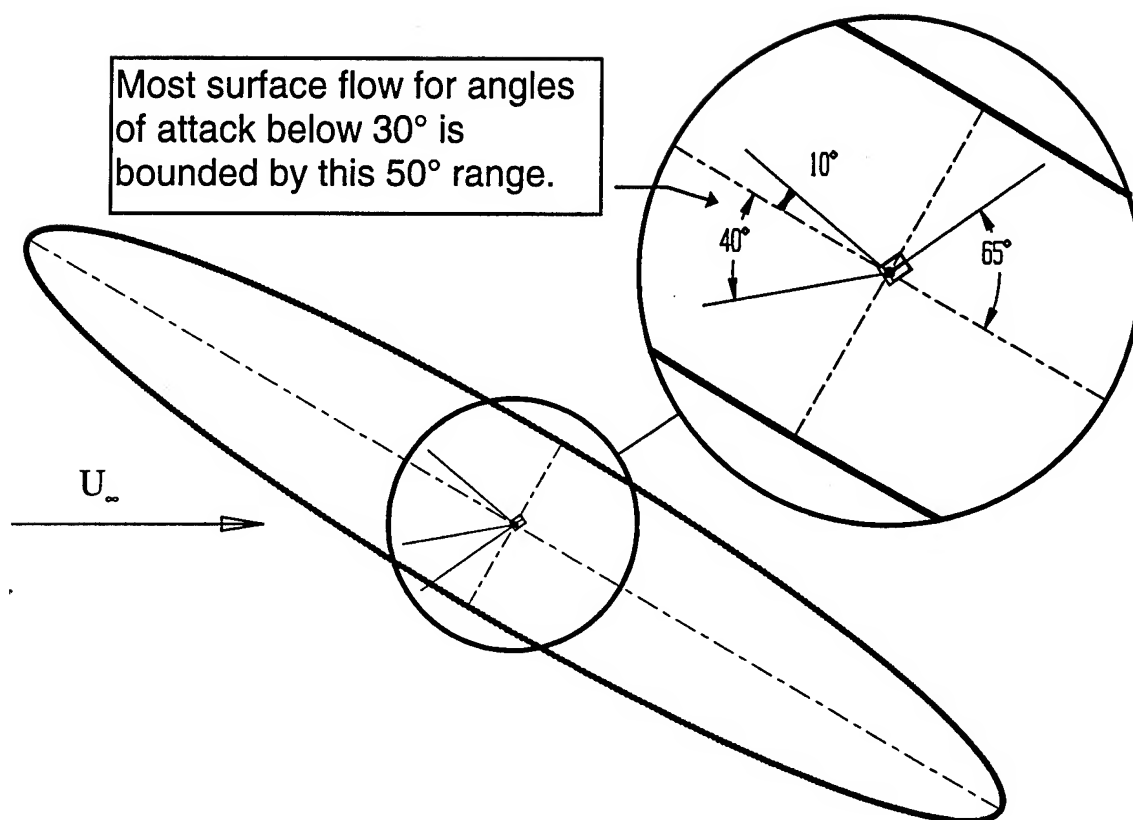


Figure 18. Hot-film sensor orientation on model. At angles of attack up to around 30°, most of the local wall shear angles are bounded in the range of 40° below 10° above longitudinal. The sensors were oriented with their centerlines 65° off longitudinal to minimize directional sensitivity.

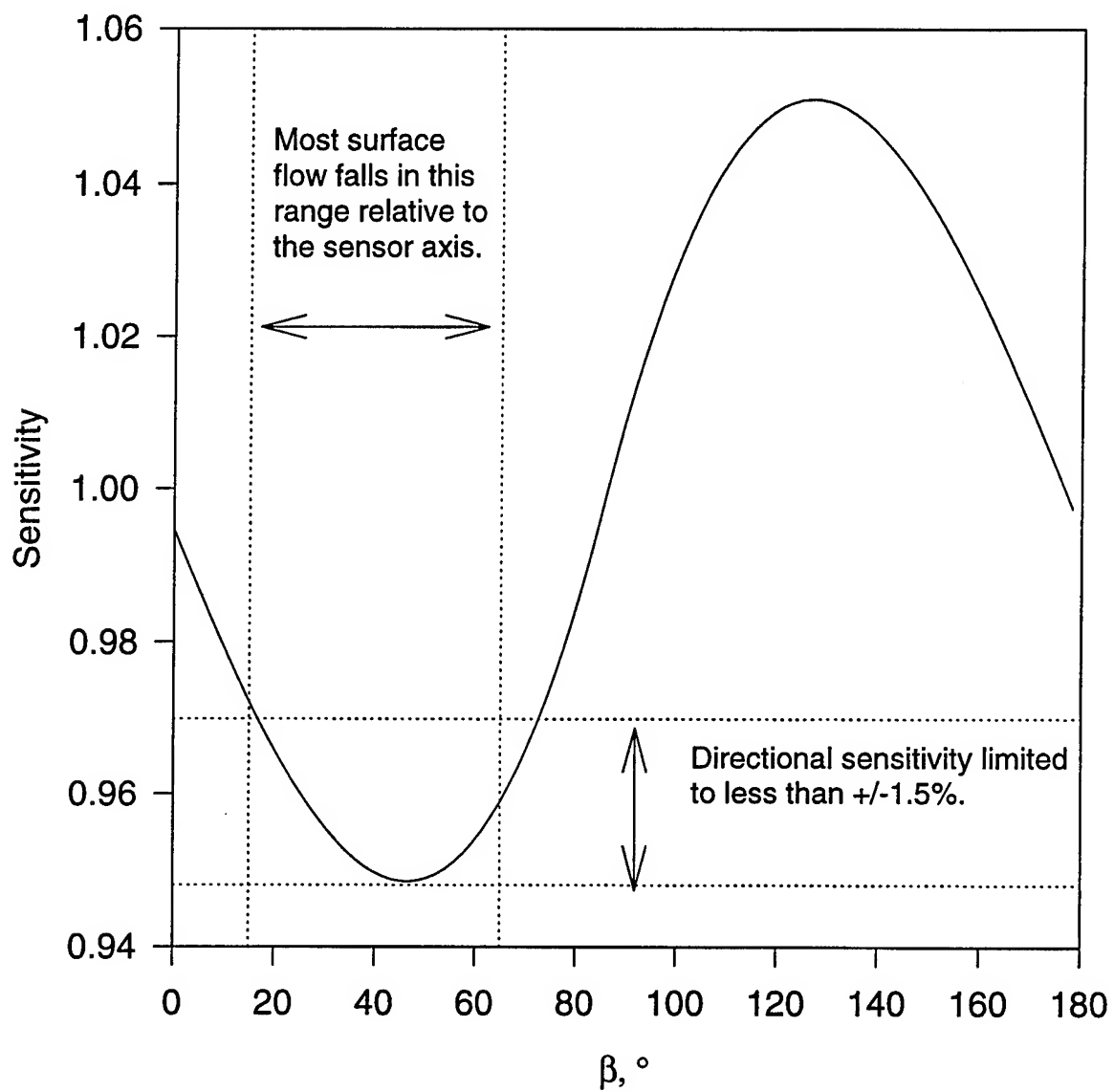


Figure 19. Hot-film sensor directional sensitivity, calculated as an effective length relative to the mean effective length. Dotted lines show bounded flow directions.



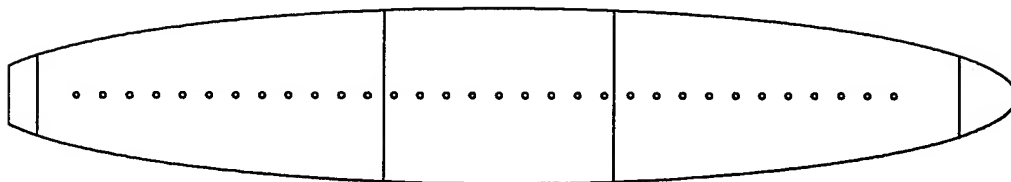


Figure 20. Locations of sensor on model for constant current tests.

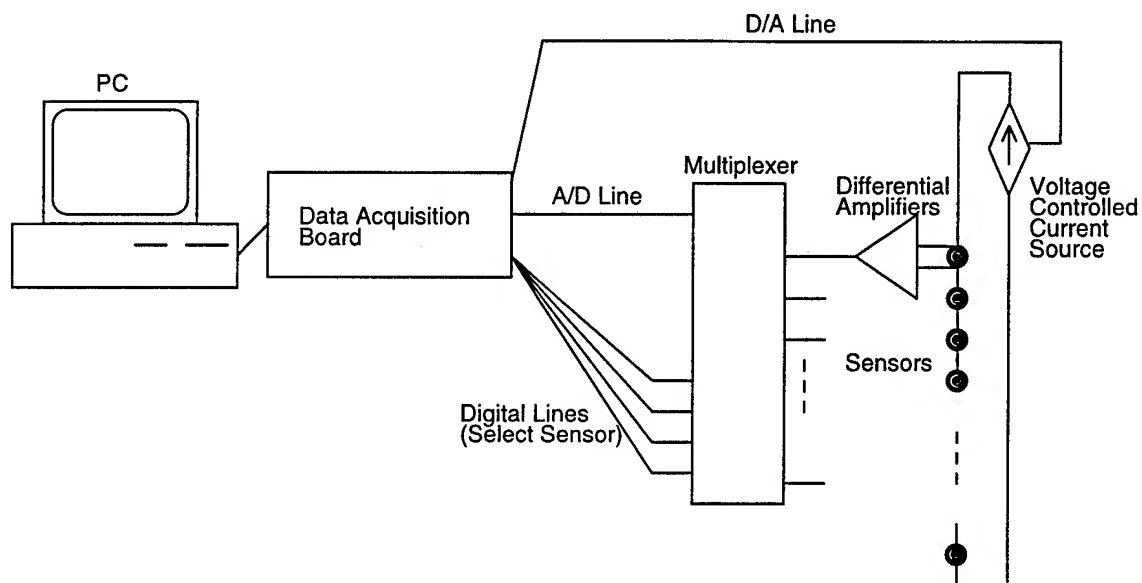


Figure 21. Constant current anemometer block diagram.

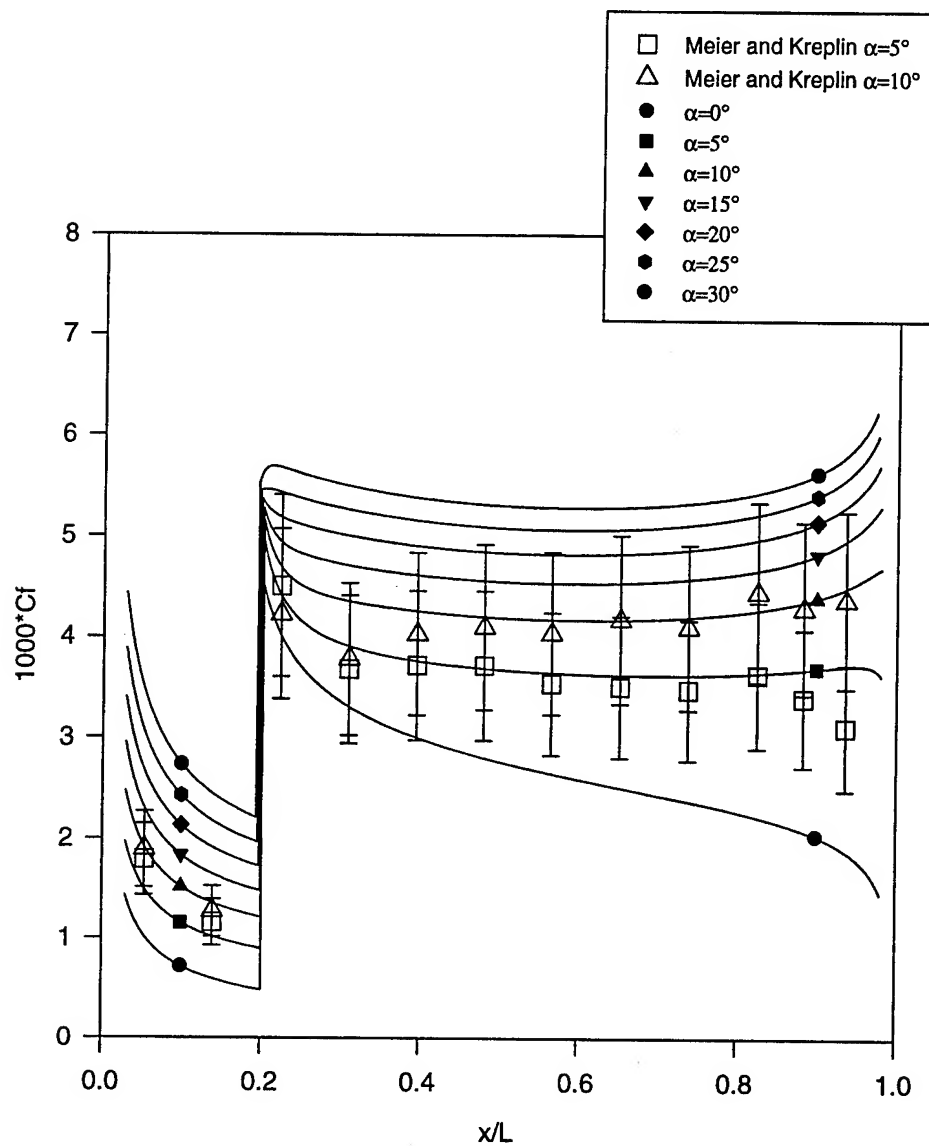


Figure 22. Line-of-symmetry  $C_f$  calculations. Calculations are for a 6:1 prolate spheroid at  $Re=4.2$  million with trip posts at  $x/L=0.20$  and the model at various angles of attack. Meier and Kreplin data from  $5^\circ$  and  $10^\circ$  shown for comparison.

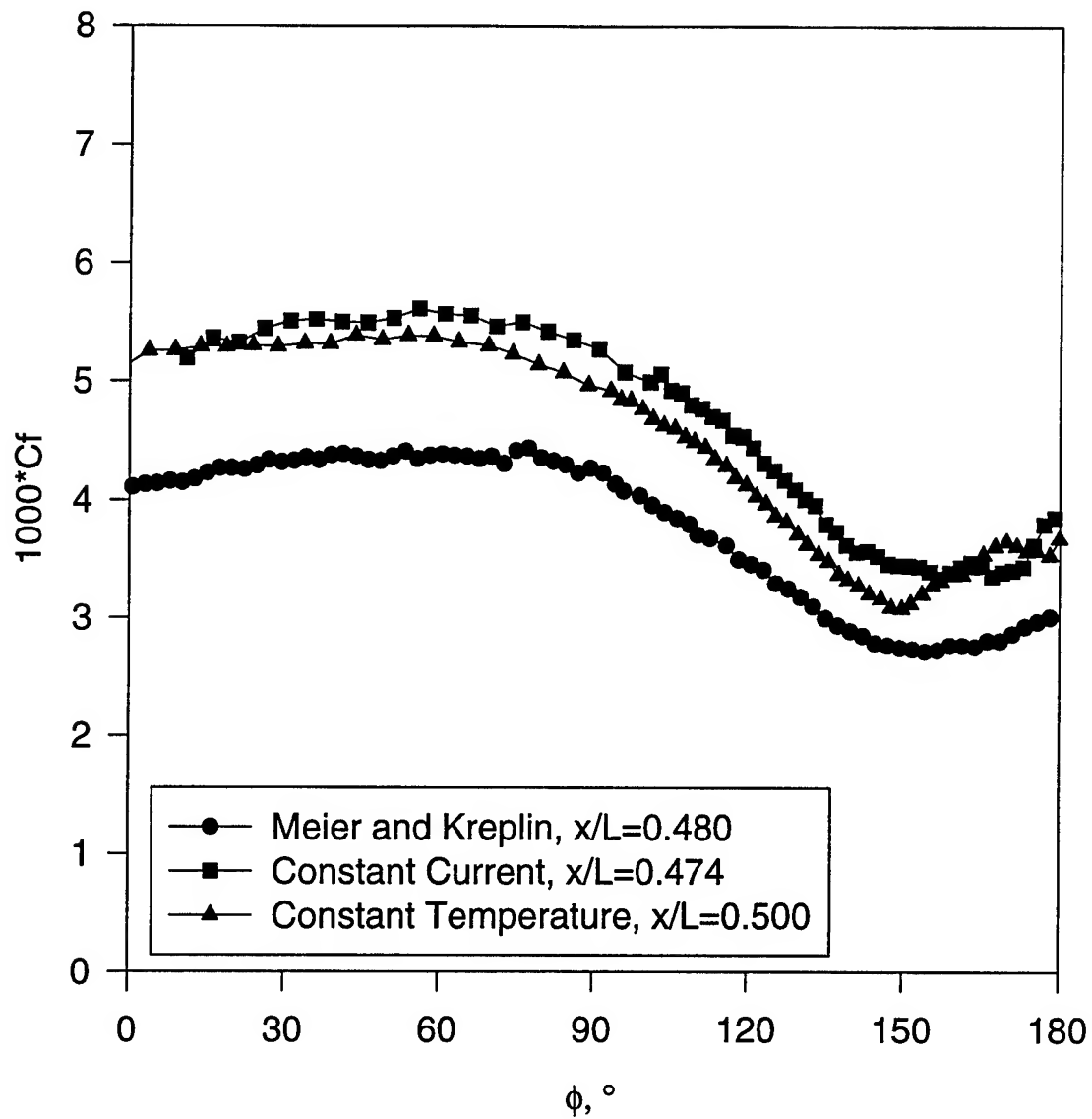


Figure 23. Comparison of present skin friction magnitudes,  $Re=4.2$  million (both constant temperature and constant current), with hot-film data from Meier and Kreplin (1984),  $Re=6.4$  million, at  $x/L=0.48$  and  $\alpha=10^\circ$ . Closest sensors from present data set are shown.

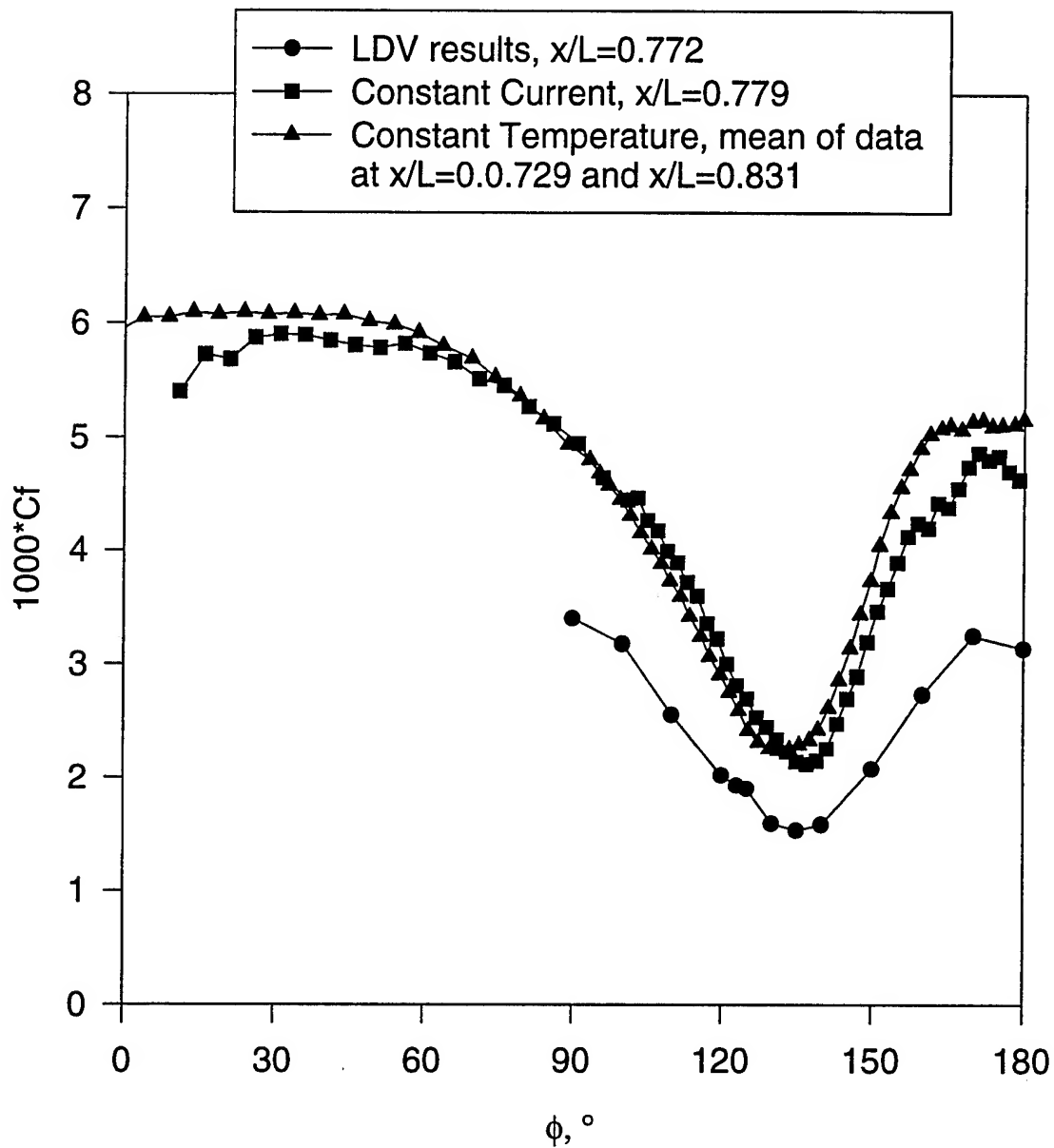


Figure 24. Comparison of present skin friction magnitudes (both constant temperature and constant current) with LDV data from Chesnakas and Simpson (1996) at  $x/L=0.77$ ,  $\alpha=10^\circ$ , and  $Re=4.2$  million. Closest sensors from present data set are shown.

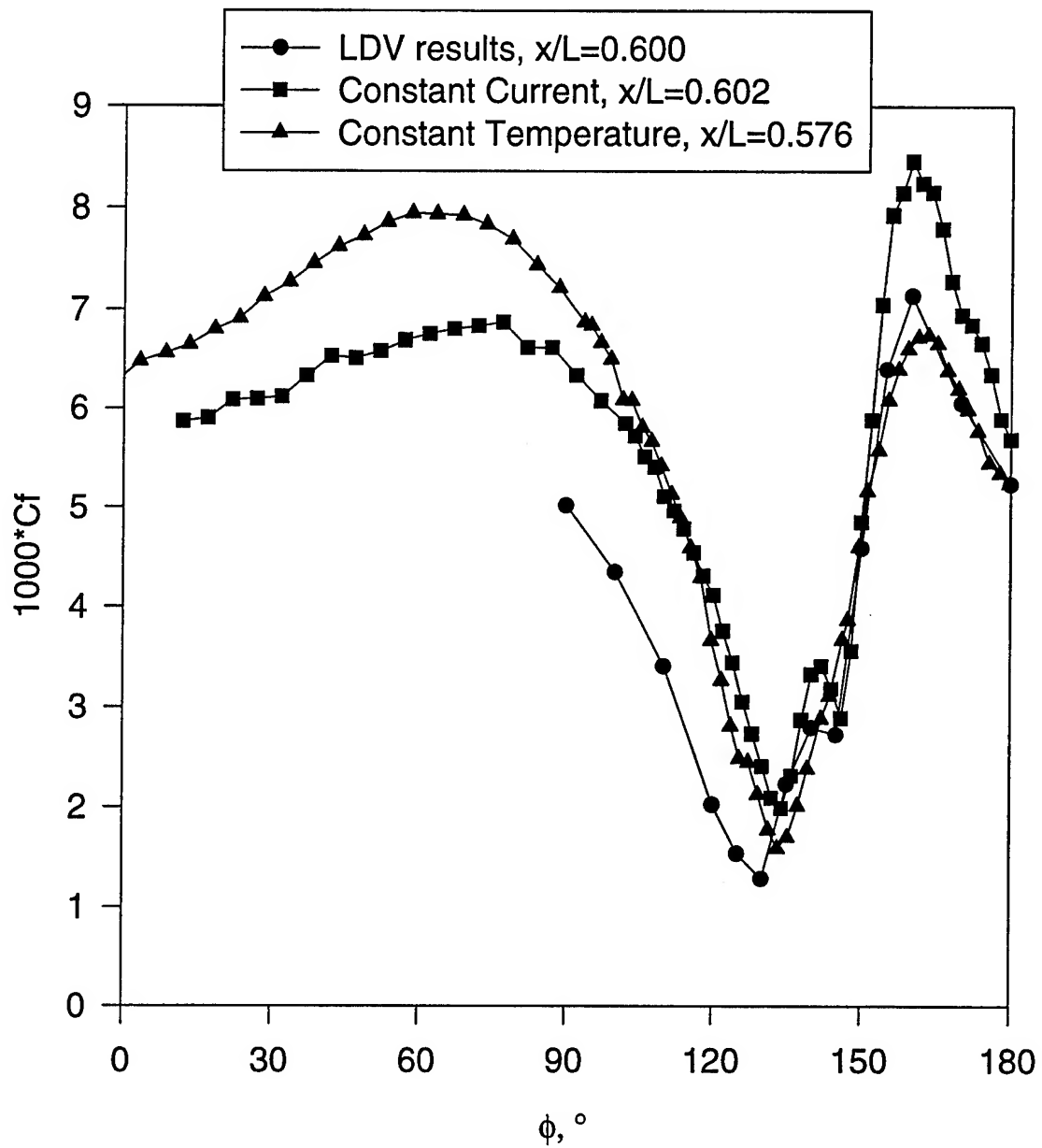


Figure 25. Comparison of present skin friction magnitudes (both constant temperature and constant current) with LDV data from Chesnakas and Simpson (1996) at  $x/L=0.60$ ,  $\alpha=20^\circ$ , and  $Re=4.2$  million. Closest sensors from present data set are shown.

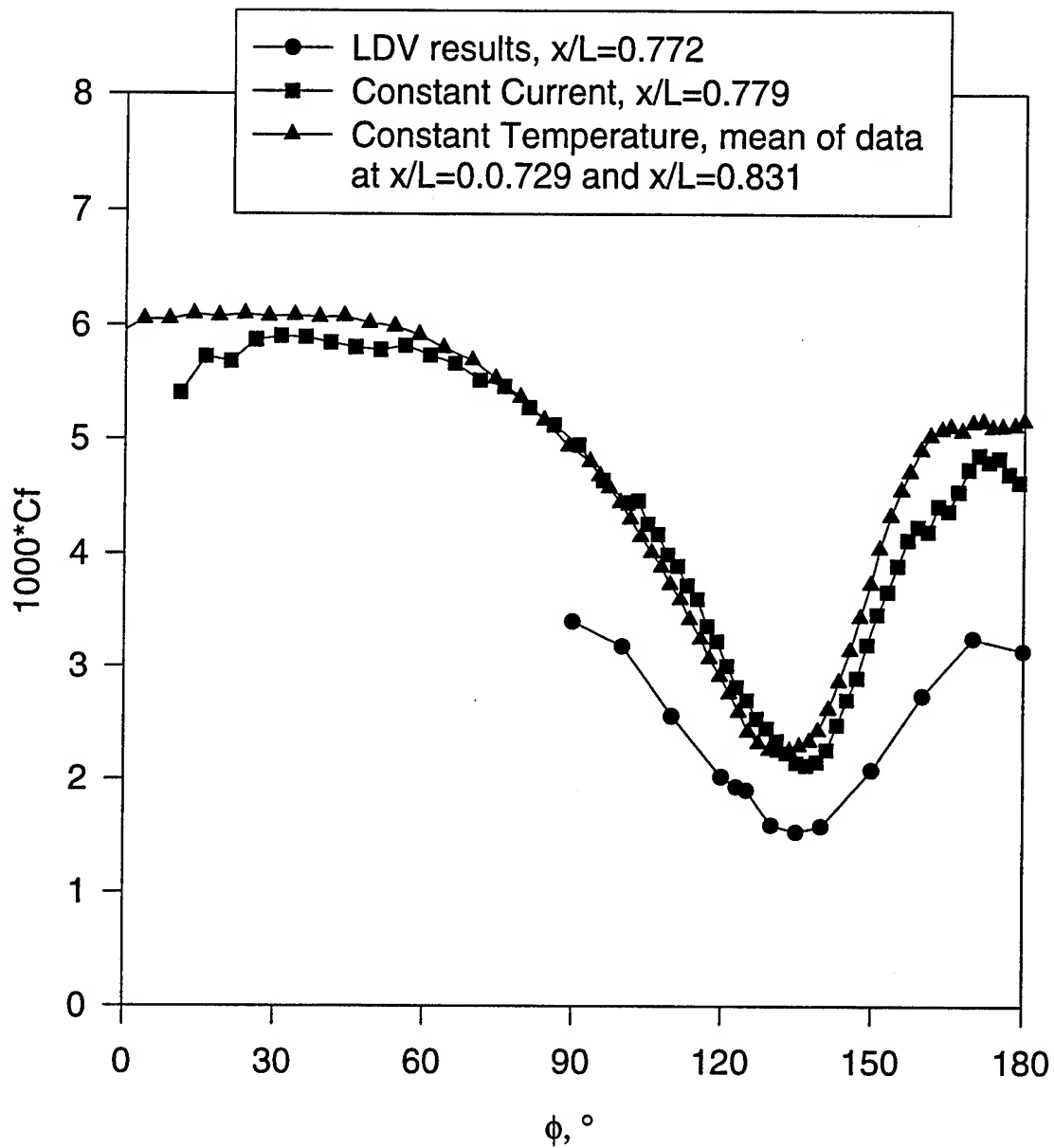


Figure 26. Comparison of present skin friction magnitudes (both constant temperature and constant current) with LDV data from Chesnakas and Simpson (1996) at  $x/L=0.77$ ,  $\alpha=20^\circ$ , and  $Re=4.2$  million. Closest sensors from present data set are shown.

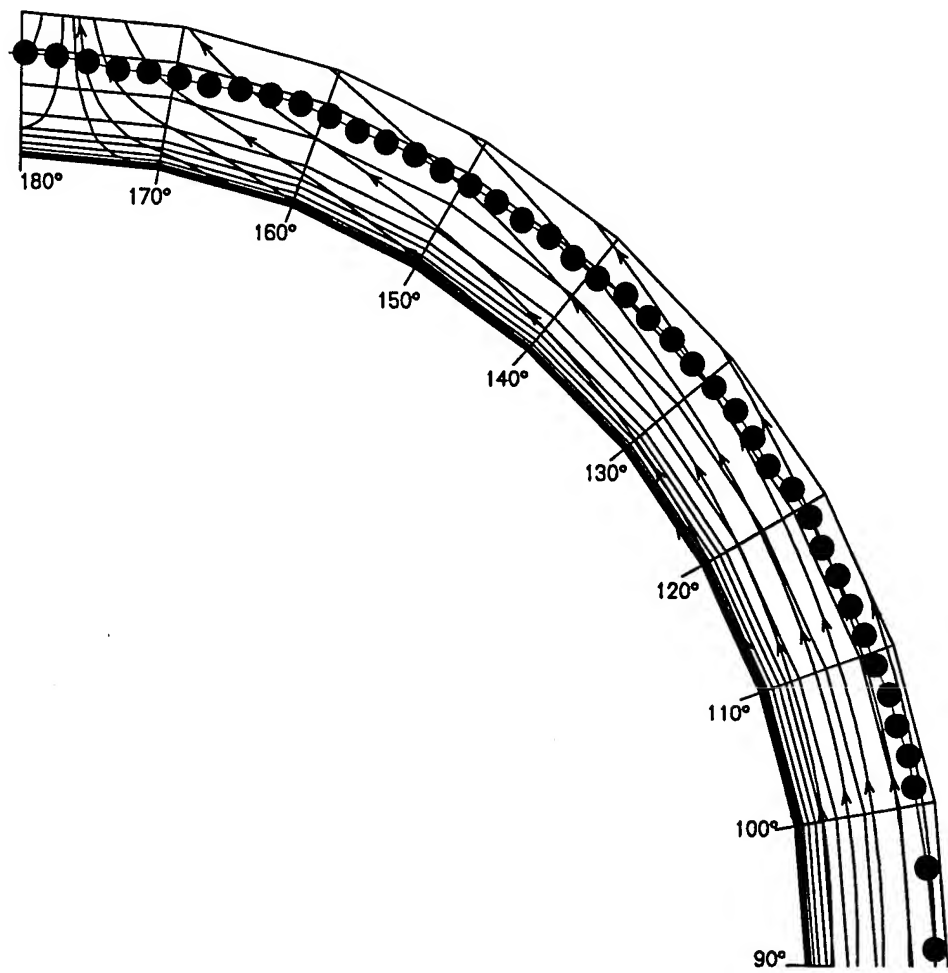


Figure 27. Skin friction values superimposed on secondary streamlines from Chesnakas and Simpson (1996) at  $x/L=0.40$  and  $\alpha=10^\circ$ .



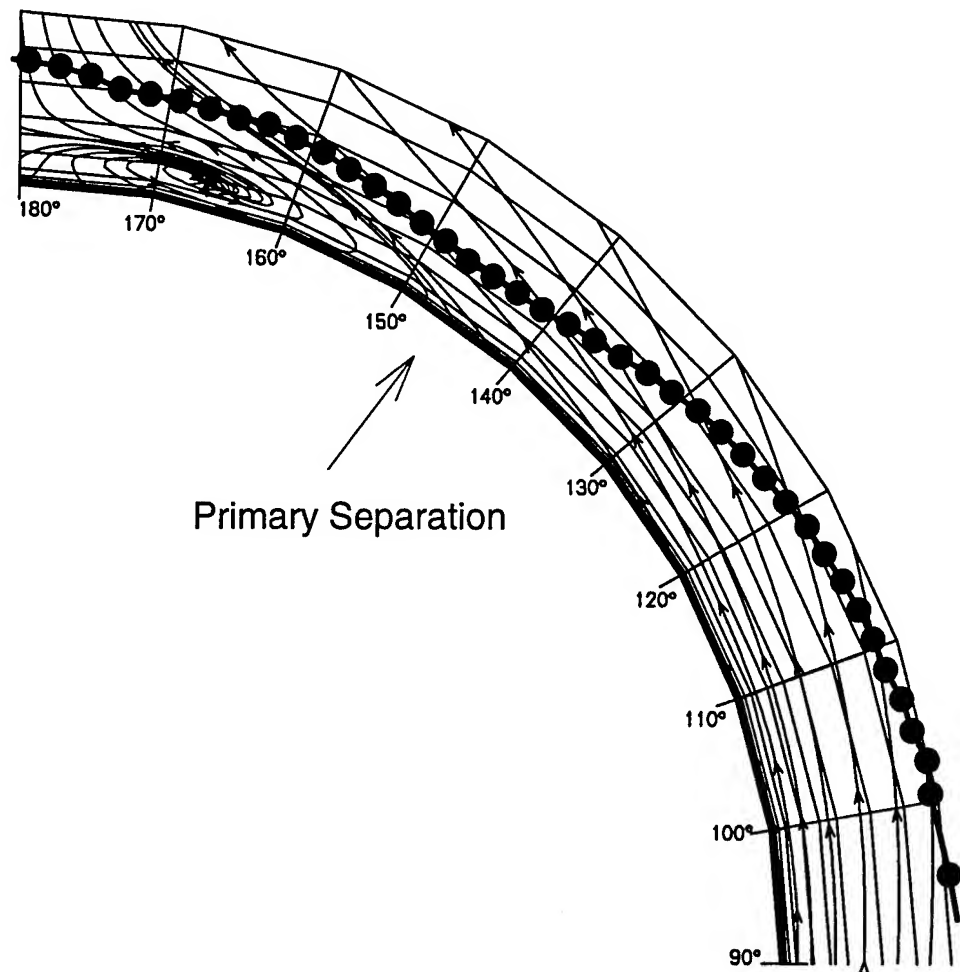


Figure 28. Skin friction values superimposed on secondary streamlines from Chesnakas and Simpson (1996) at  $x/L=0.60$  and  $\alpha=10^\circ$ .

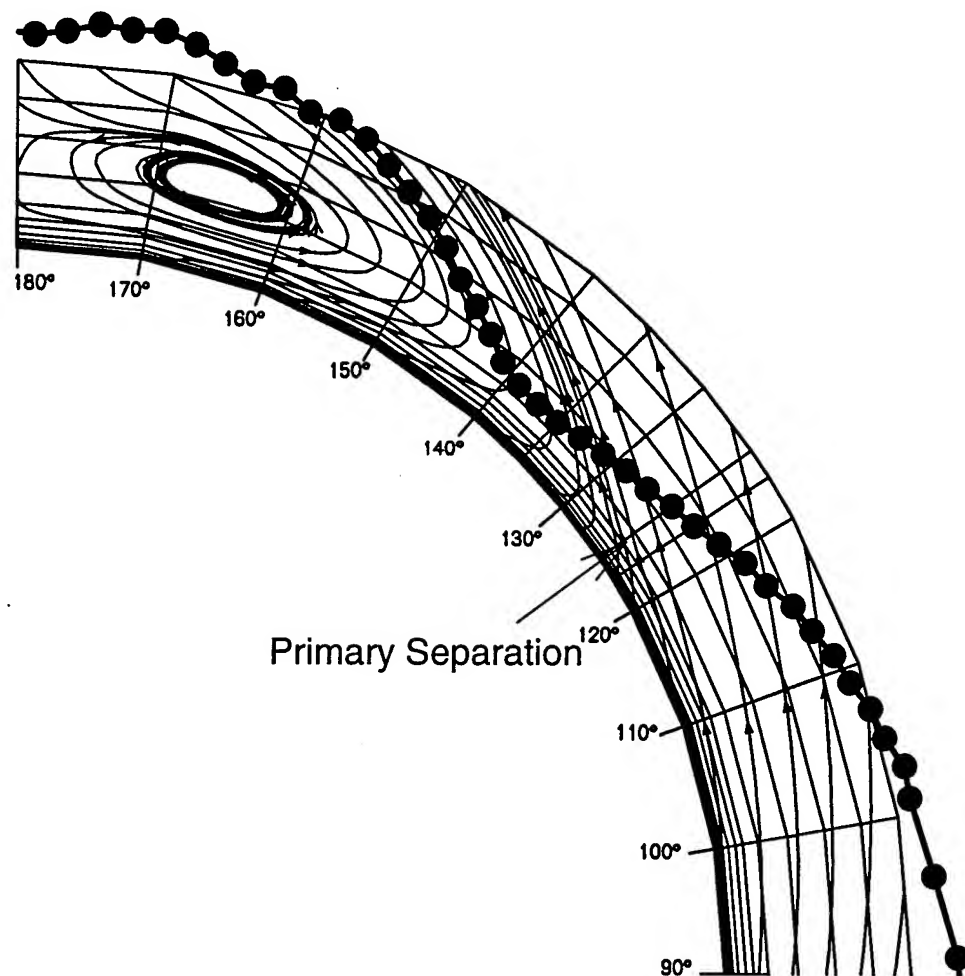


Figure 29. Skin friction values superimposed on secondary streamlines from Chesnakas and Simpson (1996) at  $x/L=0.77$  and  $\alpha=10^\circ$ .

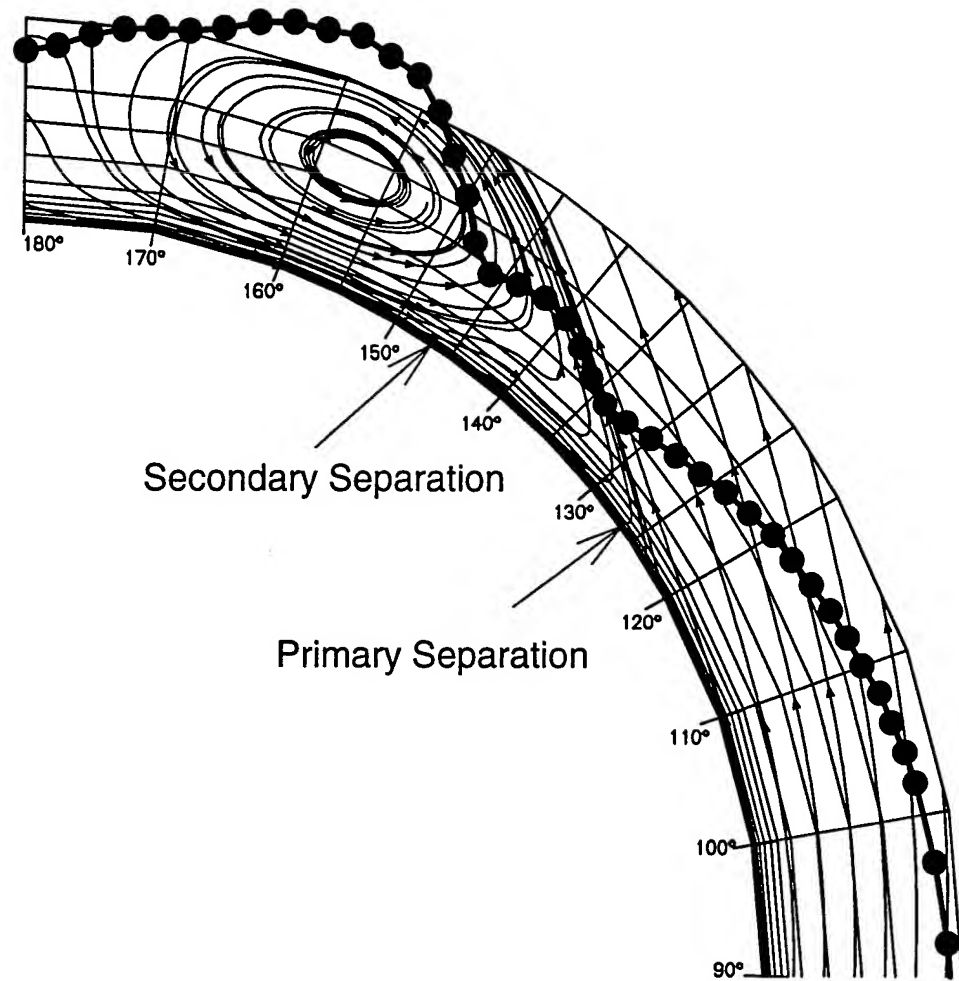


Figure 30. Skin friction values superimposed on secondary streamlines from Chesnakas and Simpson (1996) at  $x/L=0.60$  and  $\alpha=20^\circ$ .

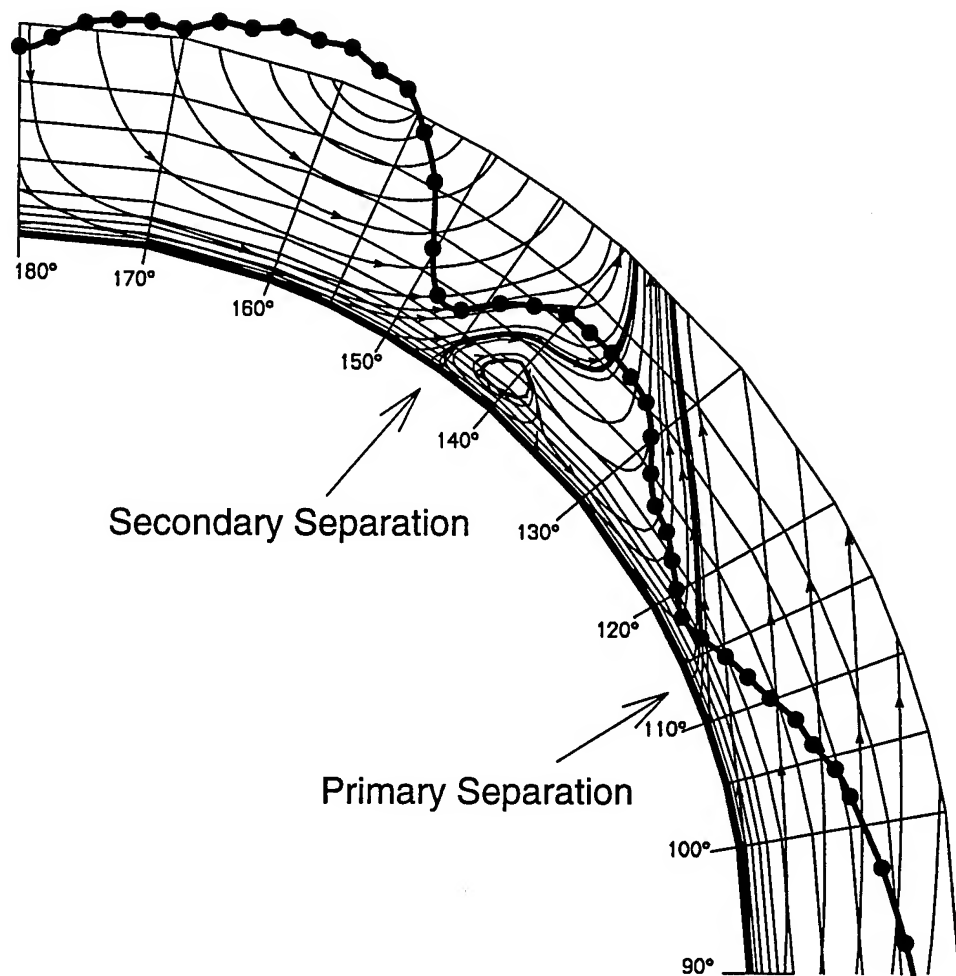


Figure 31. Skin friction values superimposed on secondary streamlines from Chesnakas and Simpson (1996) at  $x/L=0.77$  and  $\alpha=20^\circ$ .

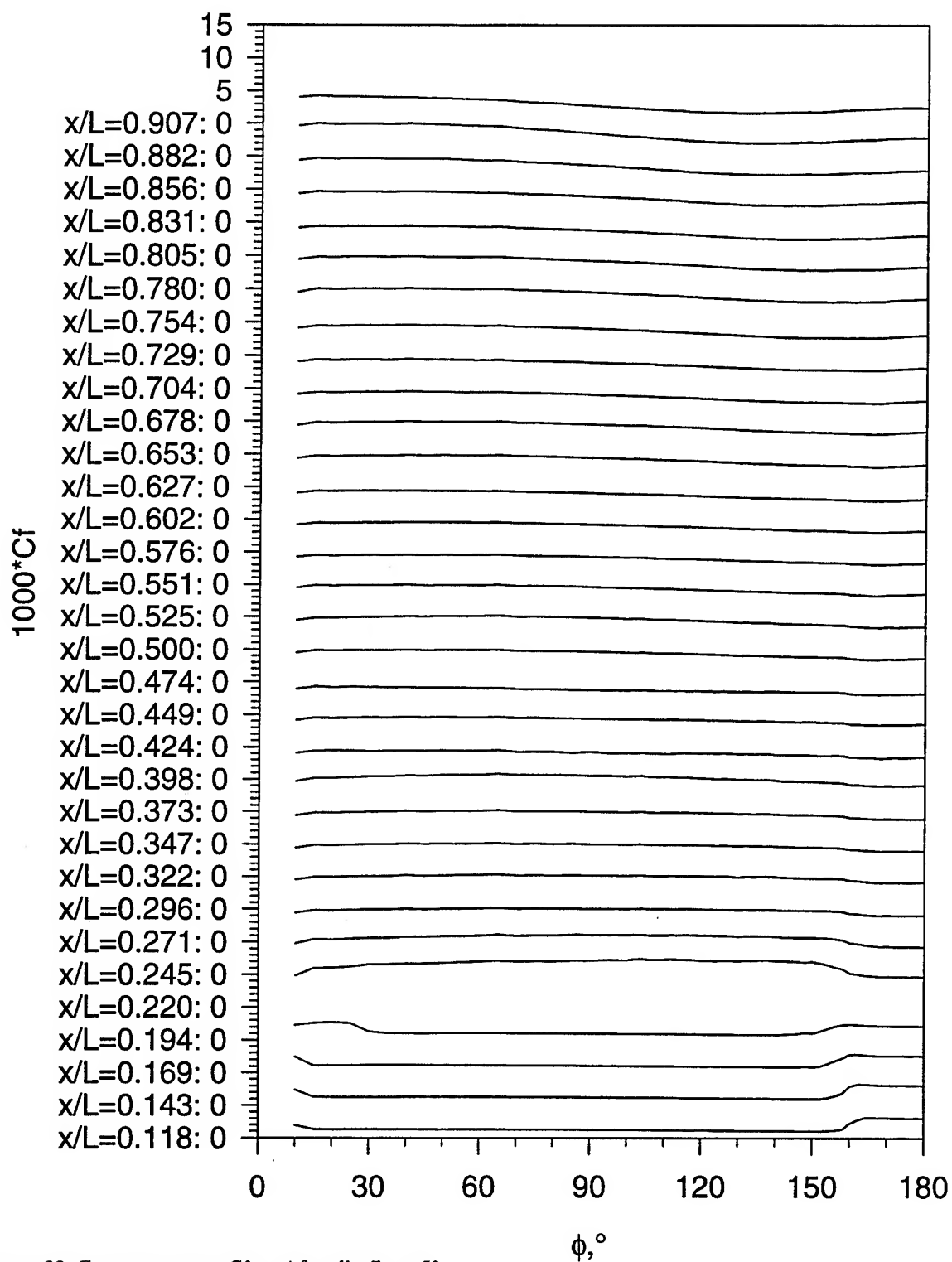


Figure 32. Constant current  $Cf$  vs.  $\phi$  for all  $x/L$ ,  $\alpha=5^\circ$ .

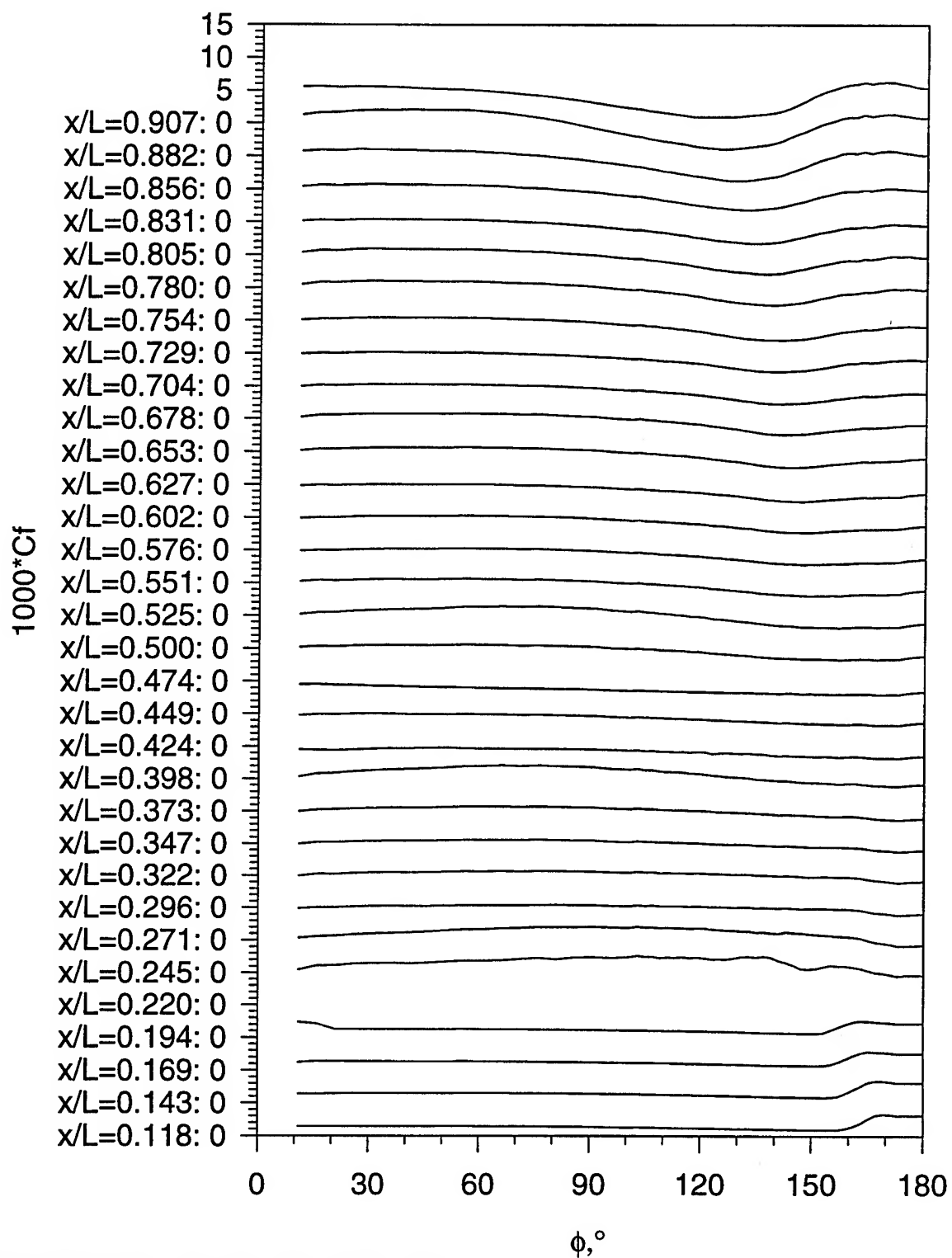


Figure 33. Constant current  $C_f$  vs.  $\phi$  for all  $x/L$ ,  $\alpha=10^\circ$ .

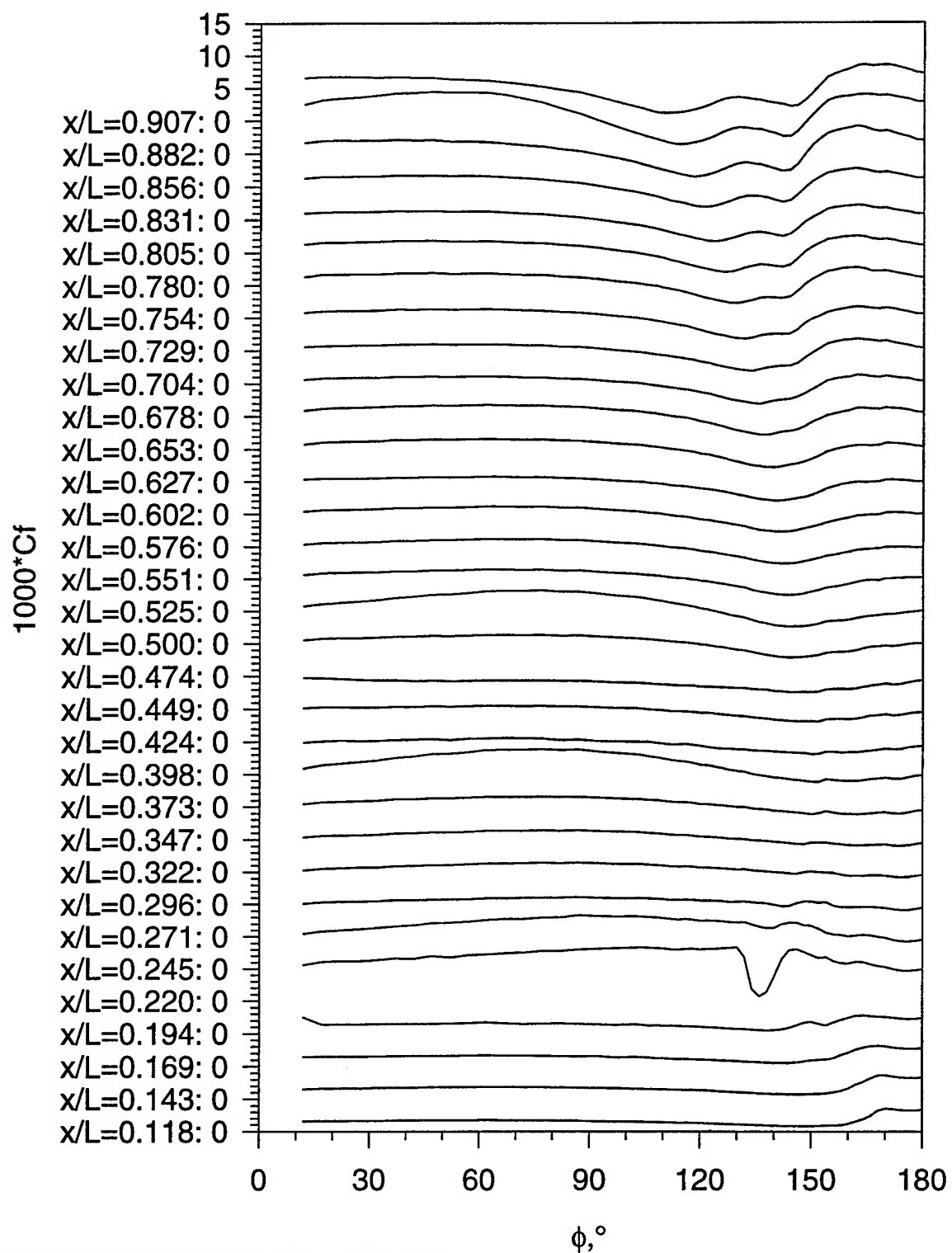


Figure 34. Constant current  $C_f$  vs.  $\phi$  for all  $x/L$ ,  $\alpha=15^\circ$ .

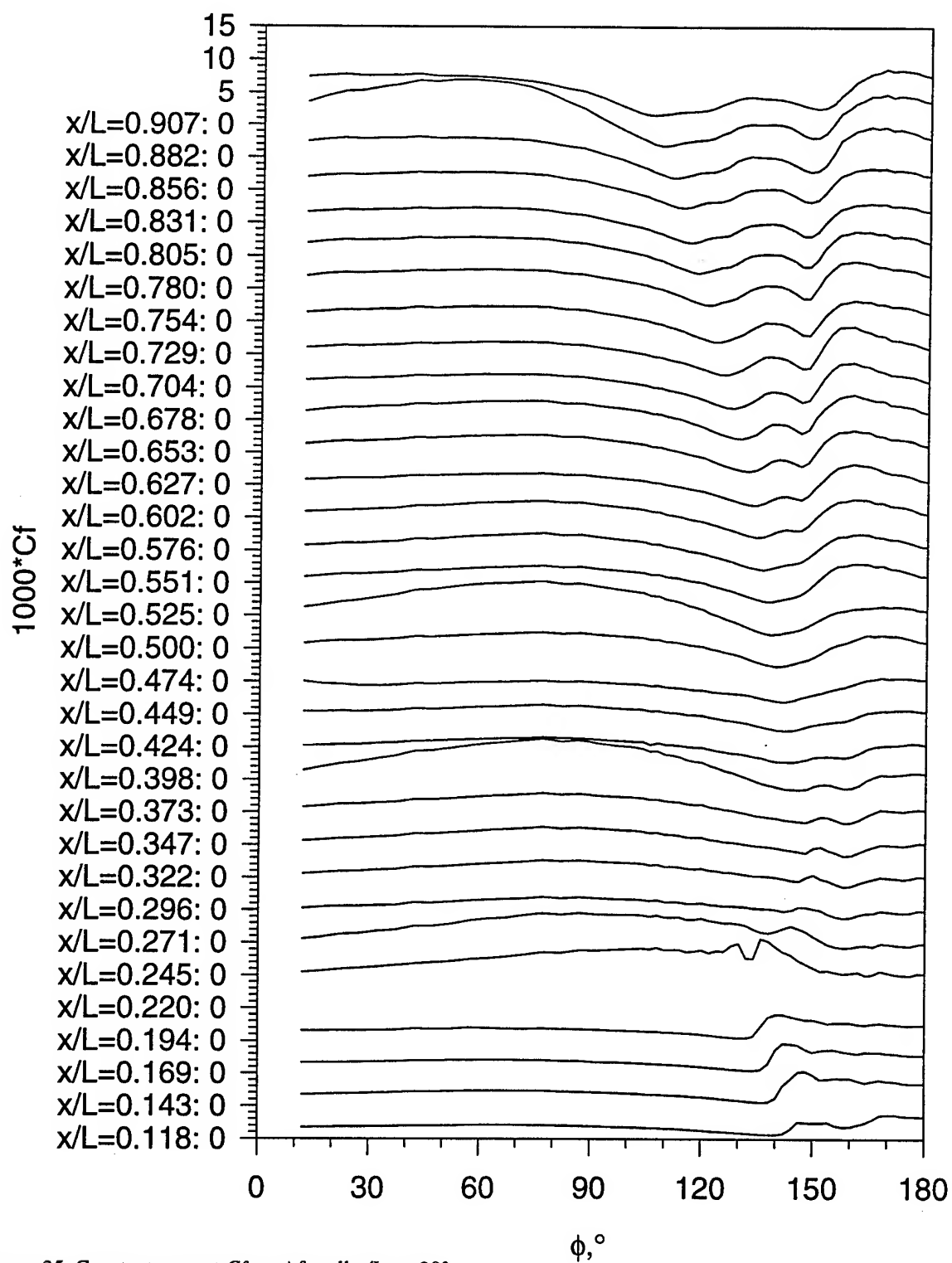


Figure 35. Constant current  $C_f$  vs.  $\phi$  for all  $x/L$ ,  $\alpha=20^\circ$ .



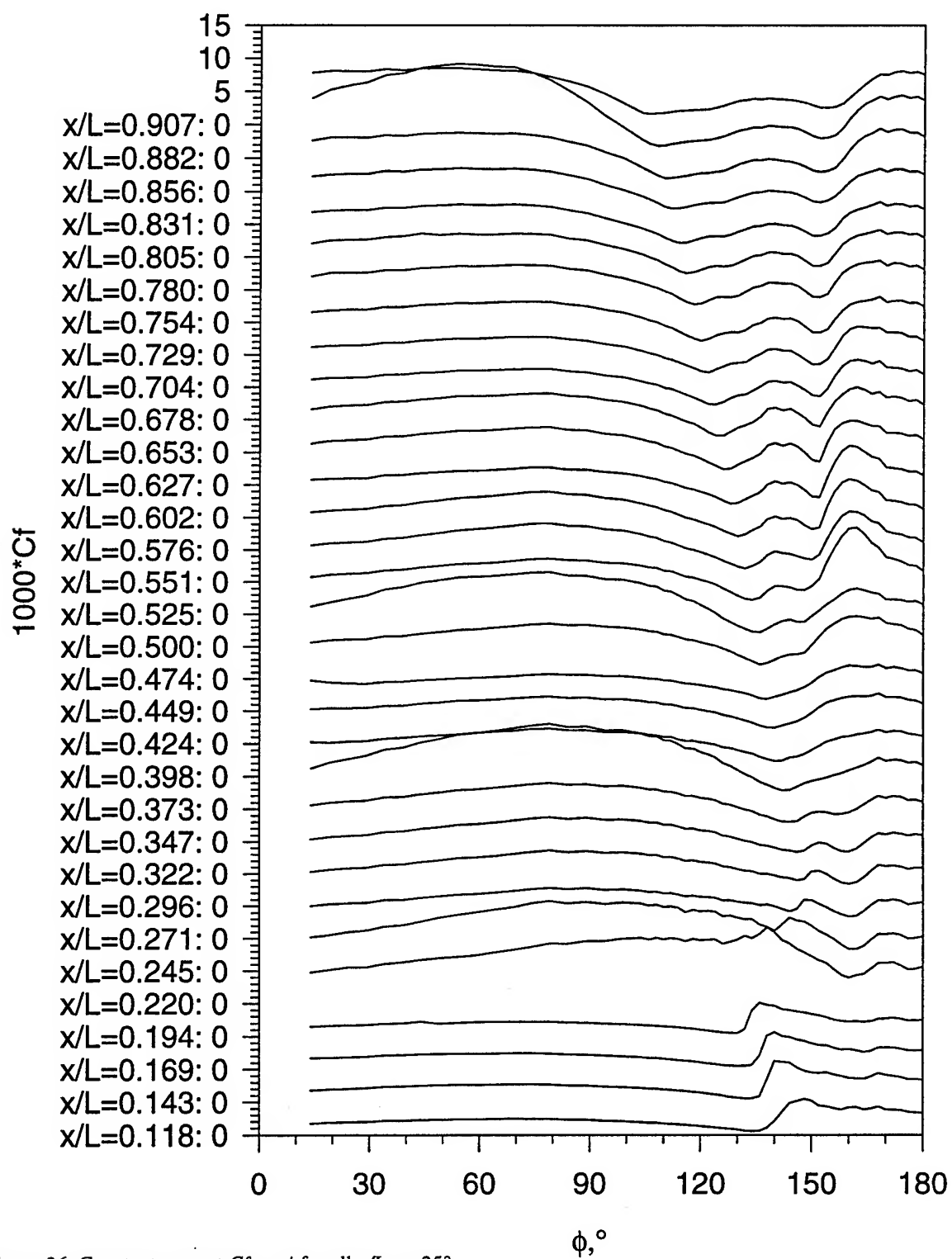


Figure 36. Constant current  $C_f$  vs.  $\phi$  for all  $x/L$ ,  $\alpha = 25^\circ$ .

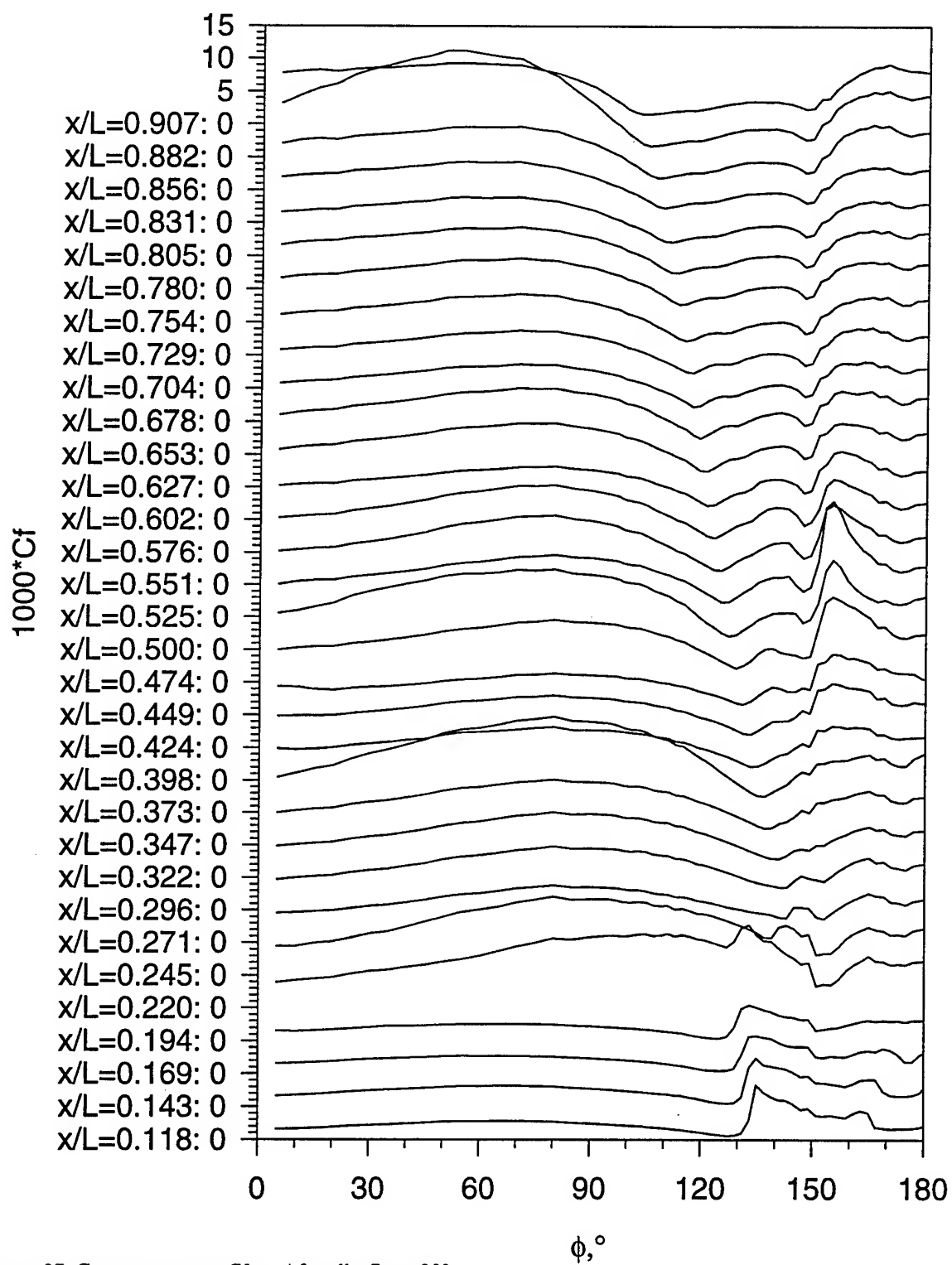


Figure 37. Constant current  $C_f$  vs.  $\phi$  for all  $x/L$ ,  $\alpha = 30^\circ$ .

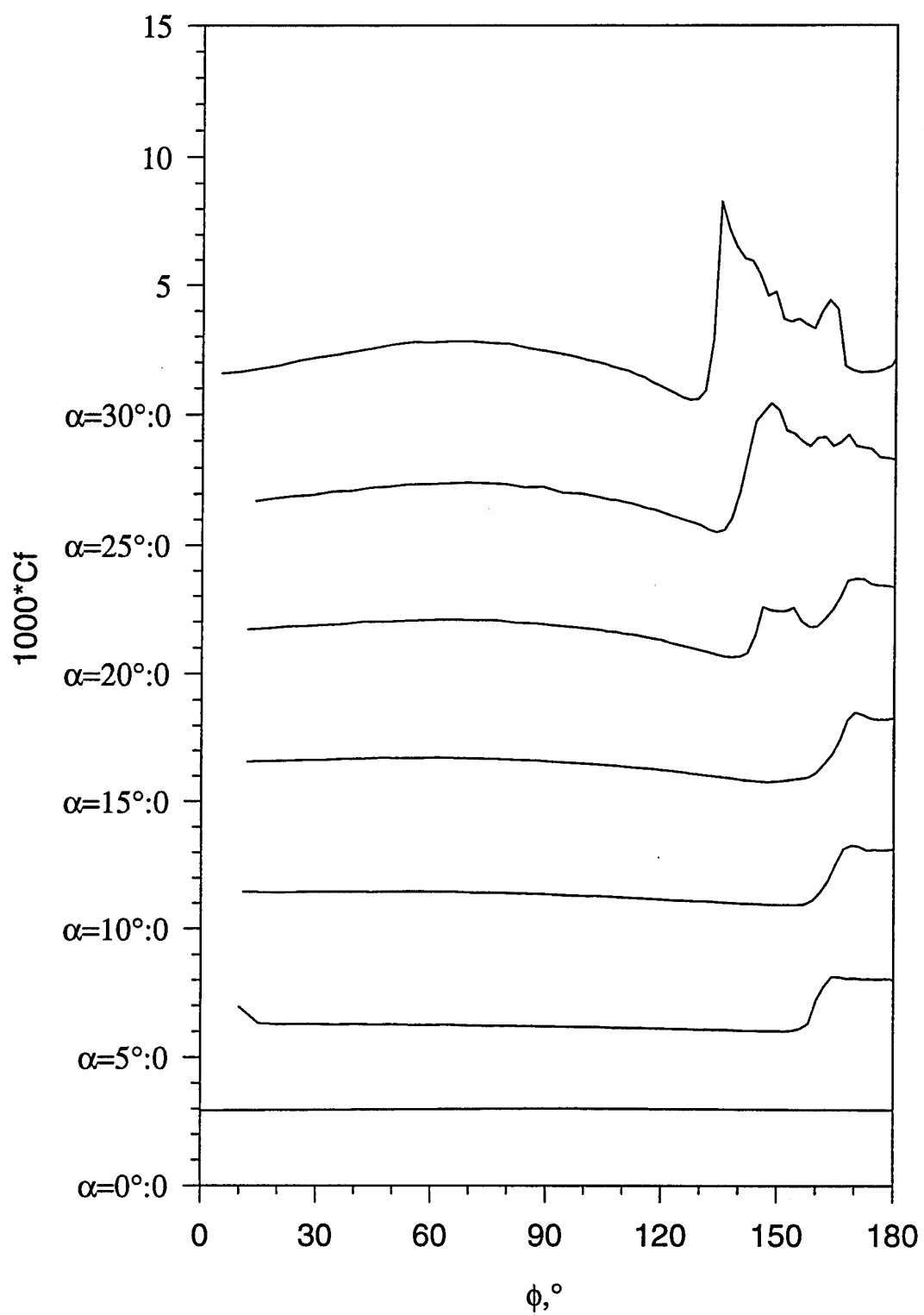


Figure 38. Constant current  $C_f$  vs.  $\phi$  for all  $\alpha$ ,  $x/L=0.118$ .

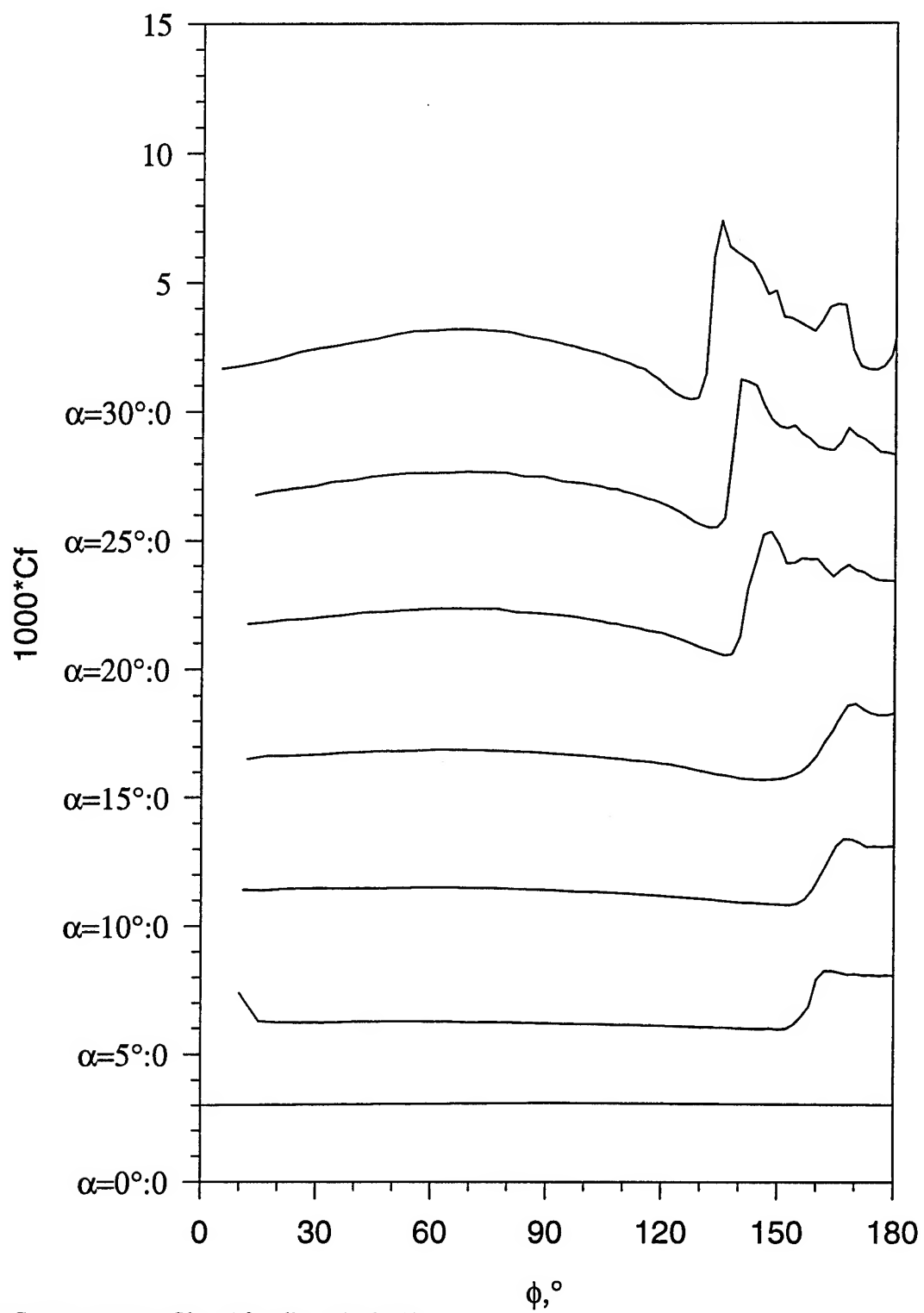


Figure 39. Constant current  $Cf$  vs.  $\phi$  for all  $\alpha$ ,  $x/L=0.143$ .

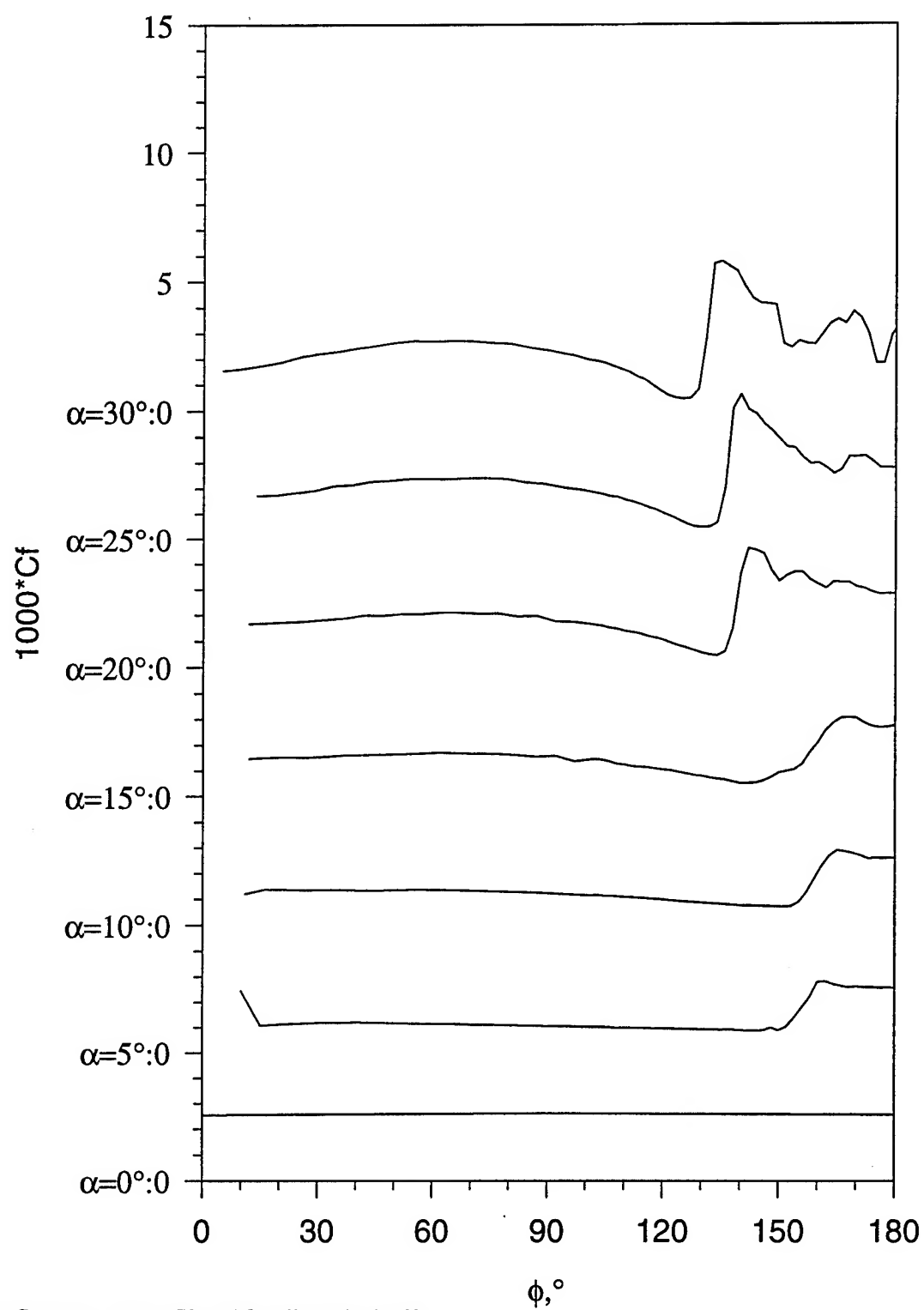


Figure 40. Constant current  $Cf$  vs.  $\phi$  for all  $\alpha$ ,  $x/L=0.169$ .

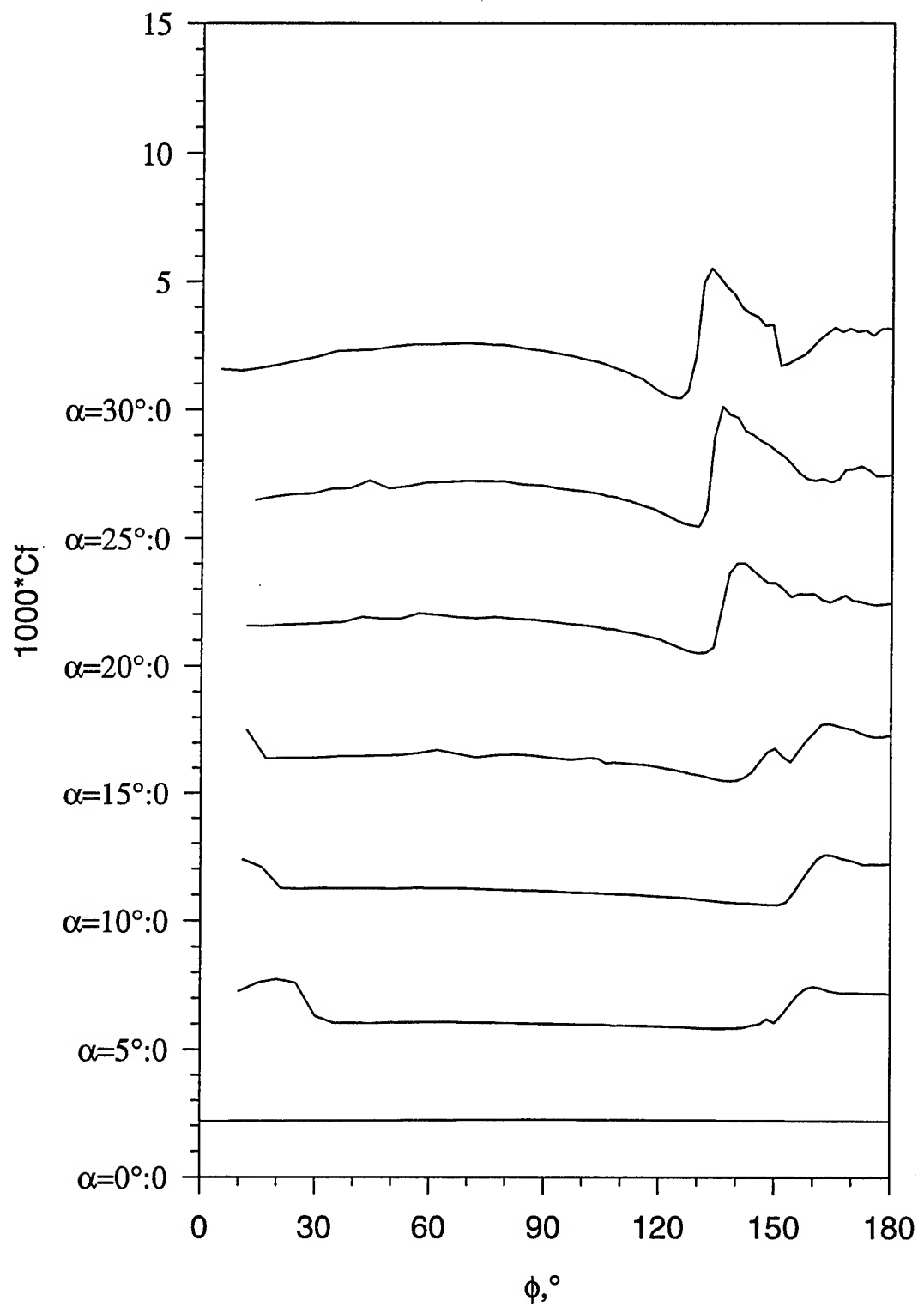


Figure 41. Constant current  $C_f$  vs.  $\phi$  for all  $\alpha$ ,  $x/L=0.194$ .

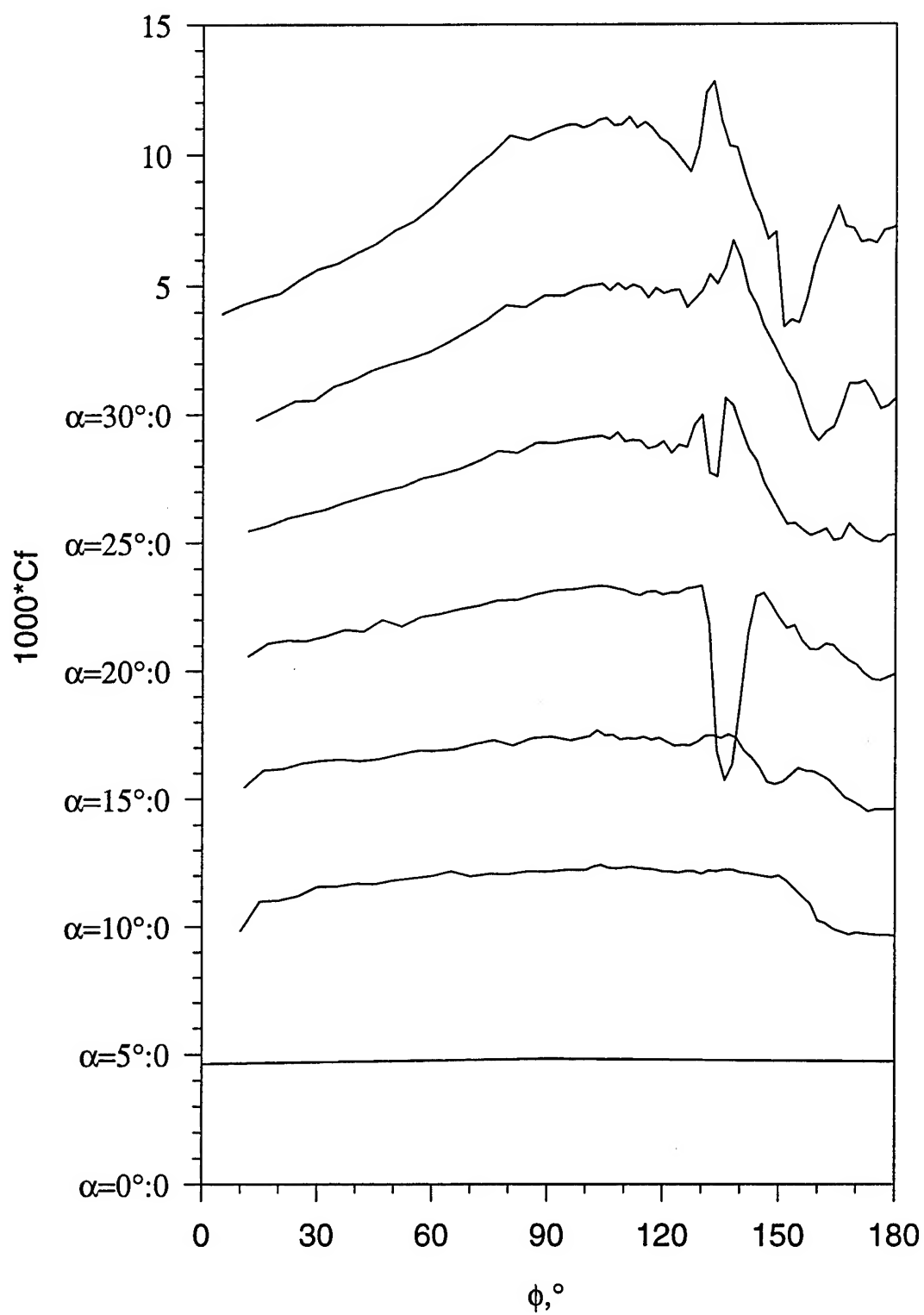


Figure 42. Constant current  $Cf$  vs.  $\phi$  for all  $\alpha$ ,  $x/L=0.220$ .

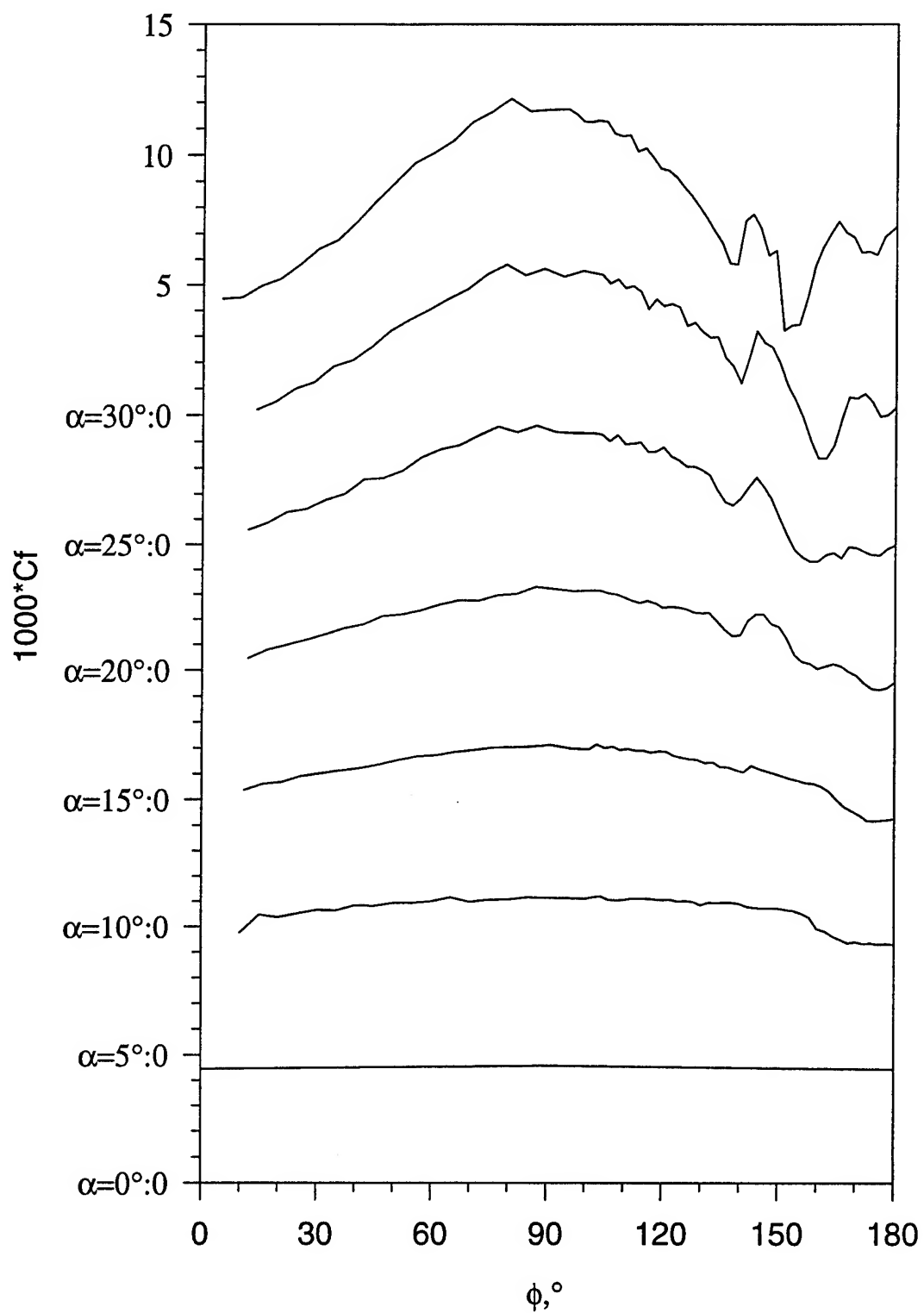


Figure 43. Constant current  $Cf$  vs.  $\phi$  for all  $\alpha$ ,  $x/L=0.245$ .



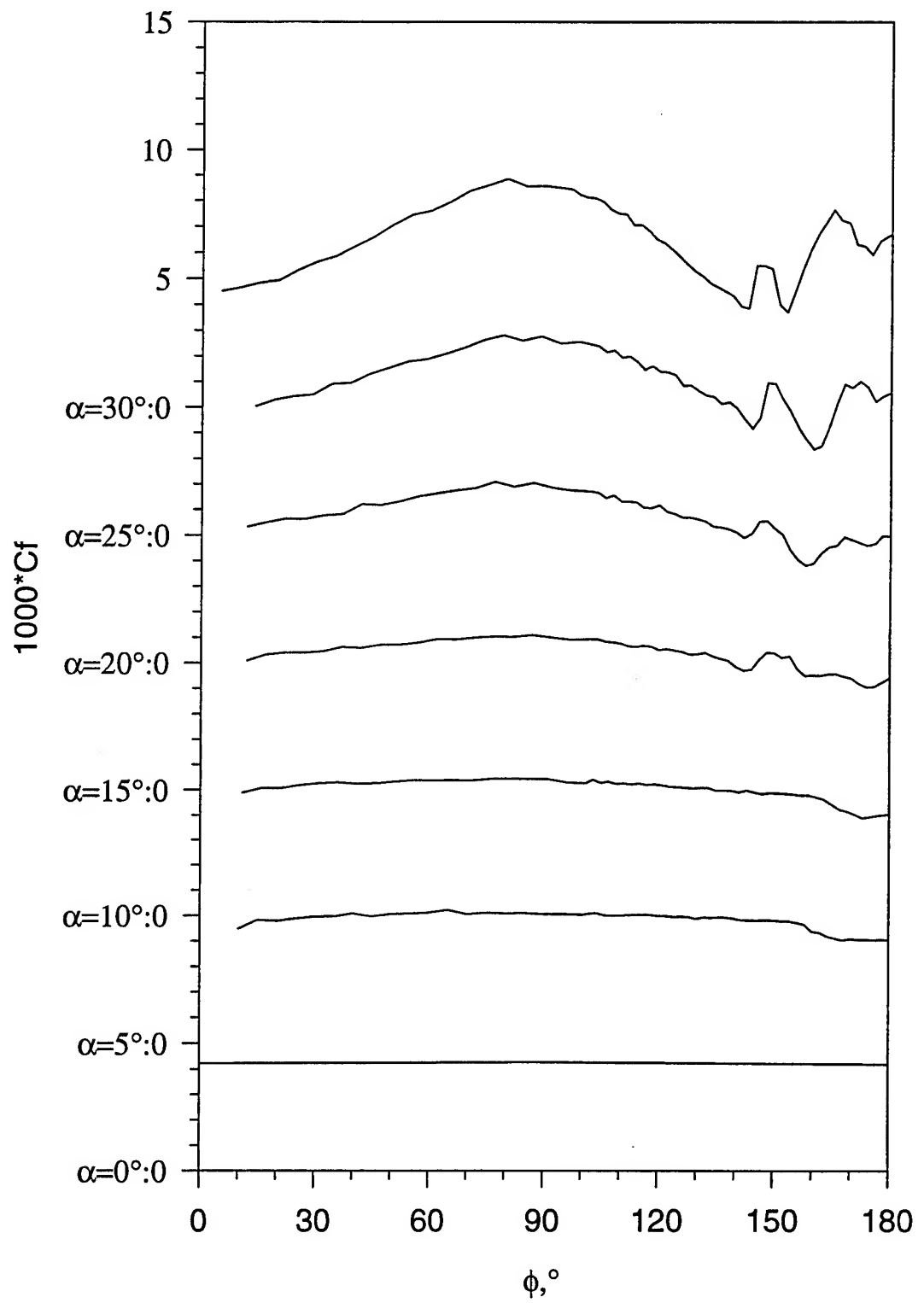


Figure 44. Constant current  $Cf$  vs.  $\phi$  for all  $\alpha$ ,  $x/L=0.271$ .

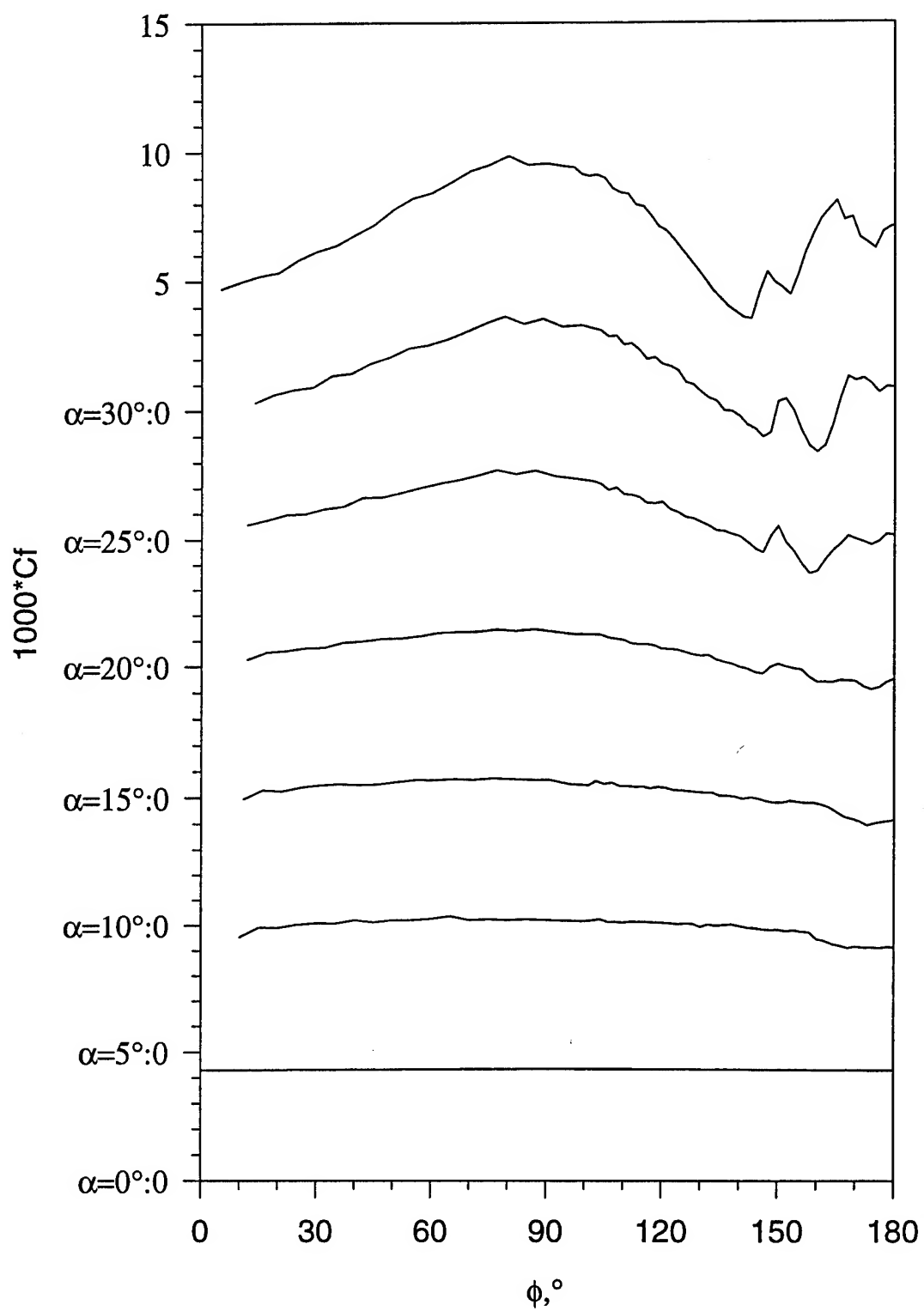


Figure 45. Constant current  $C_f$  vs.  $\phi$  for all  $\alpha$ ,  $x/L=0.296$ .

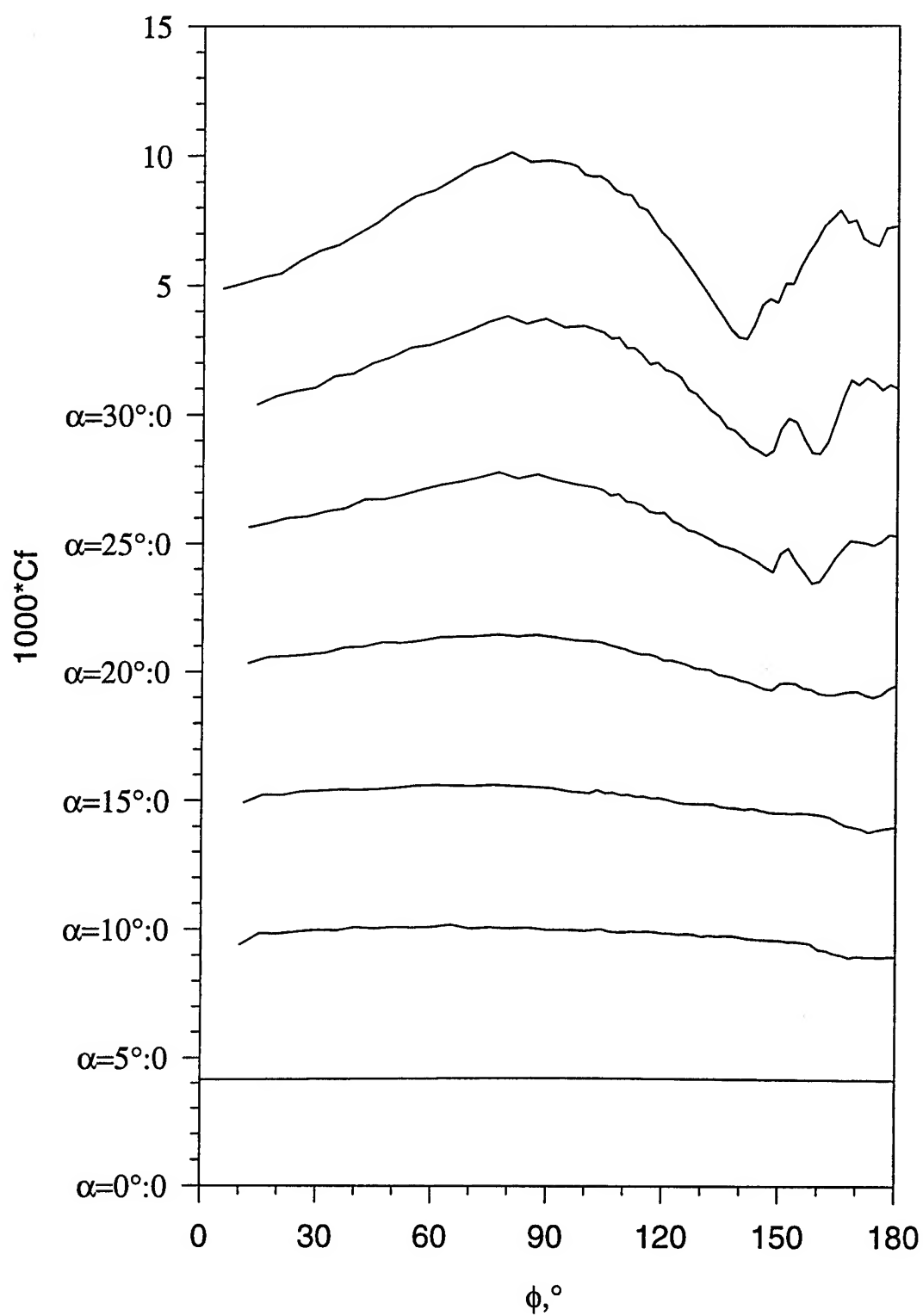


Figure 46. Constant current  $Cf$  vs.  $\phi$  for all  $\alpha$ ,  $x/L=0.322$ .

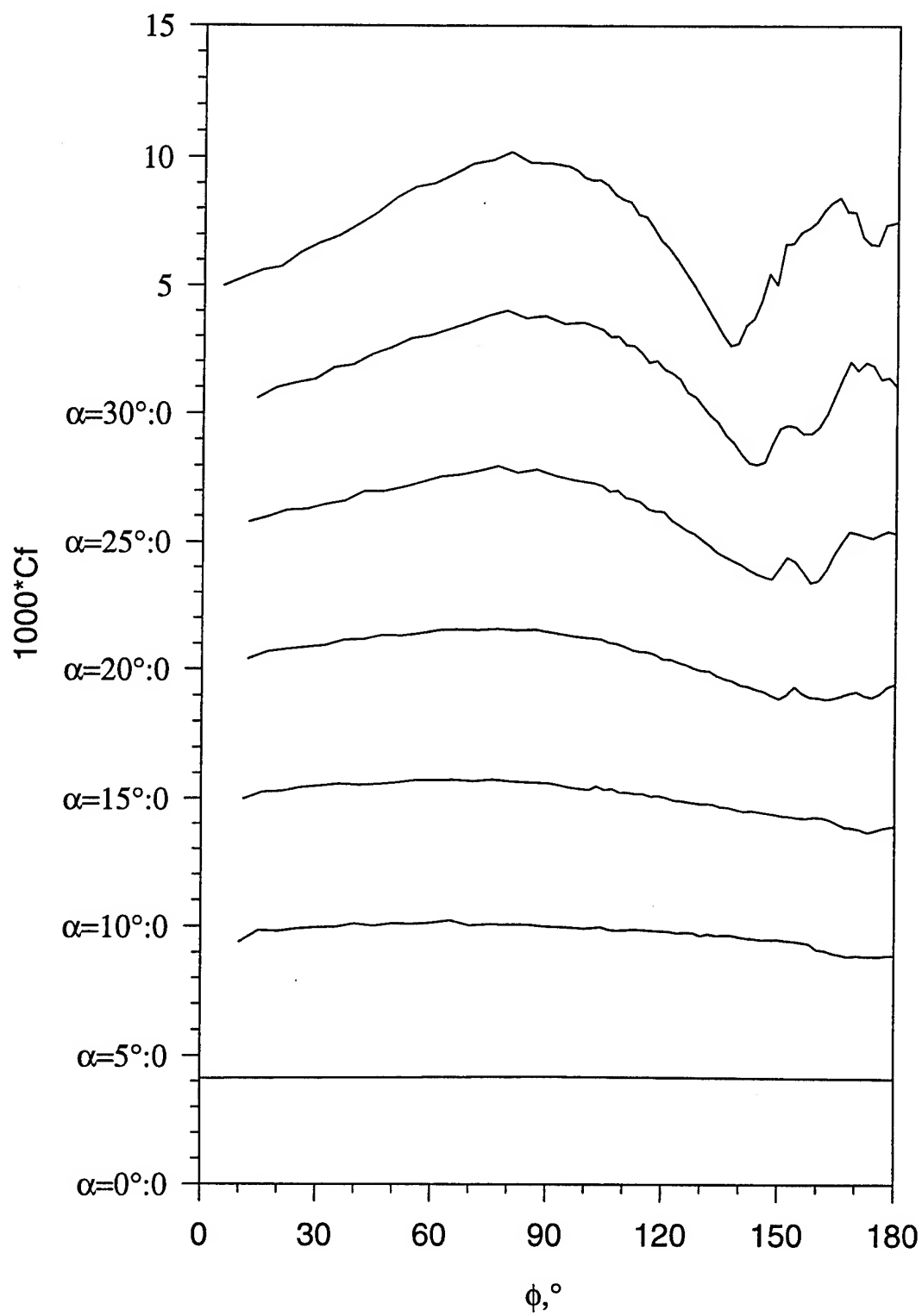


Figure 47. Constant current  $Cf$  vs.  $\phi$  for all  $\alpha$ ,  $x/L=0.347$ .

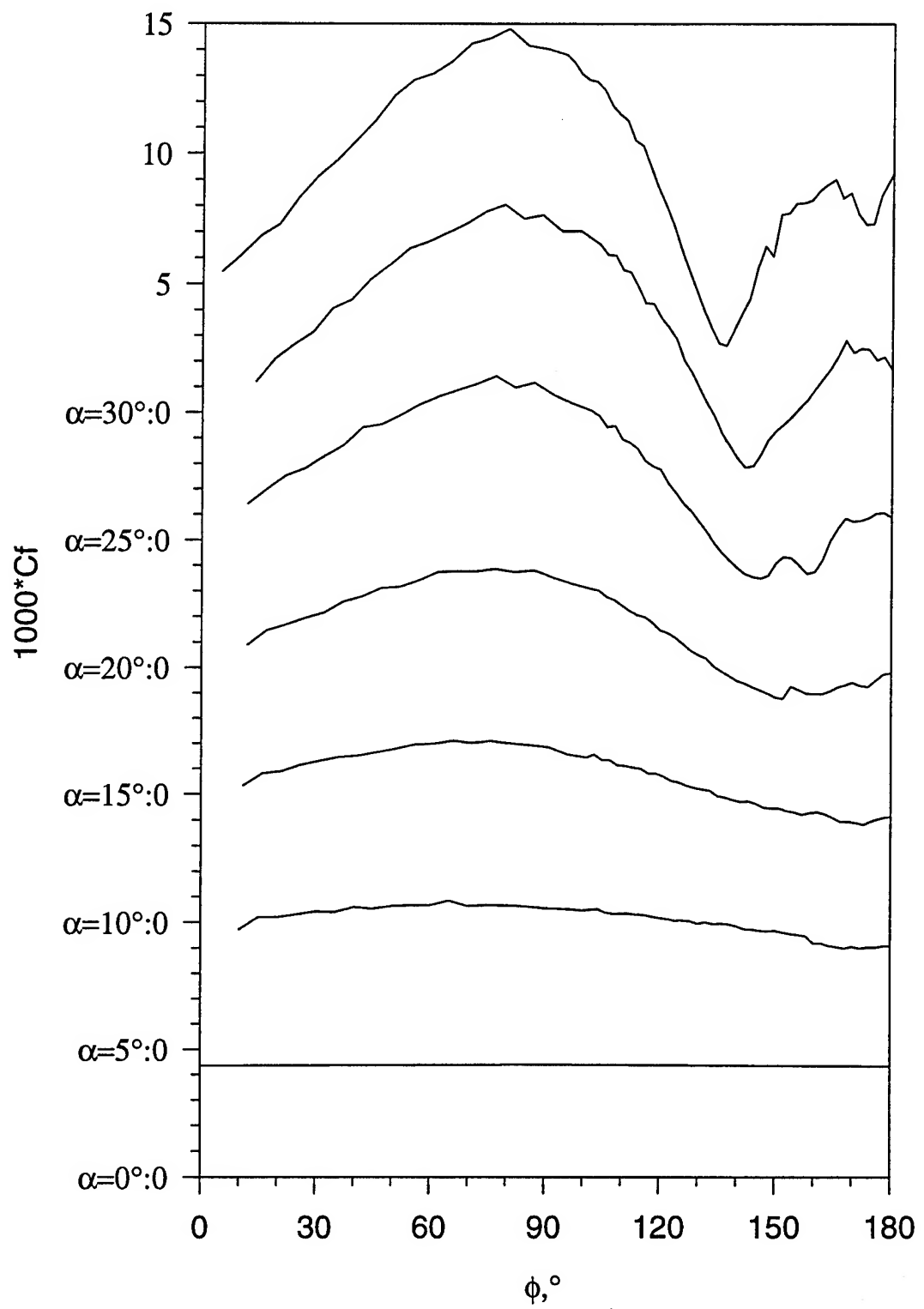


Figure 48. Constant current  $C_f$  vs.  $\phi$  for all  $\alpha$ ,  $x/L=0.373$ .

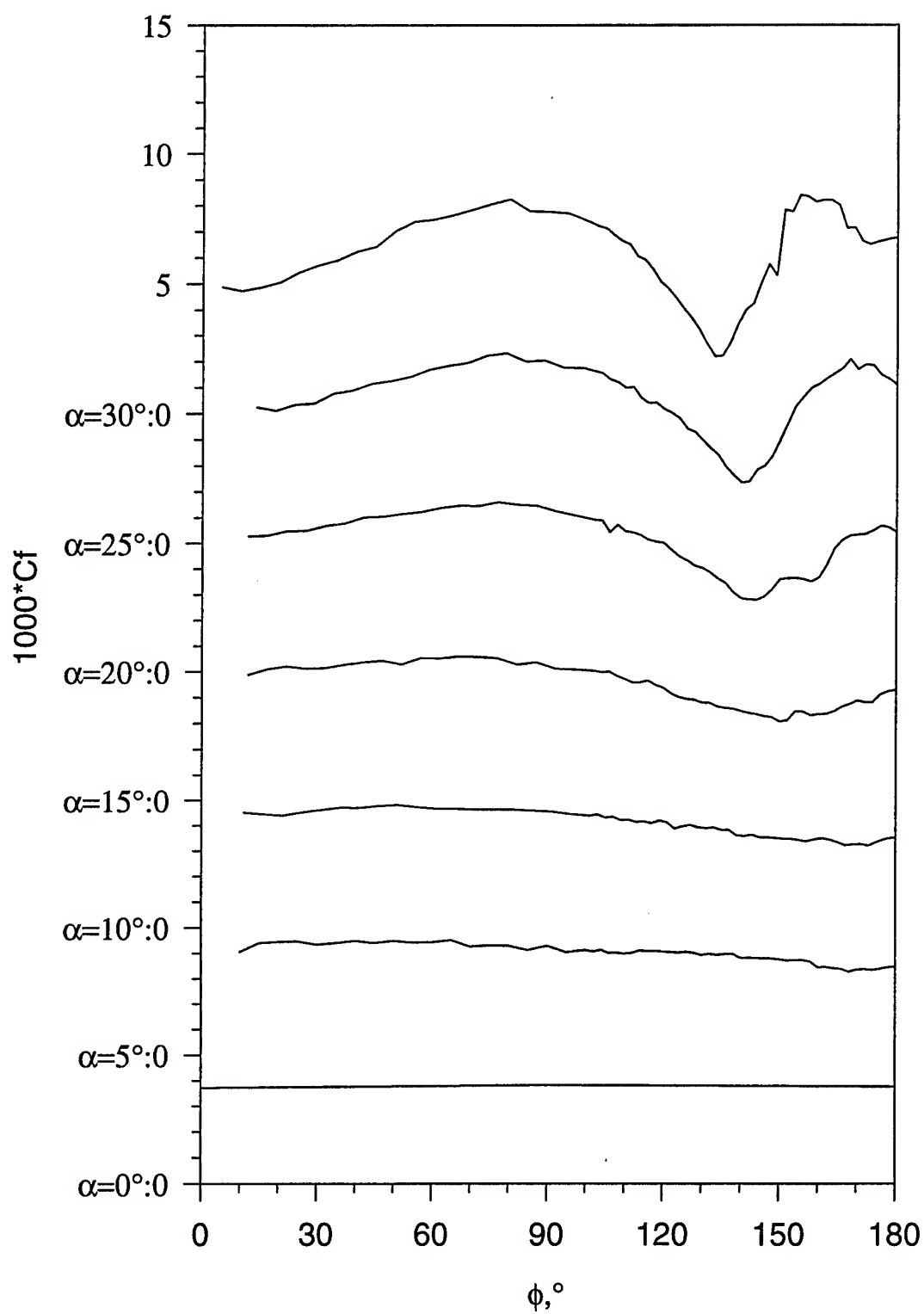


Figure 49. Constant current  $C_f$  vs.  $\phi$  for all  $\alpha$ ,  $x/L=0.398$ .

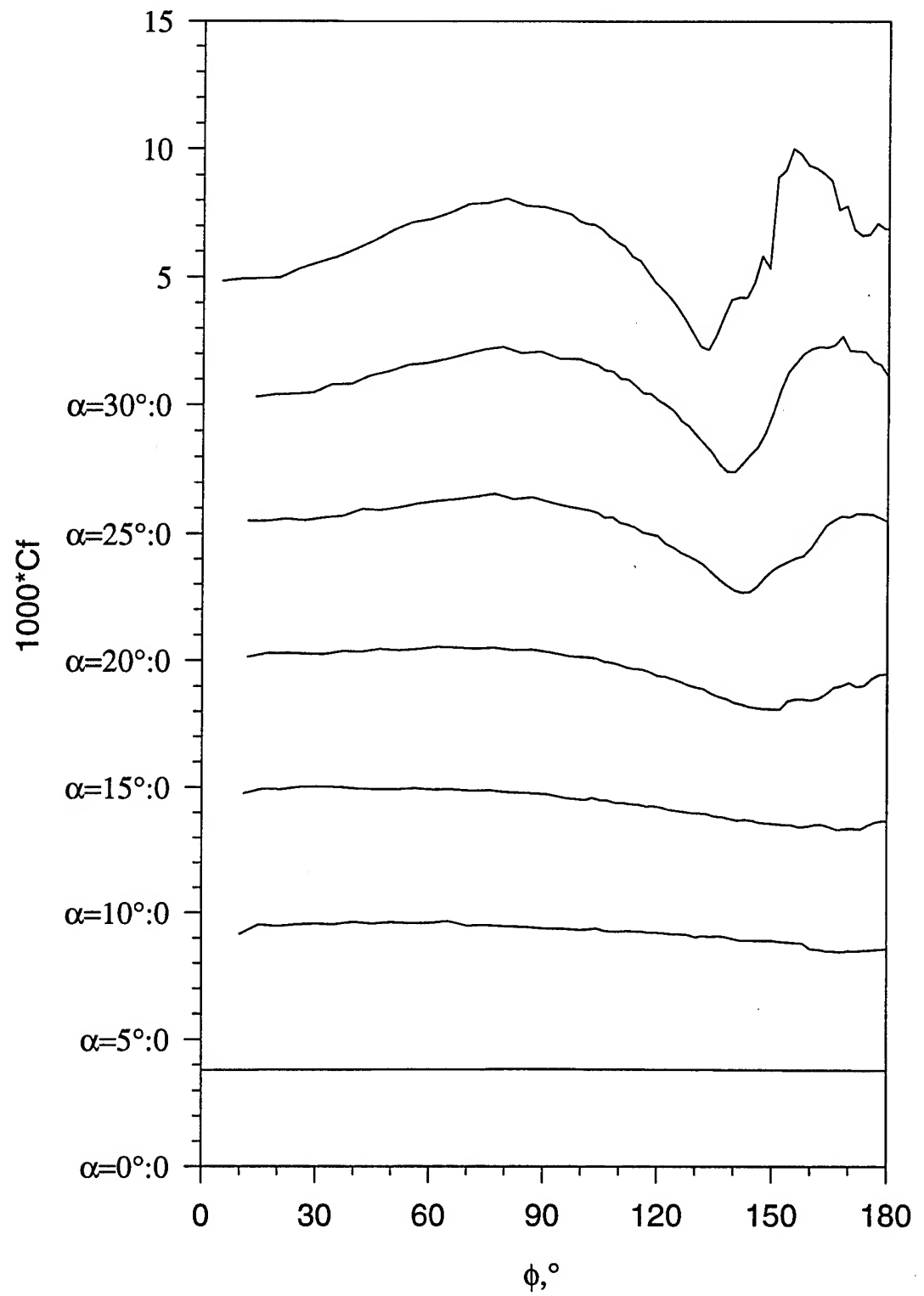


Figure 50. Constant current  $Cf$  vs.  $\phi$  for all  $\alpha$ ,  $x/L=0.424$ .

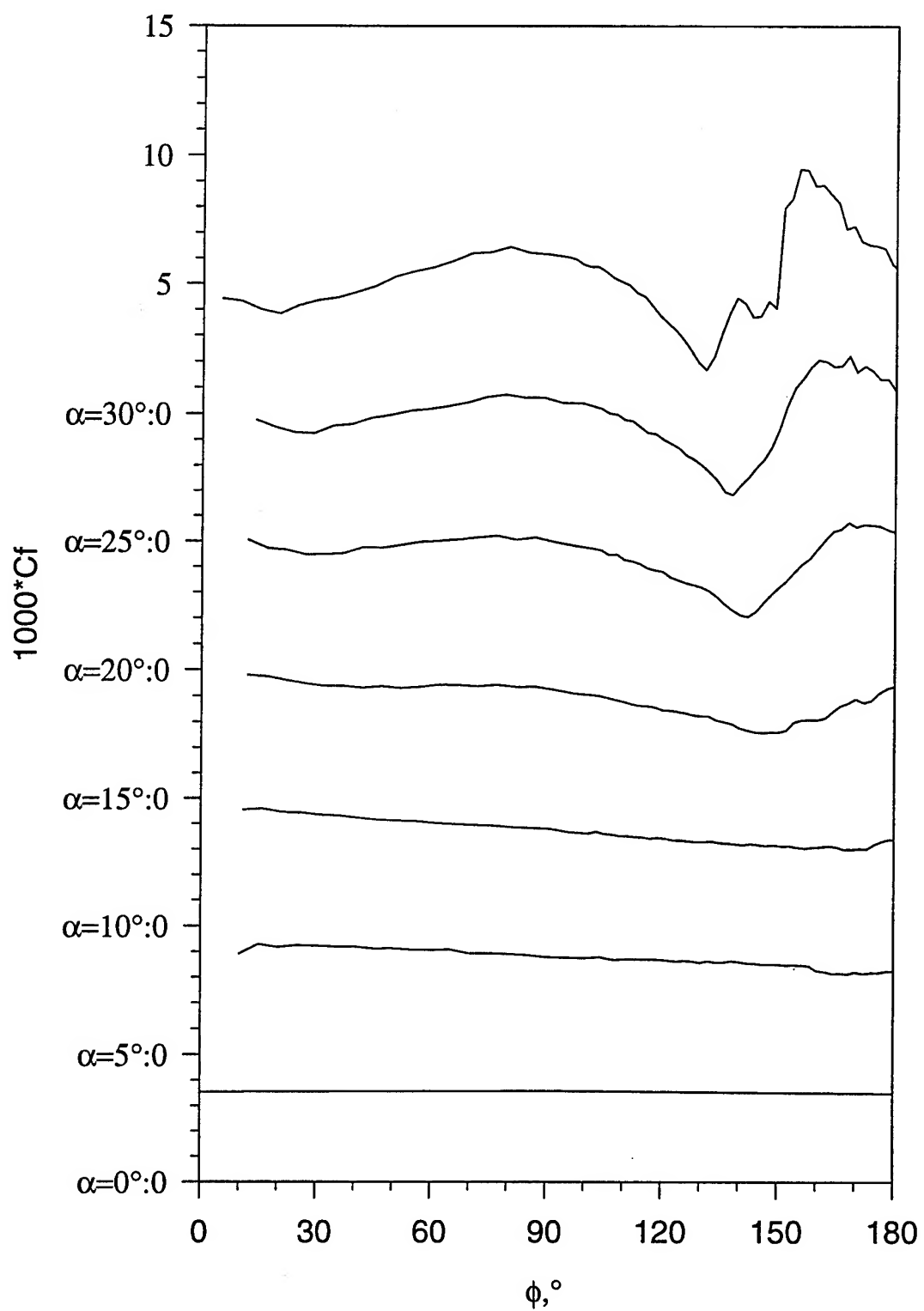


Figure 51. Constant current  $Cf$  vs.  $\phi$  for all  $\alpha$ ,  $x/L=0.449$ .



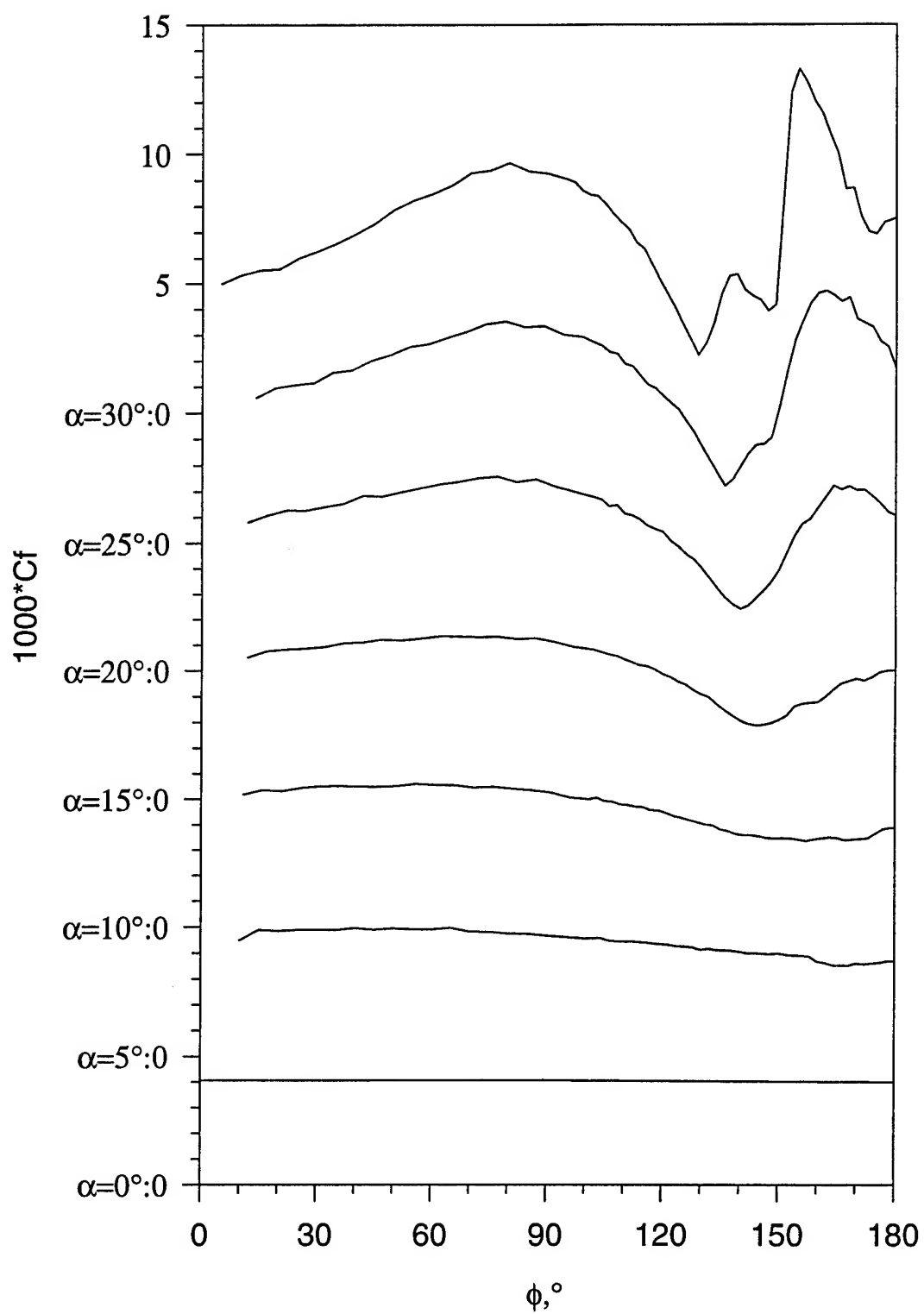


Figure 52. Constant current  $Cf$  vs.  $\phi$  for all  $\alpha$ ,  $x/L=0.474$ .

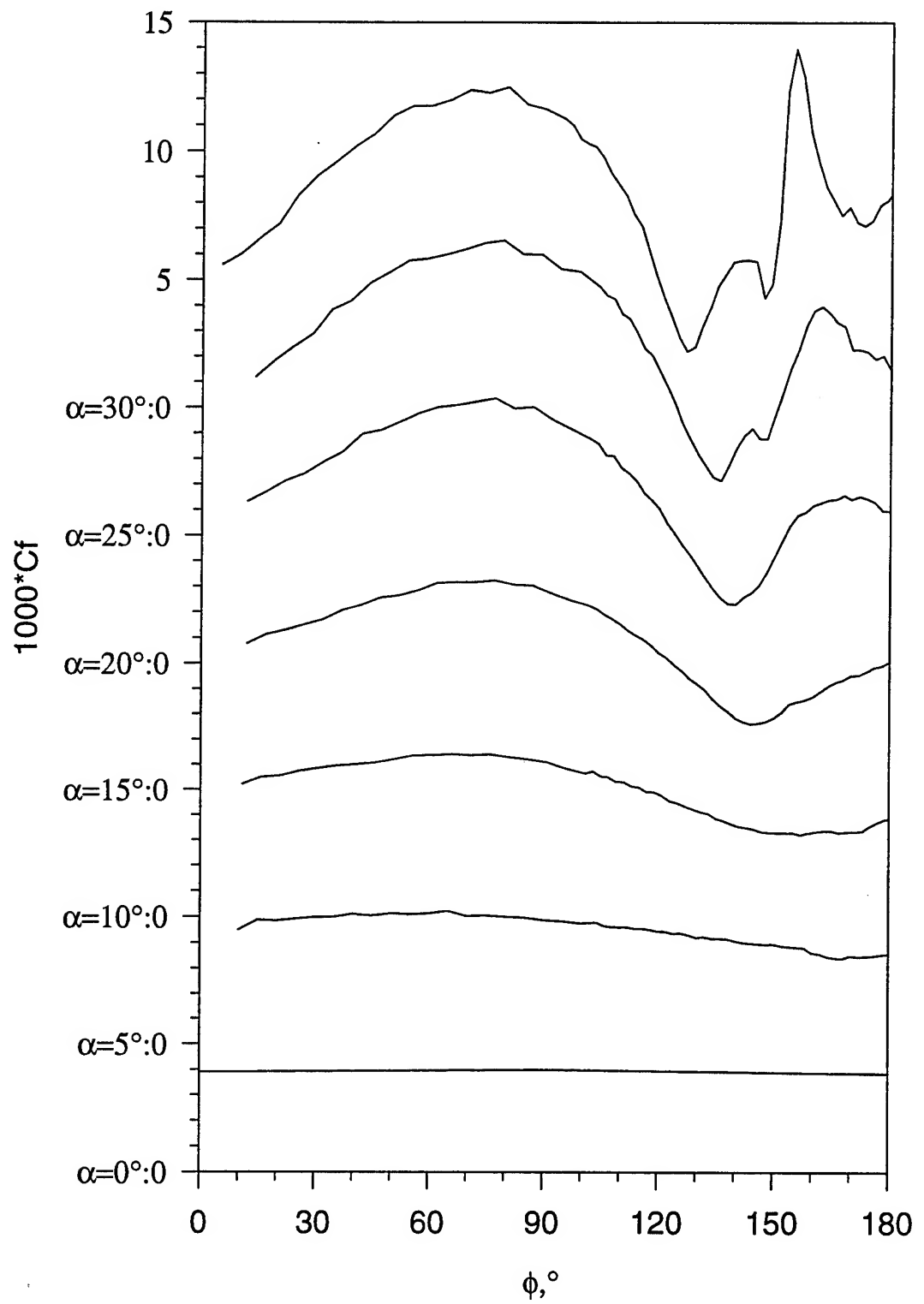


Figure 53. Constant current  $Cf$  vs.  $\phi$  for all  $\alpha$ ,  $x/L=0.500$ .

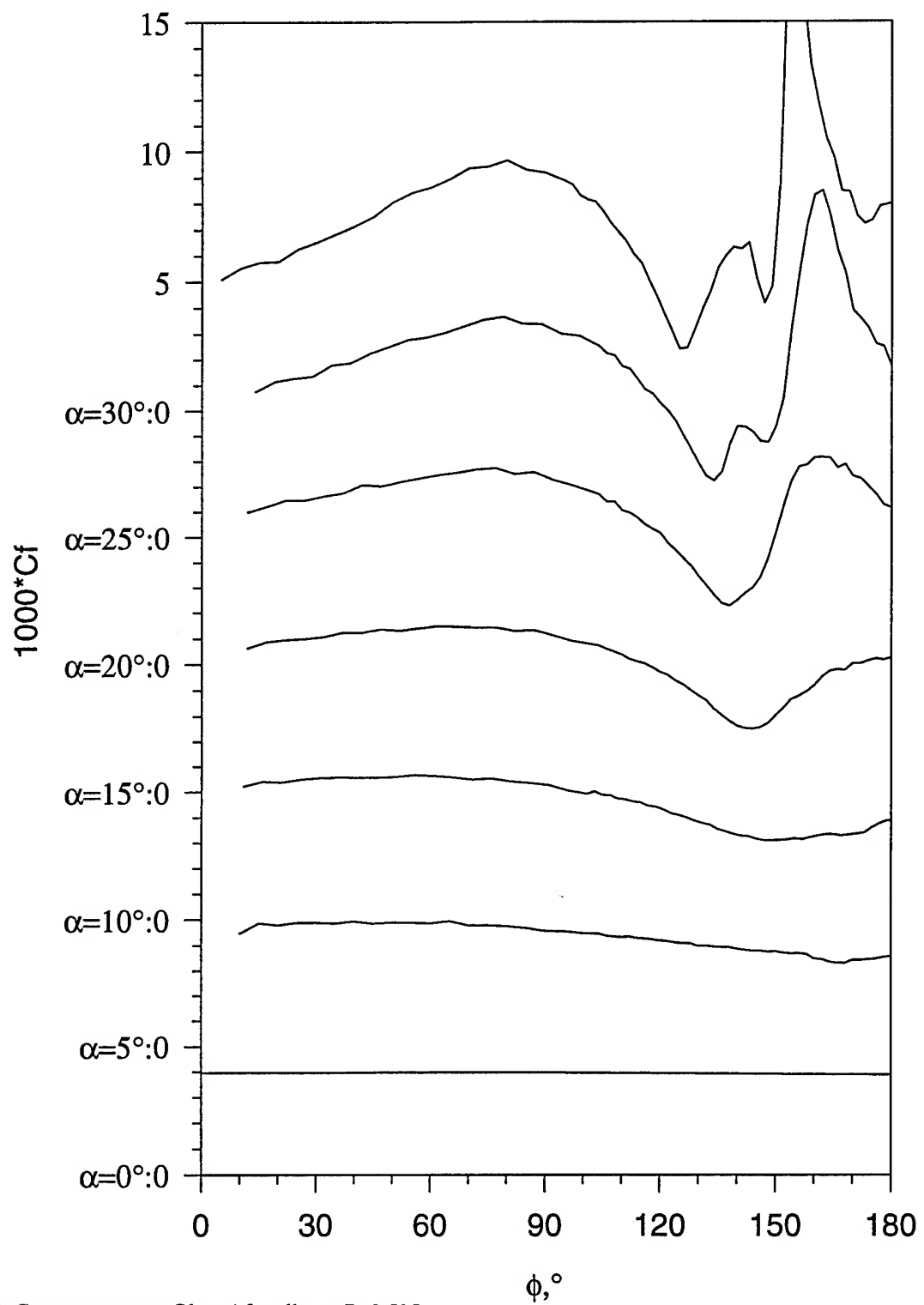


Figure 54. Constant current  $Cf$  vs.  $\phi$  for all  $\alpha$ ,  $x/L=0.525$ .

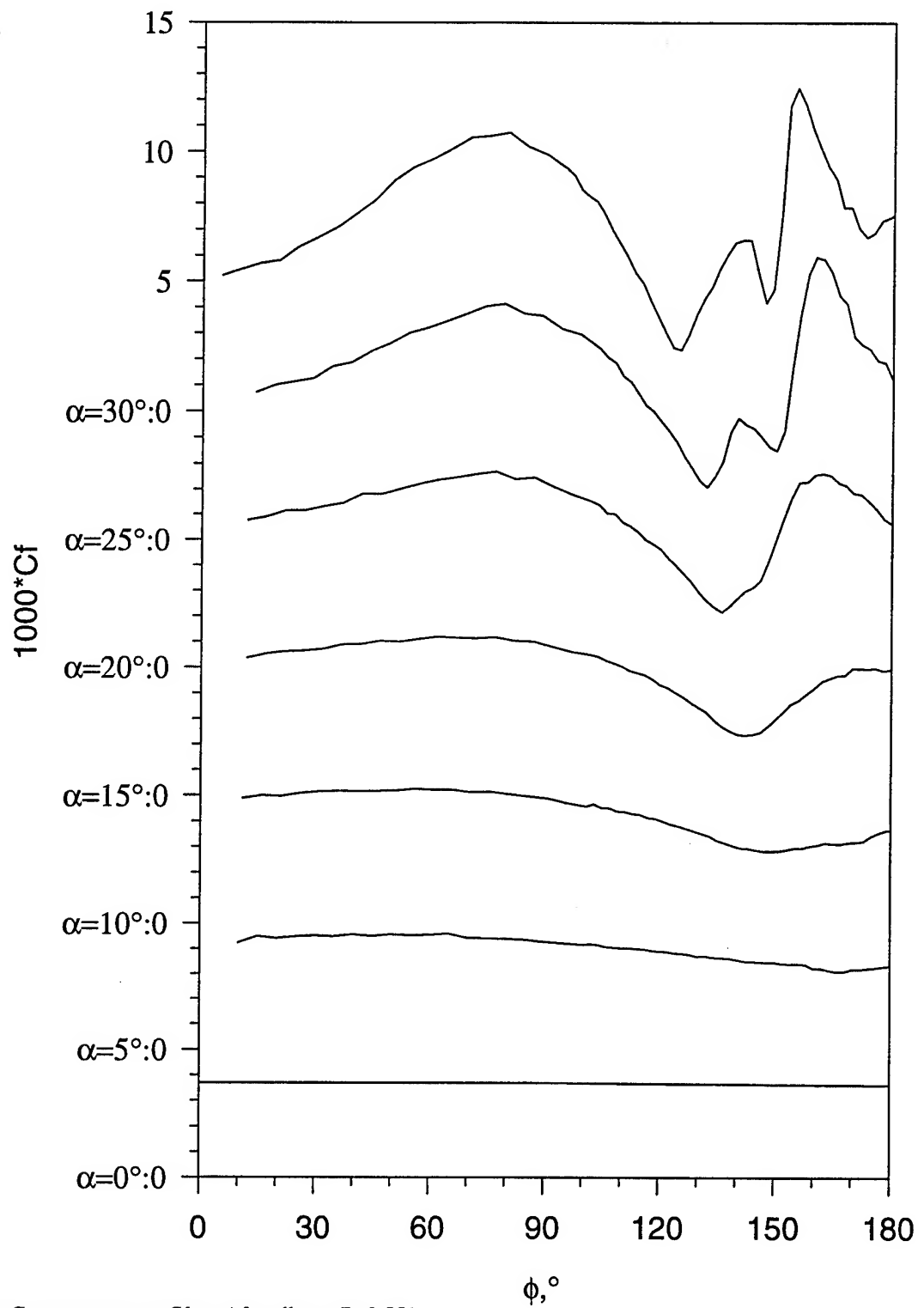


Figure 55. Constant current  $Cf$  vs.  $\phi$  for all  $\alpha$ ,  $x/L=0.551$ .

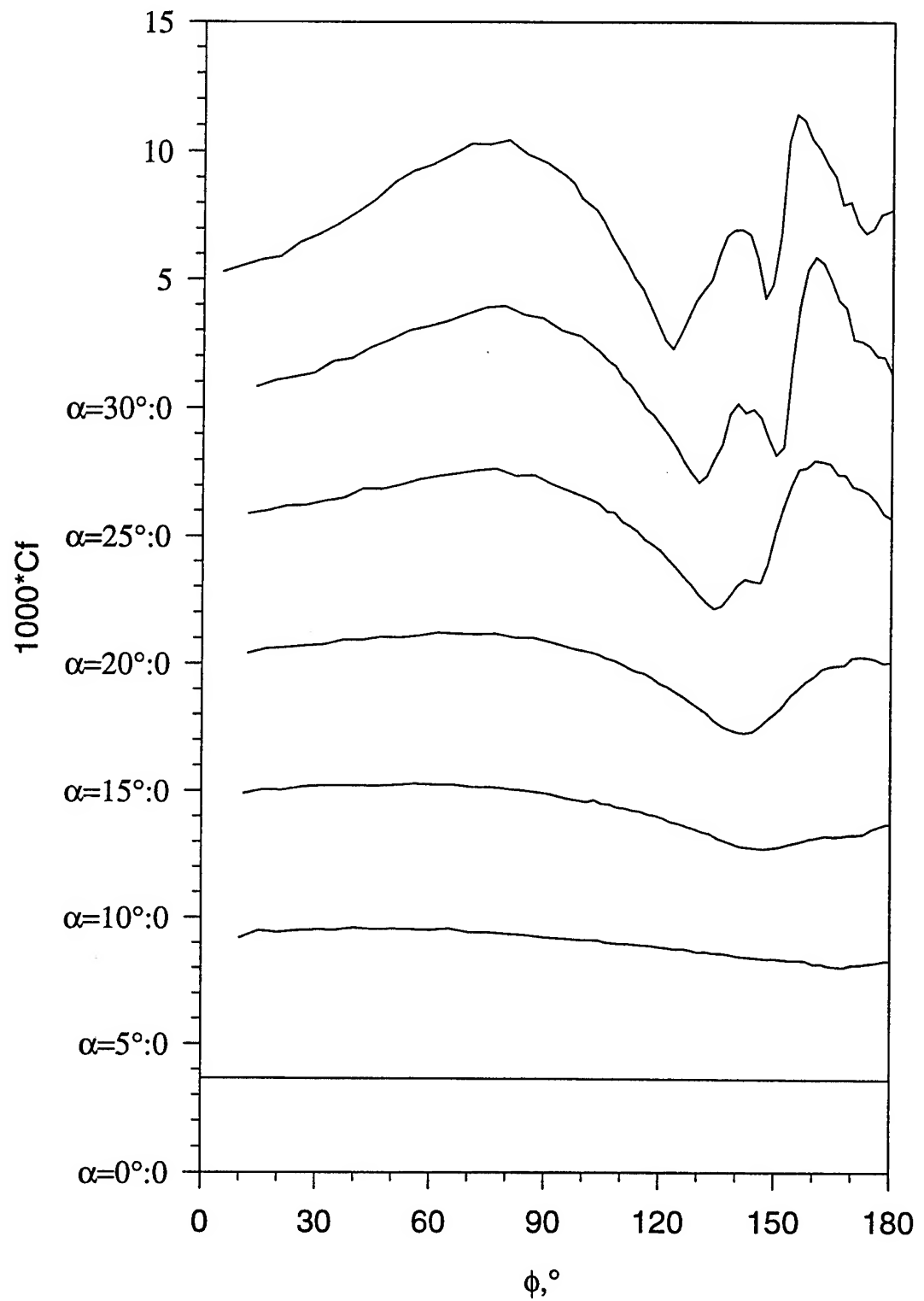


Figure 56. Constant current  $Cf$  vs.  $\phi$  for all  $\alpha$ ,  $x/L=0.576$ .

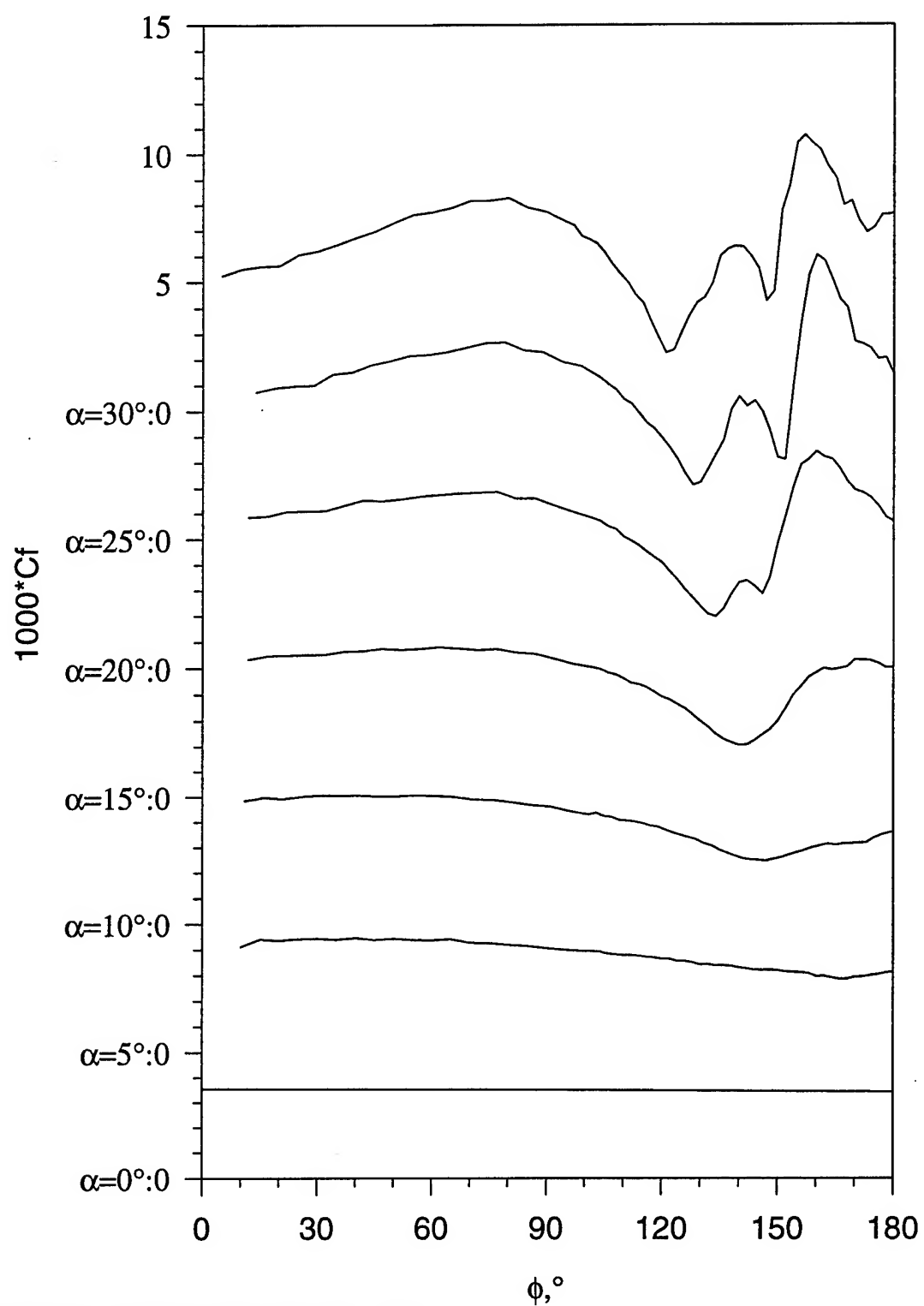


Figure 57. Constant current  $Cf$  vs.  $\phi$  for all  $\alpha$ ,  $x/L=0.602$ .

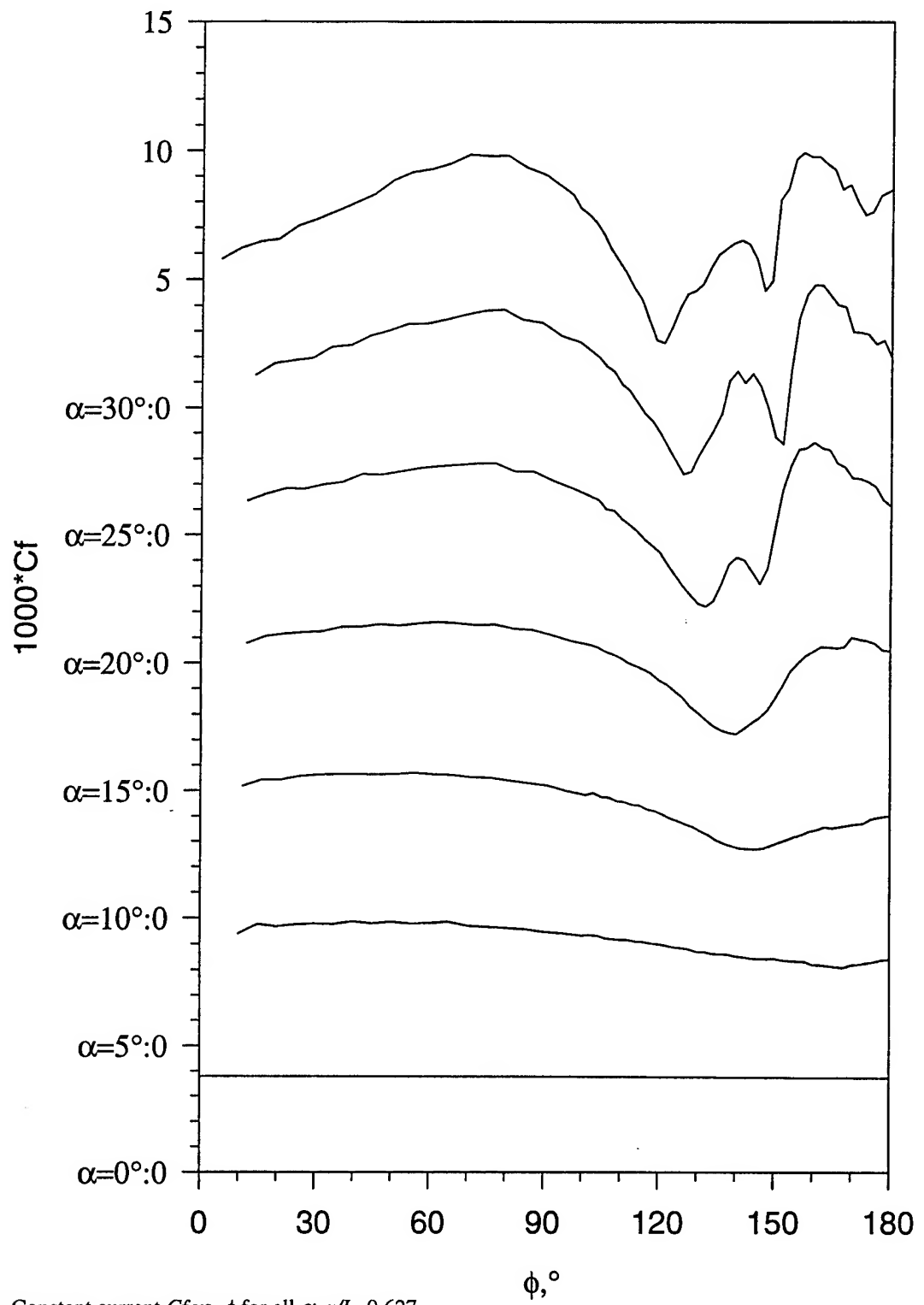


Figure 58. Constant current  $Cf$  vs.  $\phi$  for all  $\alpha$ ,  $x/L=0.627$ .

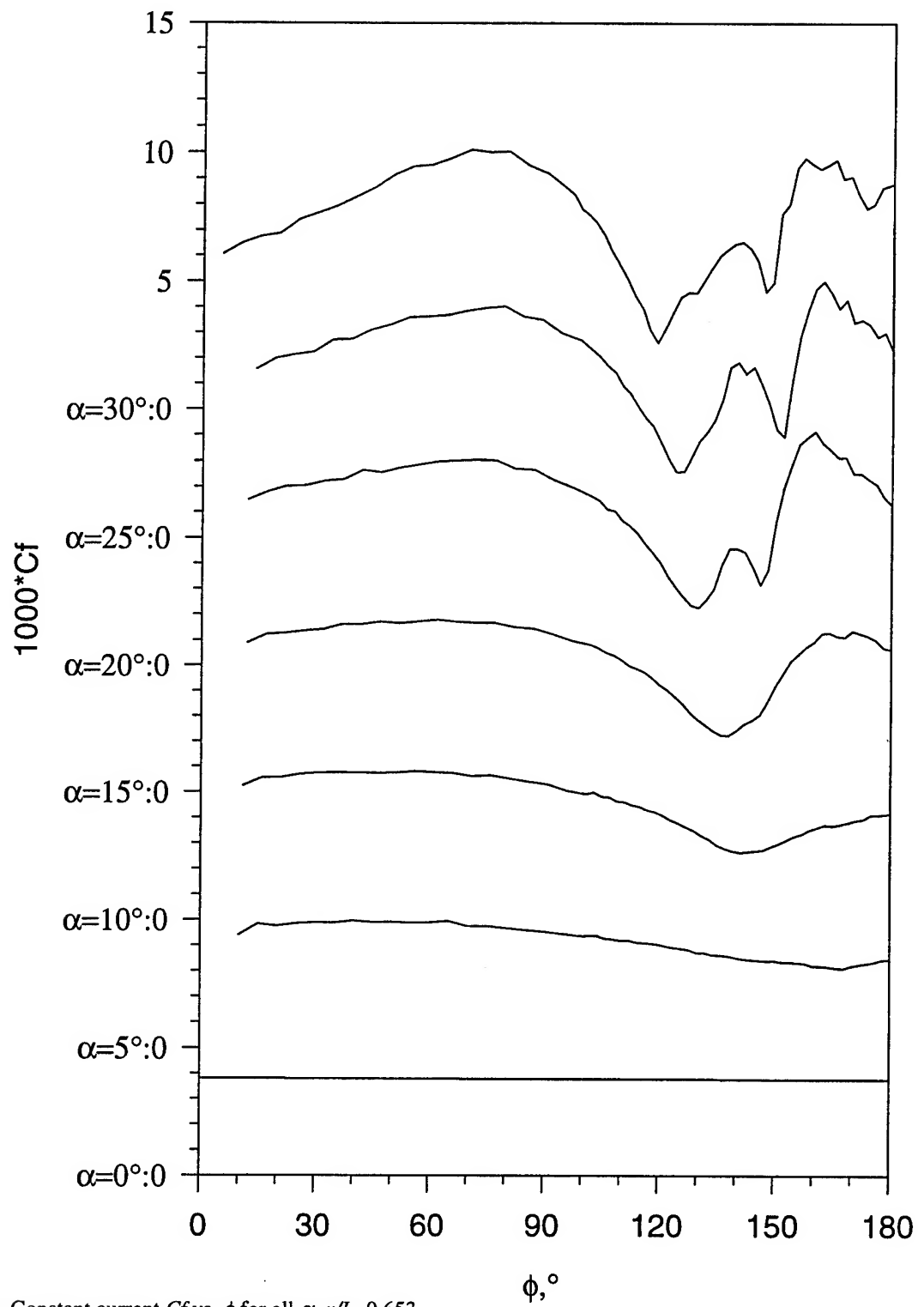


Figure 59. Constant current  $Cf$  vs.  $\phi$  for all  $\alpha$ ,  $x/L=0.653$ .



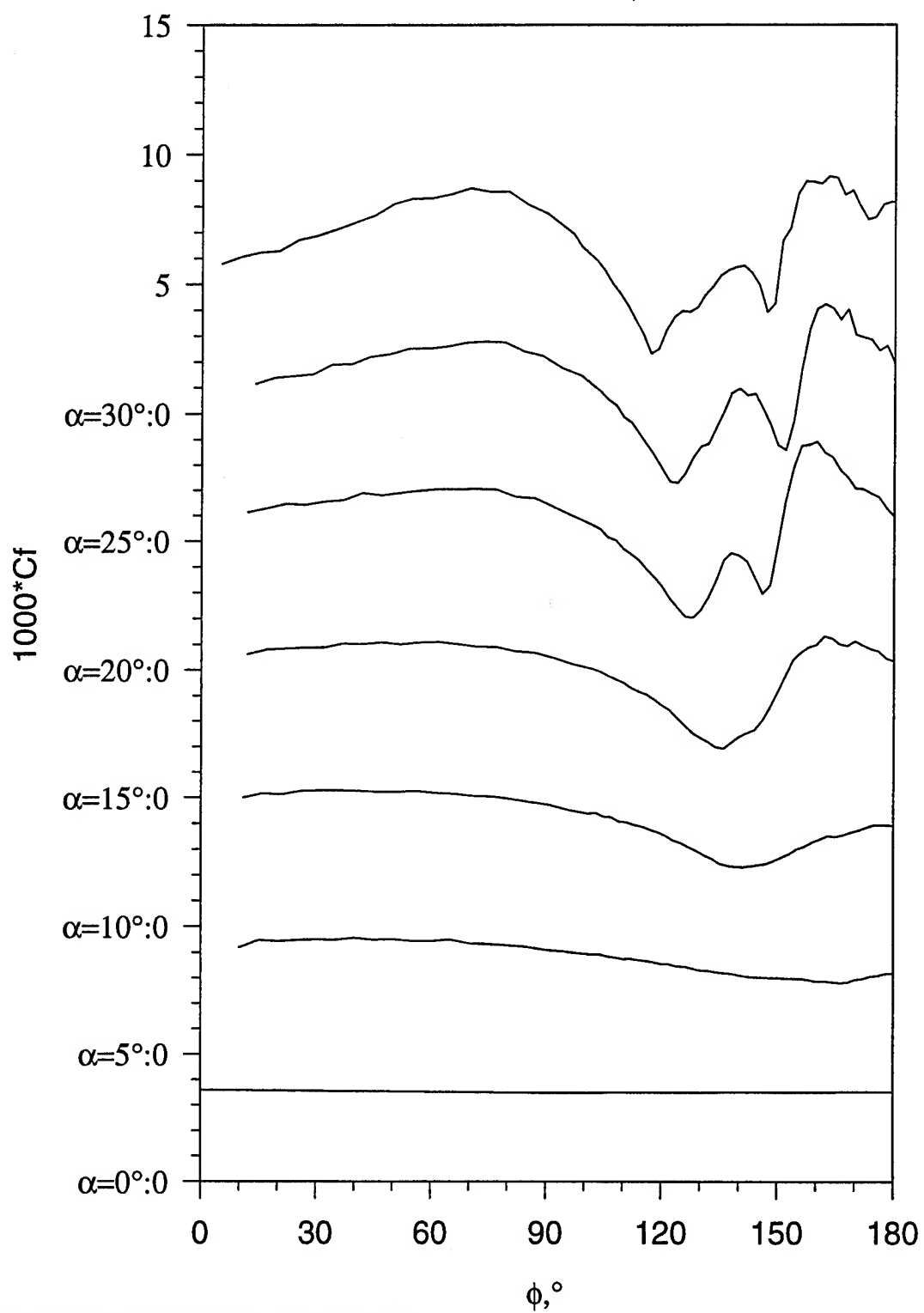


Figure 60. Constant current  $C_f$  vs.  $\phi$  for all  $\alpha$ ,  $x/L=0.678$ .

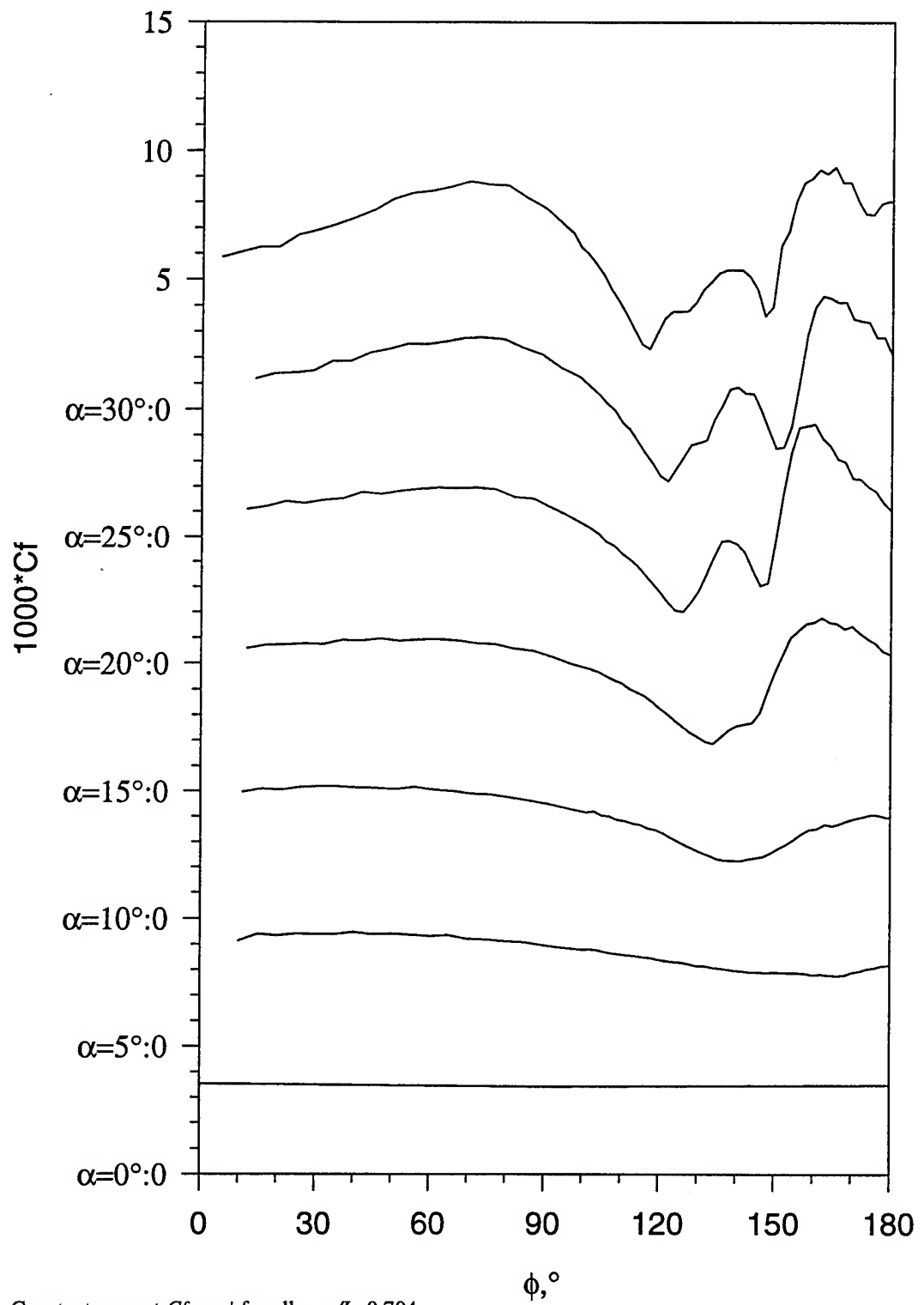


Figure 61. Constant current  $Cf$  vs.  $\phi$  for all  $\alpha$ ,  $x/L=0.704$ .

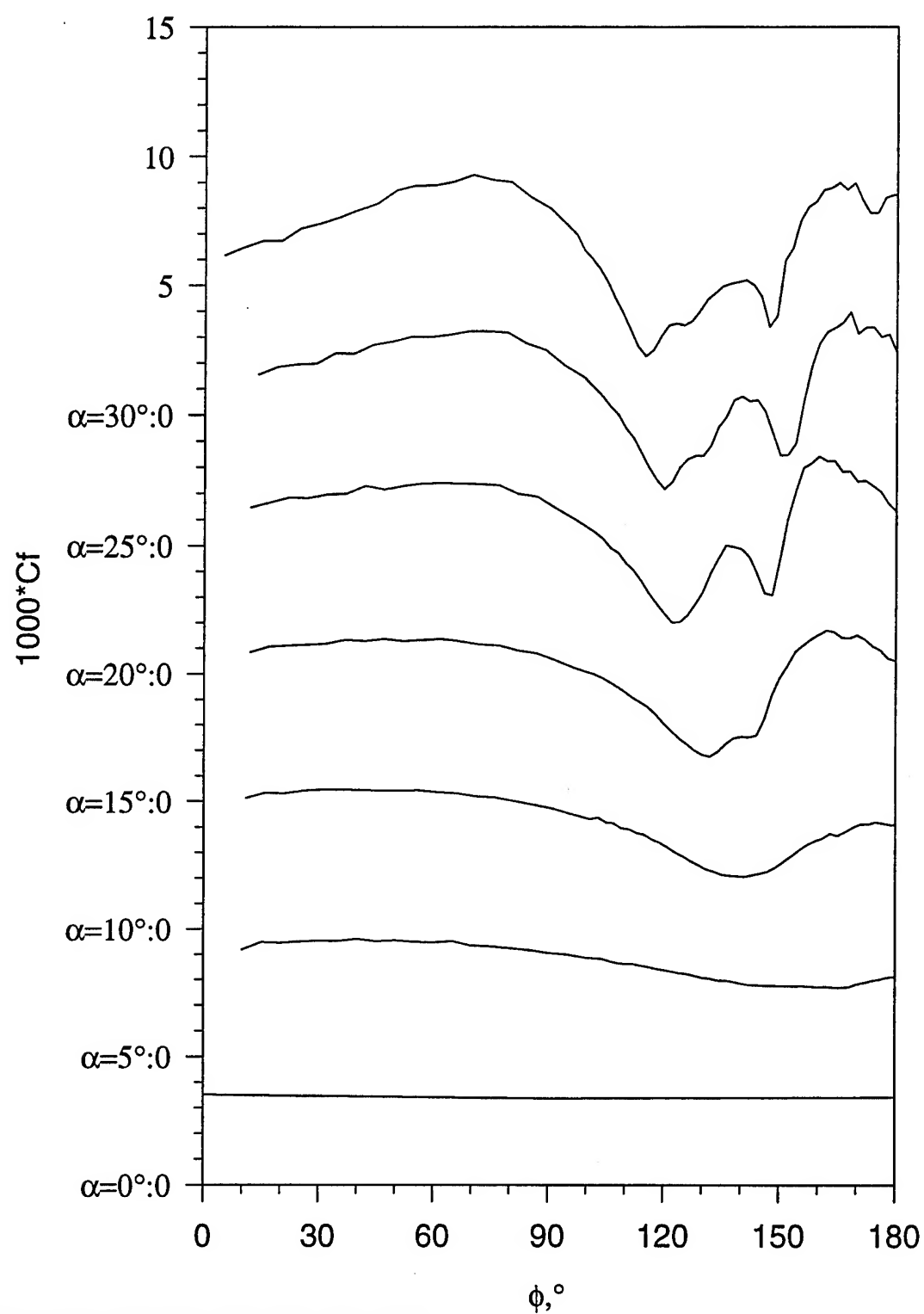


Figure 62. Constant current  $Cf$  vs.  $\phi$  for all  $\alpha$ ,  $x/L=0.729$ .

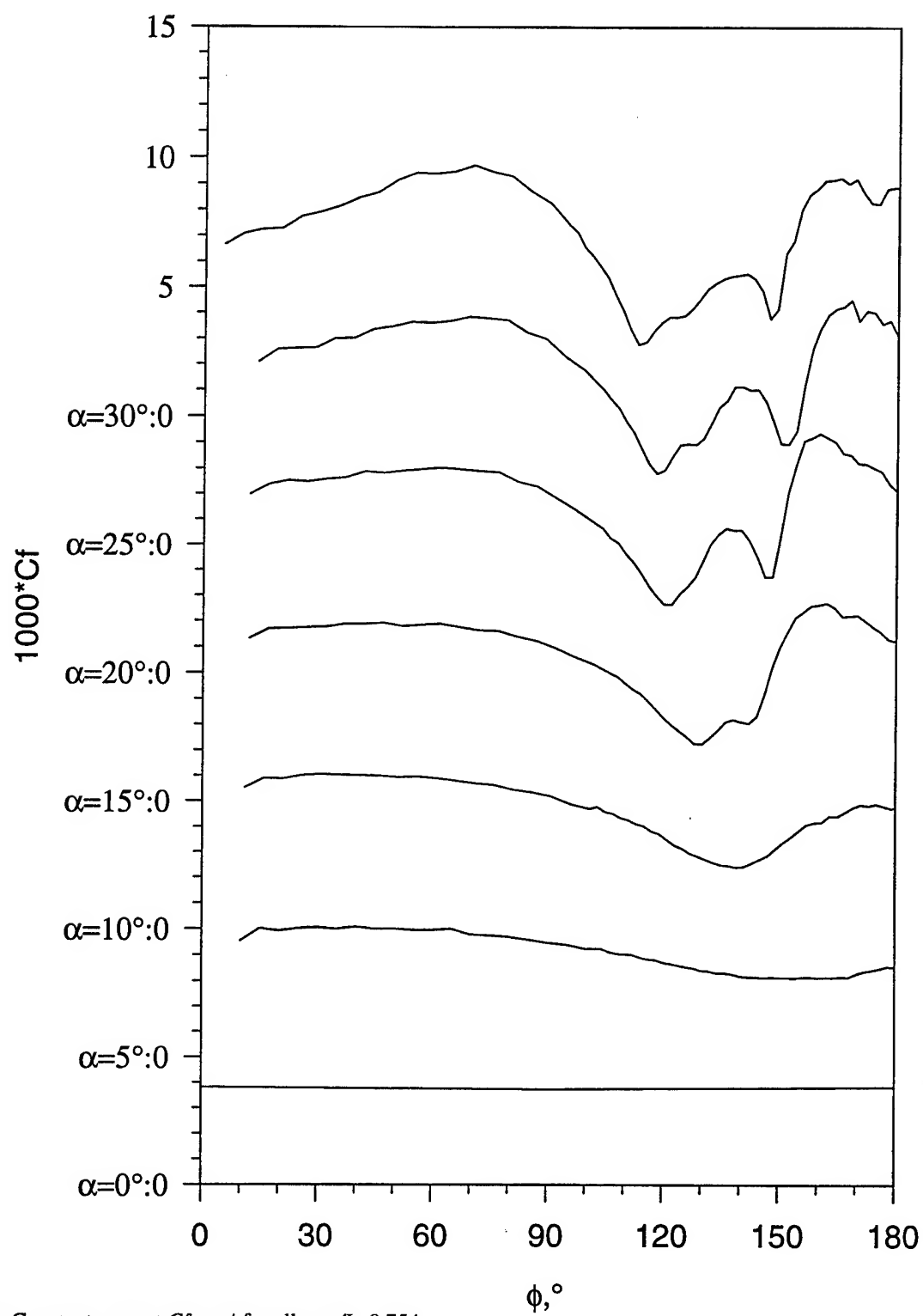


Figure 63. Constant current  $Cf$  vs.  $\phi$  for all  $\alpha$ ,  $x/L=0.754$ .

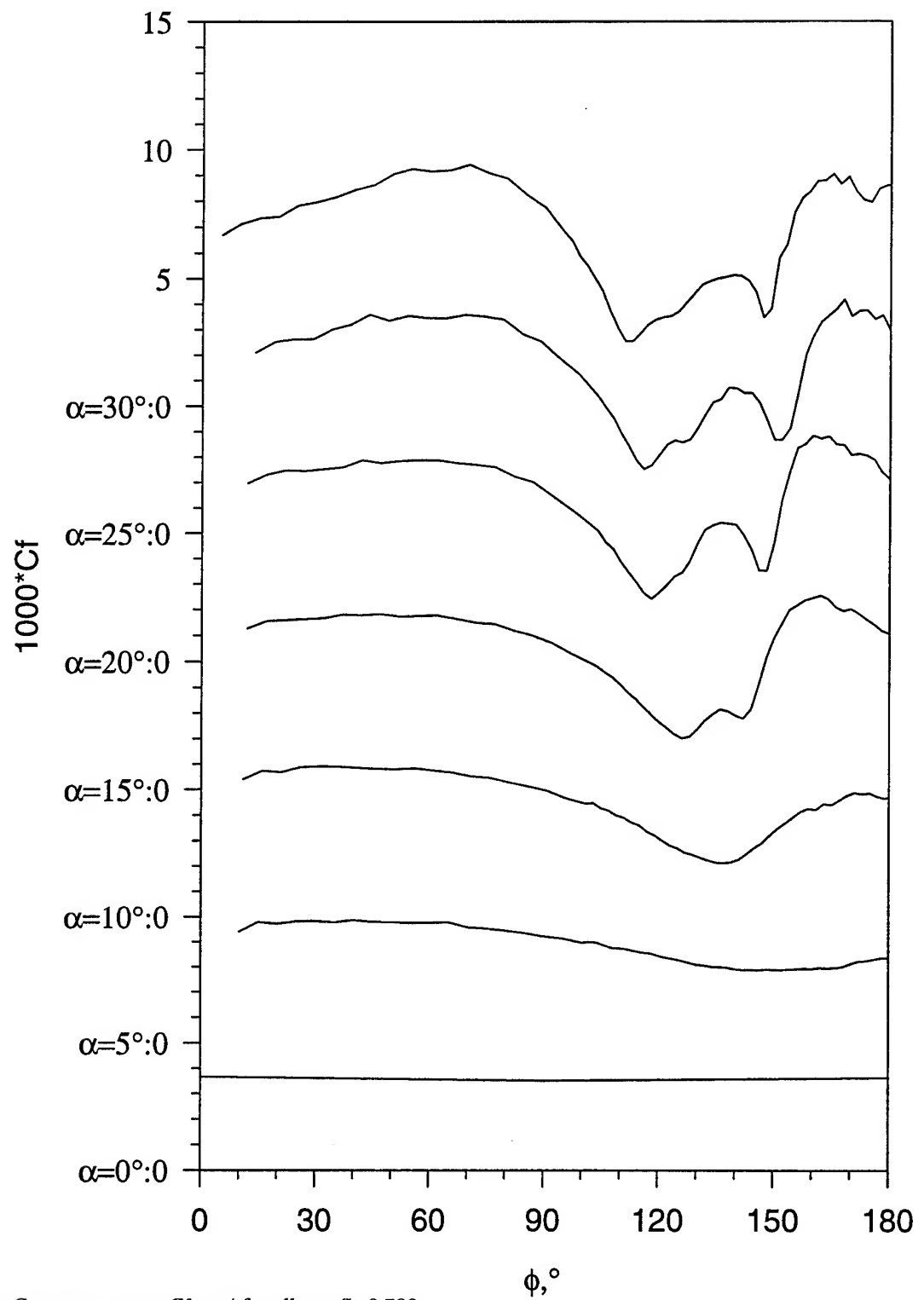


Figure 64. Constant current  $Cf$  vs.  $\phi$  for all  $\alpha$ ,  $x/L=0.780$ .

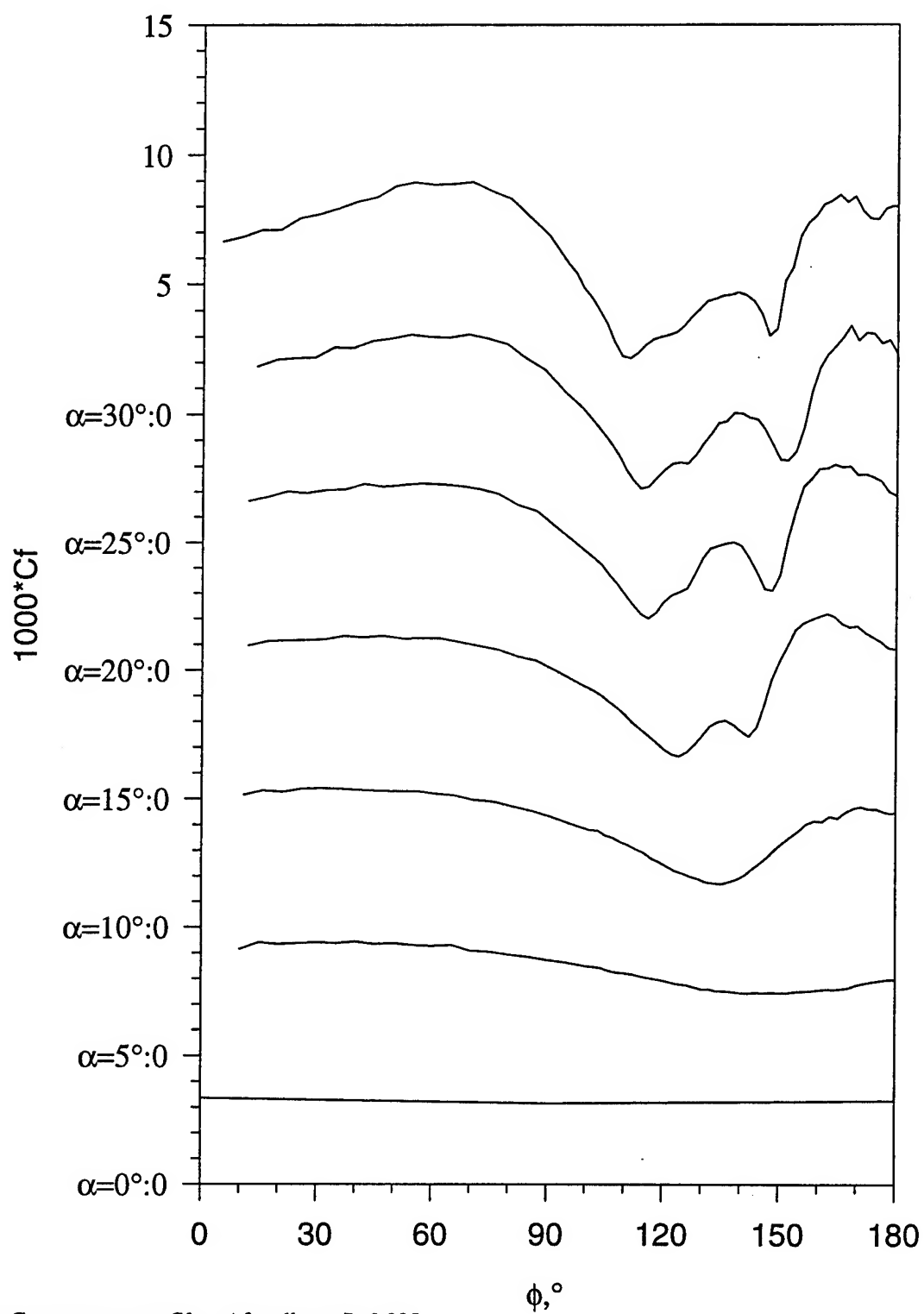


Figure 65. Constant current  $Cf$  vs.  $\phi$  for all  $\alpha$ ,  $x/L=0.805$ .

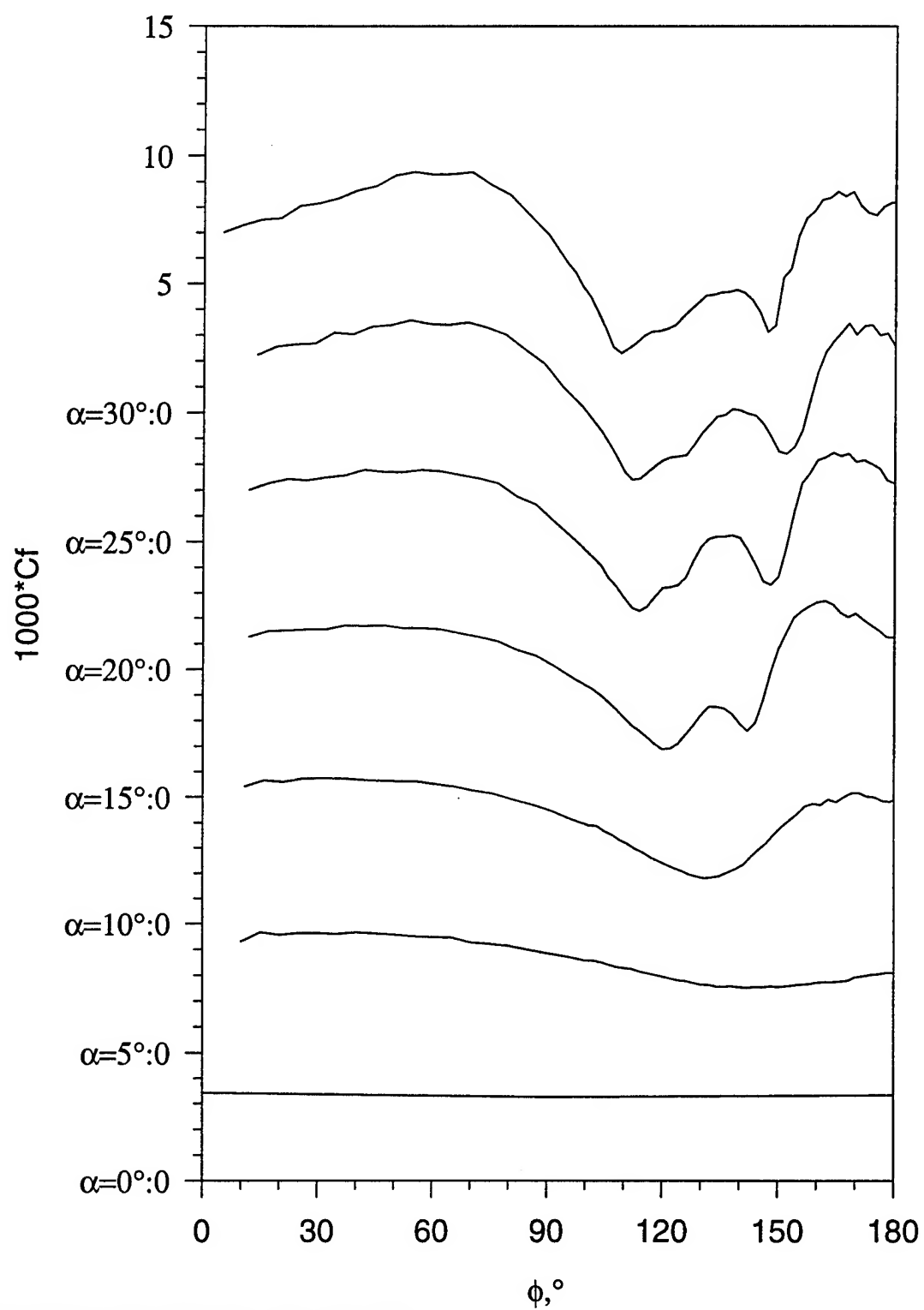


Figure 66. Constant current  $Cf$  vs.  $\phi$  for all  $\alpha$ ,  $x/L=0.831$ .

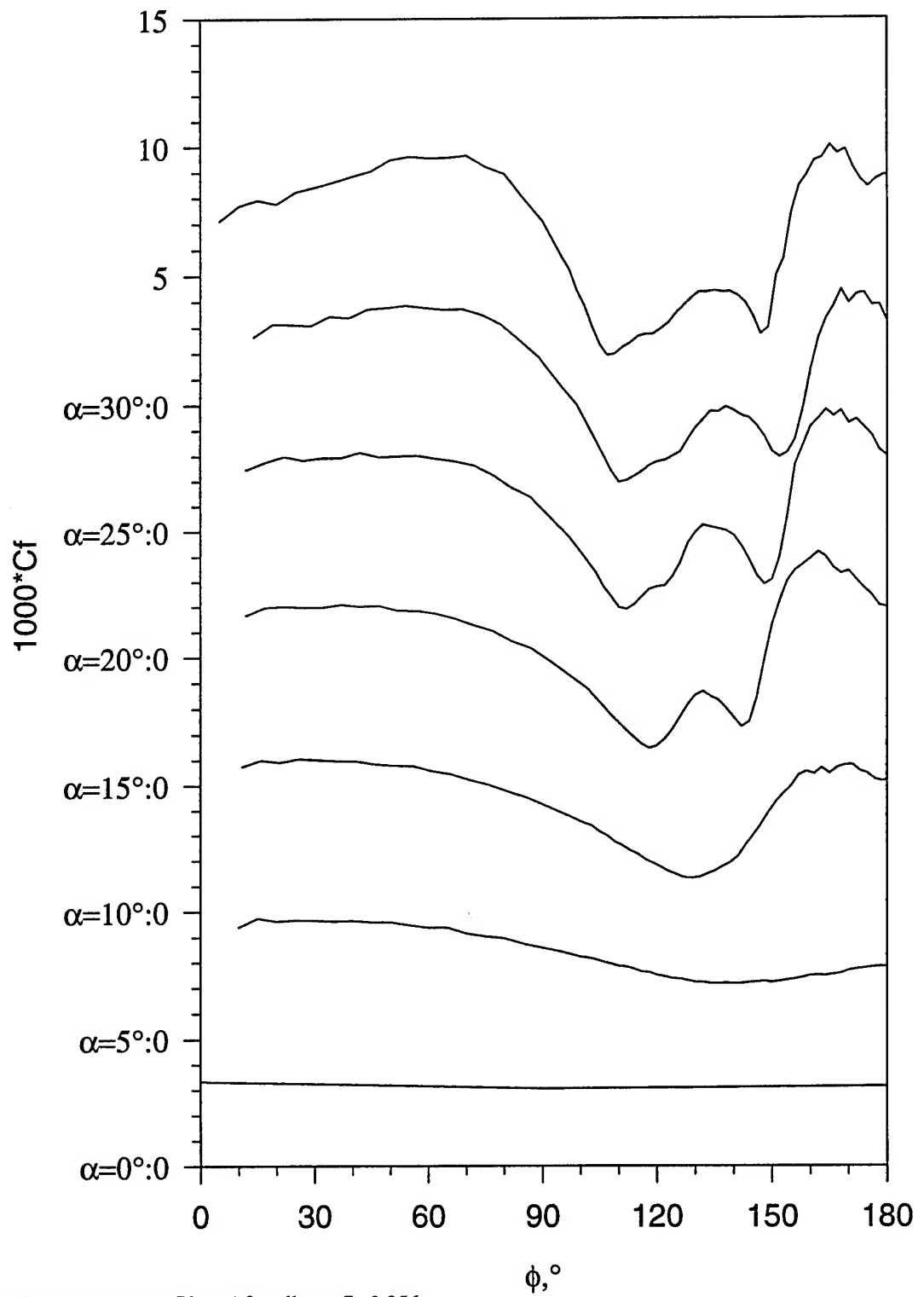


Figure 67. Constant current  $Cf$  vs.  $\phi$  for all  $\alpha$ ,  $x/L=0.856$ .



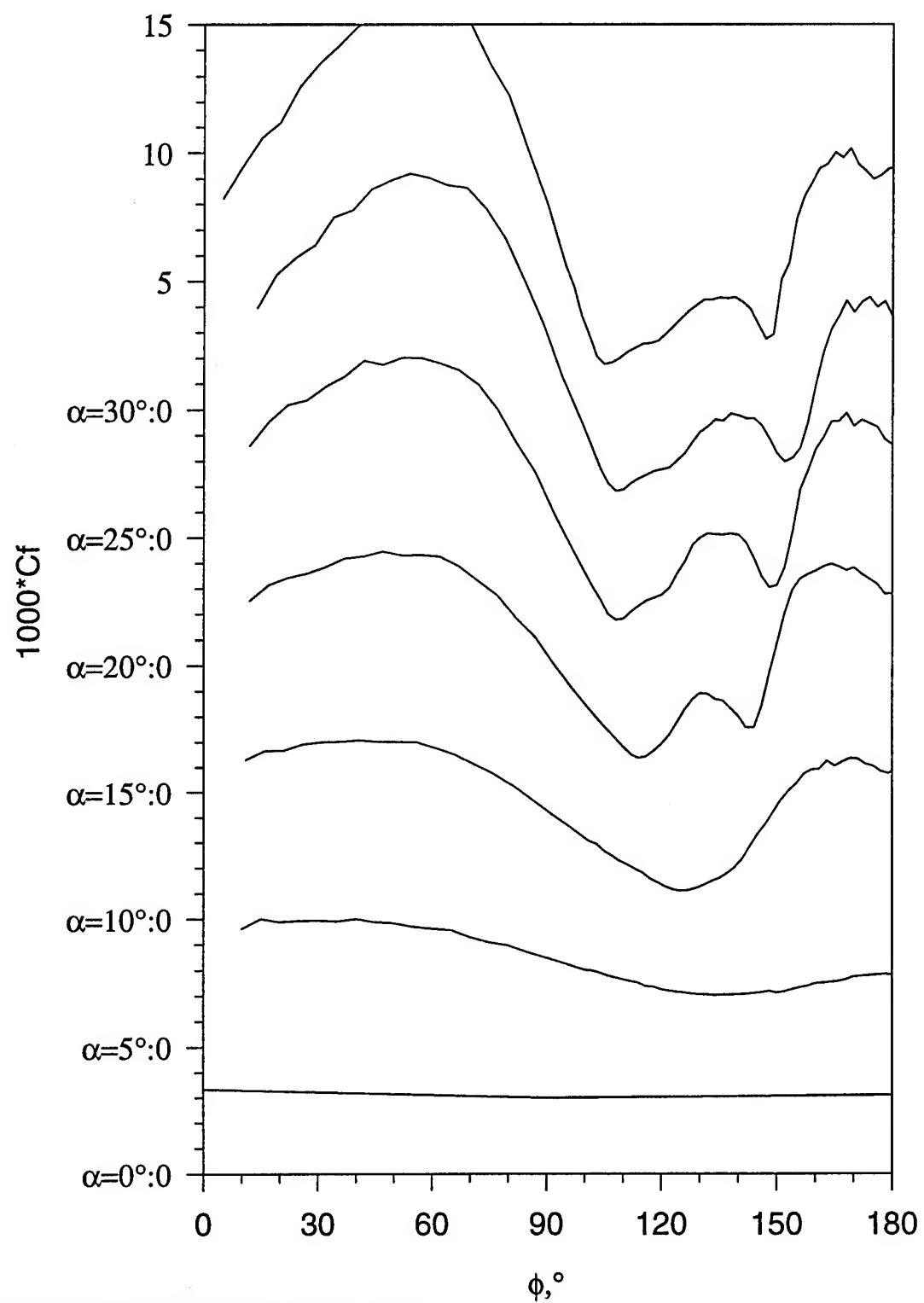


Figure 68. Constant current  $Cf$  vs.  $\phi$  for all  $\alpha$ ,  $x/L=0.882$ .

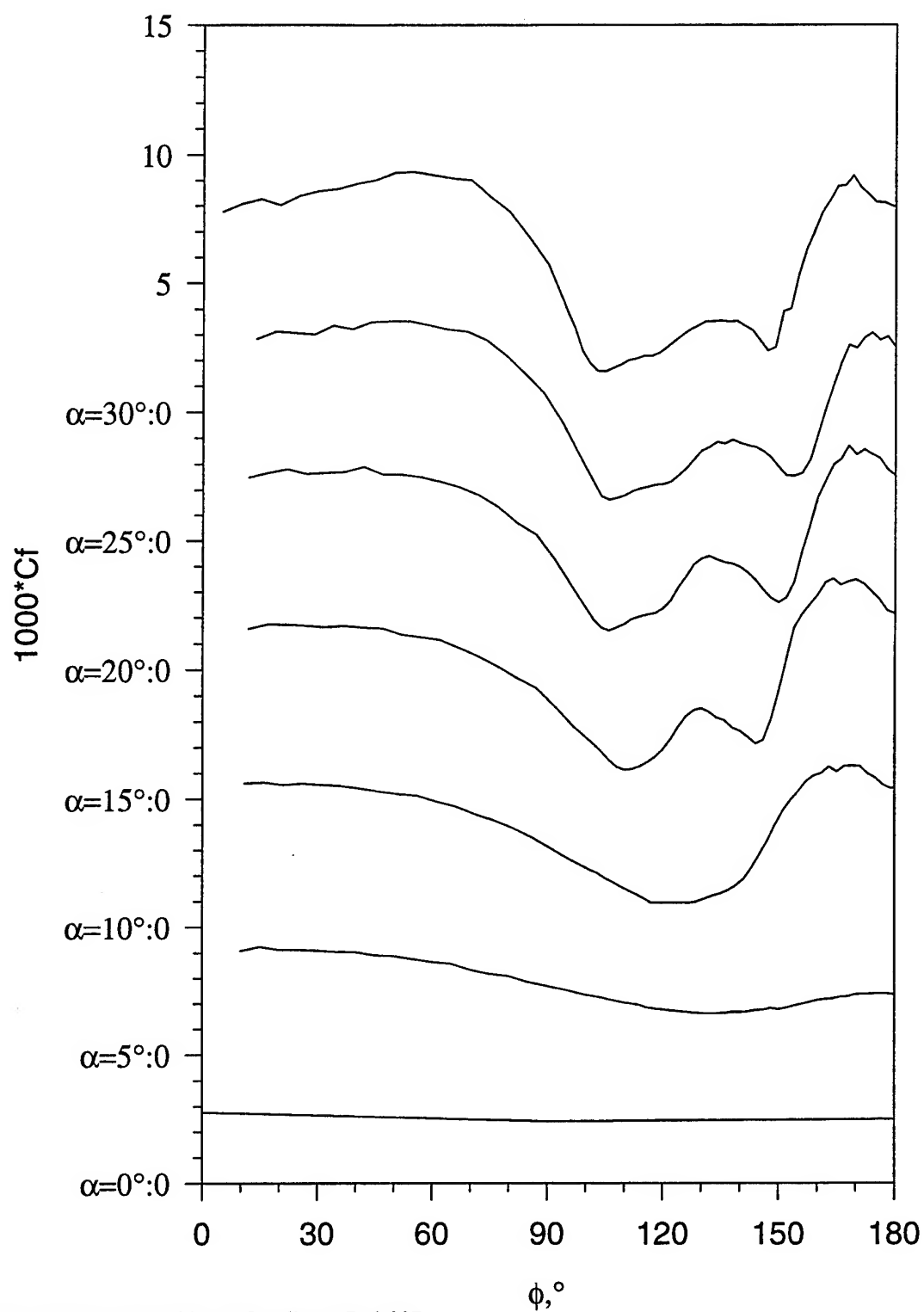


Figure 69. Constant current  $C_f$  vs.  $\phi$  for all  $\alpha$ ,  $x/L=0.907$ .

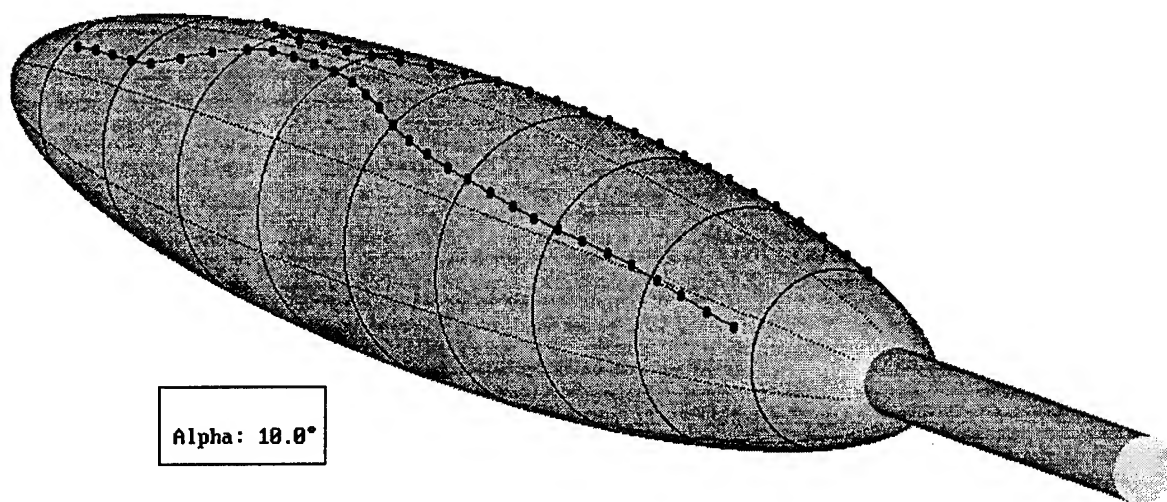


Figure 70. Constant current separation line topology for  $\alpha=10^\circ$ .

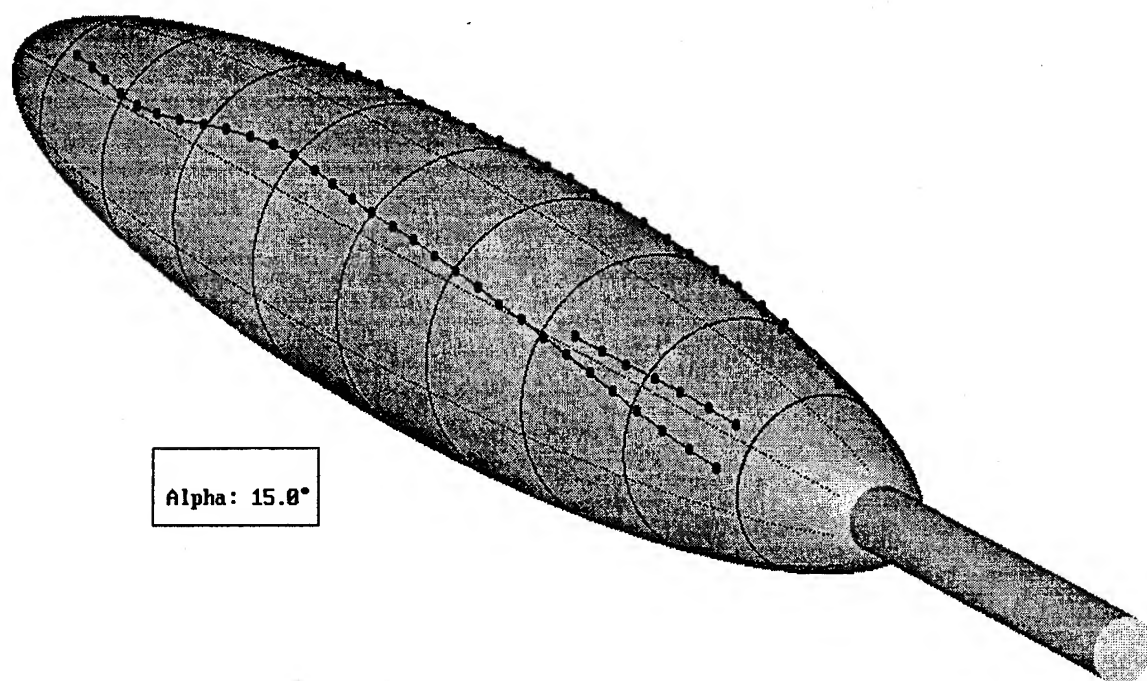


Figure 71. Constant current separation line topology for  $\alpha=15^\circ$ .

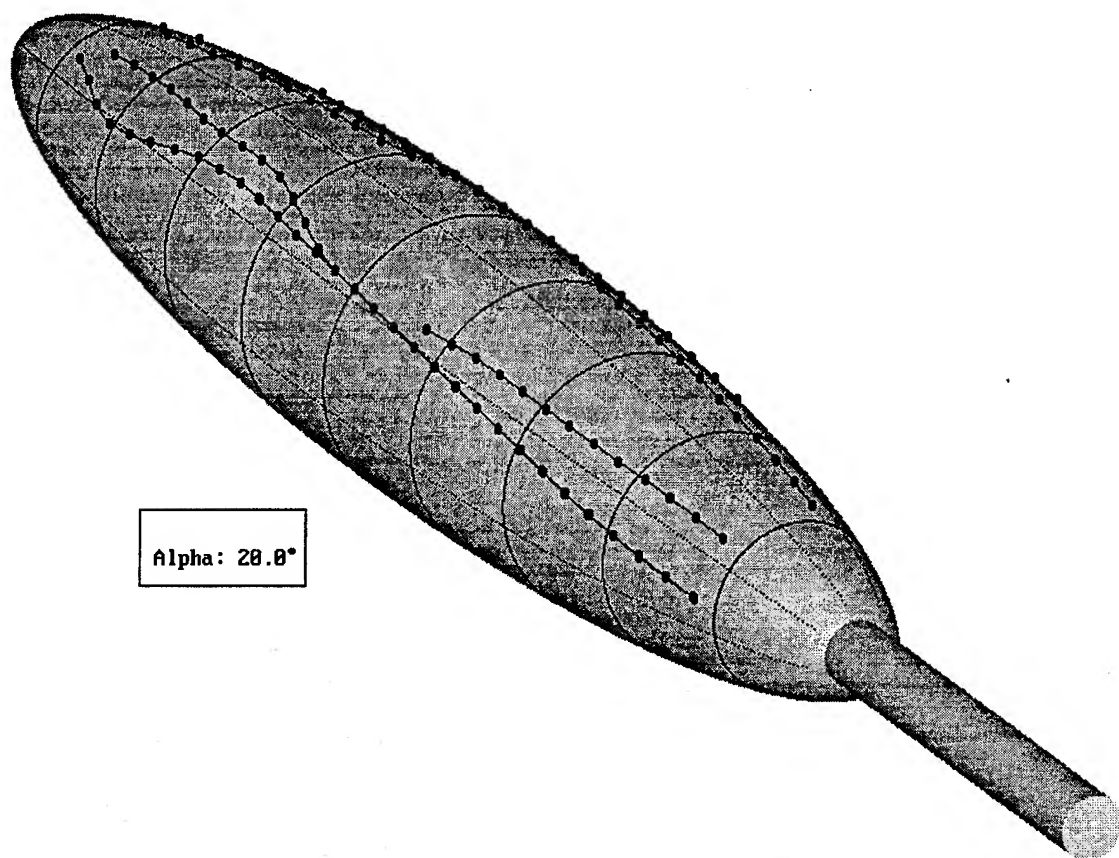


Figure 72. Constant current separation line topology for  $\alpha=20^\circ$ .

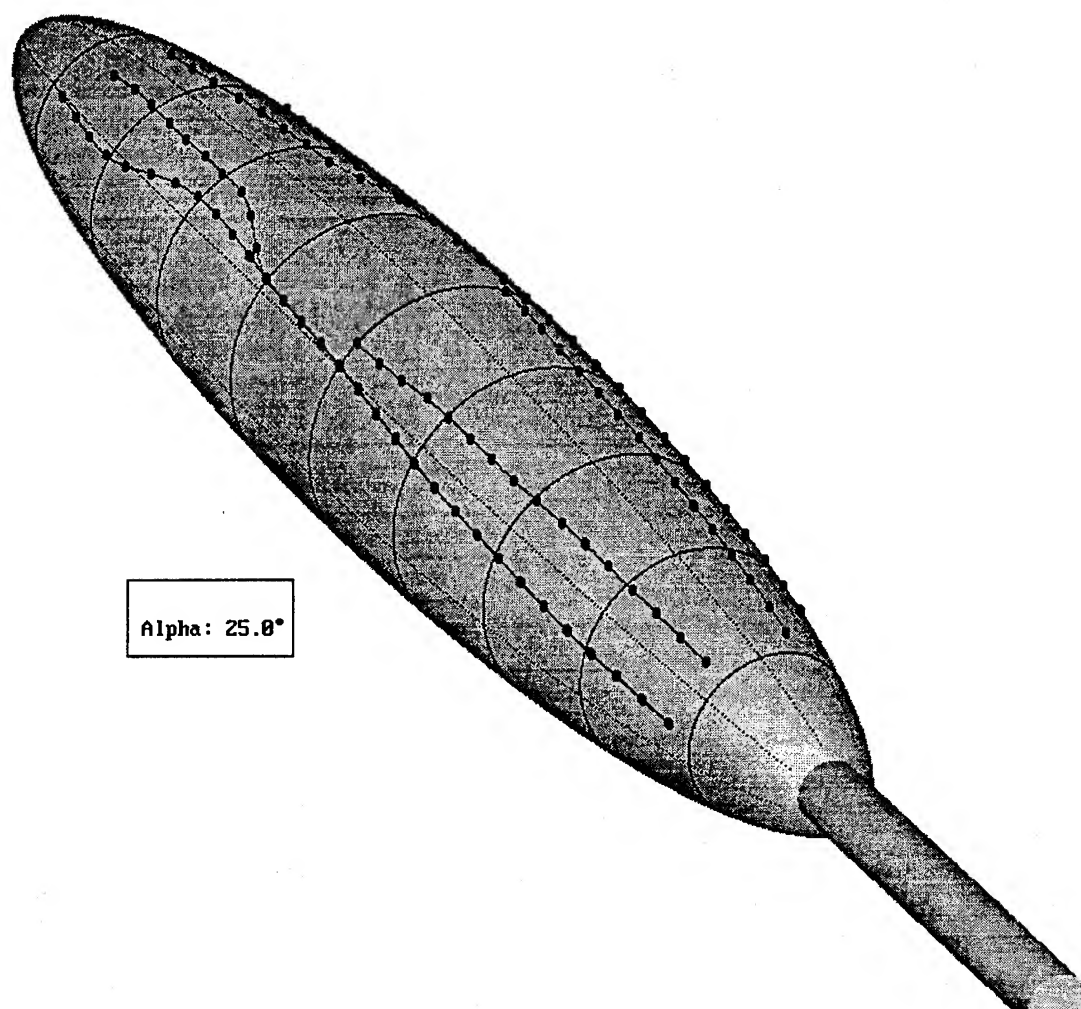


Figure 73. Constant current separation line topology for  $\alpha=25^\circ$ .

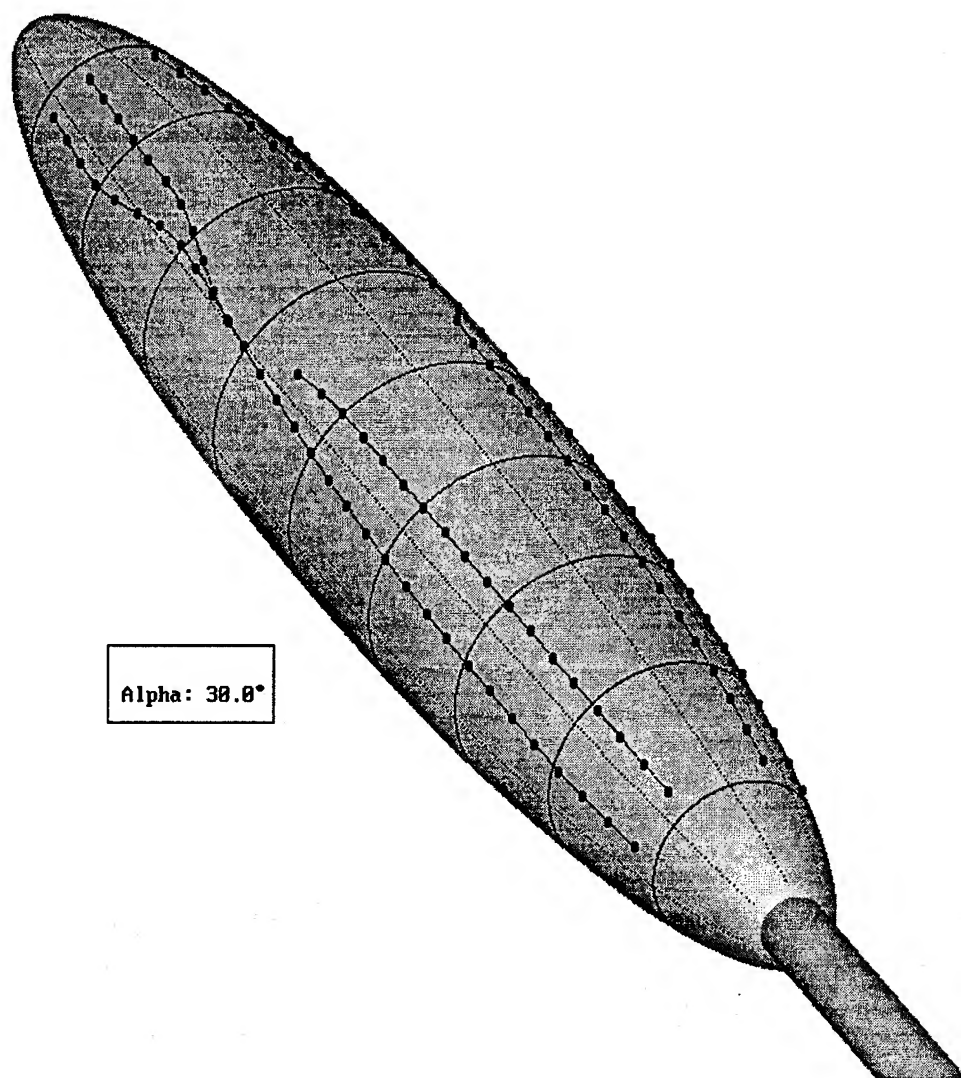


Figure 74. Constant current separation line topology for  $\alpha=30^\circ$ .

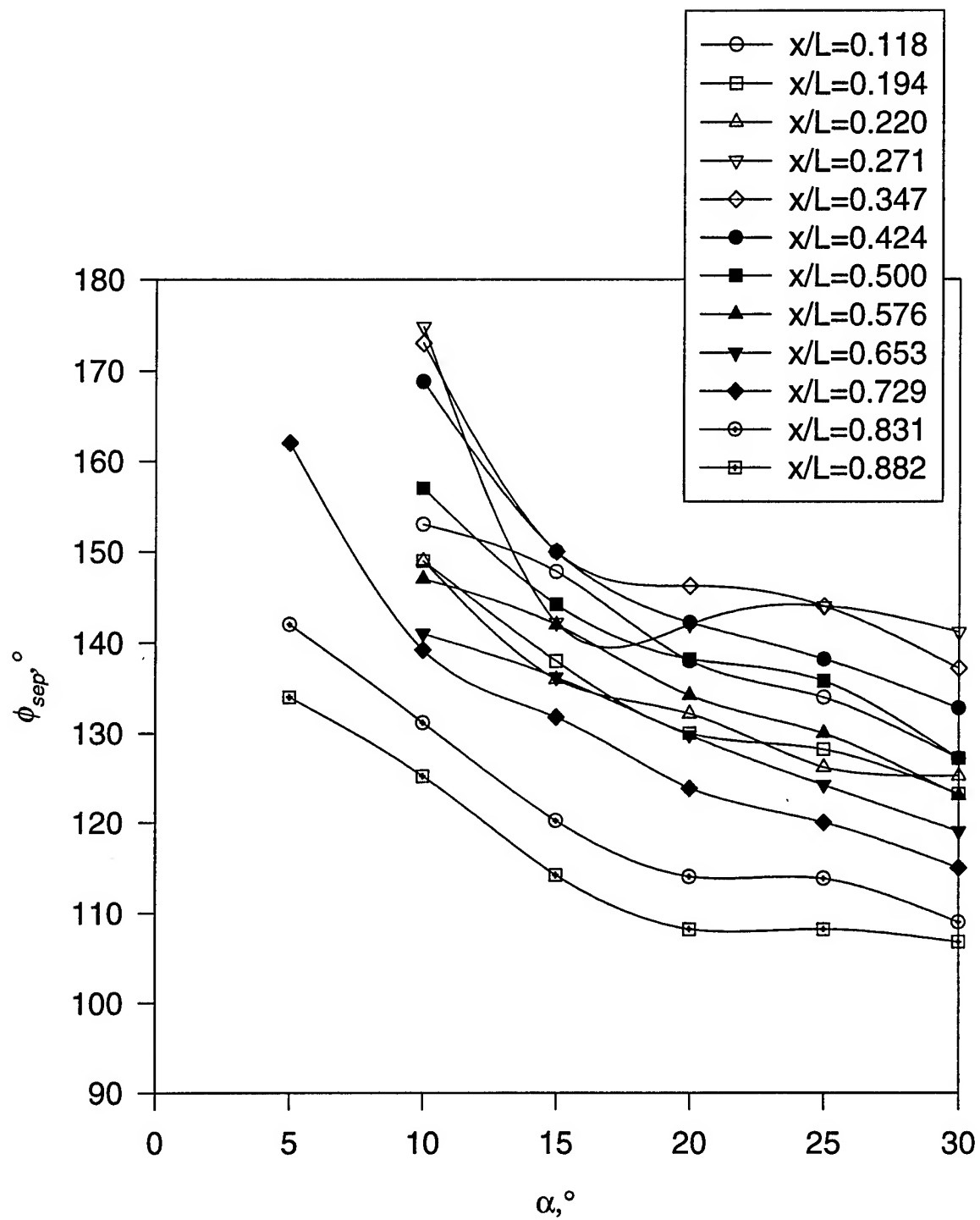


Figure 75. Primary separation location as a function of  $\alpha$  for various  $x/L$ .



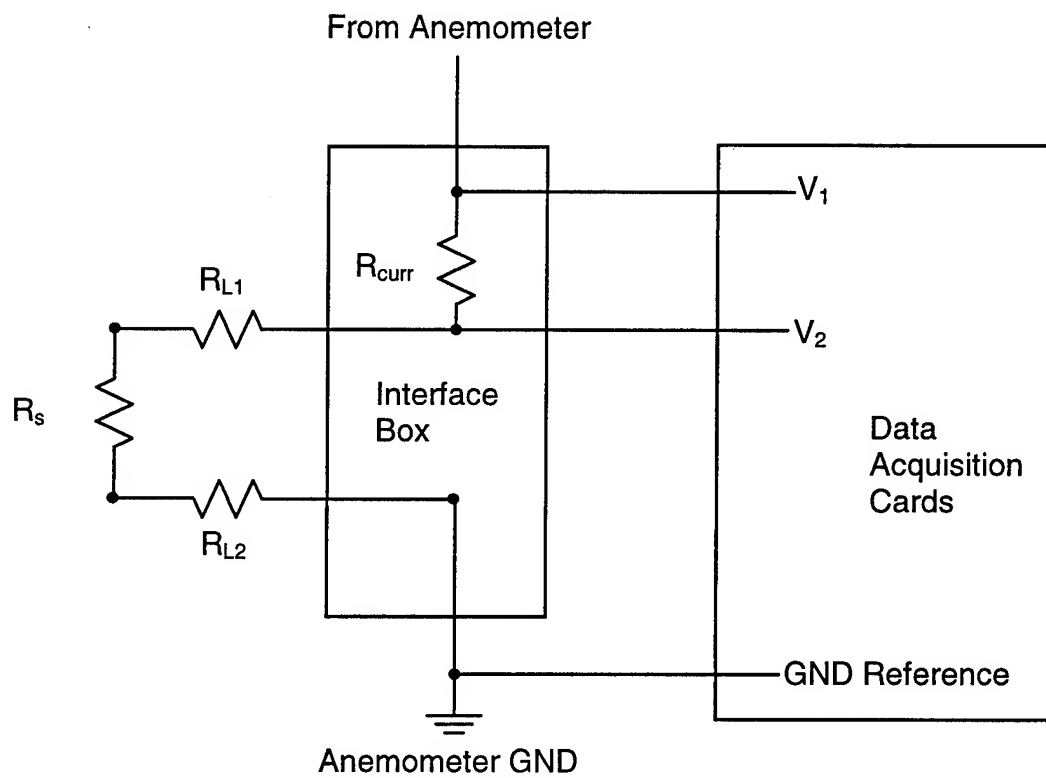


Figure 76. Constant temperature anemometer/data acquisition interface box.

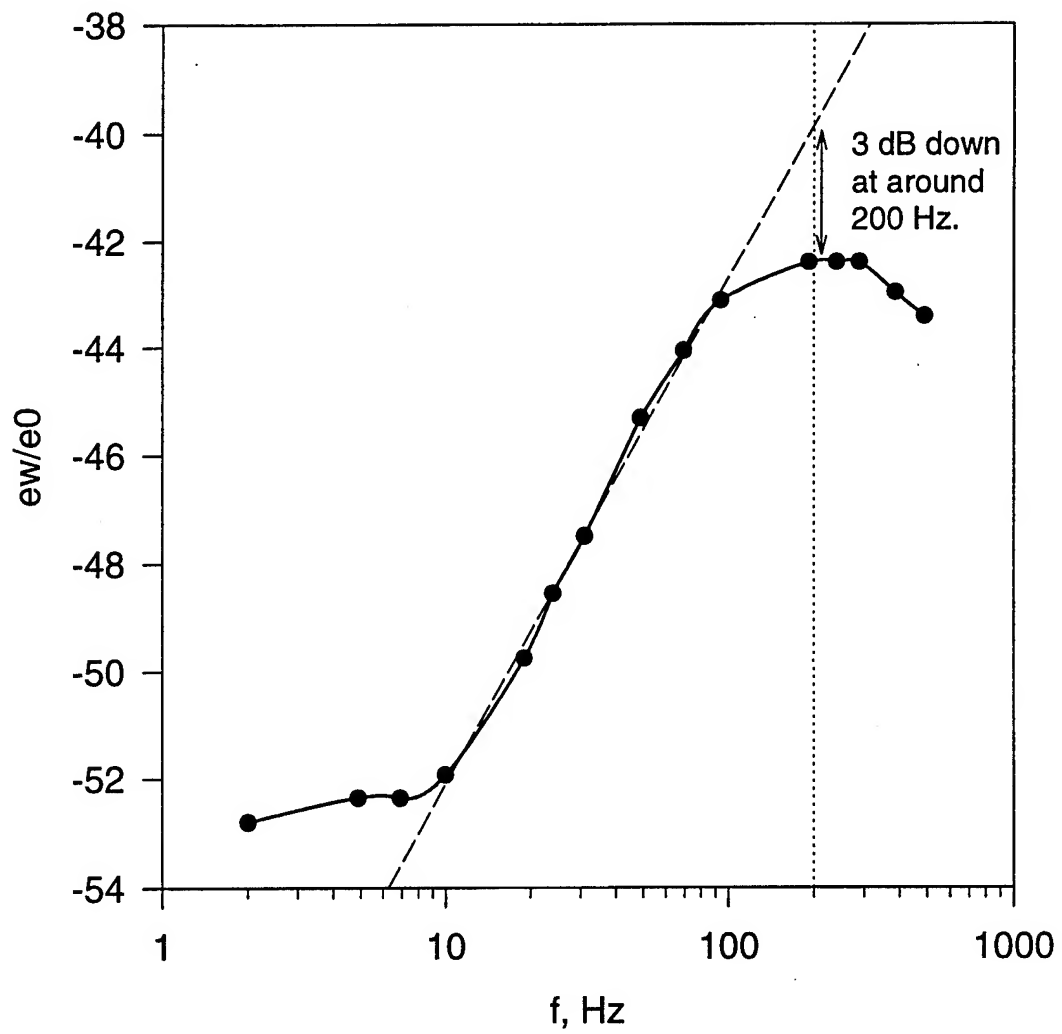


Figure 77. Typical frequency response for the Miller anemometers with the present hot-film sensors.

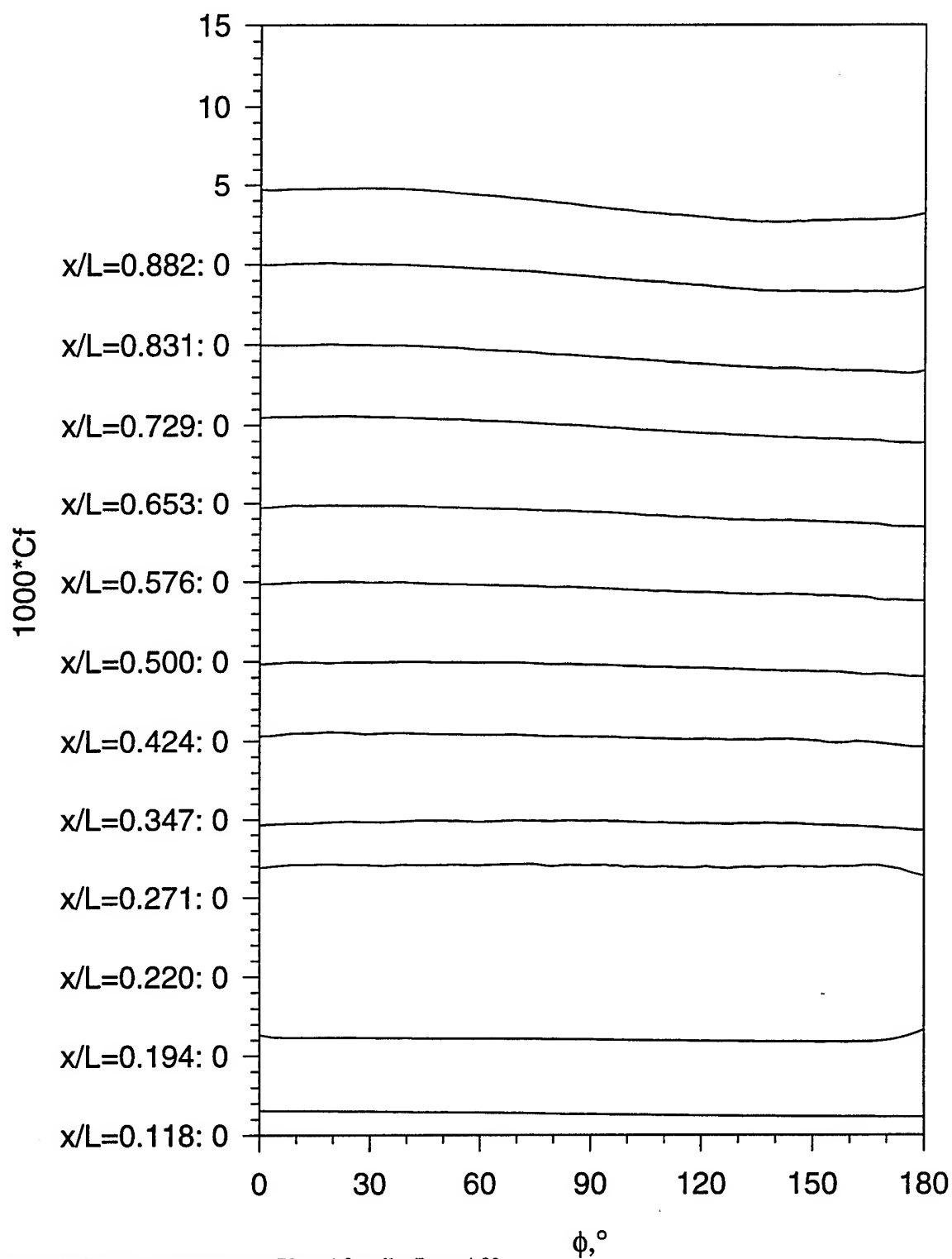


Figure 78. Constant temperature  $Cf$  vs.  $\phi$  for all  $x/L$ ,  $\alpha=4.8^\circ$ .

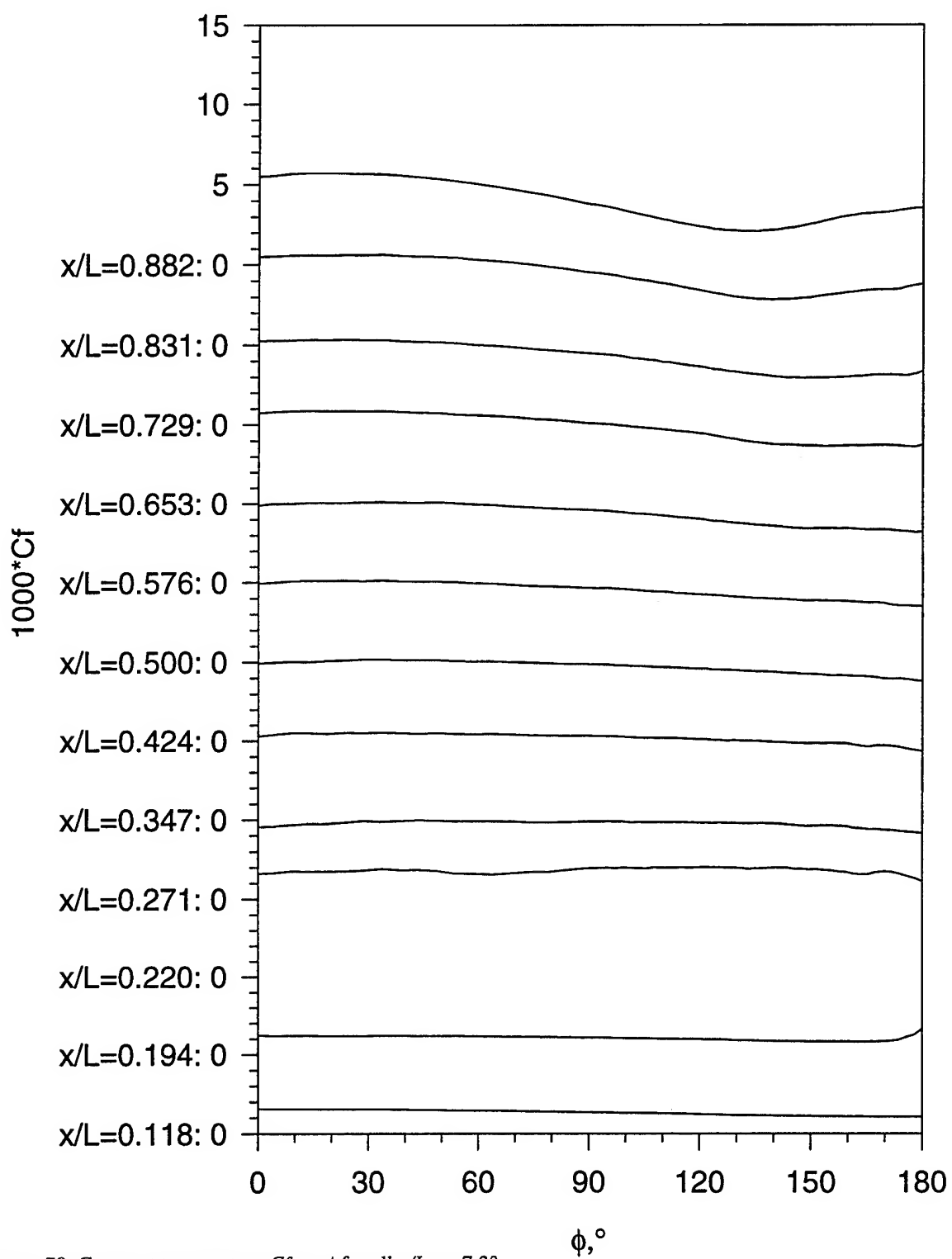


Figure 79. Constant temperature  $Cf$  vs.  $\phi$  for all  $x/L$ ,  $\alpha=7.3^\circ$ .

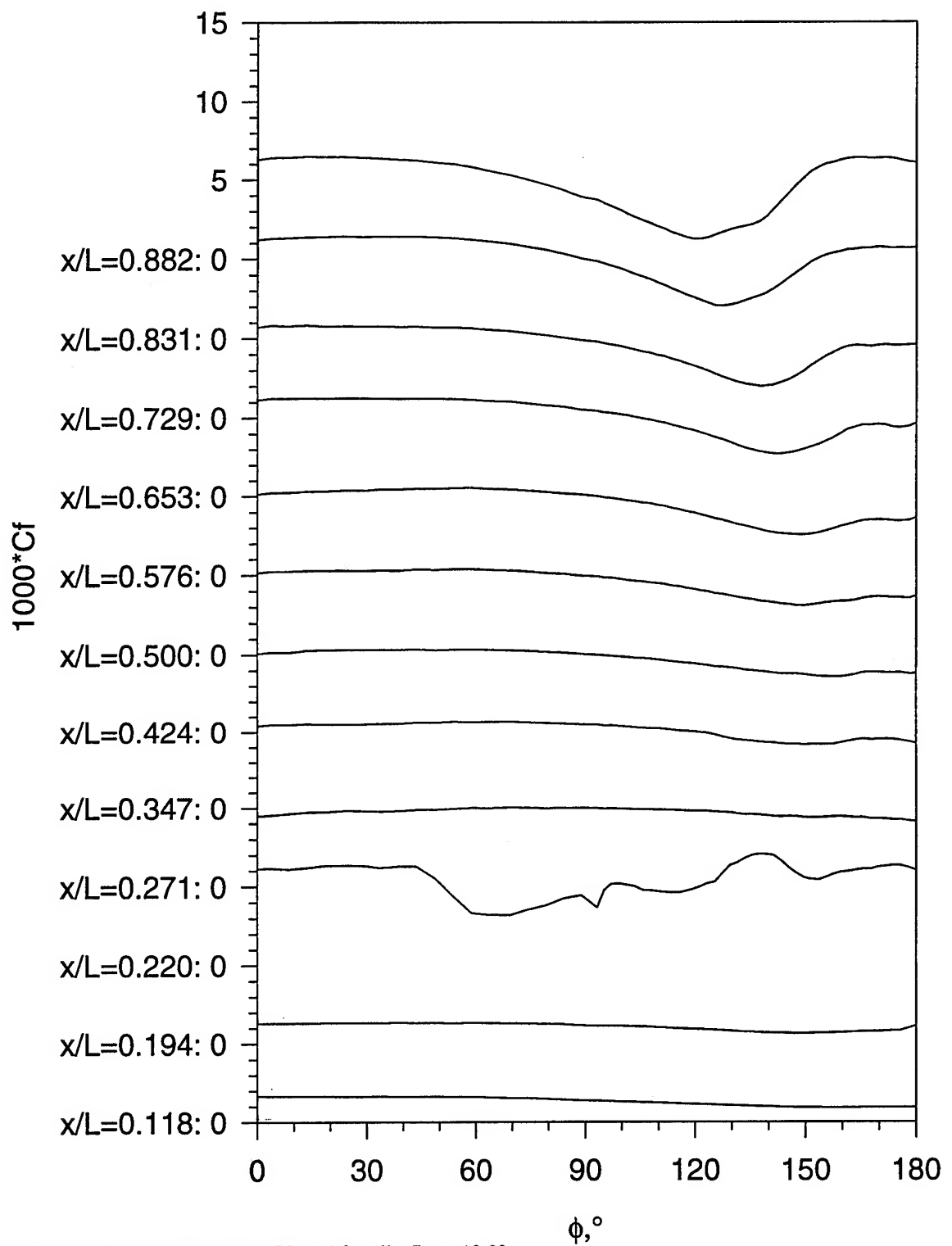


Figure 80. Constant temperature  $Cf$  vs.  $\phi$  for all  $x/L$ ,  $\alpha=12.2^\circ$ .

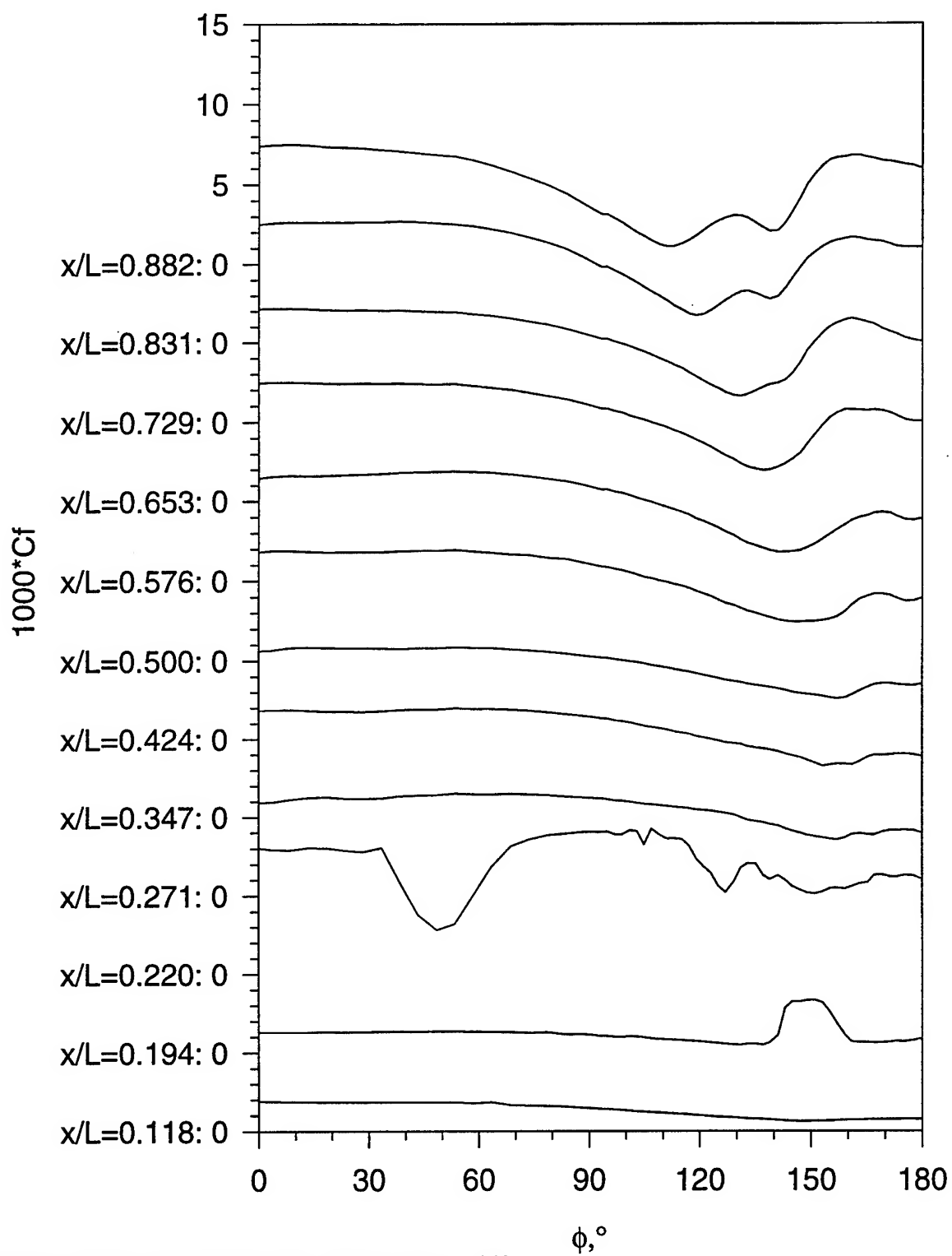


Figure 81. Constant temperature  $Cf$  vs.  $\phi$  for all  $x/L$ ,  $\alpha = 15.2^\circ$ .

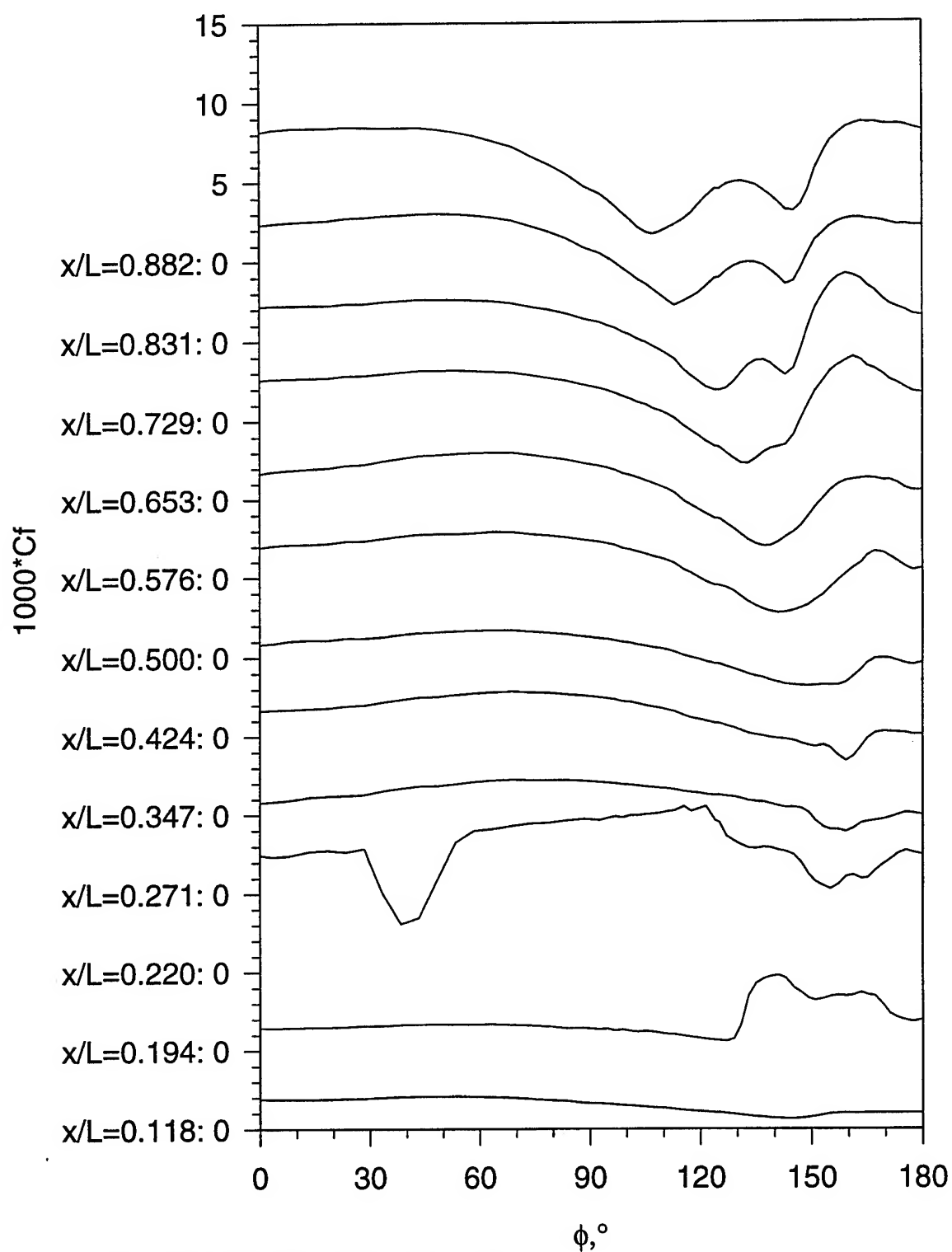


Figure 82. Constant temperature  $Cf$  vs.  $\phi$  for all  $x/L$ ,  $\alpha = 17.6^\circ$ .

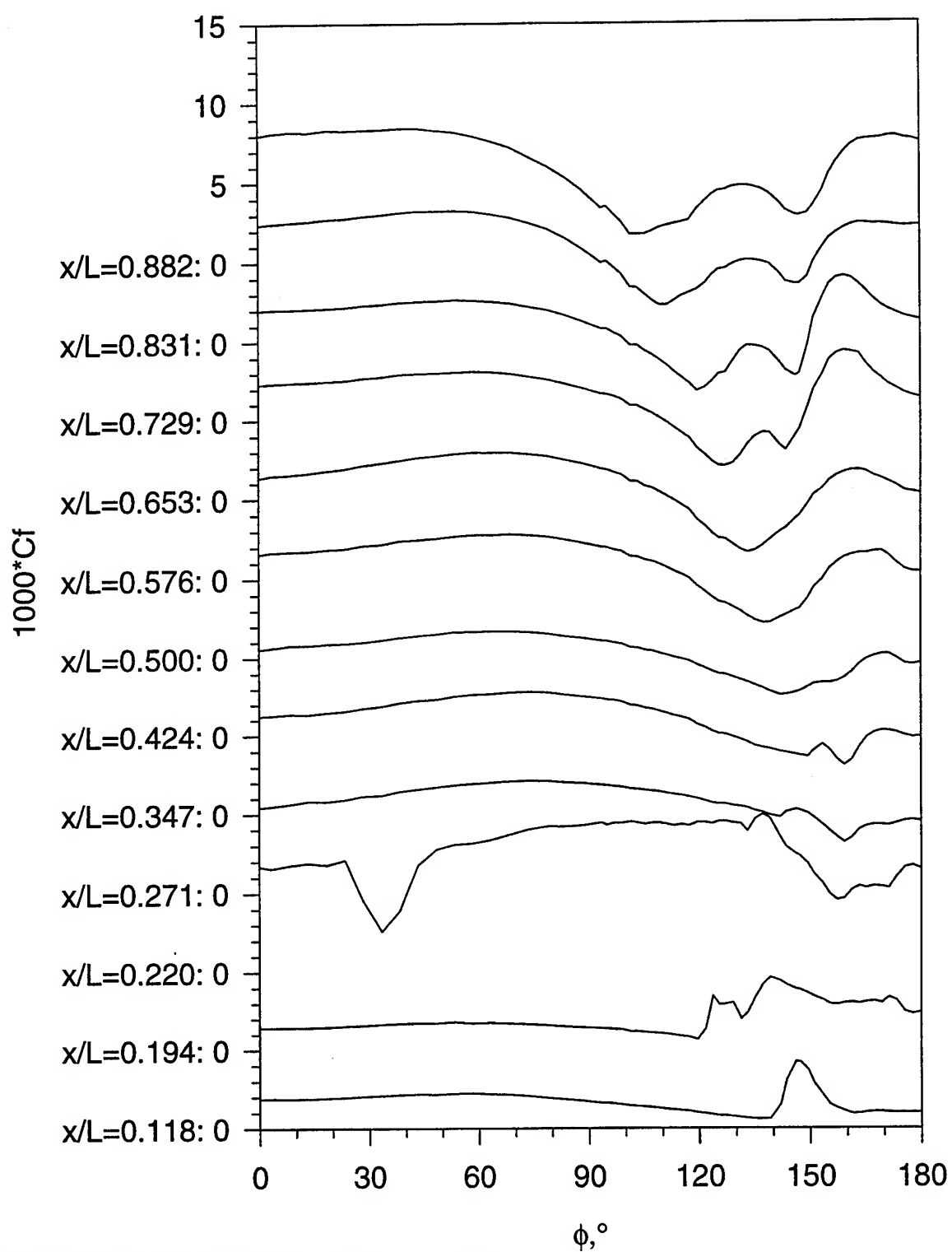


Figure 83. Constant temperature  $C_f$  vs.  $\phi$  for all  $x/L$ ,  $\alpha=20.2^\circ$ .



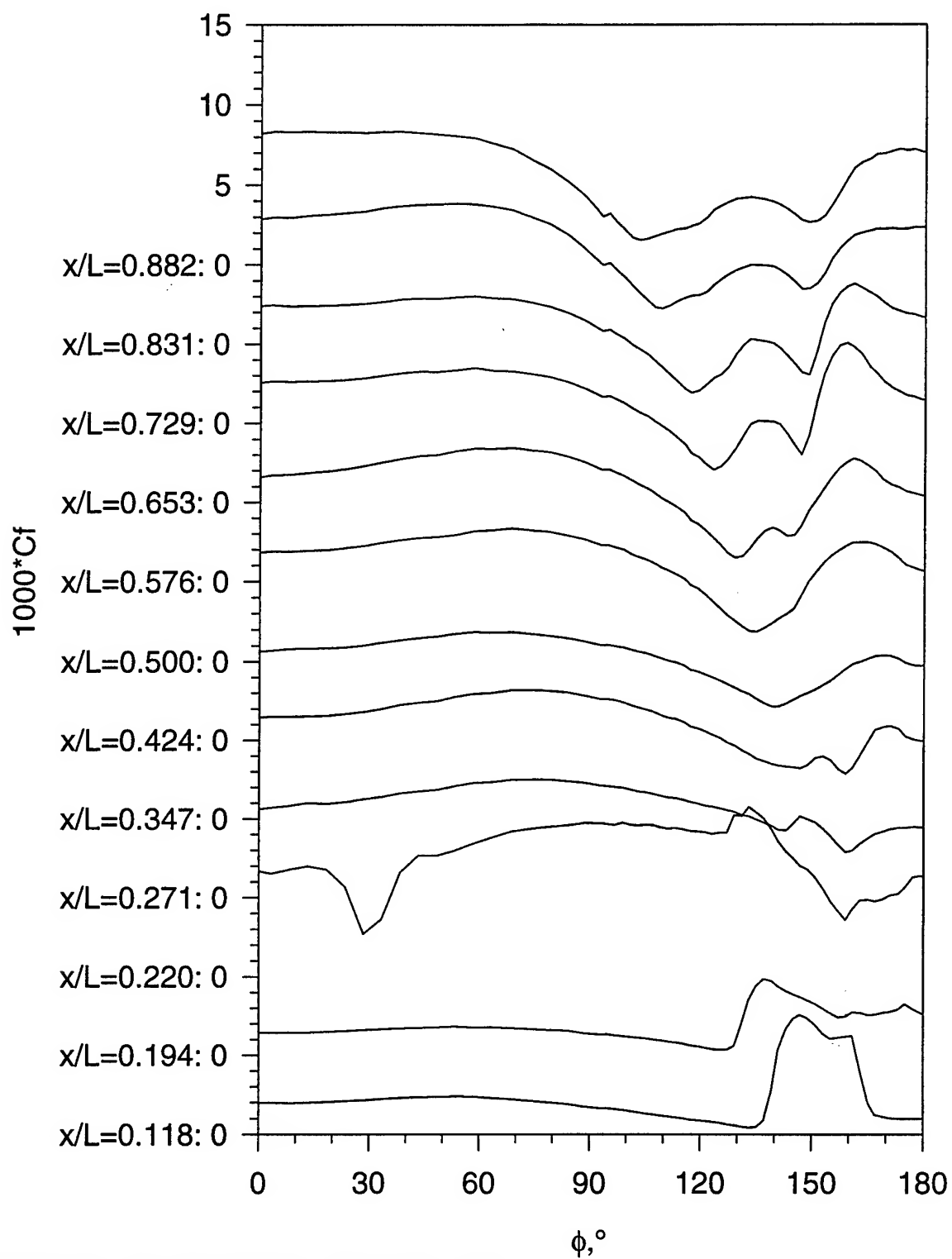


Figure 84. Constant temperature  $Cf$  vs.  $\phi$  for all  $x/L$ ,  $\alpha=22.4^\circ$ .

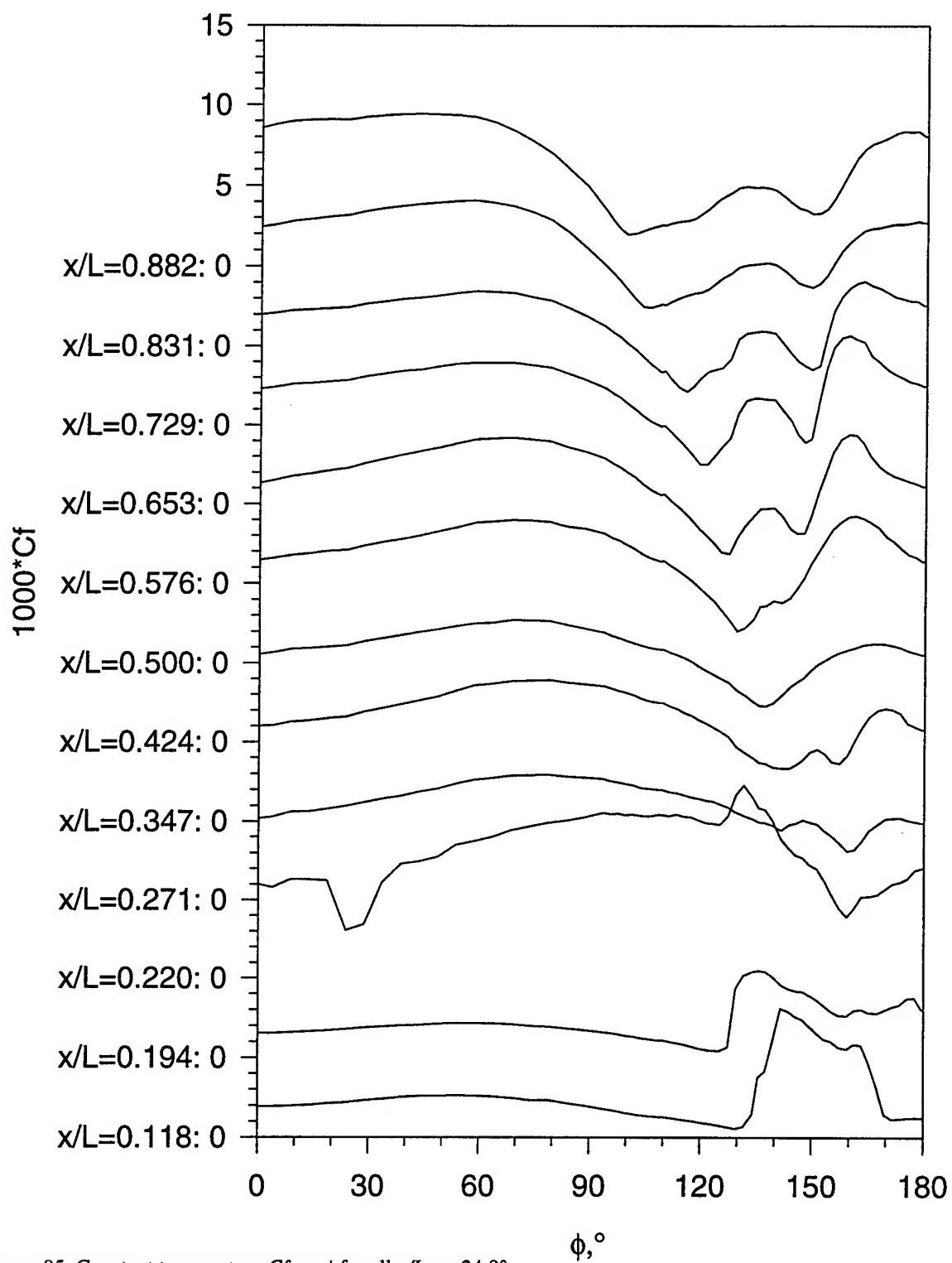


Figure 85. Constant temperature  $C_f$  vs.  $\phi$  for all  $x/L$ ,  $\alpha=24.8^\circ$ .

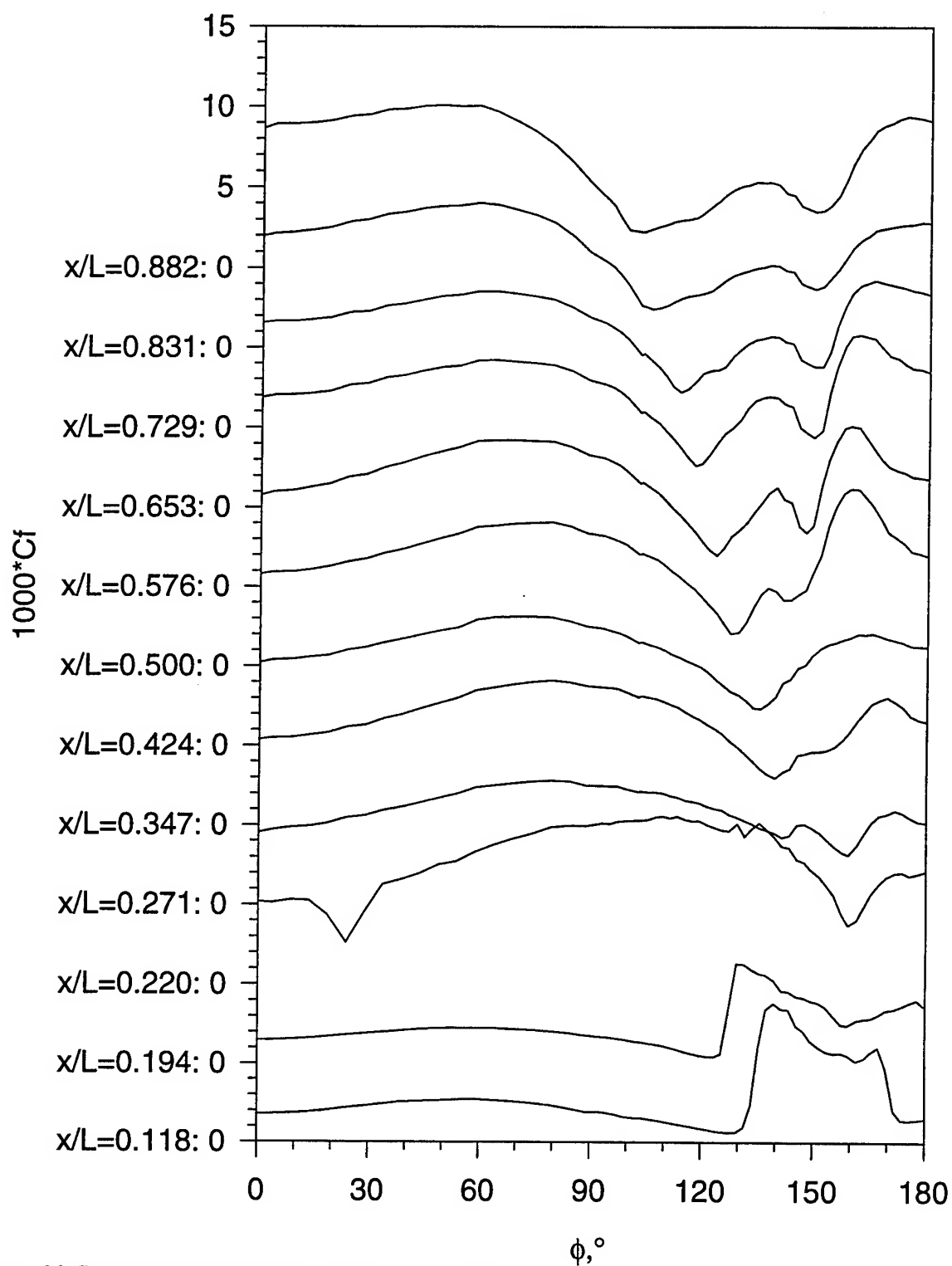


Figure 86. Constant temperature  $Cf$  vs.  $\phi$  for all  $x/L$ ,  $\alpha=27.5^\circ$ .

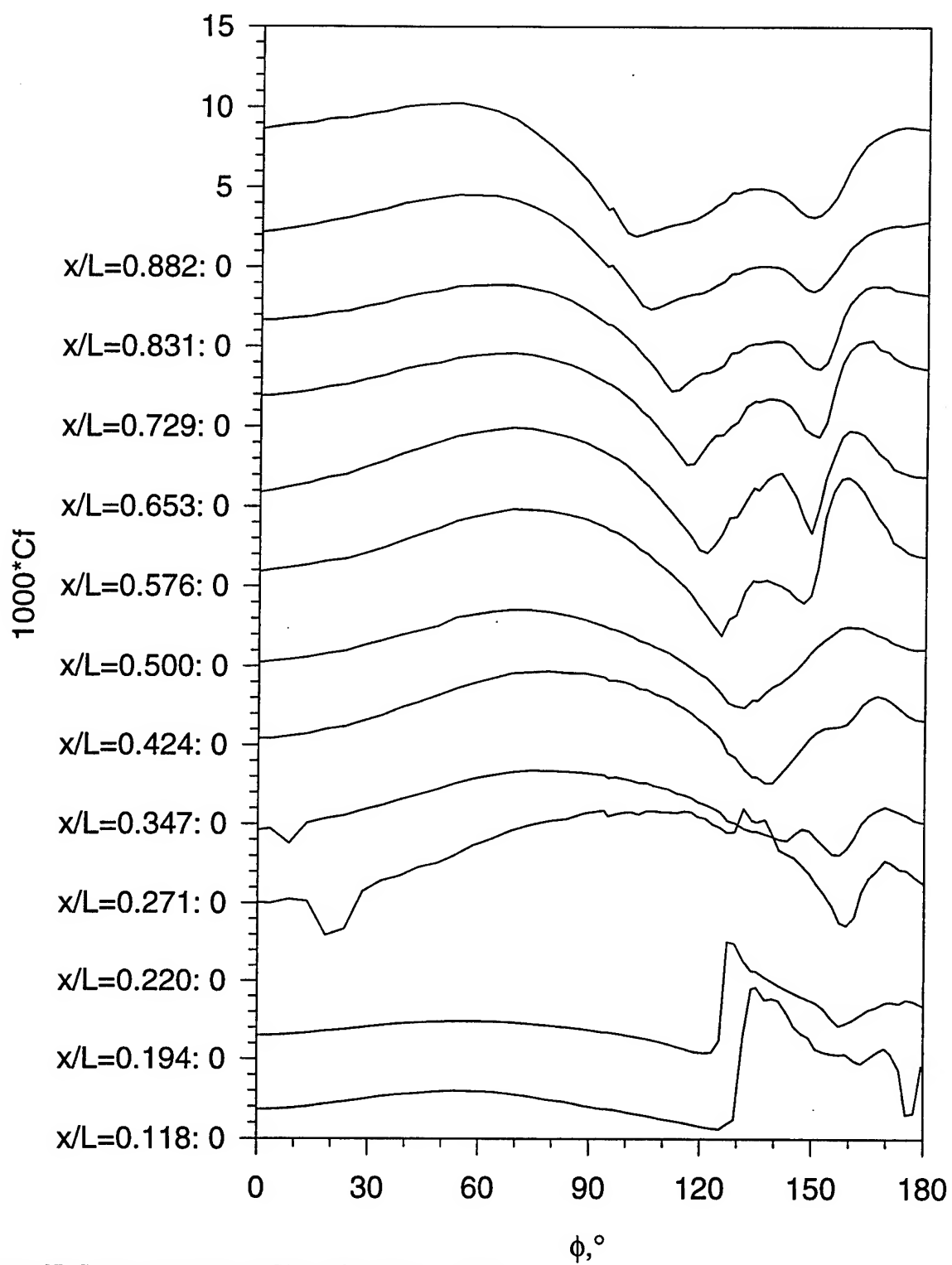


Figure 87. Constant temperature  $Cf$  vs.  $\phi$  for all  $x/L$ ,  $\alpha=29.9^\circ$ .

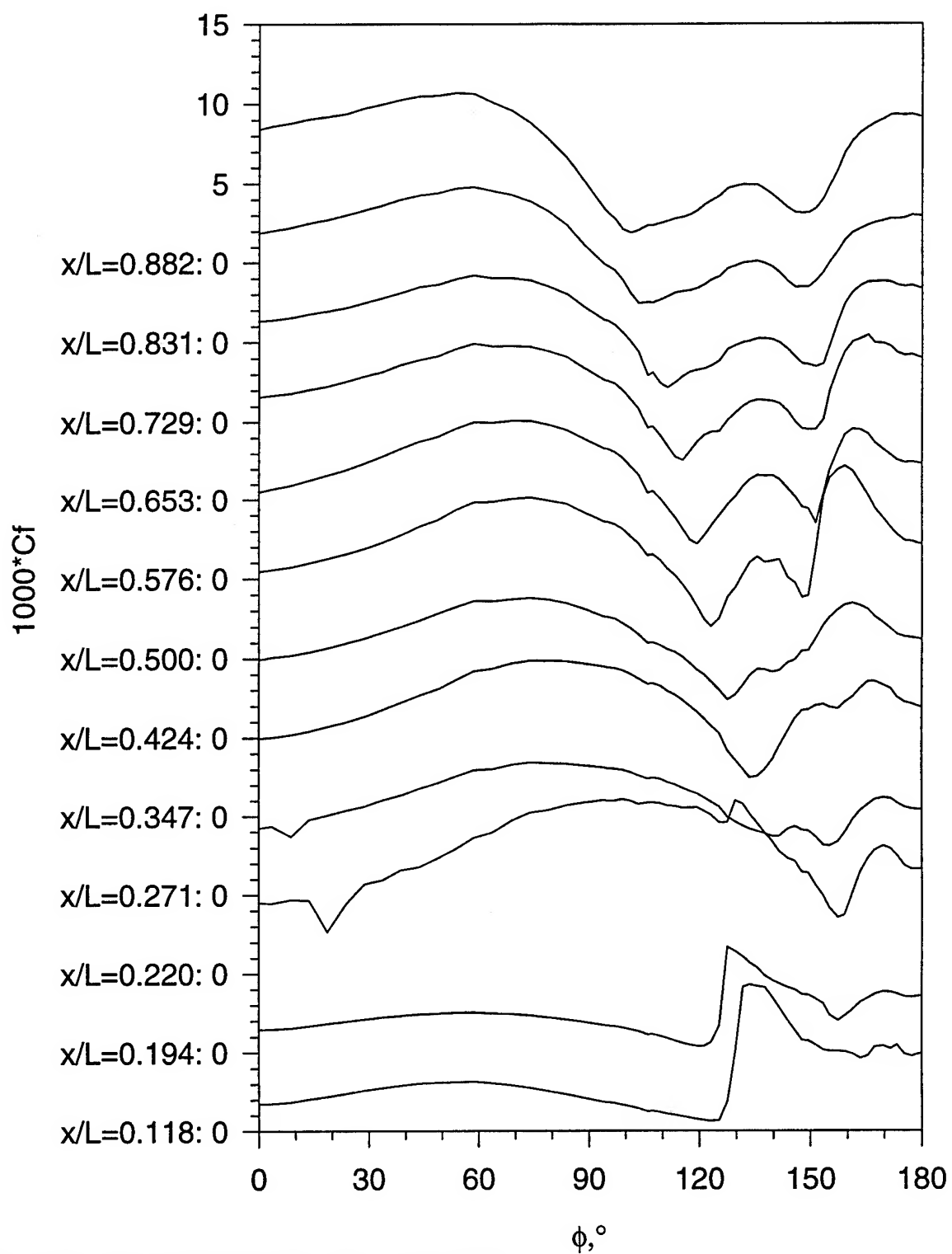


Figure 88. Constant temperature  $Cf$  vs.  $\phi$  for all  $x/L$ ,  $\alpha=32.4^\circ$ .

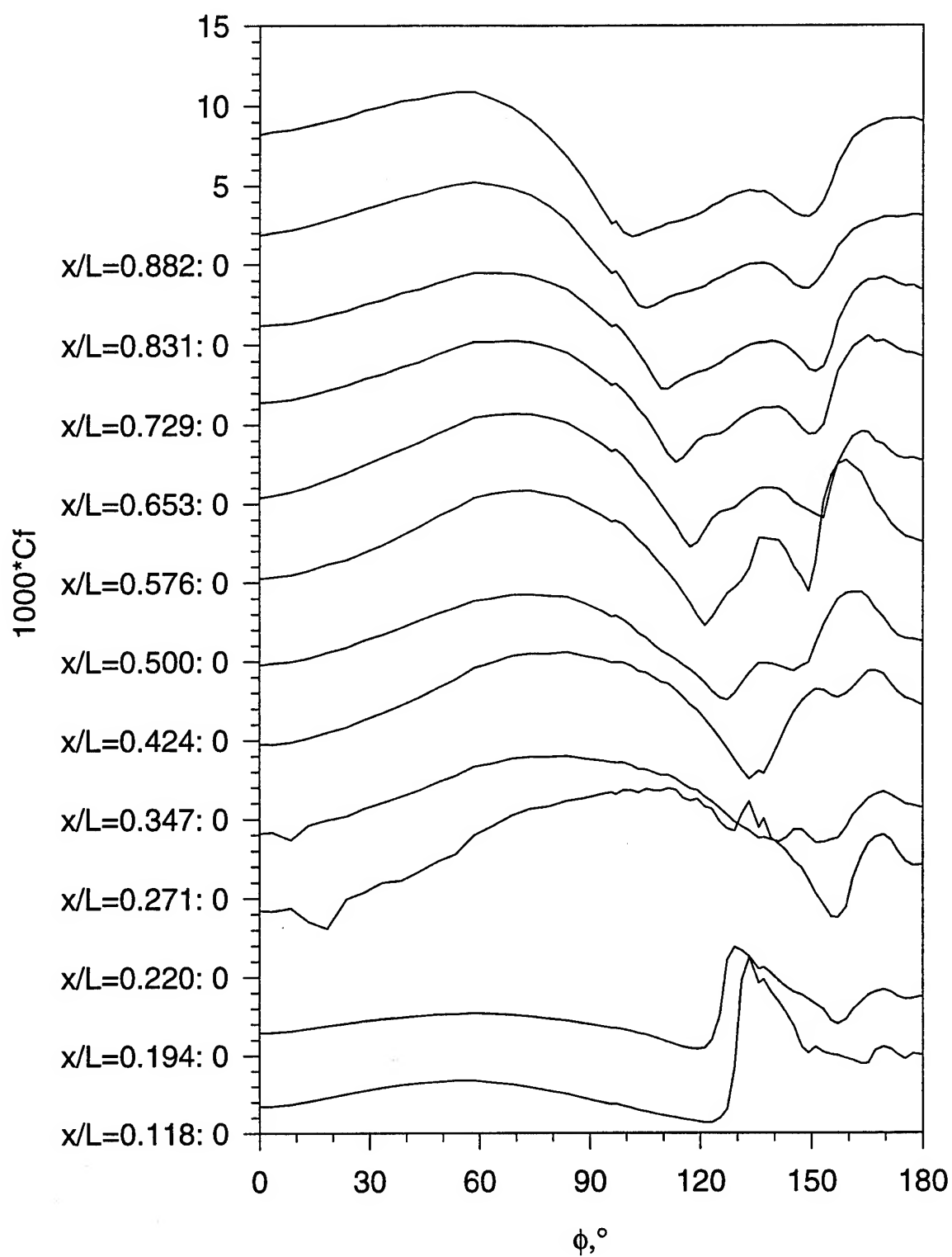


Figure 89. Constant temperature  $Cf$  vs.  $\phi$  for all  $x/L$ ,  $\alpha=34.8^\circ$ .

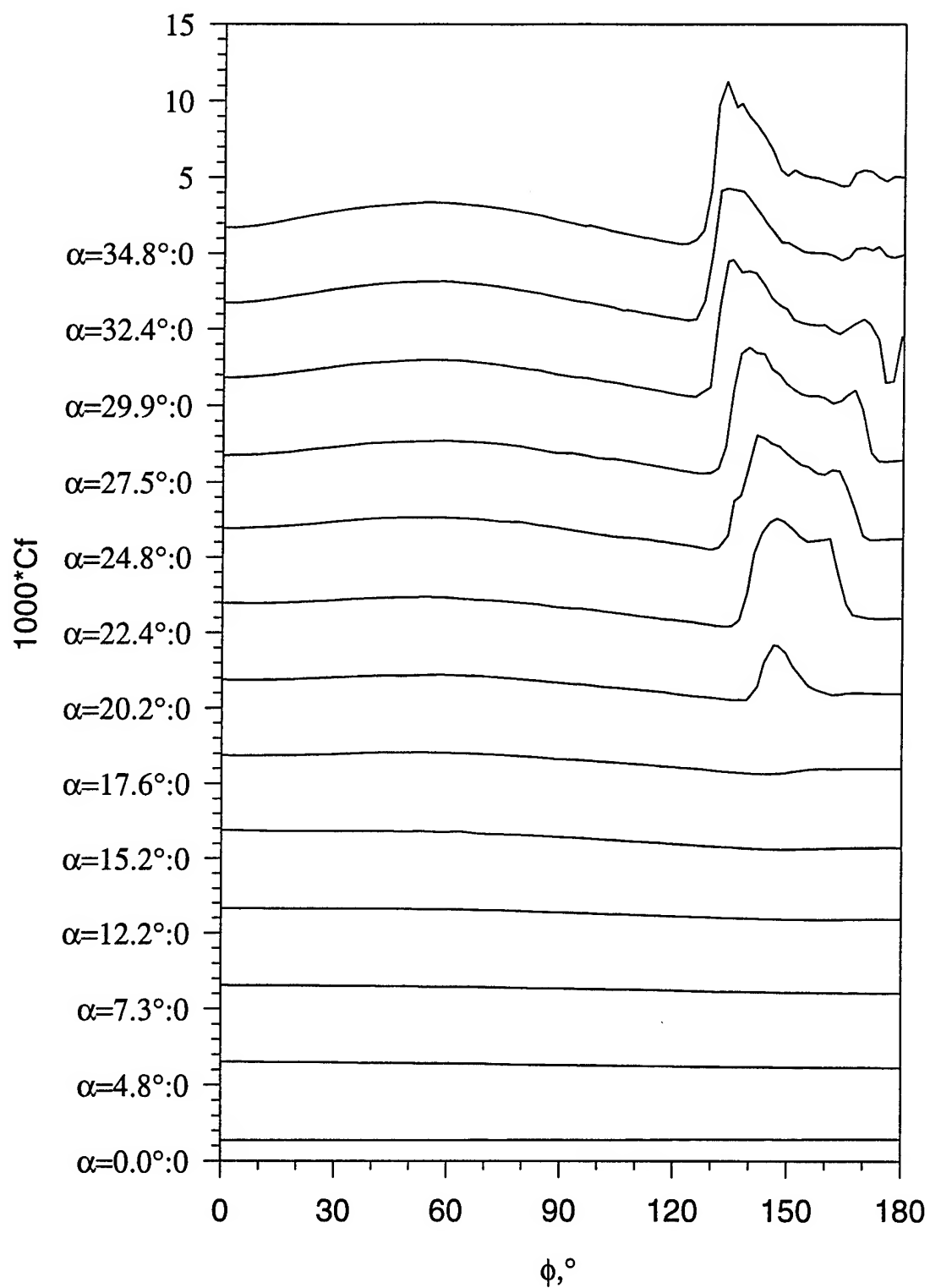


Figure 90. Constant temperature  $Cf$  vs.  $\phi$  for all  $\alpha$ ,  $x/L=0.118$ .

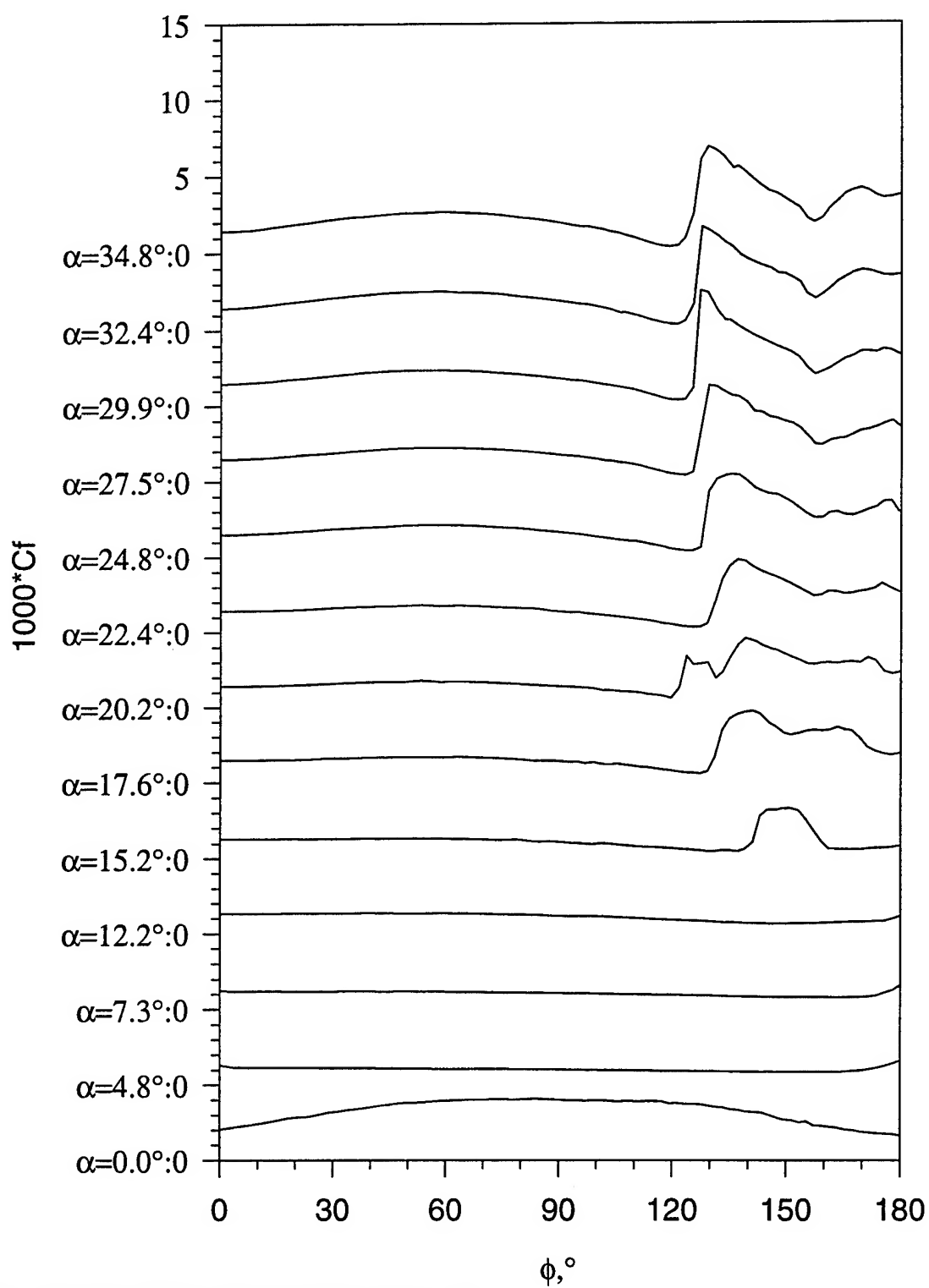


Figure 91. Constant temperature  $Cf$  vs.  $\phi$  for all  $\alpha$ ,  $x/L=0.194$ .



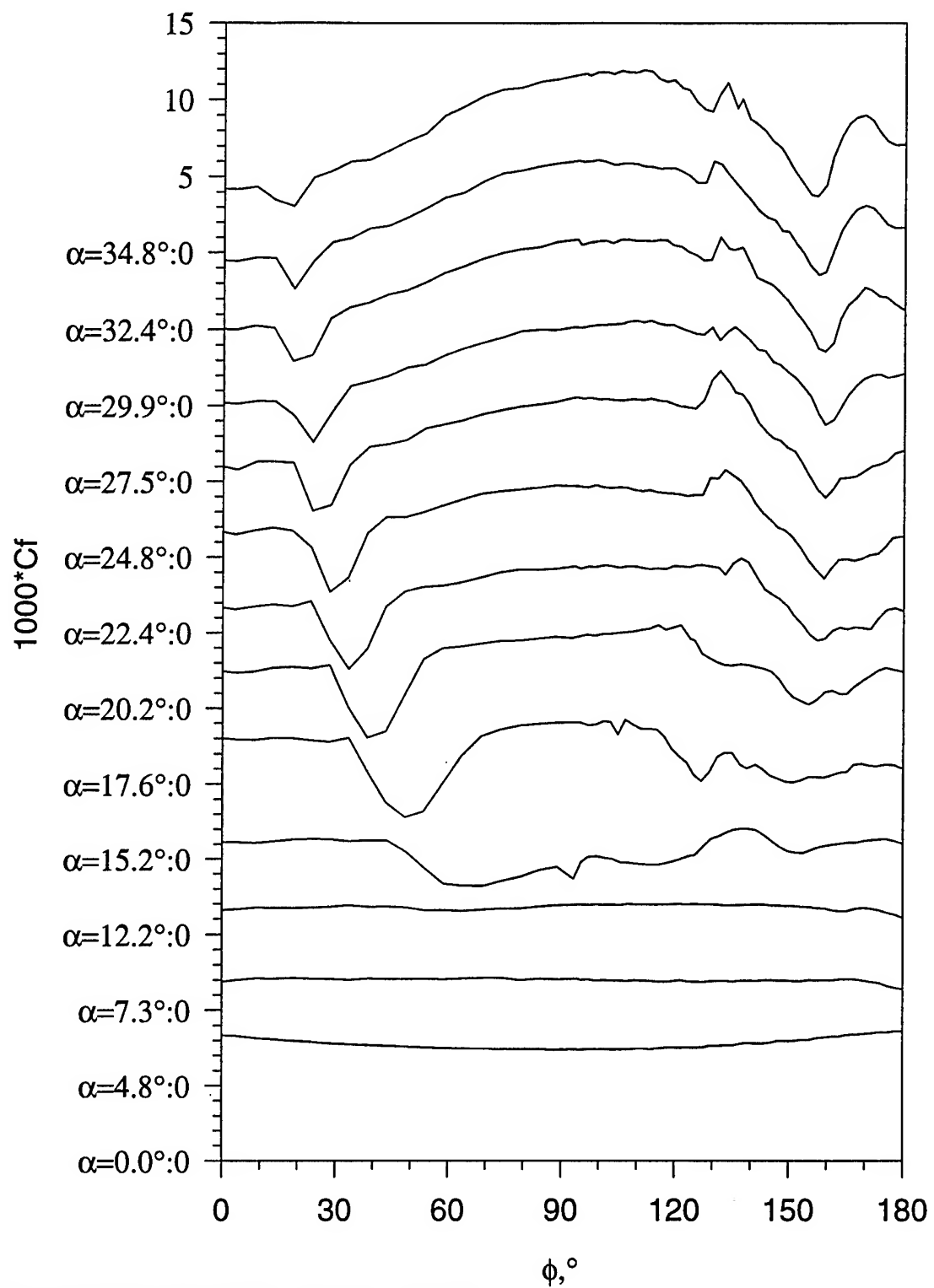


Figure 92. Constant temperature  $C_f$  vs.  $\phi$  for all  $\alpha$ ,  $x/L=0.220$ .

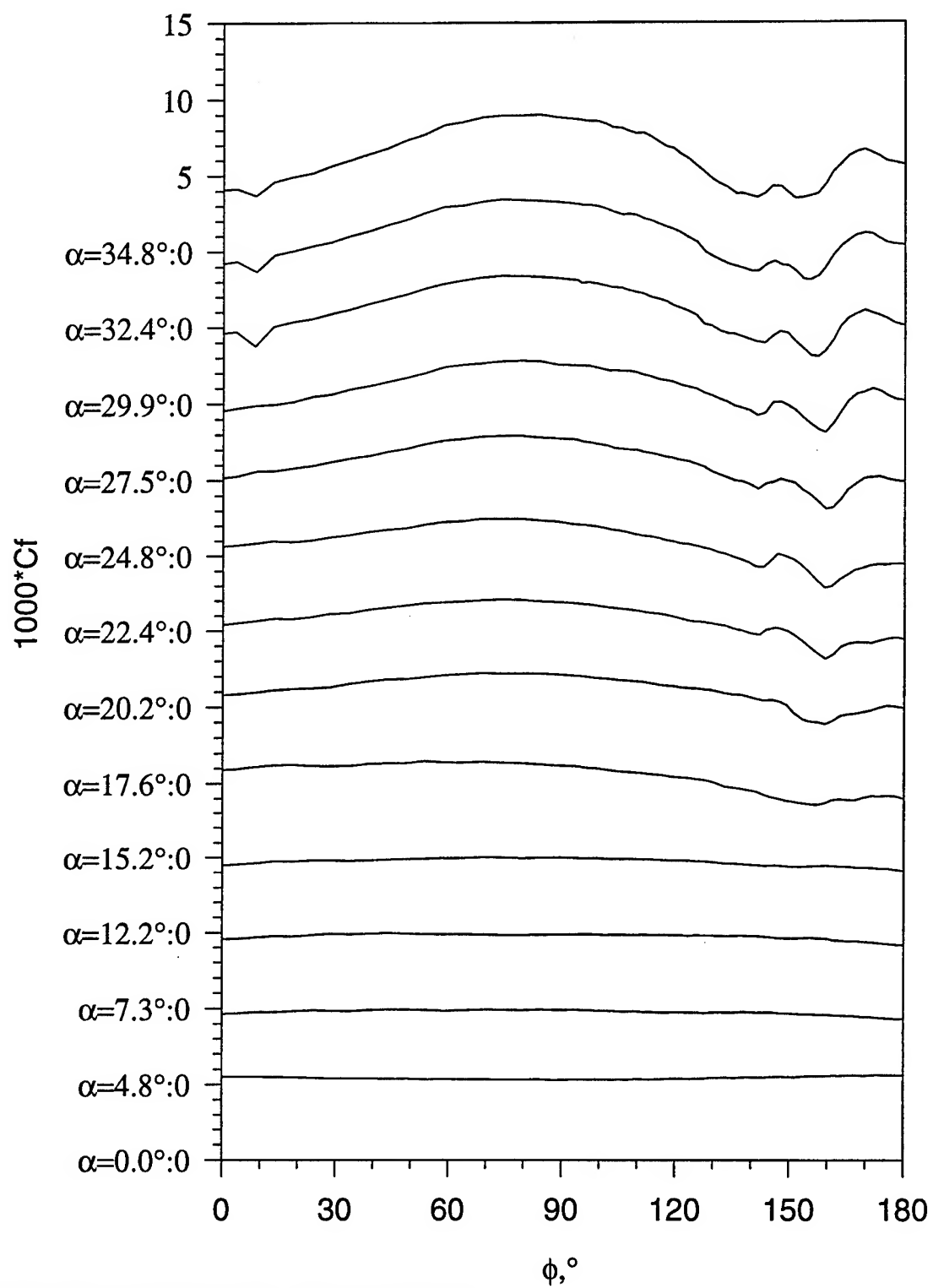


Figure 93. Constant temperature  $Cf$  vs.  $\phi$  for all  $\alpha$ ,  $x/L=0.271$ .

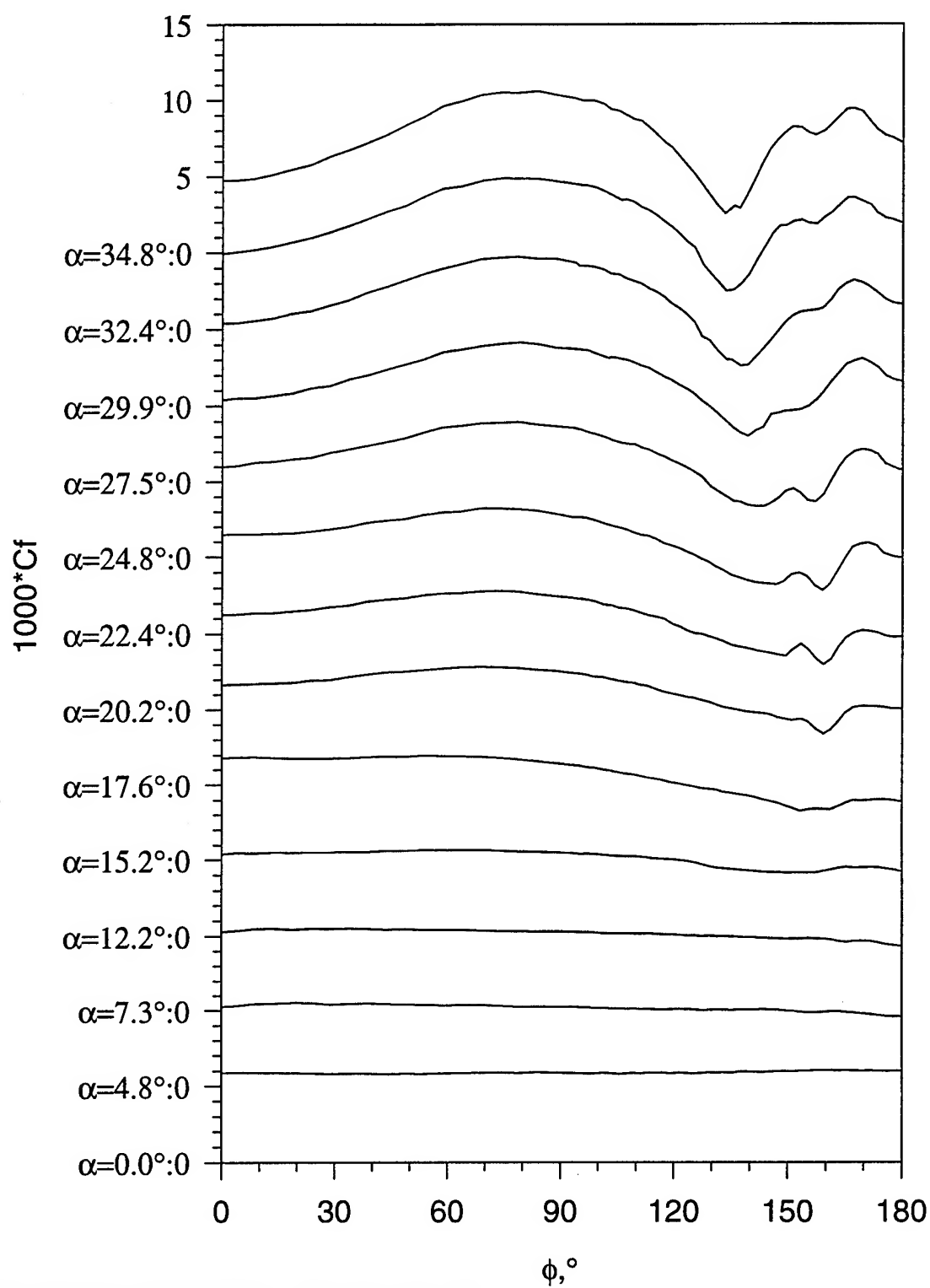


Figure 94. Constant temperature  $Cf$  vs.  $\phi$  for all  $\alpha$ ,  $x/L=0.347$ .

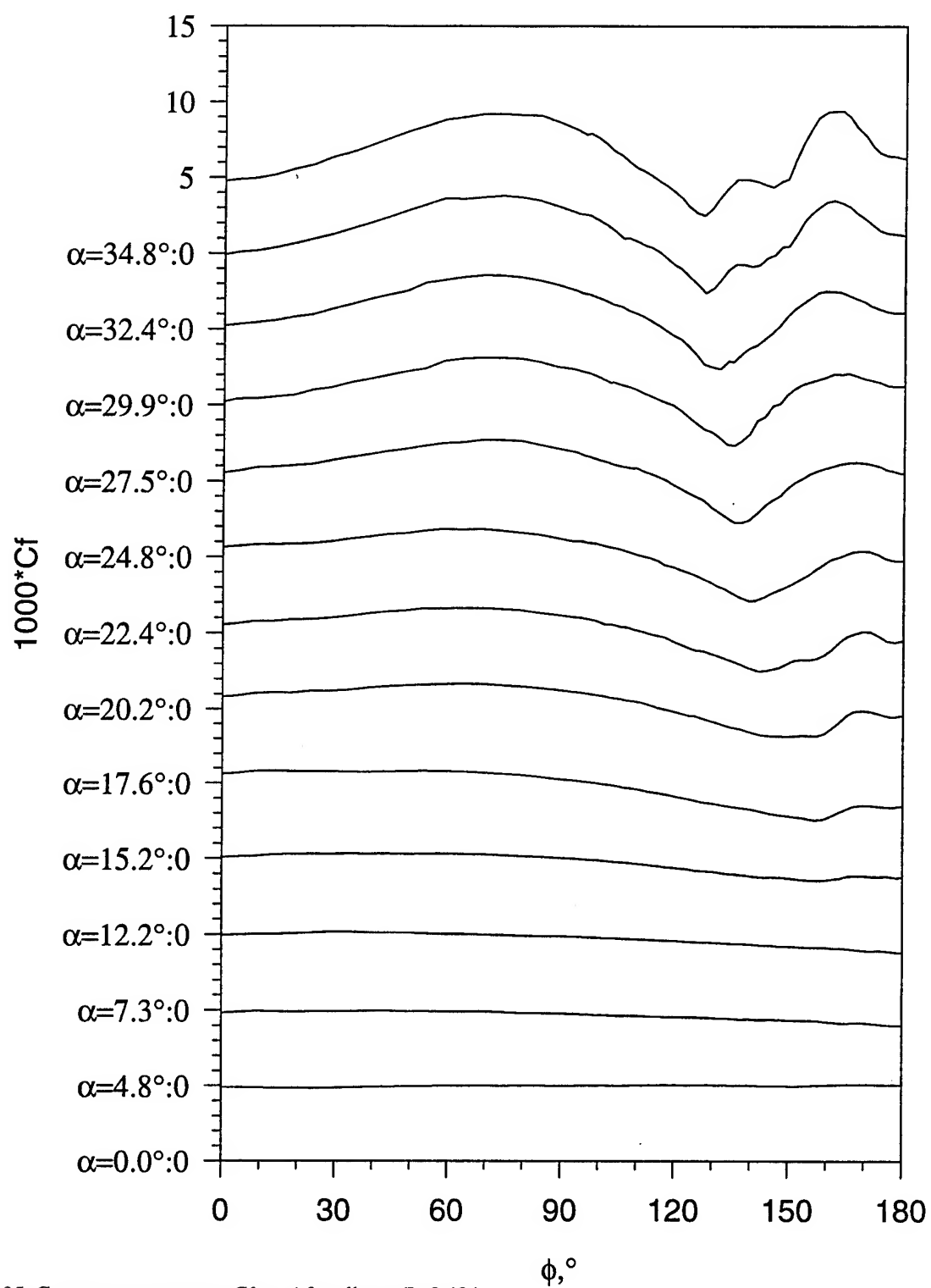


Figure 95. Constant temperature  $Cf$  vs.  $\phi$  for all  $\alpha$ ,  $x/L=0.424$ .

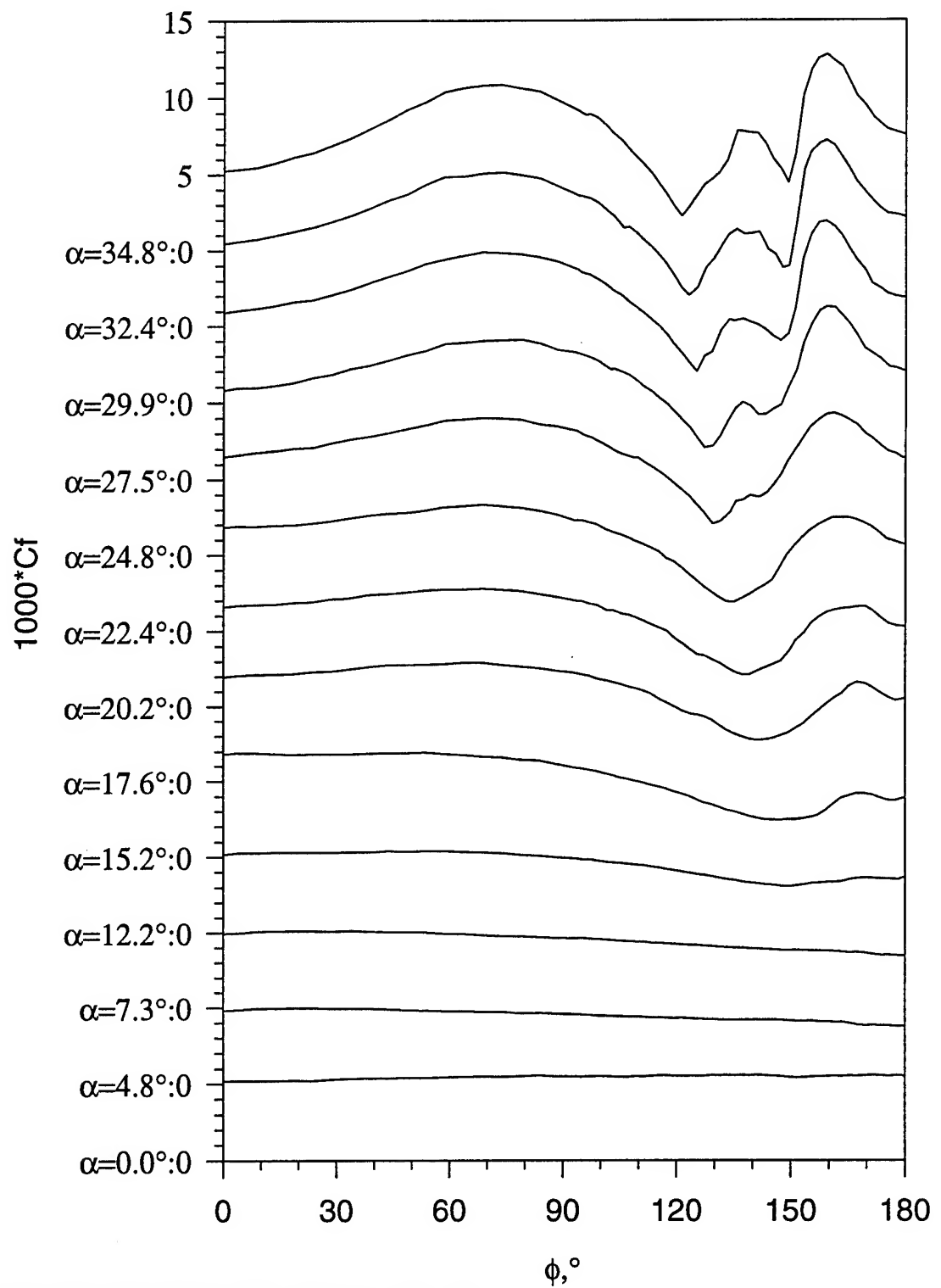


Figure 96. Constant temperature  $Cf$  vs.  $\phi$  for all  $\alpha$ ,  $x/L=0.500$ .

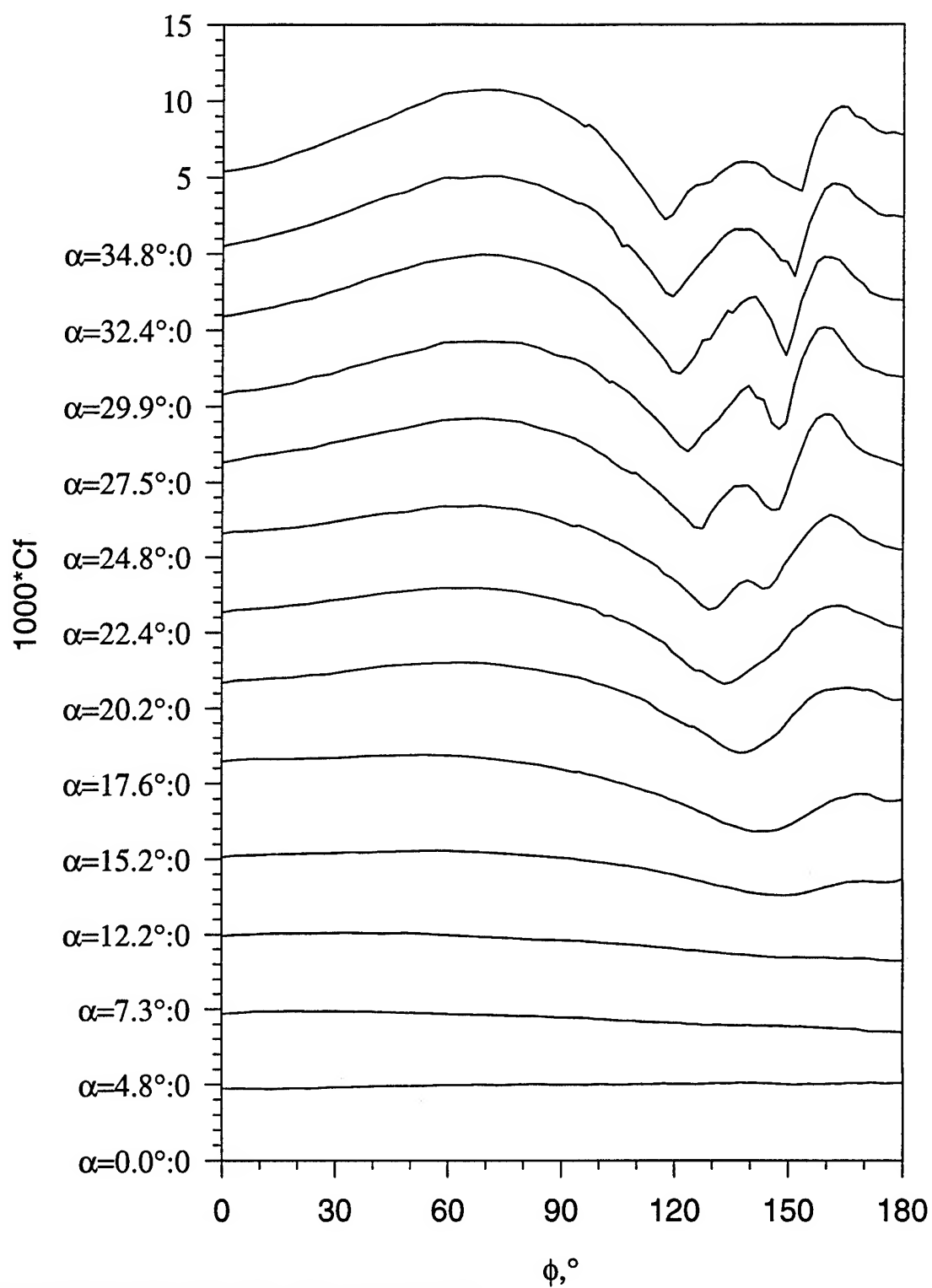


Figure 97. Constant temperature  $Cf$  vs.  $\phi$  for all  $\alpha$ ,  $x/L=0.576$ .

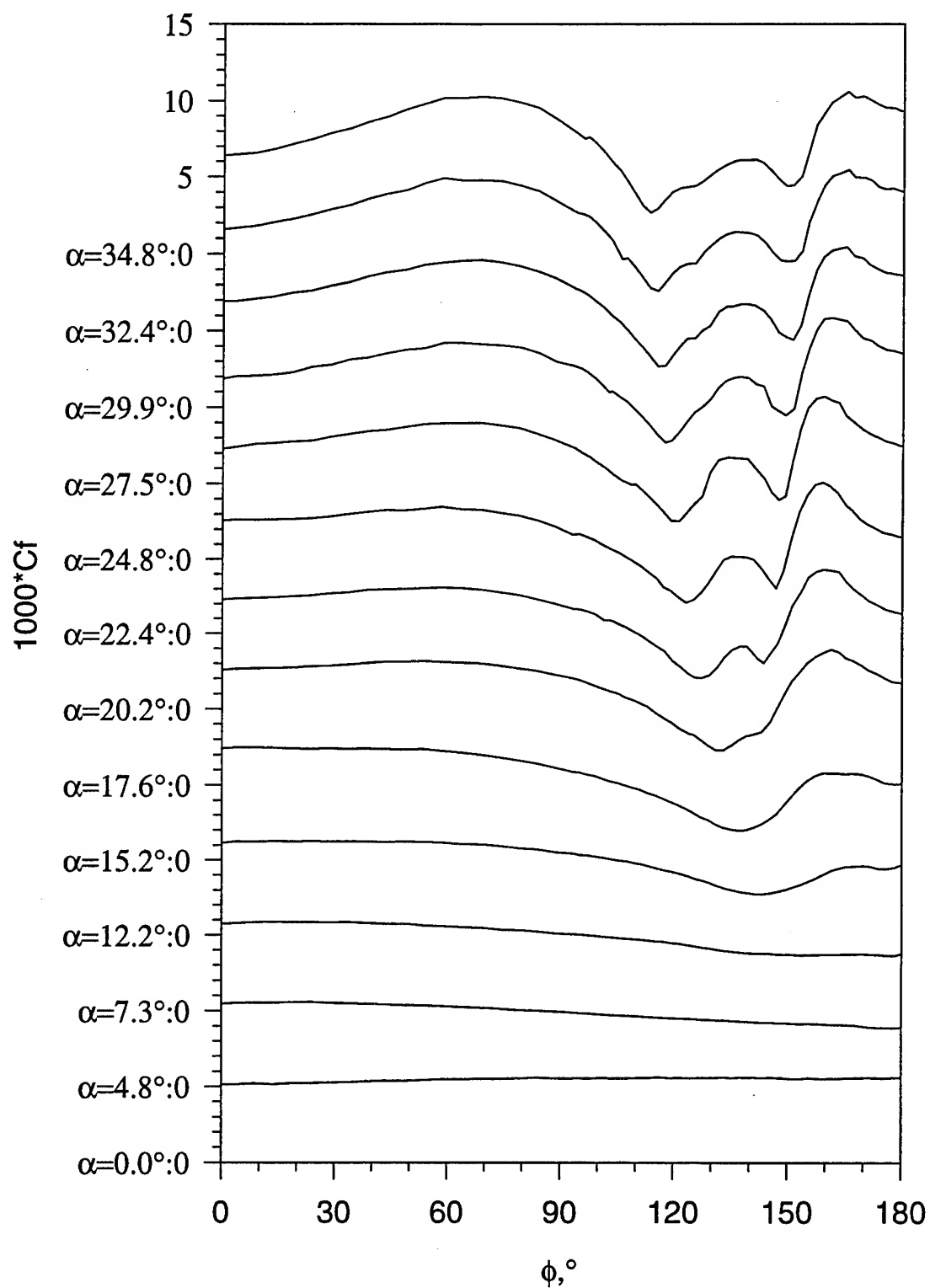


Figure 98. Constant temperature  $Cf$  vs.  $\phi$  for all  $\alpha$ ,  $x/L=0.653$ .

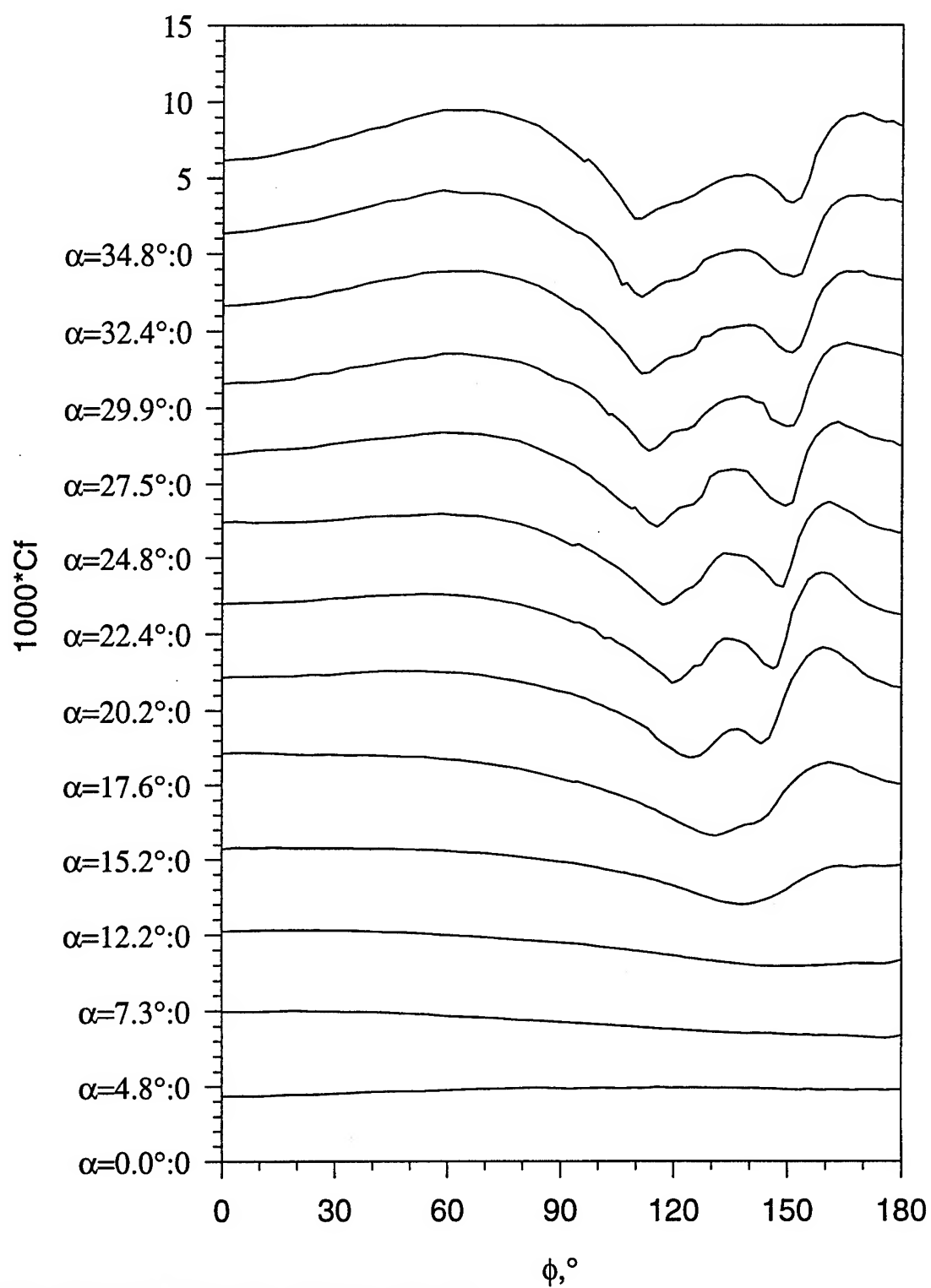


Figure 99. Constant temperature  $Cf$  vs.  $\phi$  for all  $\alpha$ ,  $x/L=0.729$ .



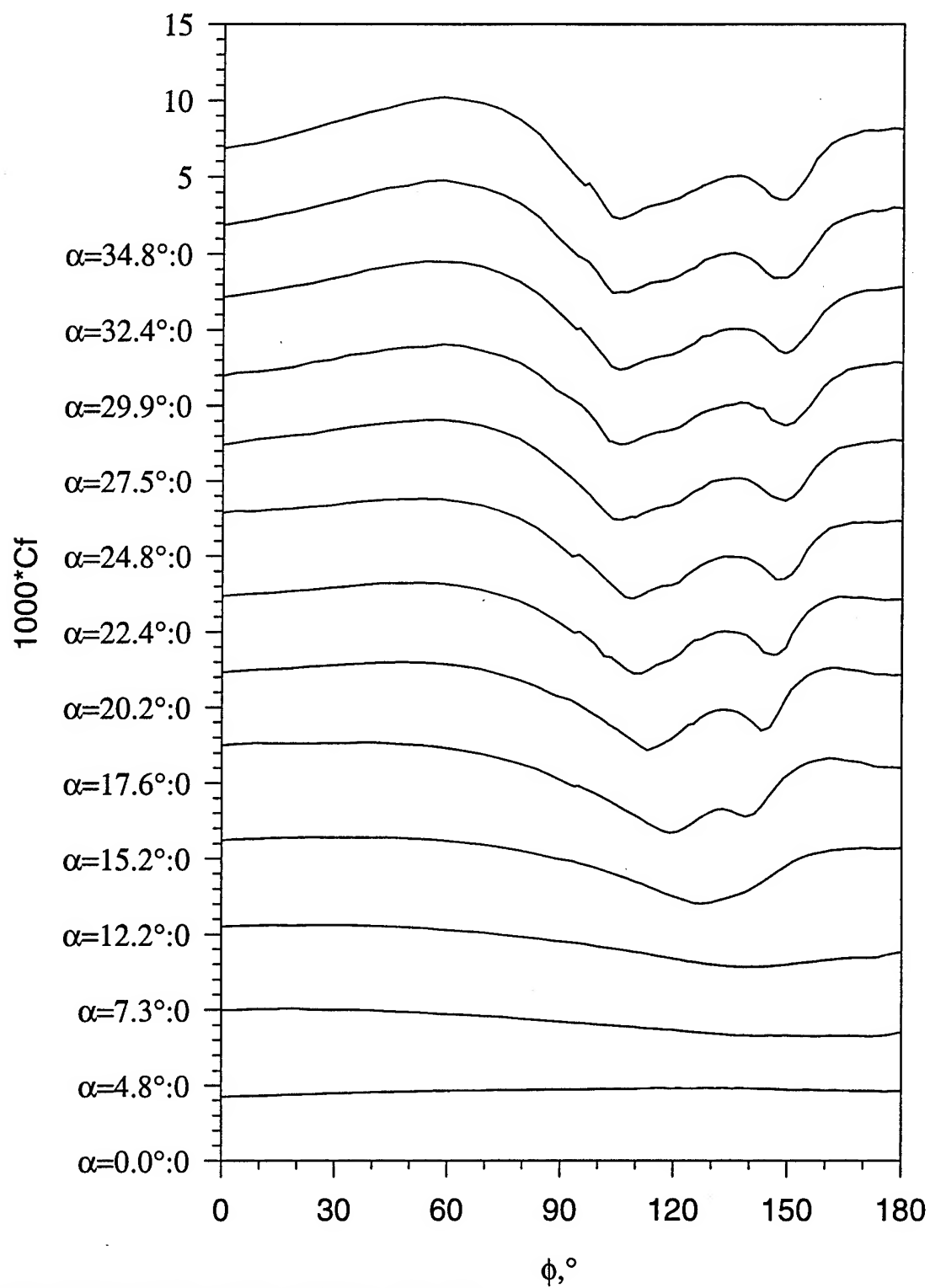


Figure 100. Constant temperature  $Cf$  vs.  $\phi$  for all  $\alpha$ ,  $x/L=0.831$ .

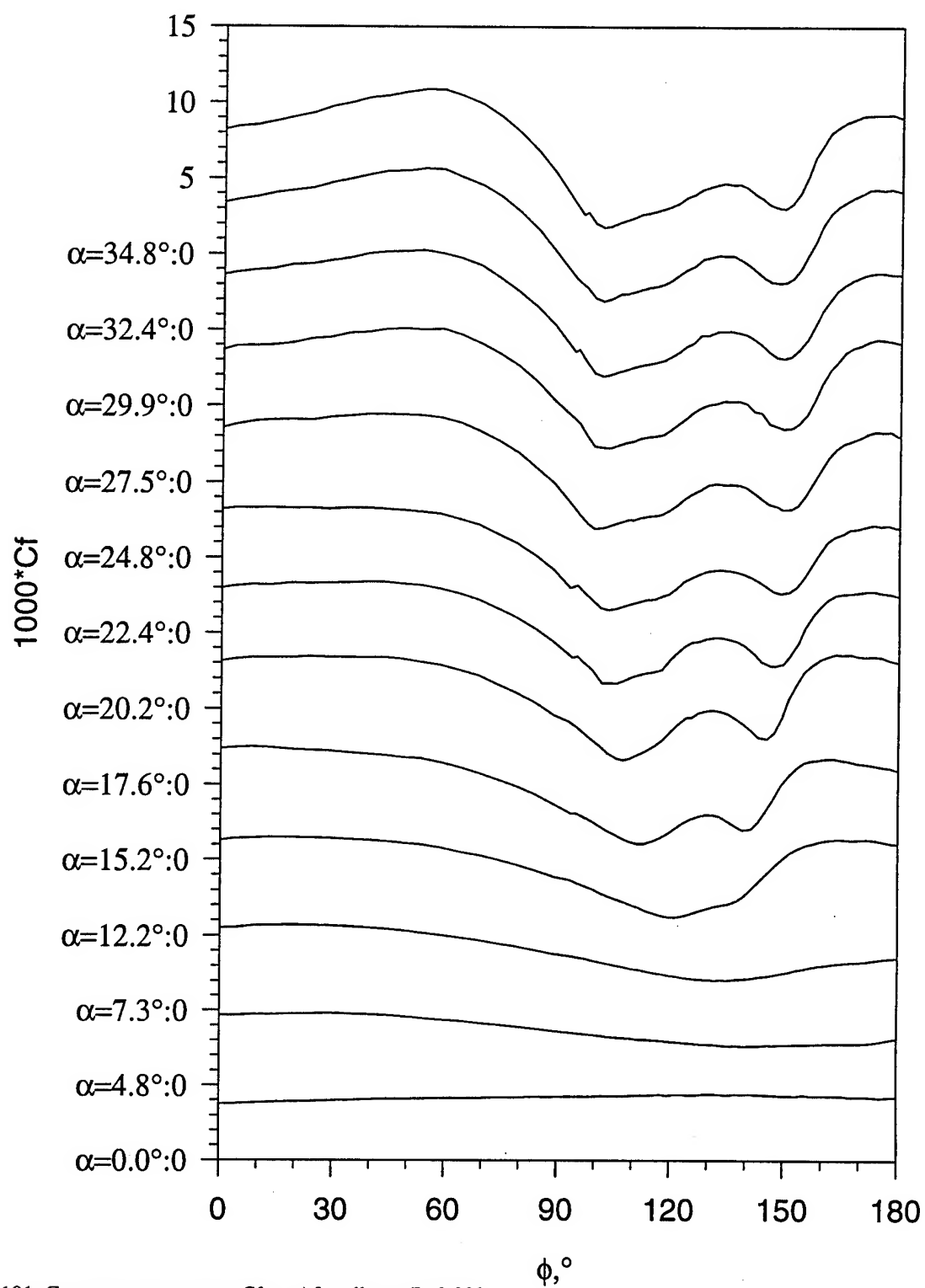


Figure 101. Constant temperature  $Cf$  vs.  $\phi$  for all  $\alpha$ ,  $x/L=0.882$ .

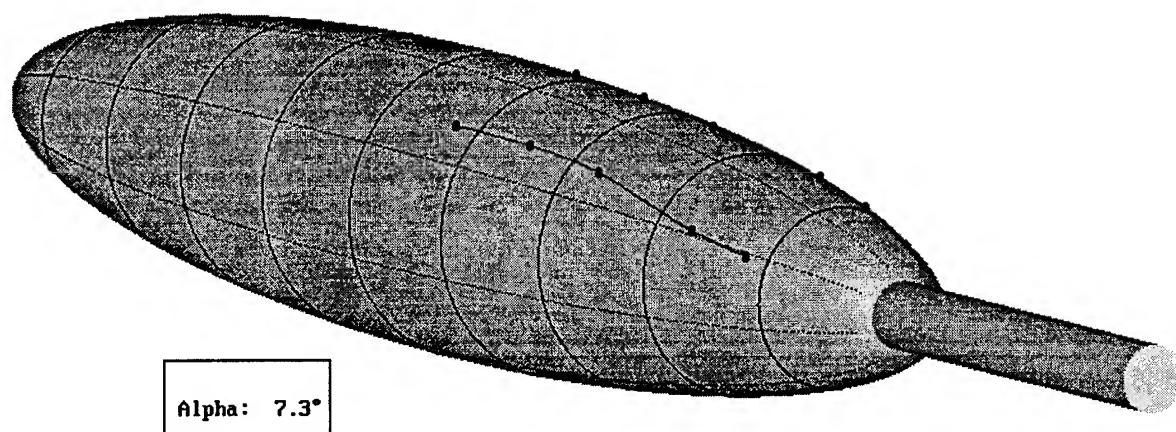


Figure 102. Constant temperature separation line topology for  $\alpha=7.3^\circ$ .

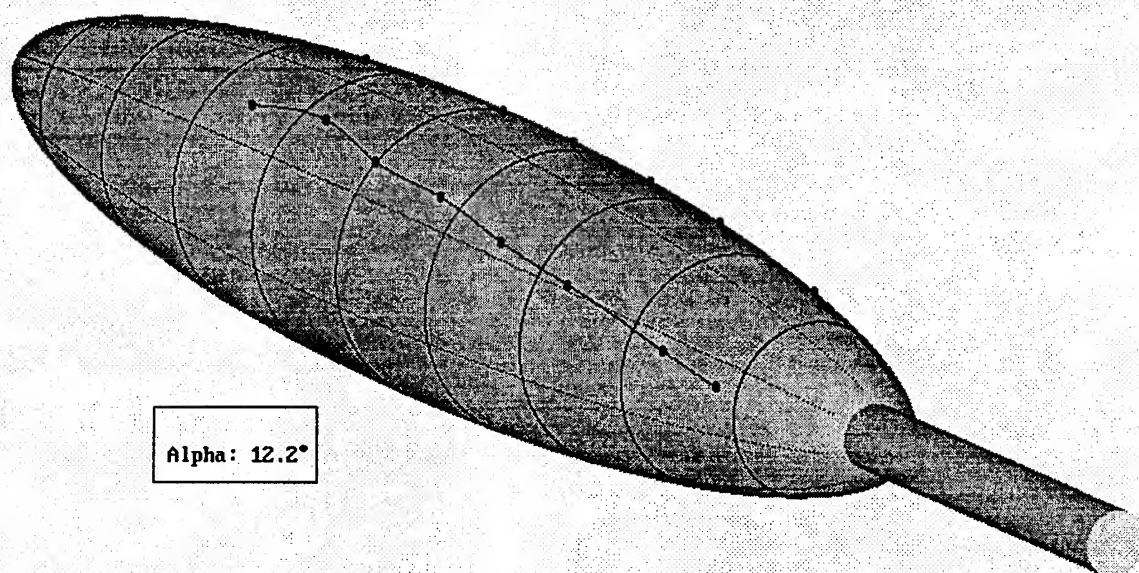


Figure 103. Constant temperature separation line topology for  $\alpha=12.2^\circ$ .

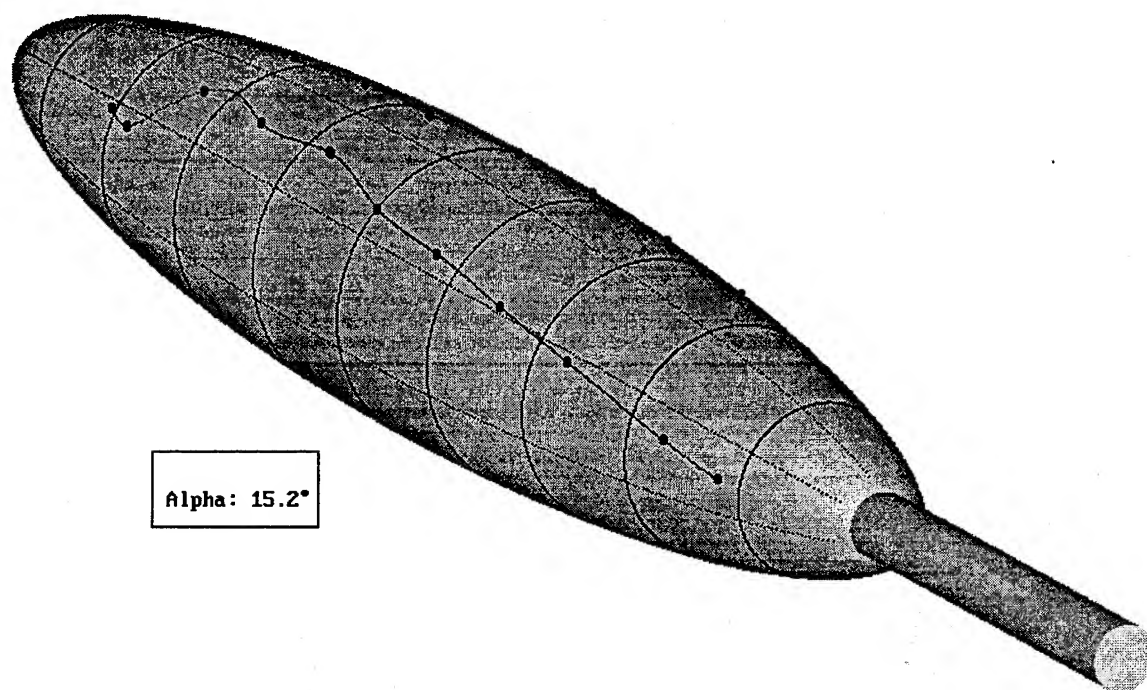


Figure 104. Constant temperature separation line topology for  $\alpha=15.2^\circ$ .

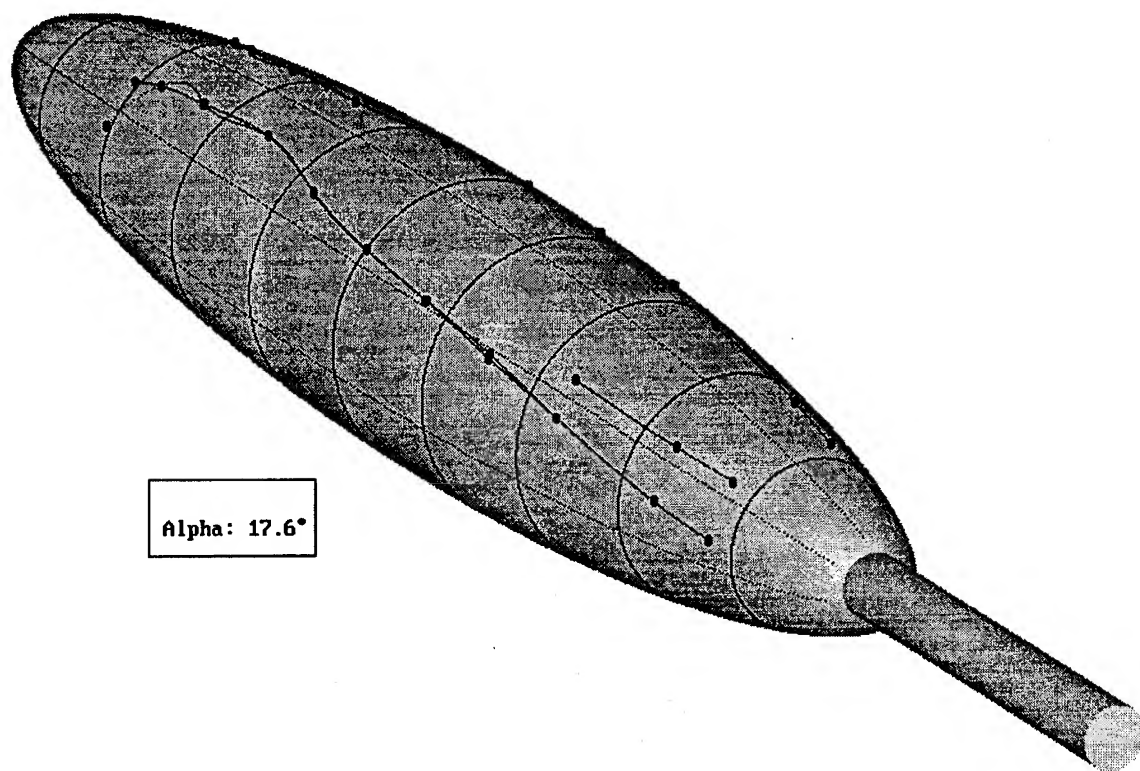


Figure 105. Constant temperature separation line topology for  $\alpha=17.6^\circ$ .

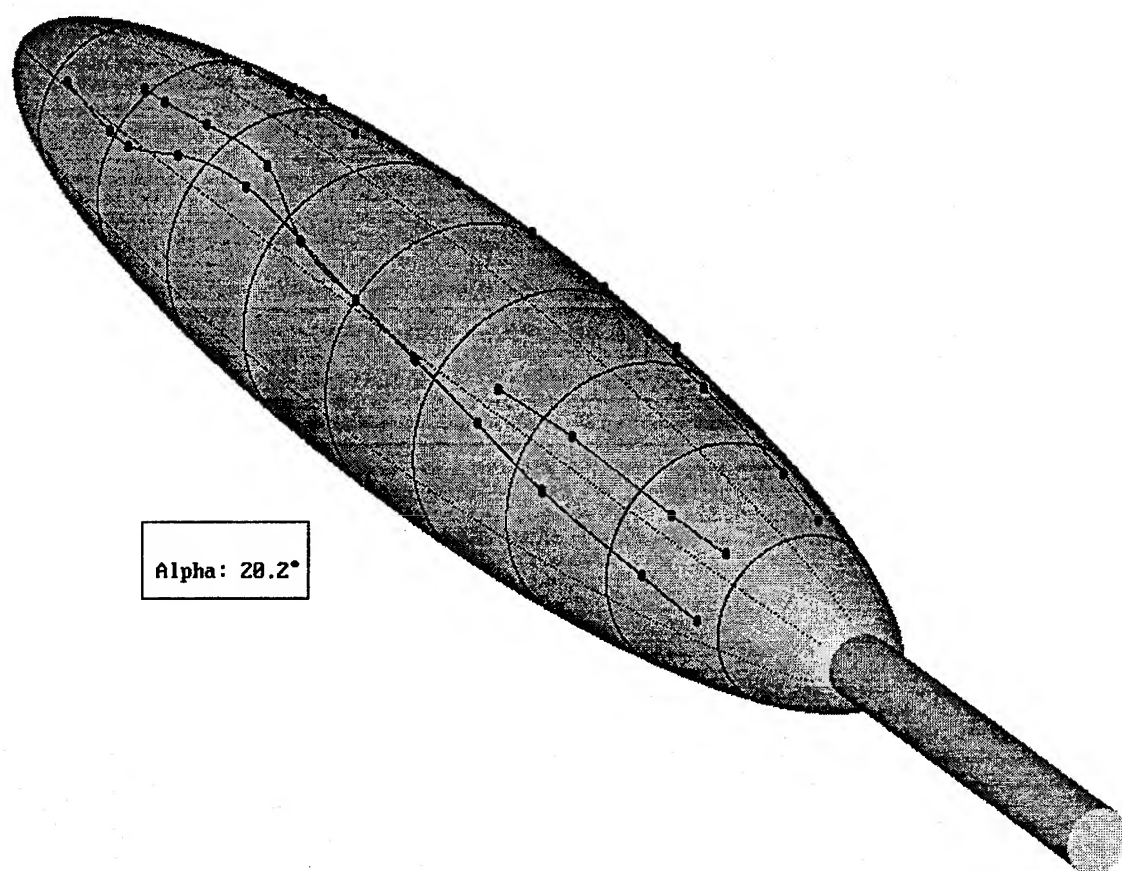


Figure 106. Constant temperature separation line topology for  $\alpha=20.2^\circ$ .

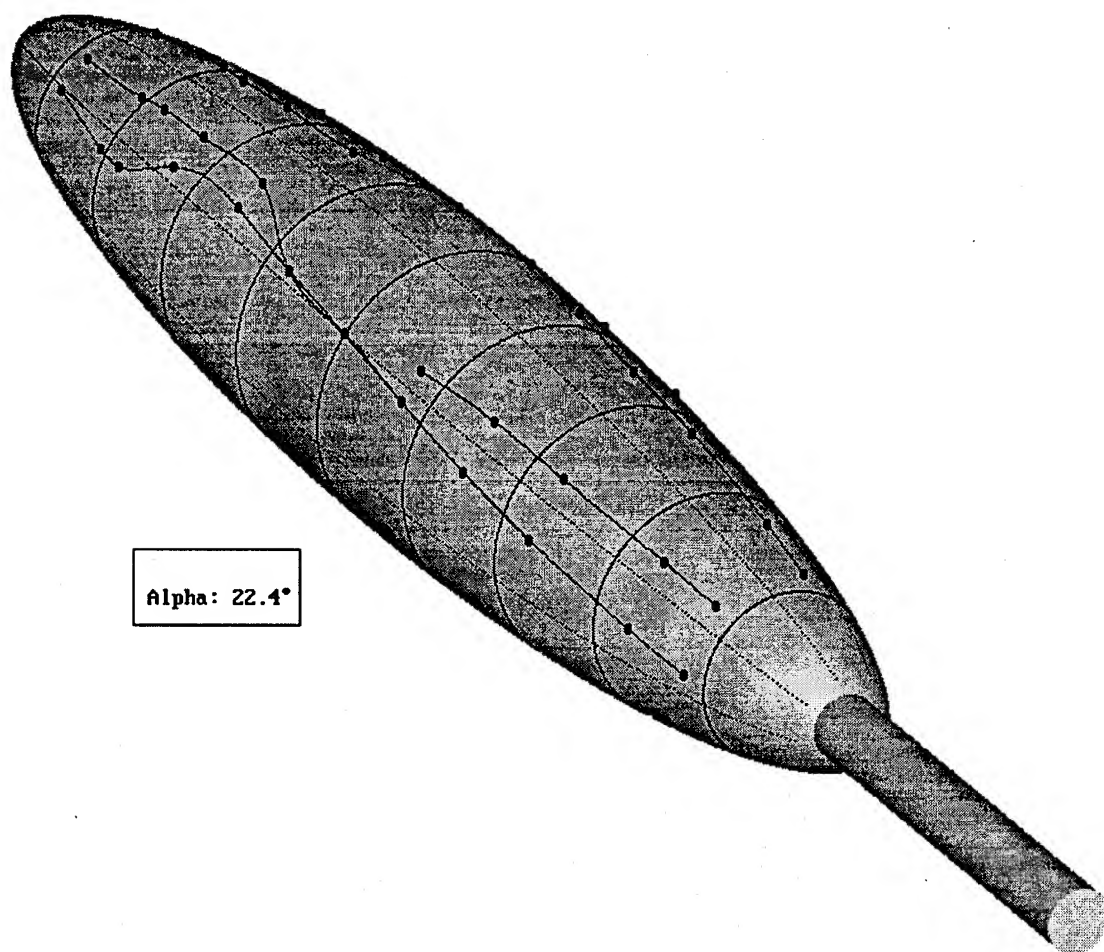


Figure 107. Constant temperature separation line topology for  $\alpha=22.4^\circ$ .



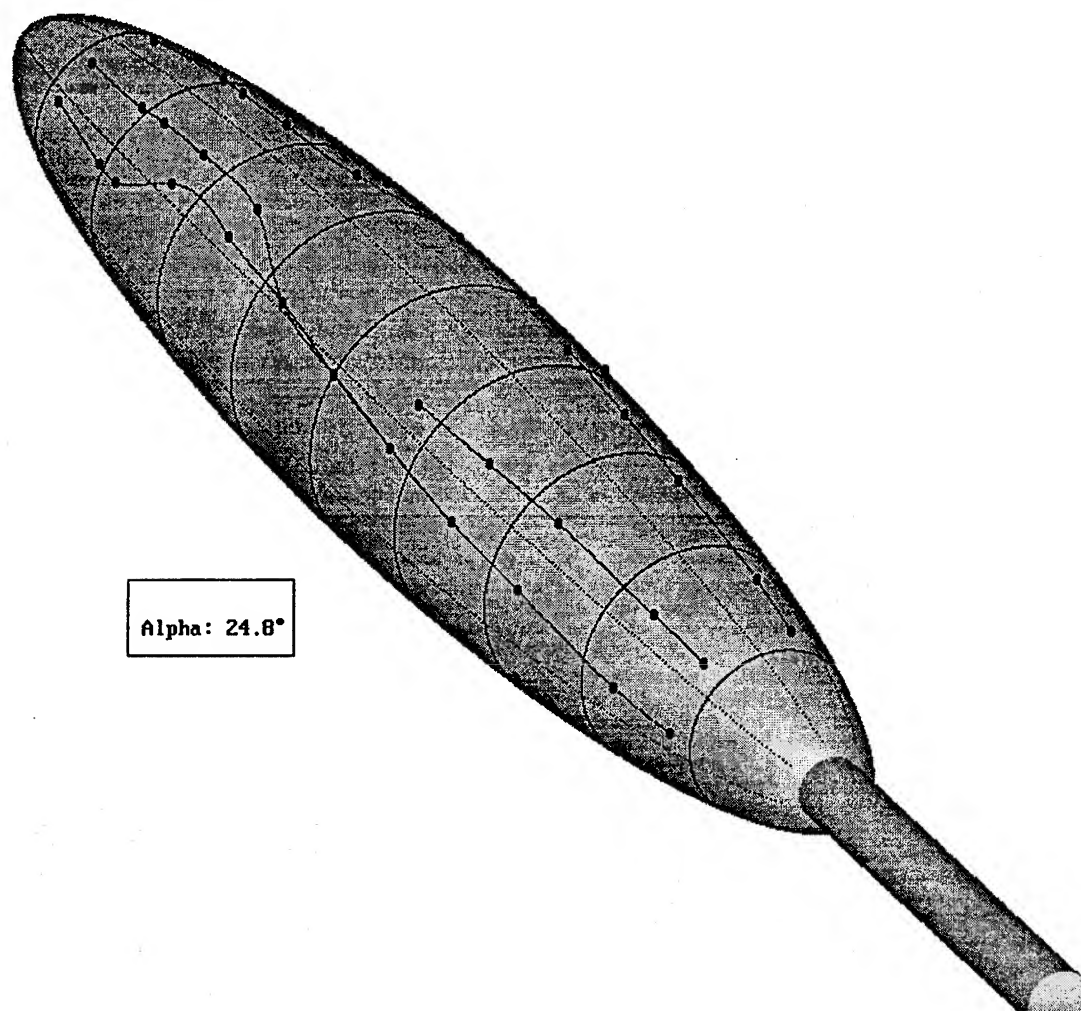


Figure 108. Constant temperature separation line topology for  $\alpha=24.8^\circ$ .

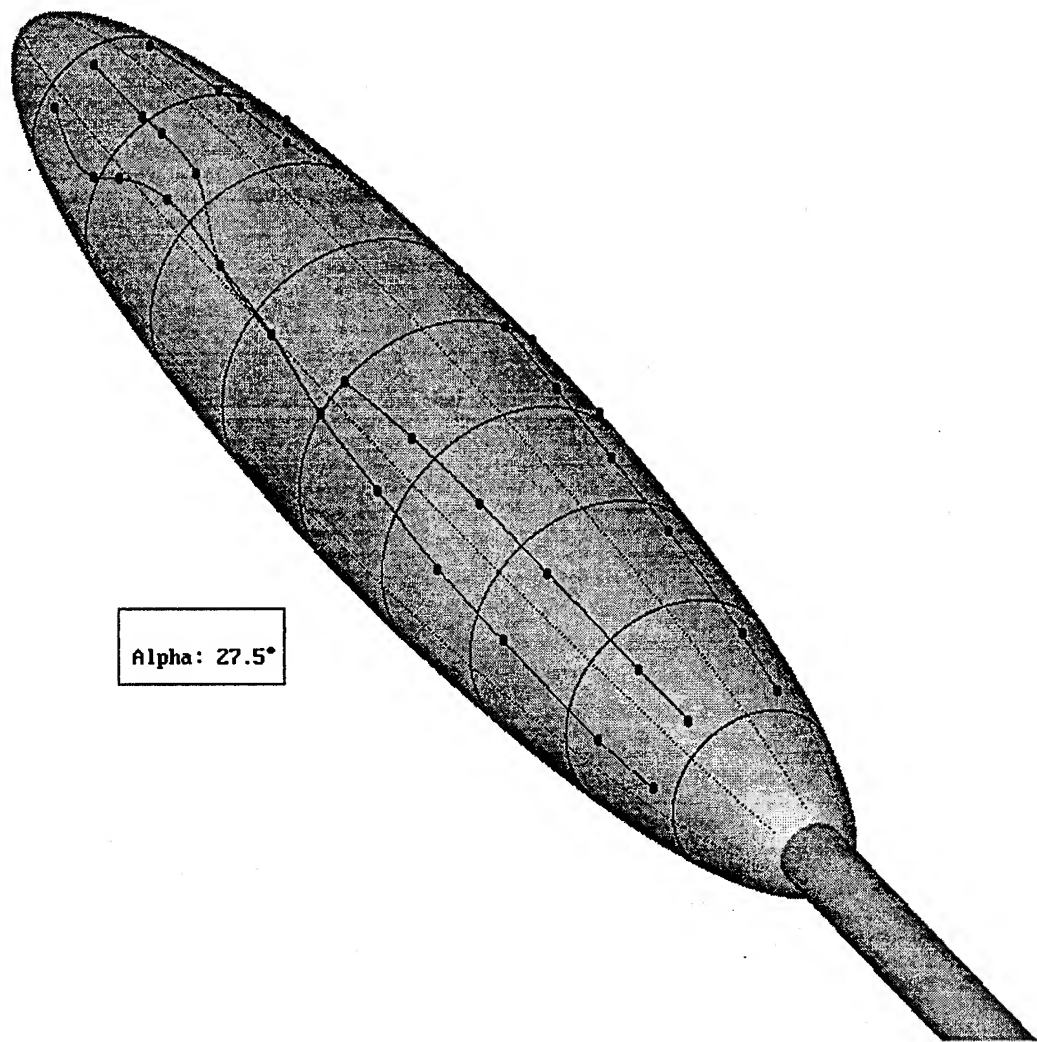


Figure 109. Constant temperature separation line topology for  $\alpha=27.5^\circ$ .

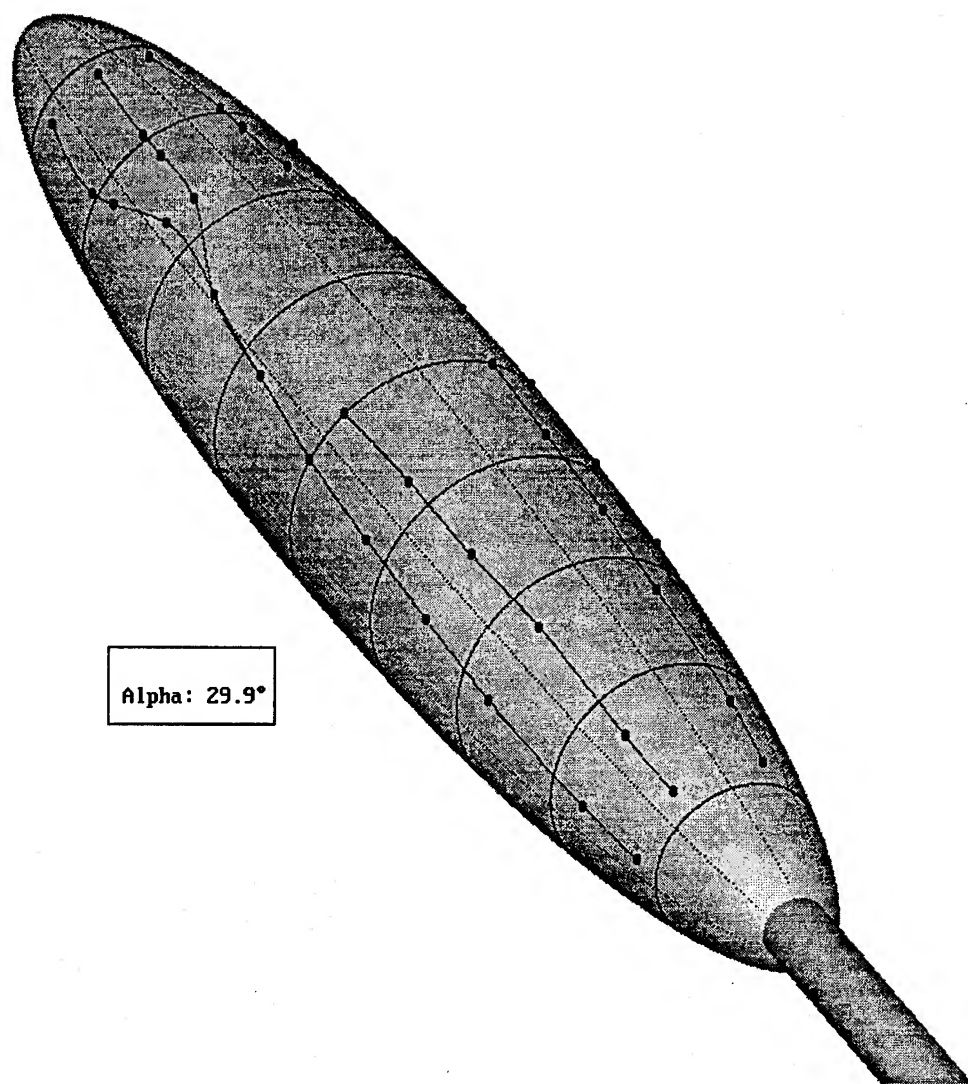


Figure 110. Constant temperature separation line topology for  $\alpha=29.9^\circ$ .

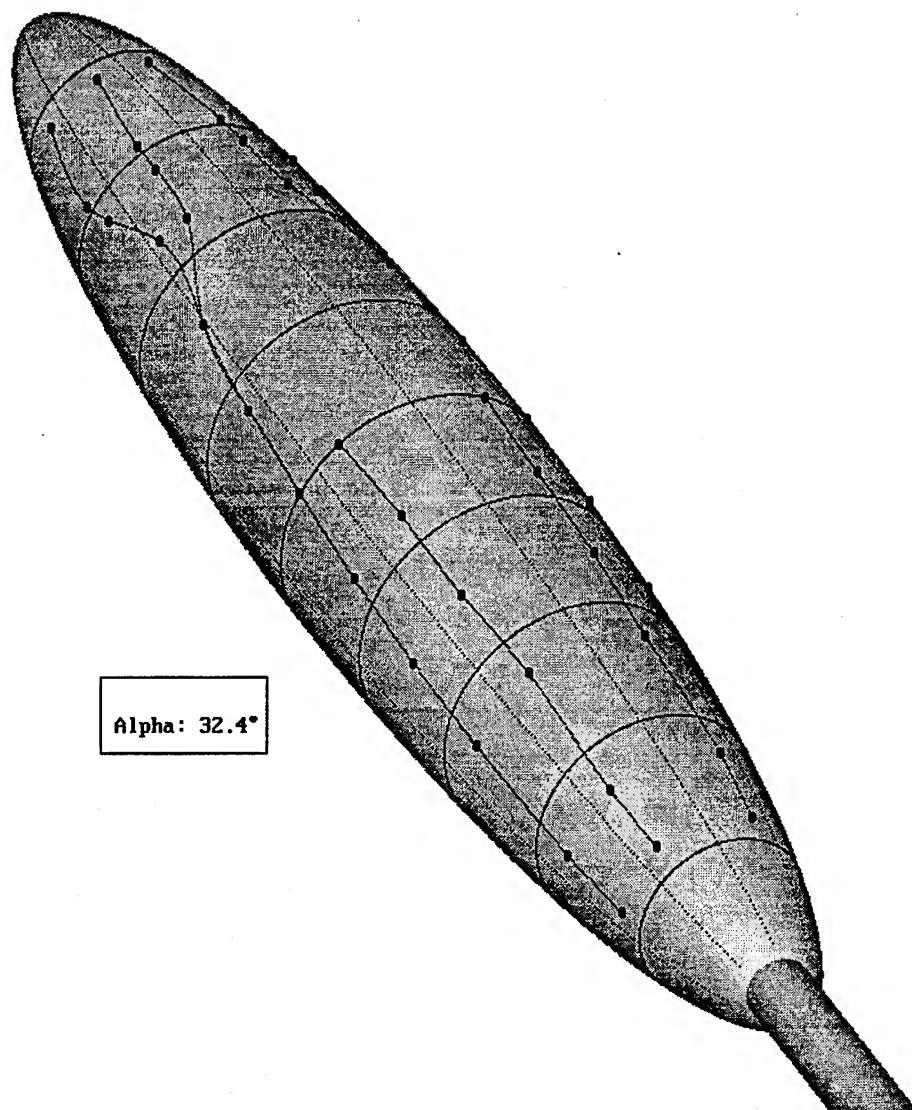


Figure 111. Constant temperature separation line topology for  $\alpha=32.4^\circ$ .

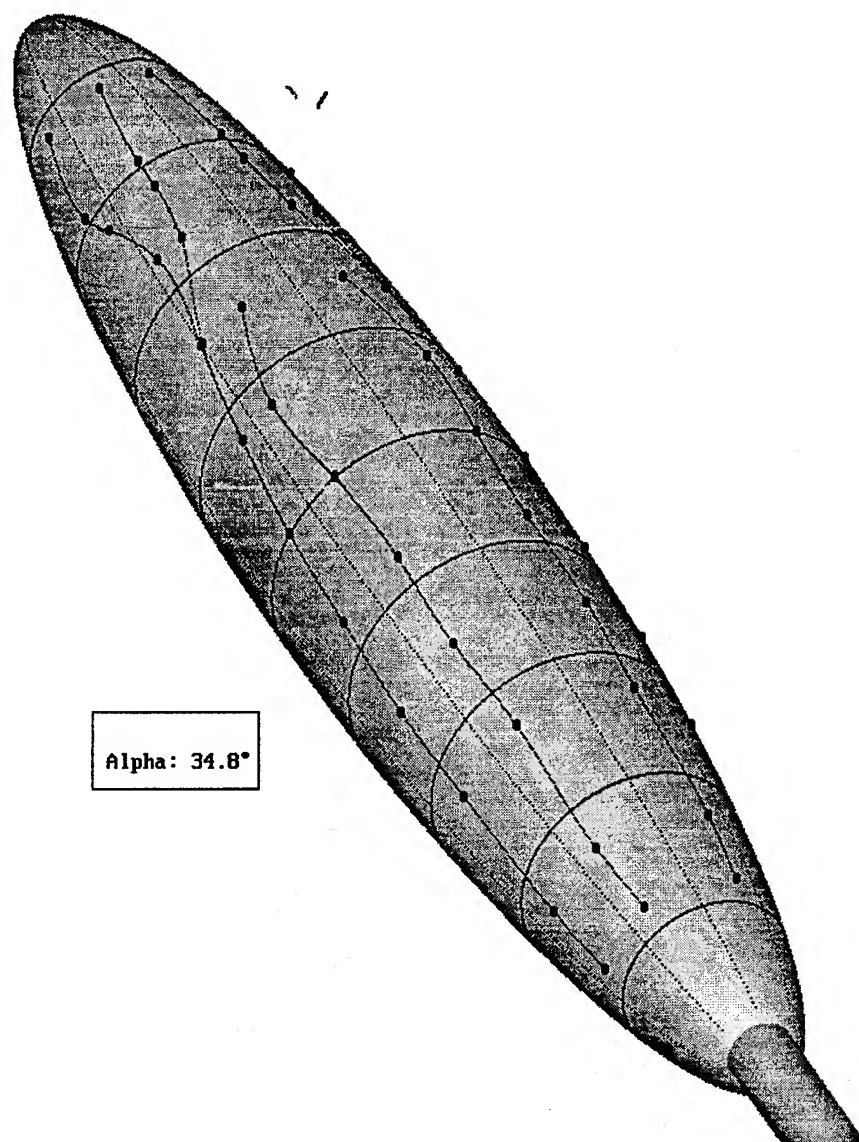


Figure 112. Constant temperature separation line topology for  $\alpha=34.8^\circ$ .

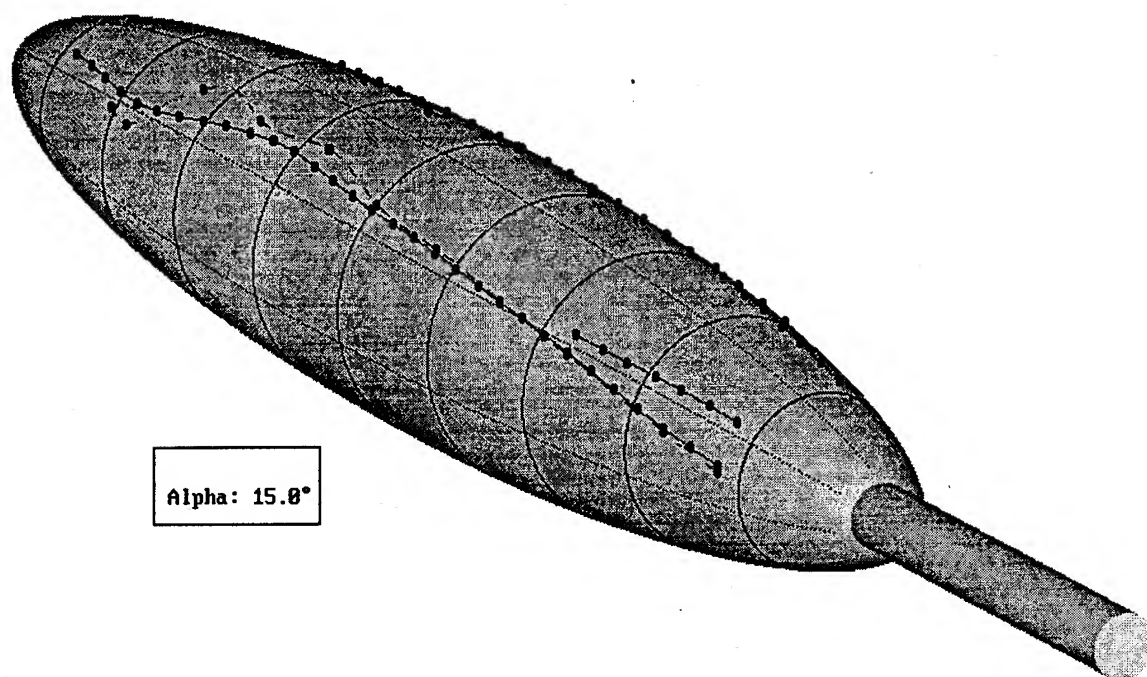


Figure 113. Comparison of constant current and constant temperature separation topology for  $\alpha=15^\circ$ . Solid lines are constant current data. Dashed lines are constant temperature data.

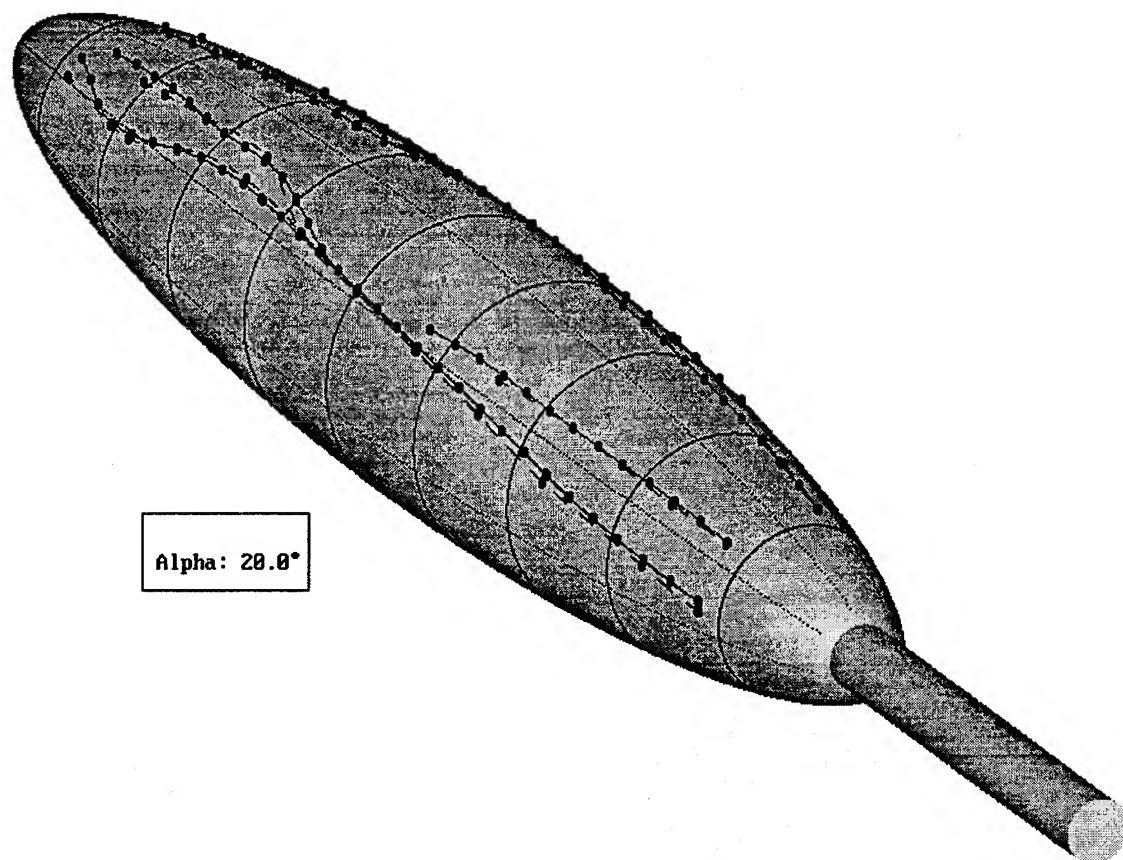


Figure 114. Comparison of constant current and constant temperature separation topology for  $\alpha=20^\circ$ . Solid lines are constant current data. Dashed lines are constant temperature data.

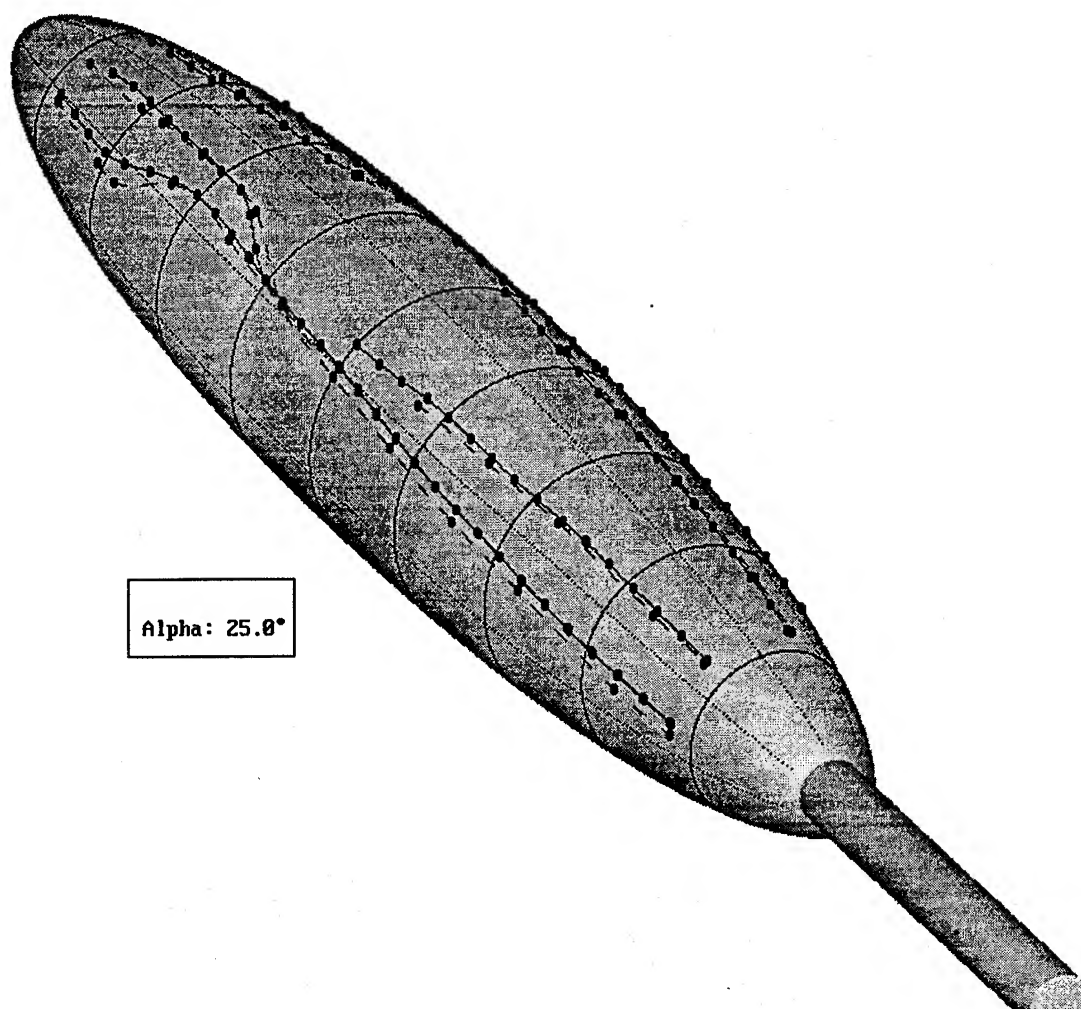


Figure 115. Comparison of constant current and constant temperature separation topology for  $\alpha=25^\circ$ . Solid lines are constant current data. Dashed lines are constant temperature data.



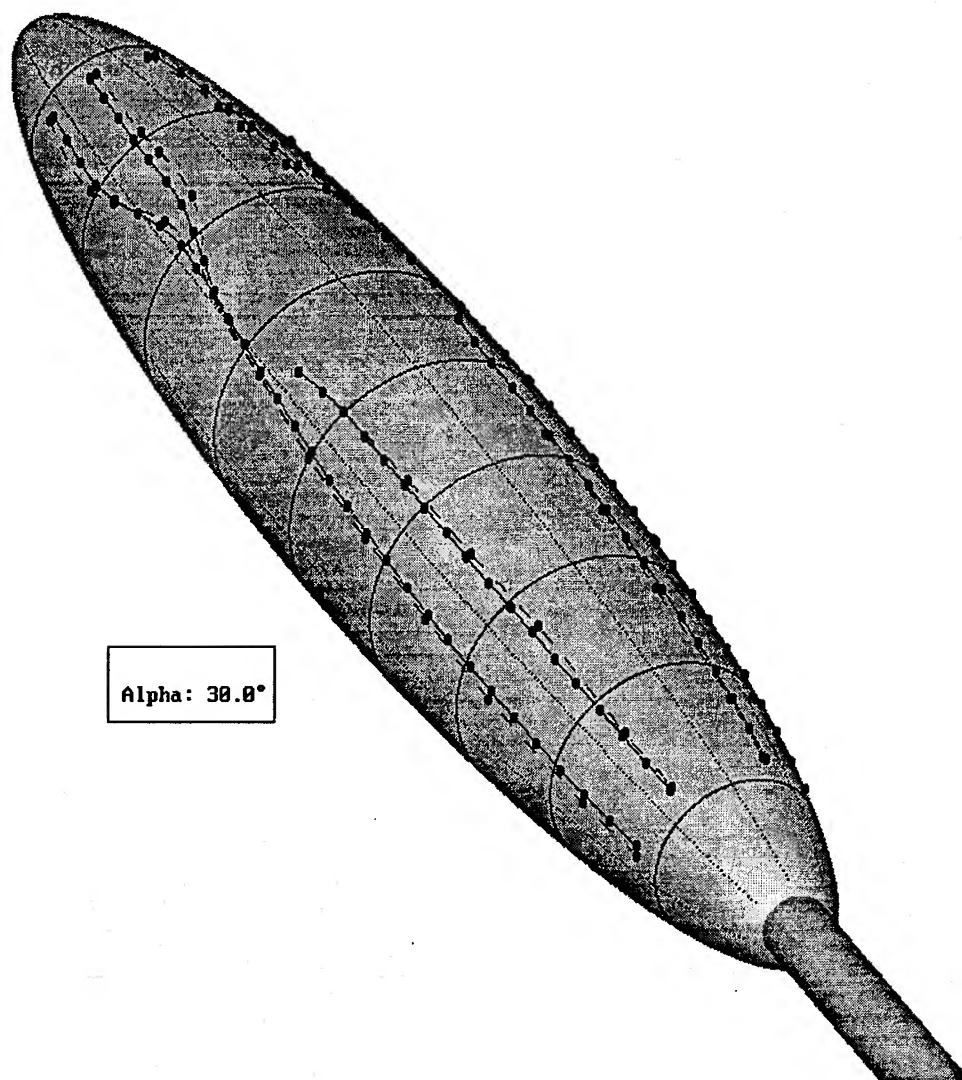


Figure 116. Comparison of constant current and constant temperature separation topology for  $\alpha=30^\circ$ . Solid lines are constant current data. Dashed lines are constant temperature data.

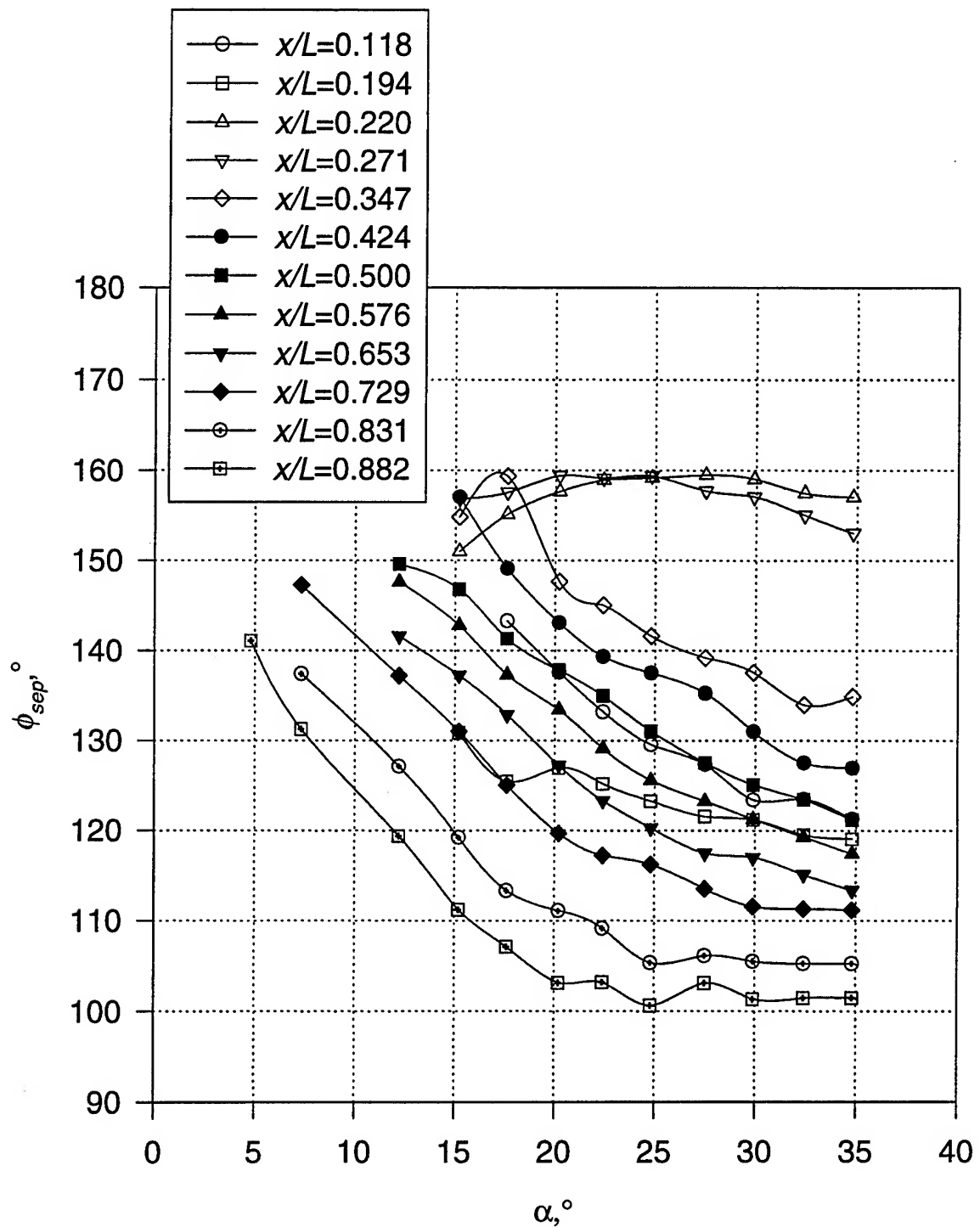


Figure 117. Constant temperature separation locations for various  $x/L$  stations sensors as a function of angle of attack.

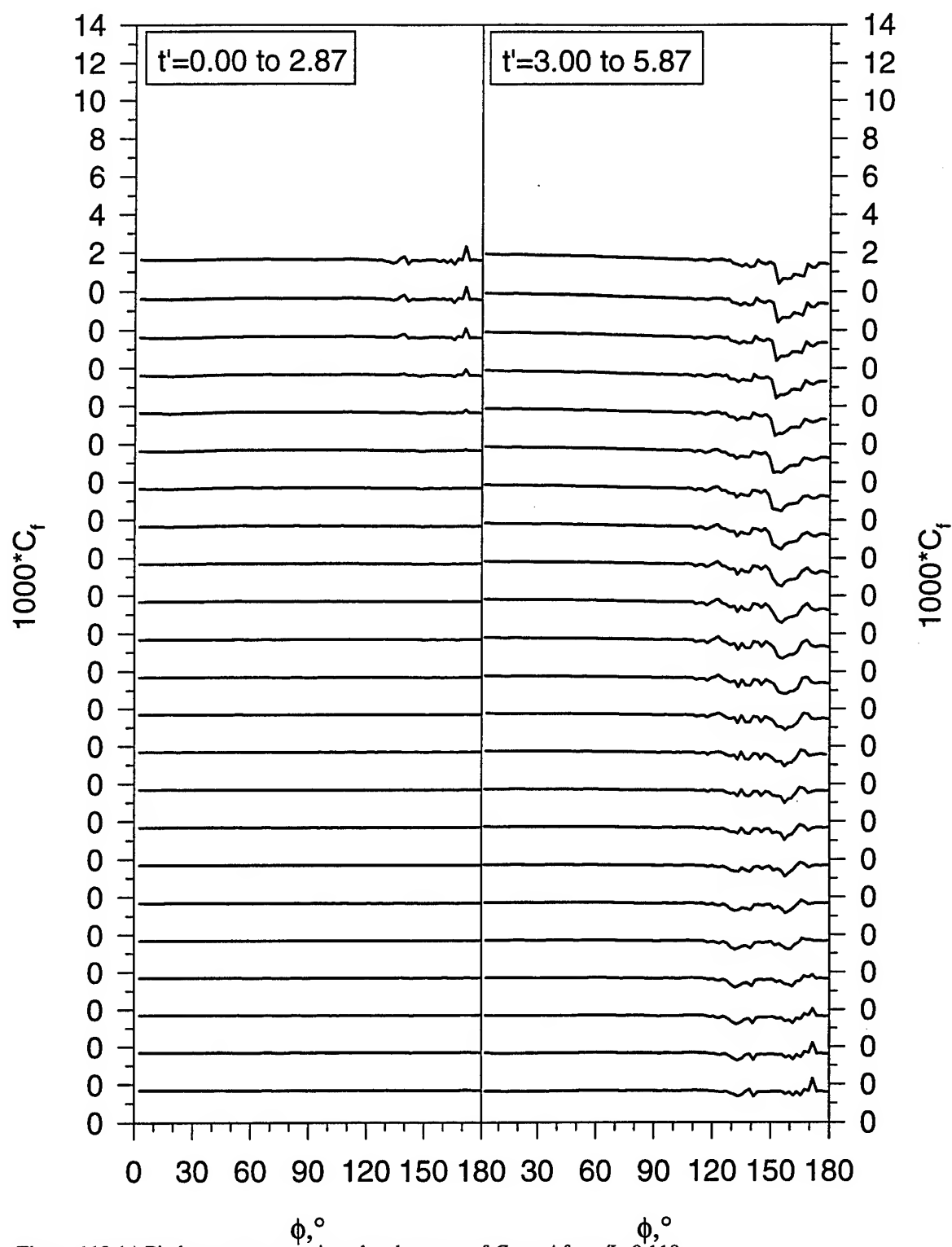


Figure 118.(a) Pitch-up maneuver time development of  $C_f$  vs.  $\phi$  for  $x/L=0.118$ .

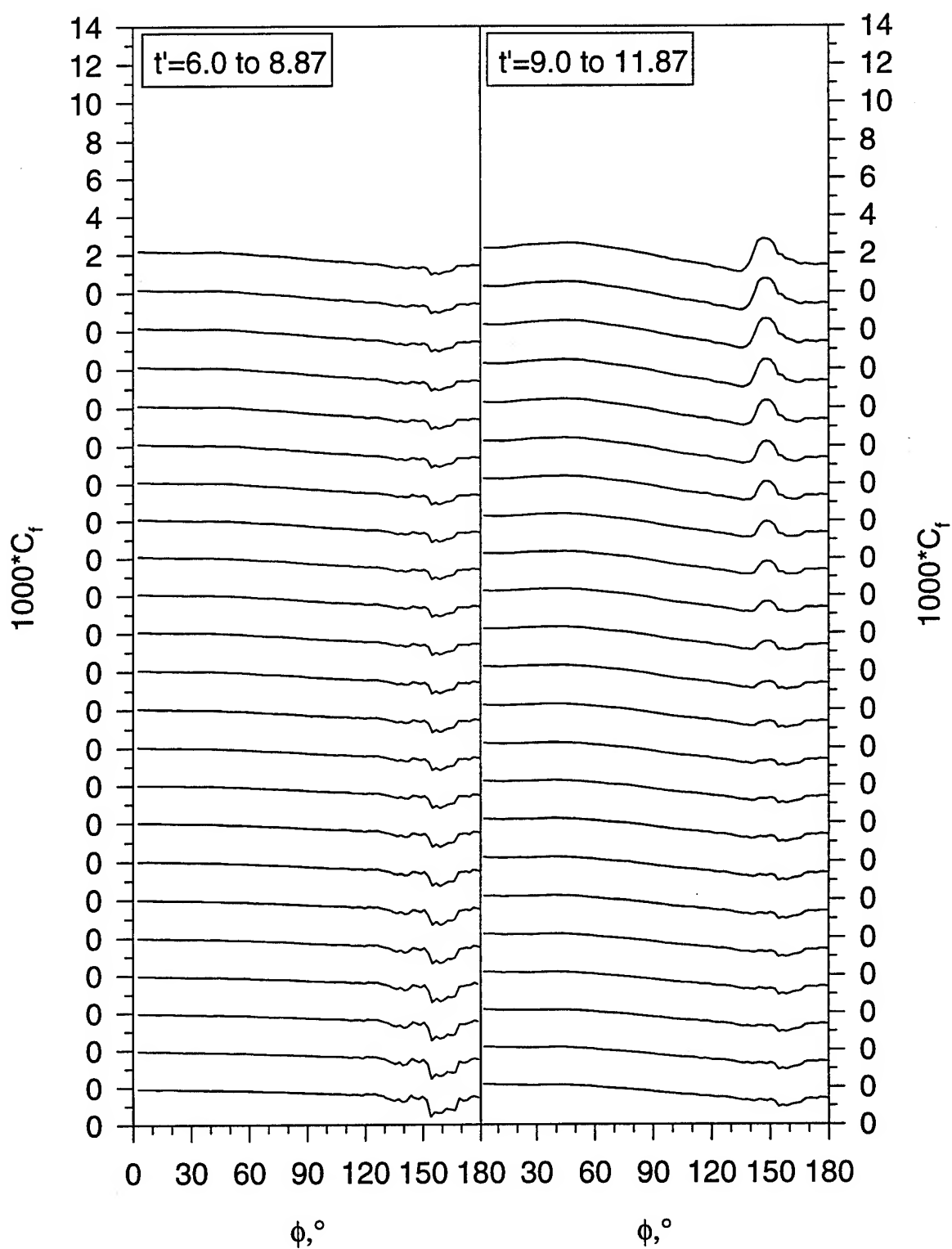


Figure 118. (b) Pitch-up maneuver time development of  $C_f$  vs.  $\phi$  for  $x/L=0.118$ .

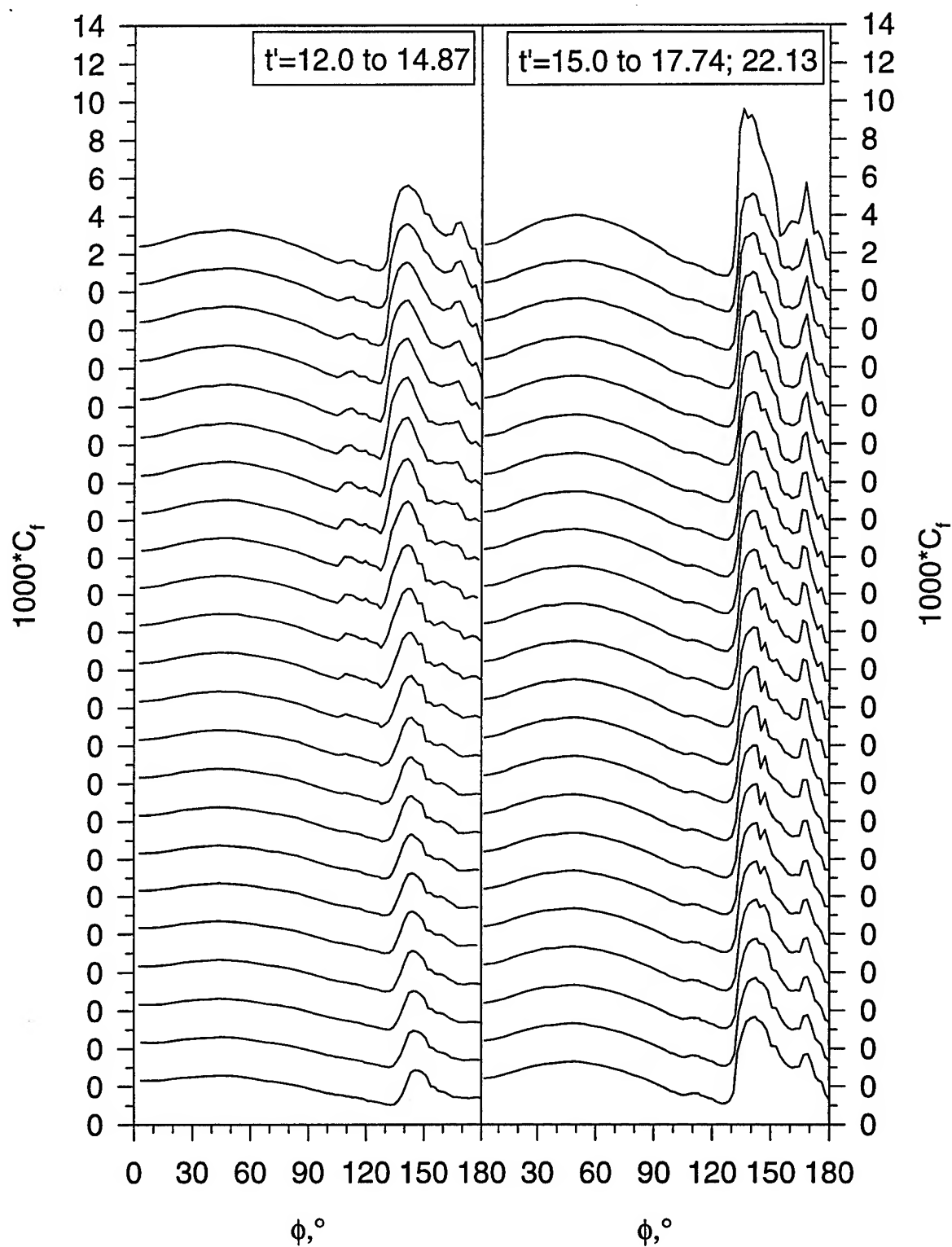


Figure 118. (c) Pitch-up maneuver time development of  $C_f$  vs.  $\phi$  for  $x/L=0.118$ .

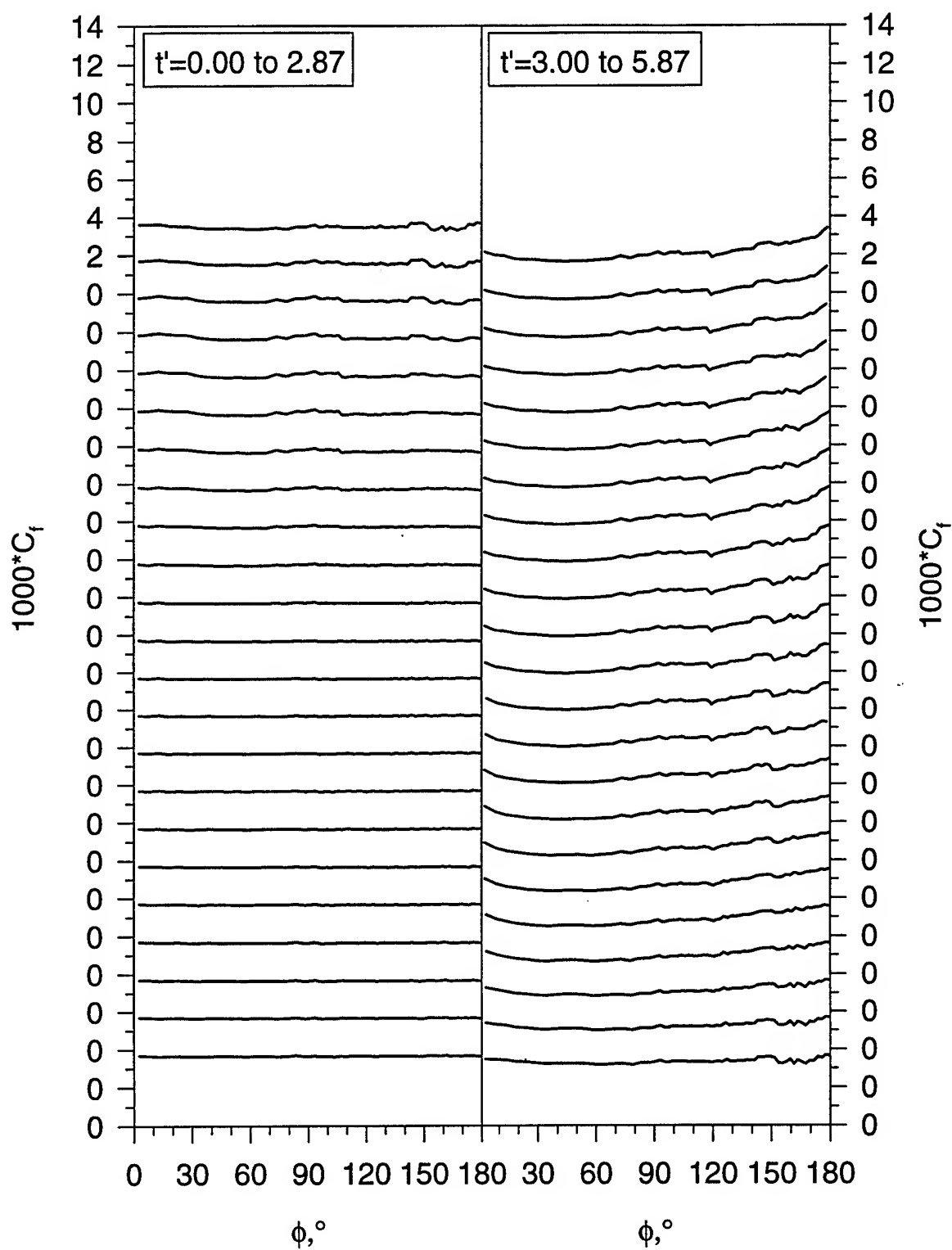


Figure 119.(a) Pitch-up maneuver time development of  $C_f$  vs.  $\phi$  for  $x/L=0.194$ .

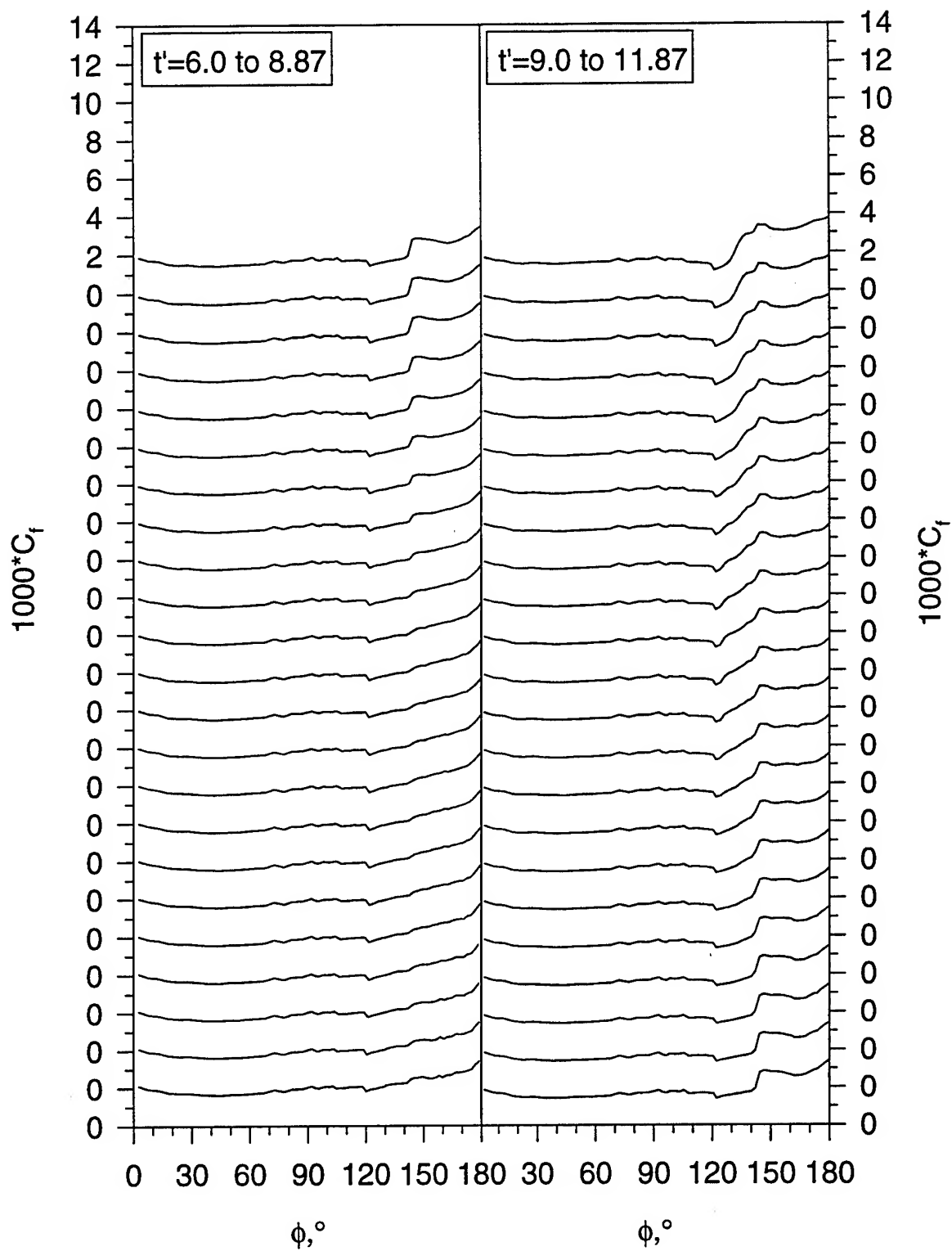


Figure 119. (b) Pitch-up maneuver time development of  $C_f$  vs.  $\phi$  for  $x/L=0.194$ .

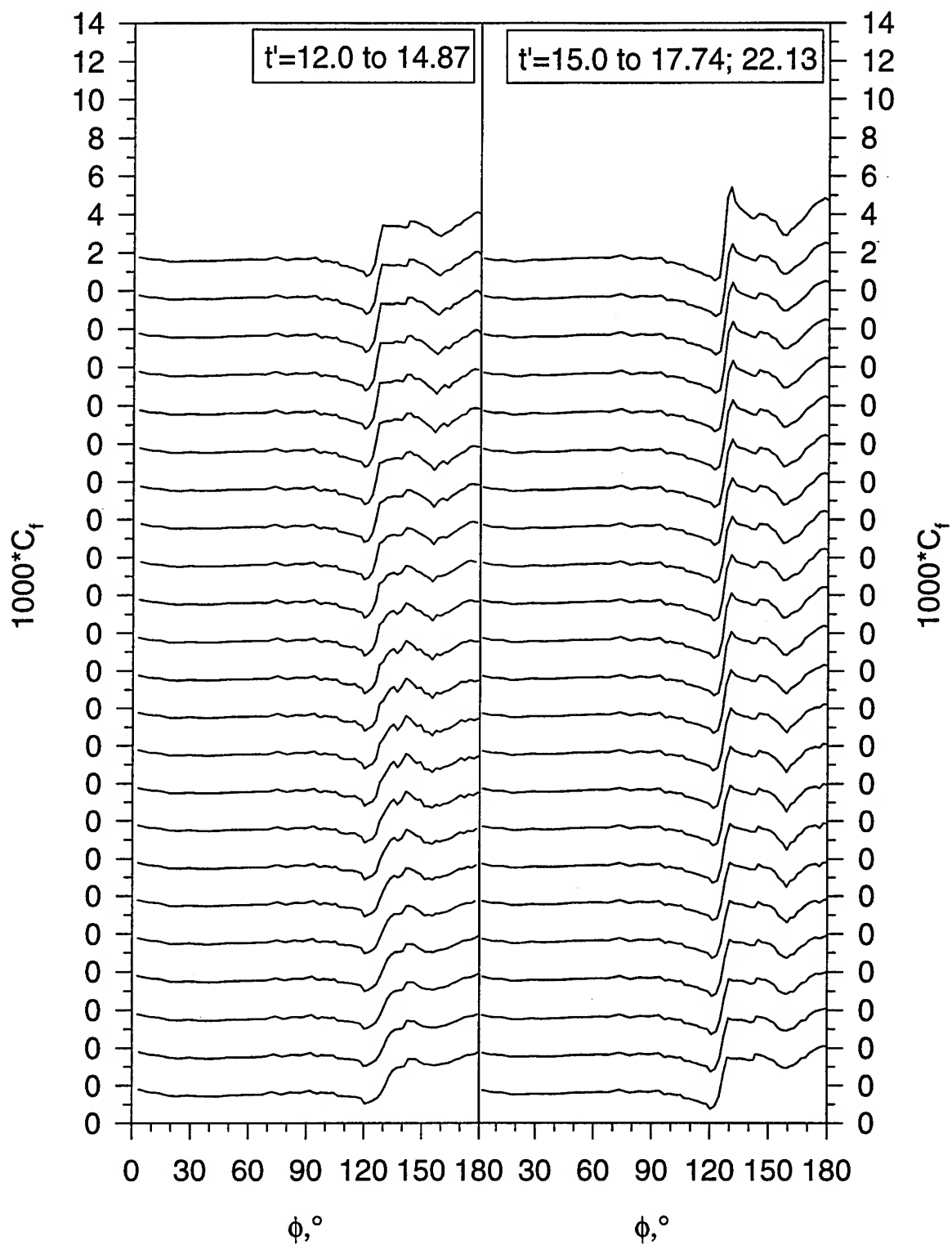


Figure 119. (c) Pitch-up maneuver time development of  $C_f$  vs.  $\phi$  for  $x/L=0.194$ .



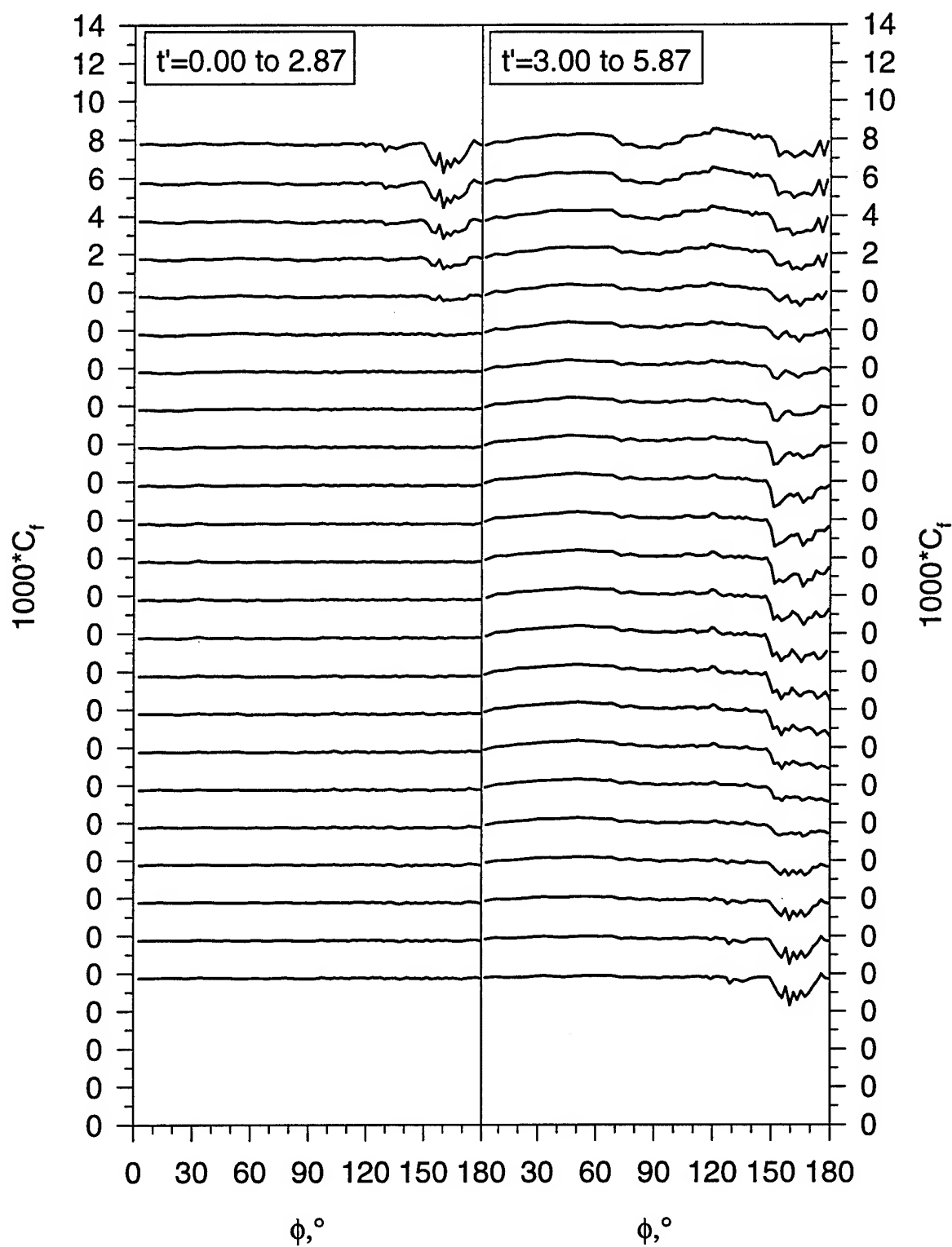


Figure 120.(a) Pitch-up maneuver time development of  $C_f$  vs.  $\phi$  for  $x/L=0.220$ .

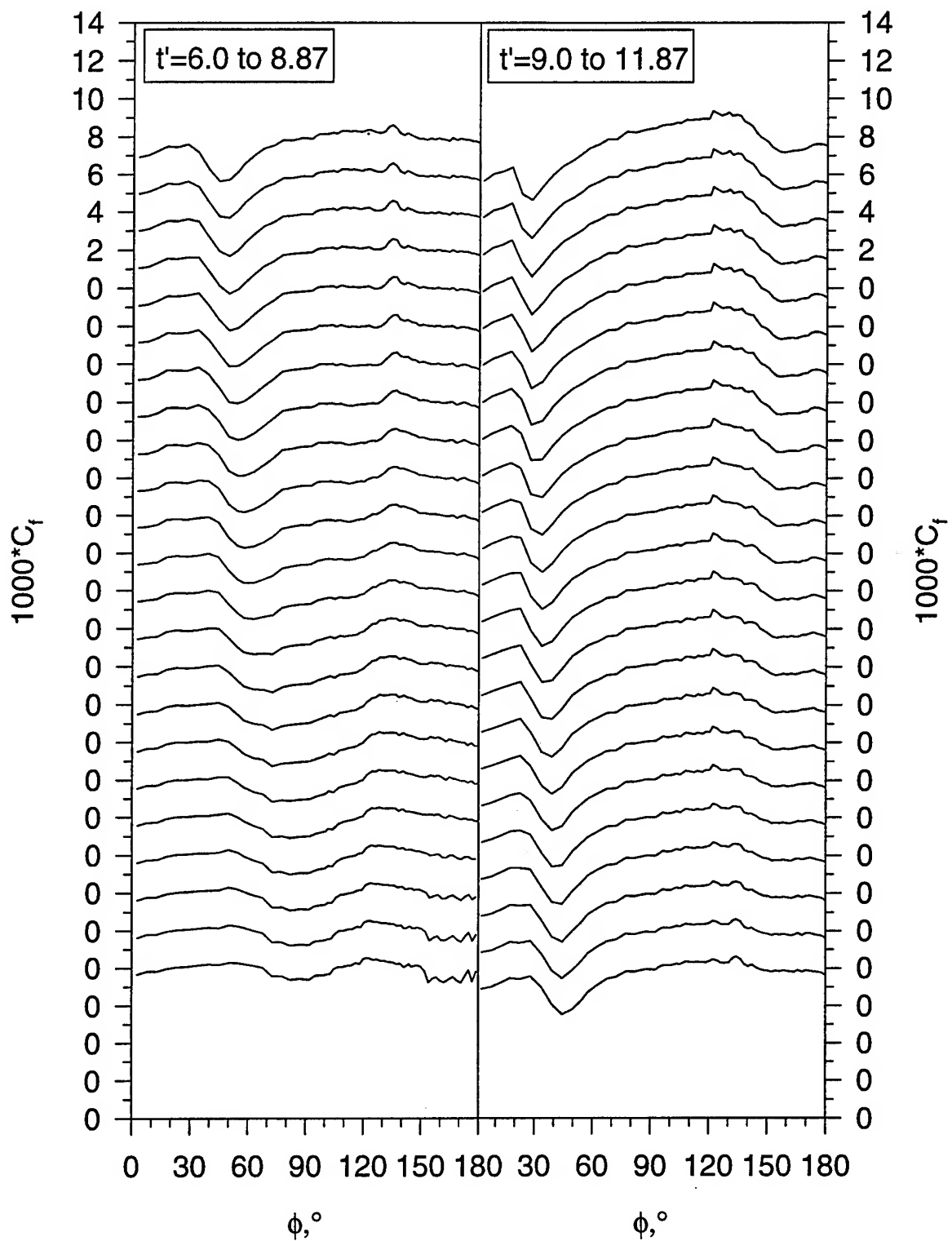


Figure 120. (b) Pitch-up maneuver time development of  $C_f$  vs.  $\phi$  for  $x/L=0.220$ .

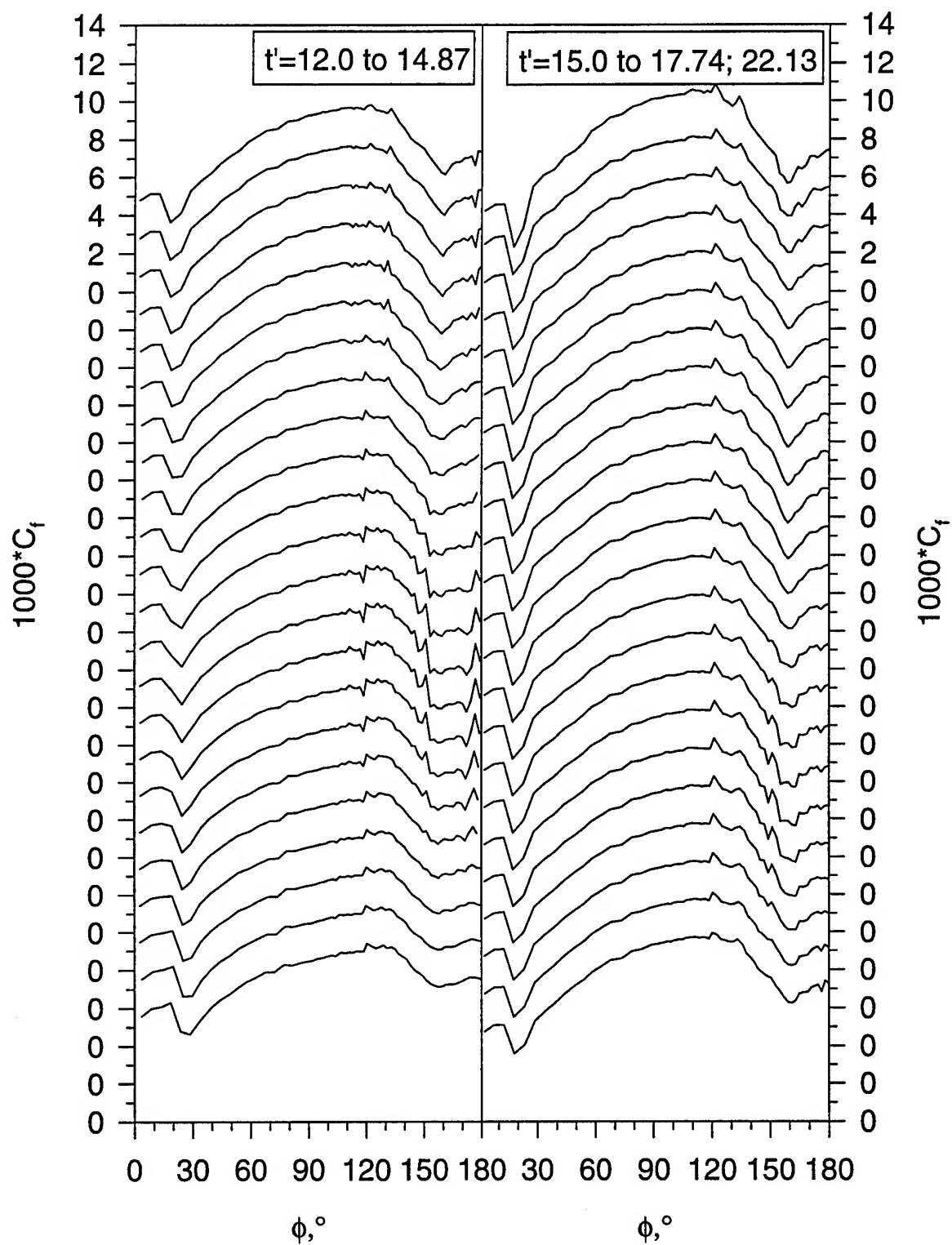


Figure 120. (c) Pitch-up maneuver time development of  $C_f$  vs.  $\phi$  for  $x/L=0.220$ .

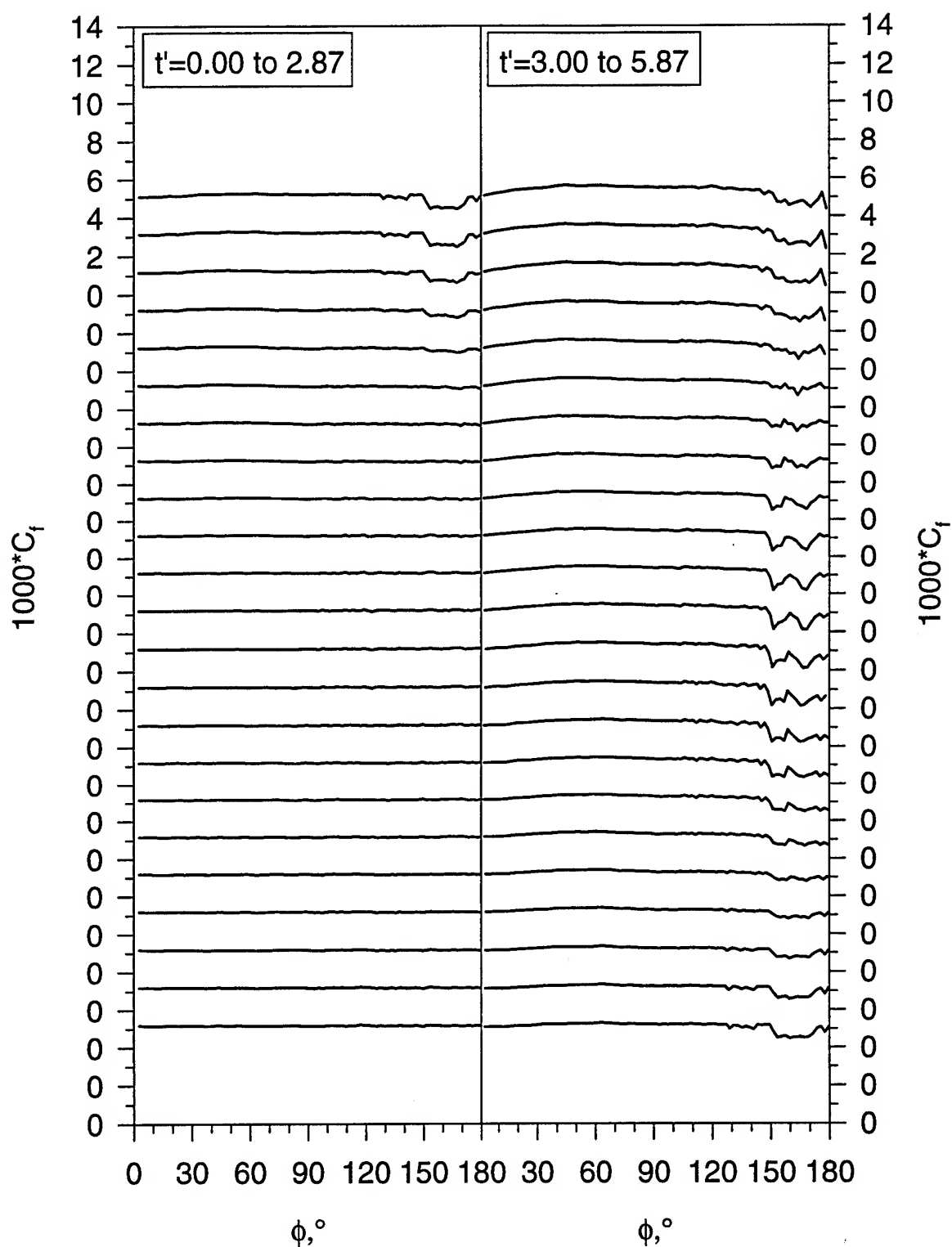


Figure 121.(a) Pitch-up maneuver time development of  $C_f$  vs.  $\phi$  for  $x/L=0.271$ .

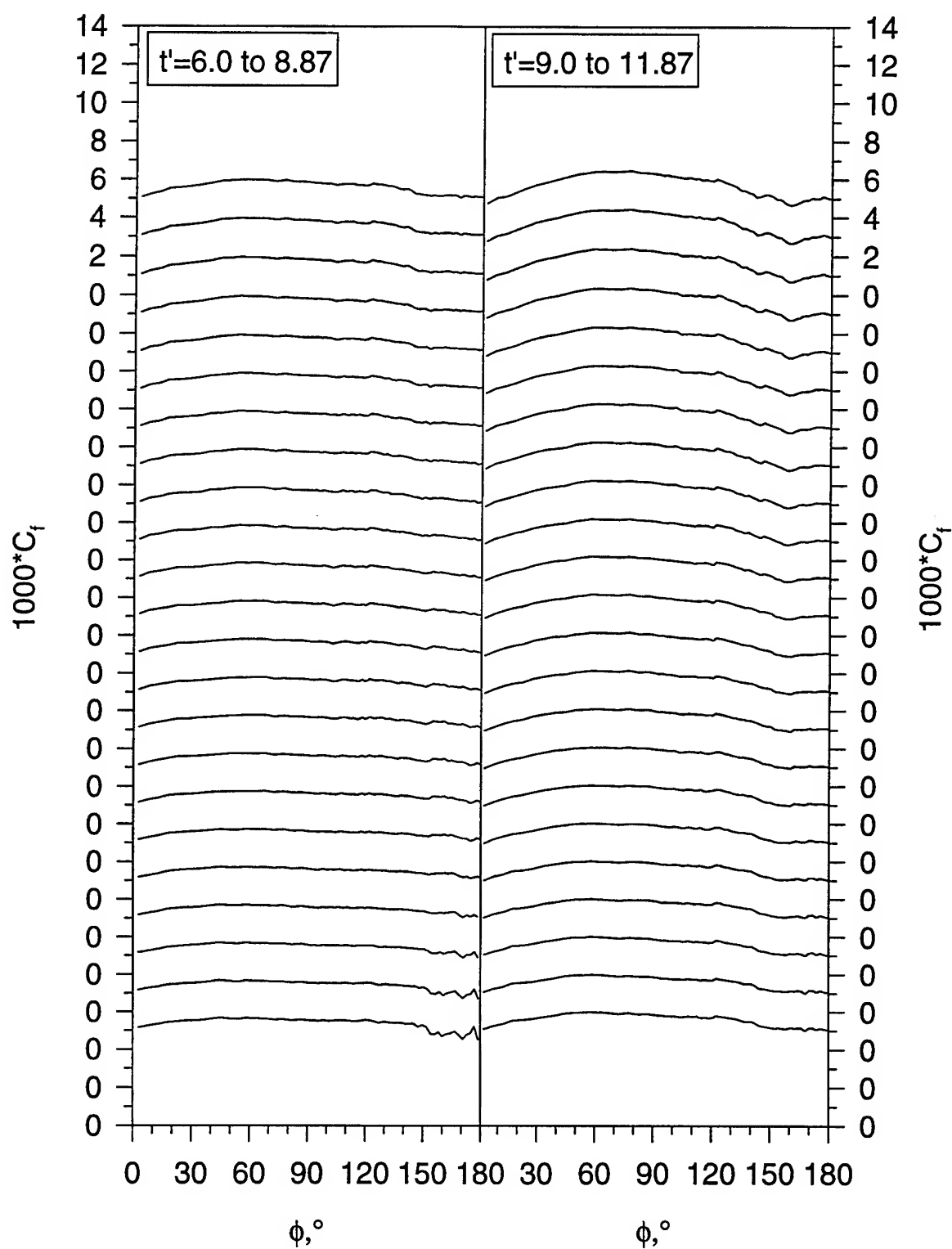


Figure 121. (b) Pitch-up maneuver time development of  $C_f$  vs.  $\phi$  for  $x/L=0.271$ .

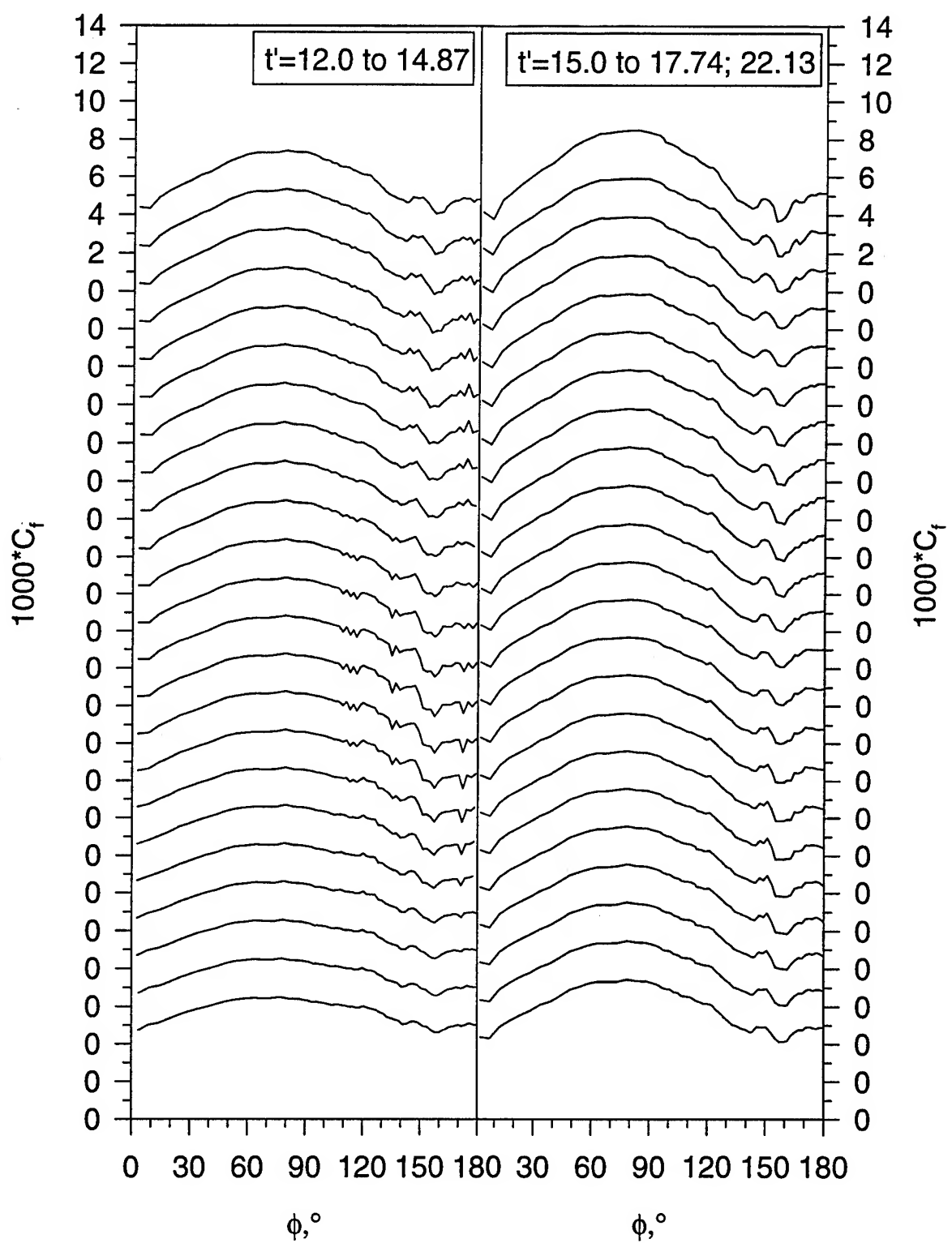


Figure 121. (c) Pitch-up maneuver time development of  $C_f$  vs.  $\phi$  for  $x/L=0.271$ .

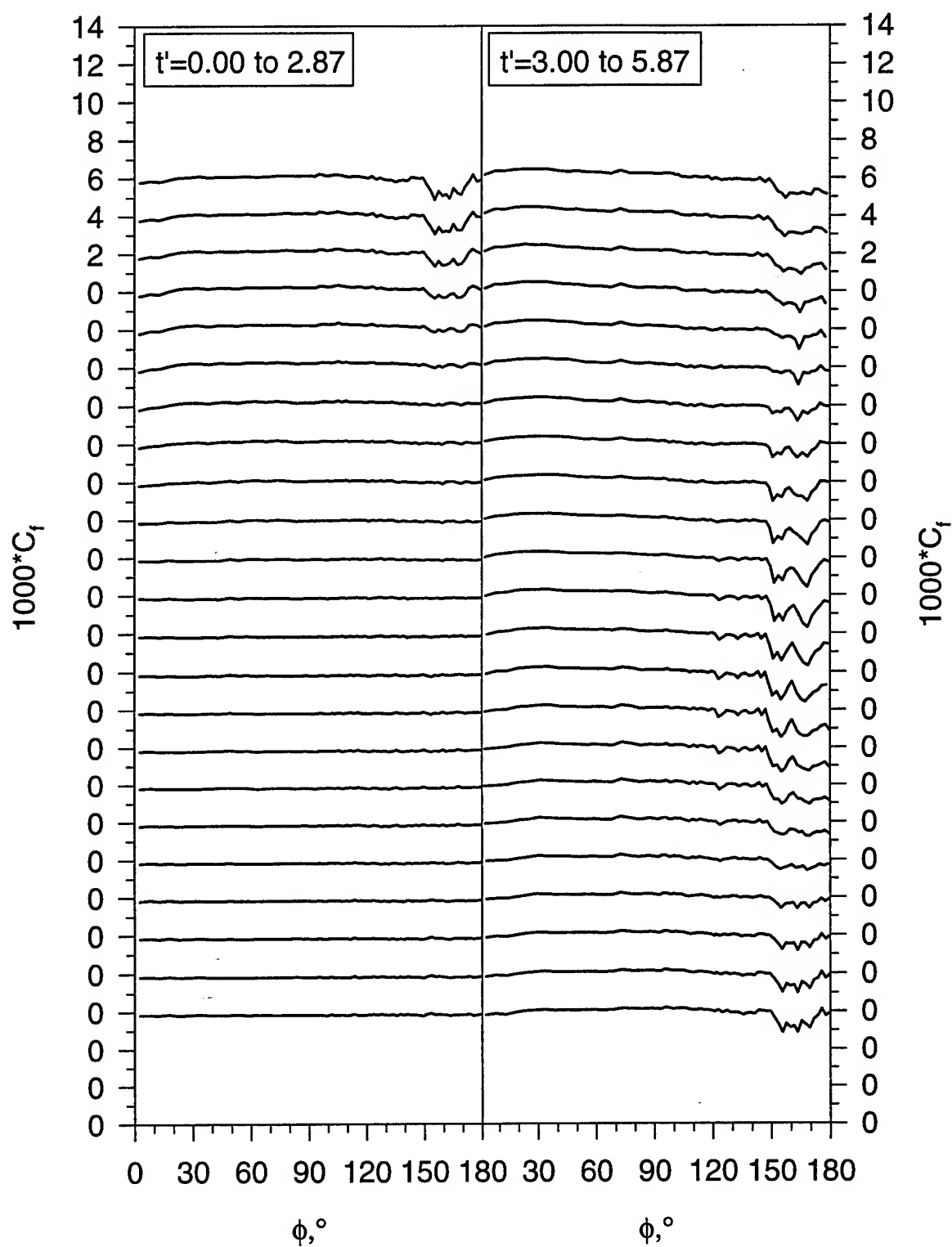


Figure 122.(a) Pitch-up maneuver time development of  $C_f$  vs.  $\phi$  for  $x/L=0.347$ .

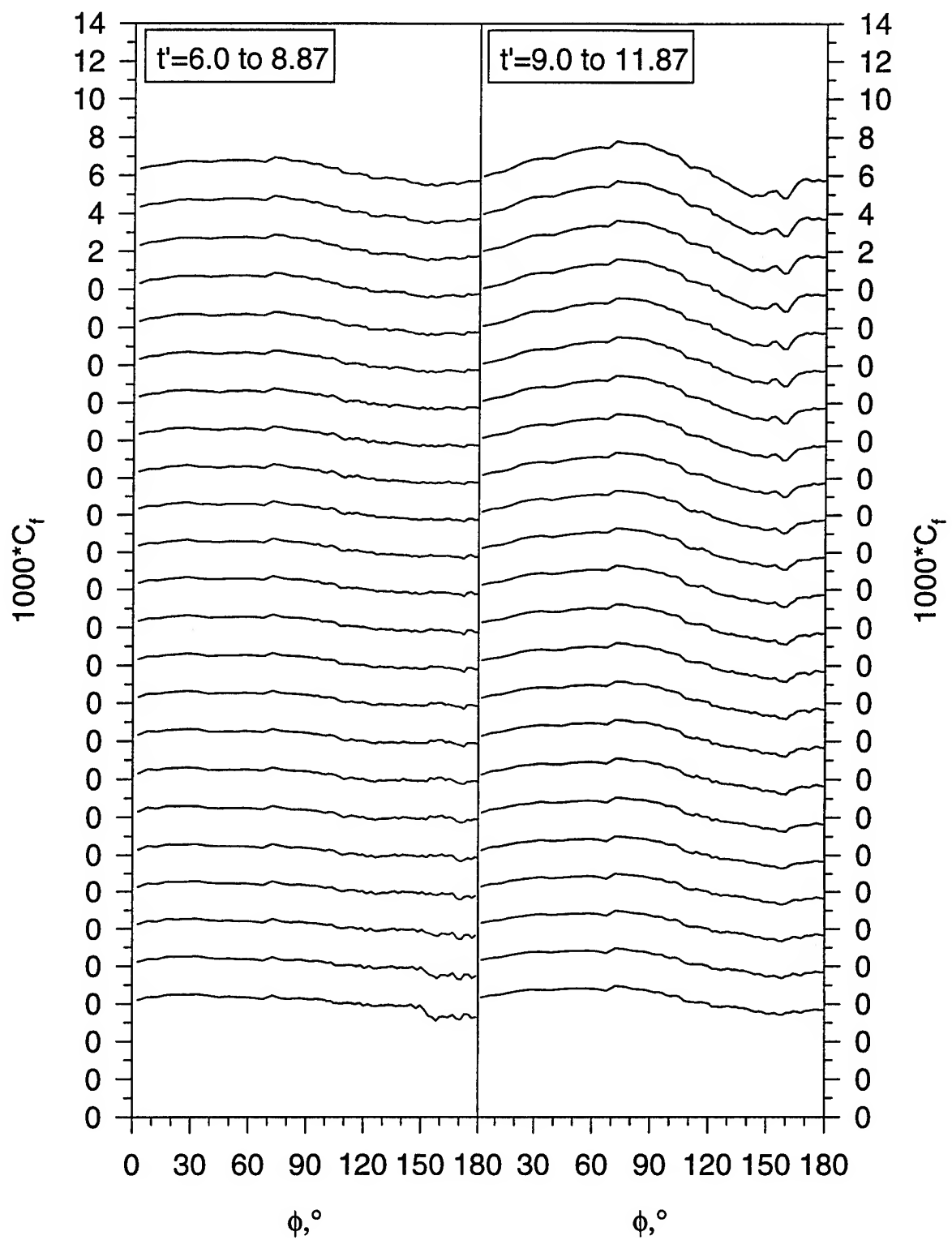


Figure 122. (b) Pitch-up maneuver time development of  $C_f$  vs.  $\phi$  for  $x/L=0.347$ .



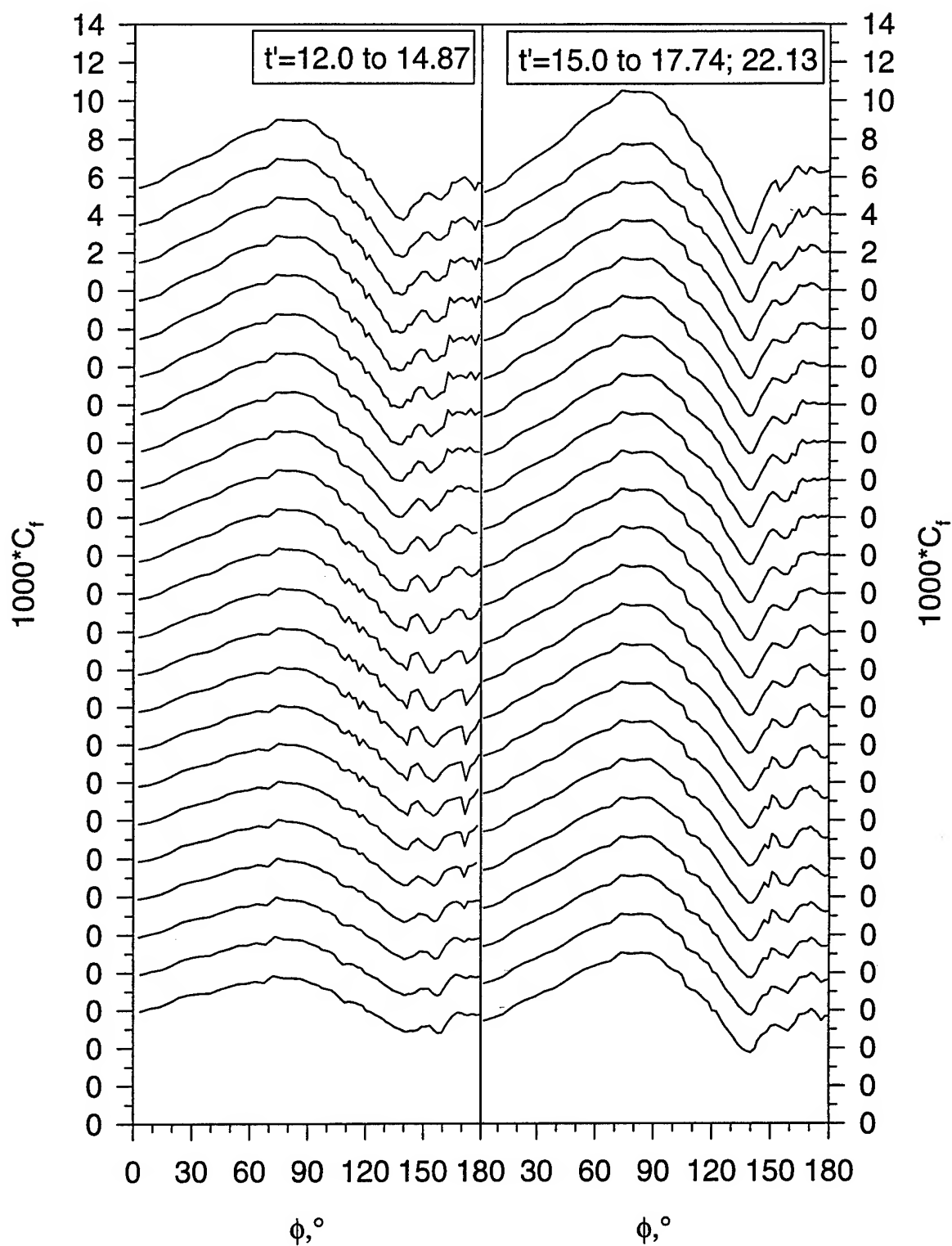


Figure 122. (c) Pitch-up maneuver time development of  $C_f$  vs.  $\phi$  for  $x/L=0.347$ .

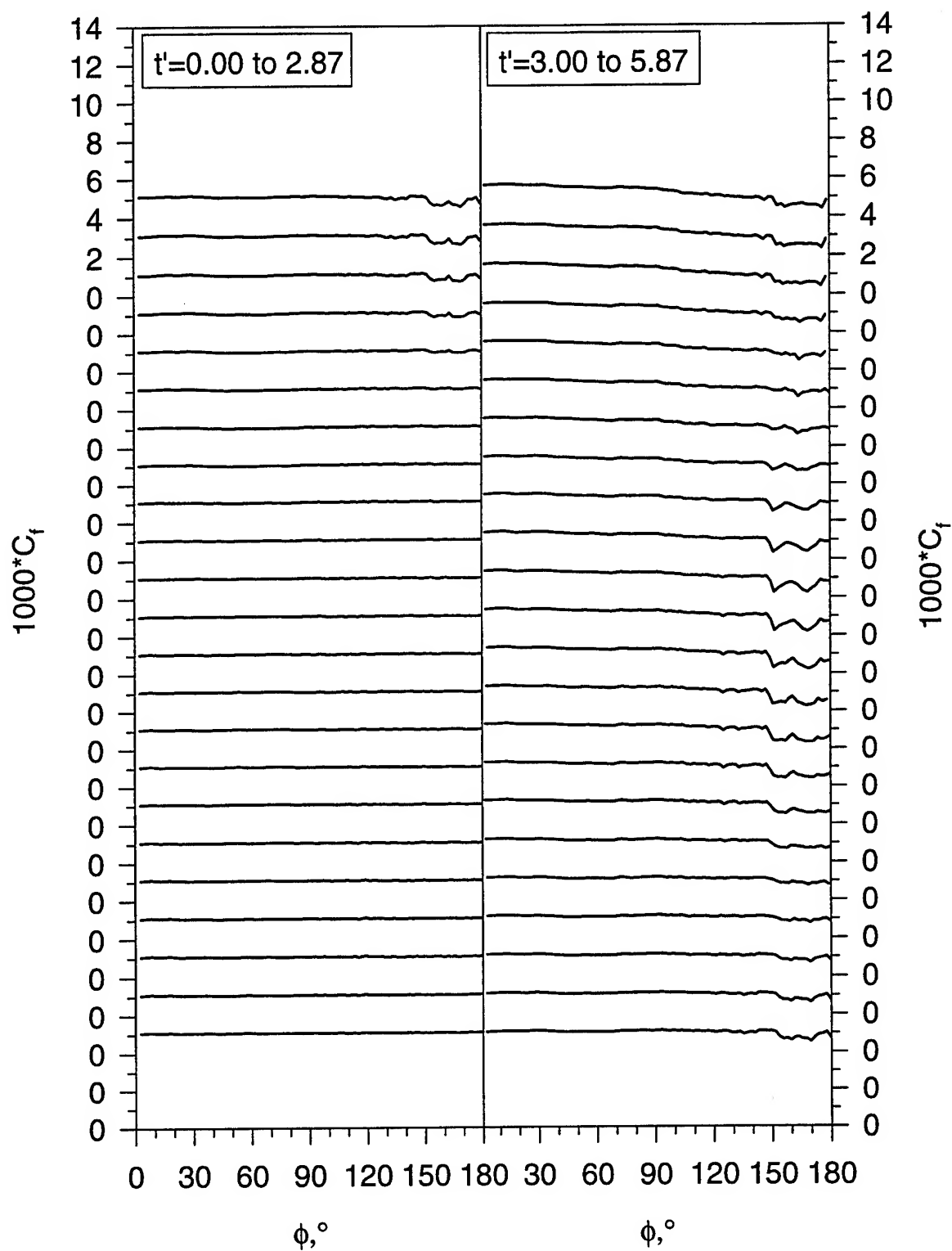


Figure 123.(a) Pitch-up maneuver time development of  $C_f$  vs.  $\phi$  for  $x/L=0.424$ .

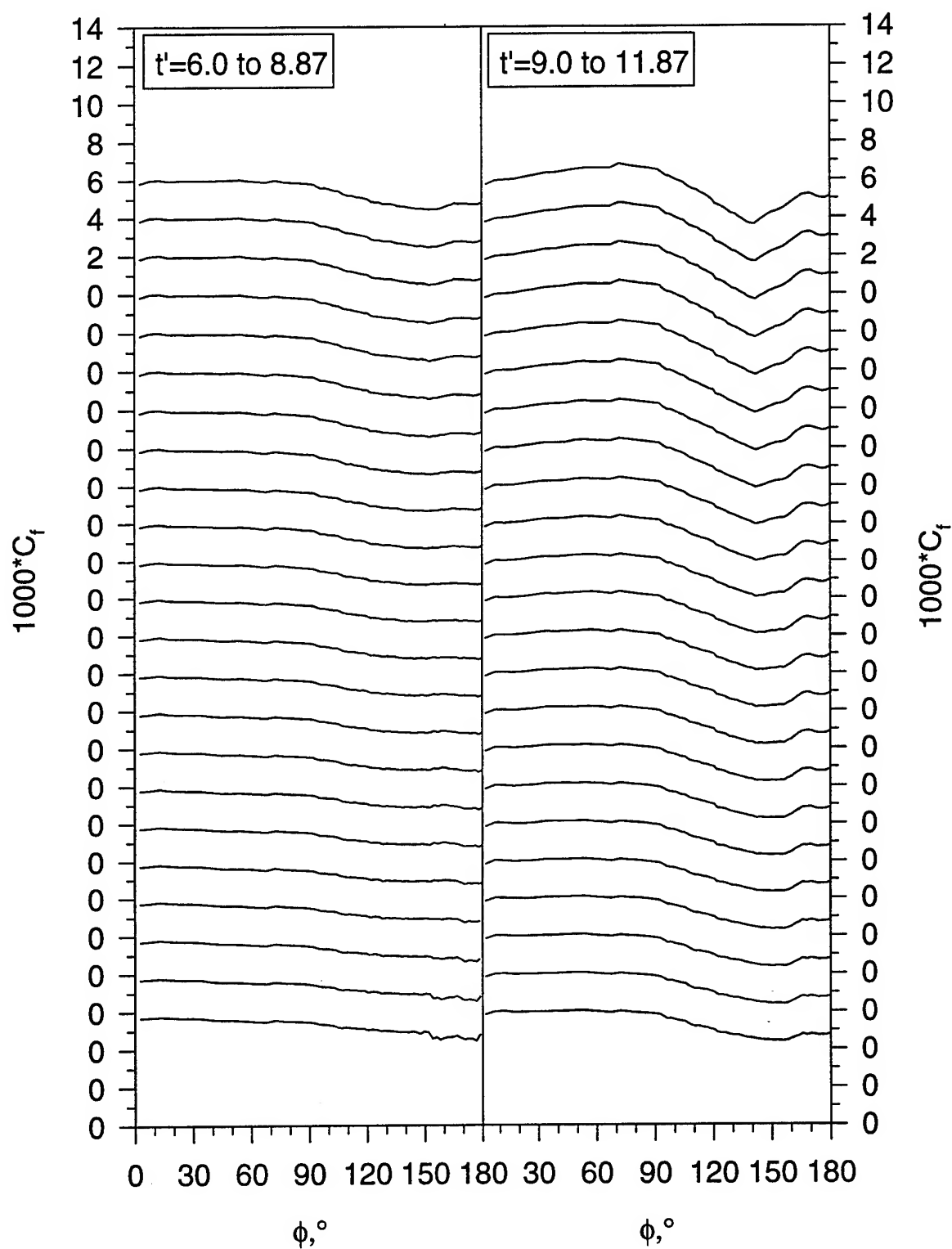


Figure 123. (b) Pitch-up maneuver time development of  $C_f$  vs.  $\phi$  for  $x/L=0.424$ .

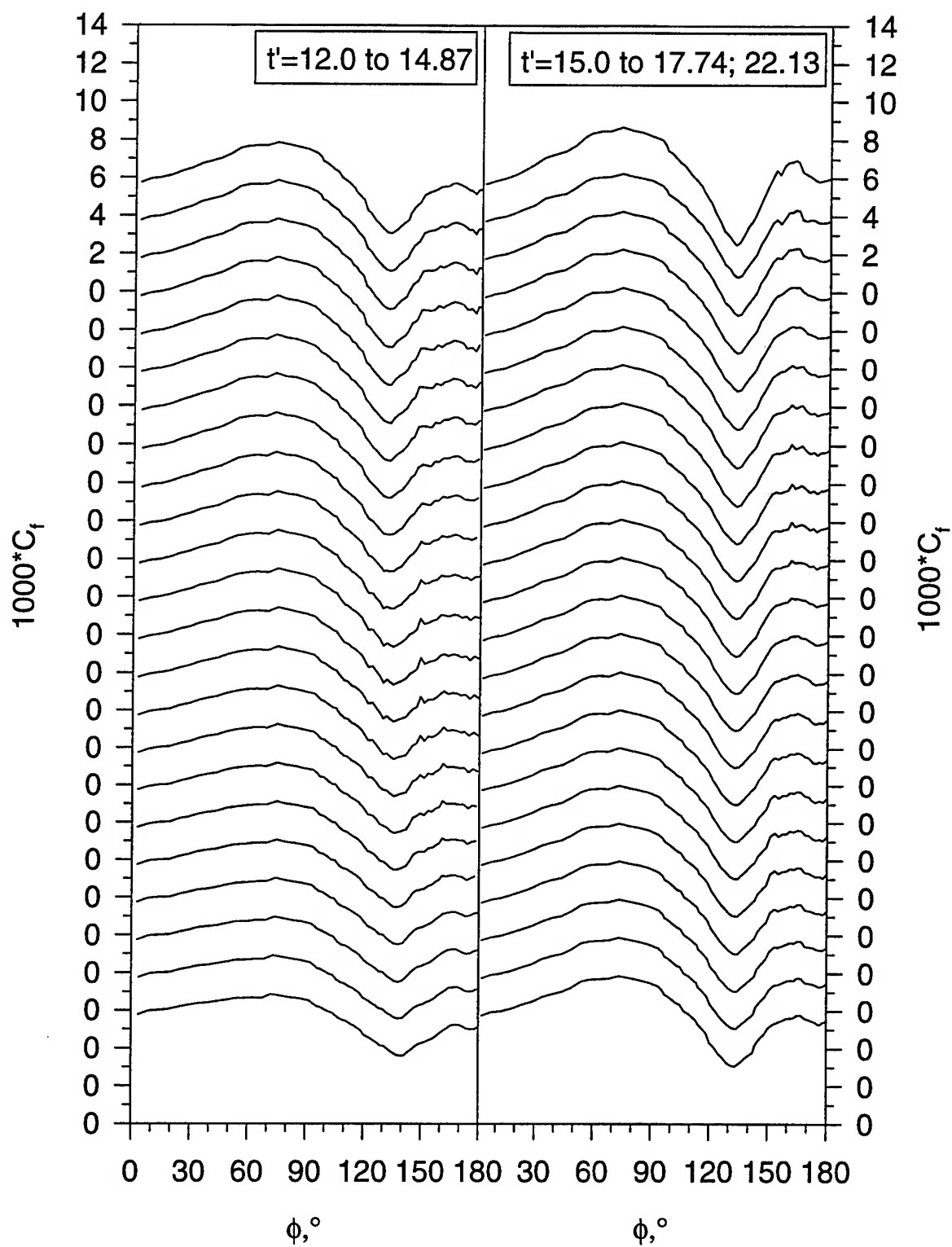


Figure 123. (c) Pitch-up maneuver time development of  $C_f$  vs.  $\phi$  for  $x/L=0.424$ .

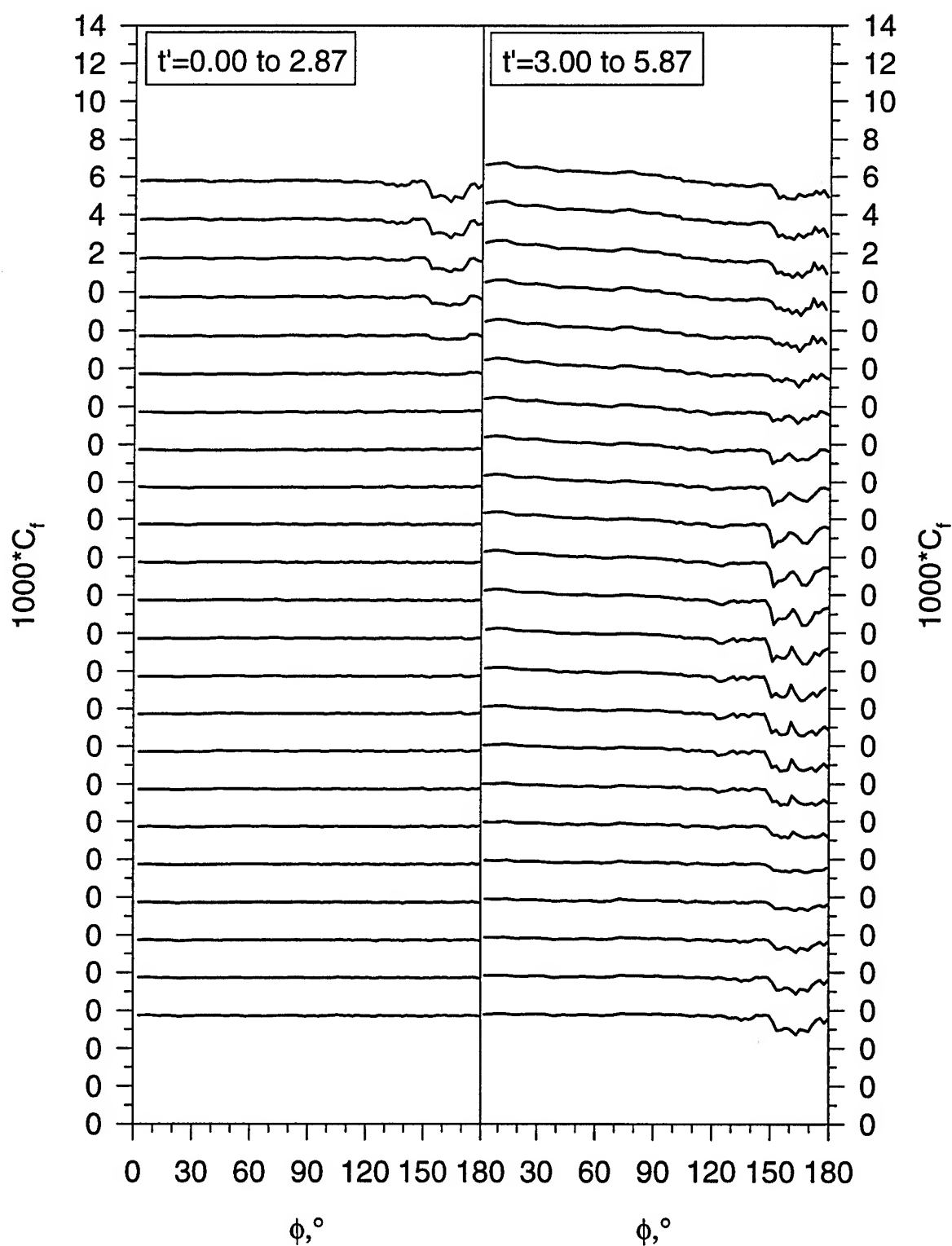


Figure 124.(a) Pitch-up maneuver time development of  $C_l$  vs.  $\phi$  for  $x/L=0.500$ .

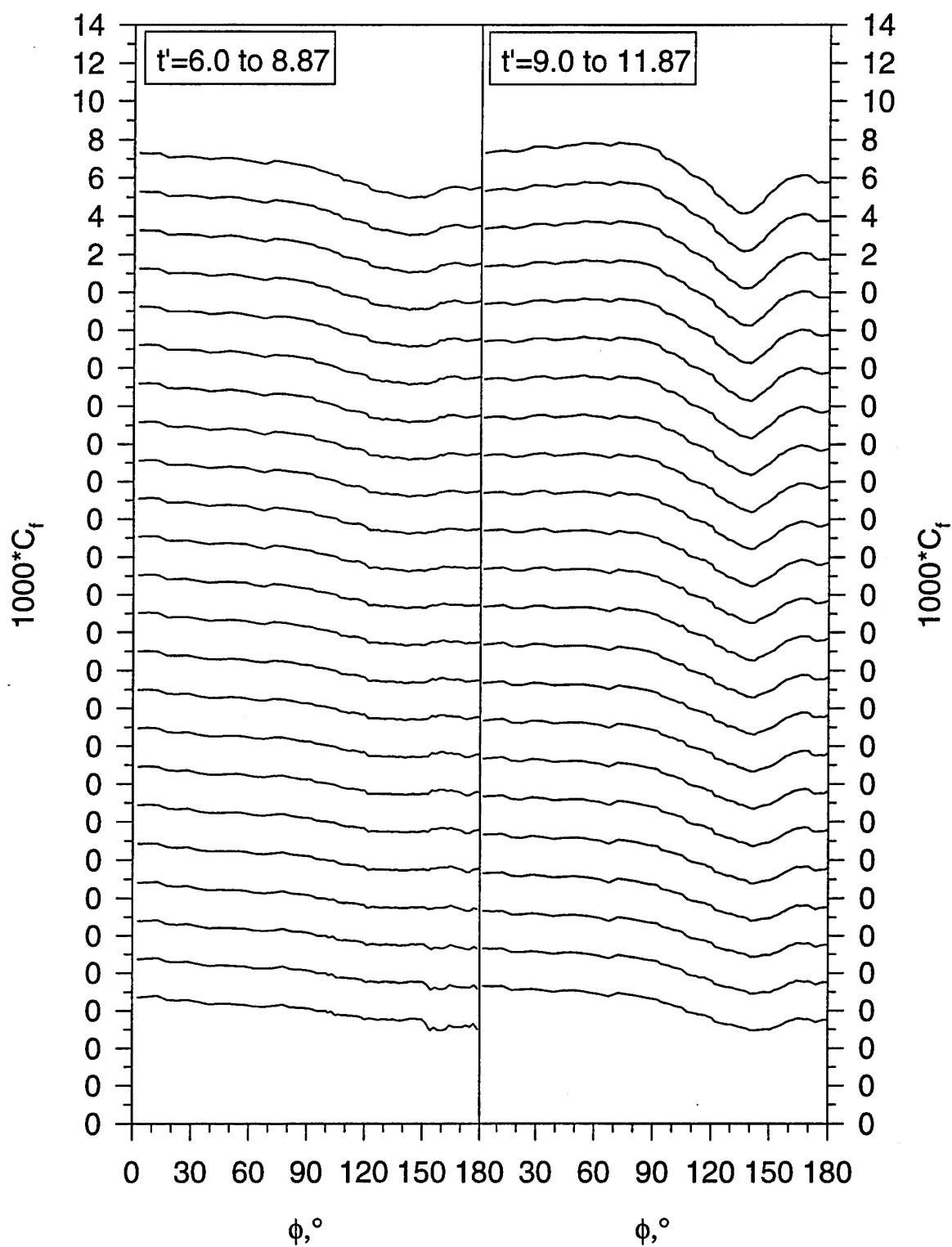


Figure 124. (b) Pitch-up maneuver time development of  $C_f$  vs.  $\phi$  for  $x/L=0.500$ .

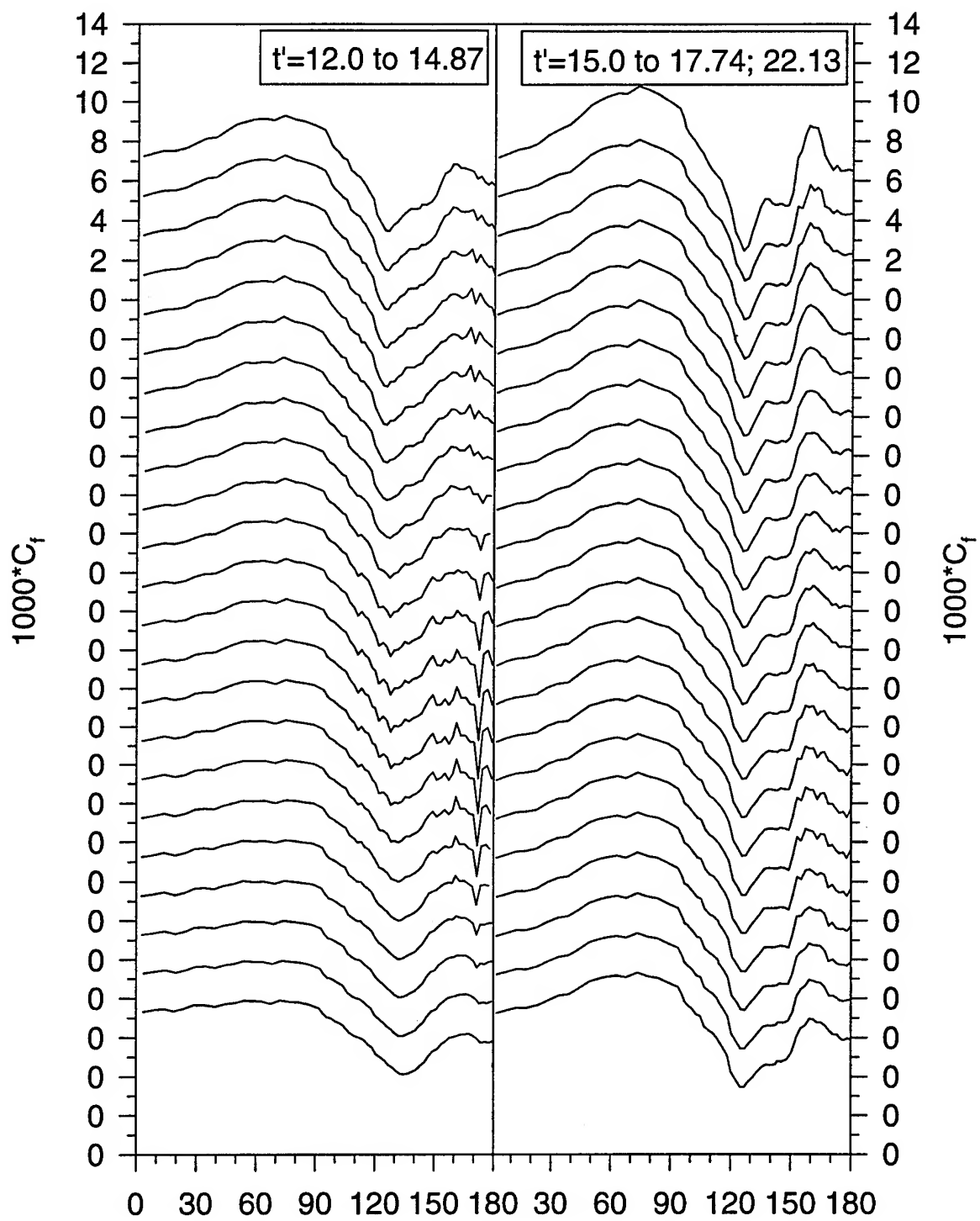


Figure 124. (c) Pitch-up maneuver time development of  $C_f$  vs.  $\phi$  for  $x/L=0.500$ .

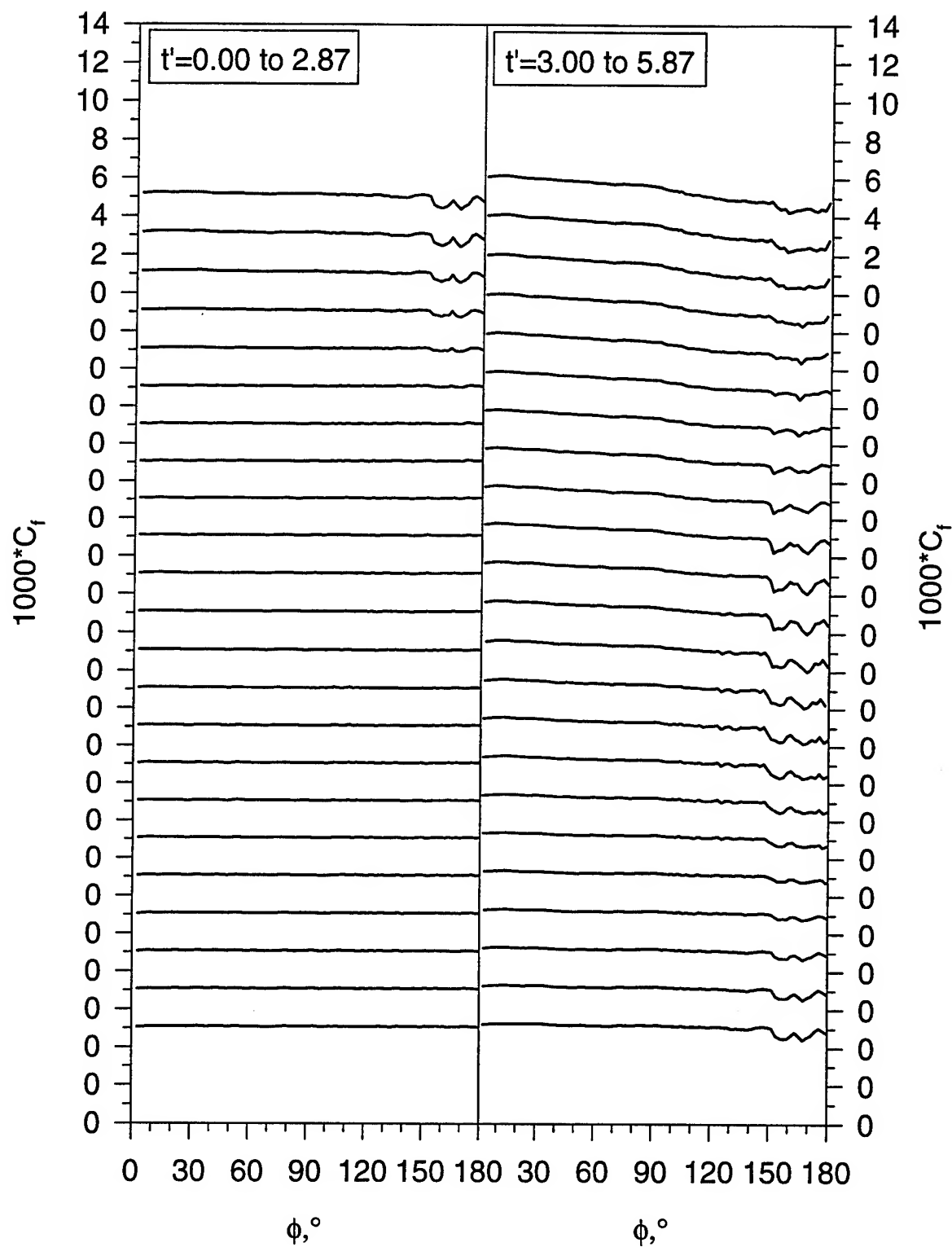


Figure 125.(a) Pitch-up maneuver time development of  $C_f$  vs.  $\phi$  for  $x/L=0.576$ .



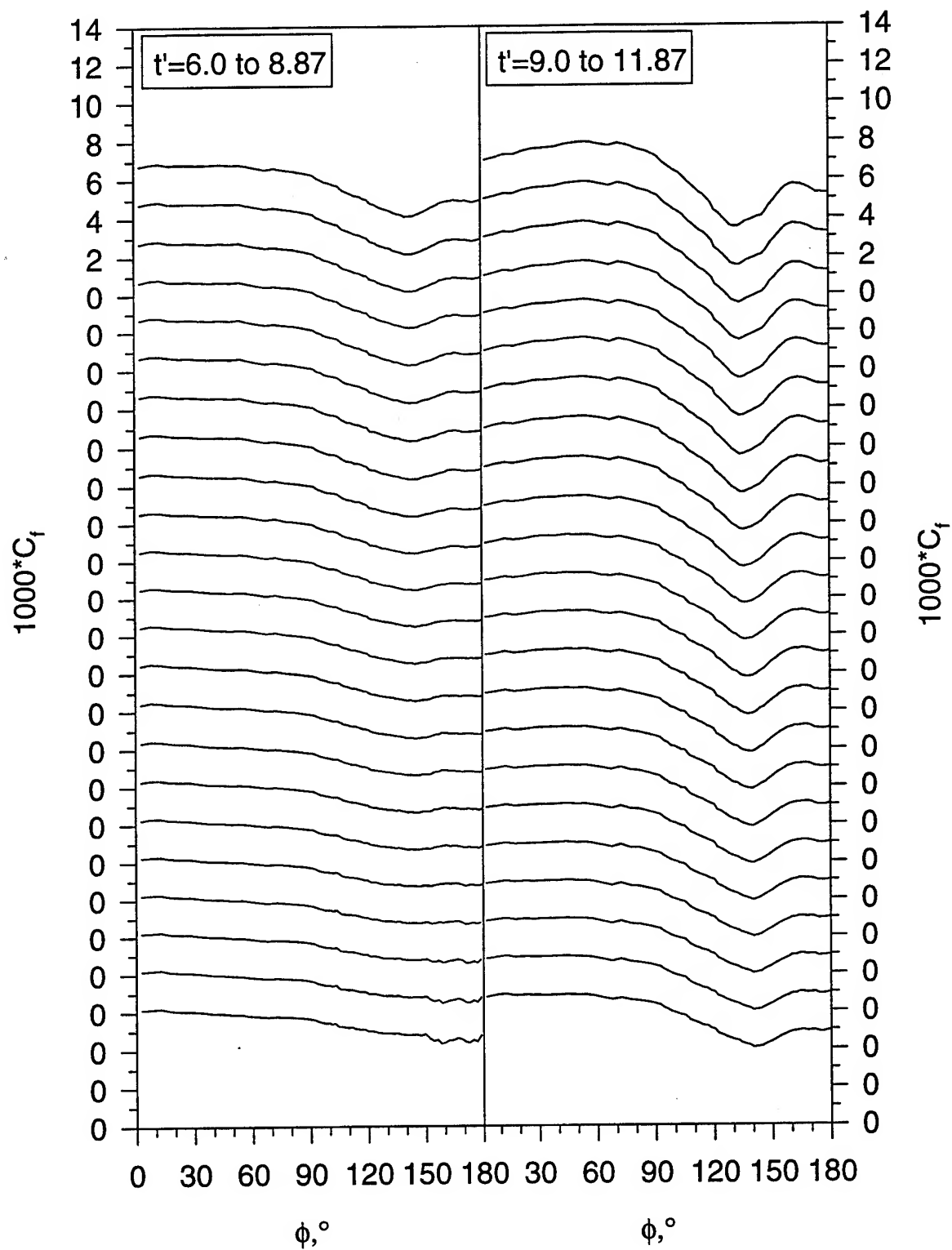


Figure 125. (b) Pitch-up maneuver time development of  $C_f$  vs.  $\phi$  for  $x/L=0.576$ .

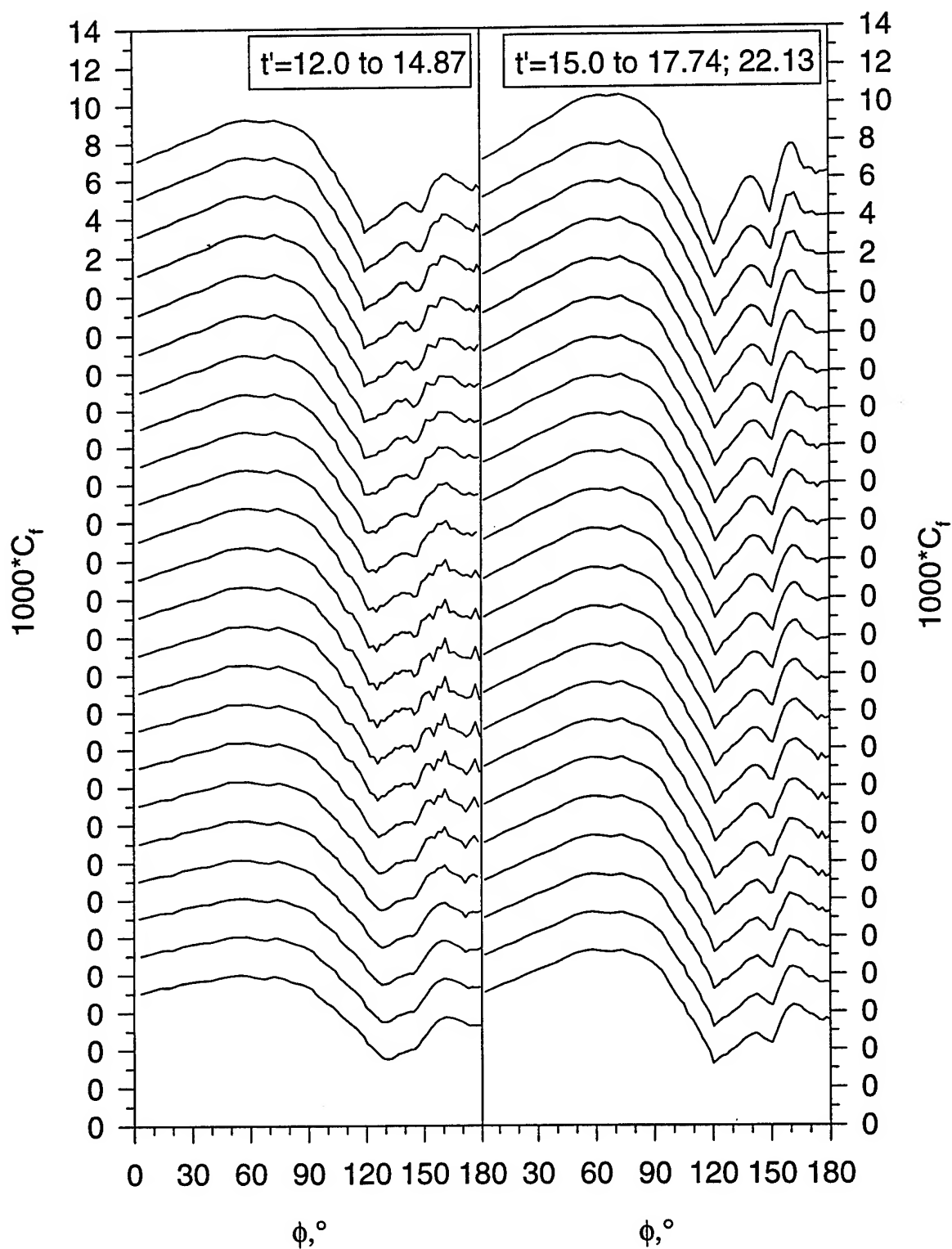


Figure 125. (c) Pitch-up maneuver time development of  $C_f$  vs.  $\phi$  for  $x/L=0.576$ .

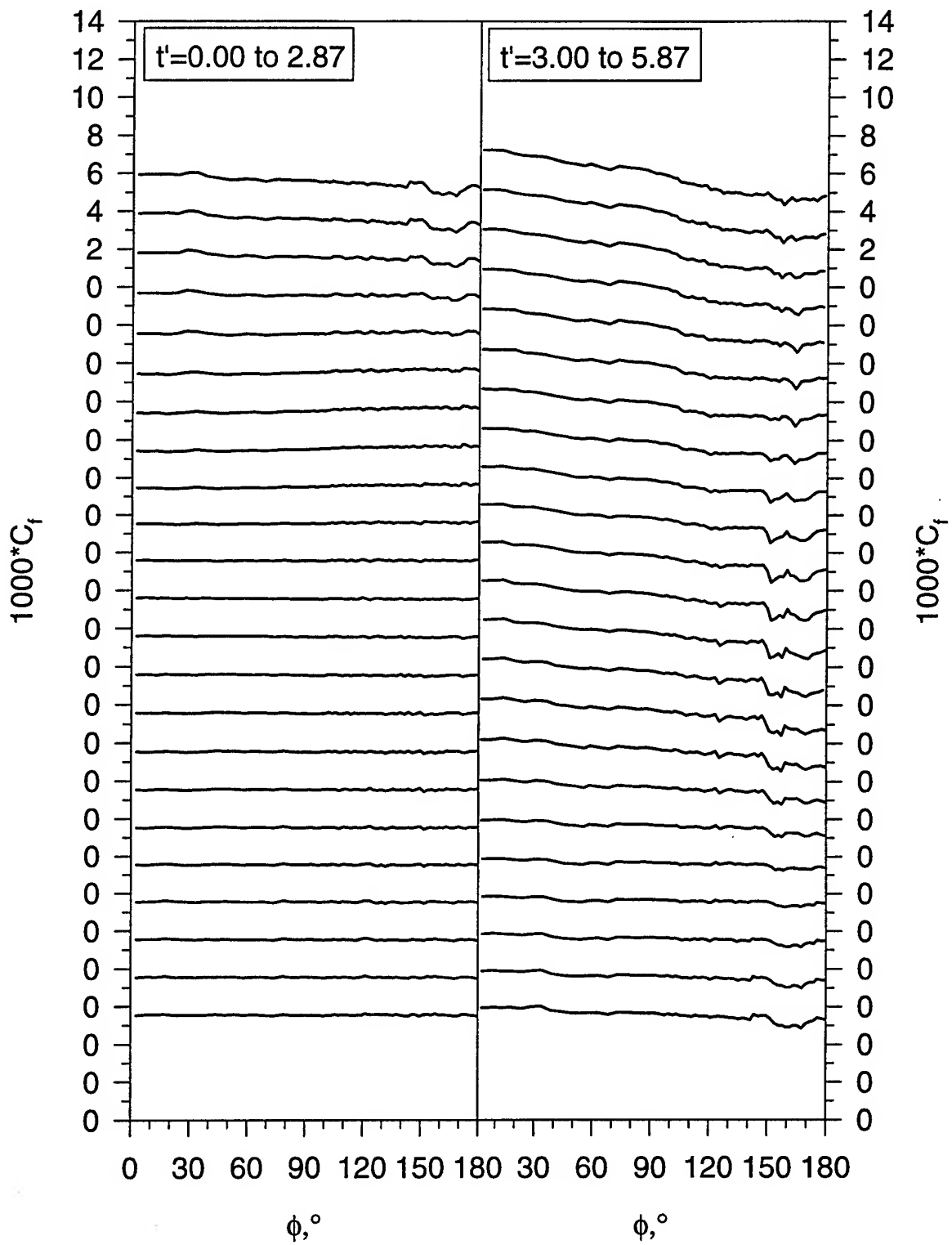


Figure 126.(a) Pitch-up maneuver time development of  $C_l$  vs.  $\phi$  for  $x/L=0.653$ .

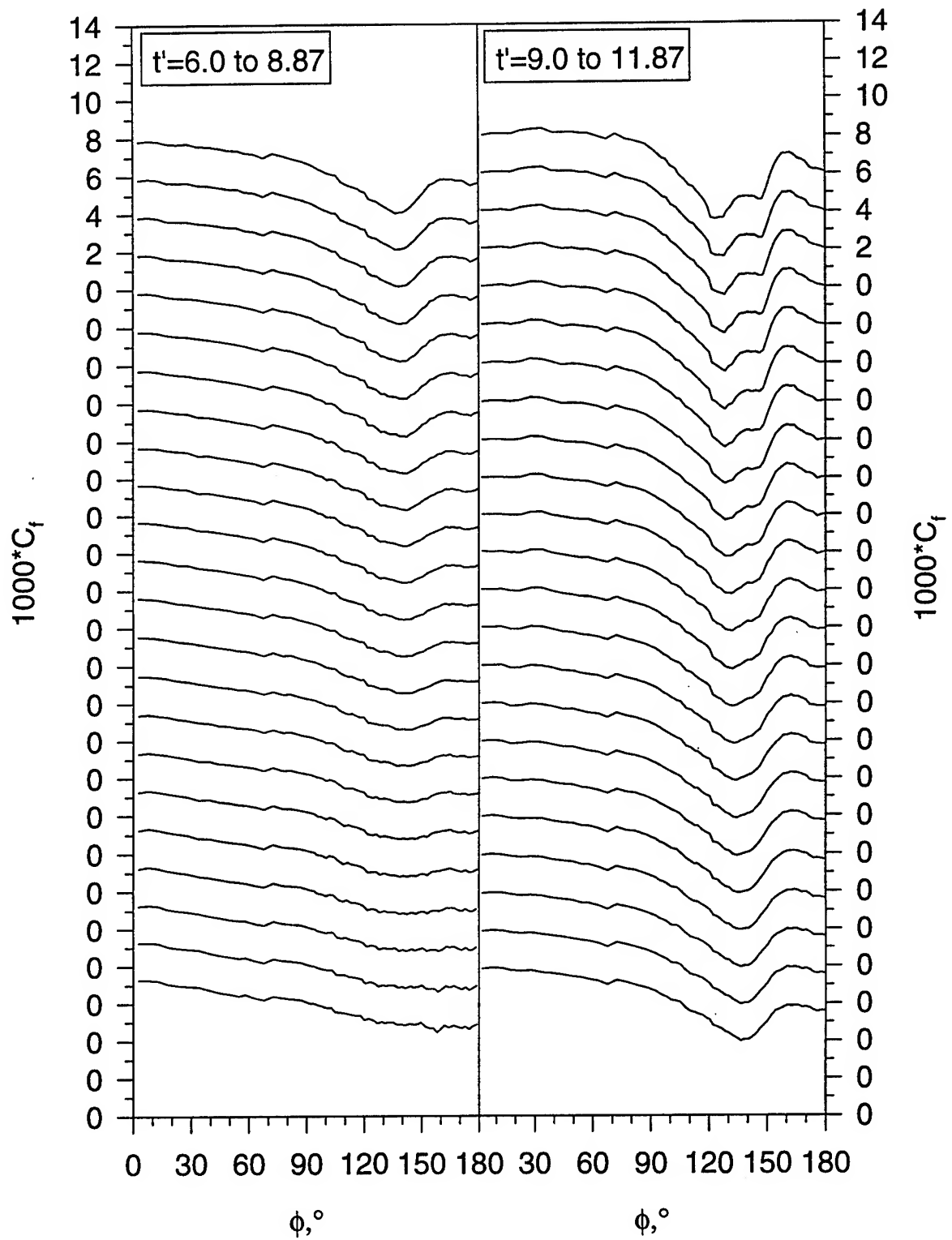


Figure 126. (b) Pitch-up maneuver time development of  $C_f$  vs.  $\phi$  for  $x/L=0.653$ .

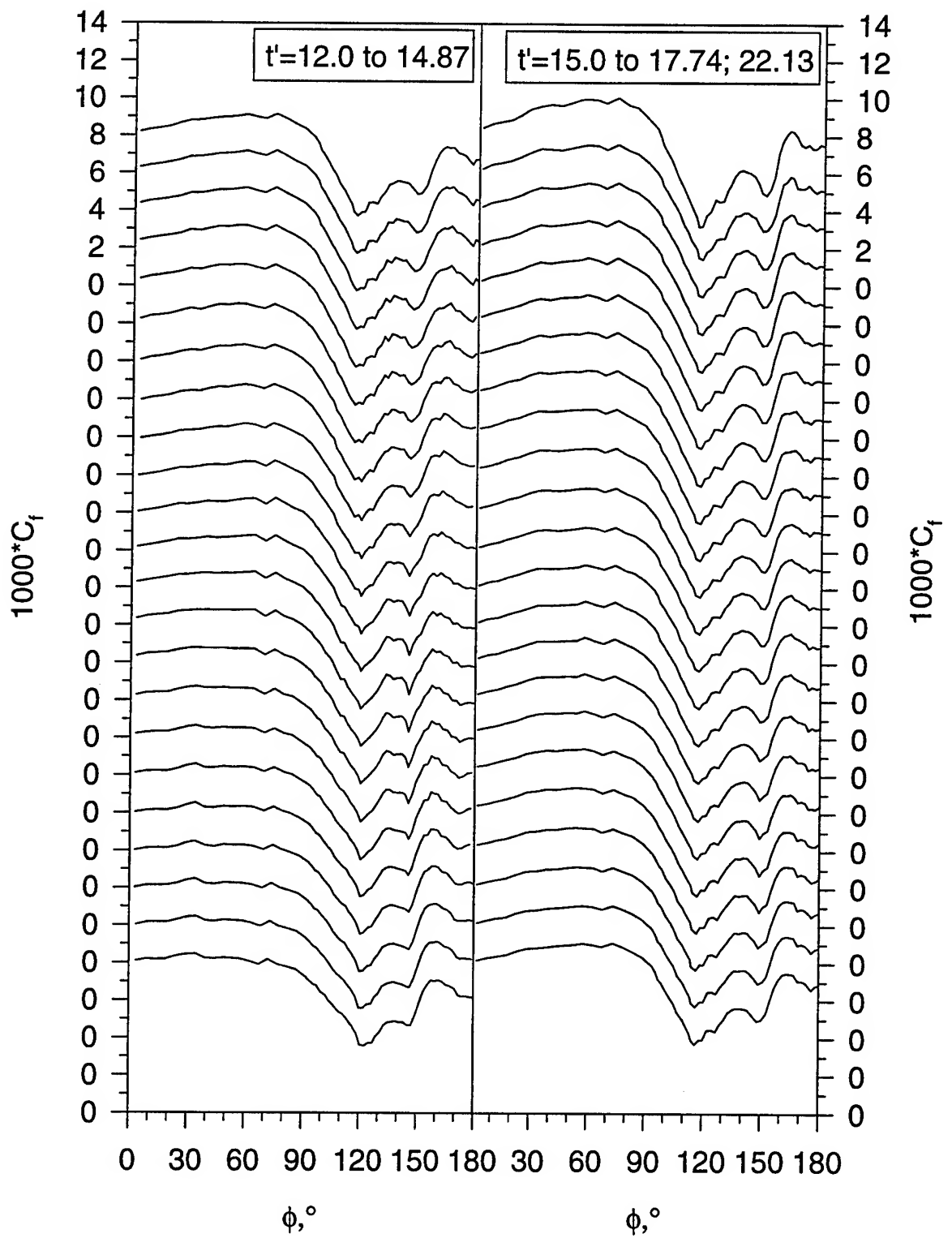


Figure 126. (c) Pitch-up maneuver time development of  $C_f$  vs.  $\phi$  for  $x/L=0.653$ .

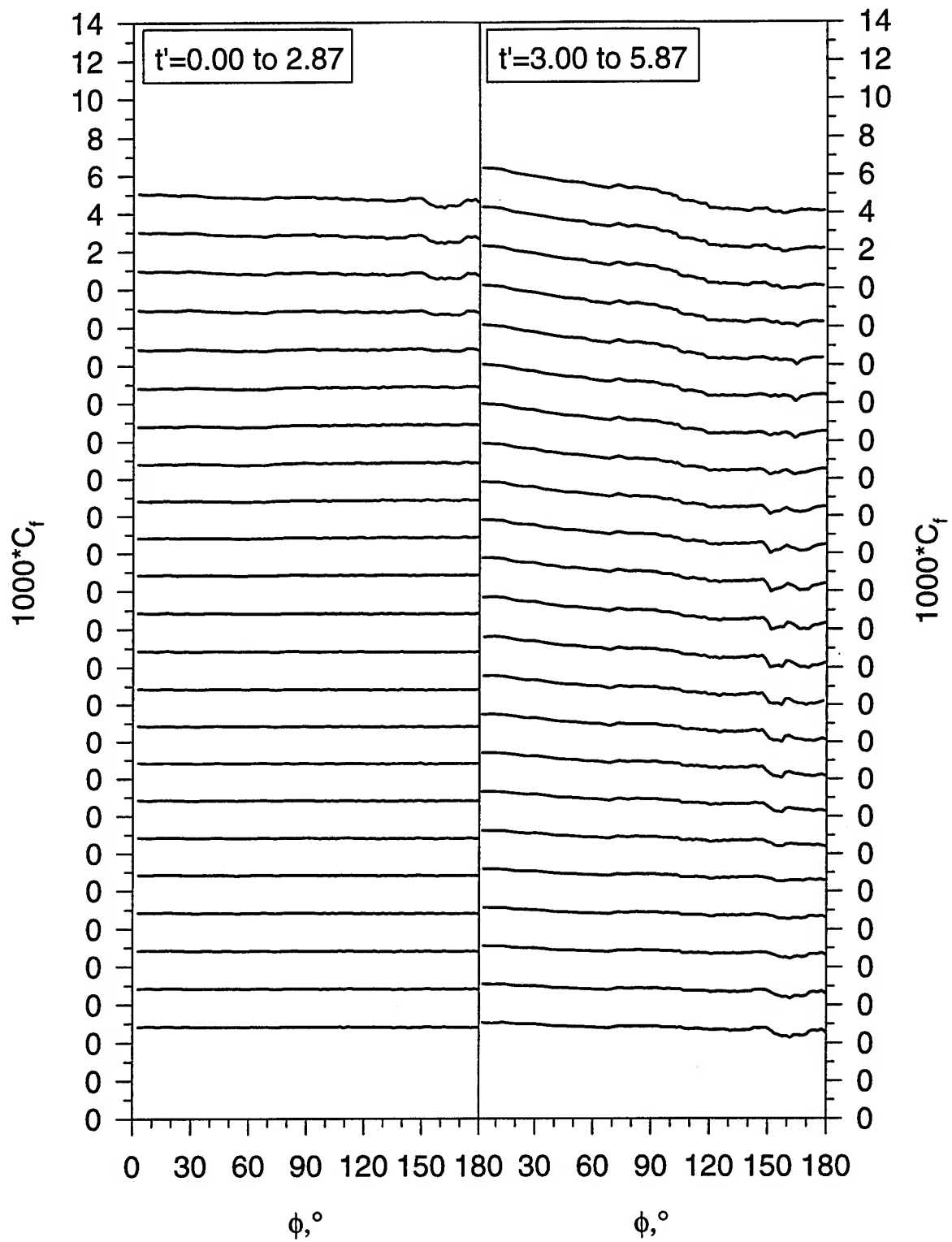


Figure 127.(a) Pitch-up maneuver time development of  $C_f$  vs.  $\phi$  for  $x/L=0.729$ .

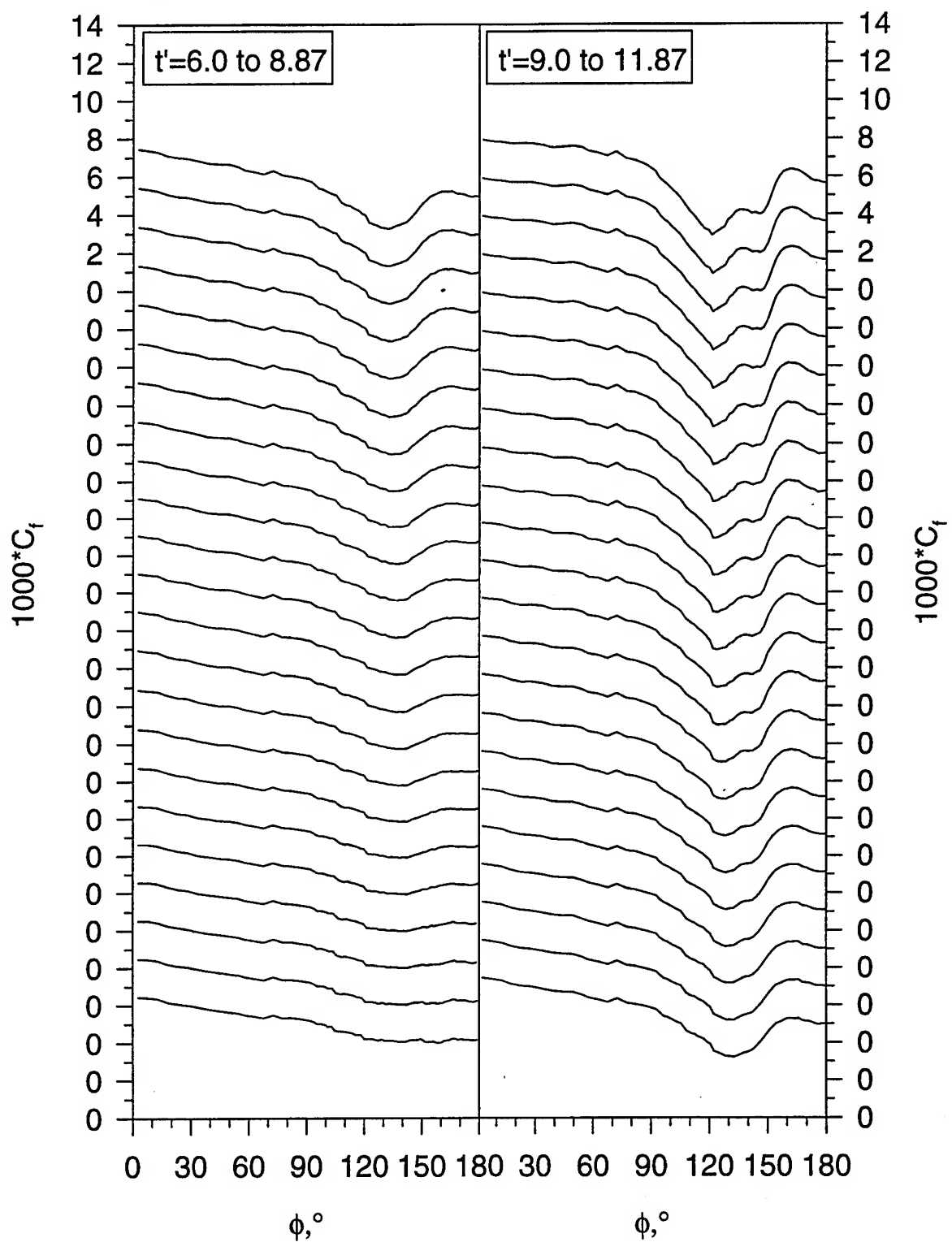


Figure 127. (b) Pitch-up maneuver time development of  $C_f$  vs.  $\phi$  for  $x/L=0.729$ .

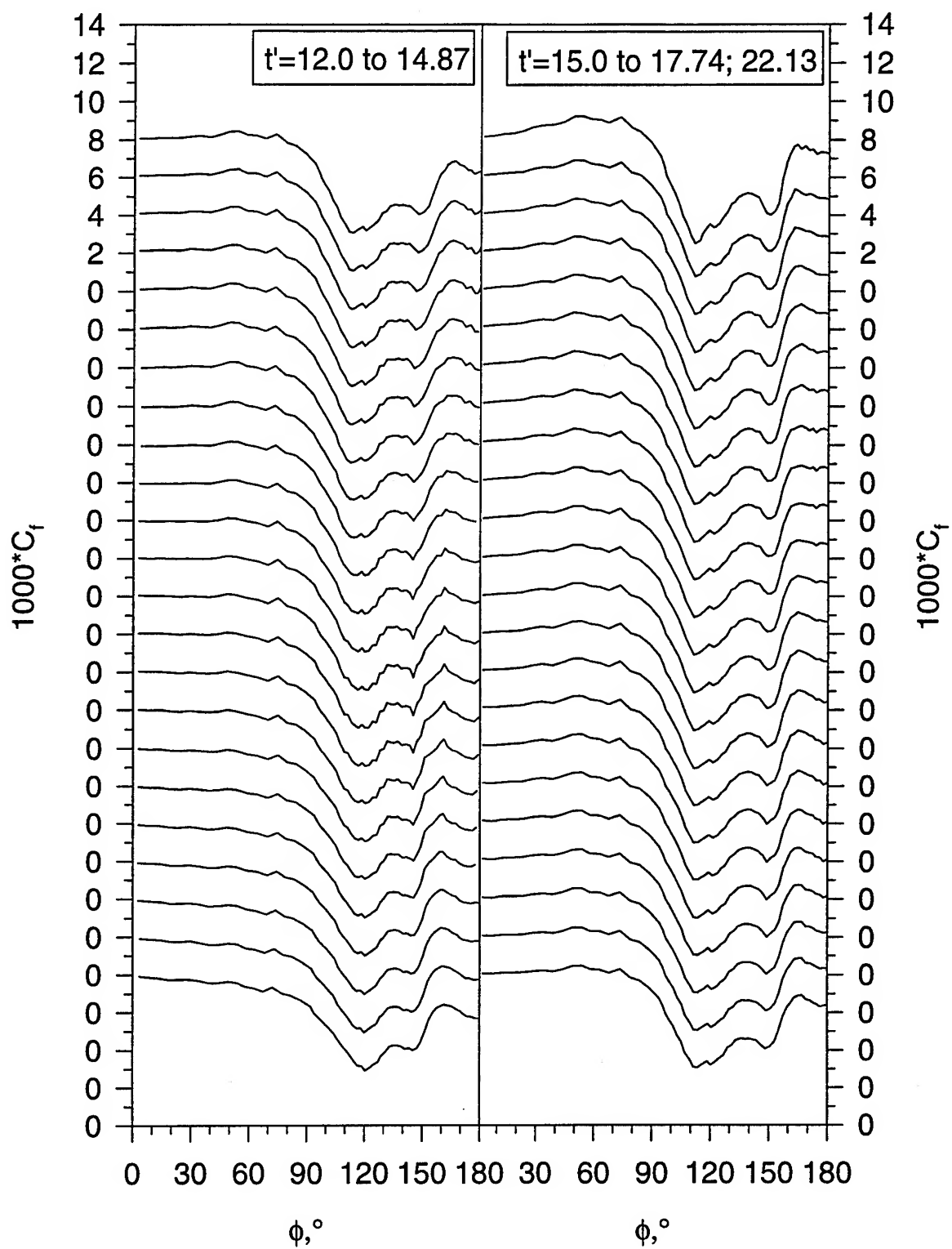


Figure 127. (c) Pitch-up maneuver time development of  $C_f$  vs.  $\phi$  for  $x/L=0.729$ .



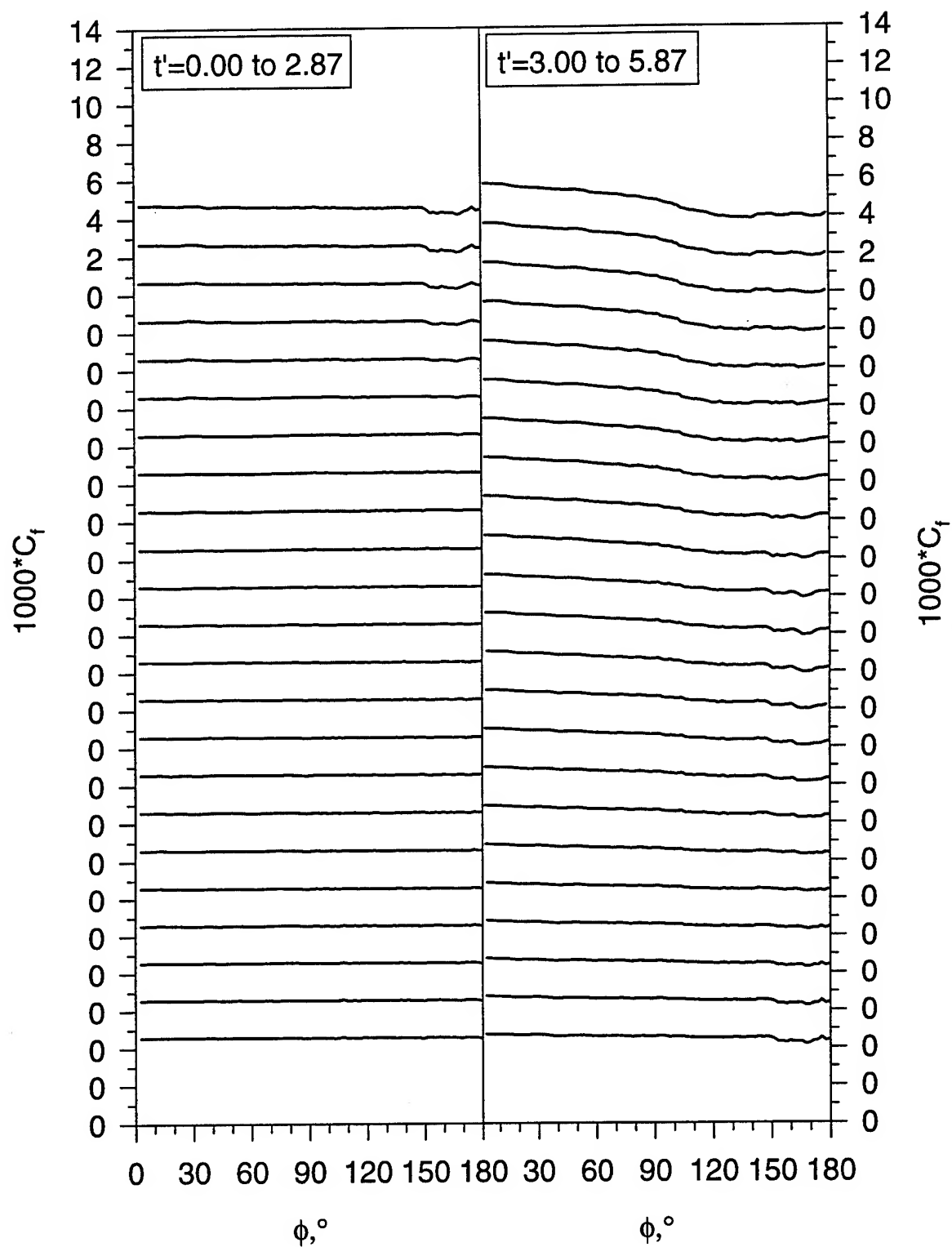


Figure 128.(a) Pitch-up maneuver time development of  $C_l$  vs.  $\phi$  for  $x/L=0.831$ .

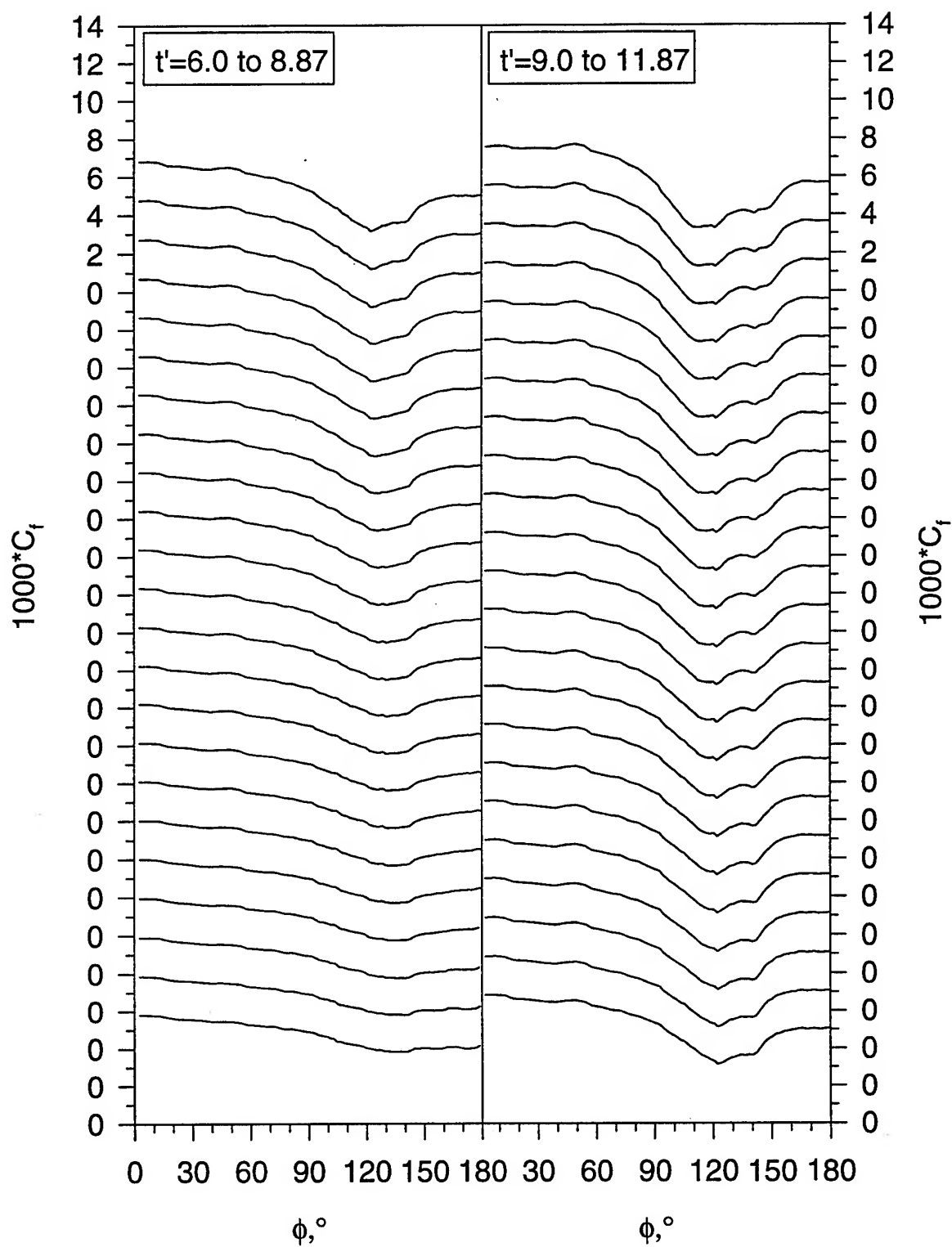


Figure 128. (b) Pitch-up maneuver time development of  $C_f$  vs.  $\phi$  for  $x/L=0.831$ .

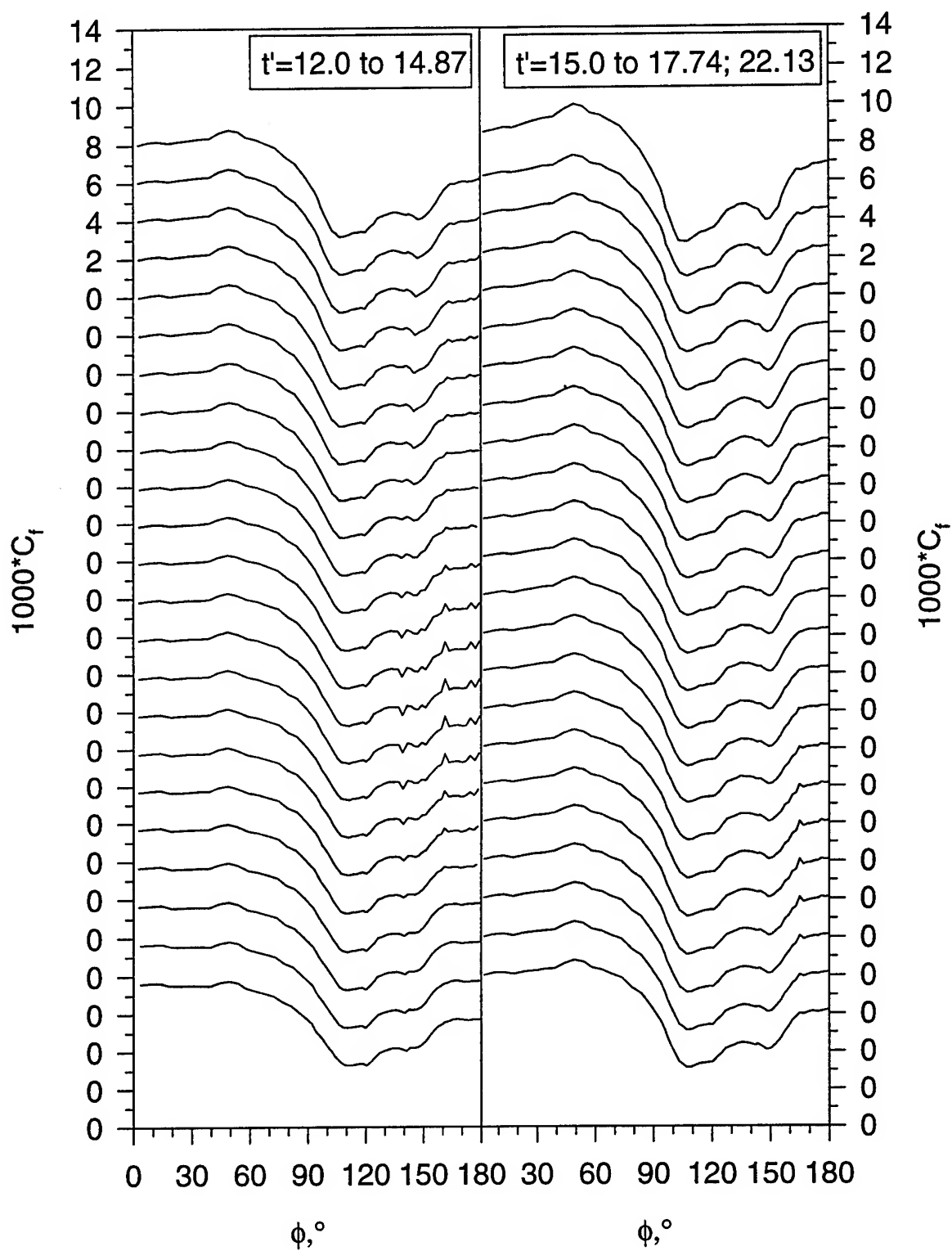


Figure 128. (c) Pitch-up maneuver time development of  $C_f$  vs.  $\phi$  for  $x/L=0.831$ .

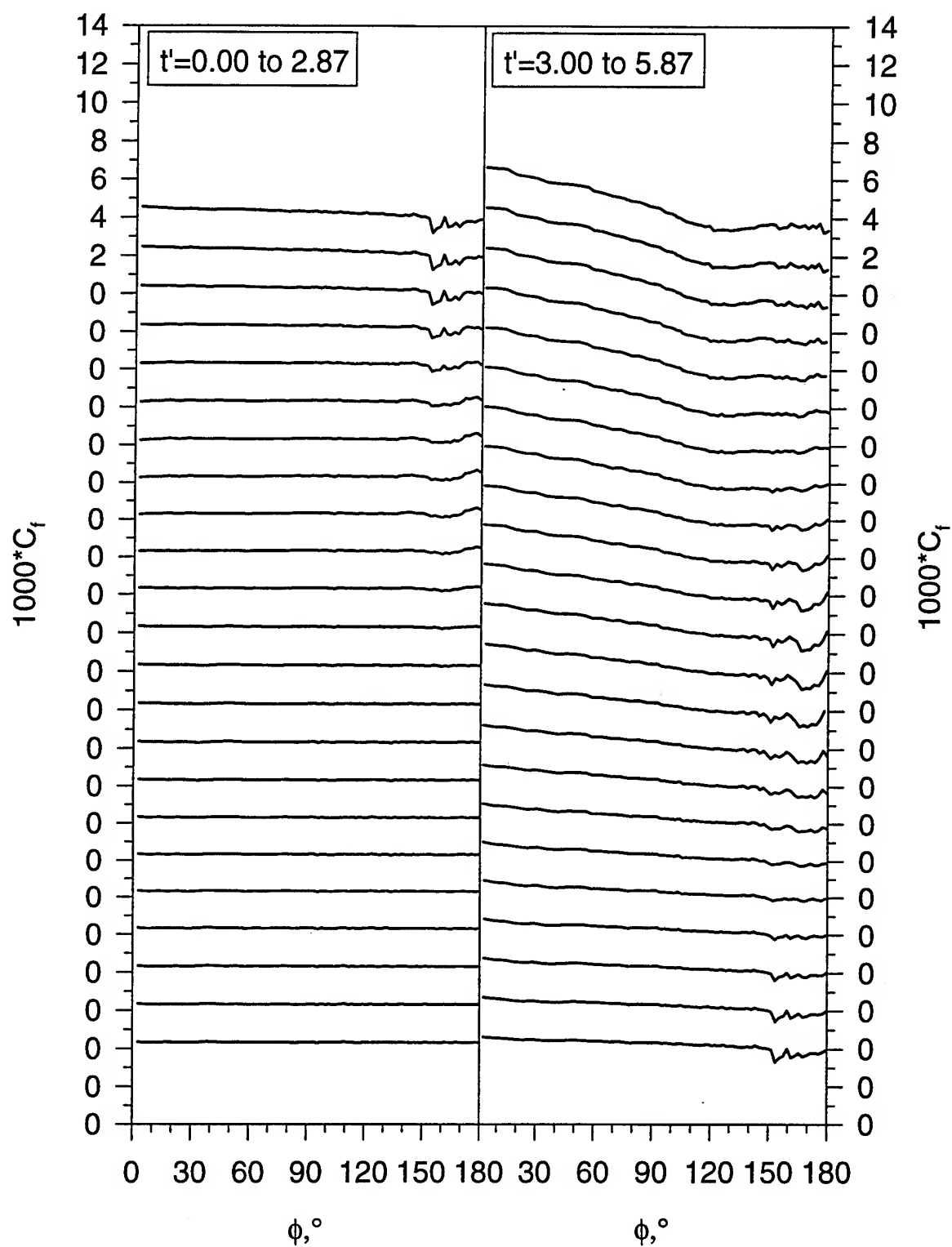


Figure 129.(a) Pitch-up maneuver time development of  $C_f$  vs.  $\phi$  for  $x/L=0.882$ .

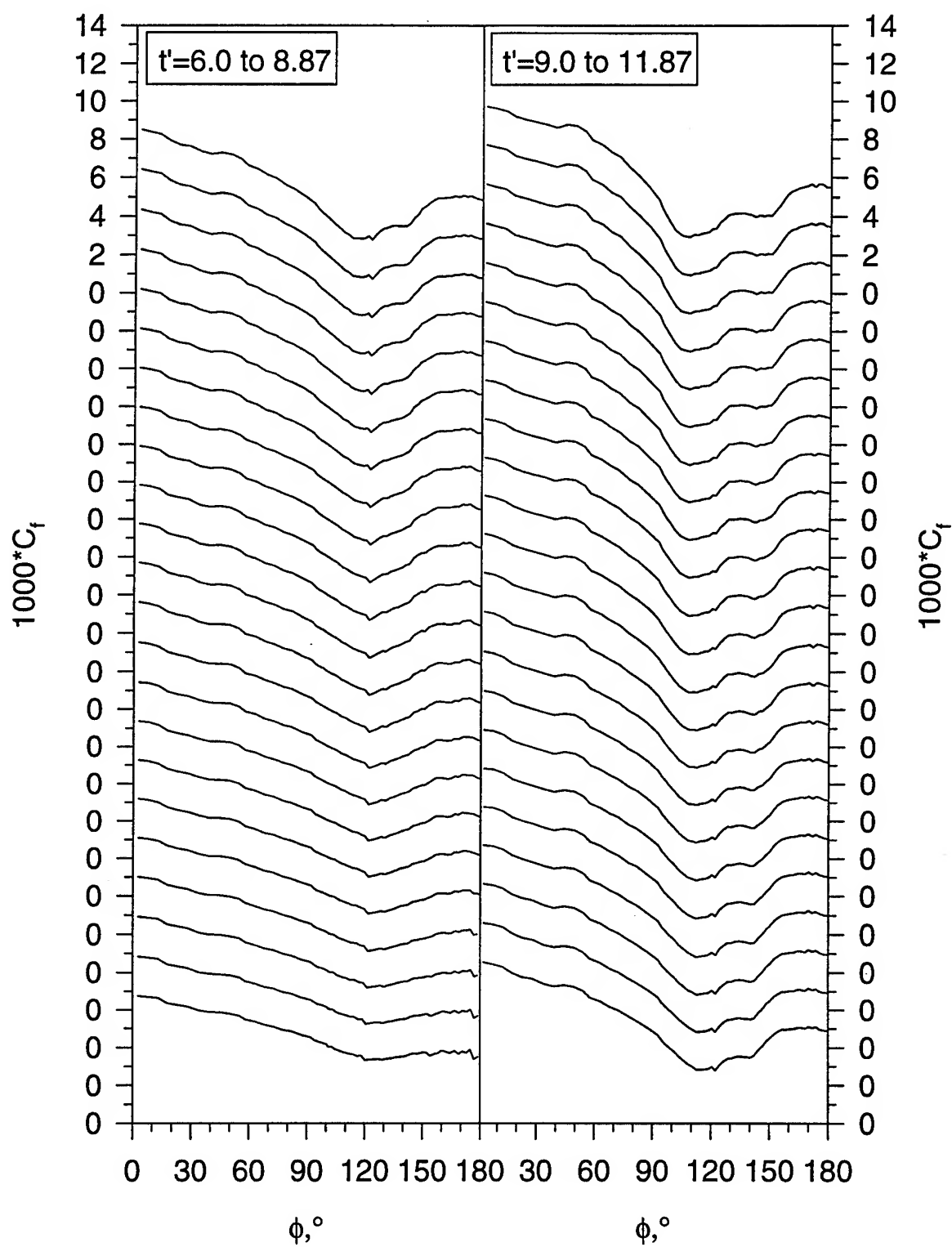


Figure 129. (b) Pitch-up maneuver time development of  $C_f$  vs.  $\phi$  for  $x/L=0.882$ .

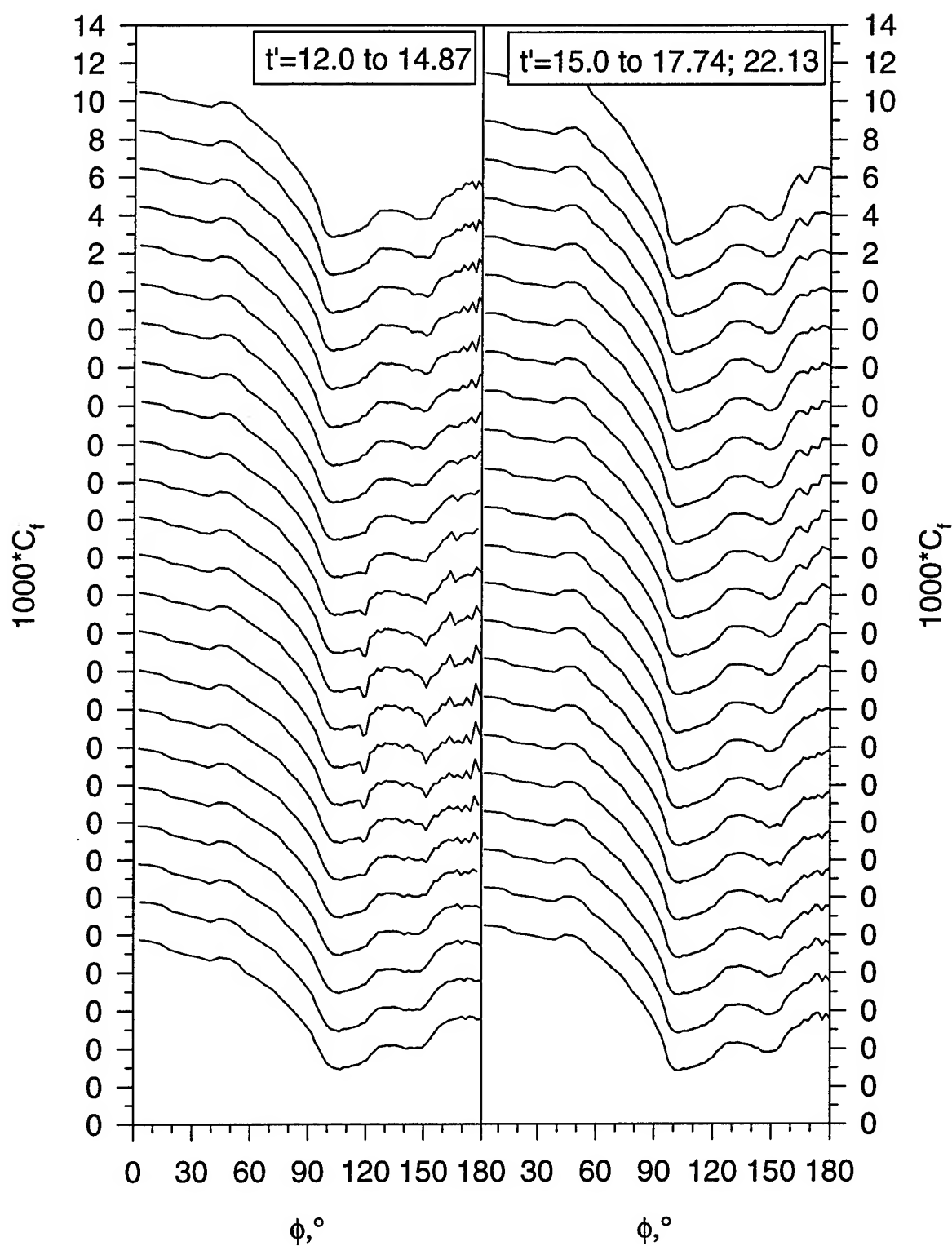


Figure 129. (c) Pitch-up maneuver time development of  $C_f$  vs.  $\phi$  for  $x/L=0.882$ .

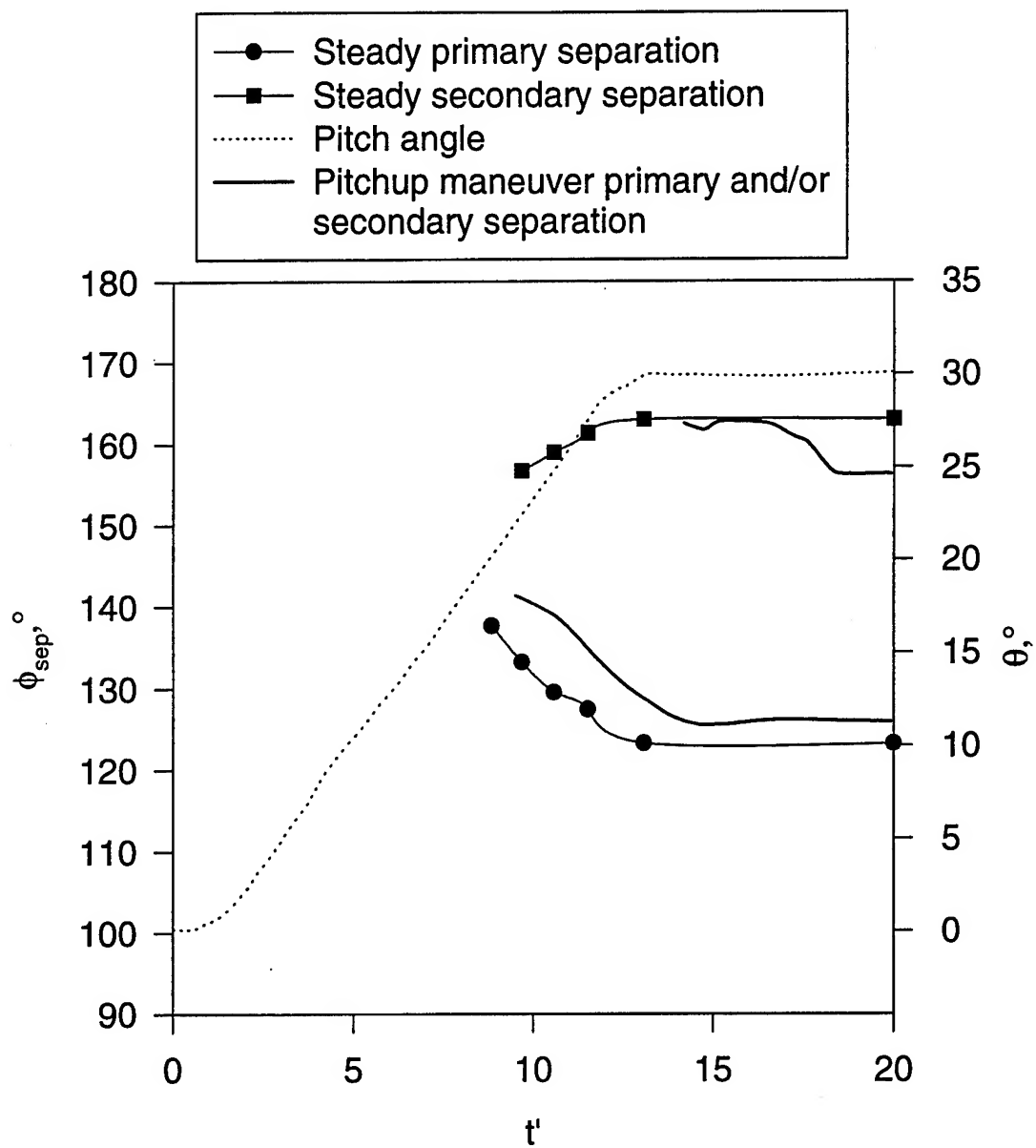


Figure 130. Separation position versus time for pitch-up maneuver at  $x/L=0.118$  compared with quasi-steady separation positions.

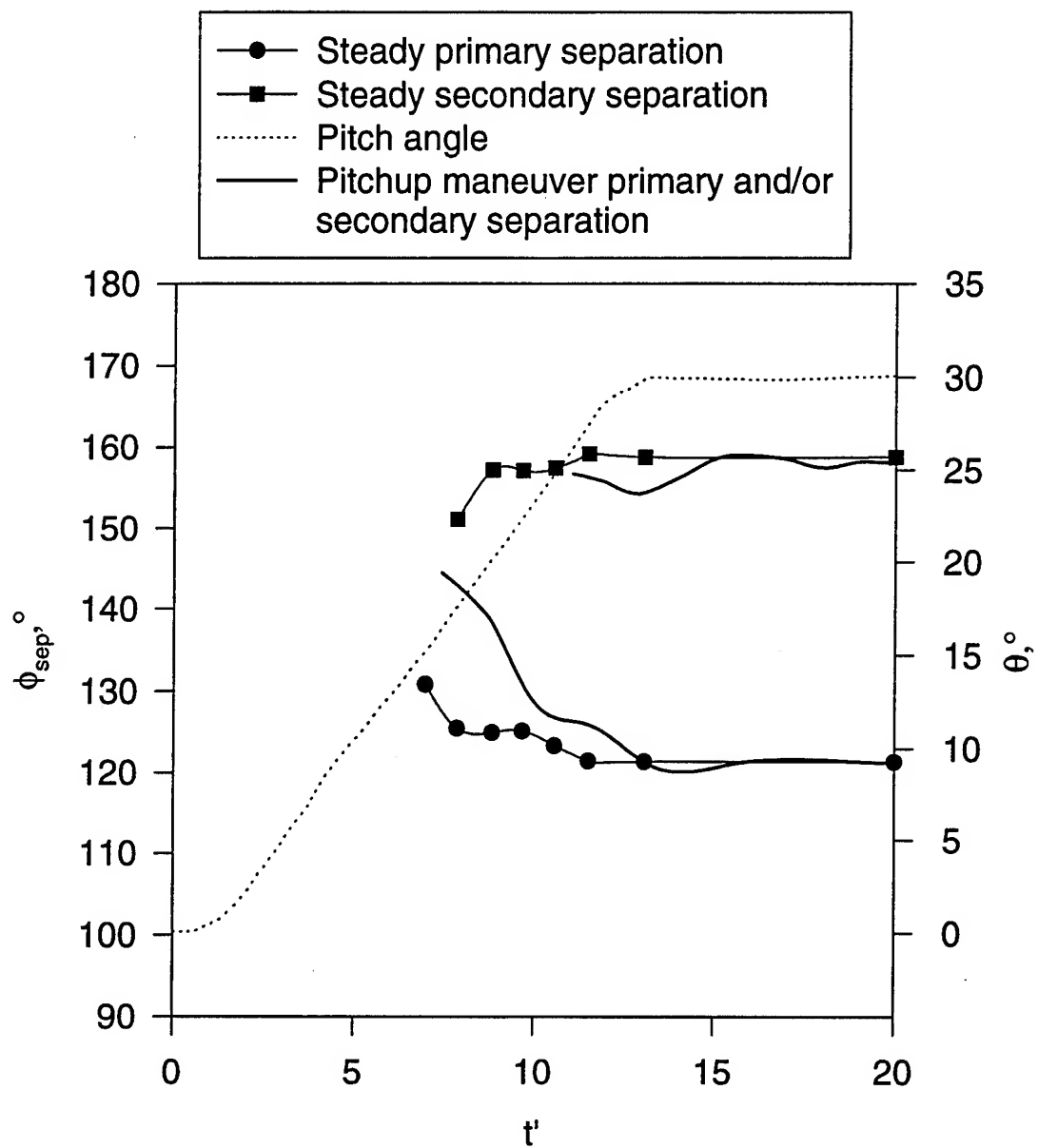


Figure 131. Separation position versus time for pitch-up maneuver at  $x/L=0.194$  compared with quasi-steady separation positions.



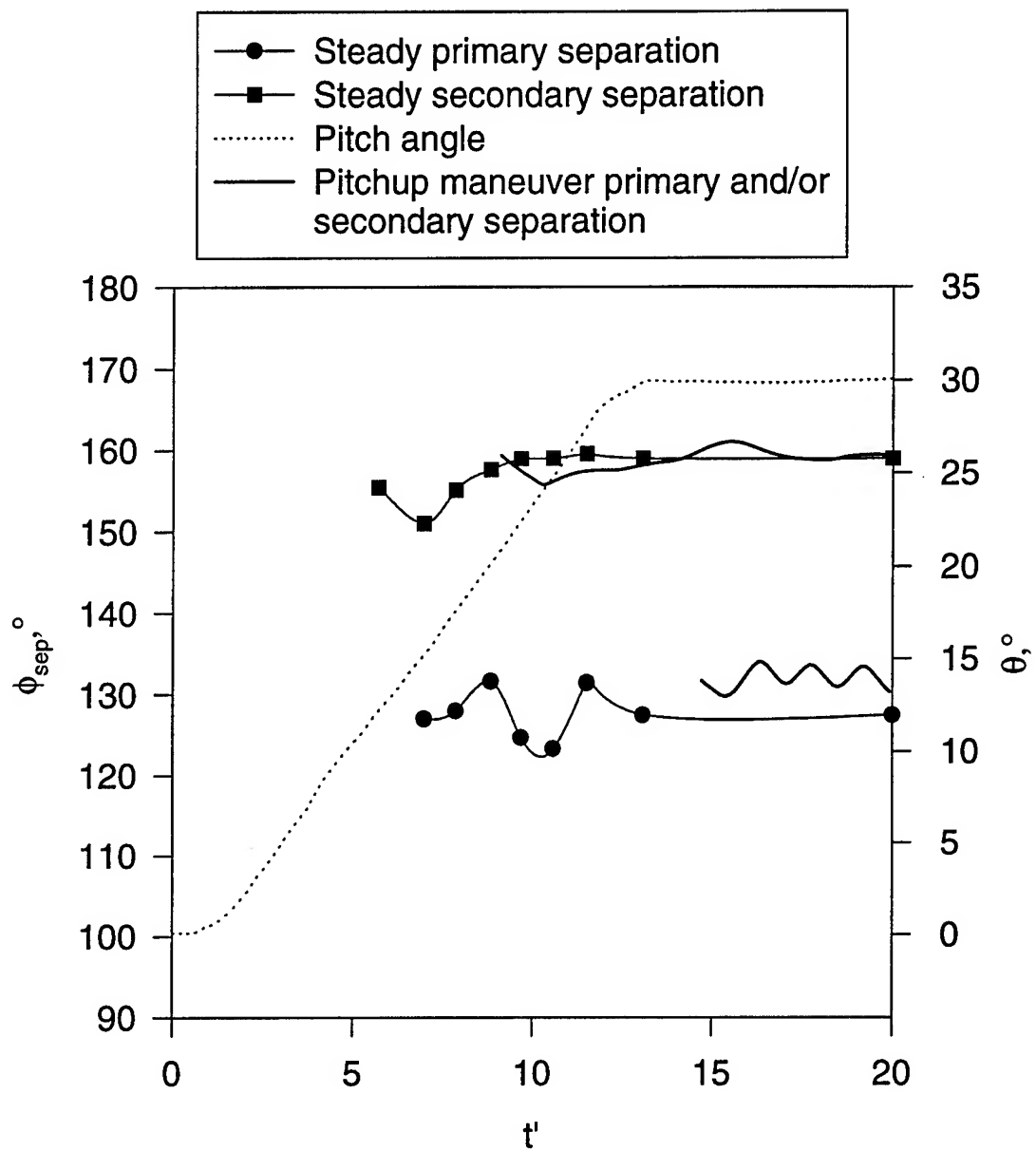


Figure 132. Separation position versus time for pitch-up maneuver at  $x/L=0.220$  compared with quasi-steady separation positions.

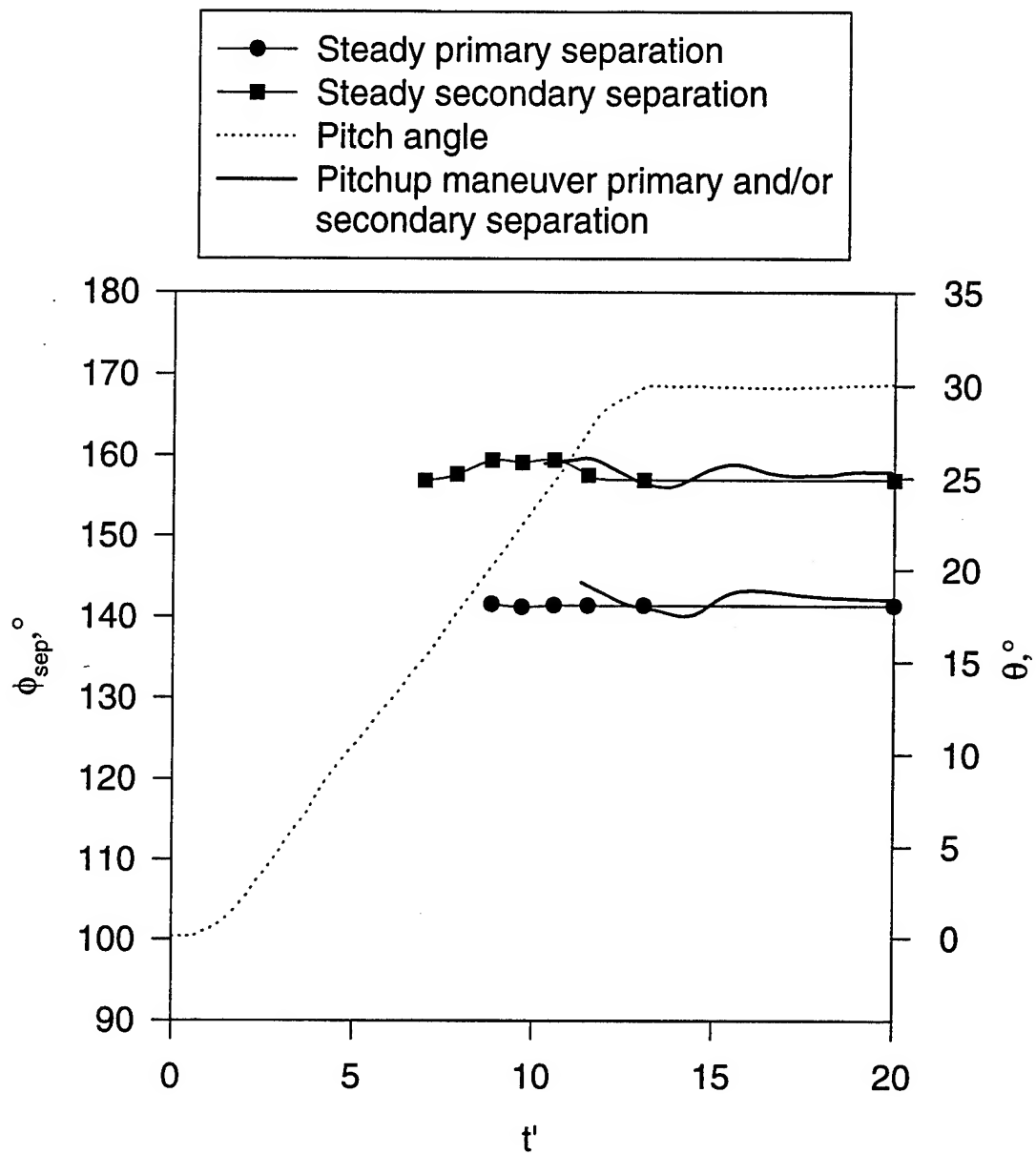


Figure 133. Separation position versus time for pitch-up maneuver at  $x/L=0.271$  compared with quasi-steady separation positions.

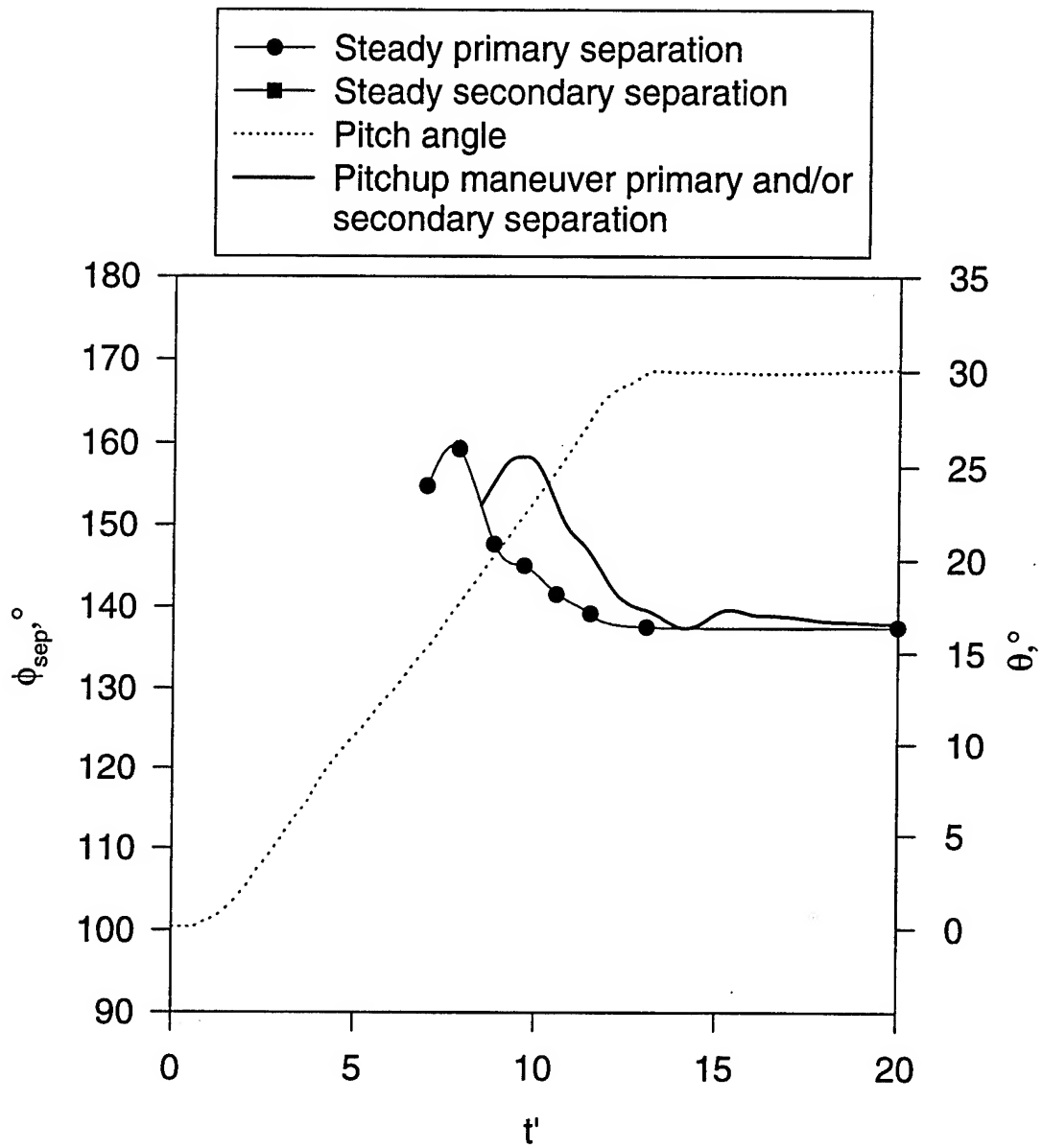


Figure 134. Separation position versus time for pitch-up maneuver at  $x/L=0.347$  compared with quasi-steady separation positions.

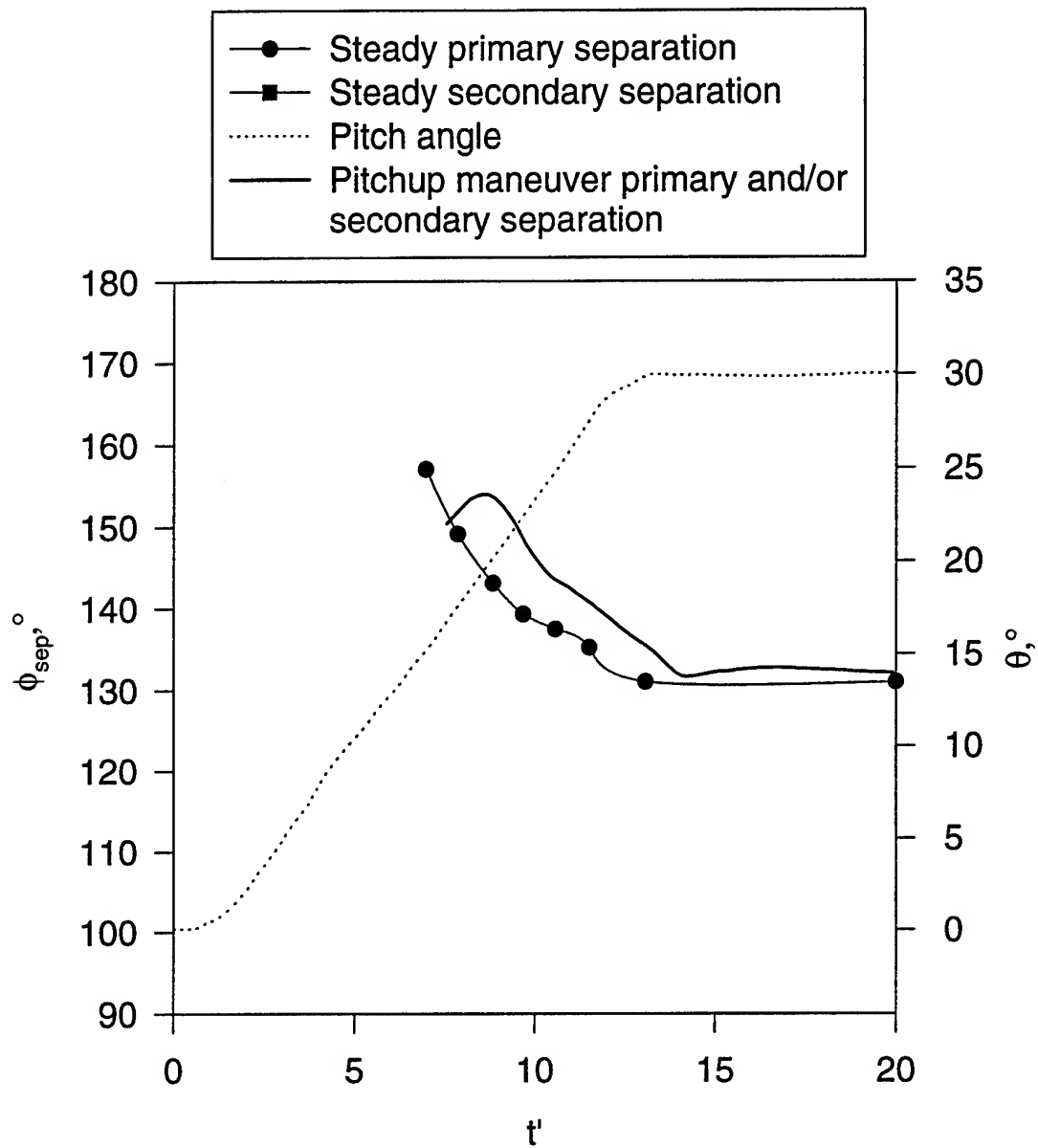


Figure 135. Separation position versus time for pitch-up maneuver at  $x/L=0.424$  compared with quasi-steady separation positions.

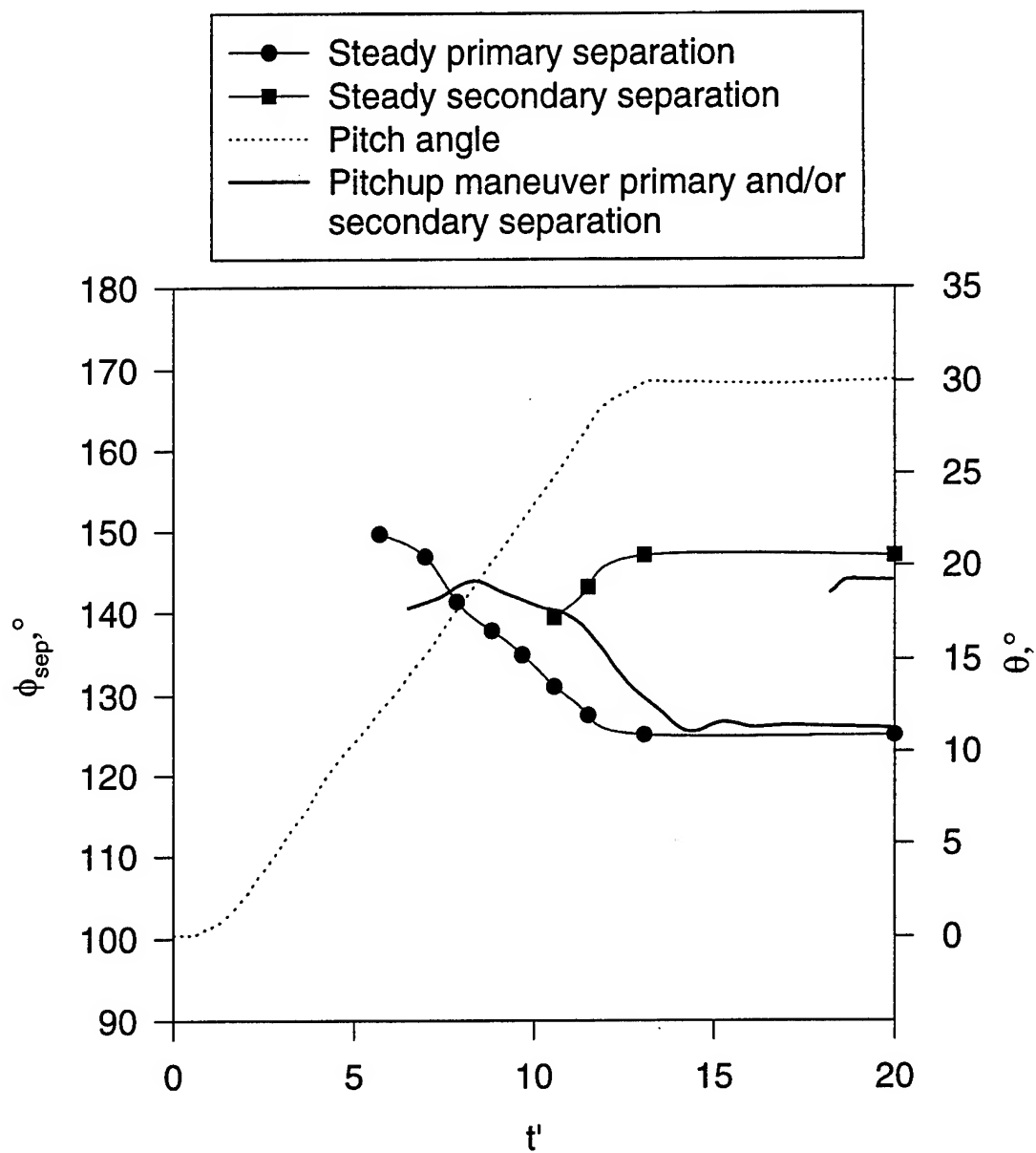


Figure 136. Separation position versus time for pitch-up maneuver at  $x/L=0.500$  compared with quasi-steady separation positions.

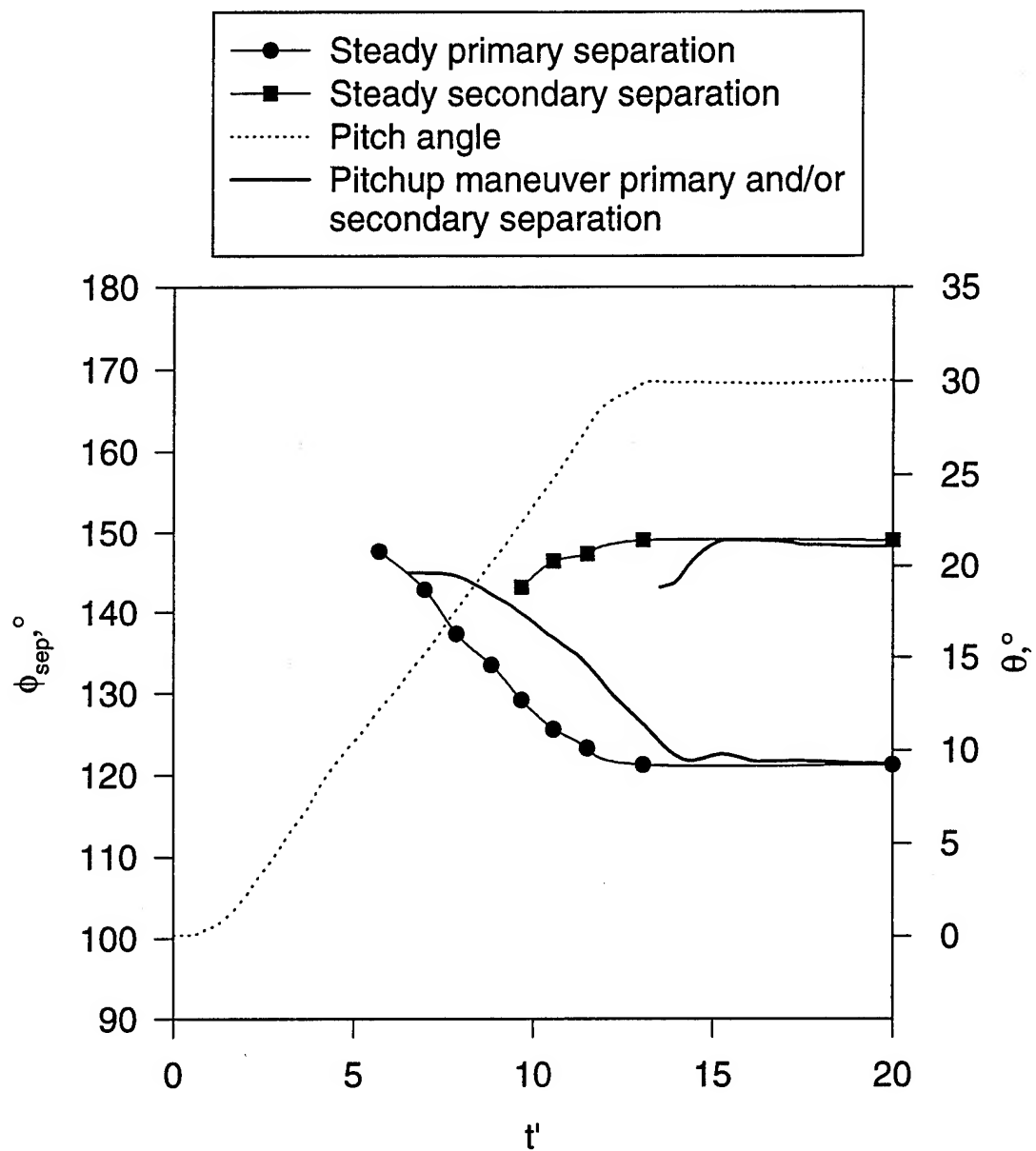


Figure 137. Separation position versus time for pitch-up maneuver at  $x/L=0.576$  compared with quasi-steady separation positions.

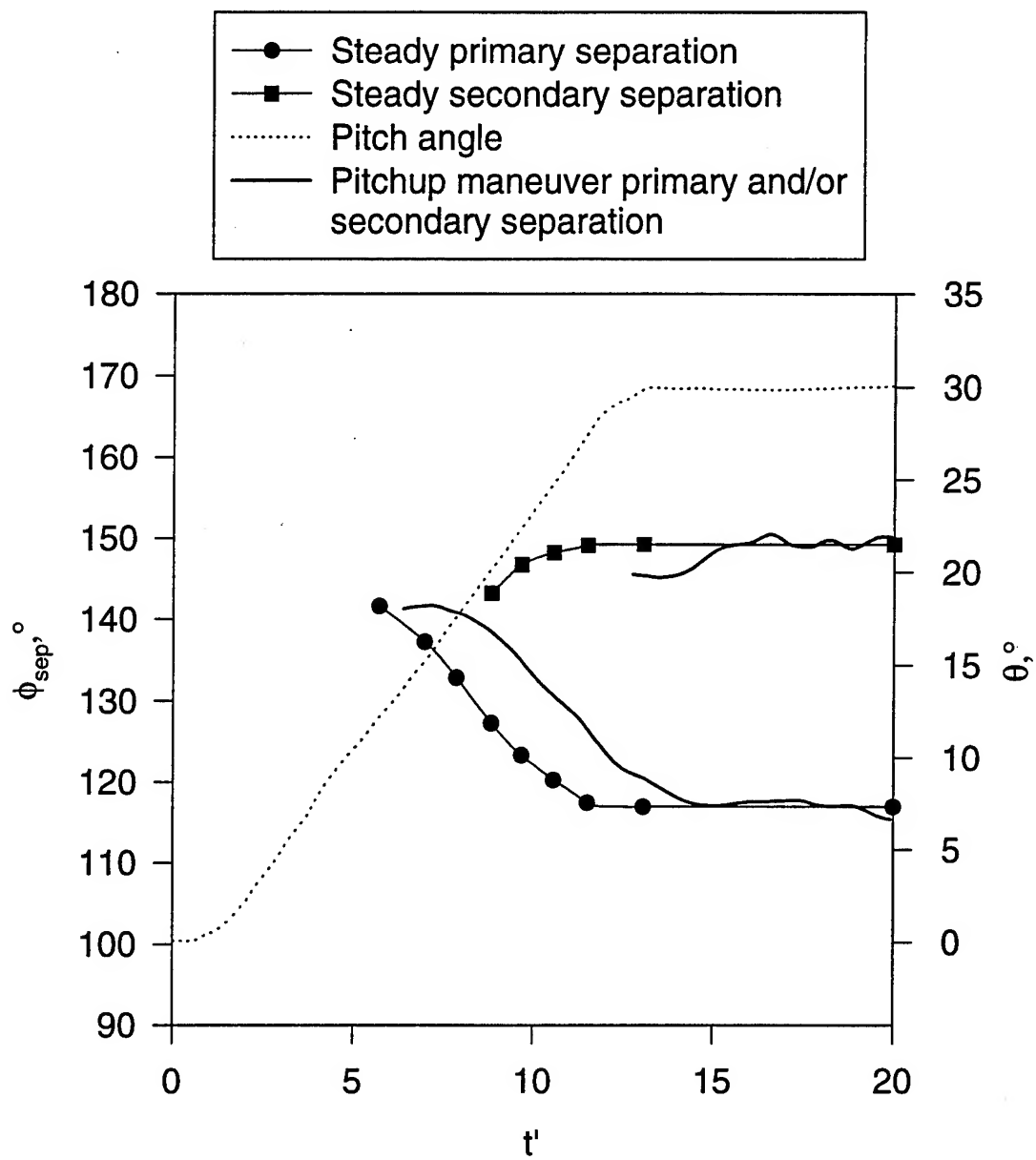


Figure 138. Separation position versus time for pitch-up maneuver at  $x/L=0.653$  compared with quasi-steady separation positions.

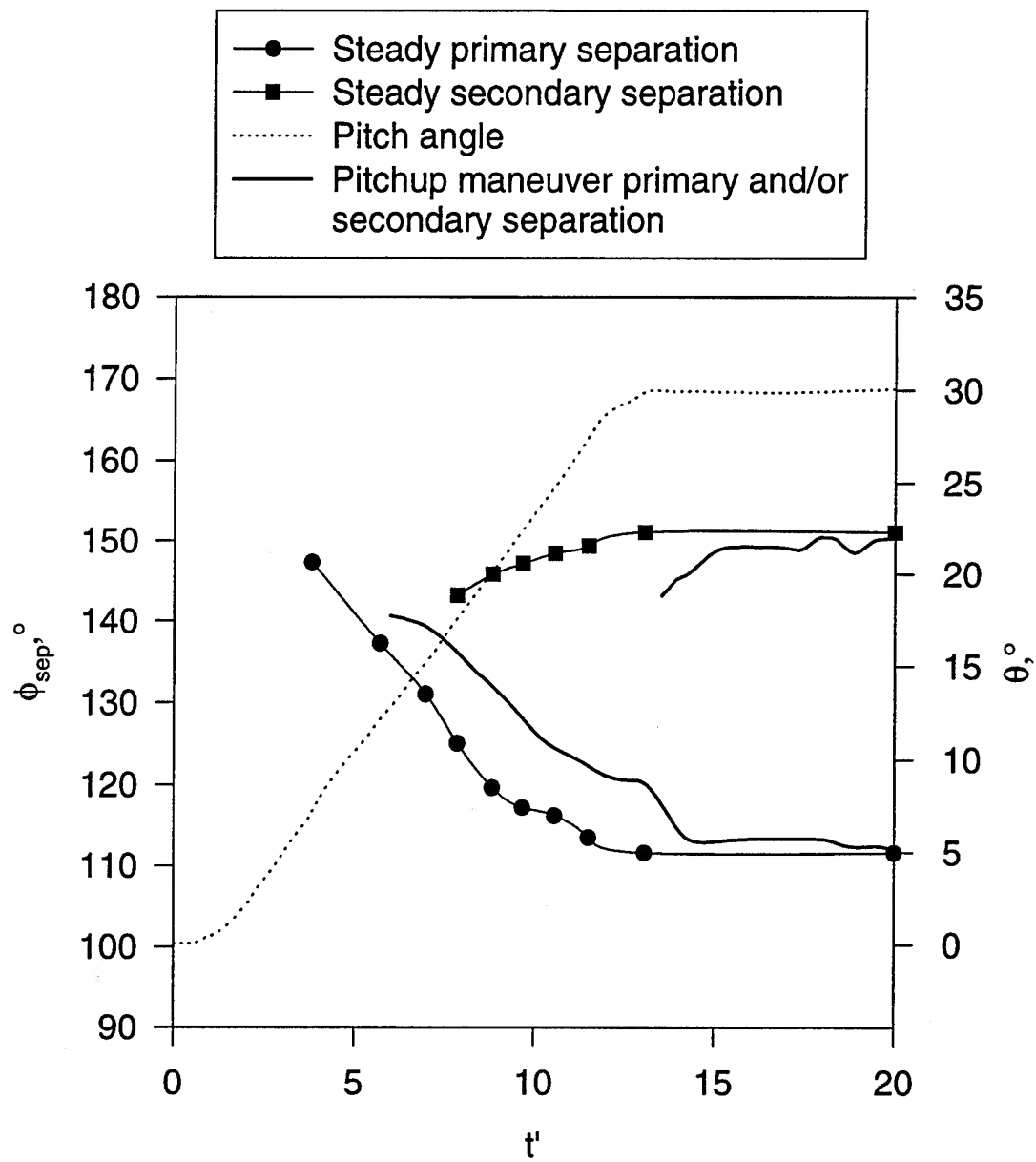


Figure 139. Separation position versus time for pitch-up maneuver at  $x/L=0.729$  compared with quasi-steady separation positions.



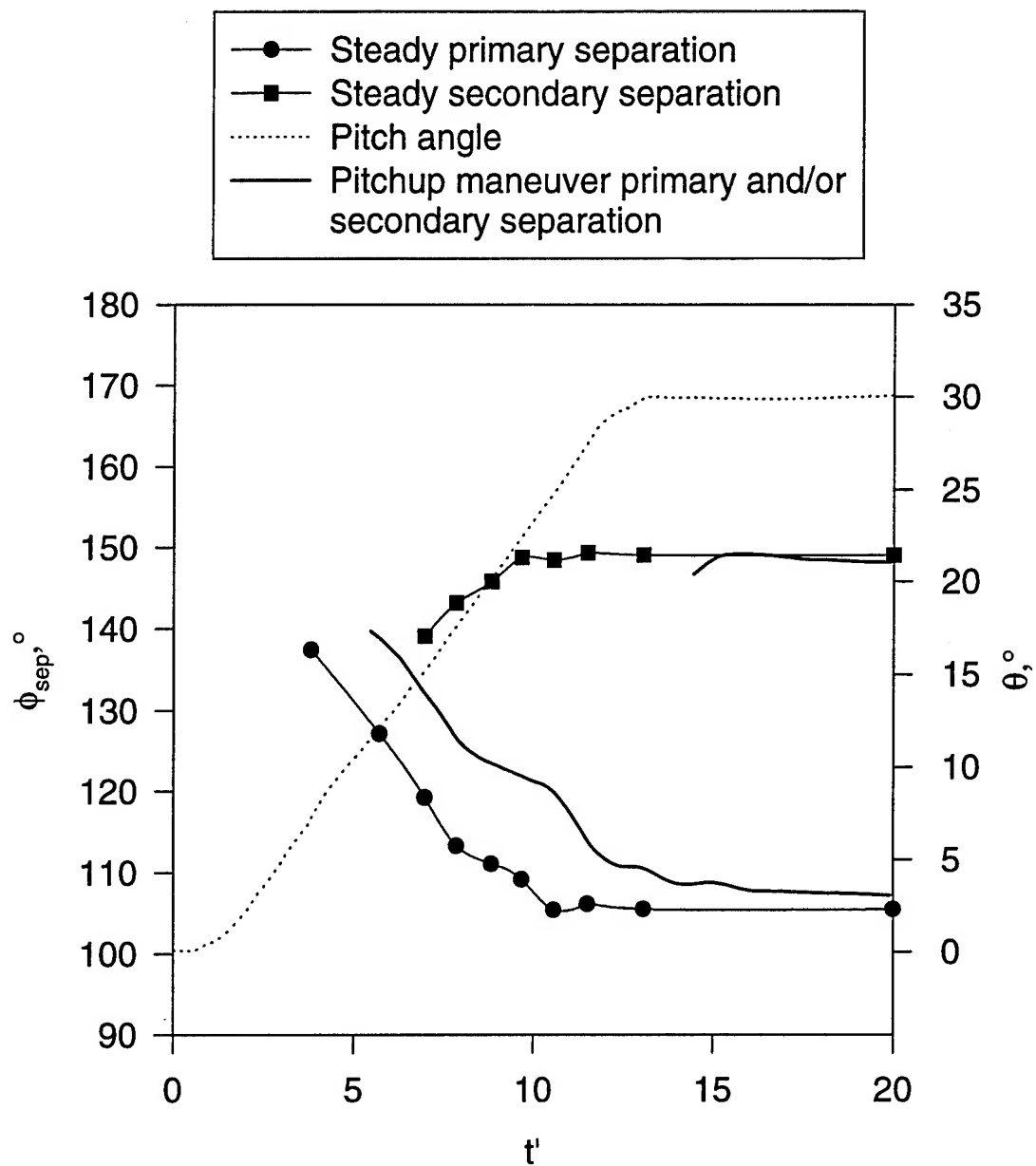


Figure 140. Separation position versus time for pitch-up maneuver at  $x/L=0.831$  compared with quasi-steady separation positions.

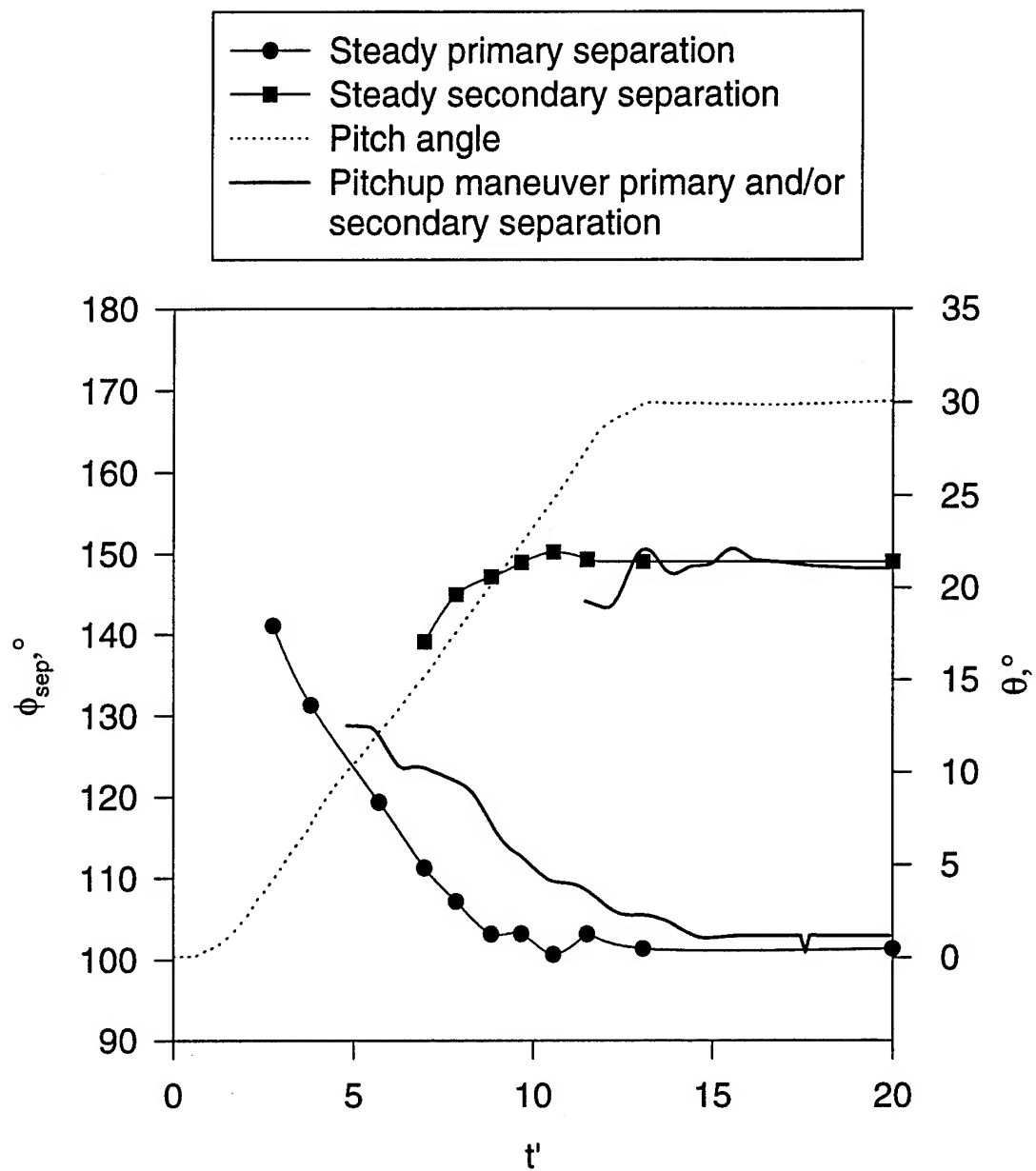


Figure 141. Separation position versus time for pitch-up maneuver at  $x/L=0.882$  compared with quasi-steady separation positions.

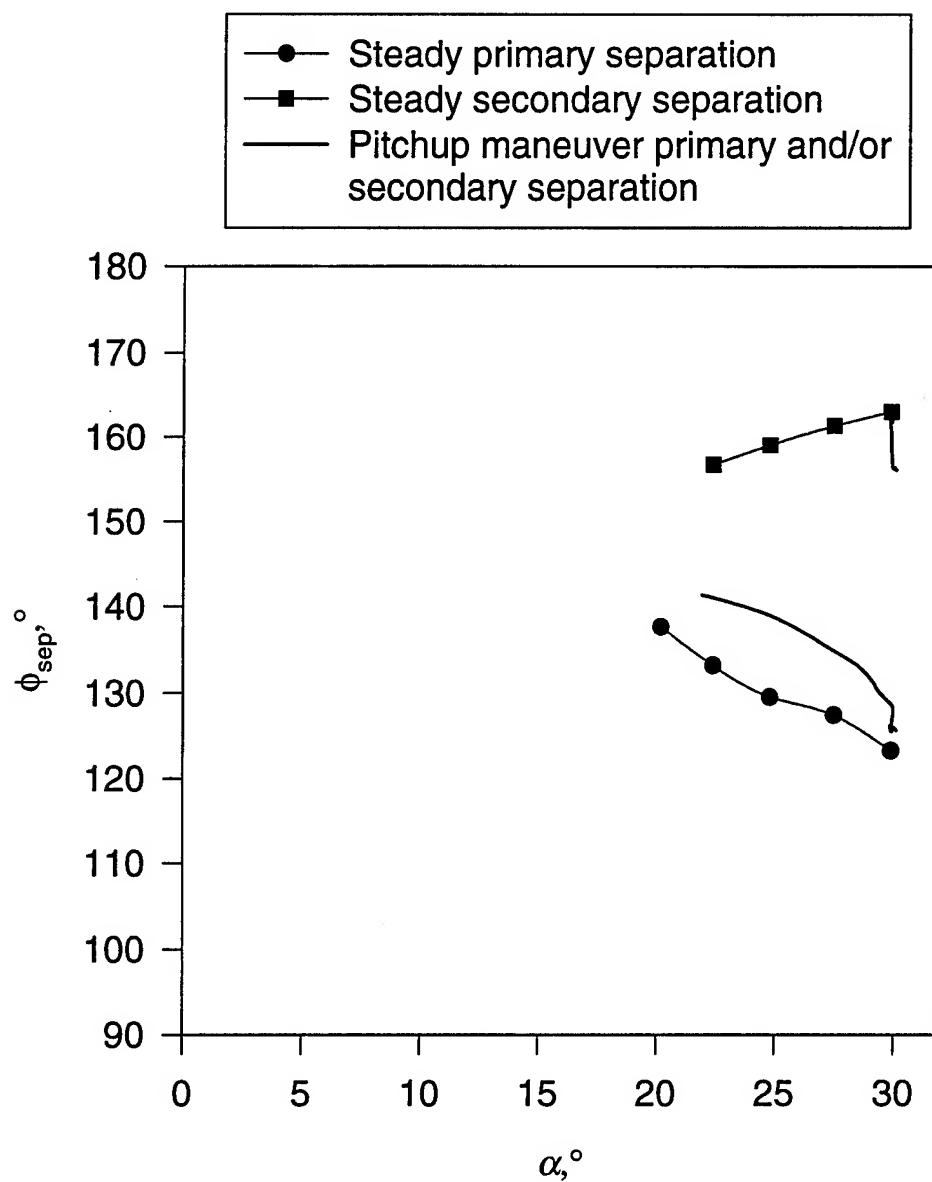


Figure 142. Separation position versus  $\alpha$  for pitch-up maneuver at  $x/L=0.118$  compared with quasi-steady separation positions.

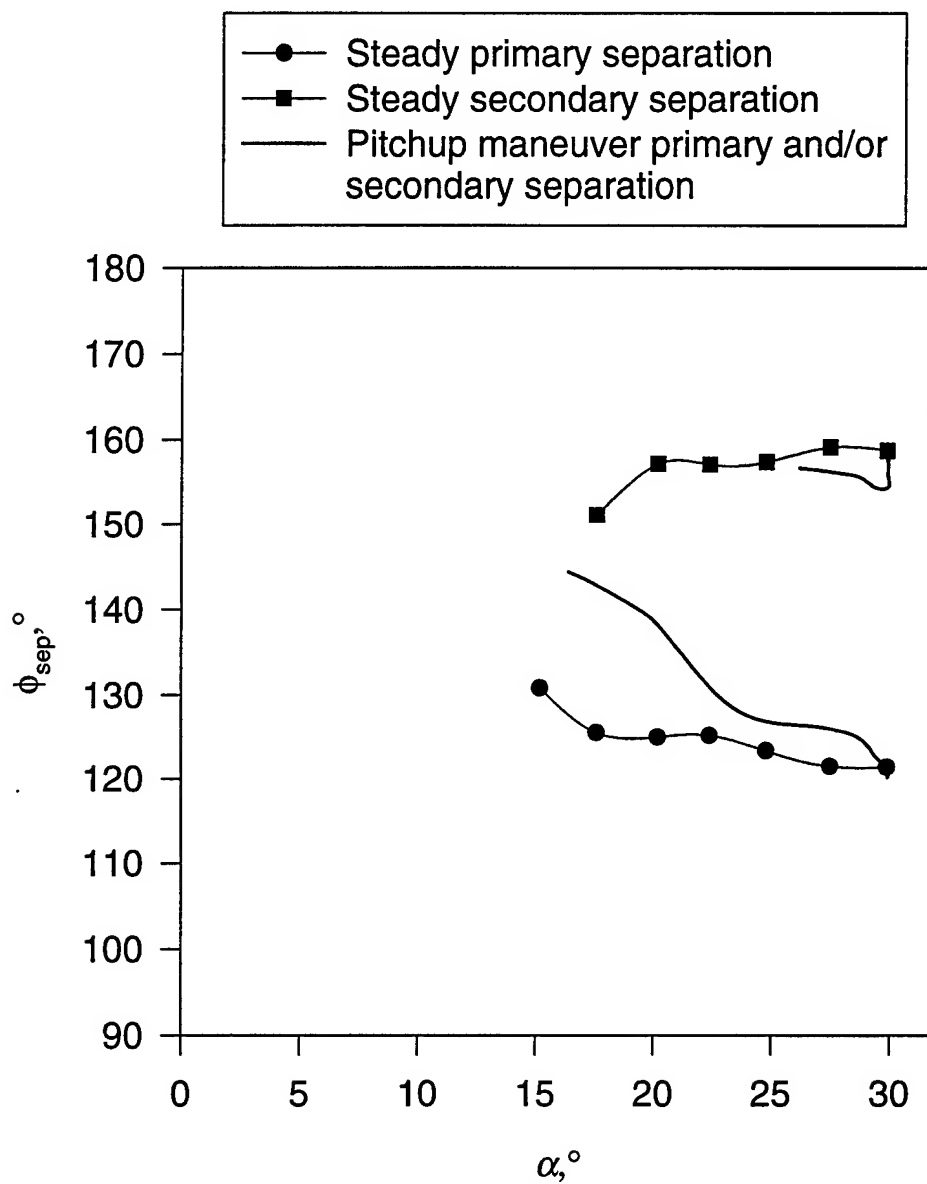


Figure 143. Separation position versus  $\alpha$  for pitch-up maneuver at  $x/L=0.194$  compared with quasi-steady separation positions.

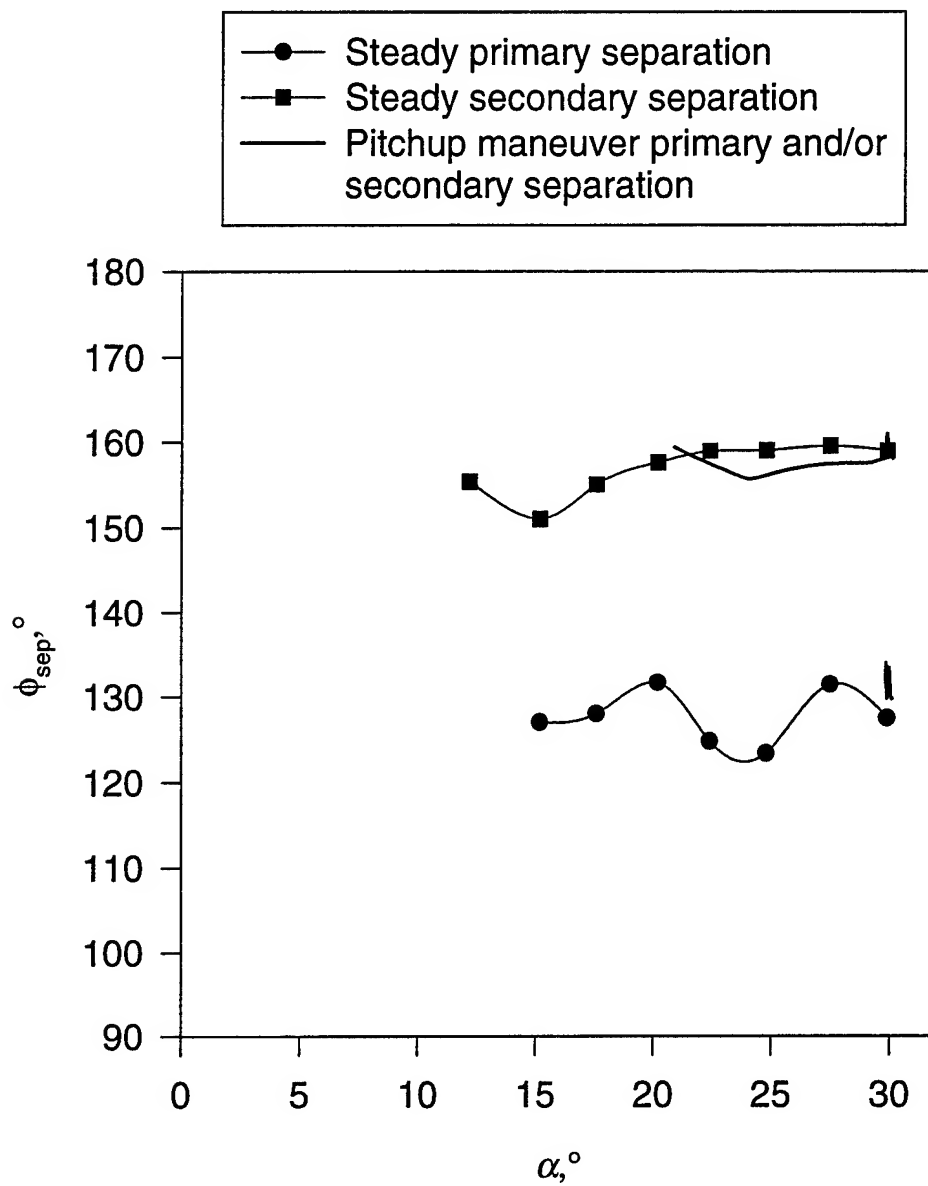


Figure 144. Separation position versus  $\alpha$  for pitch-up maneuver at  $x/L=0.220$  compared with quasi-steady separation positions.

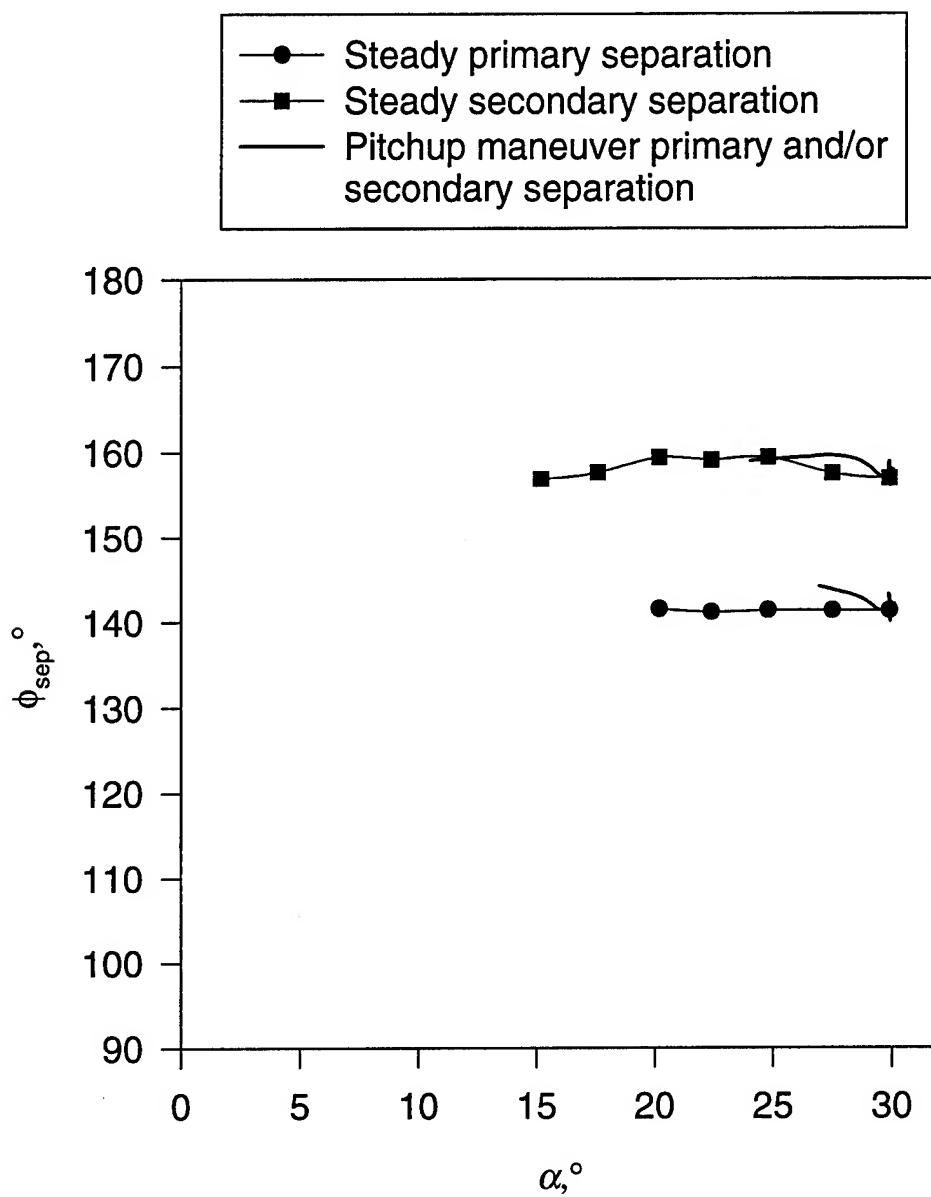


Figure 145. Separation position versus  $\alpha$  for pitch-up maneuver at  $x/L=0.271$  compared with quasi-steady separation positions.

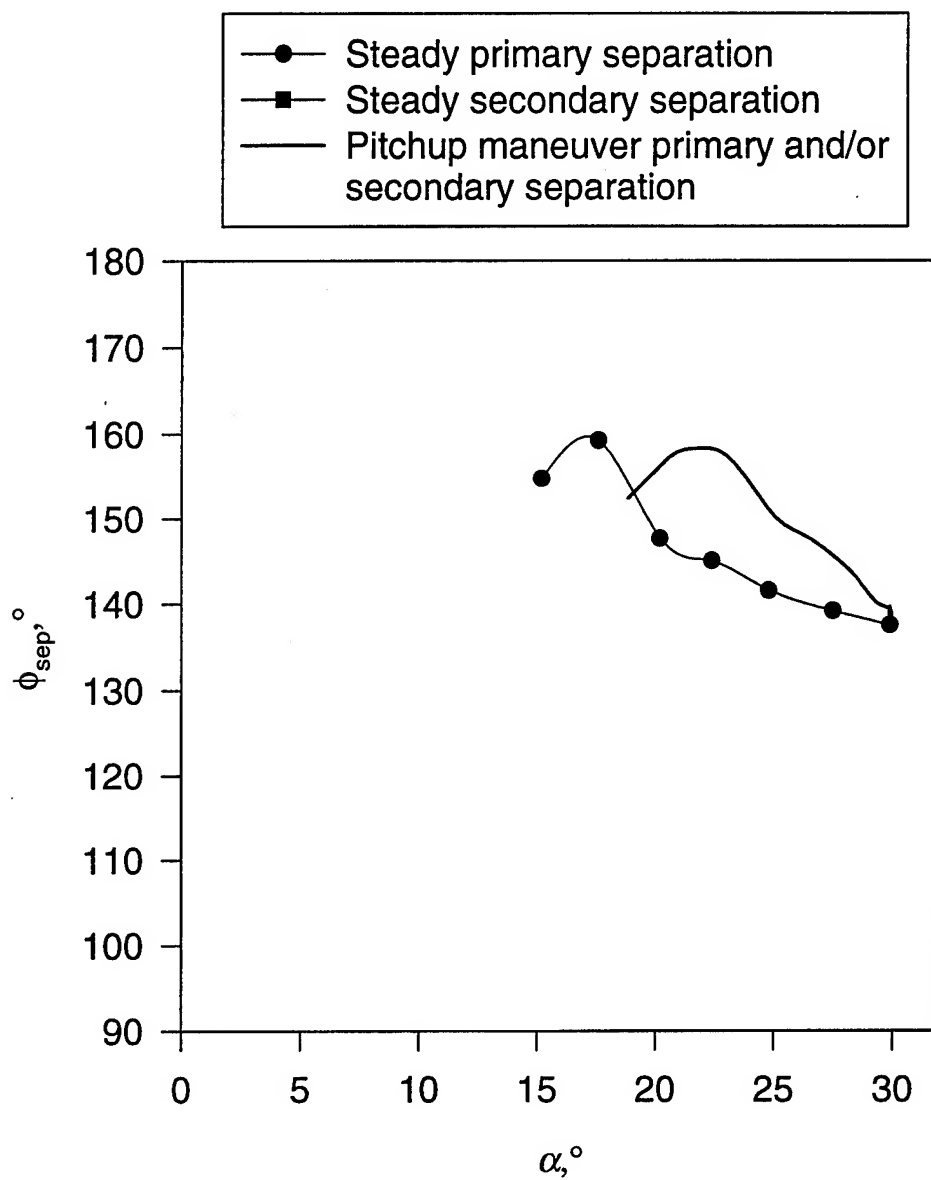


Figure 146. Separation position versus  $\alpha$  for pitch-up maneuver at  $x/L=0.347$  compared with quasi-steady separation positions.

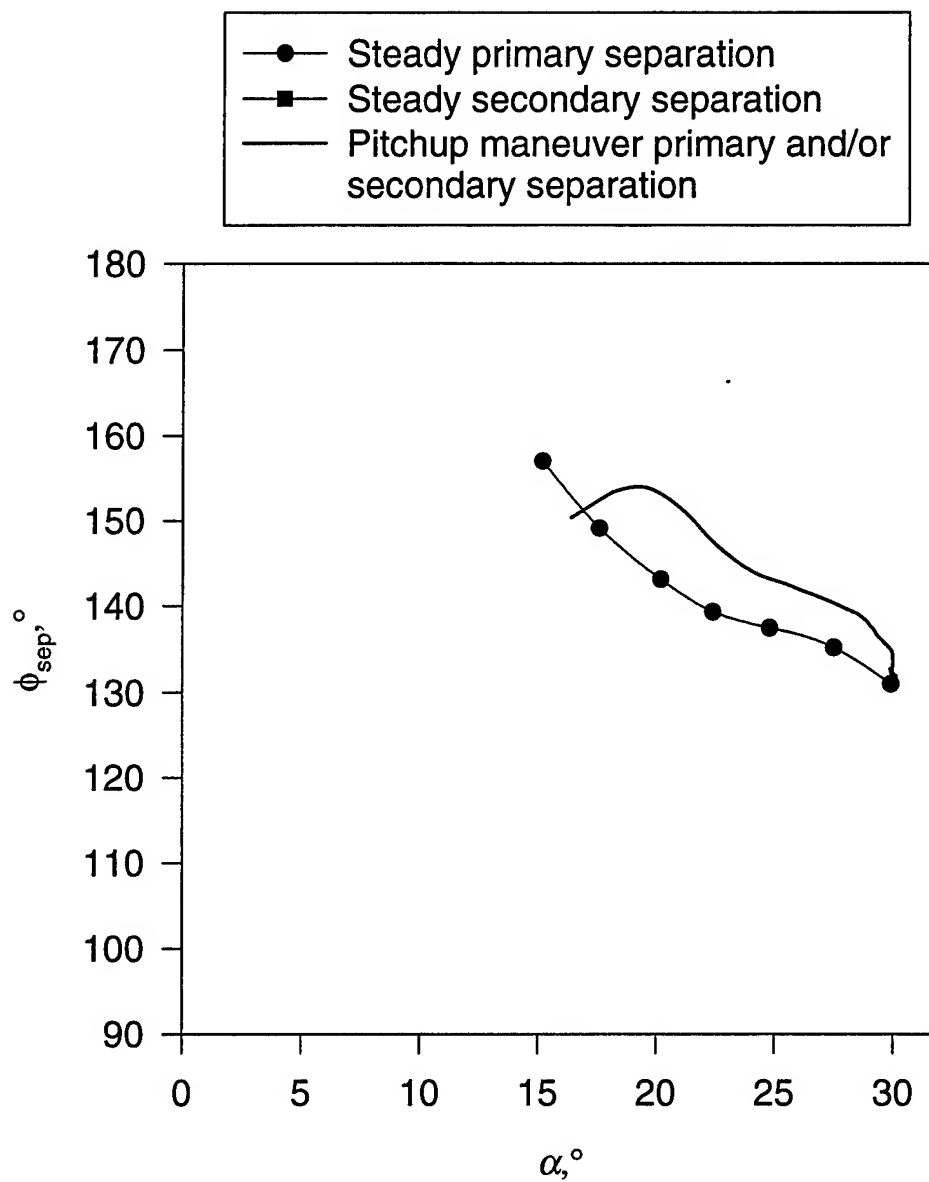


Figure 147. Separation position versus  $\alpha$  for pitch-up maneuver at  $x/L=0.424$  compared with quasi-steady separation positions.



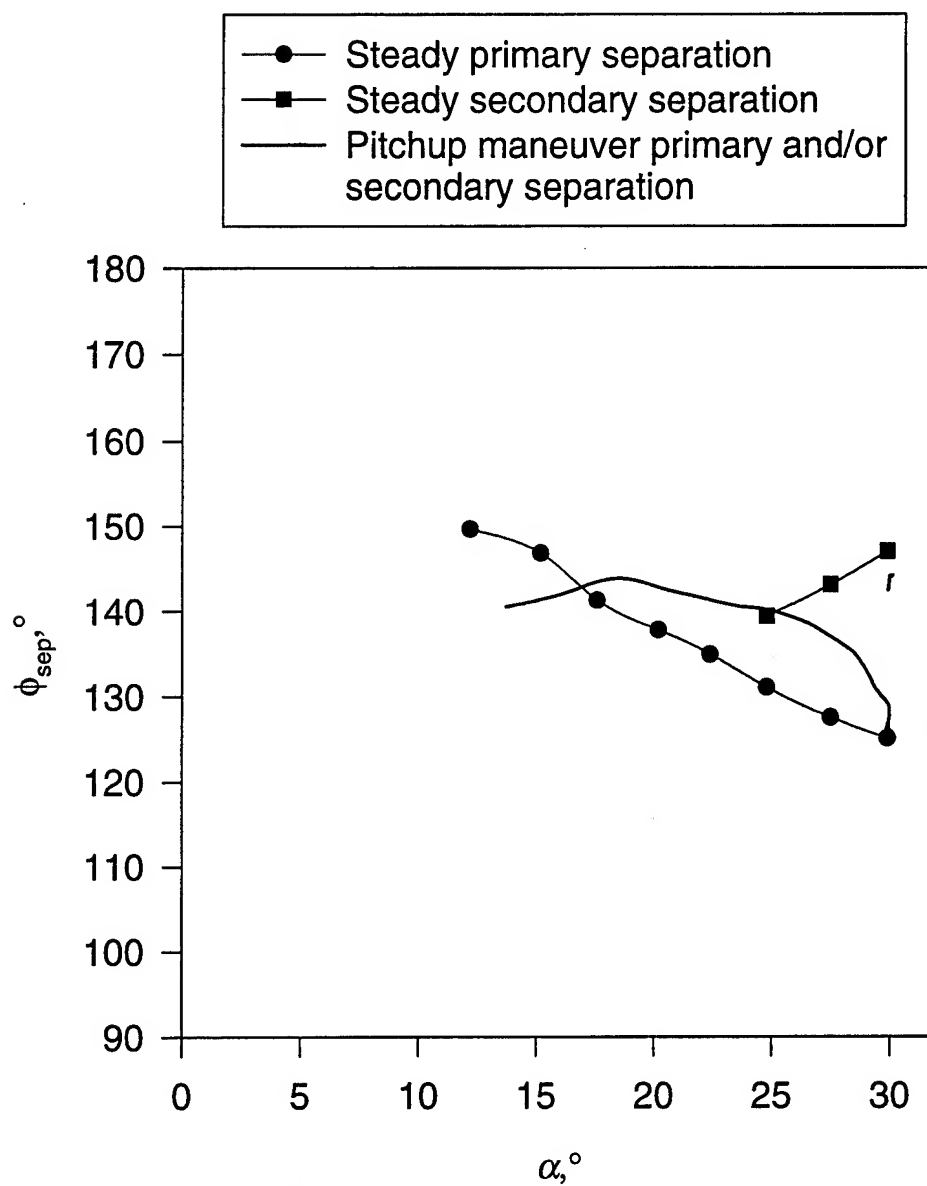


Figure 148. Separation position versus  $\alpha$  for pitch-up maneuver at  $x/L=0.500$  compared with quasi-steady separation positions.

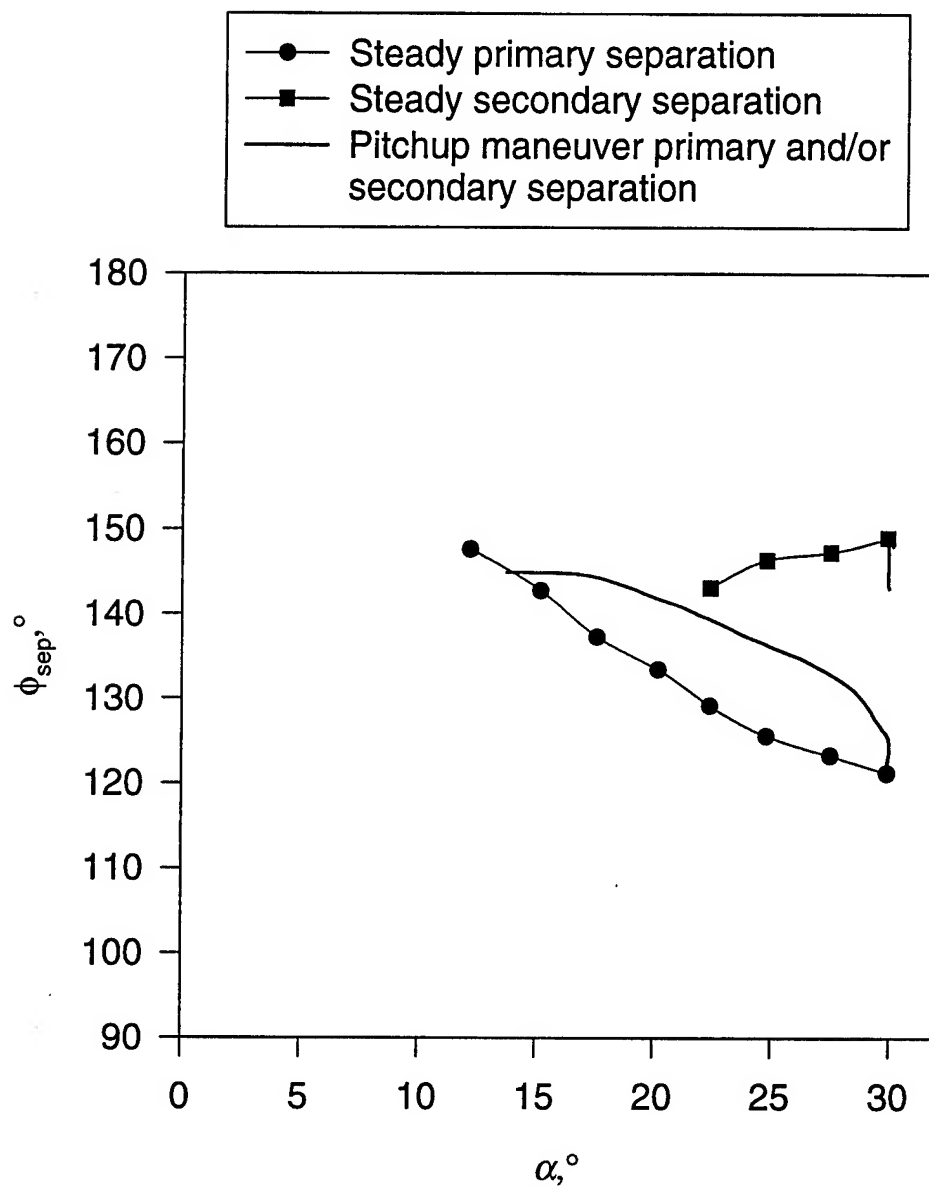


Figure 149. Separation position versus  $\alpha$  for pitch-up maneuver at  $x/L=0.576$  compared with quasi-steady separation positions.

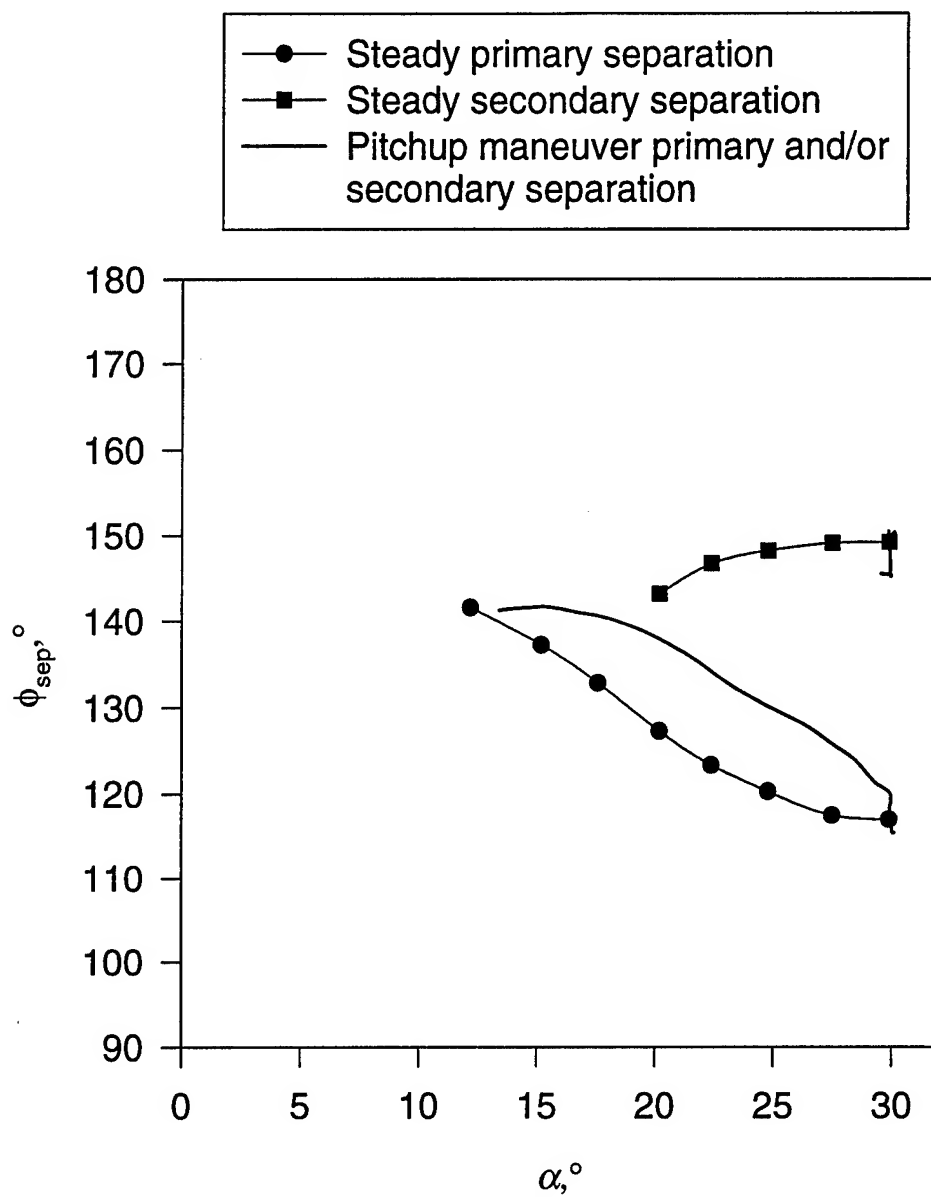


Figure 150. Separation position versus  $\alpha$  for pitch-up maneuver at  $x/L=0.653$  compared with quasi-steady separation positions.

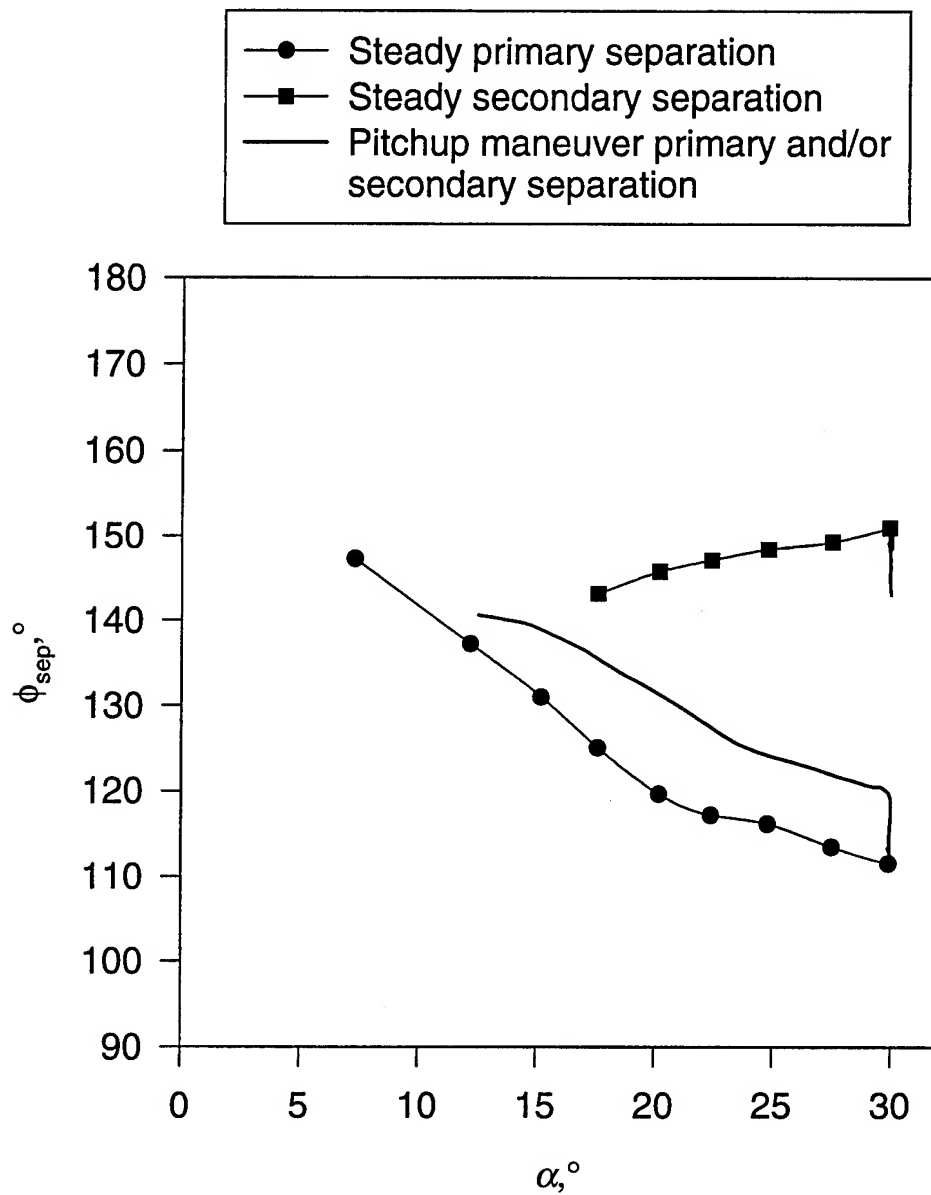


Figure 151. Separation position versus  $\alpha$  for pitch-up maneuver at  $x/L=0.729$  compared with quasi-steady separation positions.

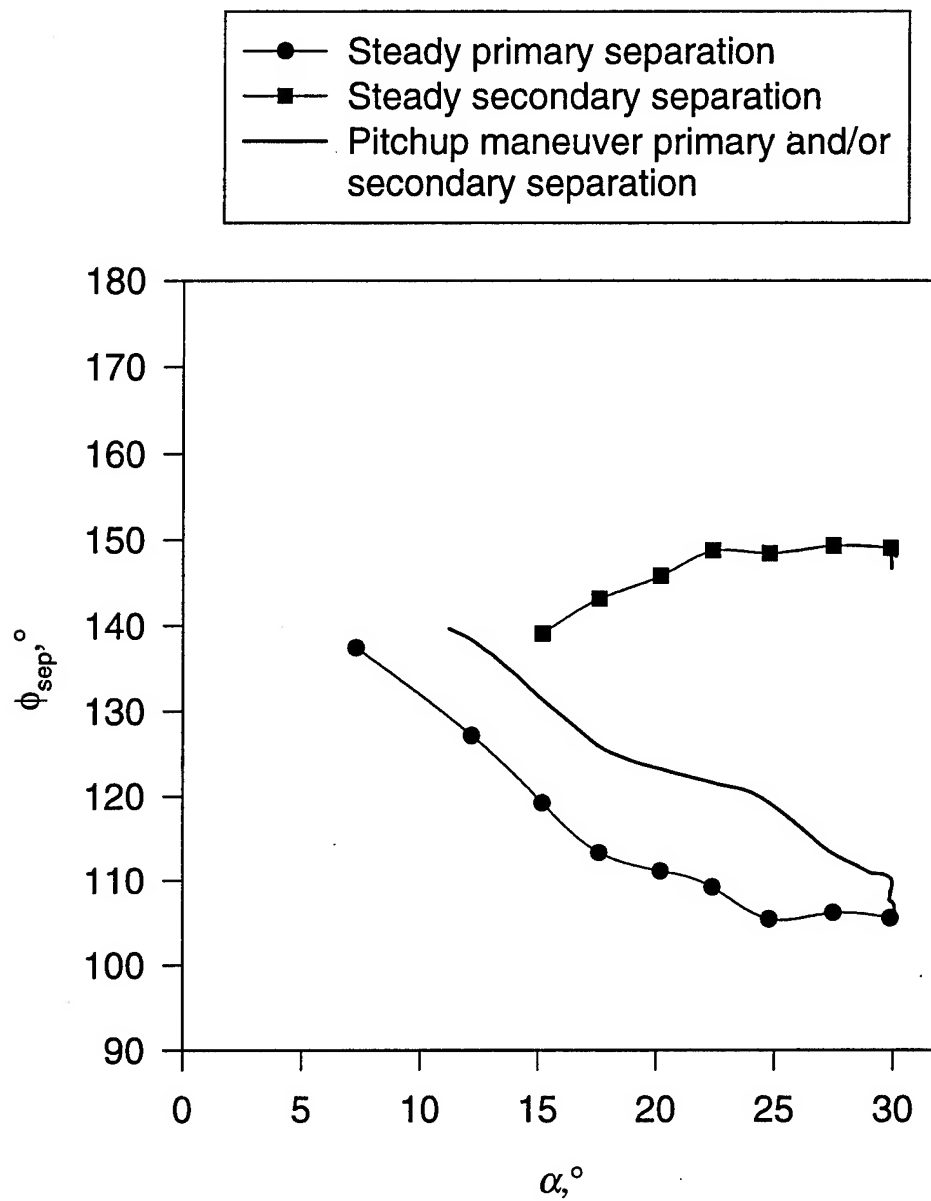


Figure 152. Separation position versus  $\alpha$  for pitch-up maneuver at  $x/L=0.831$  compared with quasi-steady separation positions.

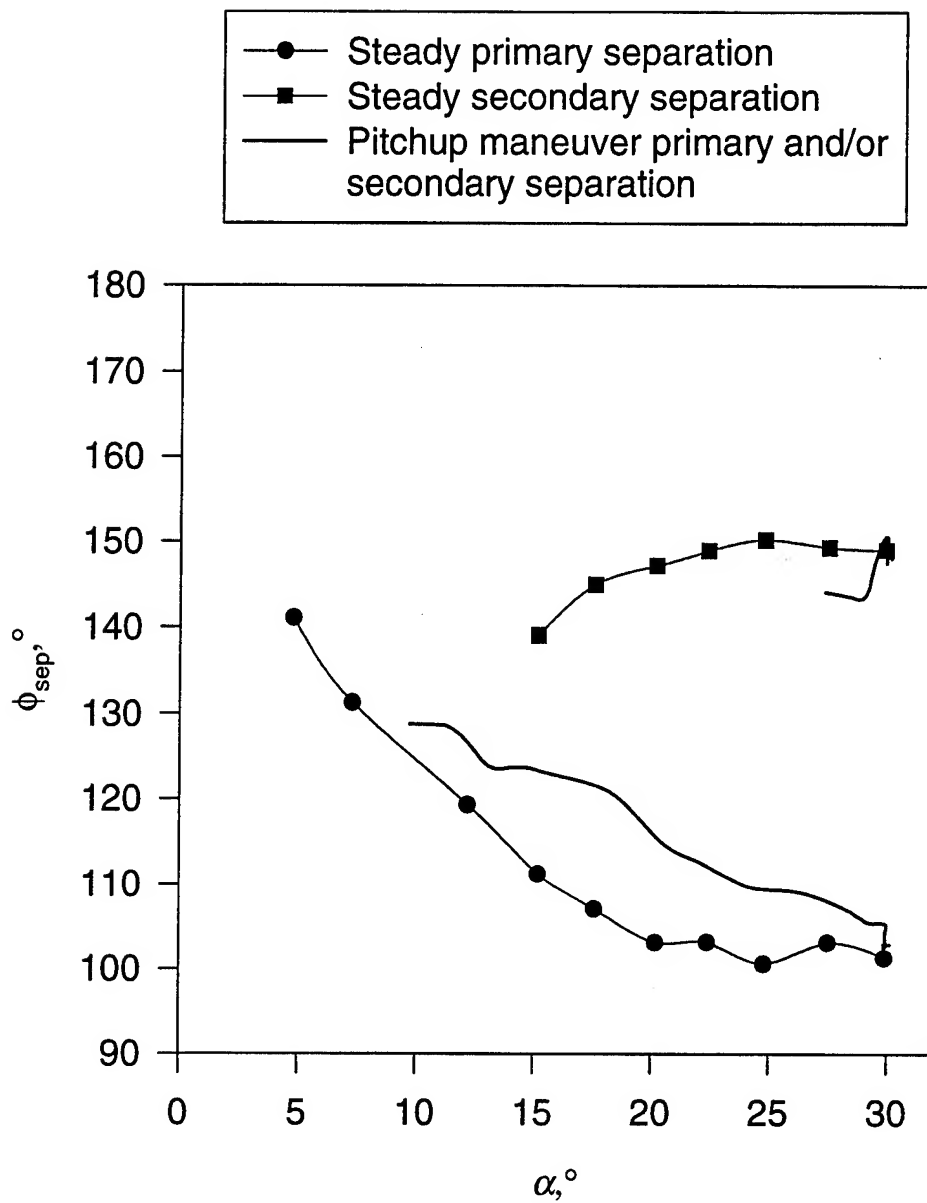


Figure 153. Separation position versus  $\alpha$  for pitch-up maneuver at  $x/L=0.882$  compared with quasi-steady separation positions.

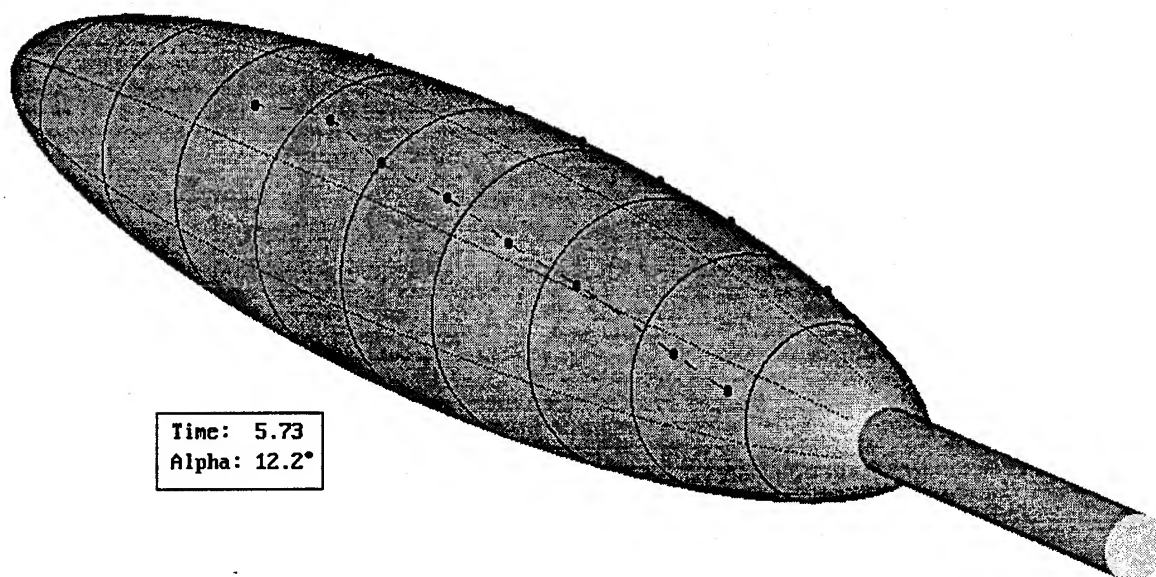


Figure 154. Comparison of steady and unsteady separation lines at  $\alpha=12.2^\circ$ . Dashed lines are equivalent steady separation lines, solid lines are instantaneous separation lines.

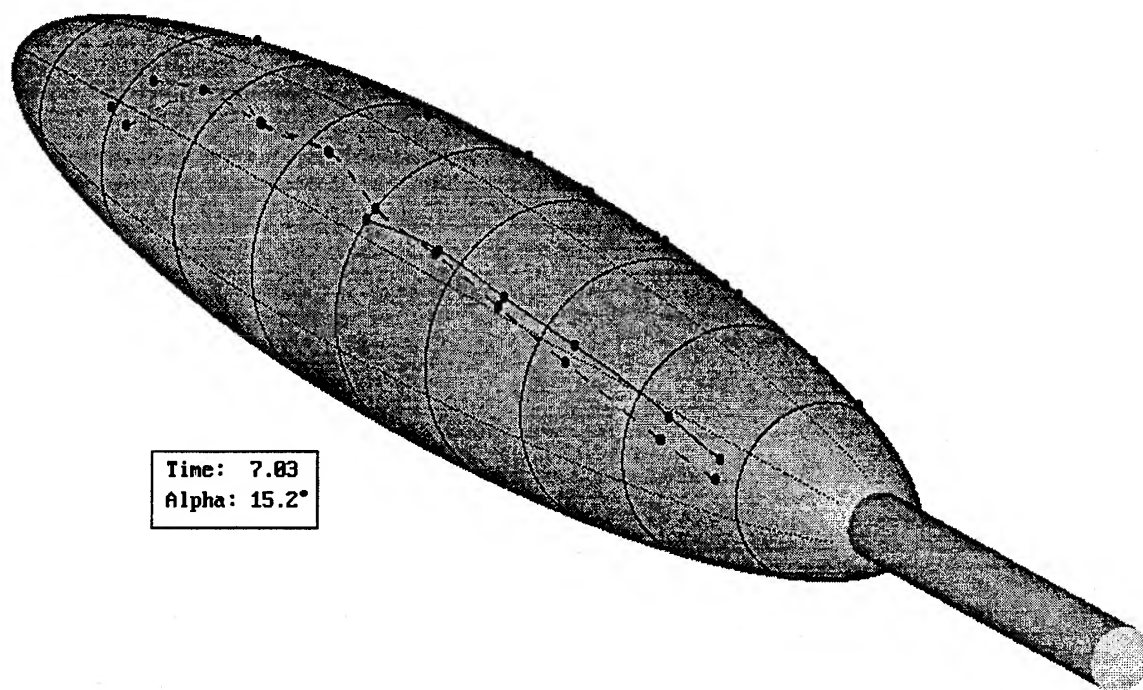


Figure 155. Comparison of steady and unsteady separation lines at  $\alpha=15.2^\circ$ . Dashed lines are equivalent steady separation lines, solid lines are instantaneous separation lines.



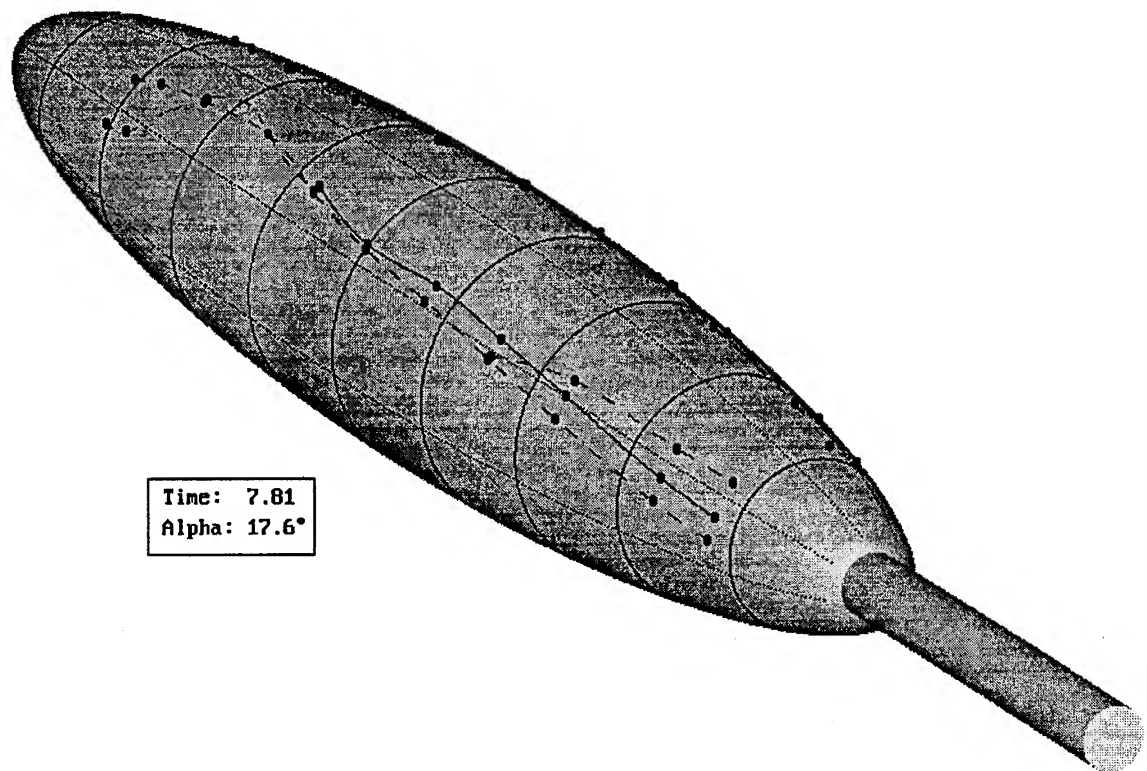


Figure 156. Comparison of steady and unsteady separation lines at  $\alpha=17.6^\circ$ . Dashed lines are equivalent steady separation lines, solid lines are instantaneous separation lines.

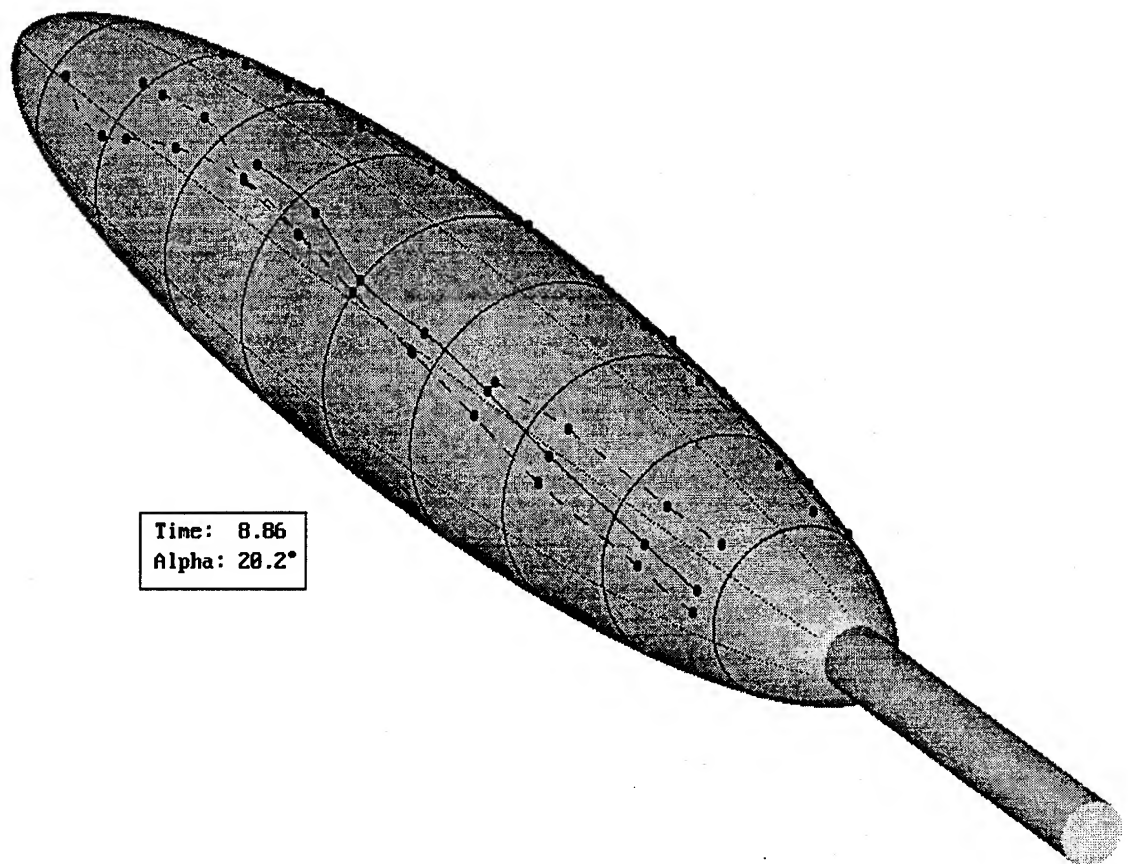


Figure 157. Comparison of steady and unsteady separation lines at  $\alpha=20.2^\circ$ . Dashed lines are equivalent steady separation lines, solid lines are instantaneous separation lines.

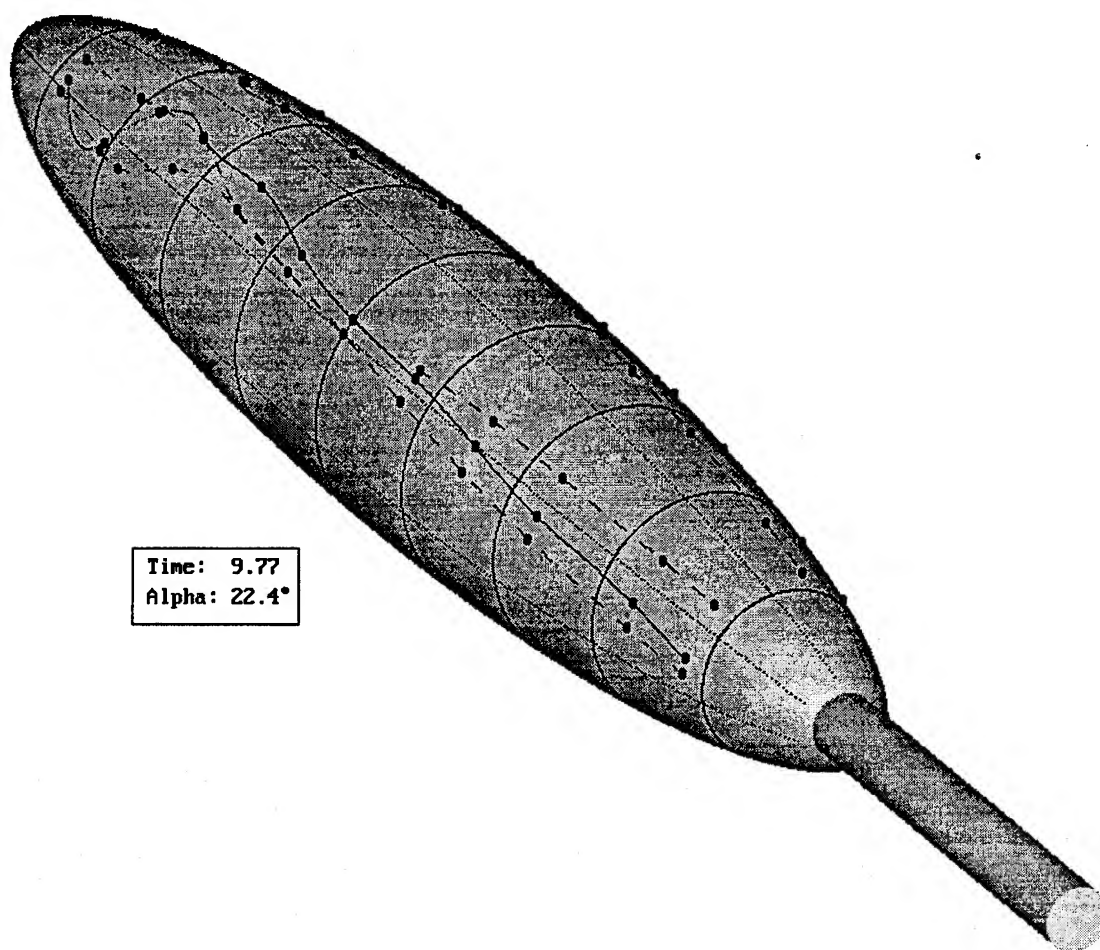


Figure 158. Comparison of steady and unsteady separation lines at  $\alpha=22.4^\circ$ . Dashed lines are equivalent steady separation lines, solid lines are instantaneous separation lines.

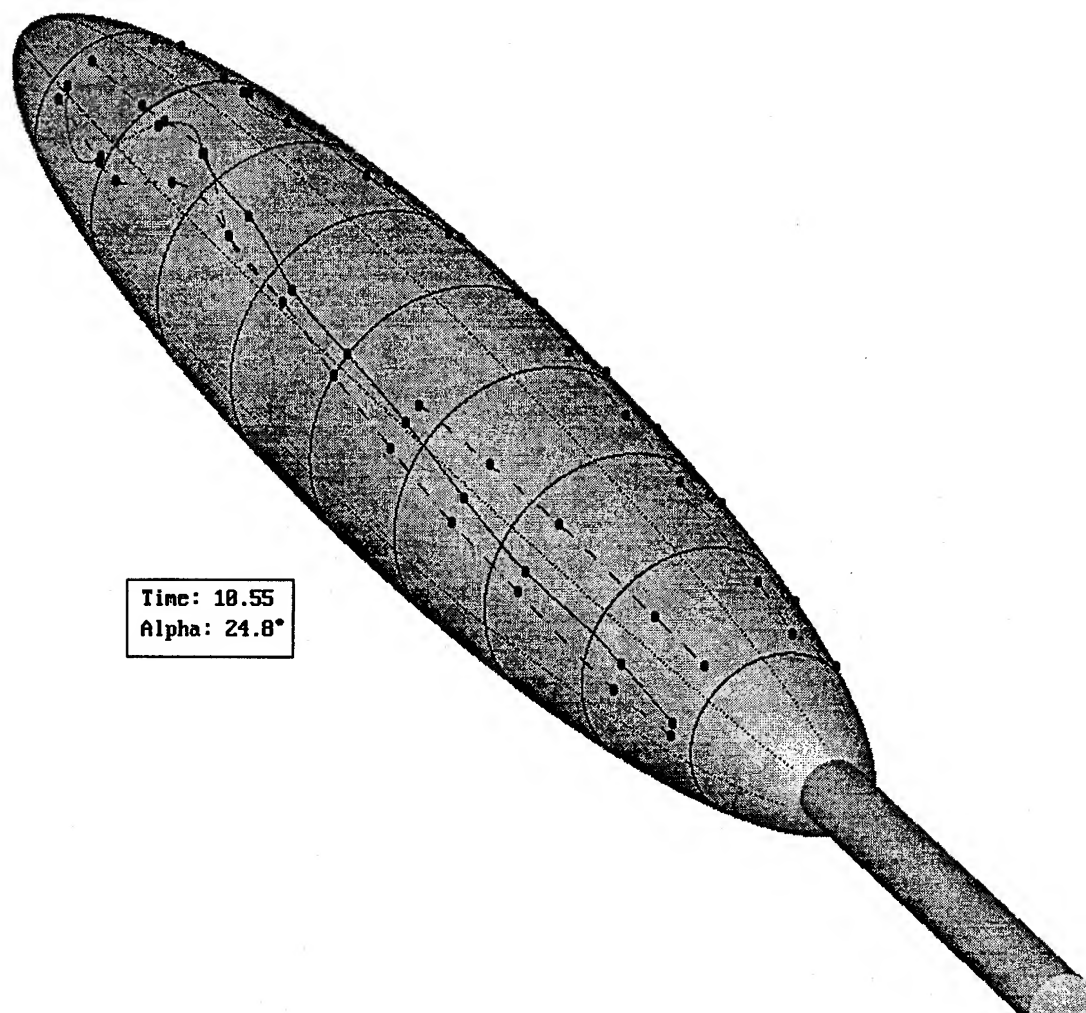


Figure 159. Comparison of steady and unsteady separation lines at  $\alpha=24.8^\circ$ . Dashed lines are equivalent steady separation lines, solid lines are instantaneous separation lines.

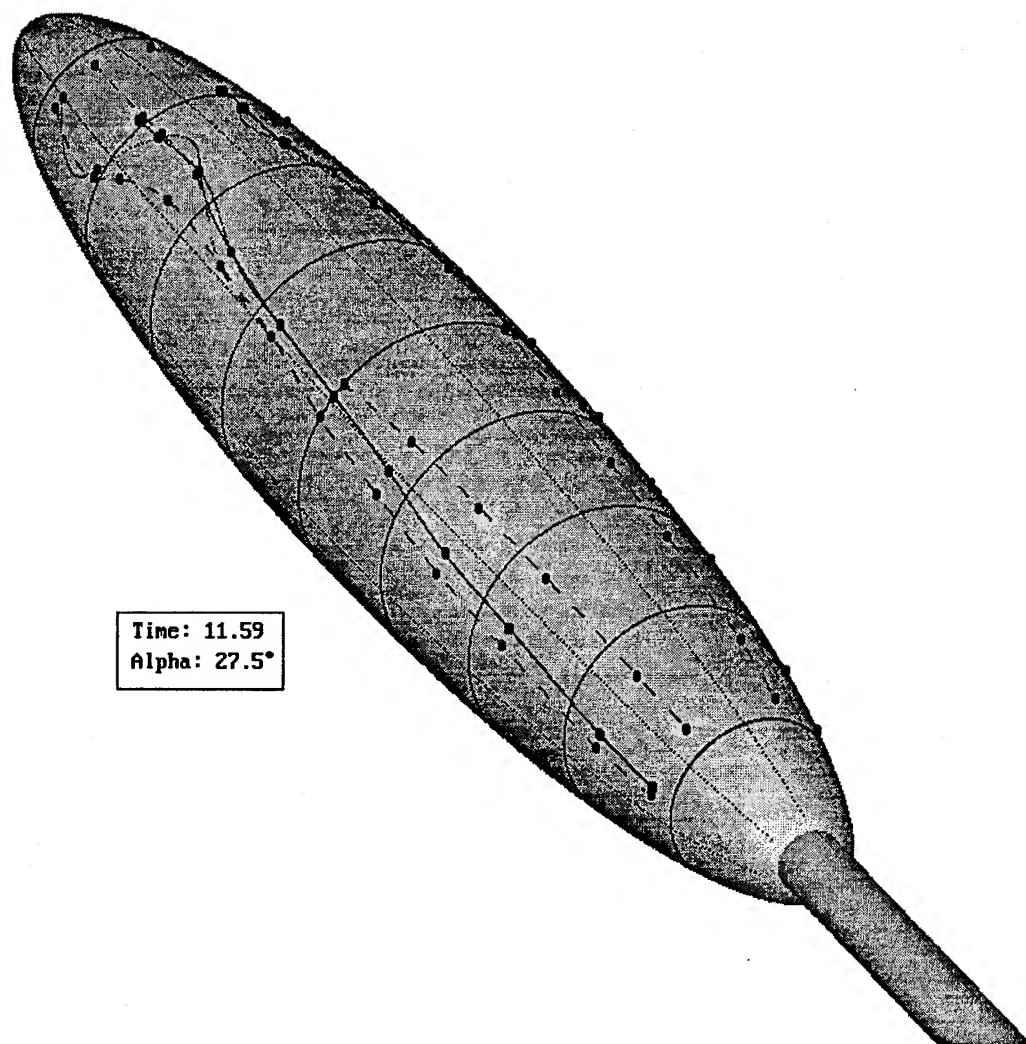


Figure 160. Comparison of steady and unsteady separation lines at  $\alpha=27.5^\circ$ . Dashed lines are equivalent steady separation lines, solid lines are instantaneous separation lines.

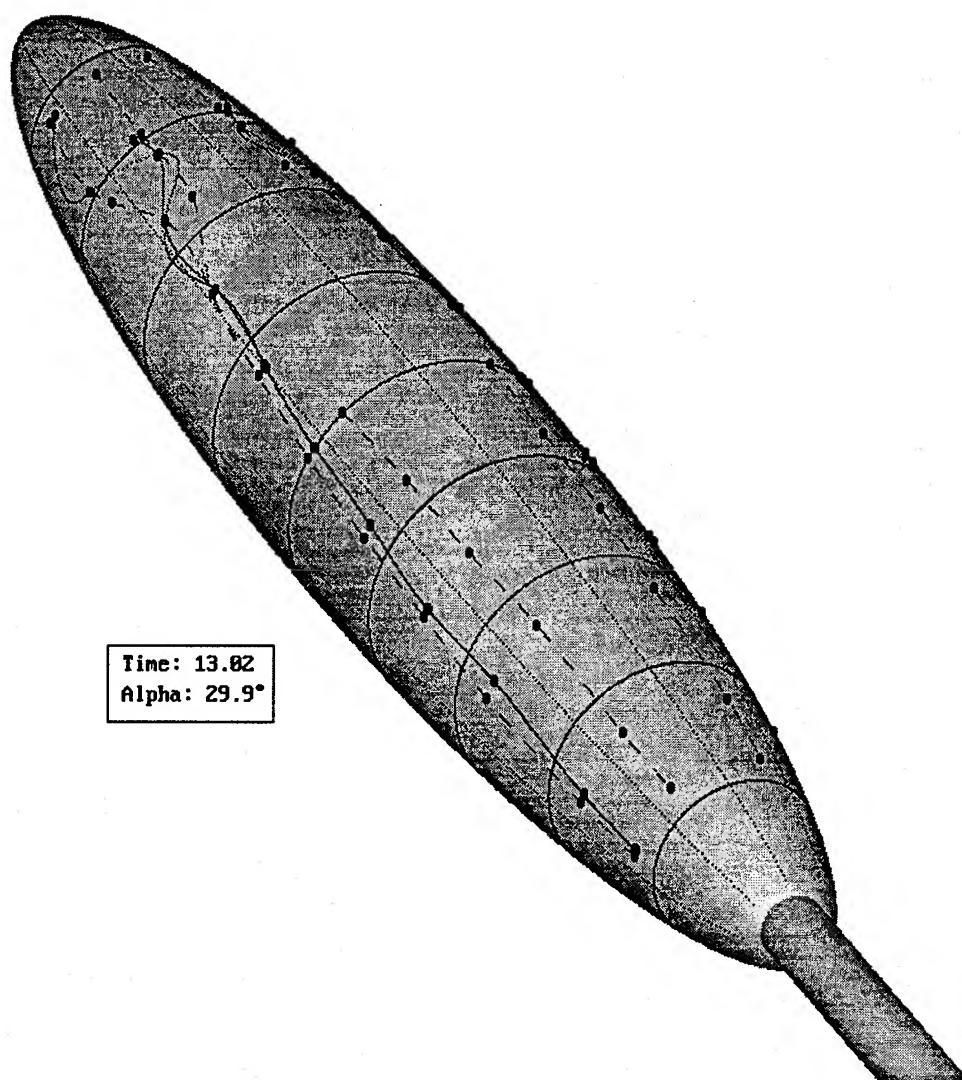


Figure 161. Comparison of steady and unsteady separation lines at  $\alpha=29.9^\circ$ . Dashed lines are equivalent steady separation lines, solid lines are instantaneous separation lines.

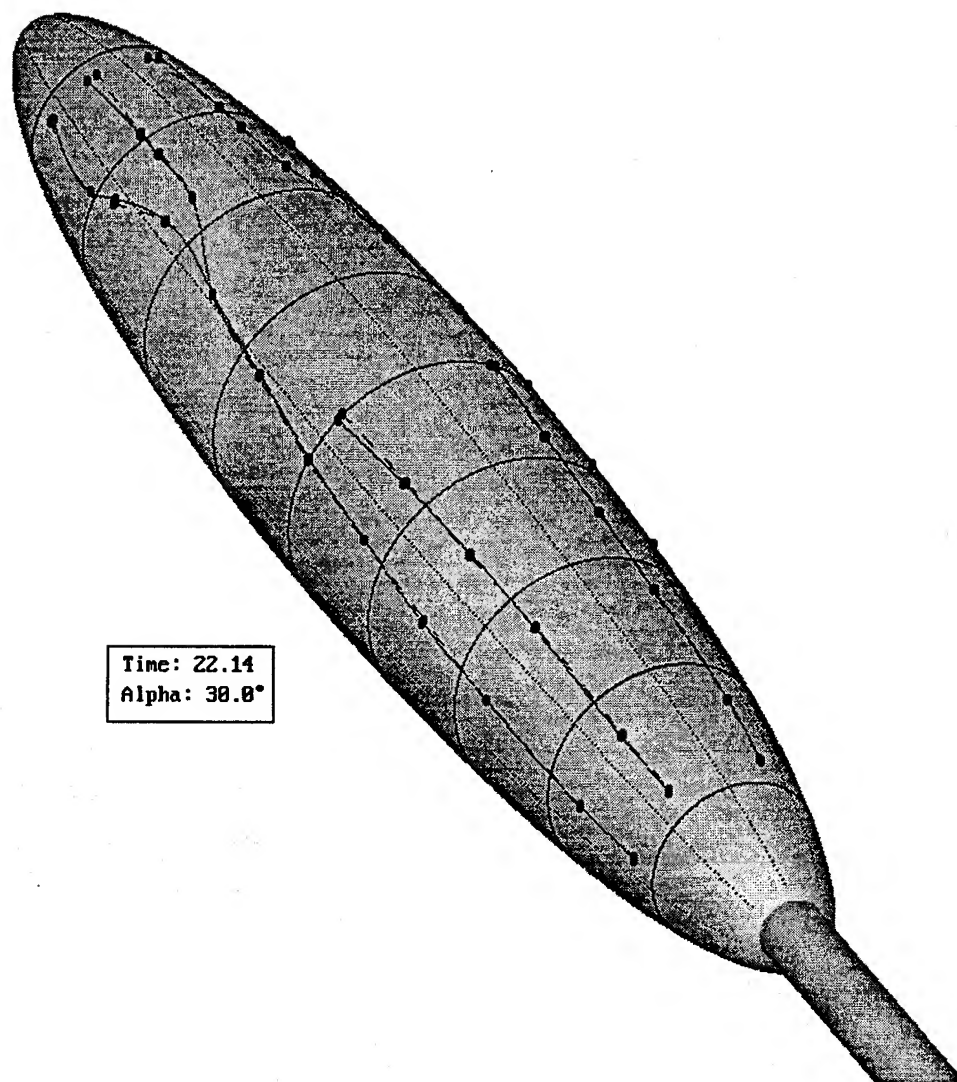


Figure 162. Comparison of steady and unsteady separation lines at  $\alpha=29.9^\circ$  at the end of the time record. Dashed lines are equivalent steady separation lines, solid lines are instantaneous separation lines.

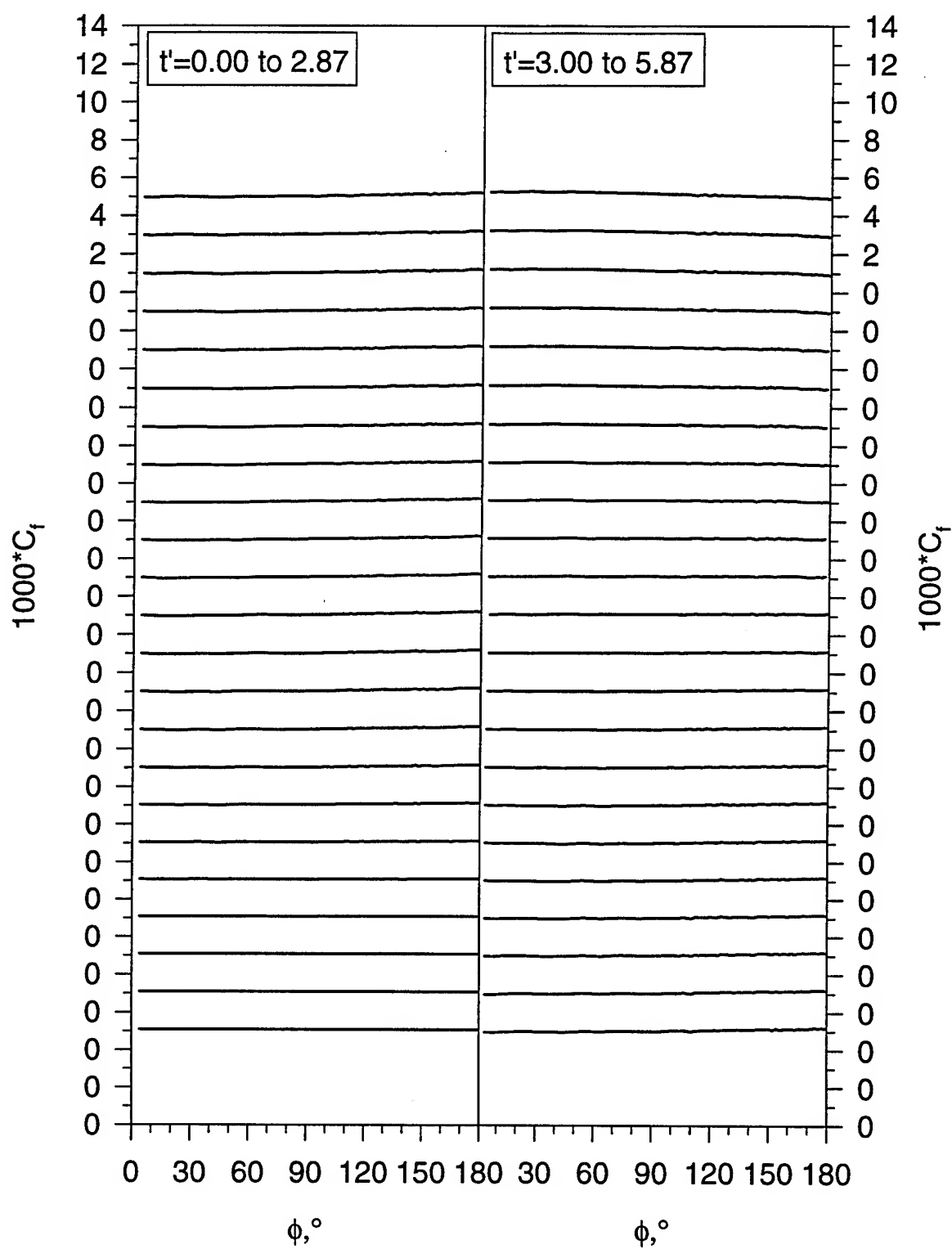


Figure 163.(a) Submarine maneuver time development of  $C_f$  vs.  $\phi$  for  $x/L=0.424$ .



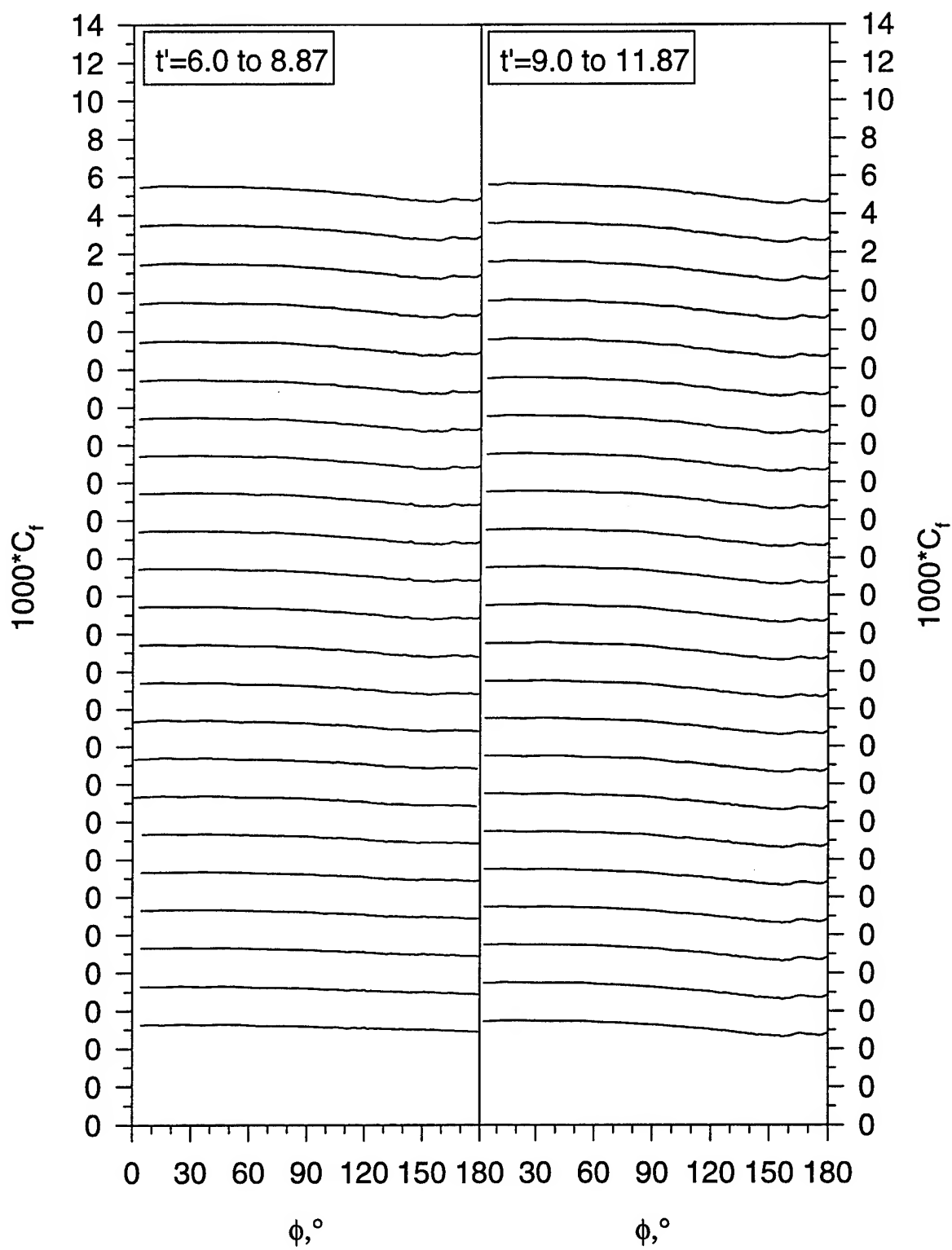


Figure 163. (b) Submarine maneuver time development of  $C_f$  vs.  $\phi$  for  $x/L=0.424$ .

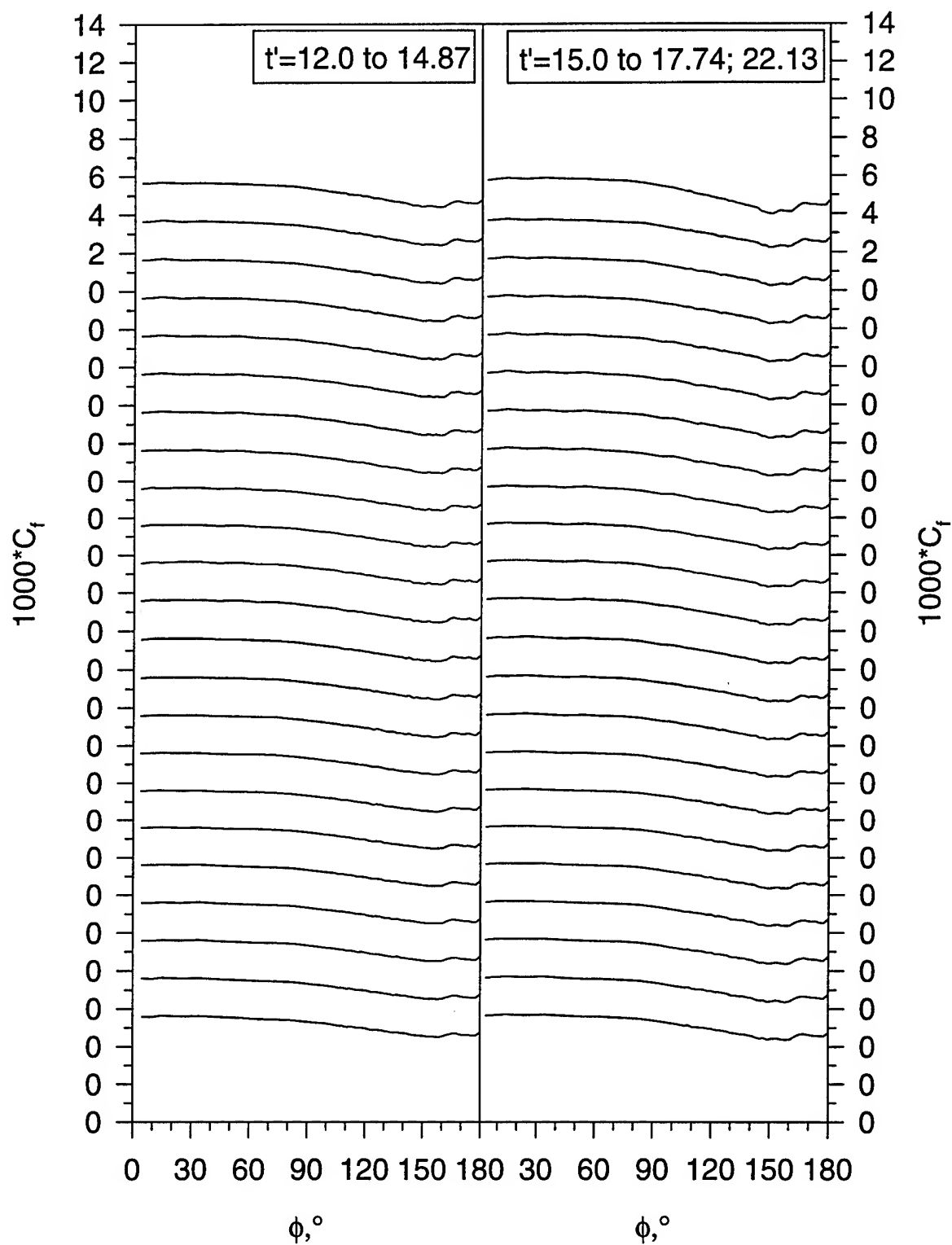


Figure 163. (c) Submarine maneuver time development of  $C_f$  vs.  $\phi$  for  $x/L=0.424$ .

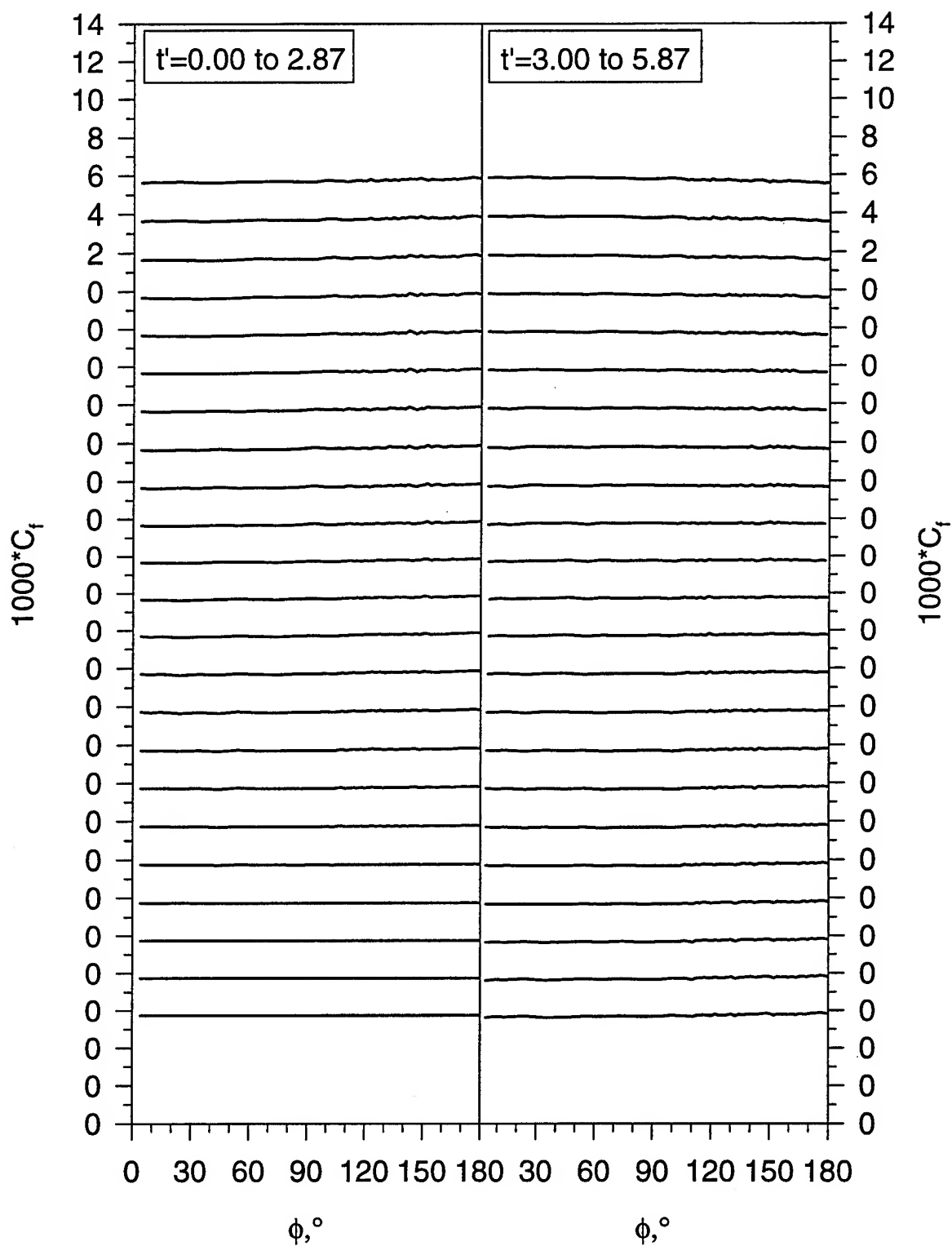


Figure 164.(a) Submarine maneuver time development of  $C_f$  vs.  $\phi$  for  $x/L=0.500$ .

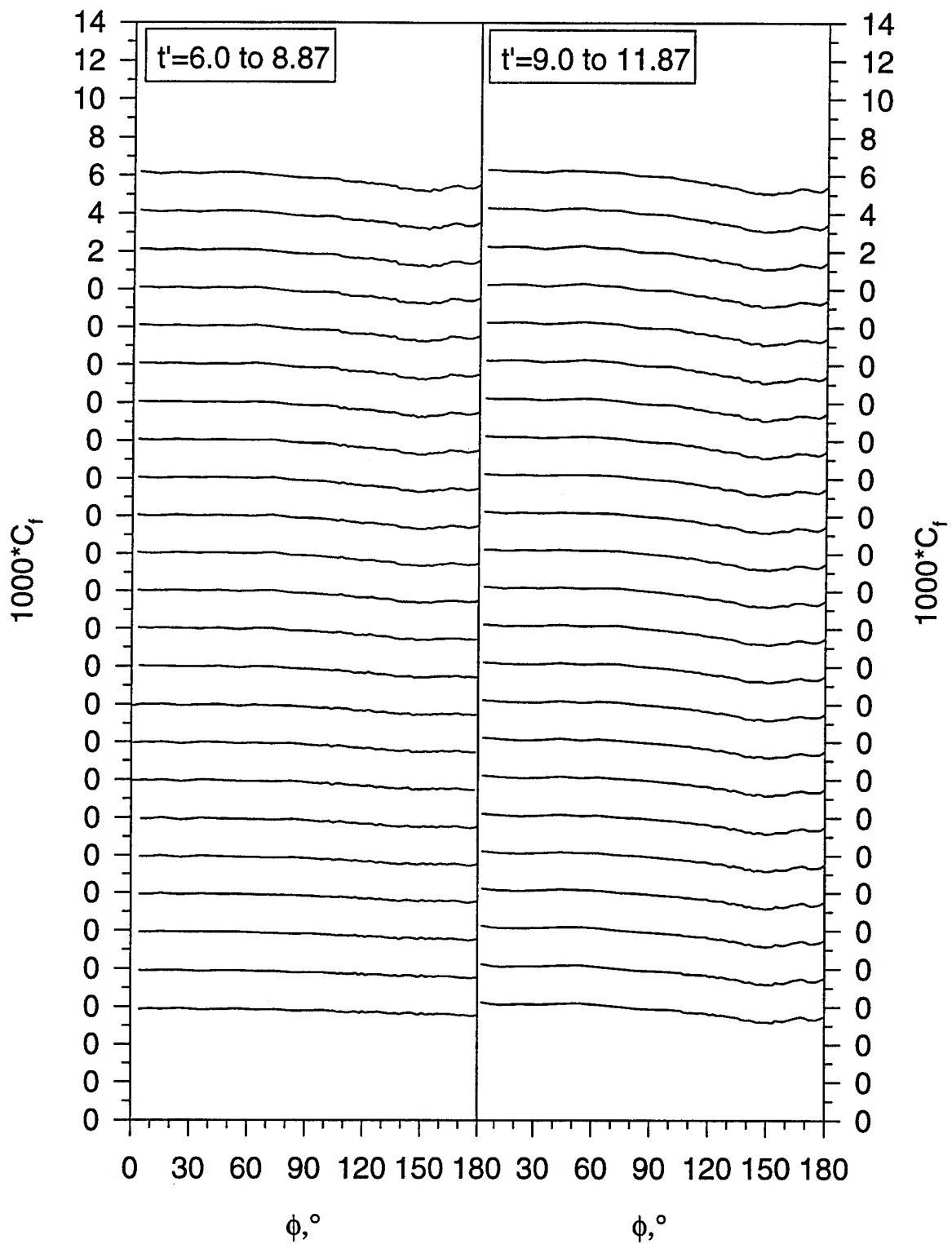


Figure 164. (b) Submarine maneuver time development of  $C_f$  vs.  $\phi$  for  $x/L=0.500$ .

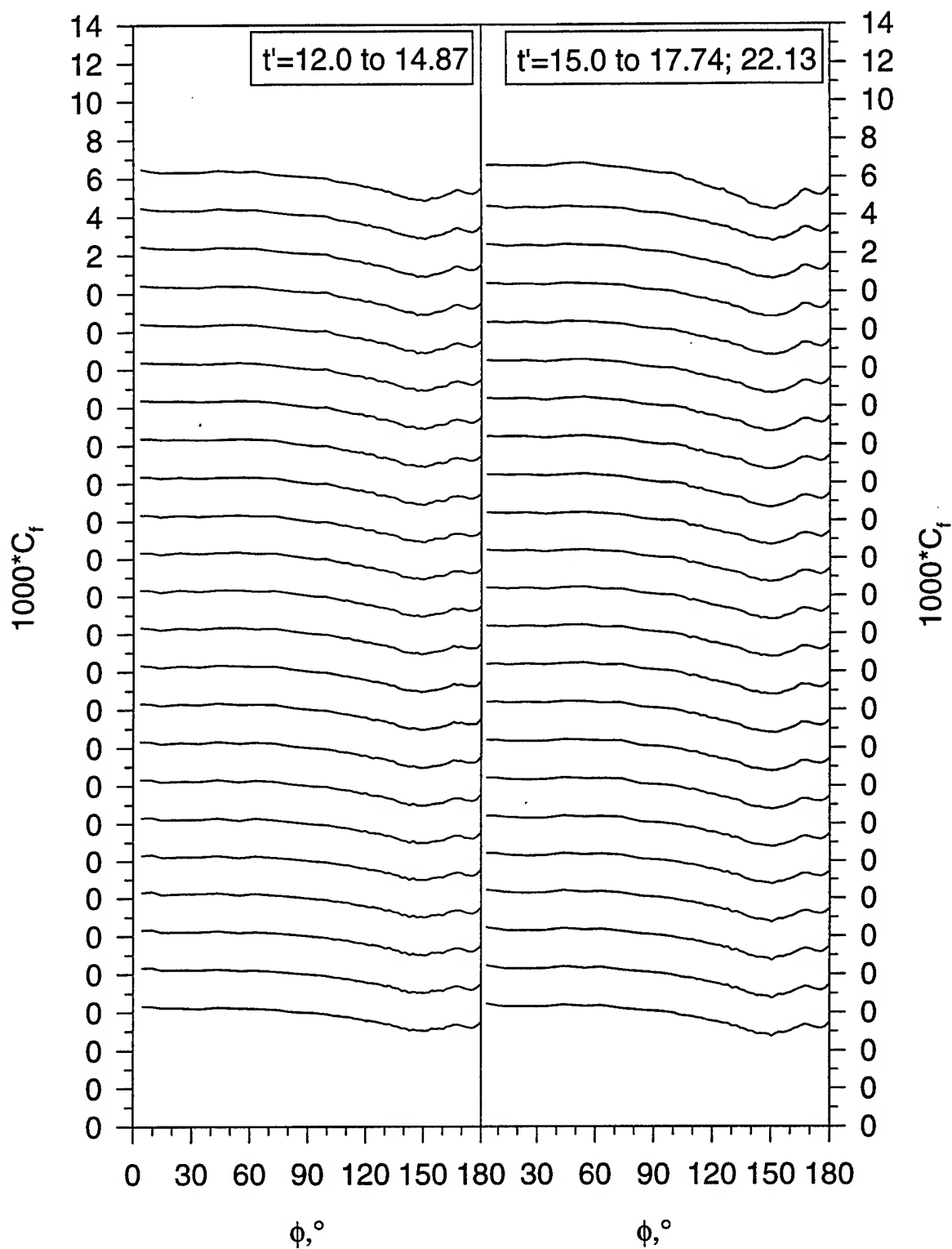


Figure 164. (c) Submarine maneuver time development of  $C_f$  vs.  $\phi$  for  $x/L=0.500$ .

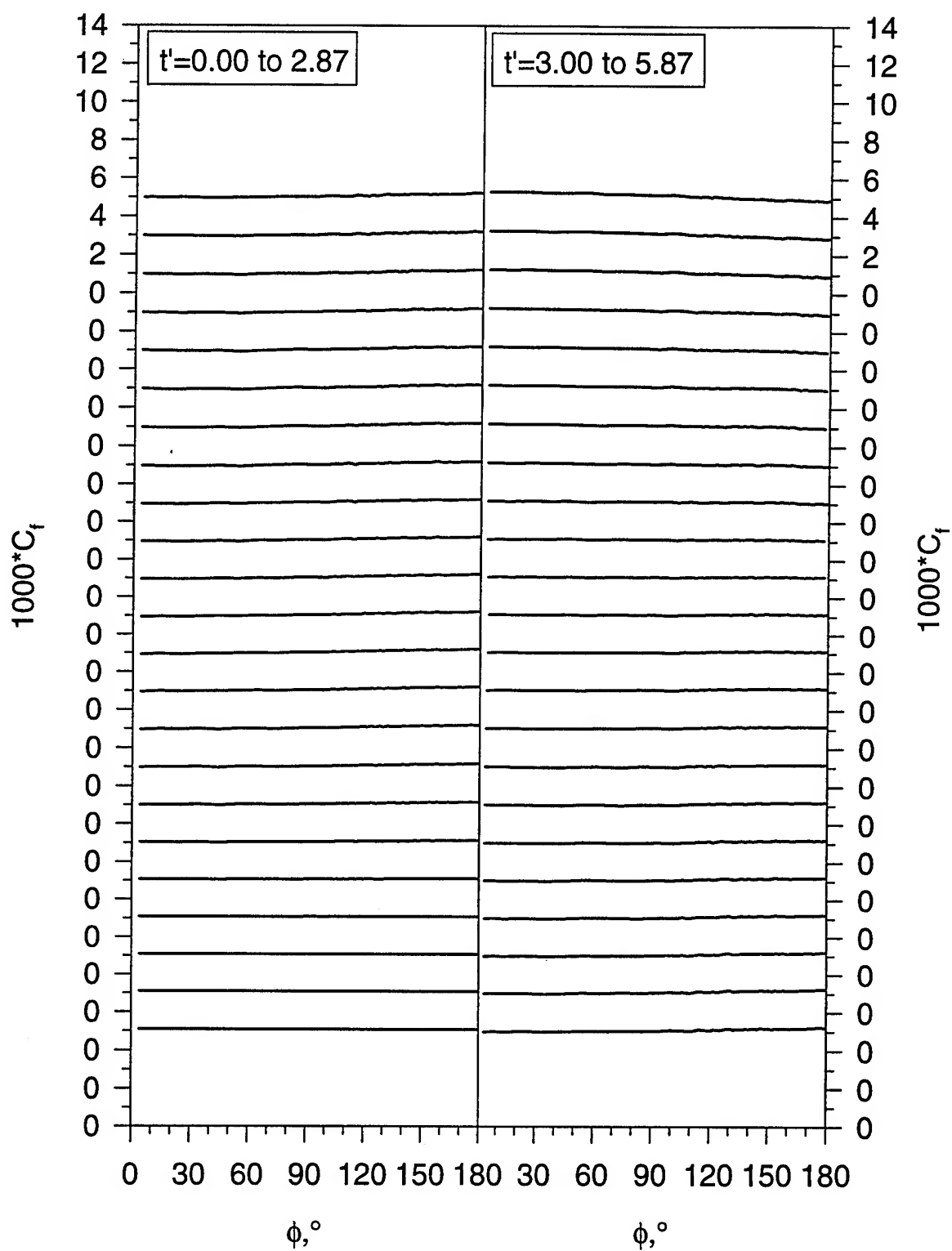


Figure 165.(a) Submarine maneuver time development of  $C_f$  vs.  $\phi$  for  $x/L=0.576$ .

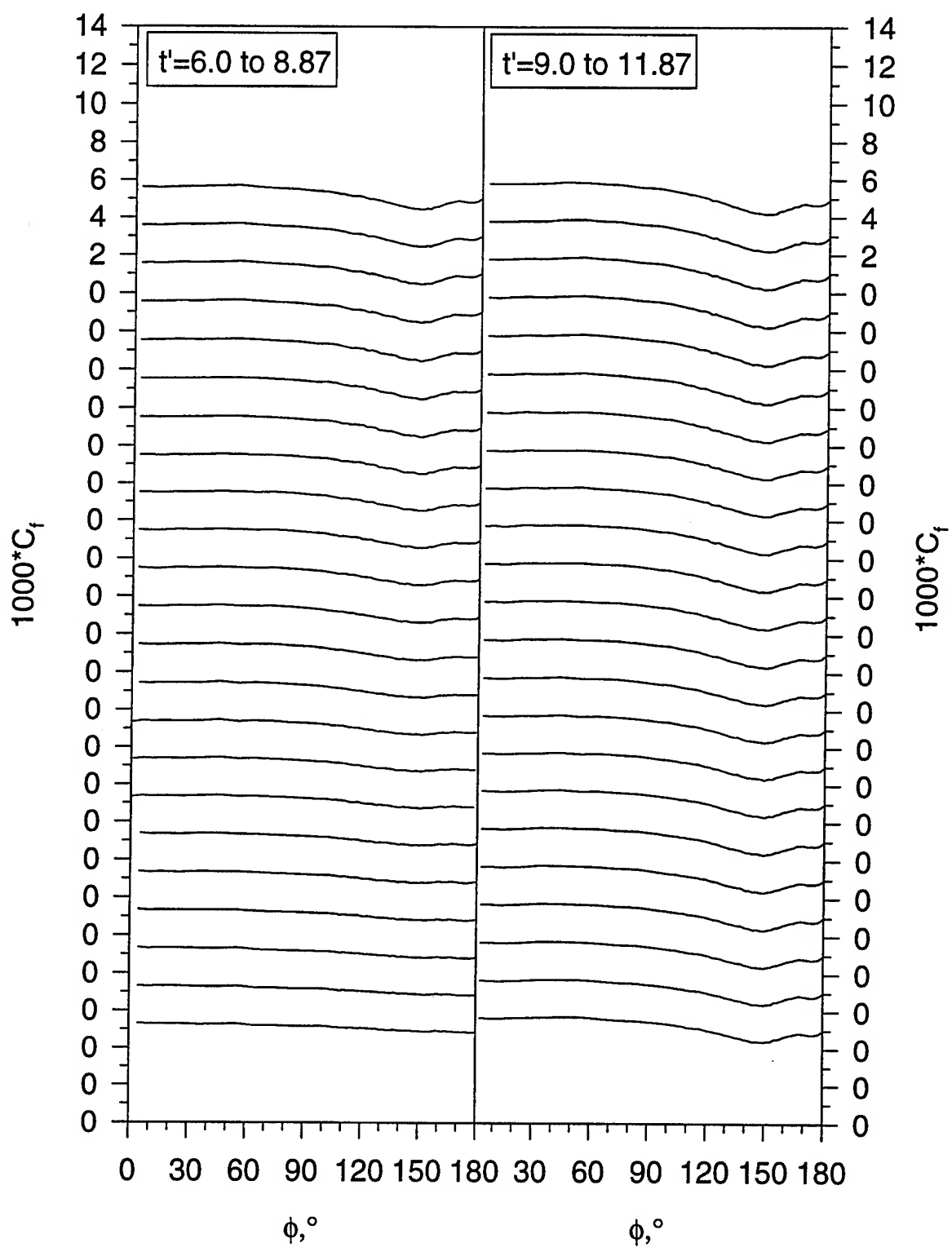


Figure 165. (b) Submarine maneuver time development of  $C_f$  vs.  $\phi$  for  $x/L=0.576$ .

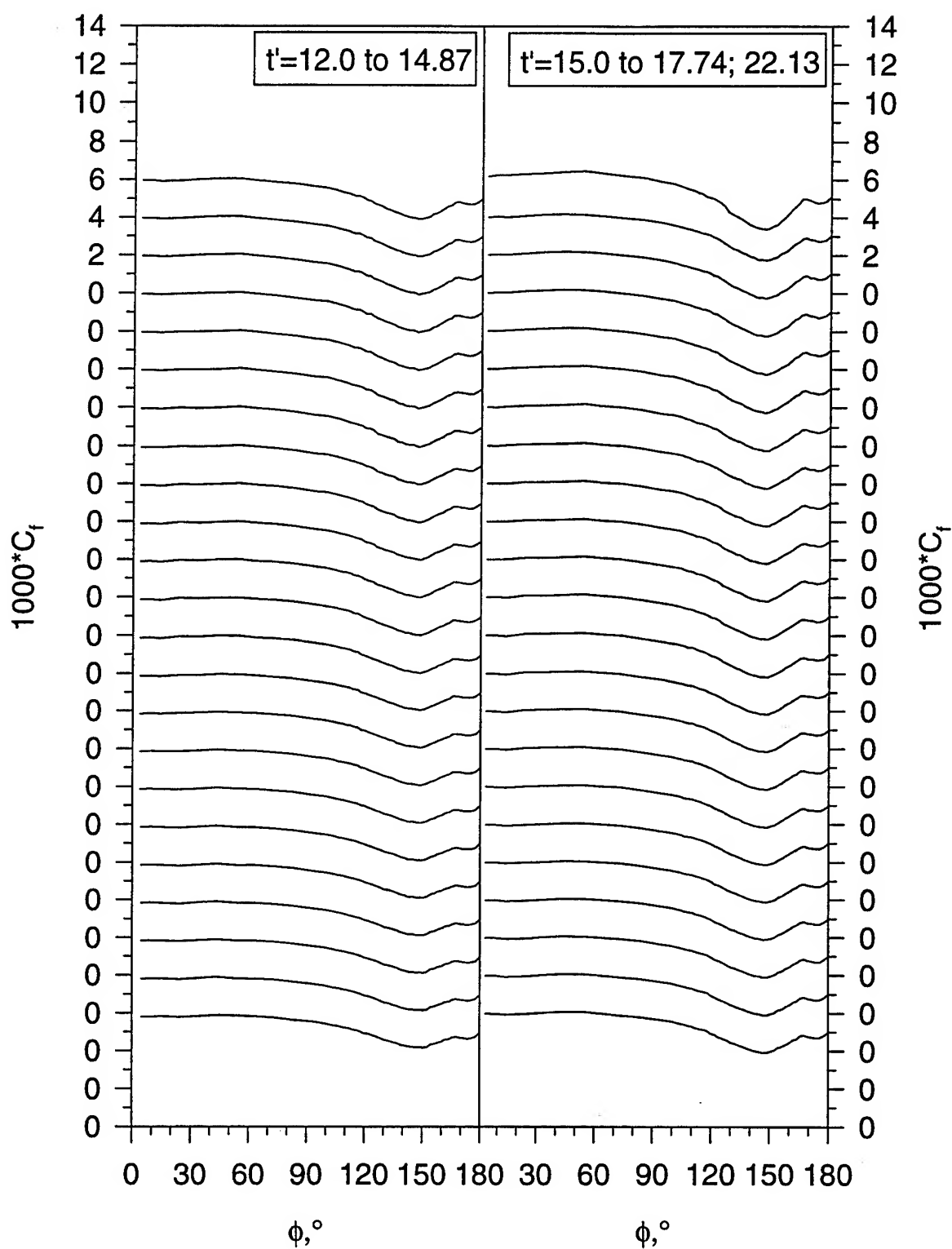


Figure 165. (c) Submarine maneuver time development of  $C_f$  vs.  $\phi$  for  $x/L=0.576$ .



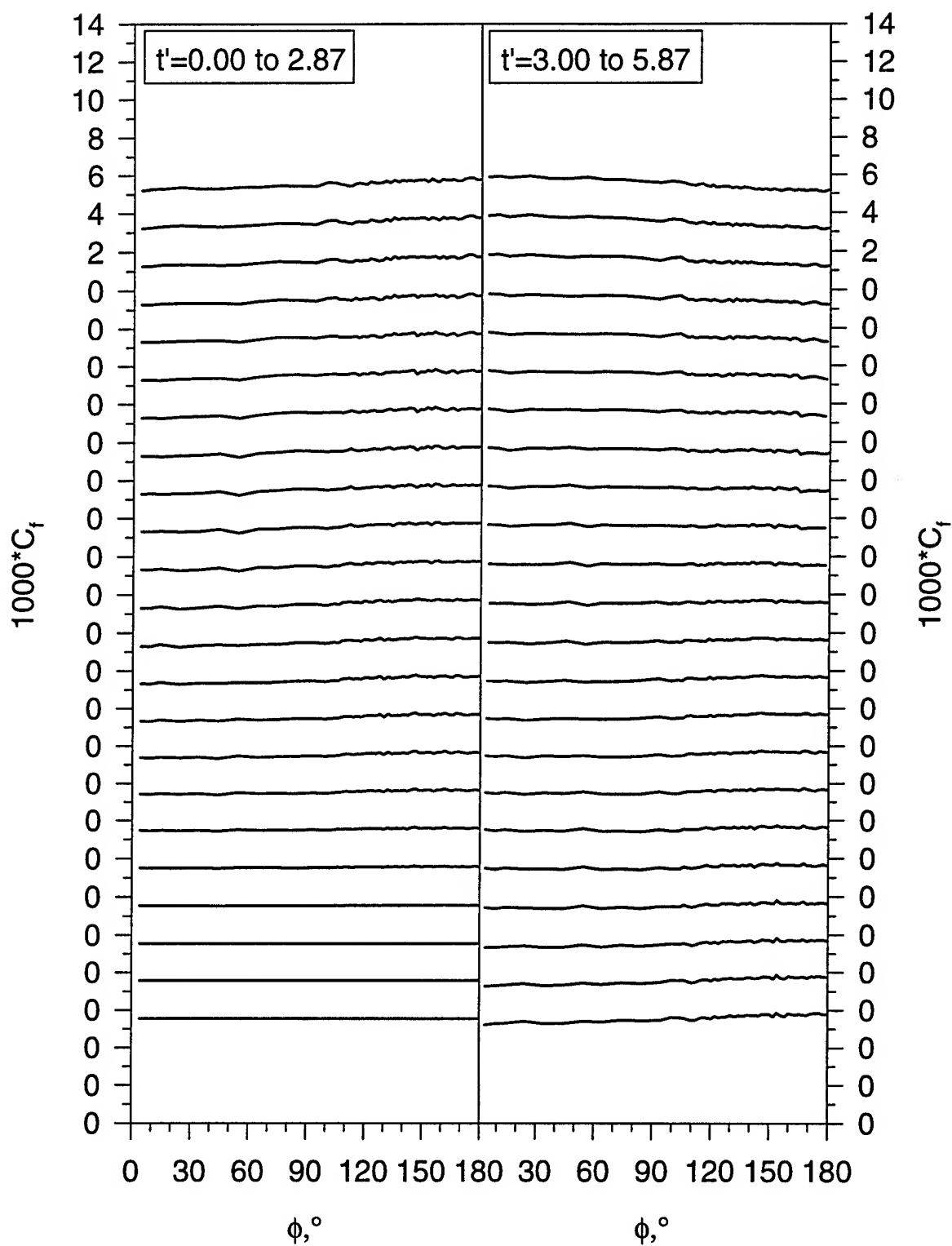


Figure 166.(a) Submarine maneuver time development of  $C_f$  vs.  $\phi$  for  $x/L=0.653$ .

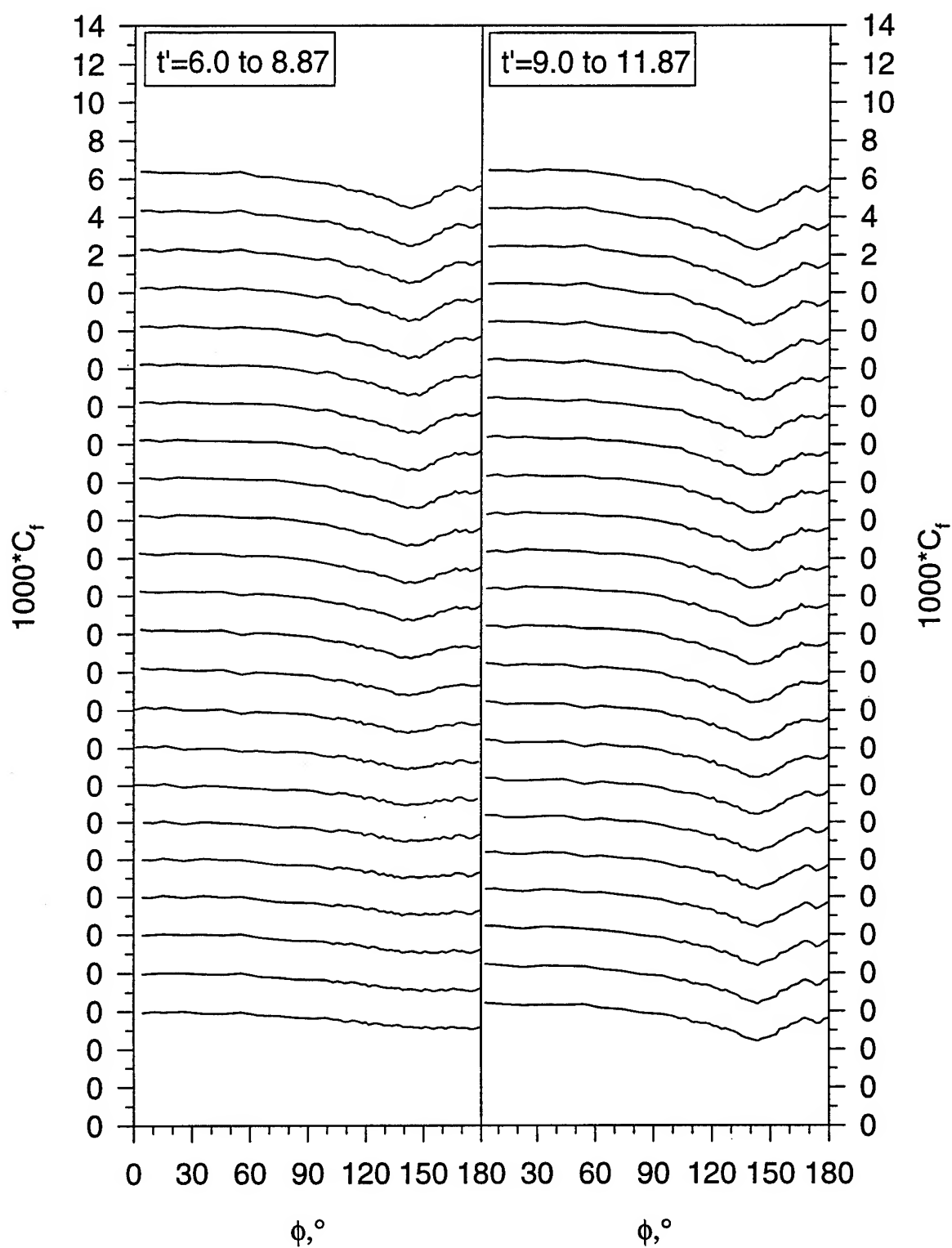


Figure 166. (b) Submarine maneuver time development of  $C_f$  vs.  $\phi$  for  $x/L=0.653$ .

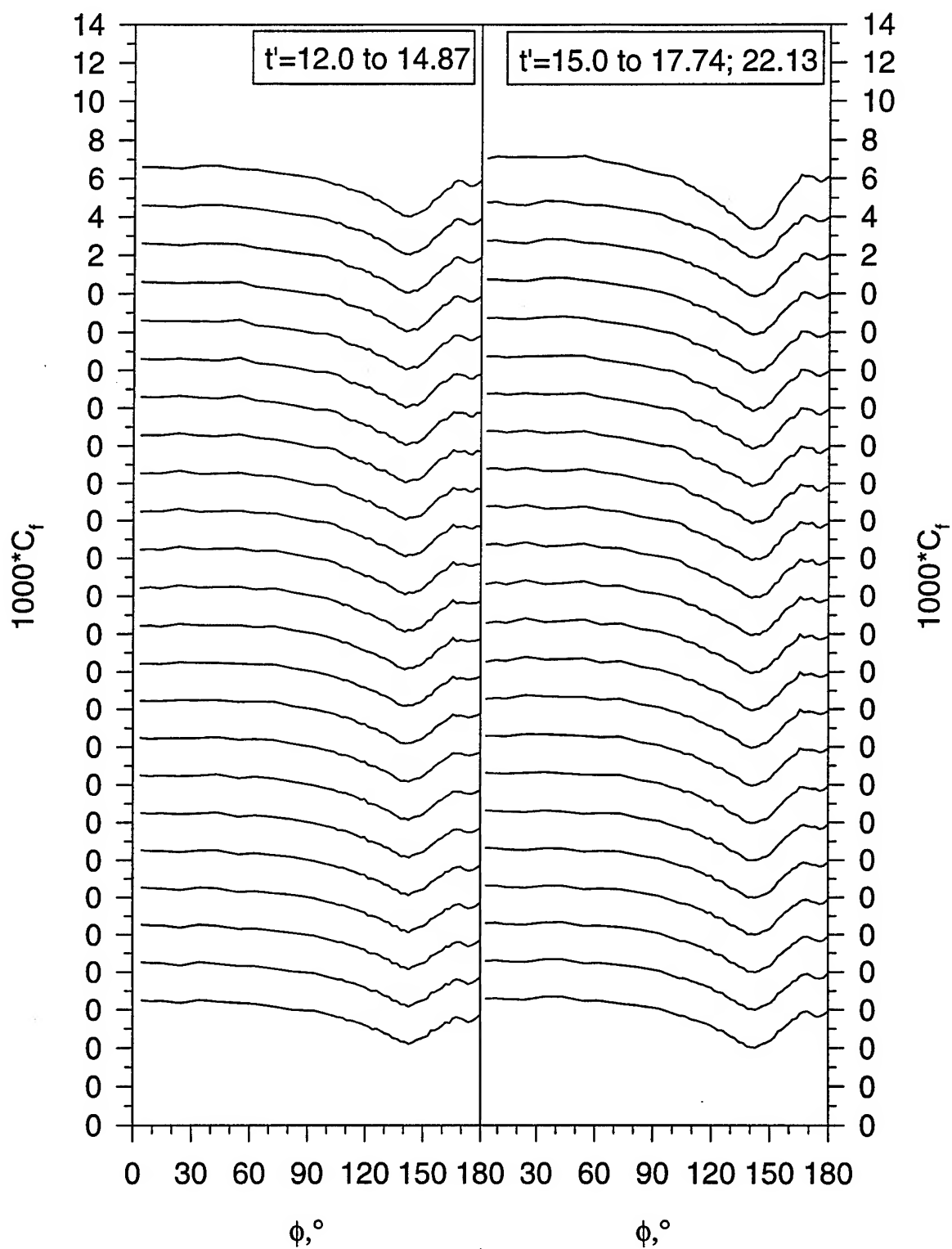


Figure 166. (c) Submarine maneuver time development of  $C_f$  vs.  $\phi$  for  $x/L=0.653$ .

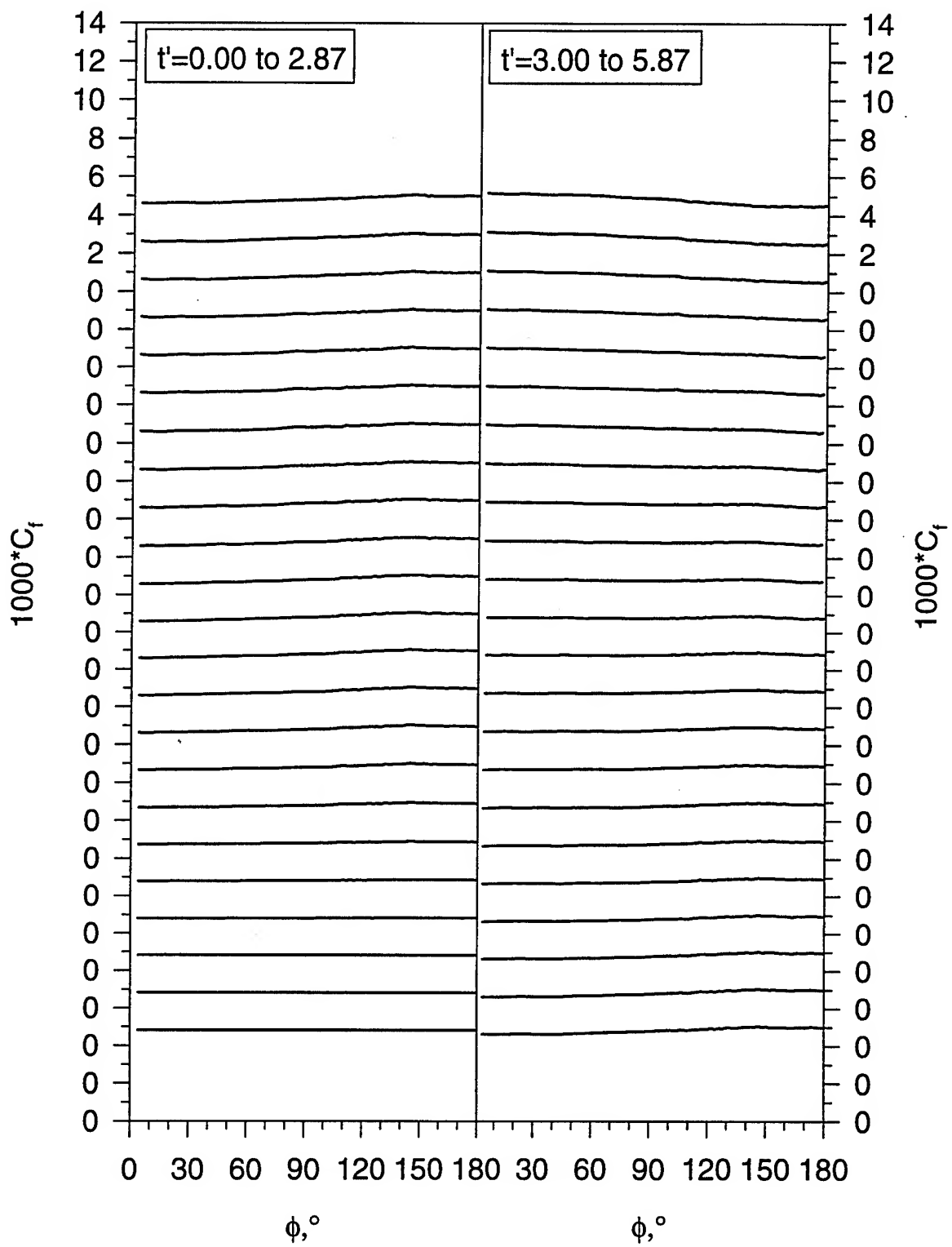


Figure 167.(a) Submarine maneuver time development of  $C_f$  vs.  $\phi$  for  $x/L=0.729$ .

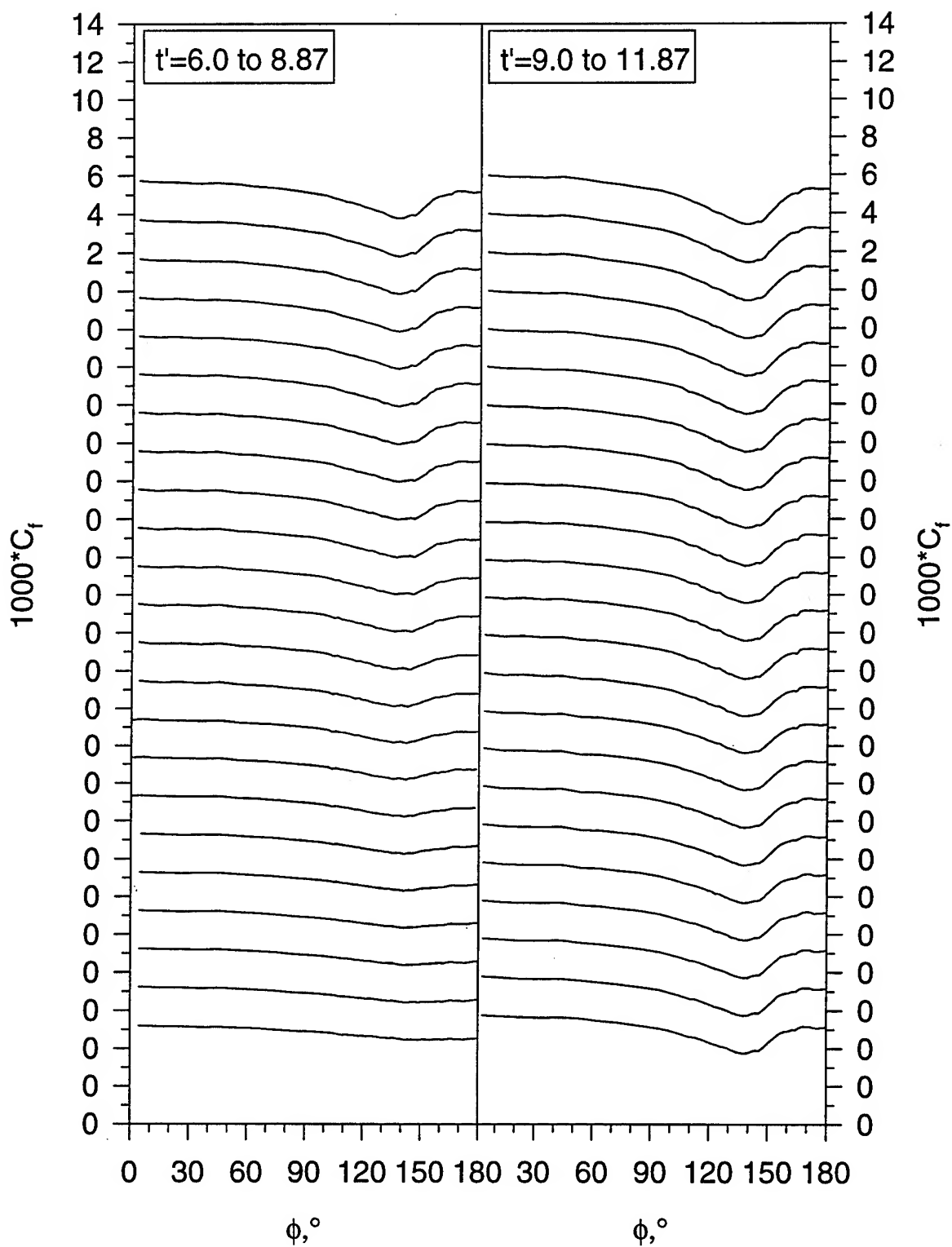


Figure 167. (b) Submarine maneuver time development of  $C_f$  vs.  $\phi$  for  $x/L=0.729$ .

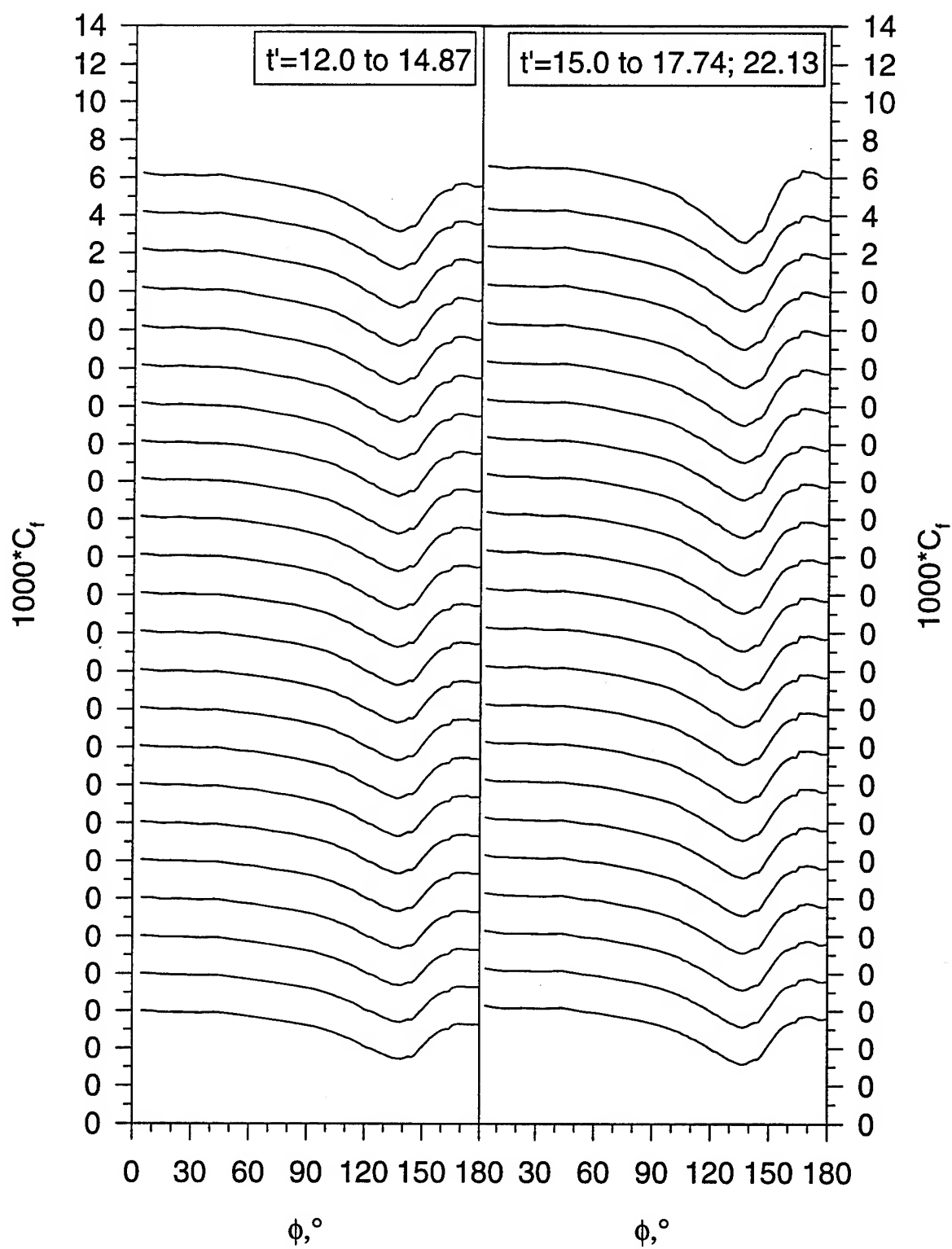


Figure 167. (c) Submarine maneuver time development of  $C_f$  vs.  $\phi$  for  $x/L=0.729$ .

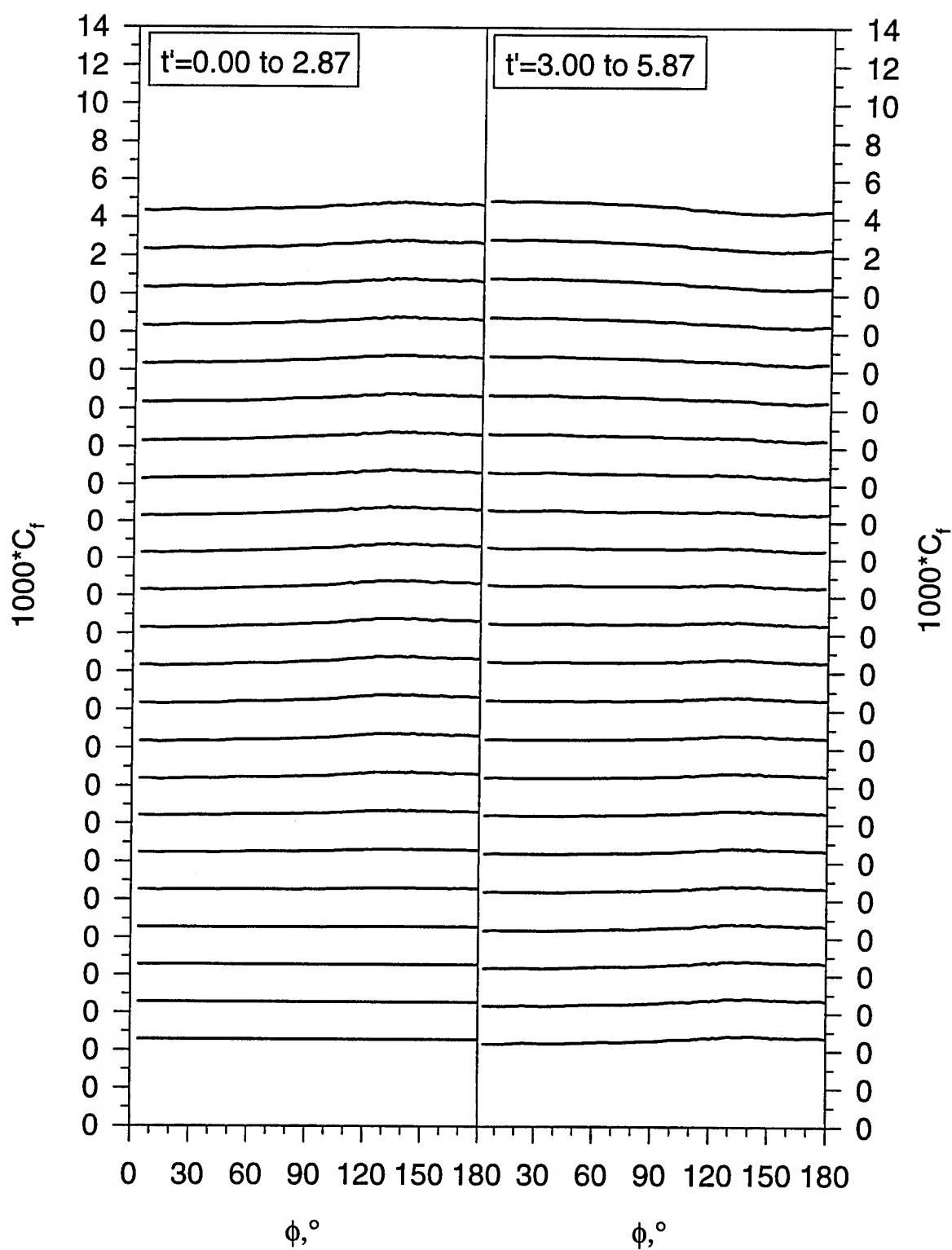


Figure 168.(a) Submarine maneuver time development of  $C_f$  vs.  $\phi$  for  $x/L=0.831$ .

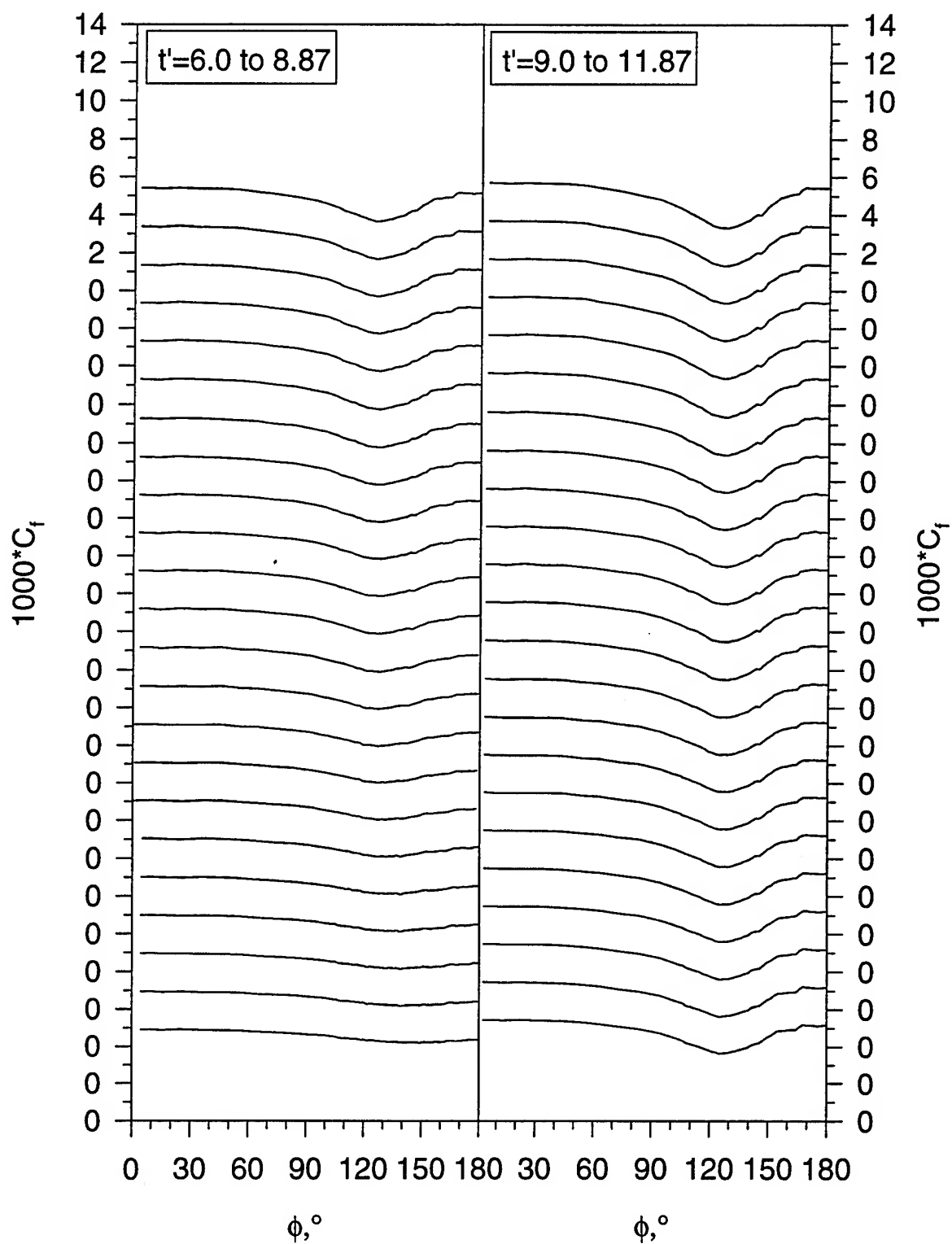


Figure 168. (b) Submarine maneuver time development of  $C_f$  vs.  $\phi$  for  $x/L=0.831$ .



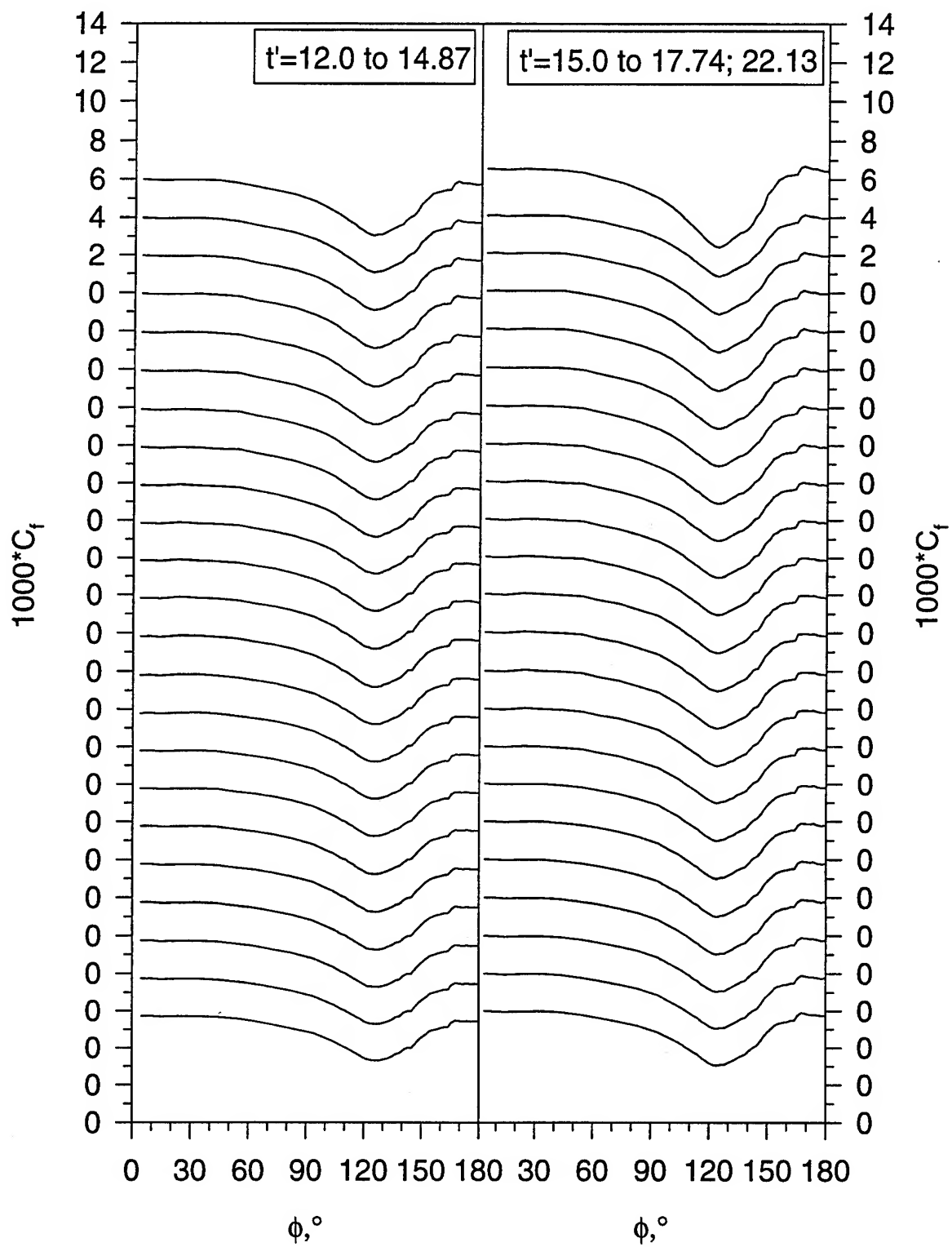


Figure 168. (c) Submarine maneuver time development of  $C_f$  vs.  $\phi$  for  $x/L=0.831$ .

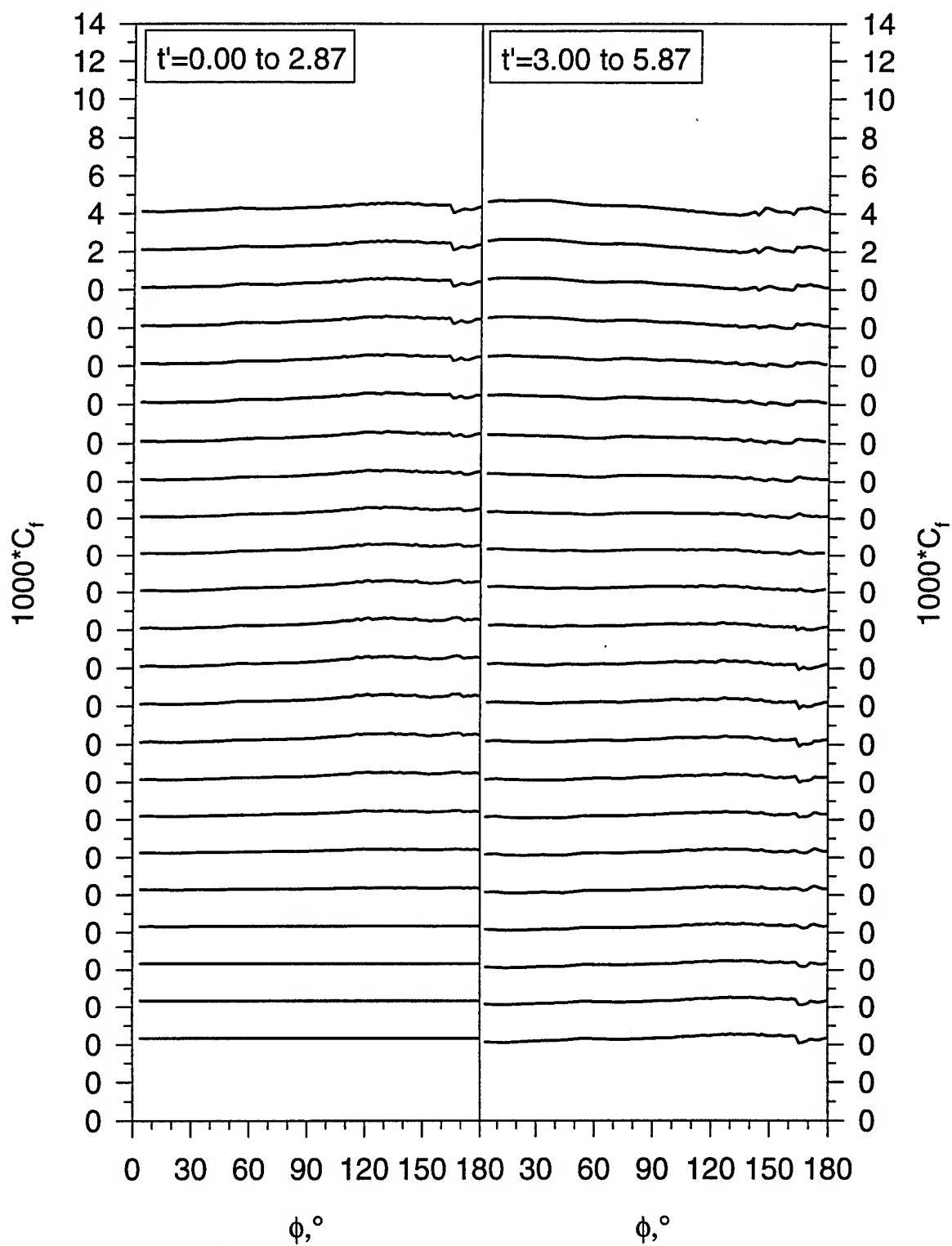


Figure 169.(a) Submarine maneuver time development of  $C_f$  vs.  $\phi$  for  $x/L=0.882$ .

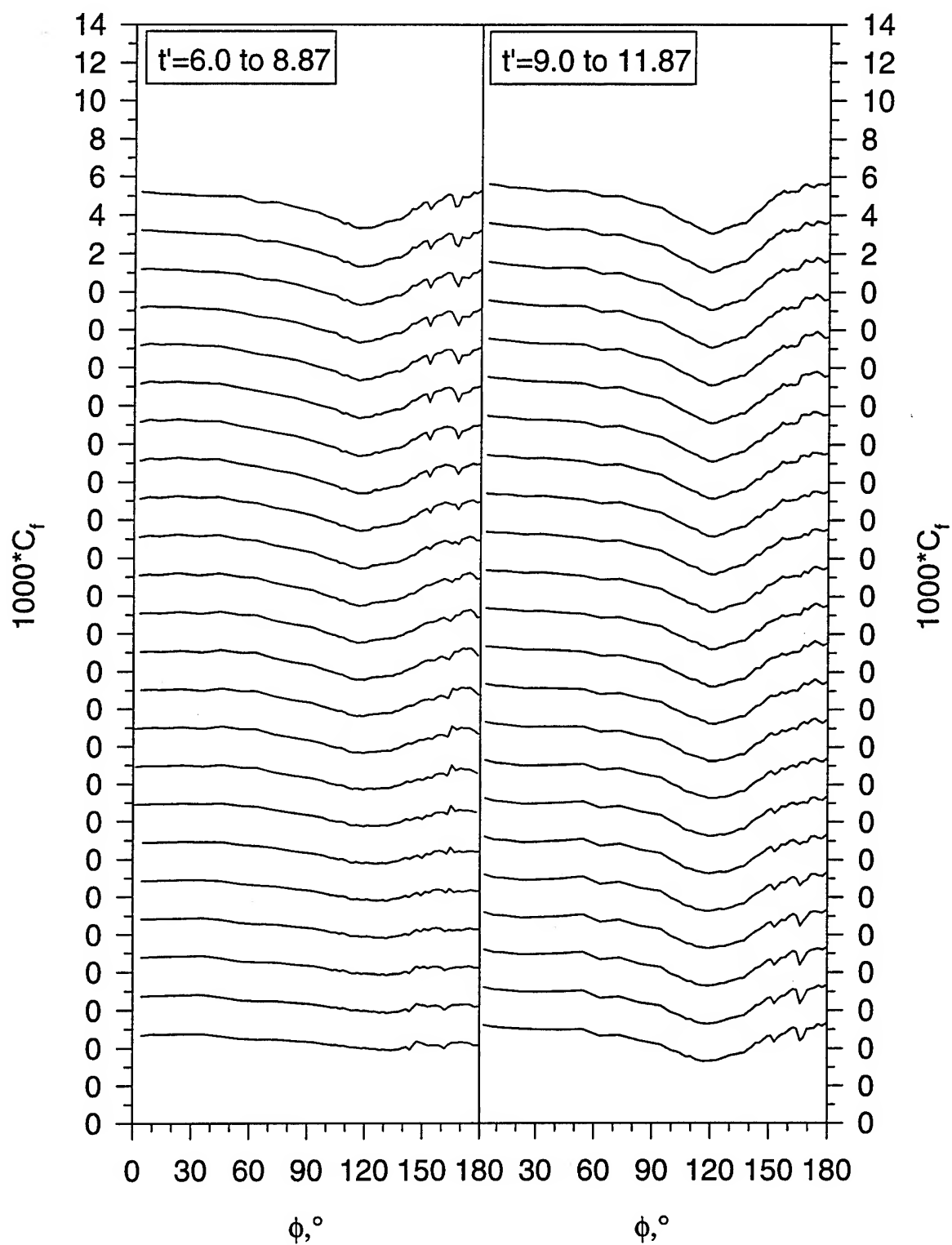


Figure 169. (b) Submarine maneuver time development of  $C_f$  vs.  $\phi$  for  $x/L=0.882$ .

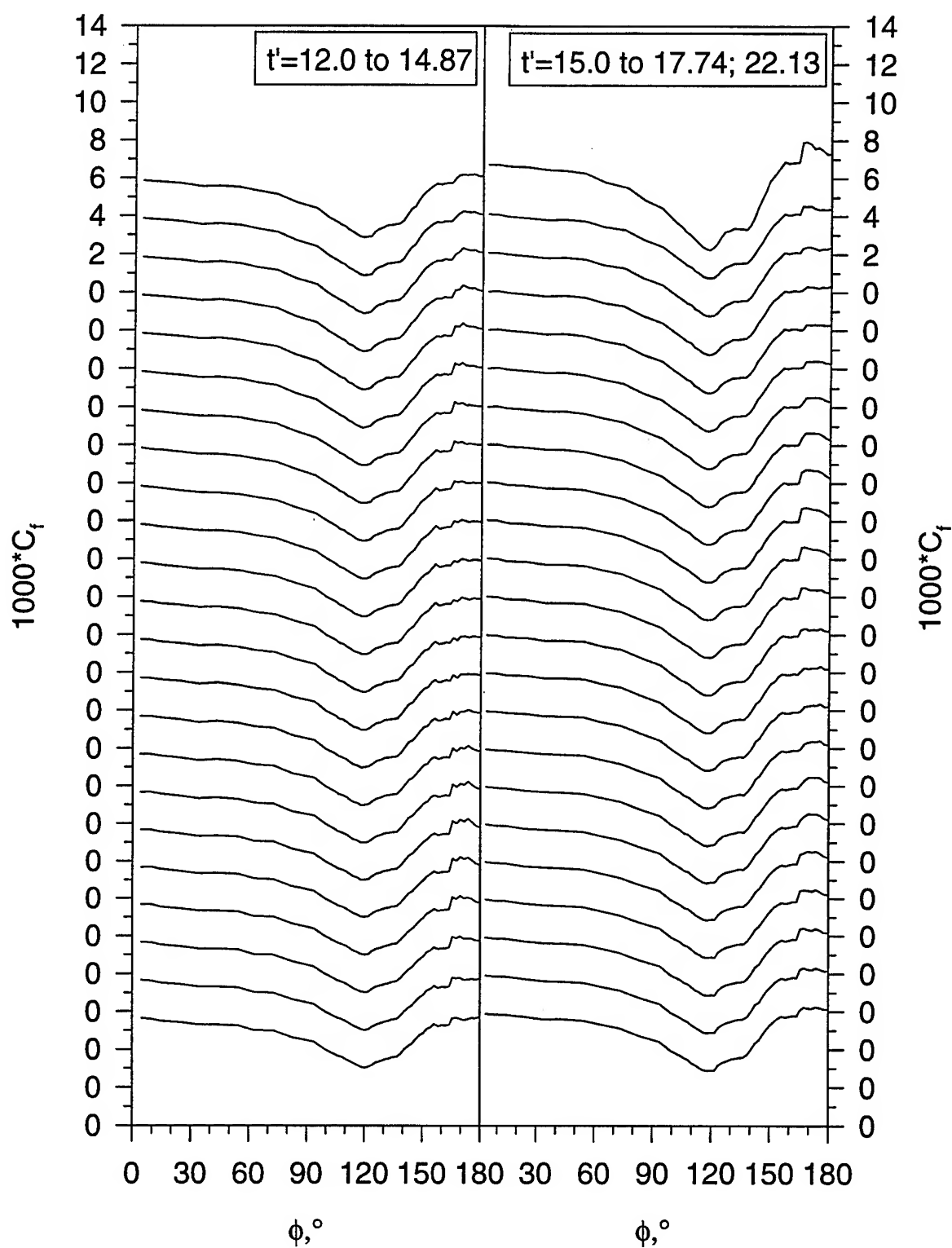


Figure 169. (c) Submarine maneuver time development of  $C_f$  vs.  $\phi$  for  $x/L=0.882$ .

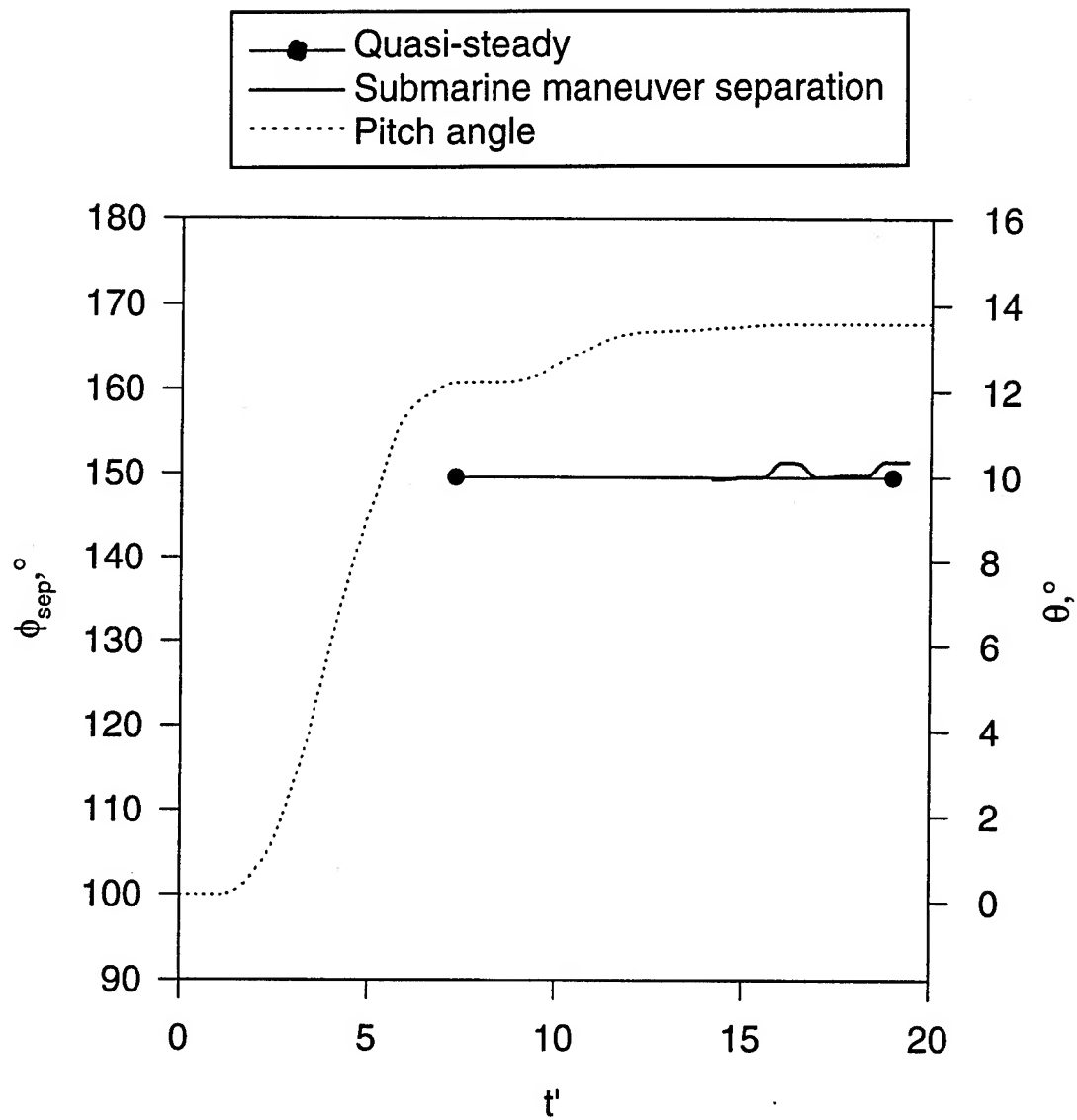


Figure 170. Separation position versus time for submarine maneuver at  $x/L=0.500$  compared with quasi-steady separation positions.

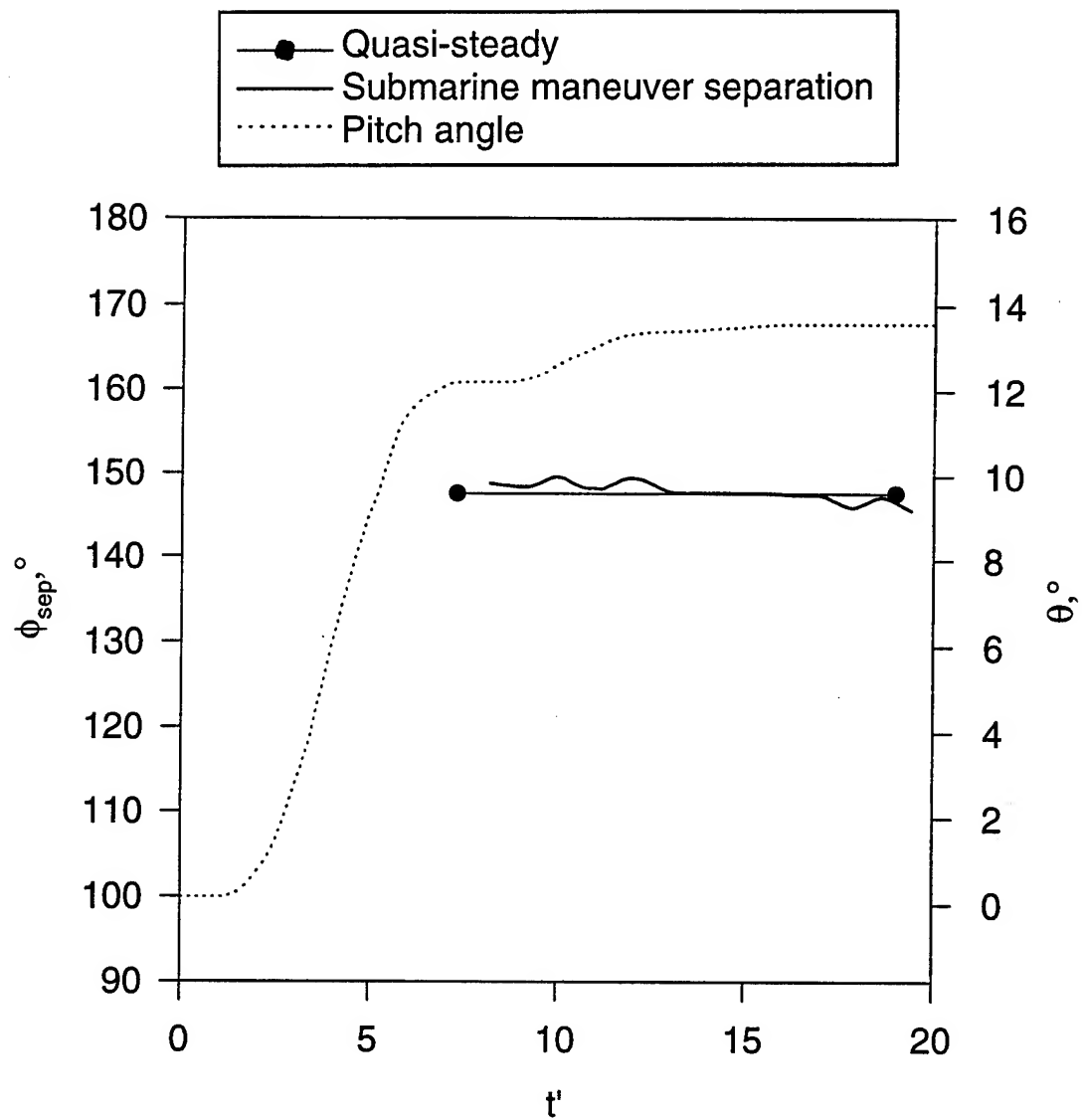


Figure 171. Separation position versus time for submarine maneuver at  $x/L=0.576$  compared with quasi-steady separation positions.

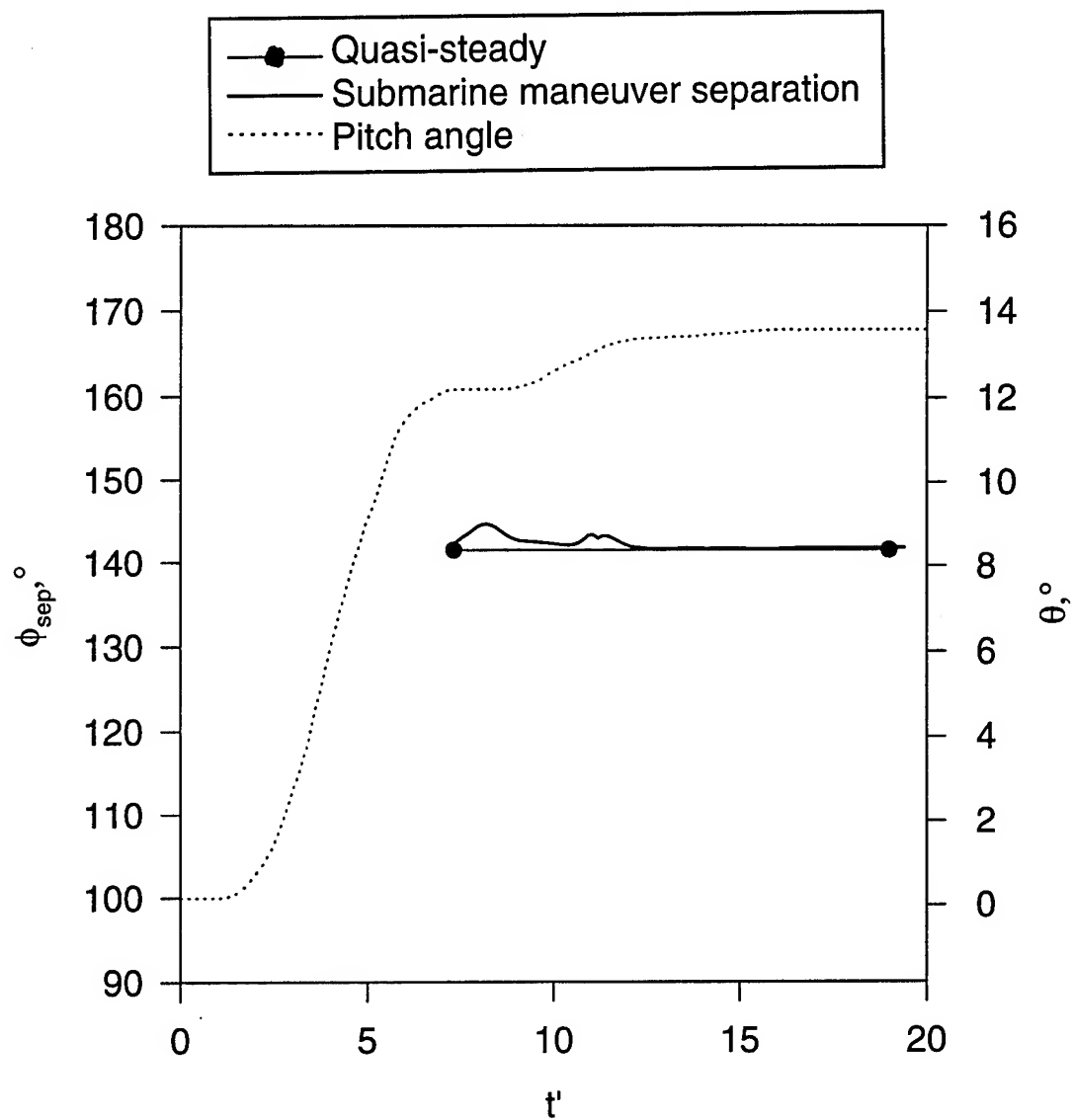


Figure 172. Separation position versus time for submarine maneuver at  $x/L=0.653$  compared with quasi-steady separation positions.

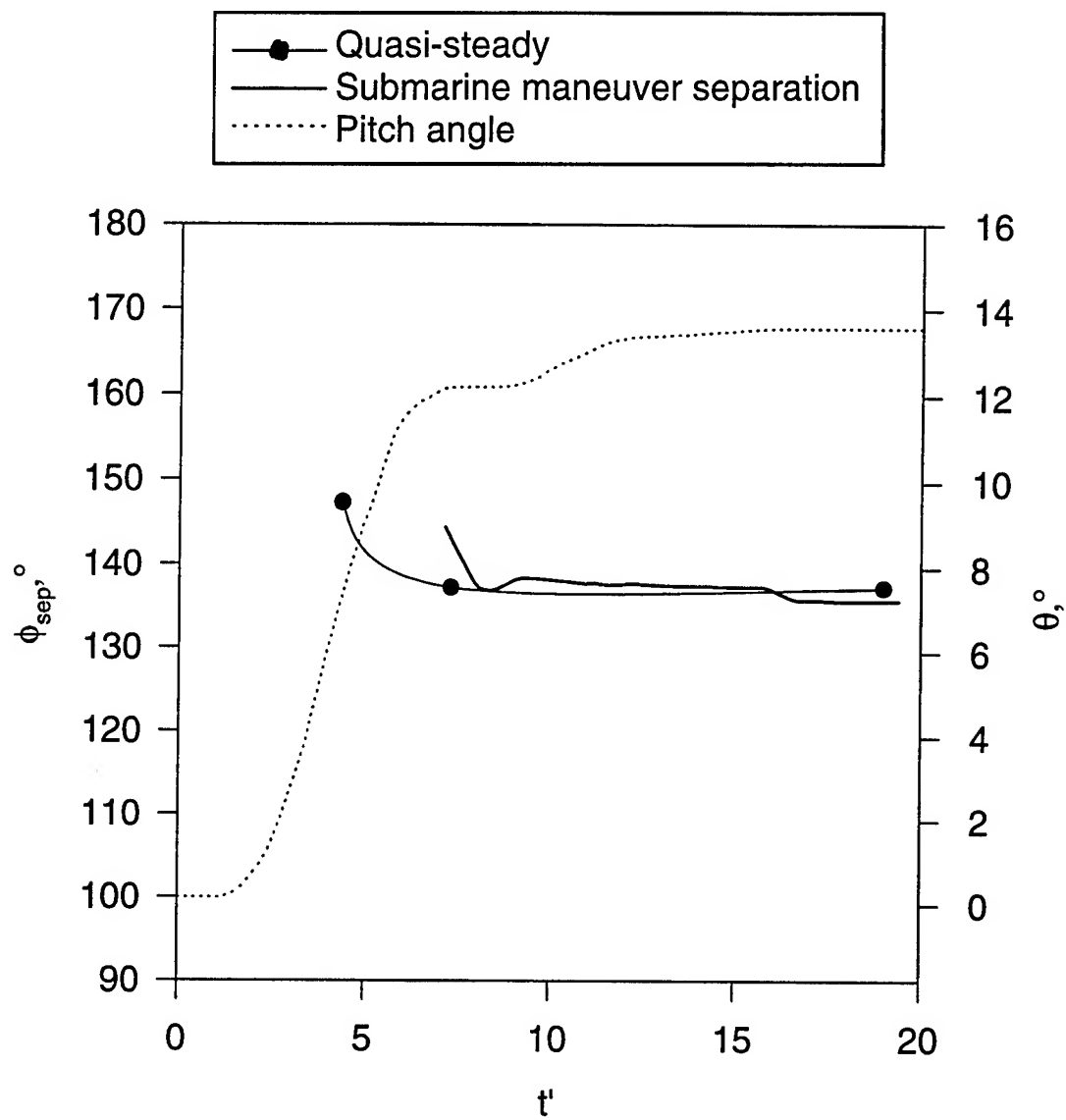


Figure 173. Separation position versus time for submarine maneuver at  $x/L=0.729$  compared with quasi-steady separation positions.



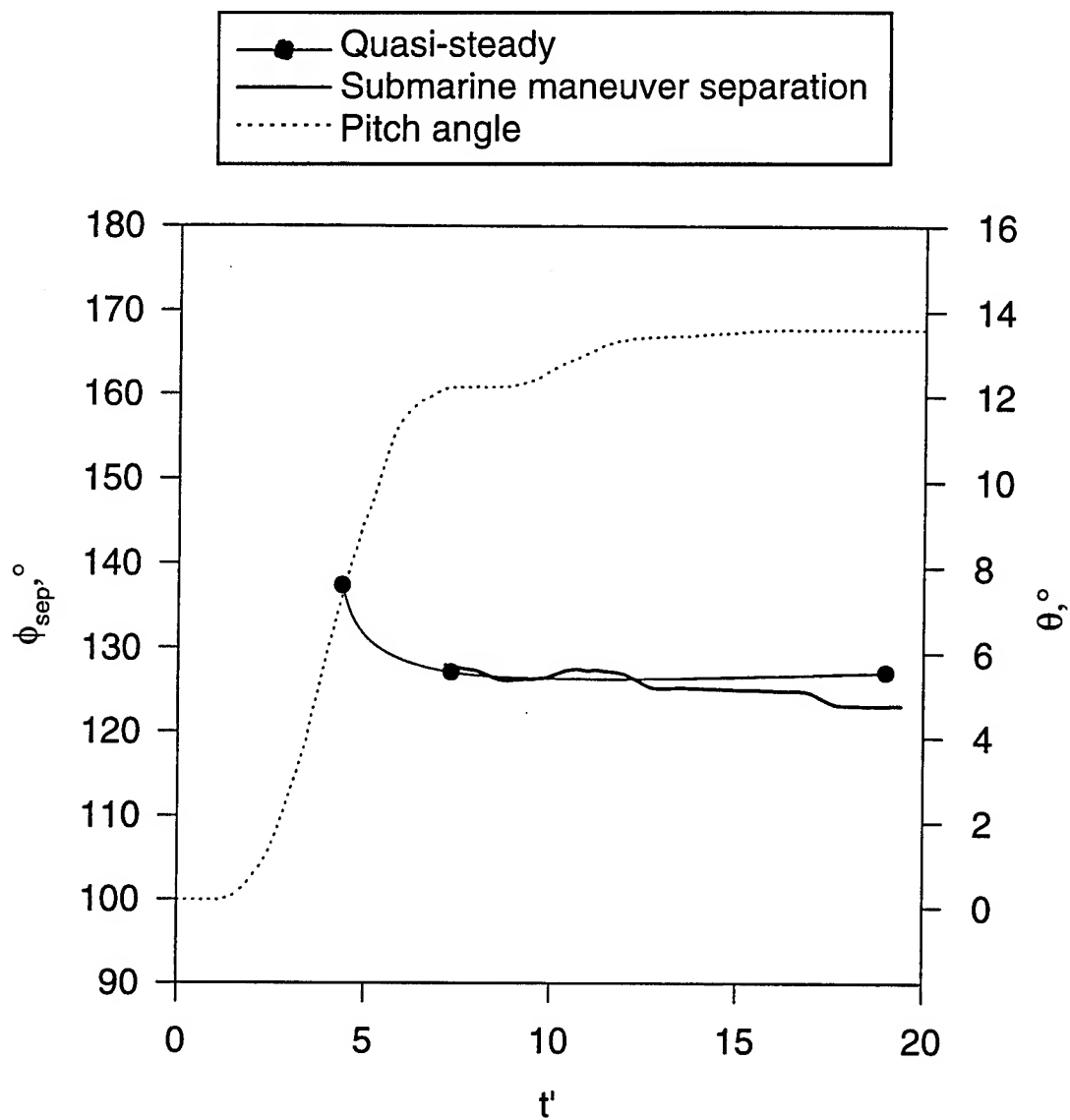


Figure 174. Separation position versus time for submarine maneuver at  $x/L=0.831$  compared with quasi-steady separation positions.

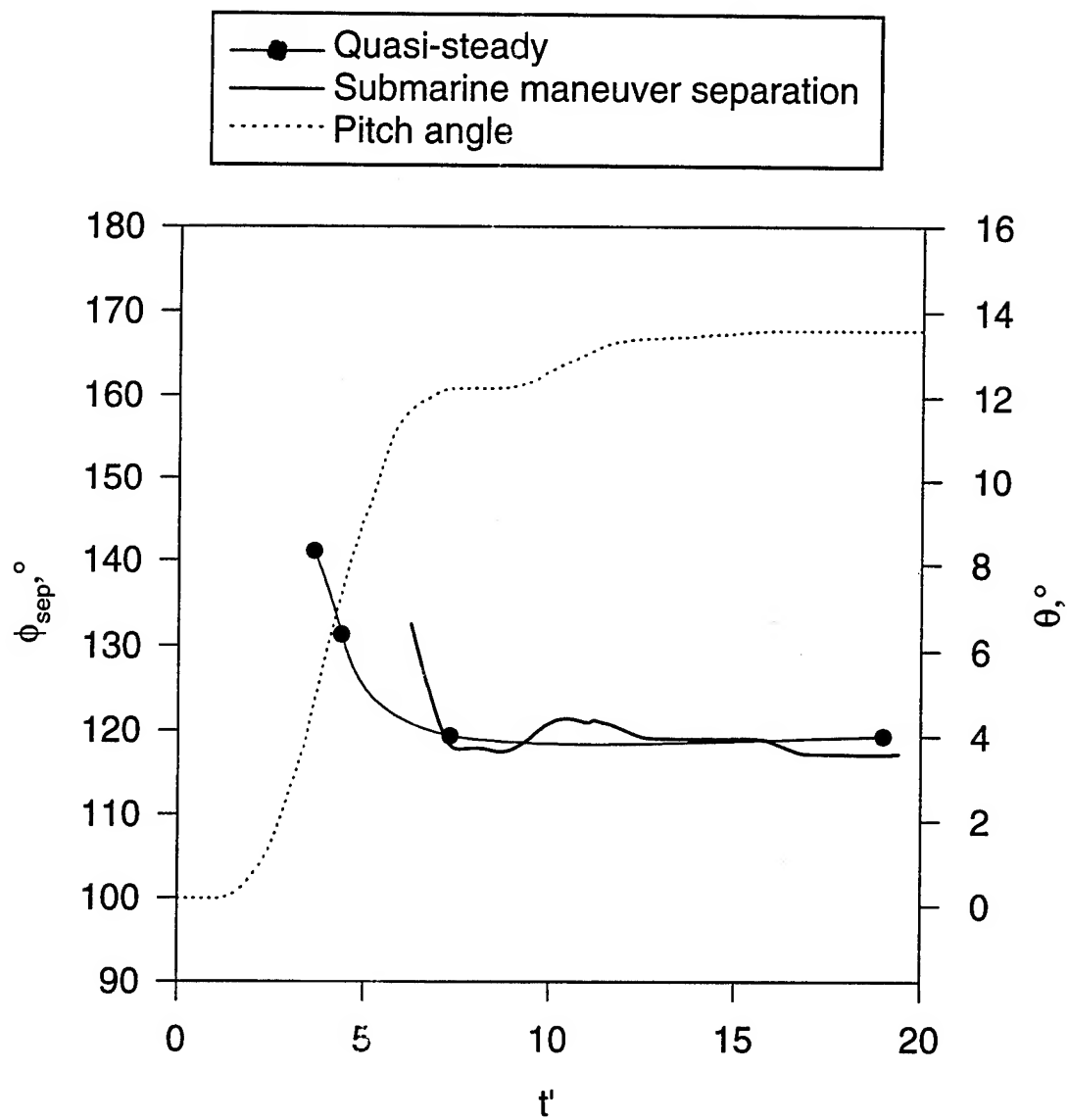


Figure 175. Separation position versus time for submarine maneuver at  $x/L=0.882$  compared with quasi-steady separation positions.

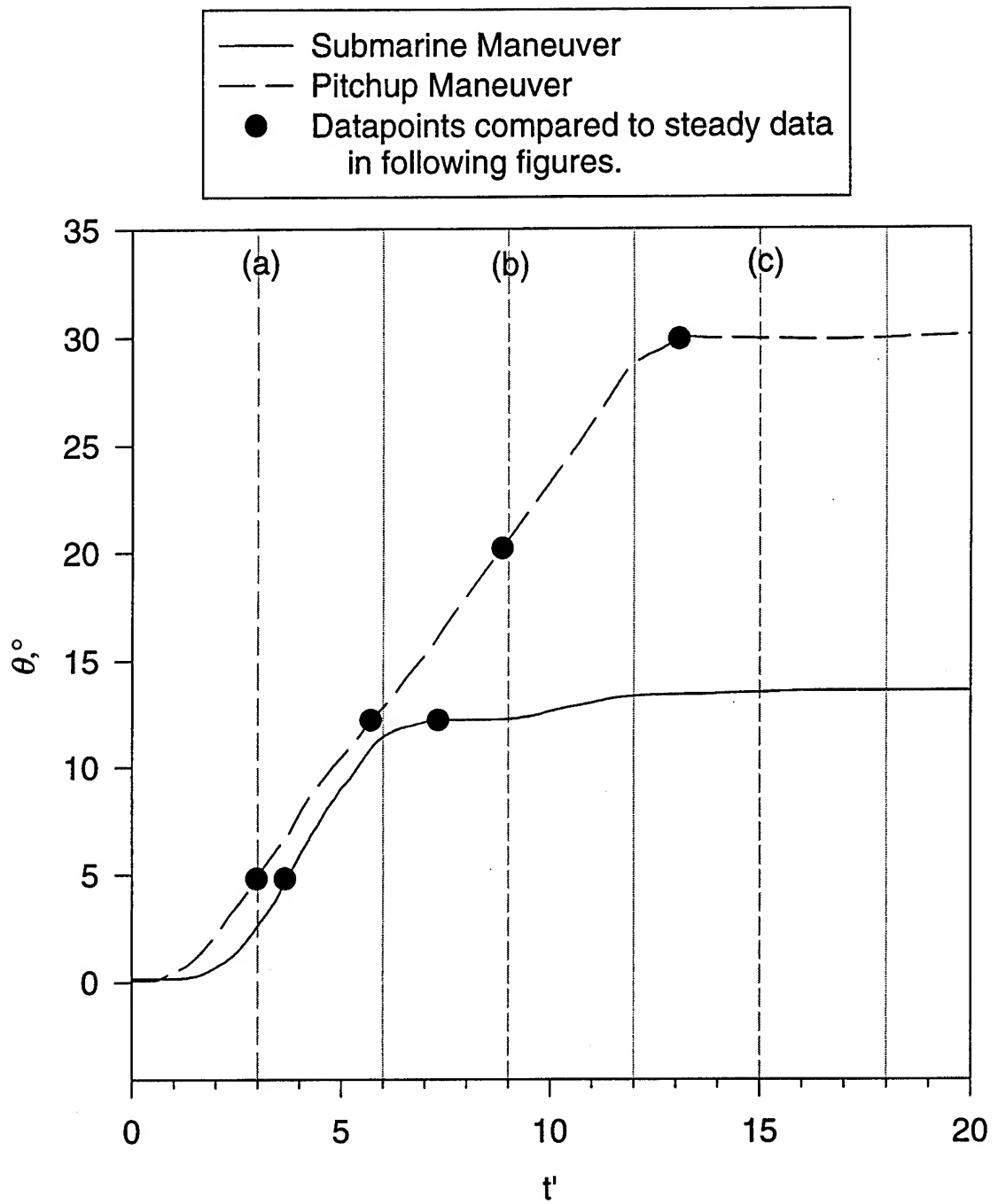


Figure 176. Comparison of pitch angle schedules for pitchup and submarine maneuvers.

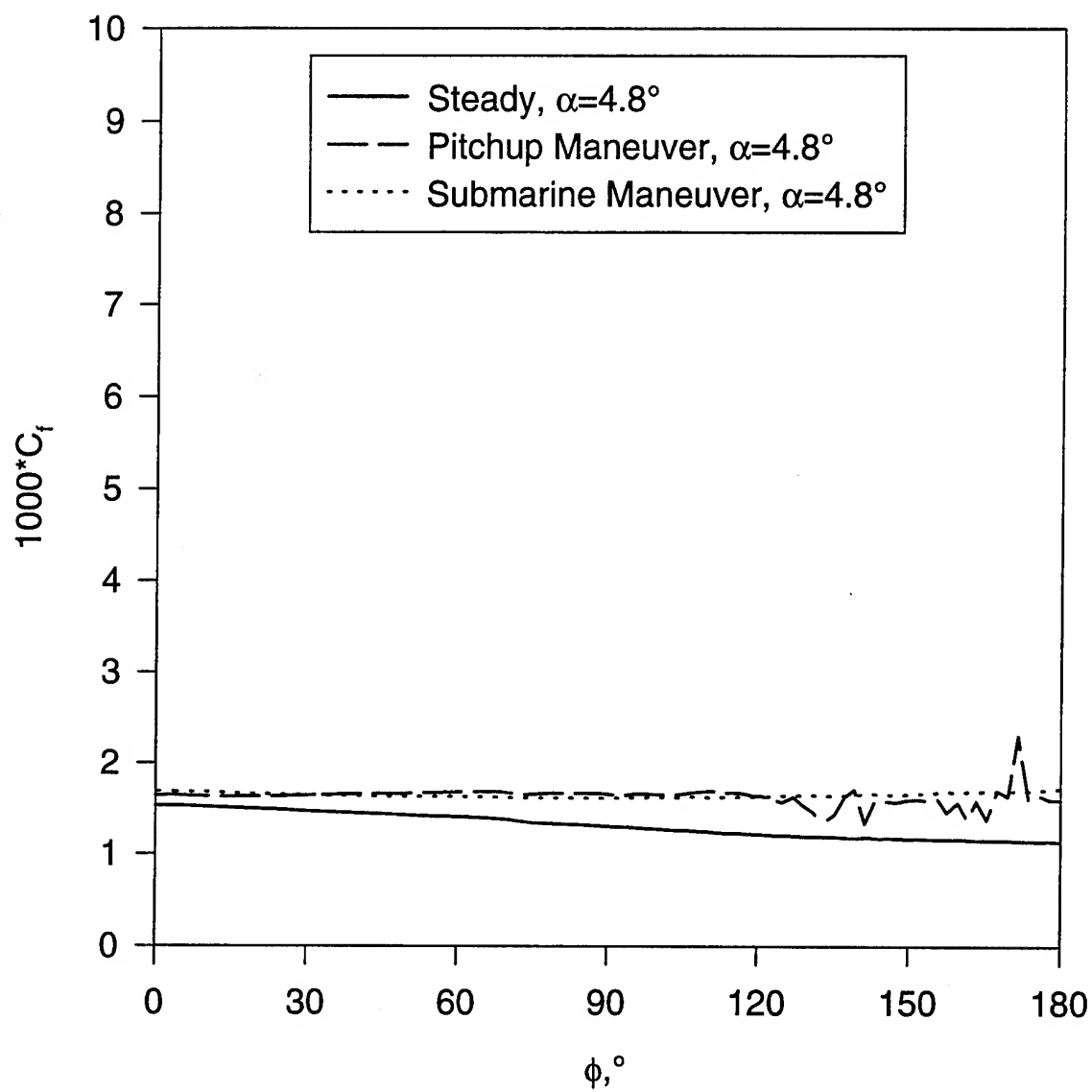


Figure 177. Comparison of wall shear distribution at  $x/L=0.118$  for steady data, pitchup maneuver, and submarine maneuver at  $\alpha=4.8^\circ$ .

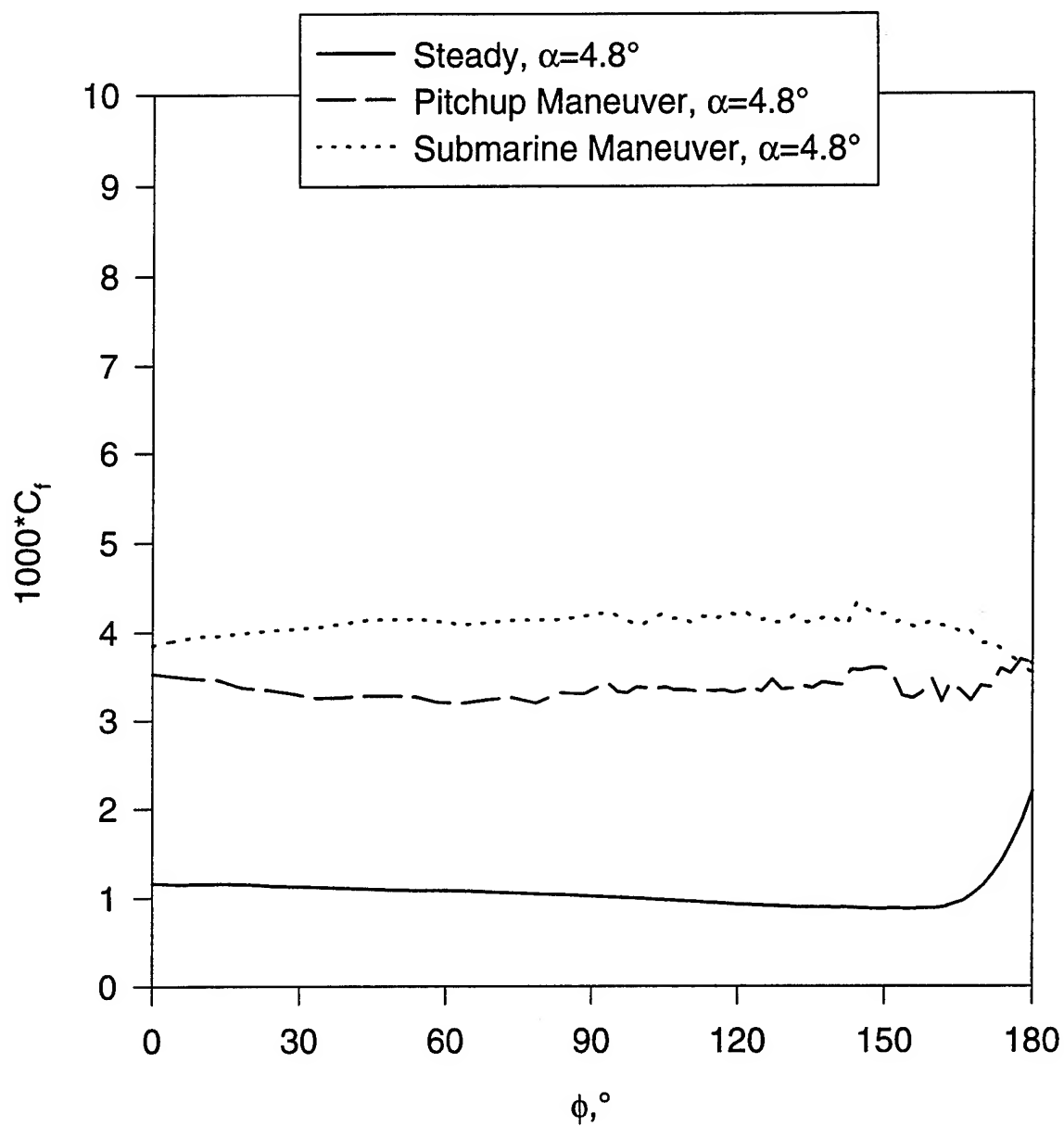


Figure 178. Comparison of wall shear distribution at  $x/L=0.194$  for steady data, pitchup maneuver, and submarine maneuver at  $\alpha=4.8^\circ$ .

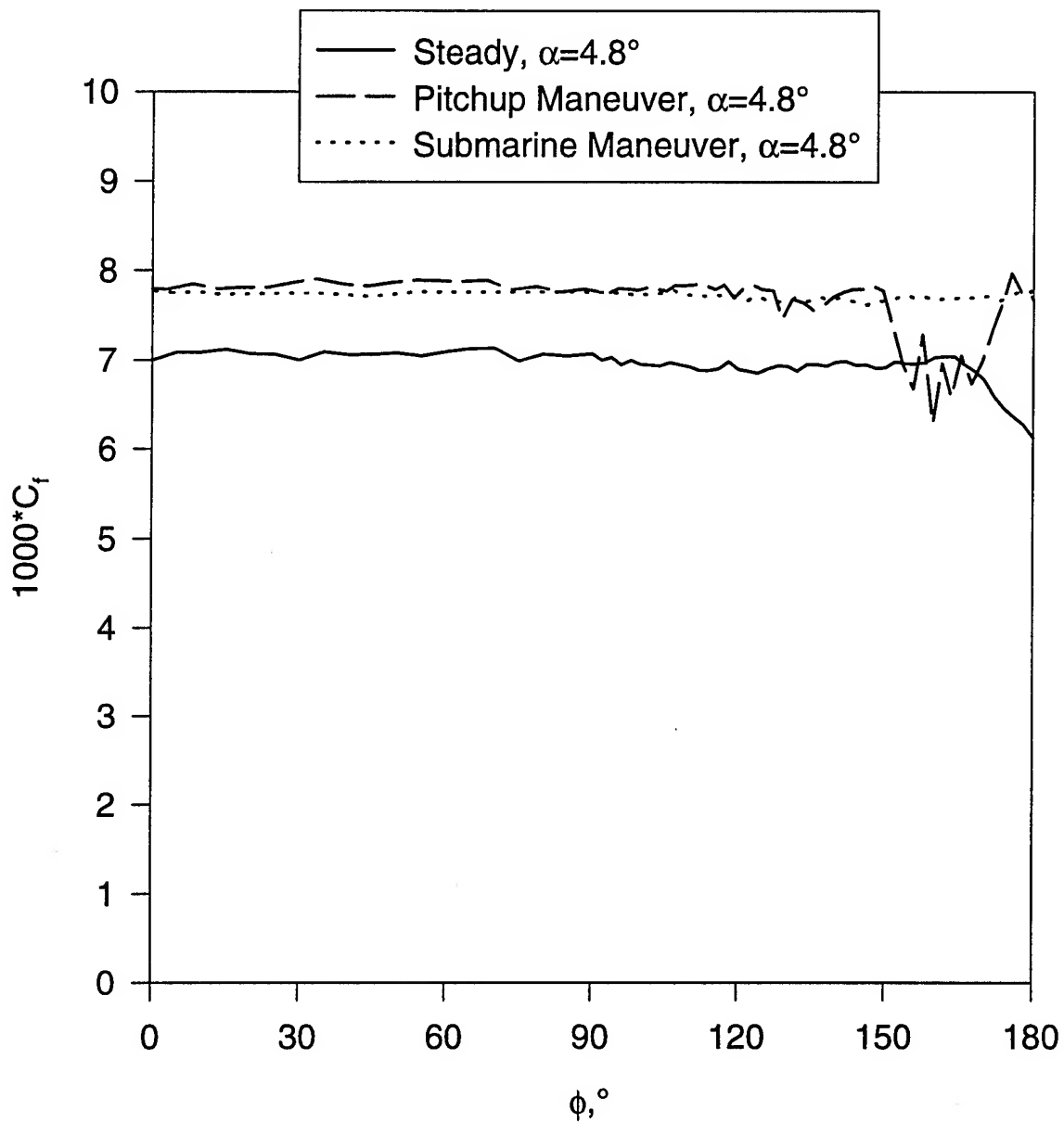


Figure 179. Comparison of wall shear distribution at  $x/L=0.220$  for steady data, pitchup maneuver, and submarine maneuver at  $\alpha=4.8^\circ$ .

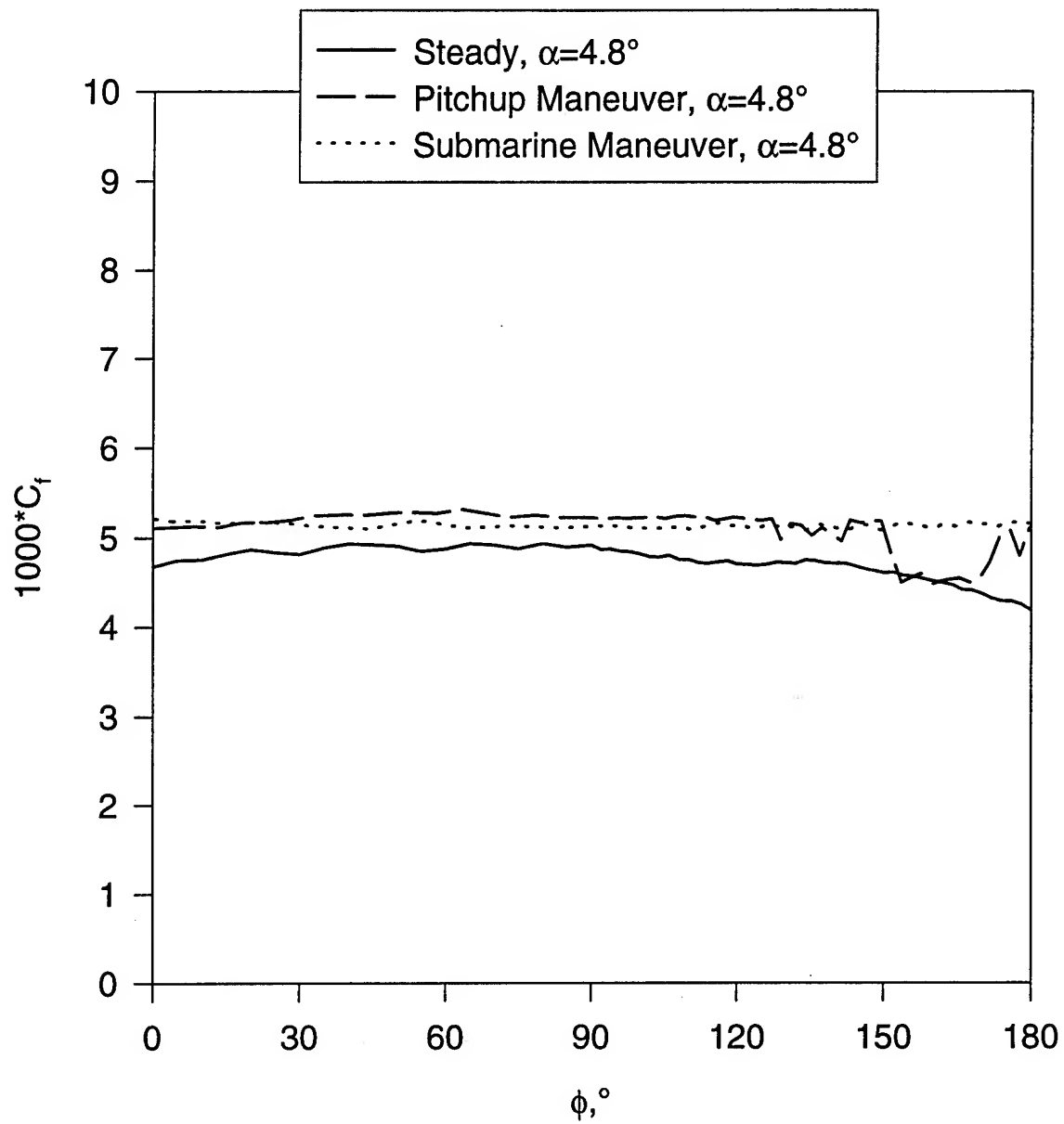


Figure 180. Comparison of wall shear distribution at  $x/L=0.271$  for steady data, pitchup maneuver, and submarine maneuver at  $\alpha=4.8^\circ$ .

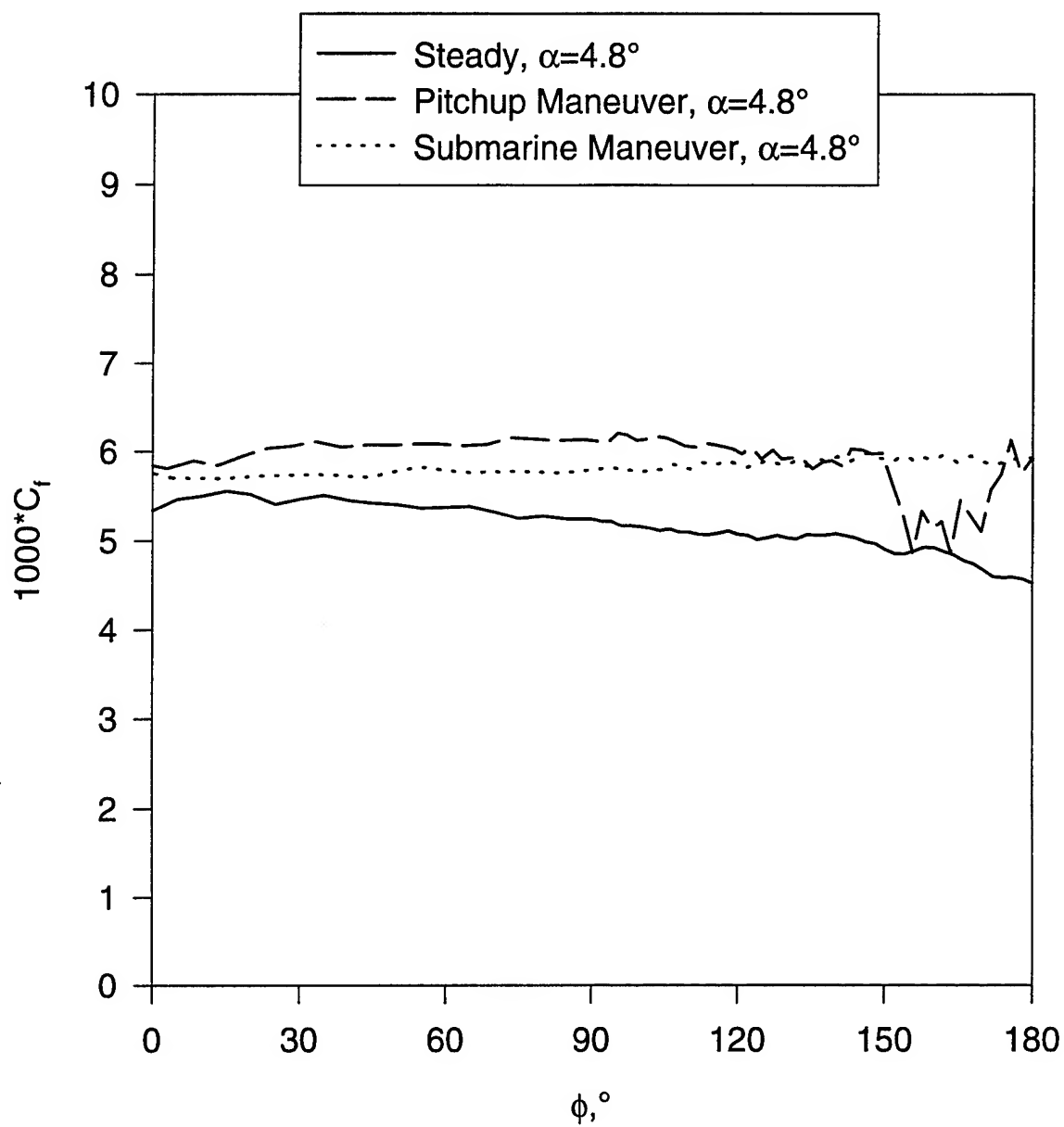


Figure 181. Comparison of wall shear distribution at  $x/L=0.347$  for steady data, pitchup maneuver, and submarine maneuver at  $\alpha=4.8^\circ$ .



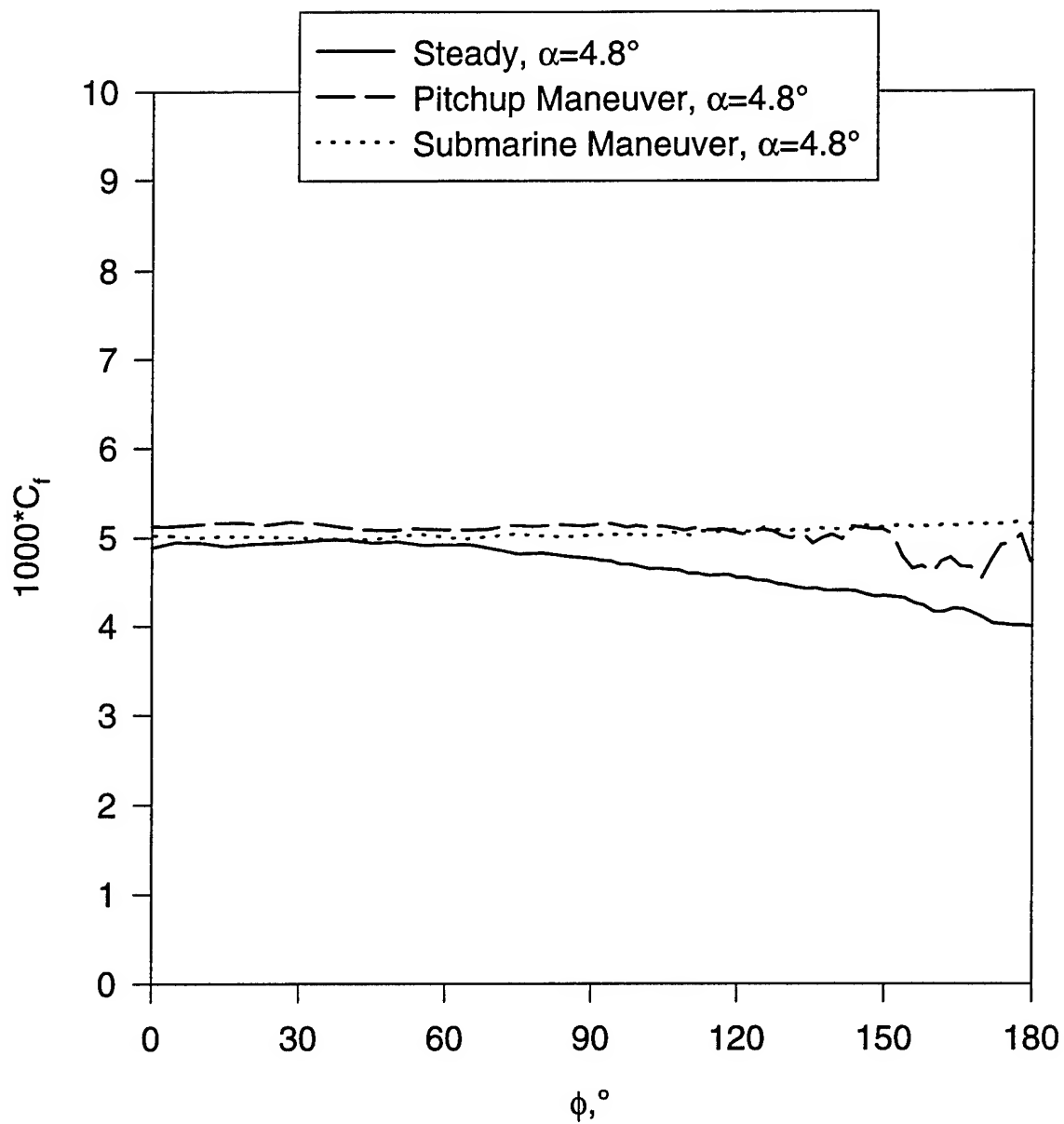


Figure 182. Comparison of wall shear distribution at  $x/L=0.424$  for steady data, pitchup maneuver, and submarine maneuver at  $\alpha=4.8^\circ$ .

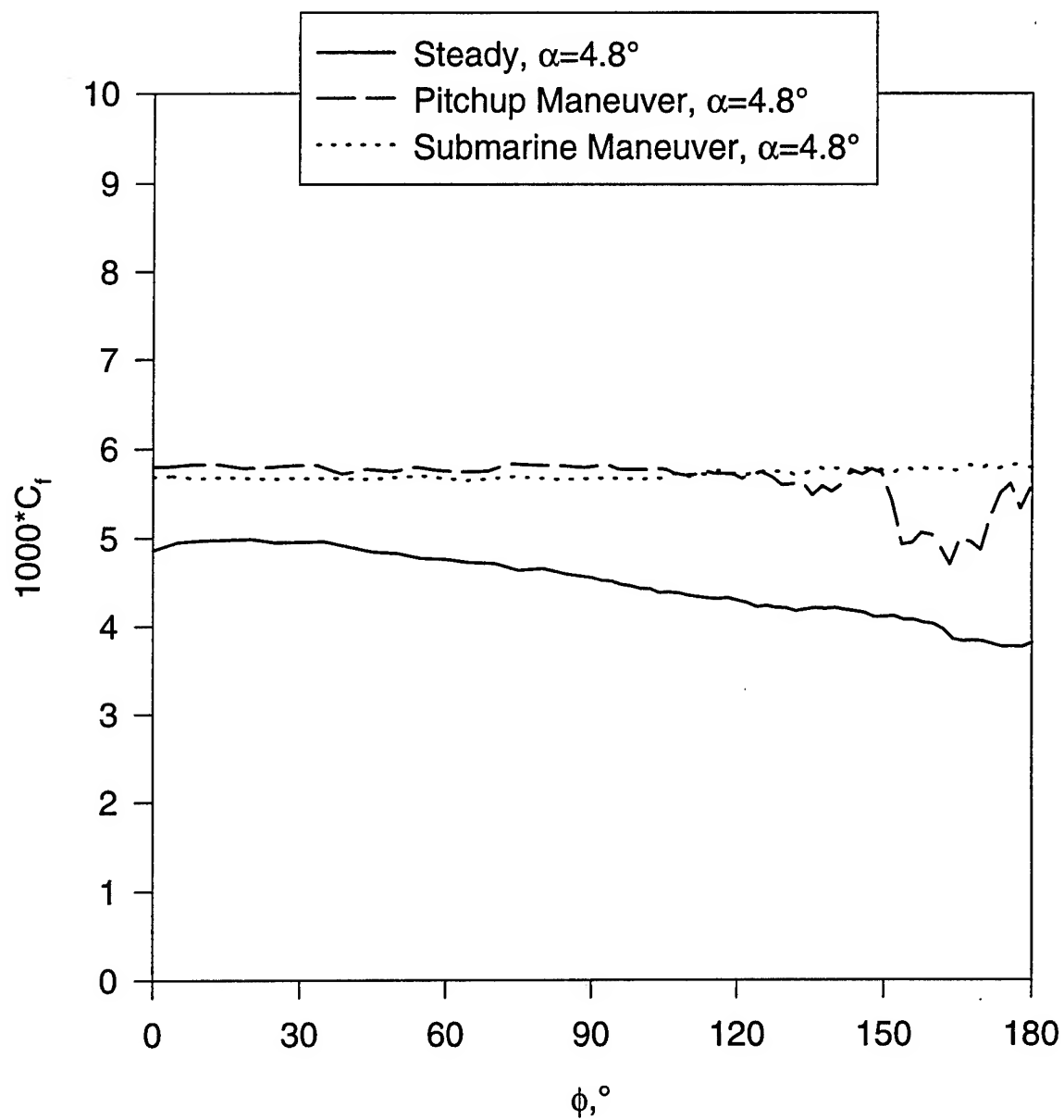


Figure 183. Comparison of wall shear distribution at  $x/L=0.500$  for steady data, pitchup maneuver, and submarine maneuver at  $\alpha=4.8^\circ$ .

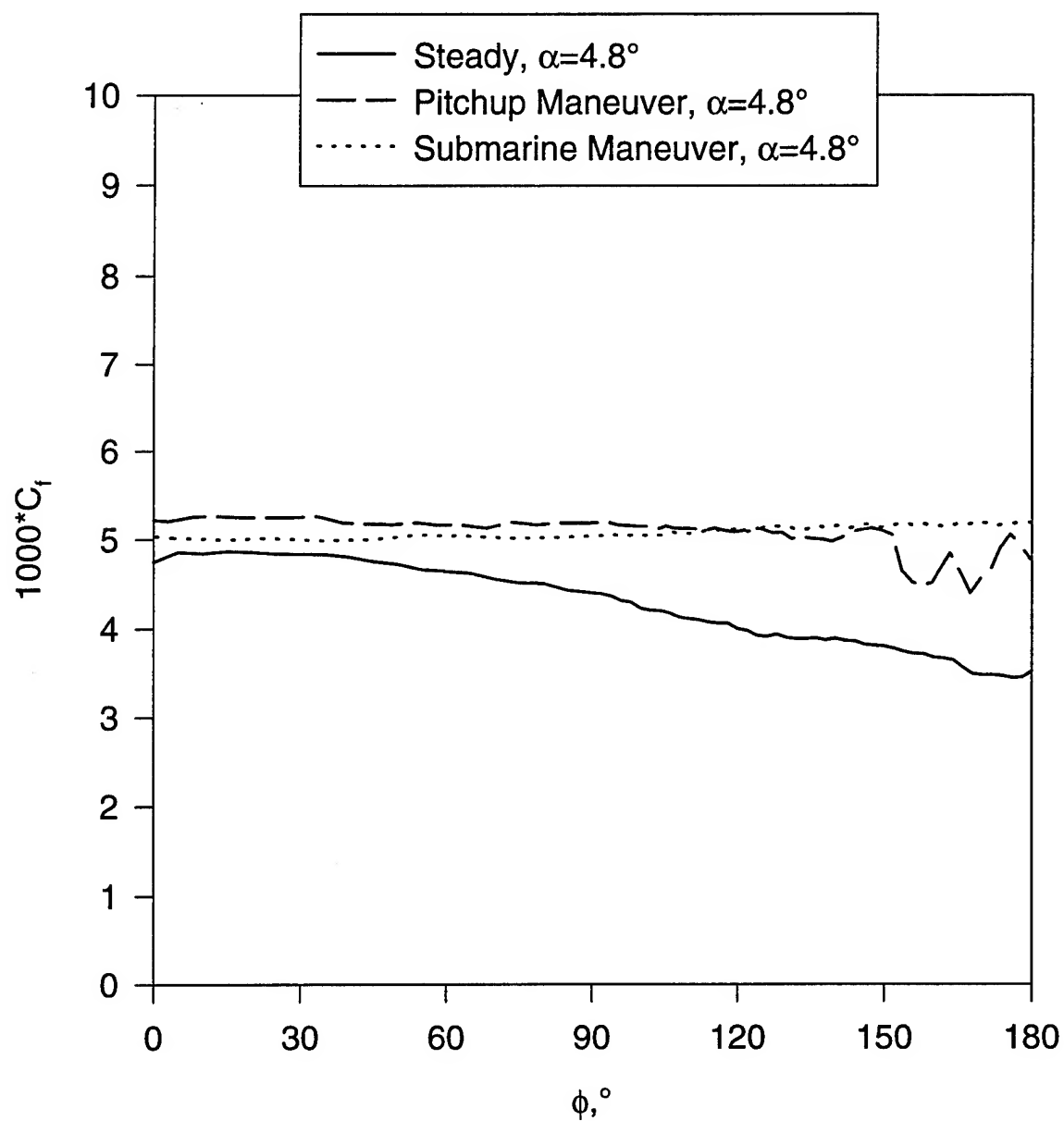


Figure 184. Comparison of wall shear distribution at  $x/L=0.576$  for steady data, pitchup maneuver, and submarine maneuver at  $\alpha=4.8^\circ$ .

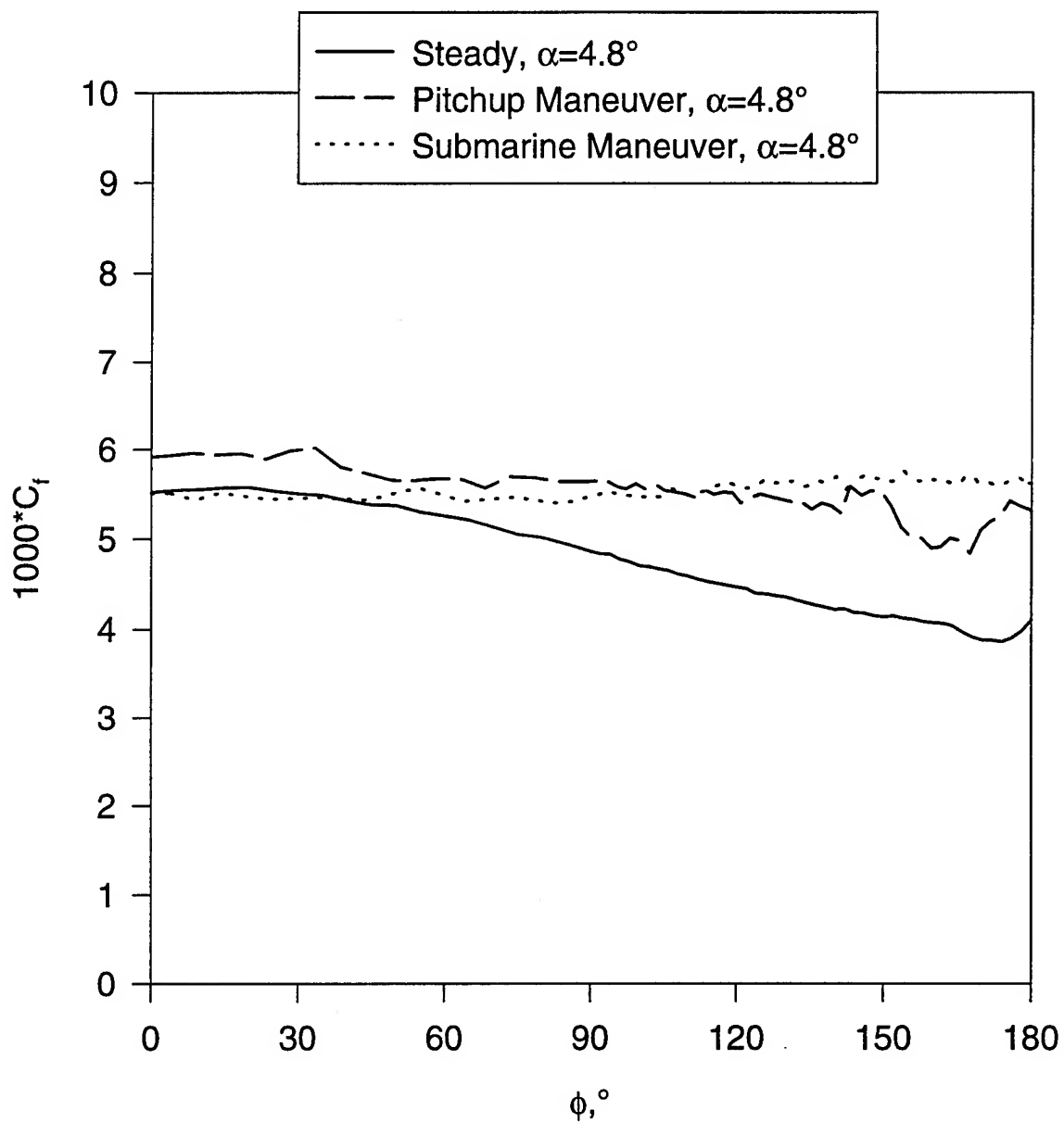


Figure 185. Comparison of wall shear distribution at  $x/L=0.653$  for steady data, pitchup maneuver, and submarine maneuver at  $\alpha=4.8^\circ$ .

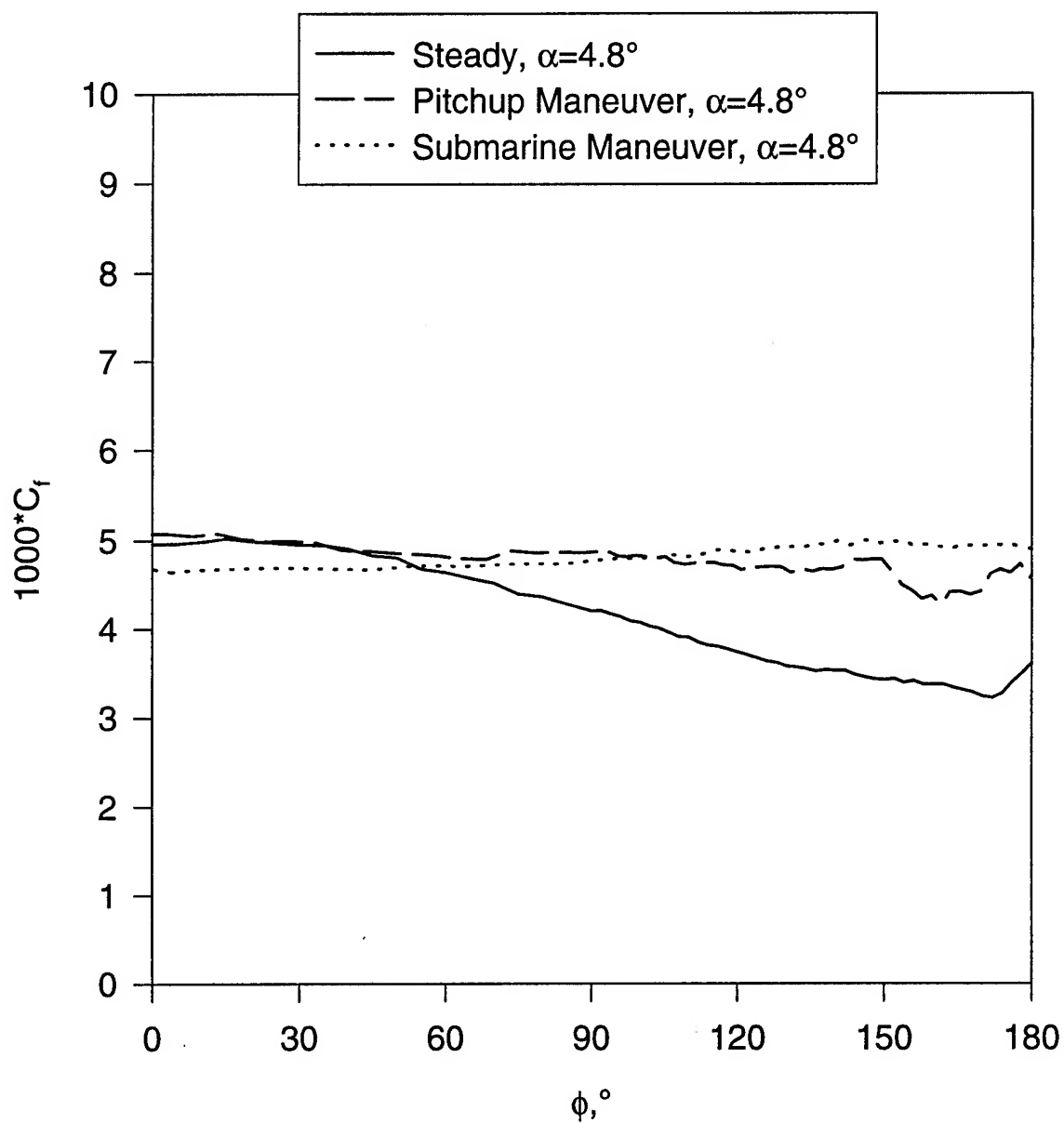


Figure 186. Comparison of wall shear distribution at  $x/L=0.729$  for steady data, pitchup maneuver, and submarine maneuver at  $\alpha=4.8^\circ$ .

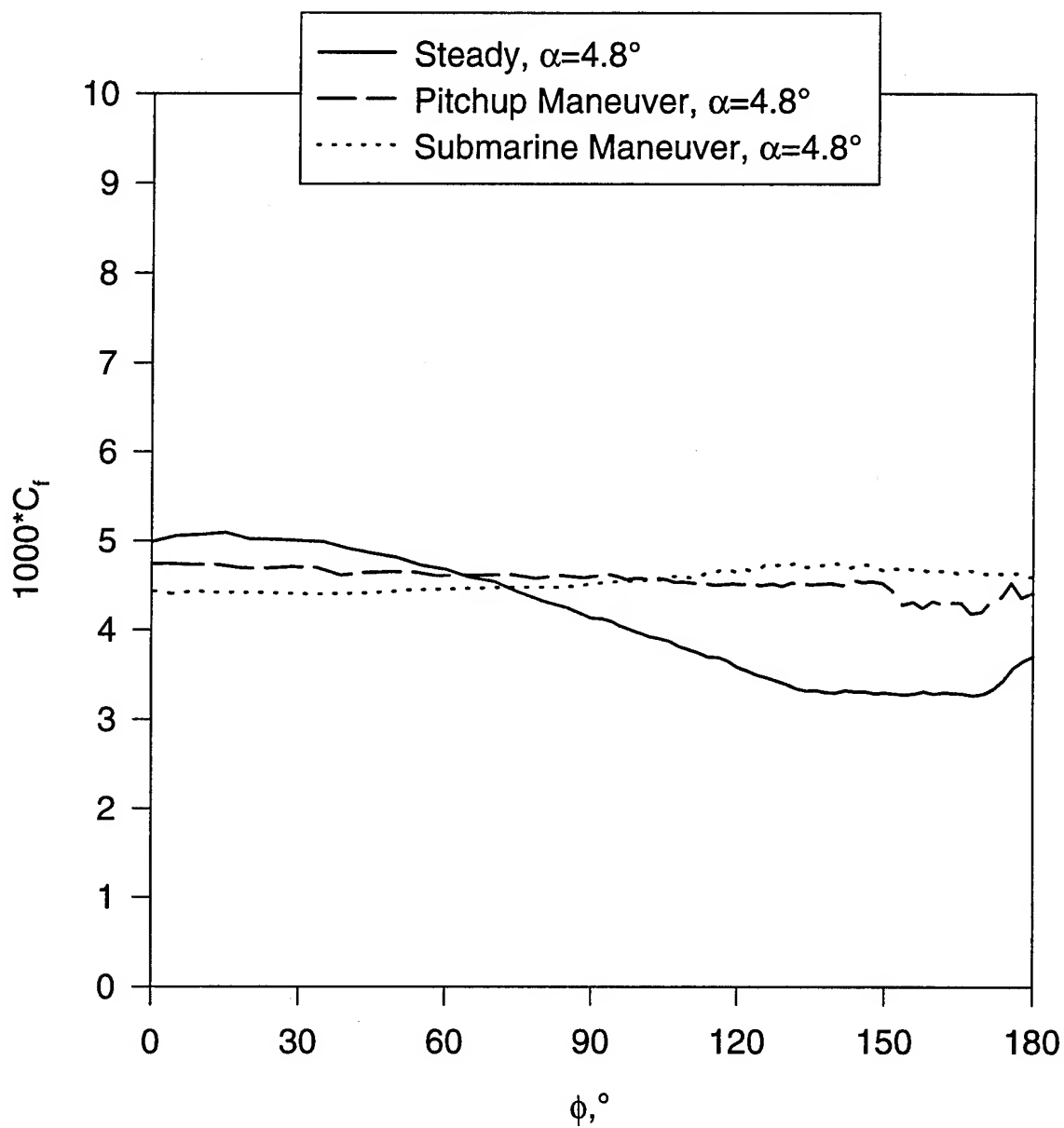


Figure 187. Comparison of wall shear distribution at  $x/L=0.831$  for steady data, pitchup maneuver, and submarine maneuver at  $\alpha=4.8^\circ$ .

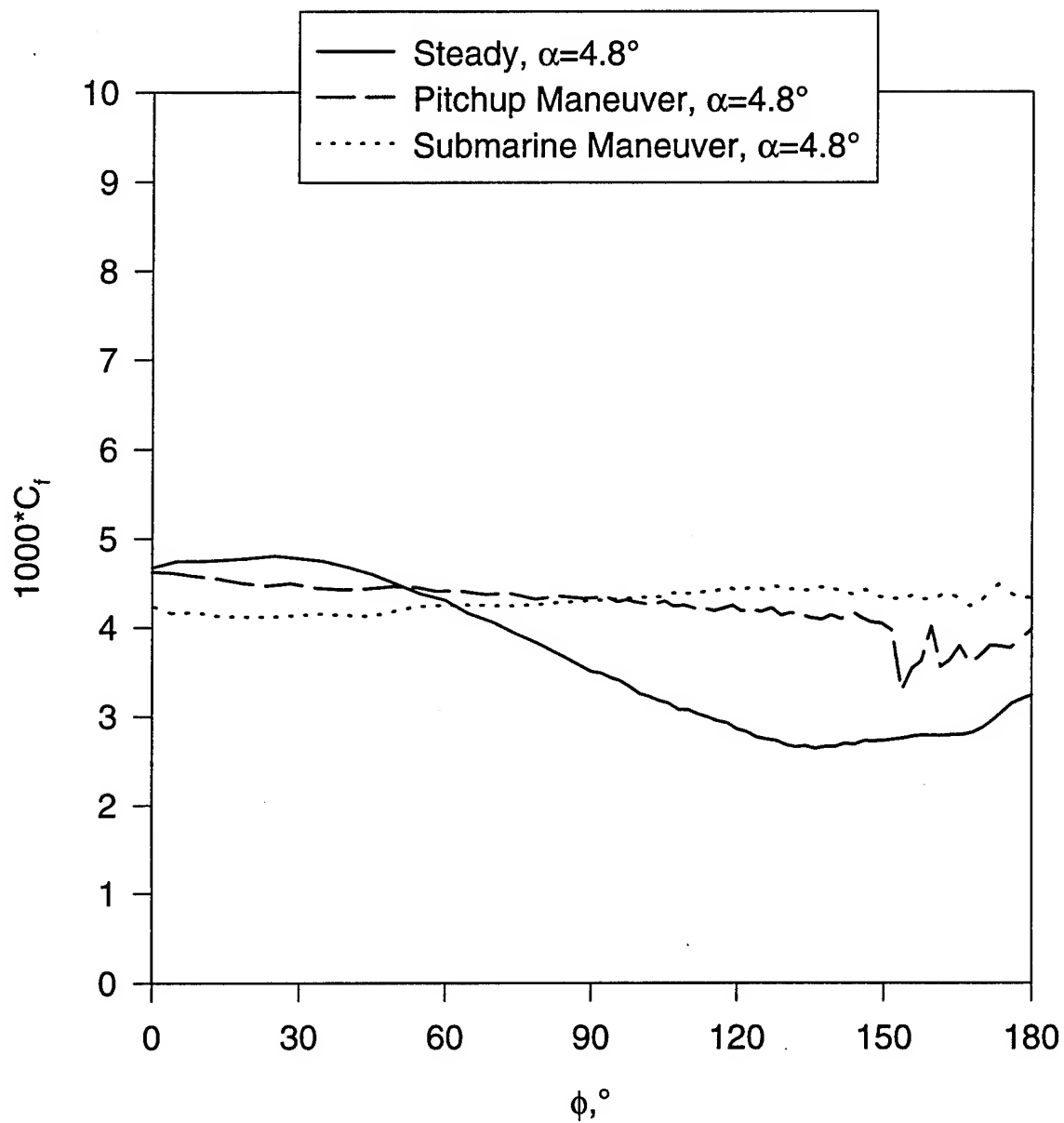


Figure 188. Comparison of wall shear distribution at  $x/L=0.882$  for steady data, pitchup maneuver, and submarine maneuver at  $\alpha=4.8^\circ$ .

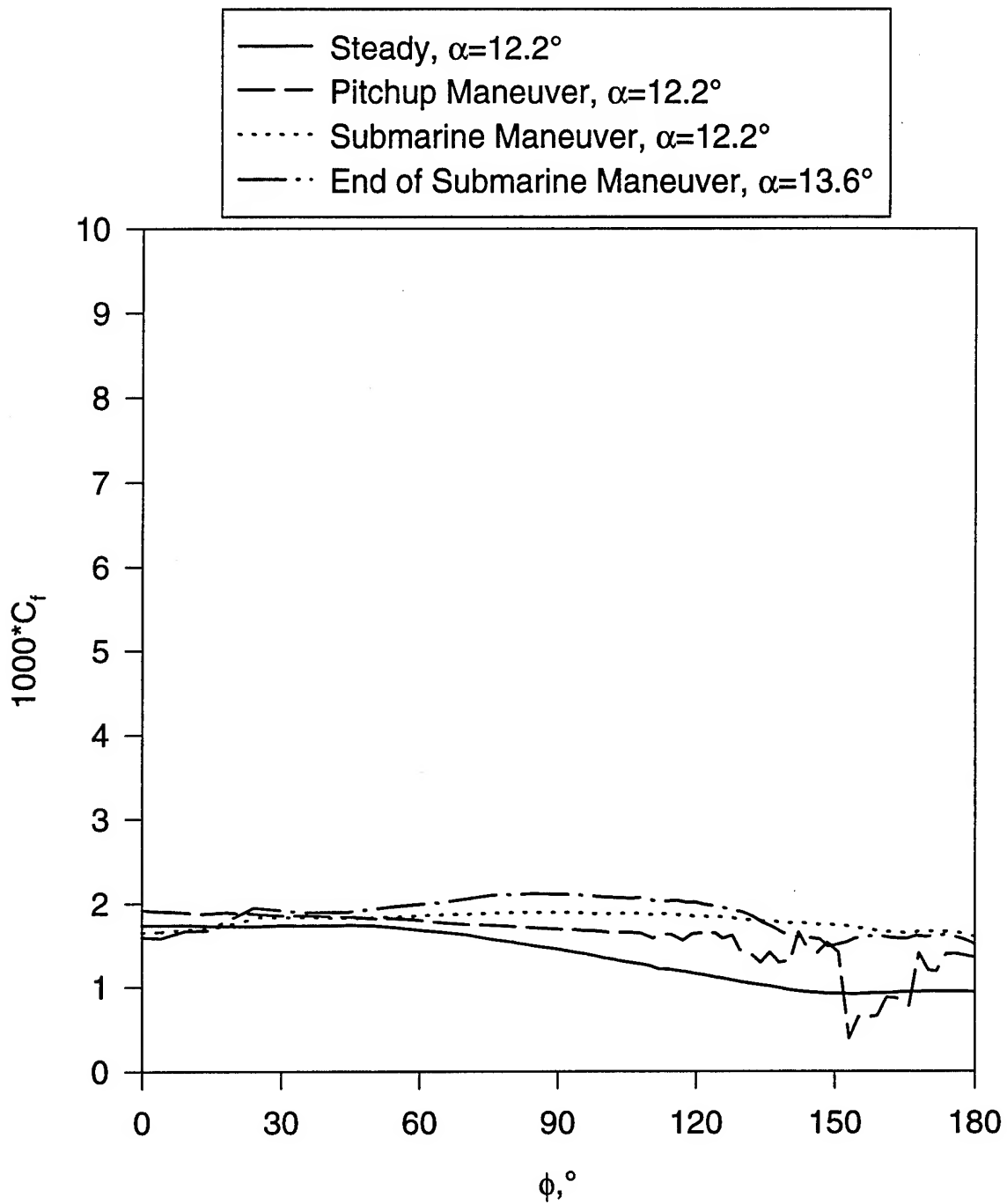


Figure 189. Comparison of wall shear distribution at  $x/L=0.118$  for steady data, pitchup maneuver, and submarine maneuver at  $\alpha=12.2^\circ$ .



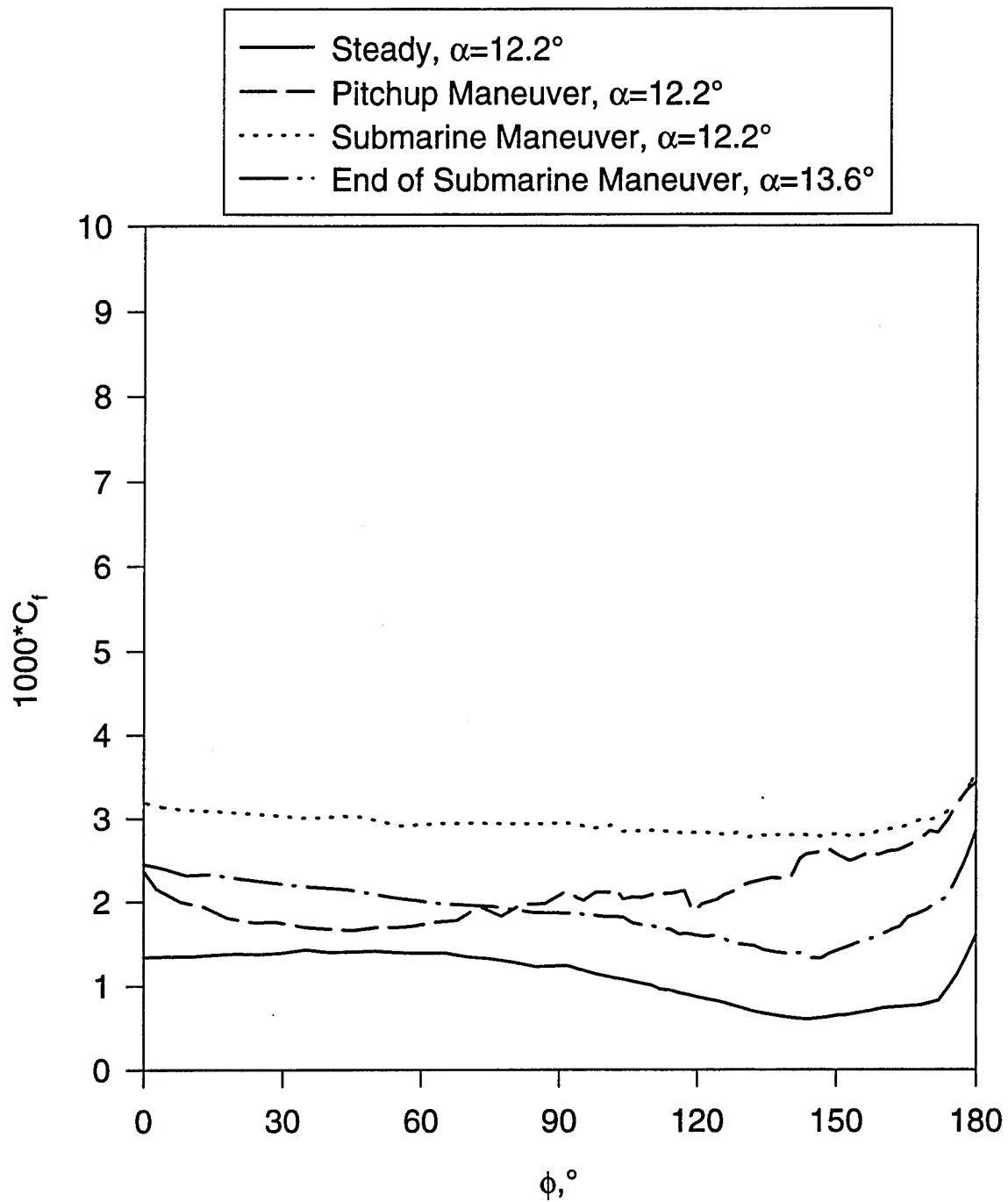


Figure 190. Comparison of wall shear distribution at  $x/L=0.194$  for steady data, pitchup maneuver, and submarine maneuver at  $\alpha=12.2^\circ$ .

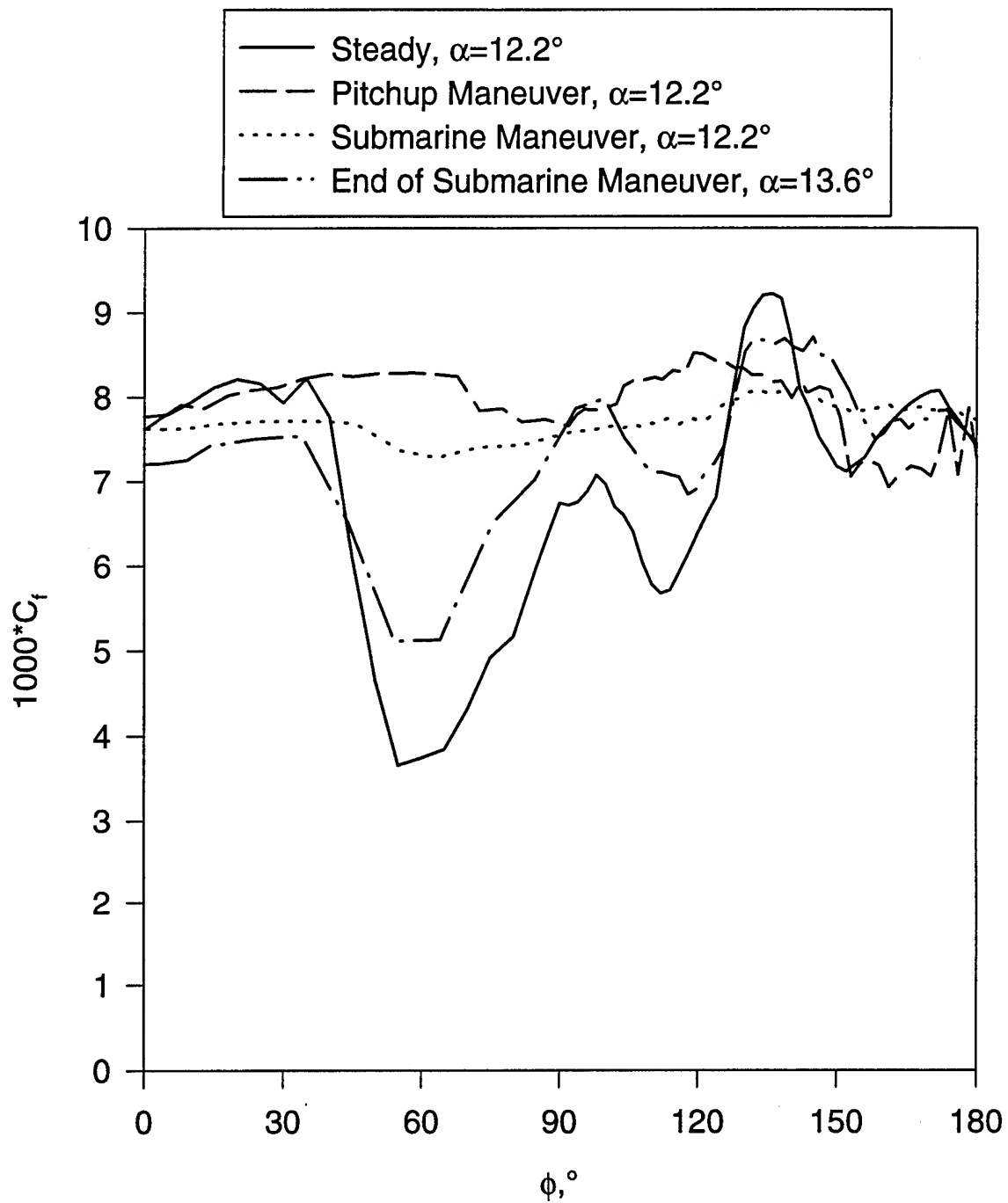


Figure 191. Comparison of wall shear distribution at  $x/L=0.220$  for steady data, pitchup maneuver, and submarine maneuver at  $\alpha=12.2^\circ$ .

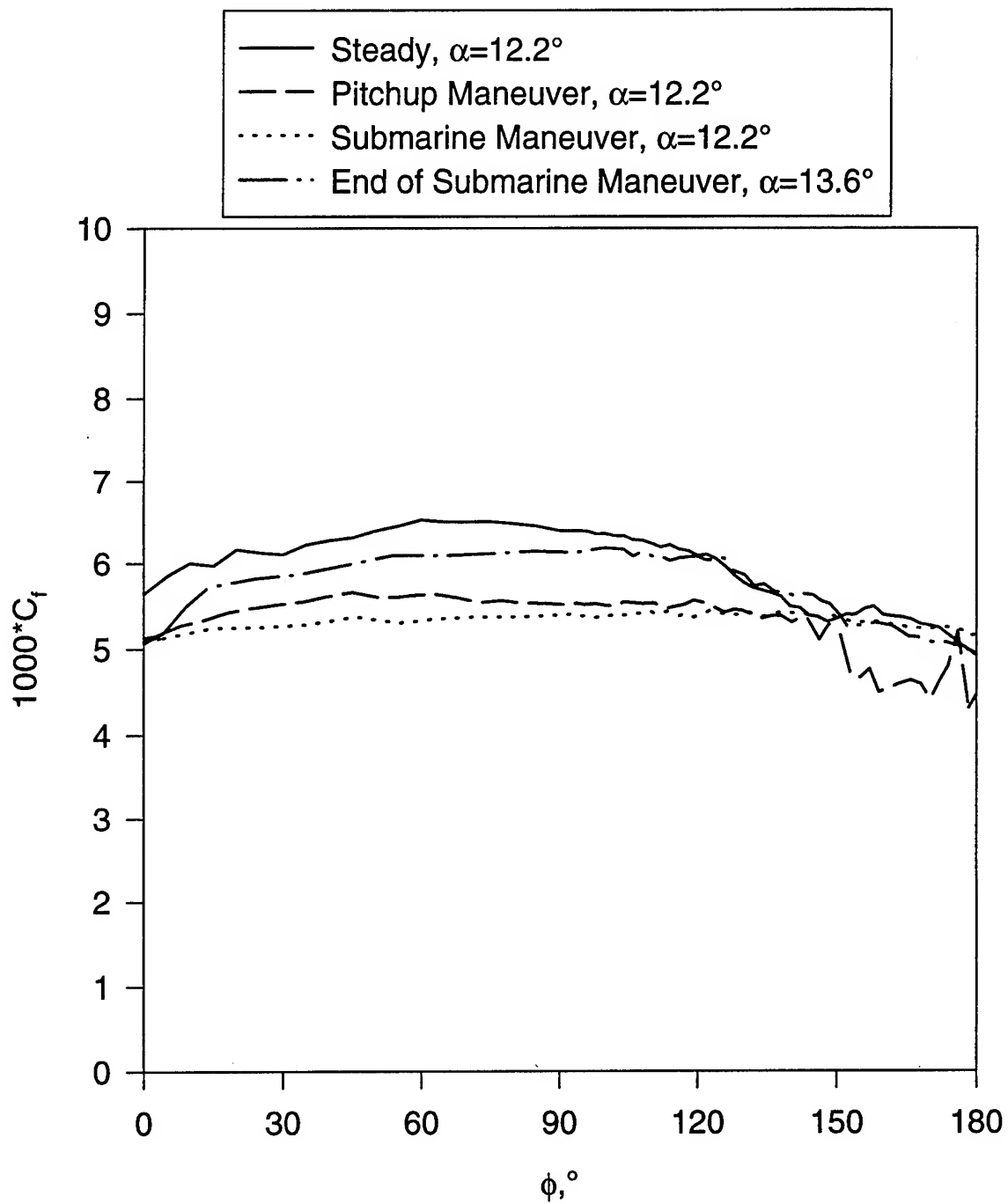


Figure 192. Comparison of wall shear distribution at  $x/L=0.271$  for steady data, pitchup maneuver, and submarine maneuver at  $\alpha=12.2^\circ$ .

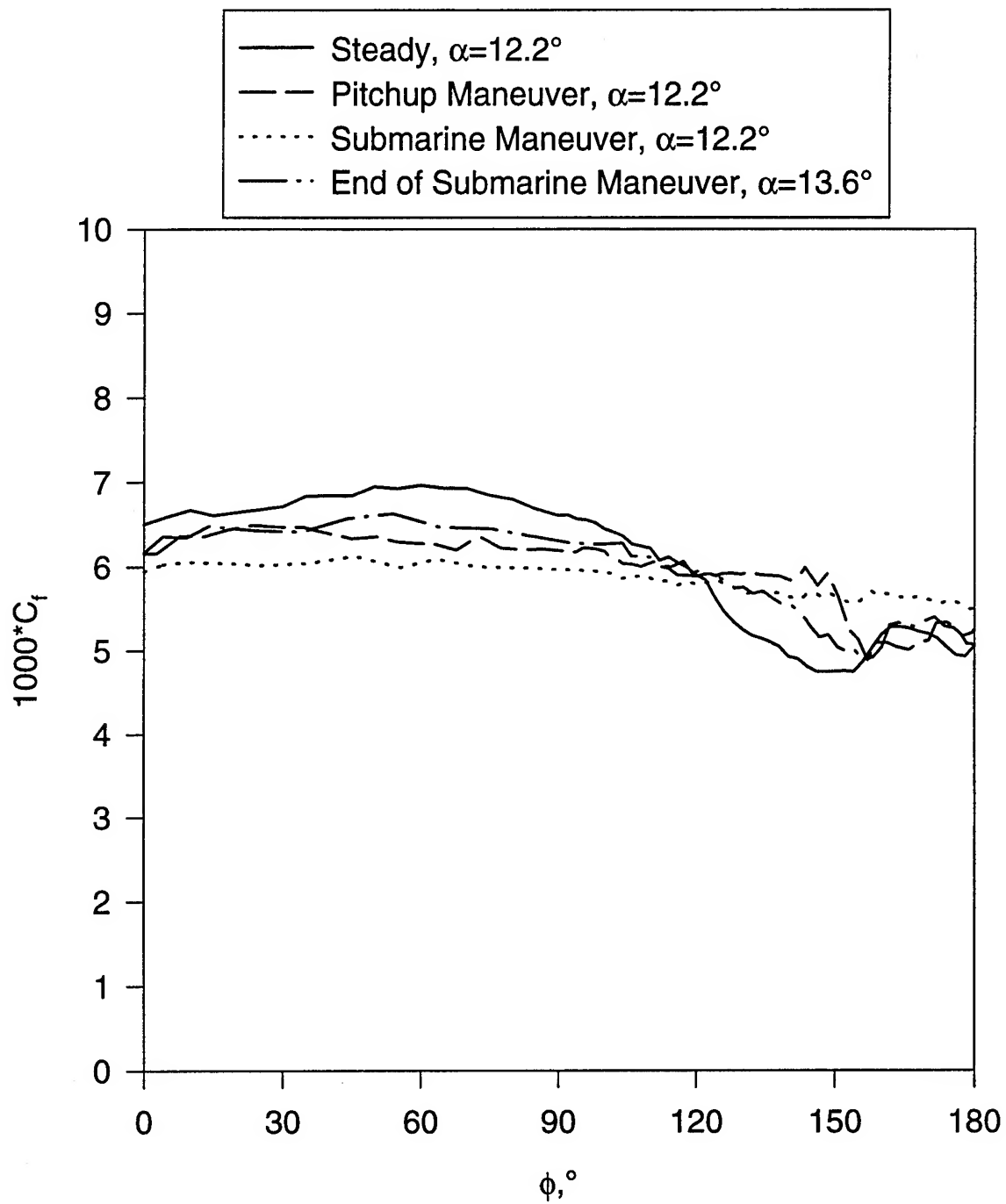


Figure 193. Comparison of wall shear distribution at  $x/L=0.347$  for steady data, pitchup maneuver, and submarine maneuver at  $\alpha=12.2^\circ$ .

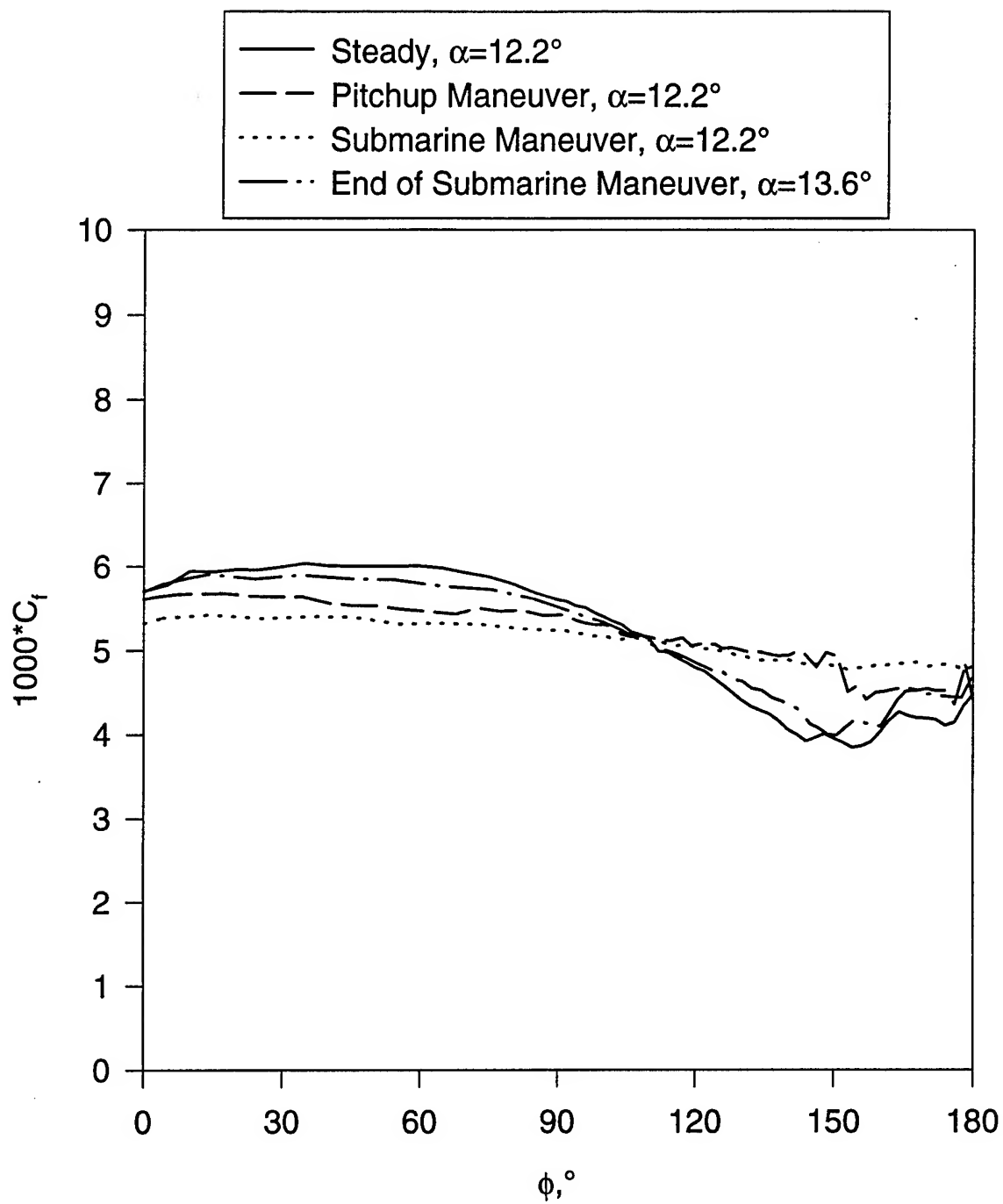


Figure 194. Comparison of wall shear distribution at  $x/L=0.424$  for steady data, pitchup maneuver, and submarine maneuver at  $\alpha=12.2^\circ$ .

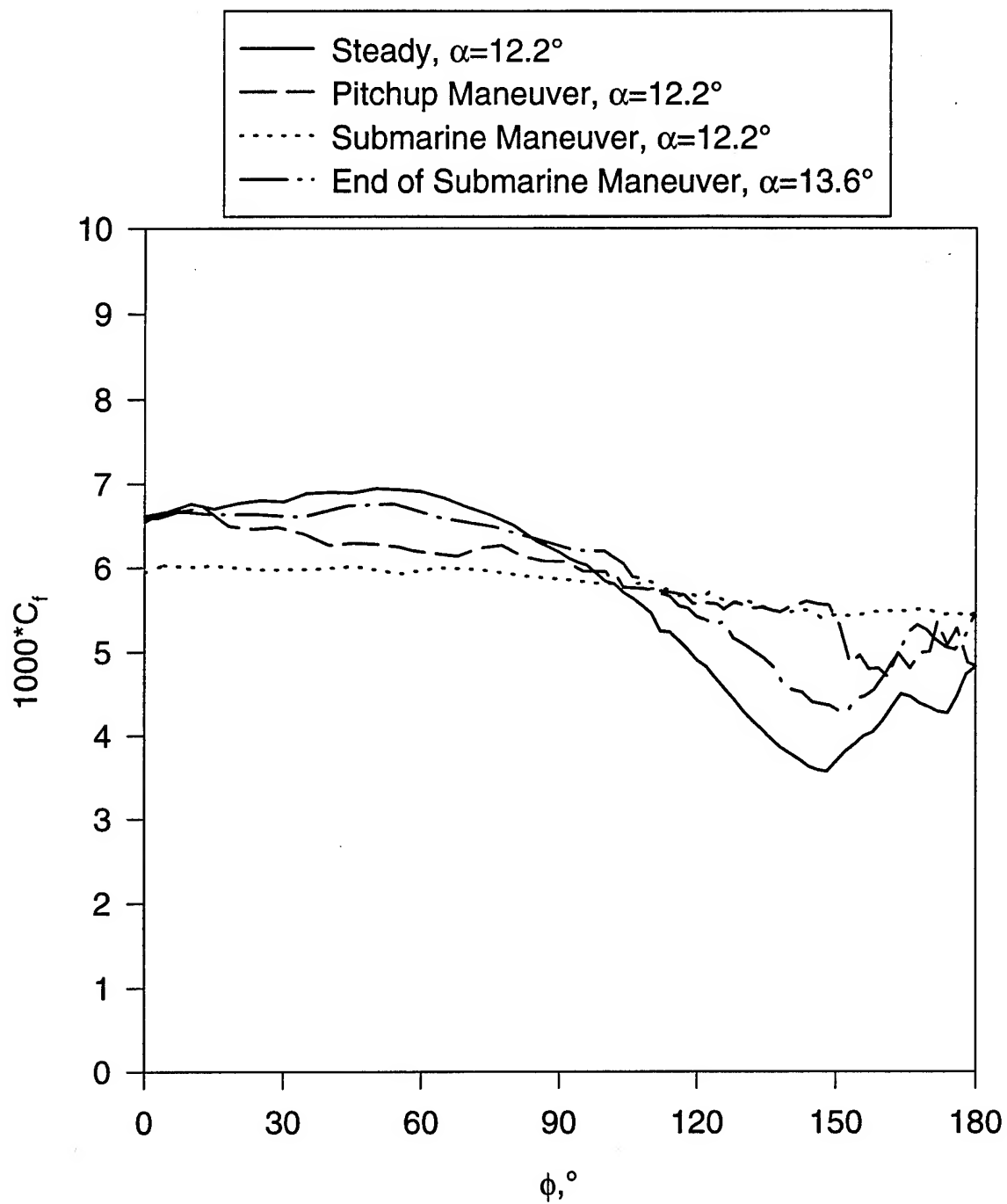


Figure 195. Comparison of wall shear distribution at  $x/L=0.500$  for steady data, pitchup maneuver, and submarine maneuver at  $\alpha=12.2^\circ$ .

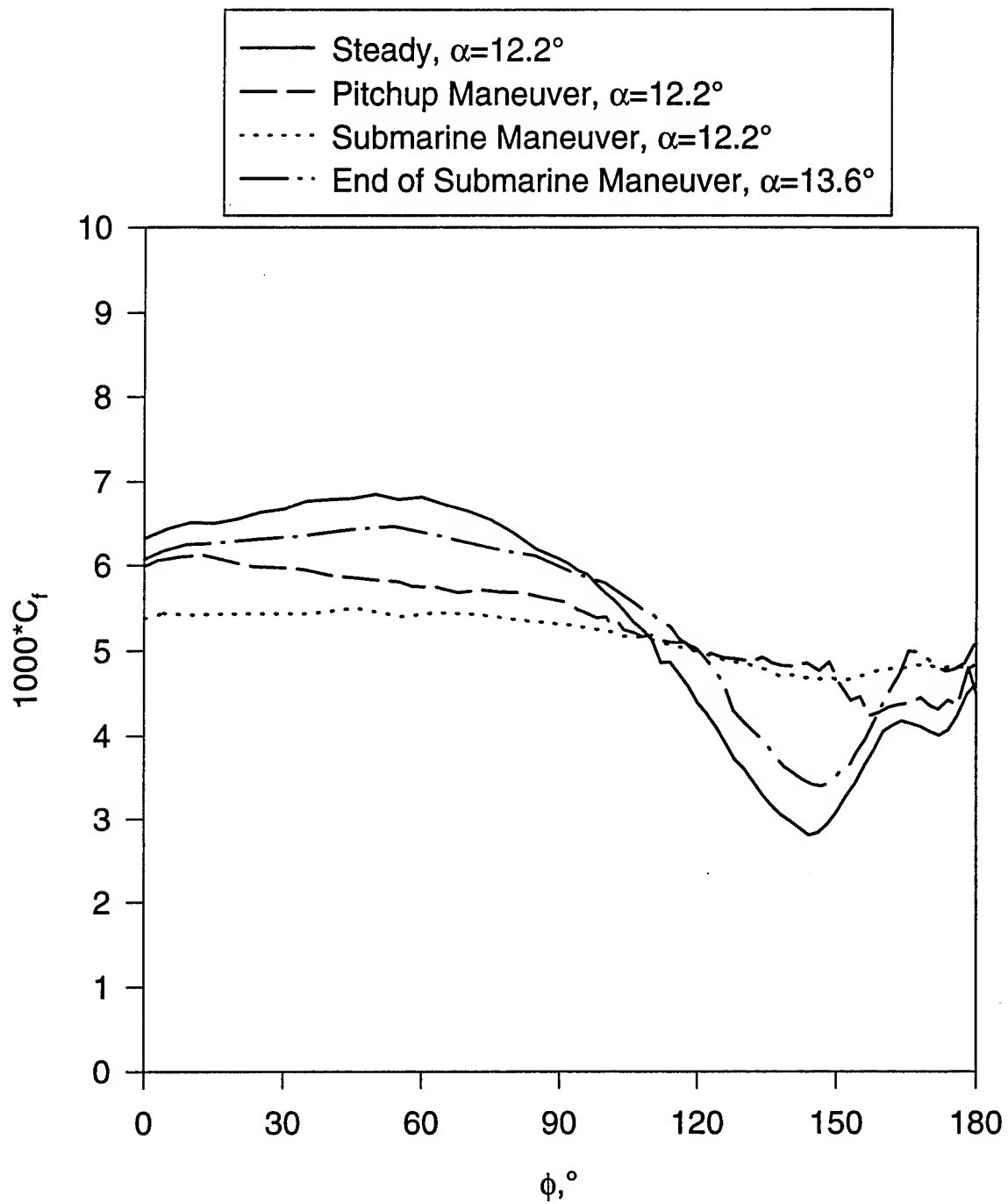


Figure 196. Comparison of wall shear distribution at  $x/L=0.576$  for steady data, pitchup maneuver, and submarine maneuver at  $\alpha=12.2^\circ$ .

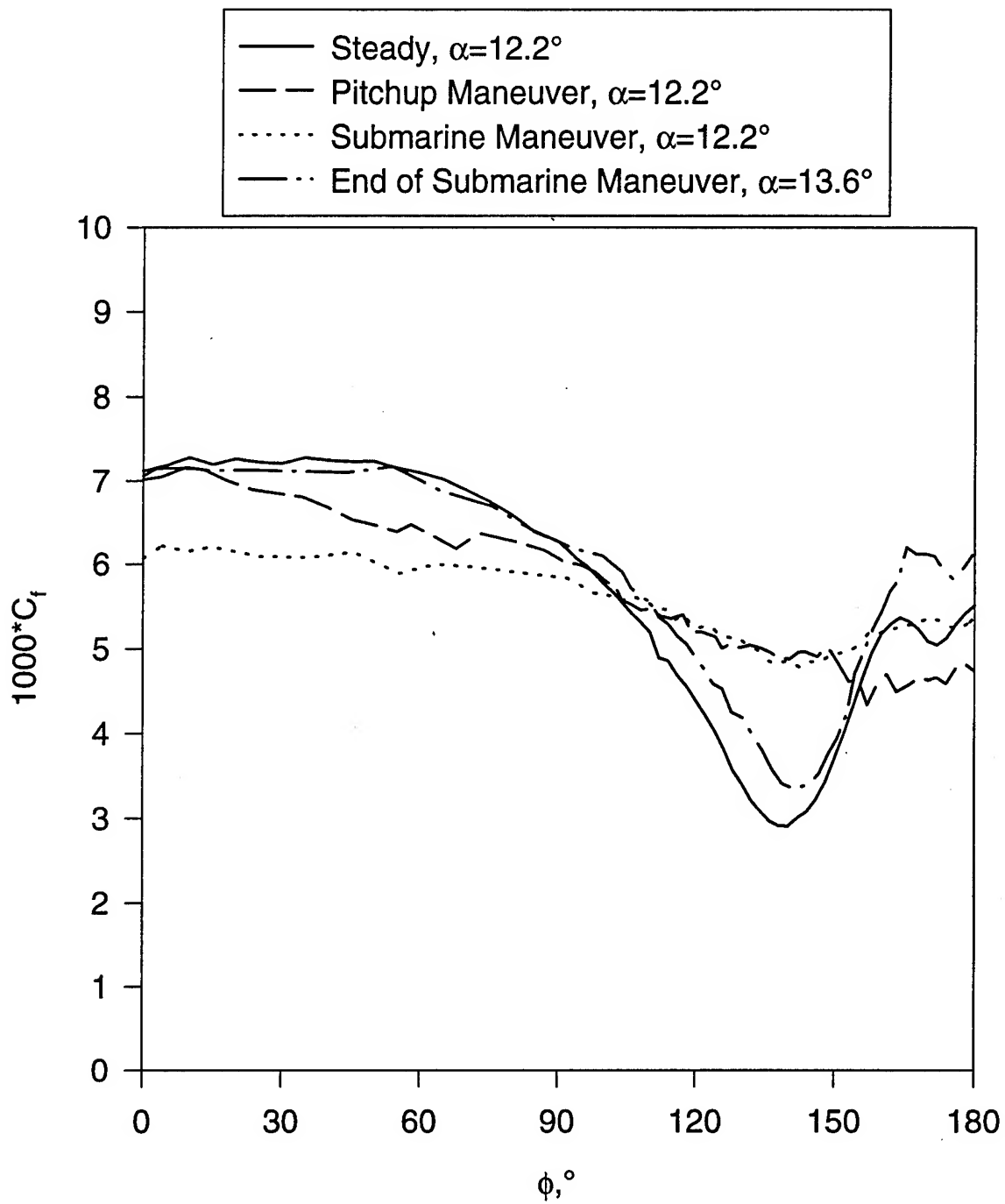


Figure 197. Comparison of wall shear distribution at  $x/L=0.653$  for steady data, pitchup maneuver, and submarine maneuver at  $\alpha=12.2^\circ$ .



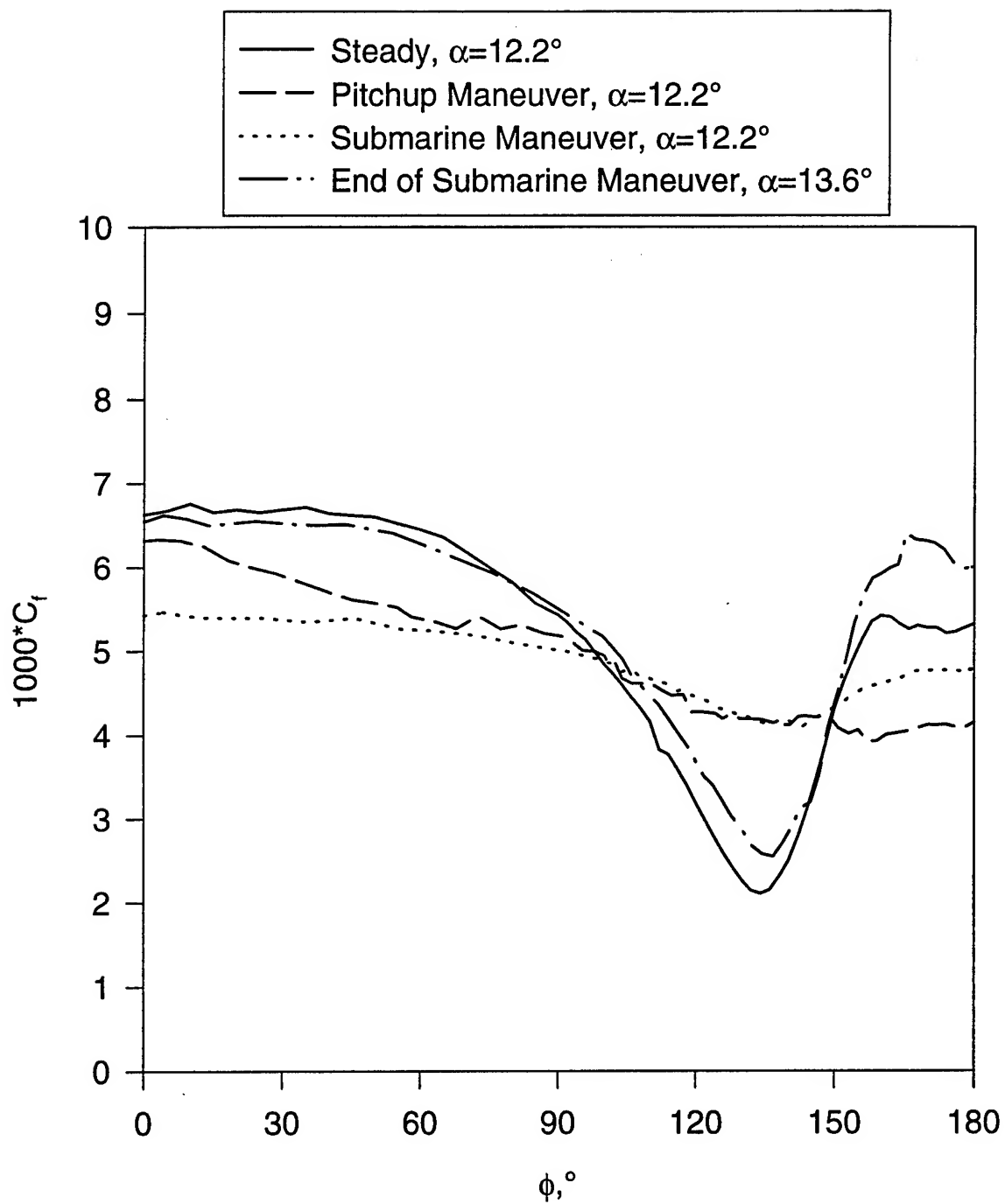


Figure 198. Comparison of wall shear distribution at  $x/L=0.729$  for steady data, pitchup maneuver, and submarine maneuver at  $\alpha=12.2^\circ$ .

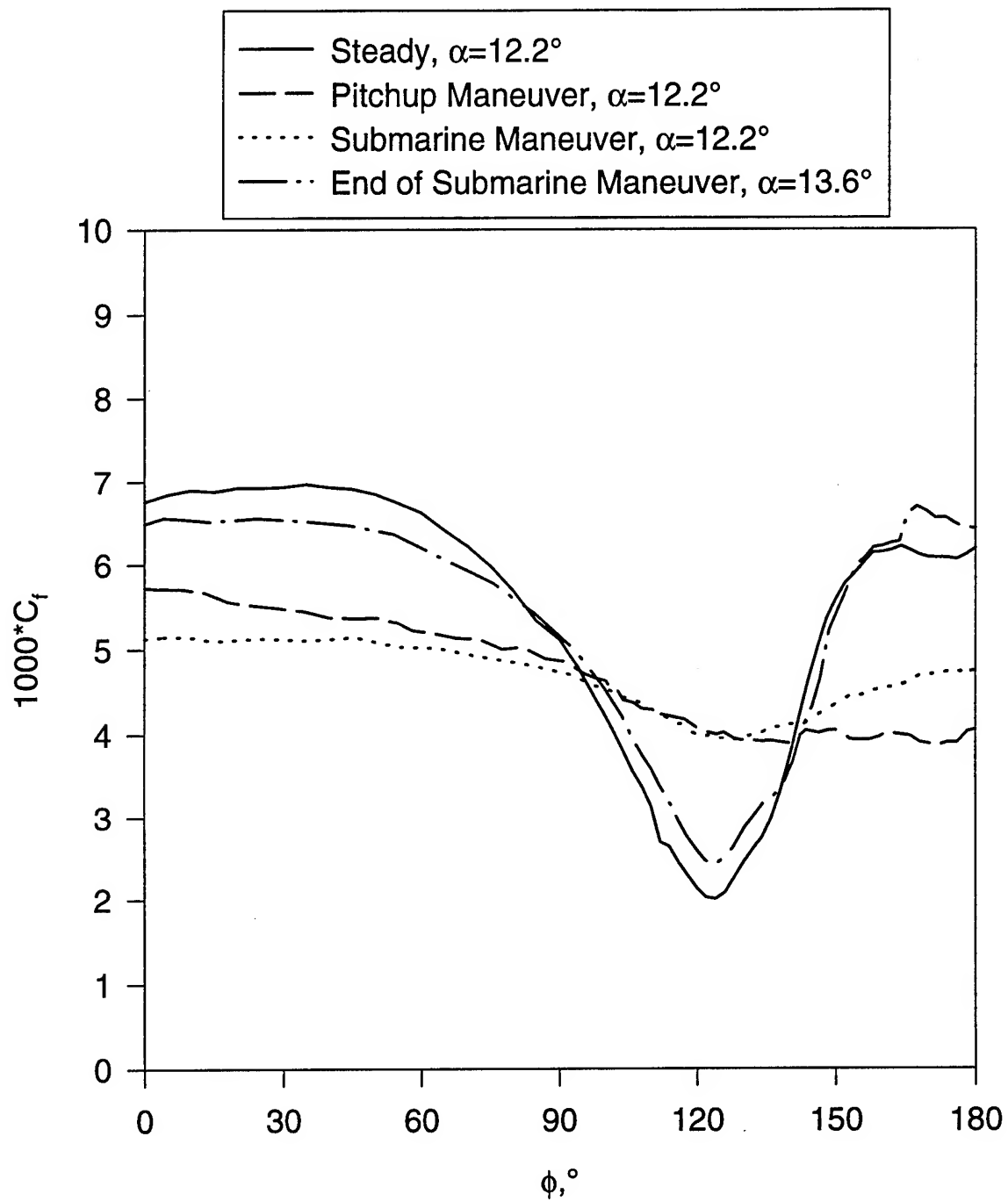


Figure 199. Comparison of wall shear distribution at  $x/L=0.831$  for steady data, pitchup maneuver, and submarine maneuver at  $\alpha=12.2^\circ$ .

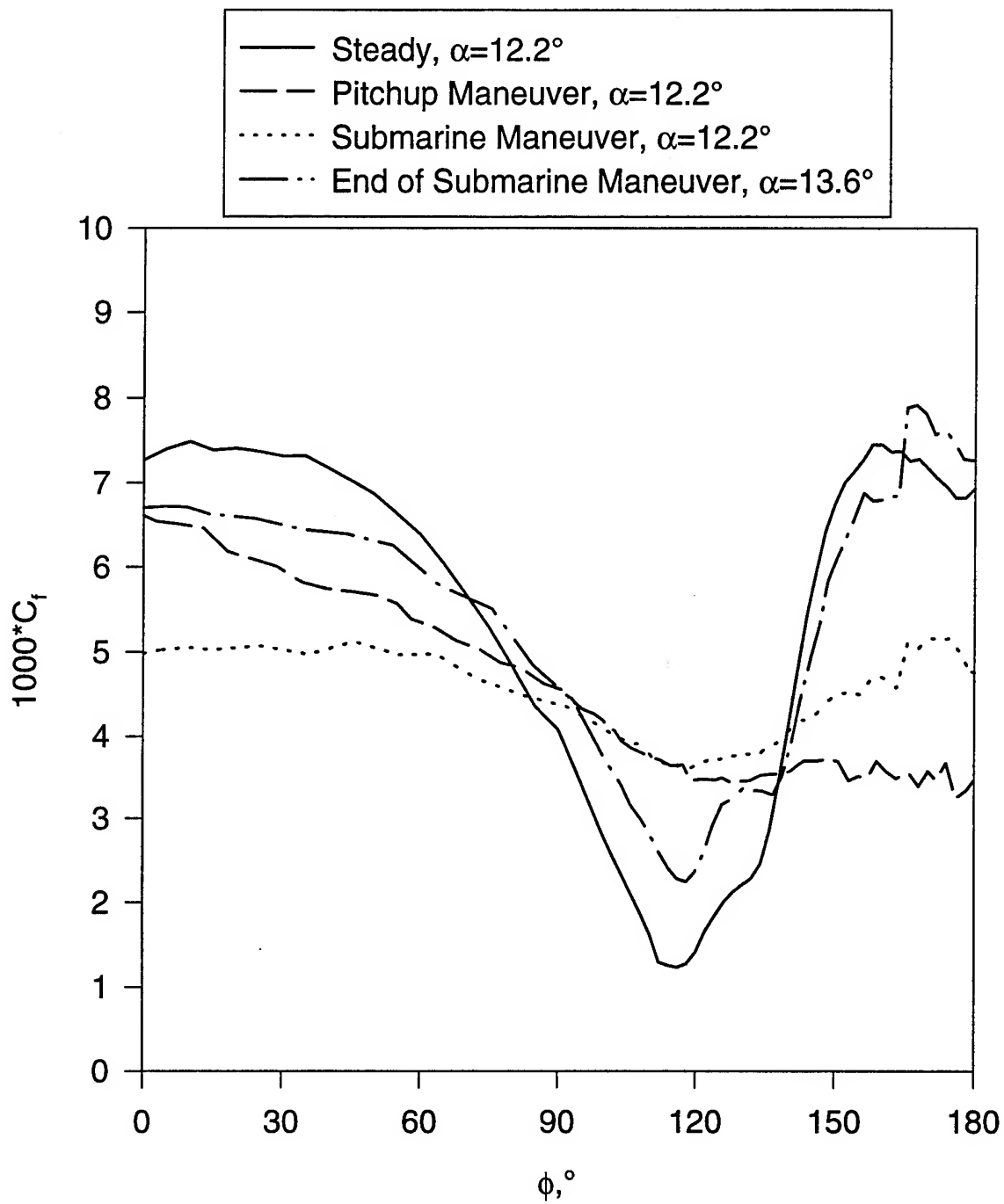


Figure 200. Comparison of wall shear distribution at  $x/L=0.882$  for steady data, pitchup maneuver, and submarine maneuver at  $\alpha=12.2^\circ$ .

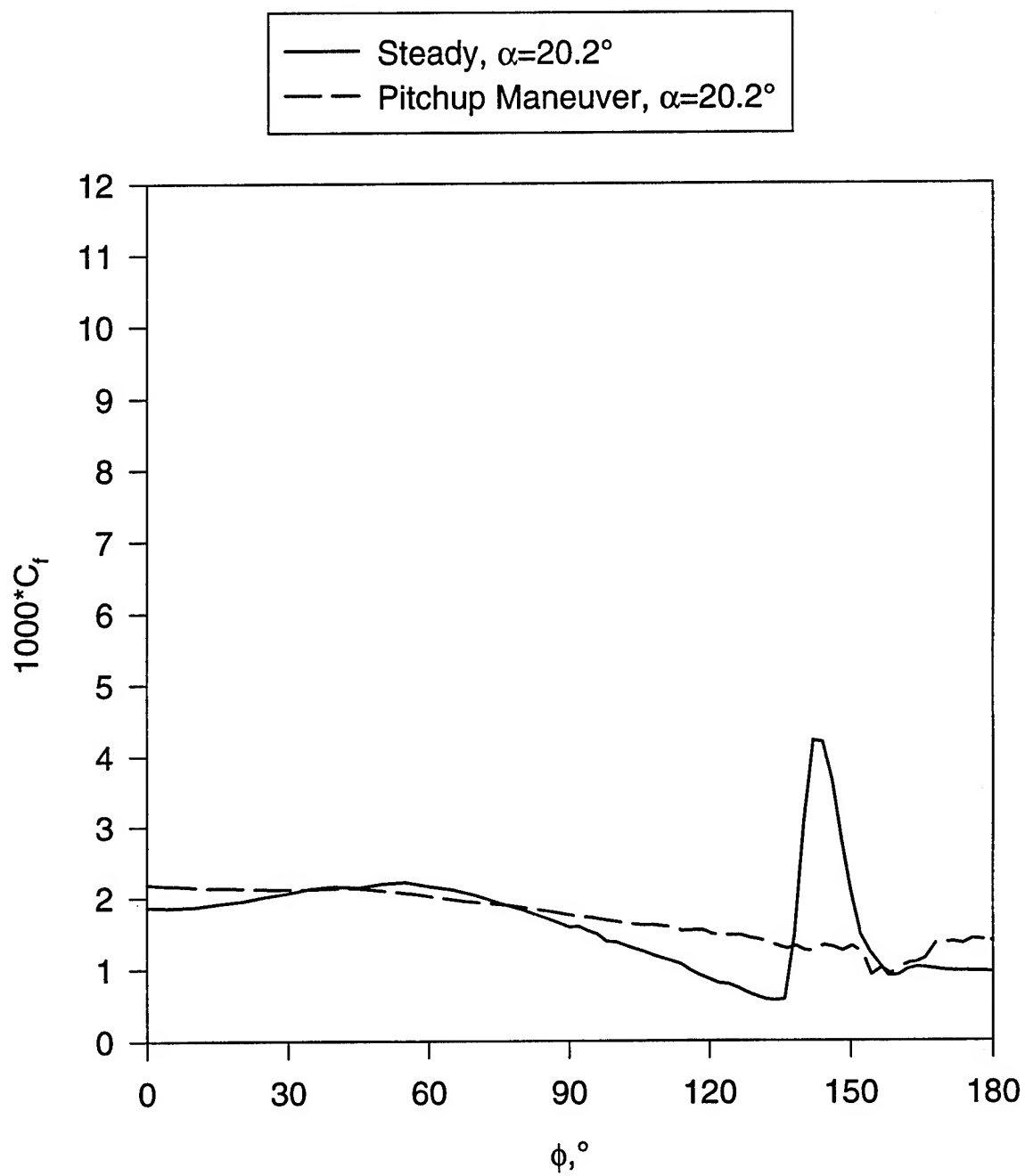


Figure 201. Comparison of wall shear distribution at  $x/L=0.118$  for steady data and pitchup maneuver at  $\alpha=20.2^\circ$ .

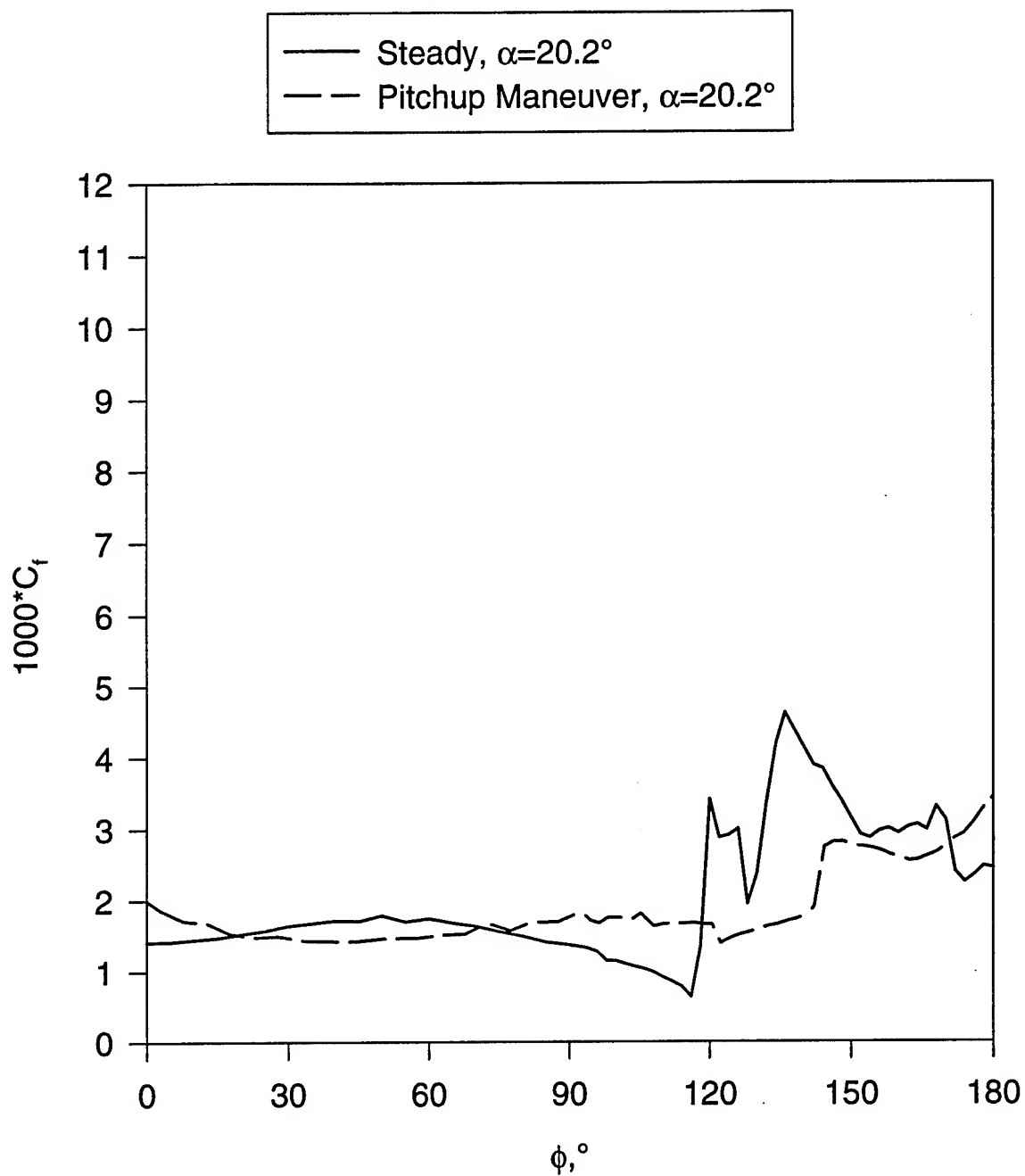


Figure 202. Comparison of wall shear distribution at  $x/L=0.194$  for steady data and pitchup maneuver at  $\alpha=20.2^\circ$ .

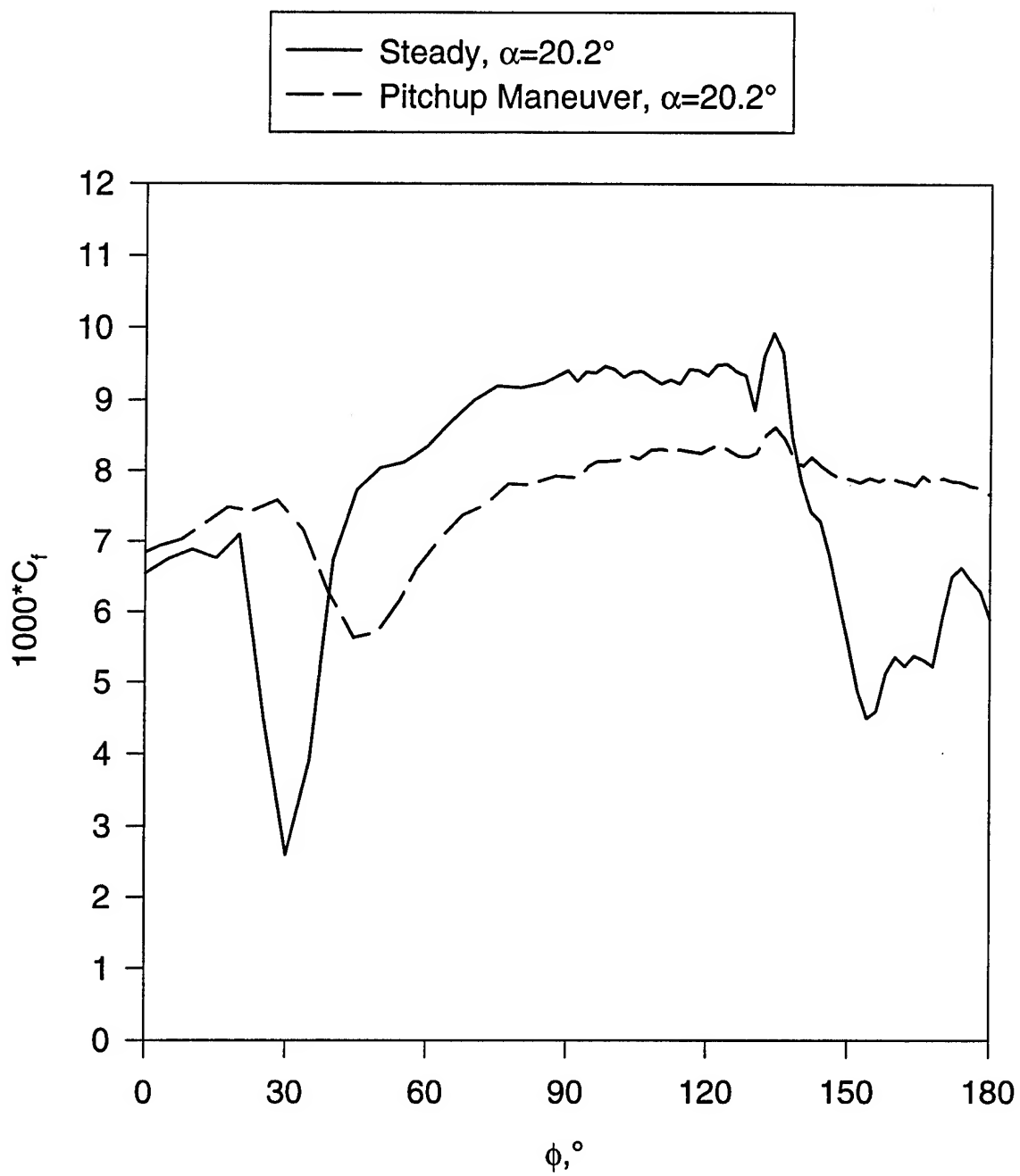


Figure 203. Comparison of wall shear distribution at  $x/L=0.220$  for steady data and pitchup maneuver at  $\alpha=20.2^\circ$ .

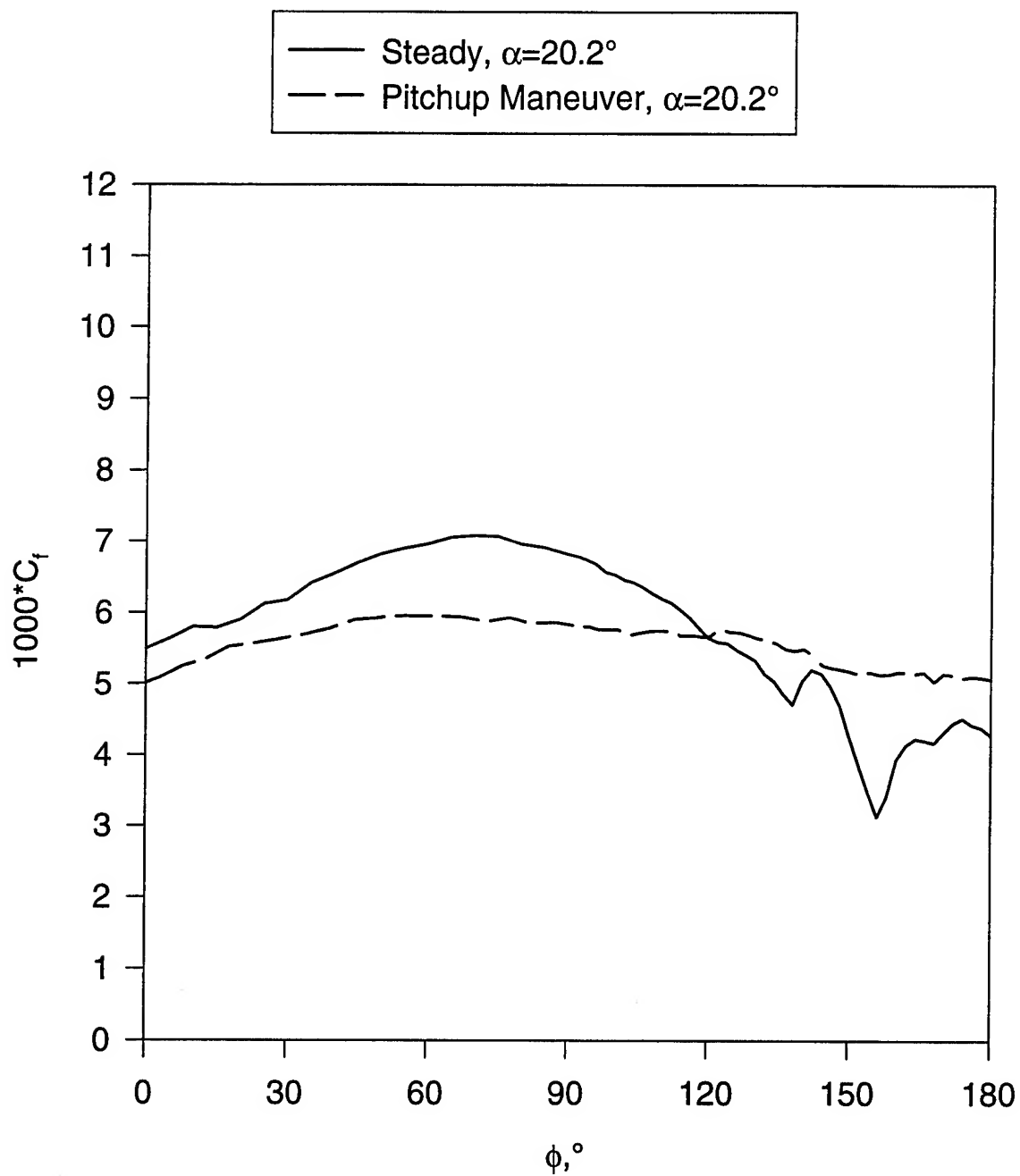


Figure 204. Comparison of wall shear distribution at  $x/L=0.271$  for steady data and pitchup maneuver at  $\alpha=20.2^\circ$ .

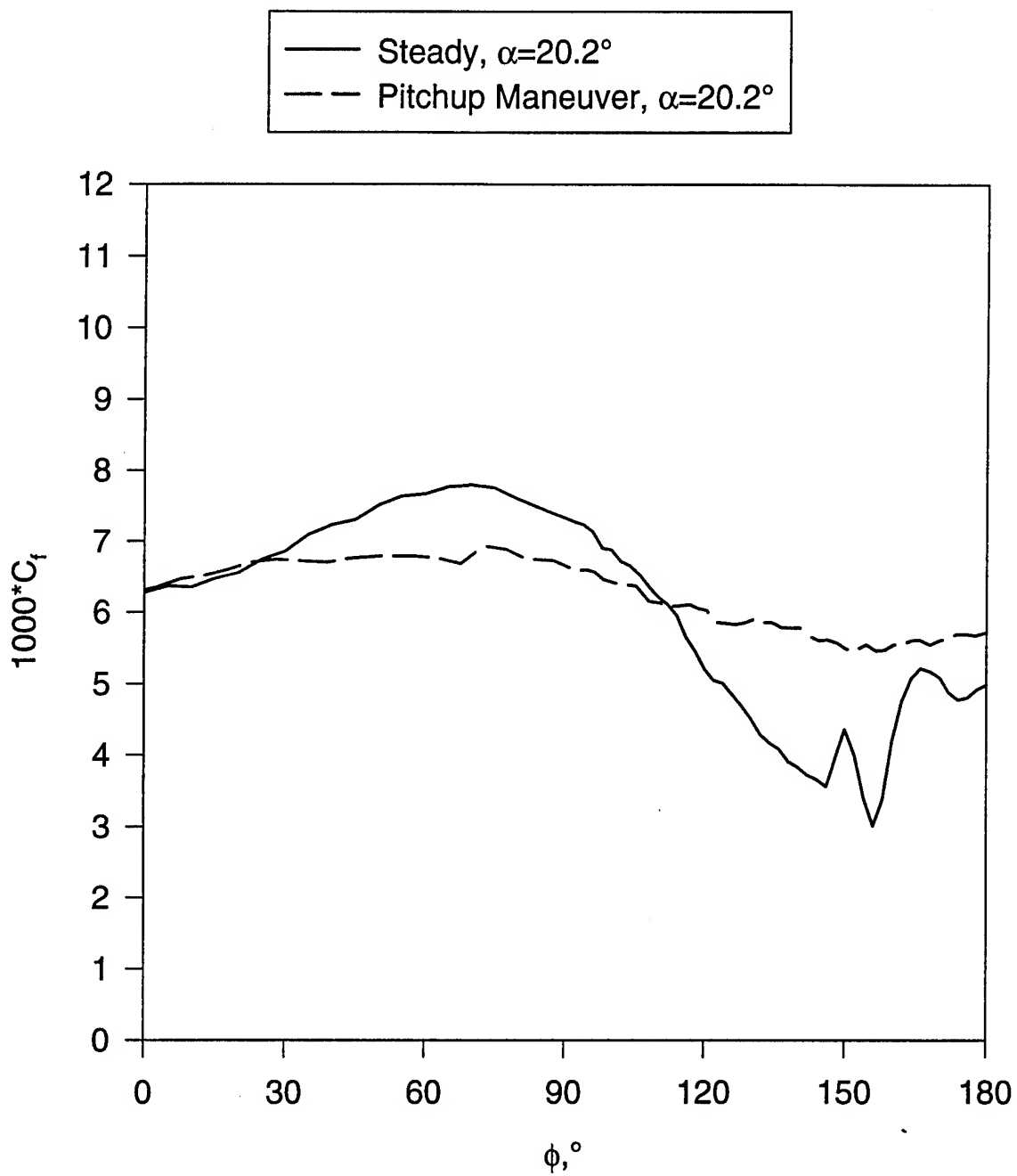


Figure 205. Comparison of wall shear distribution at  $x/L=0.347$  for steady data and pitchup maneuver at  $\alpha=20.2^\circ$ .



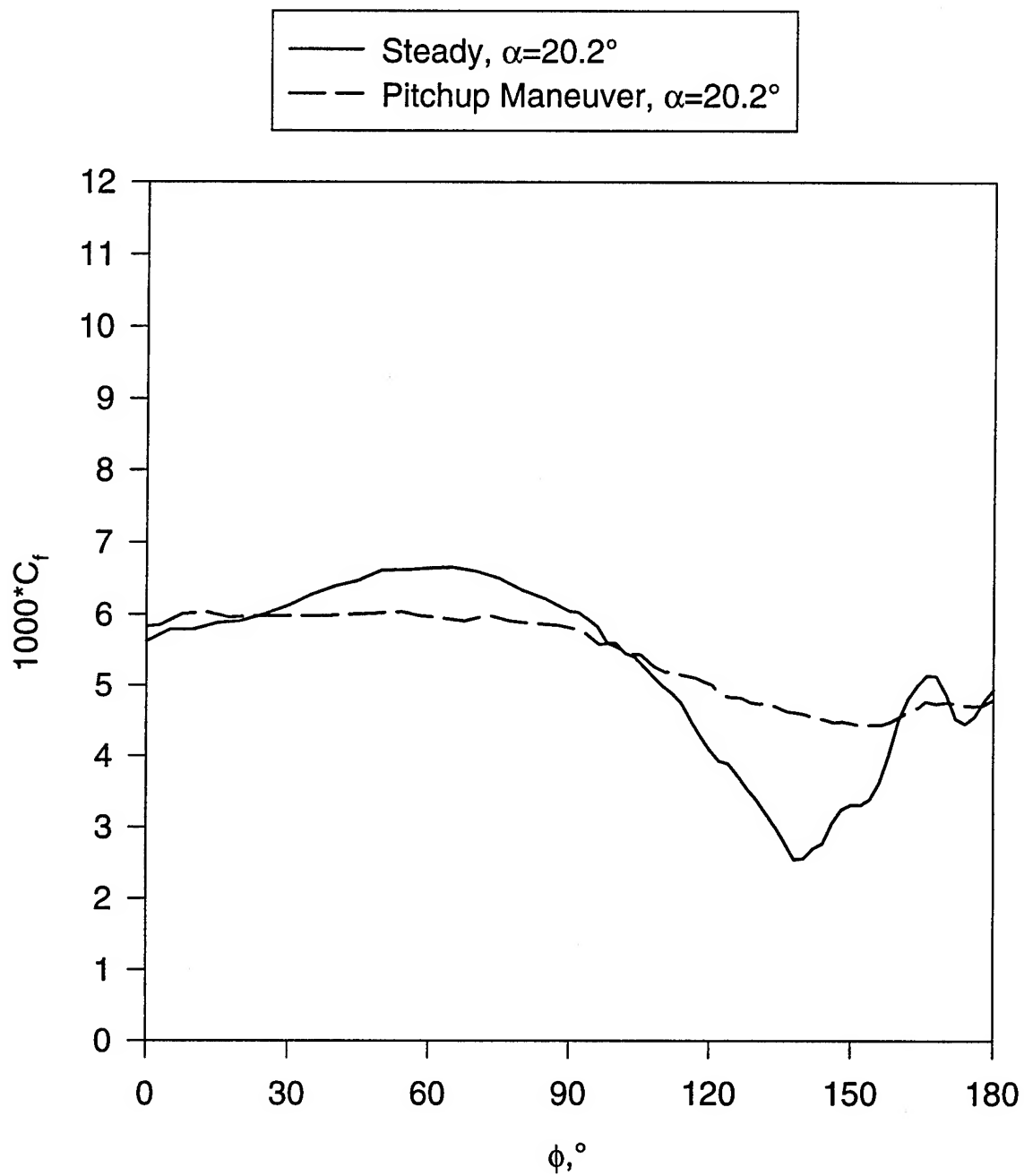


Figure 206. Comparison of wall shear distribution at  $x/L=0.424$  for steady data and pitchup maneuver at  $\alpha=20.2^\circ$ .

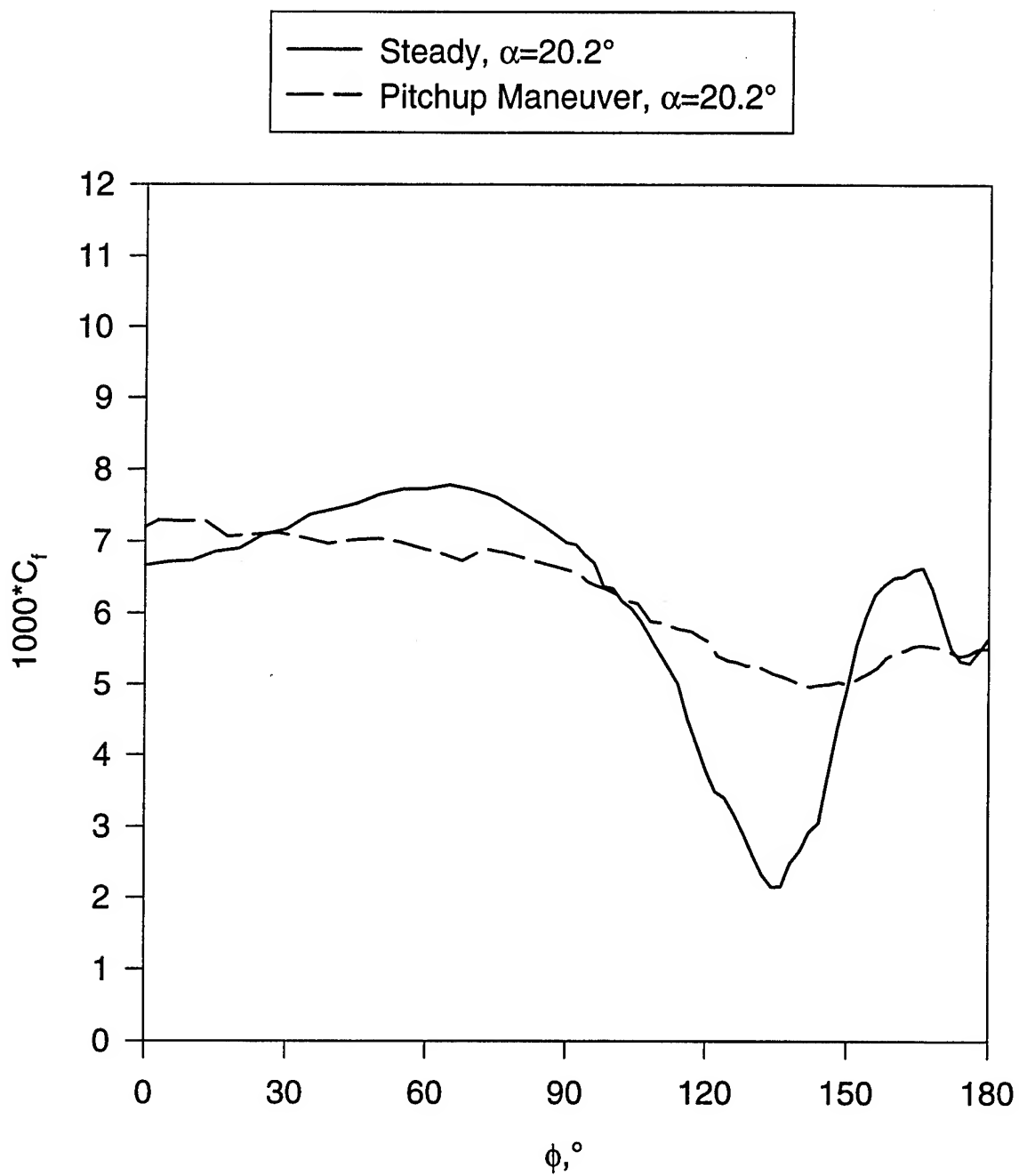


Figure 207. Comparison of wall shear distribution at  $x/L=0.500$  for steady data and pitchup maneuver at  $\alpha=20.2^\circ$ .

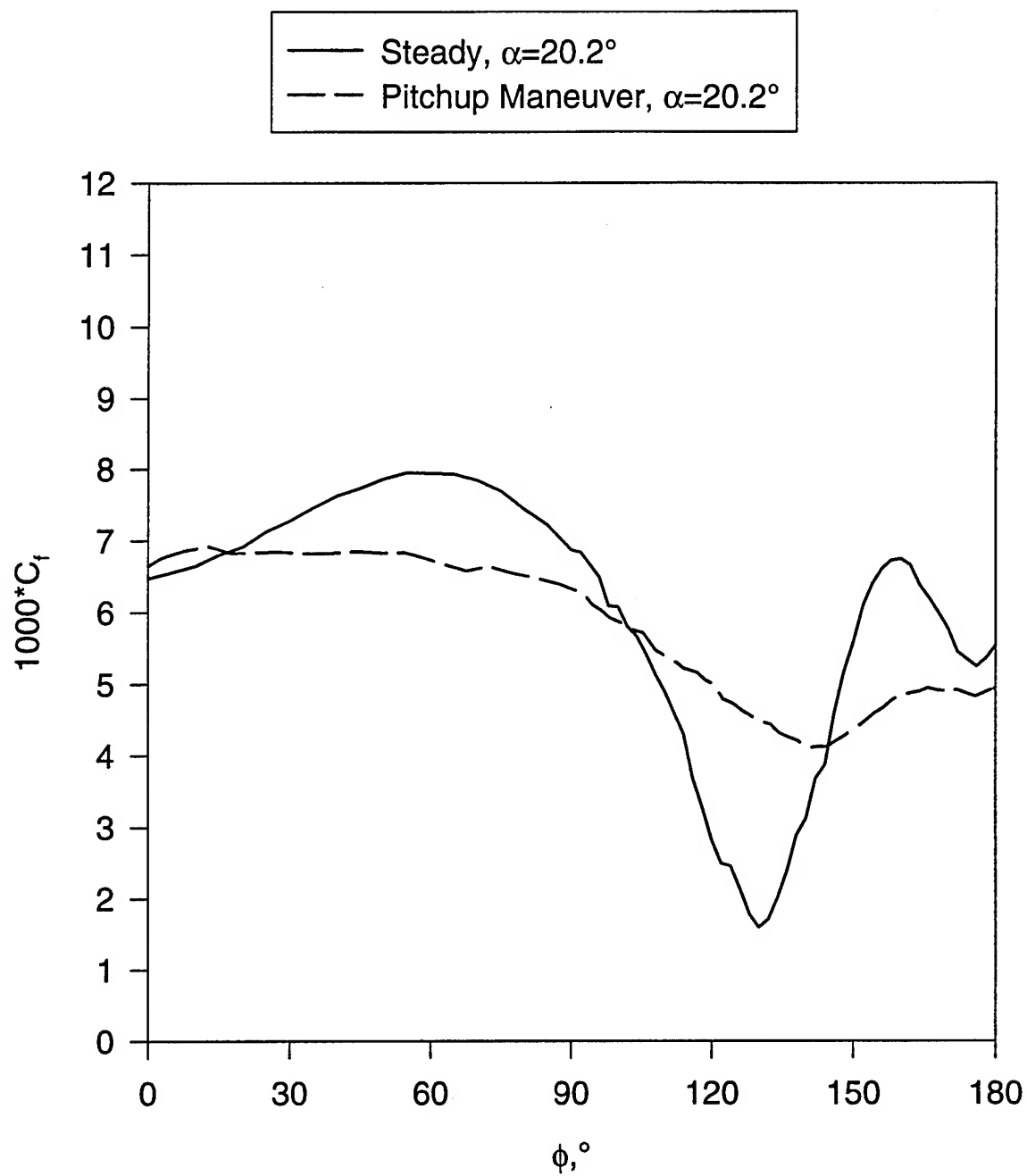


Figure 208. Comparison of wall shear distribution at  $x/L=0.576$  for steady data and pitchup maneuver at  $\alpha=20.2^\circ$ .

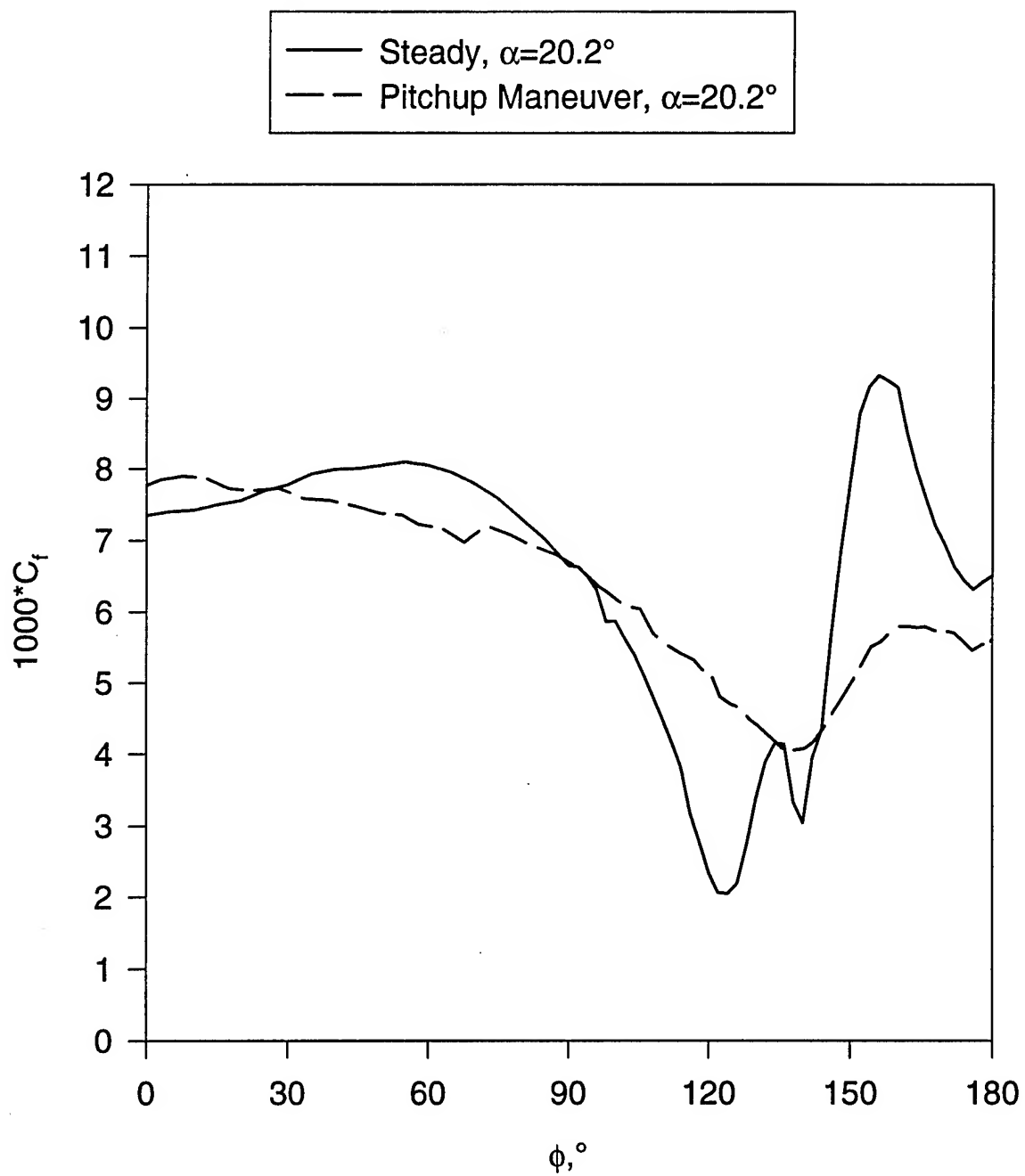


Figure 209. Comparison of wall shear distribution at  $x/L=0.653$  for steady data and pitchup maneuver at  $\alpha=20.2^\circ$ .

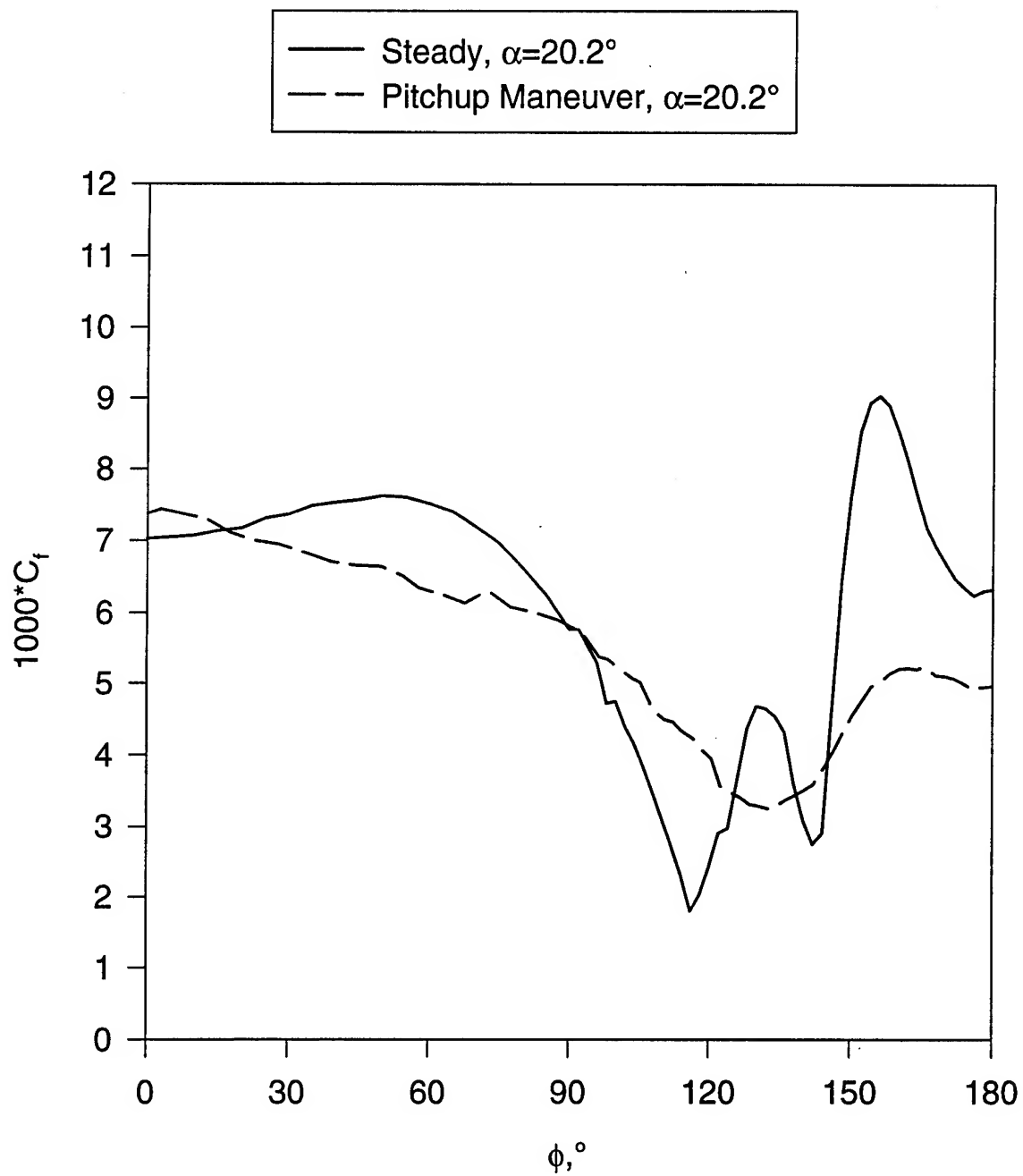


Figure 210. Comparison of wall shear distribution at  $x/L=0.729$  for steady data and pitchup maneuver at  $\alpha=20.2^\circ$ .

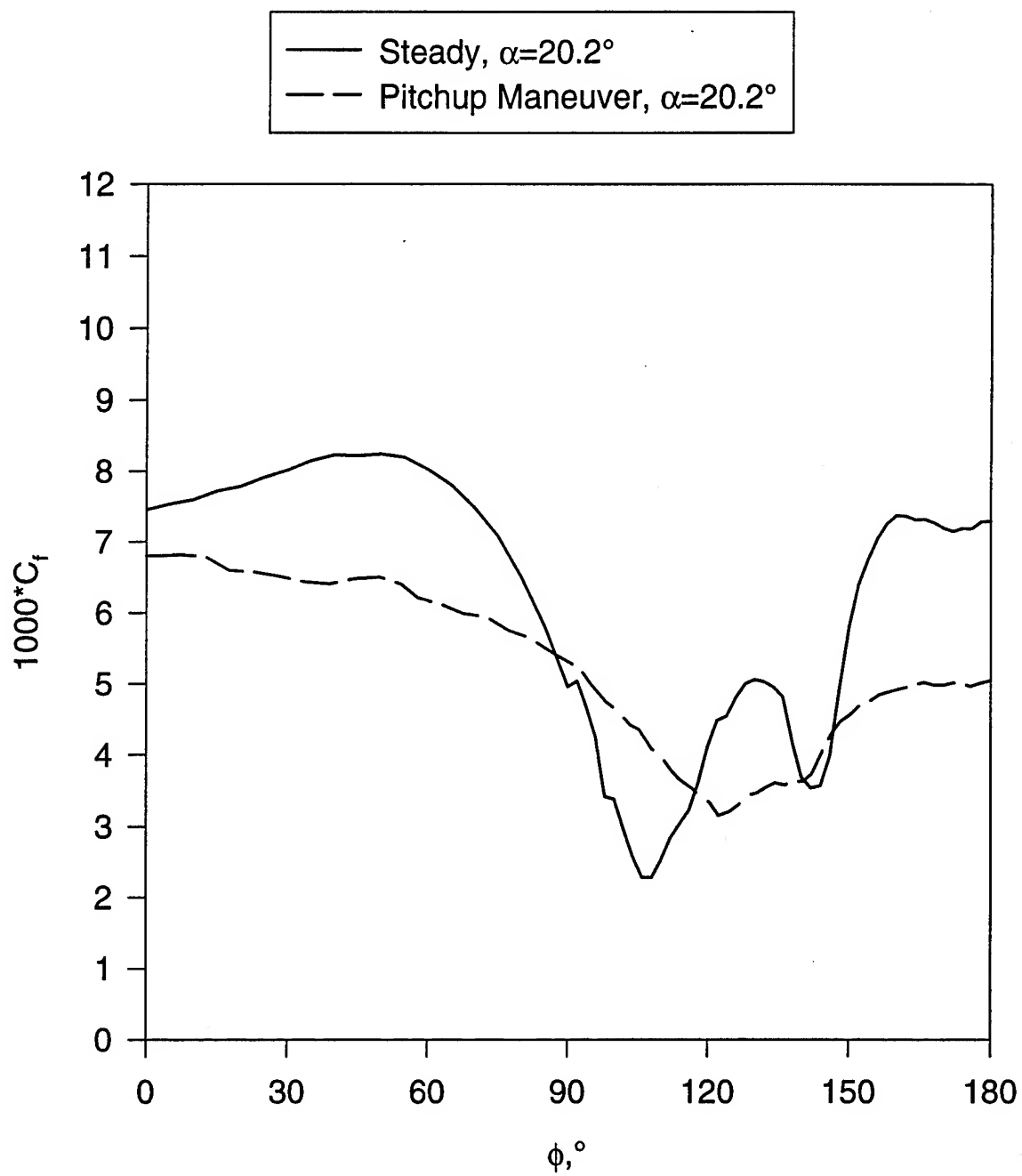


Figure 211. Comparison of wall shear distribution at  $x/L=0.831$  for steady data and pitchup maneuver at  $\alpha=20.2^\circ$ .

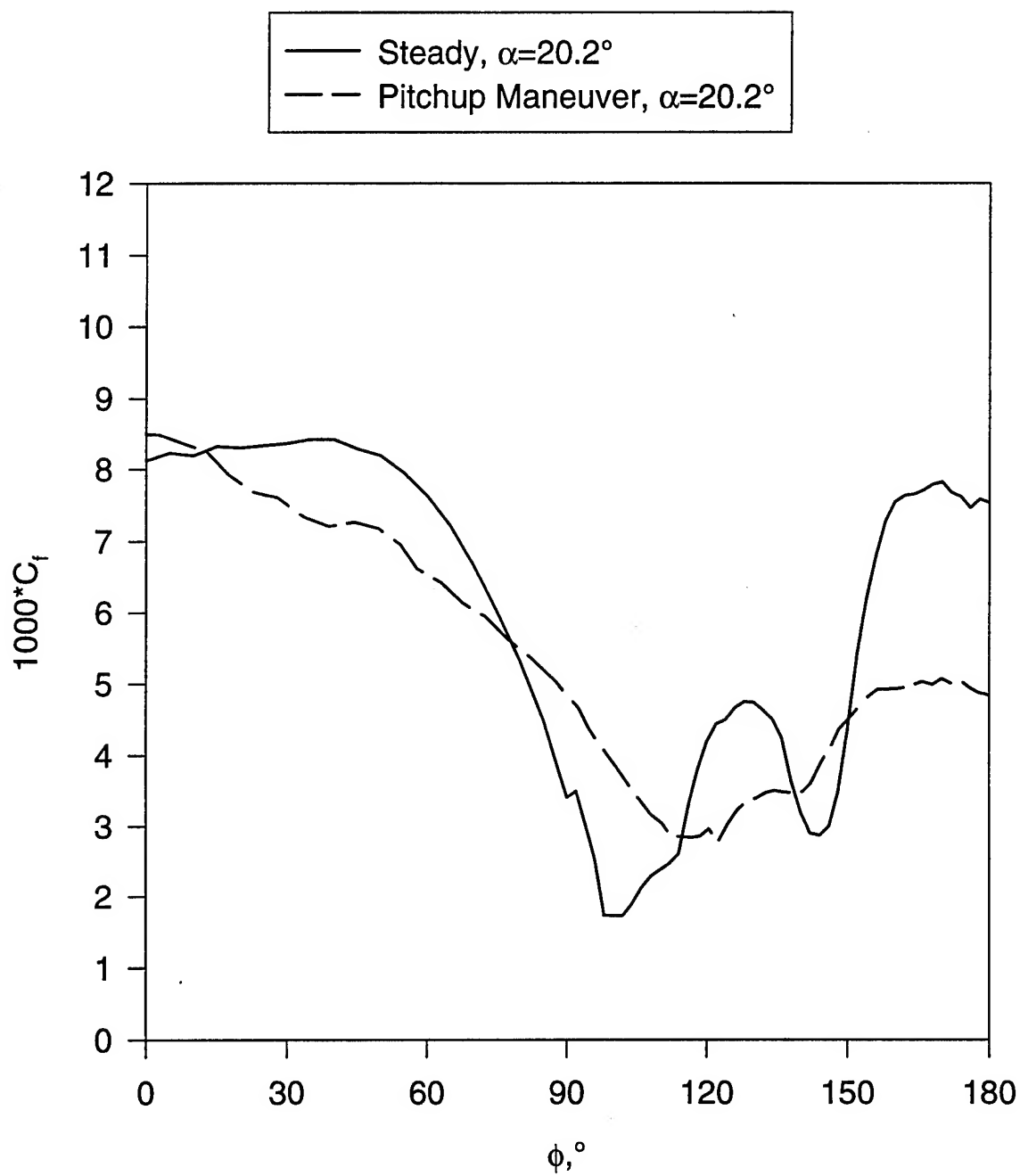


Figure 212. Comparison of wall shear distribution at  $x/L=0.882$  for steady data and pitchup maneuver at  $\alpha=20.2^\circ$ .

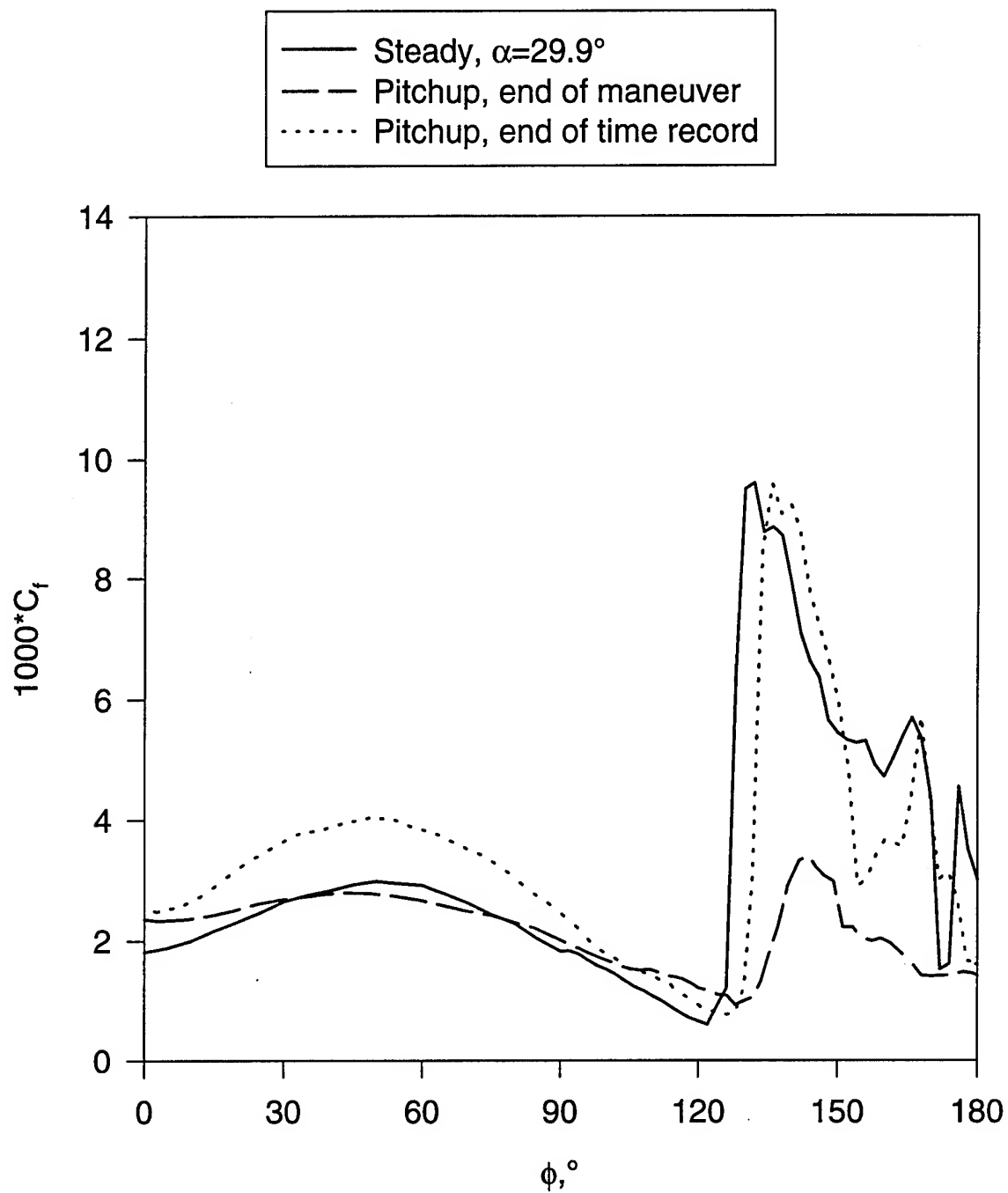


Figure 213. Comparison of wall shear distribution at  $x/L=0.118$  for steady data and pitchup maneuver at  $\alpha=29.9^\circ$ .



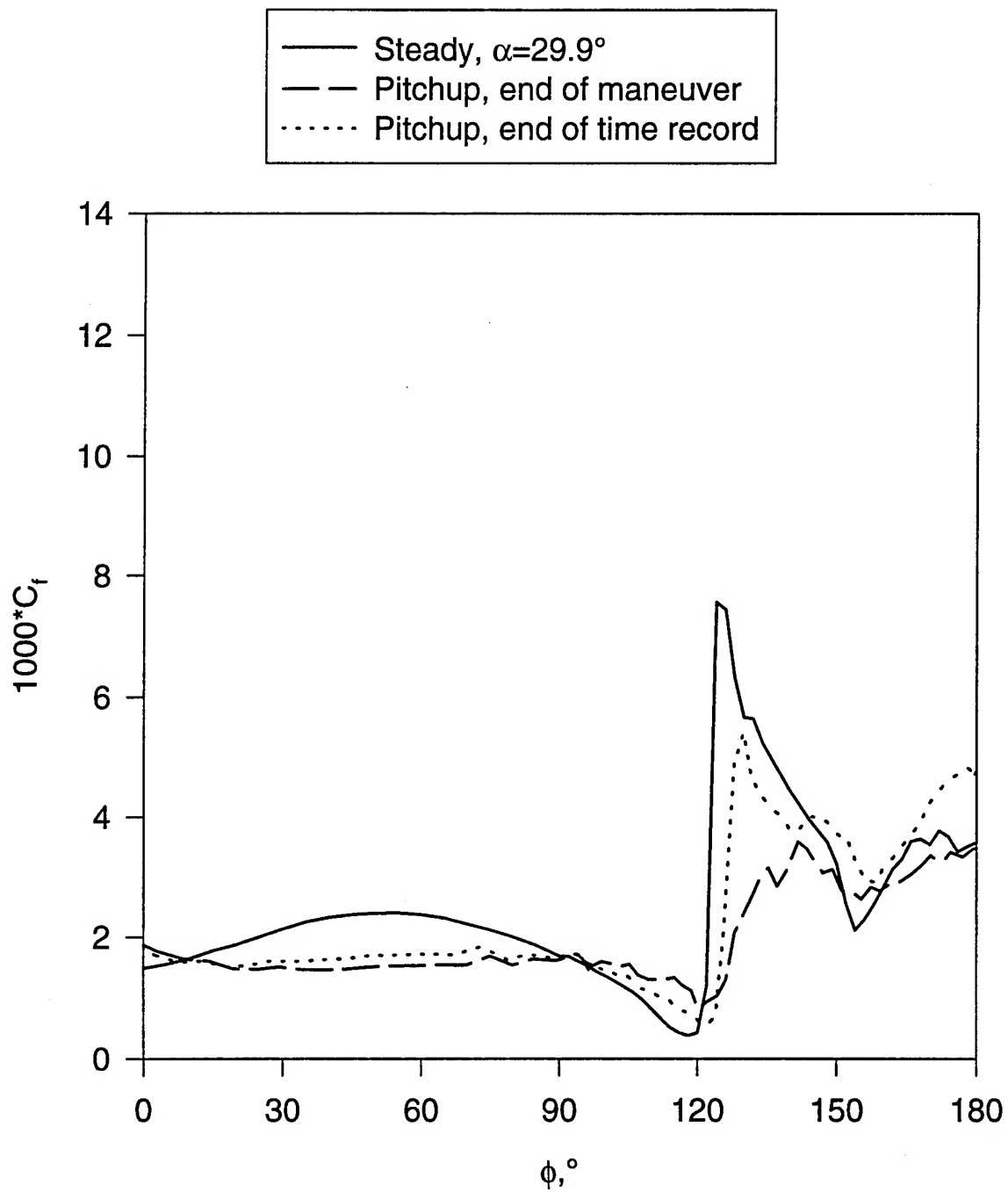


Figure 214. Comparison of wall shear distribution at  $x/L=0.194$  for steady data and pitchup maneuver at  $\alpha=29.9^\circ$ .

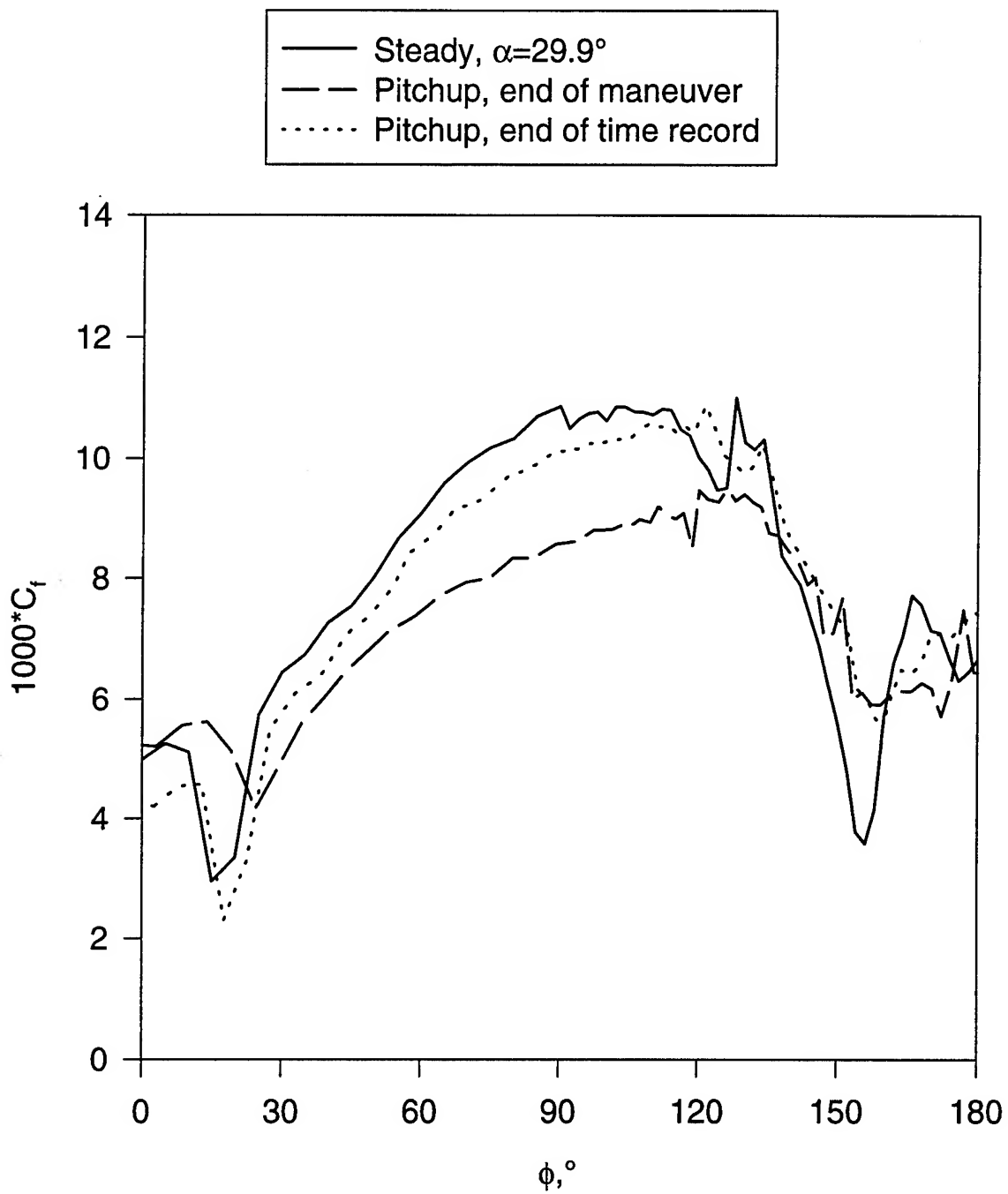


Figure 215. Comparison of wall shear distribution at  $x/L=0.220$  for steady data and pitchup maneuver at  $\alpha=29.9^\circ$ .

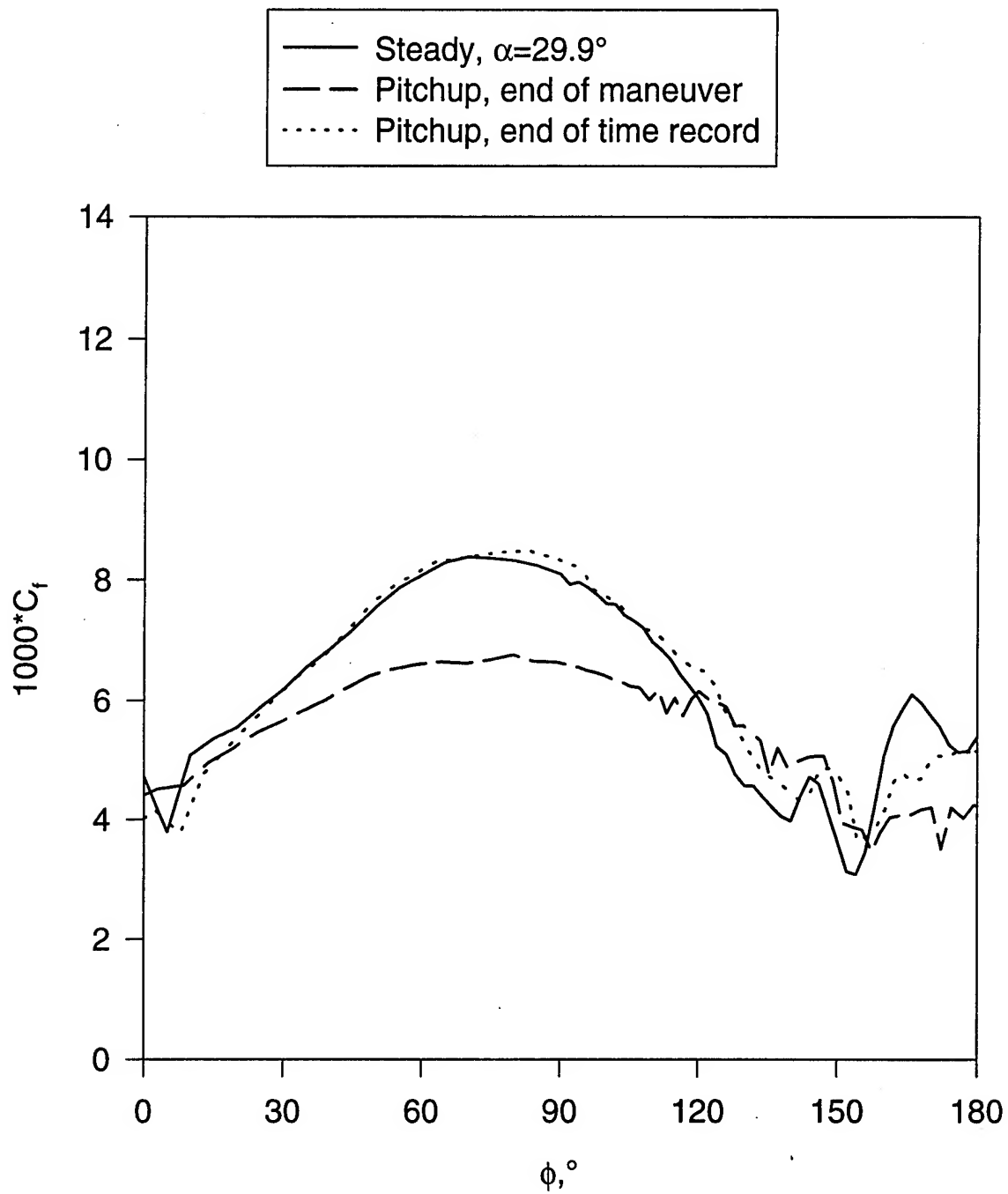


Figure 216. Comparison of wall shear distribution at  $x/L=0.271$  for steady data and pitchup maneuver at  $\alpha=29.9^\circ$ .

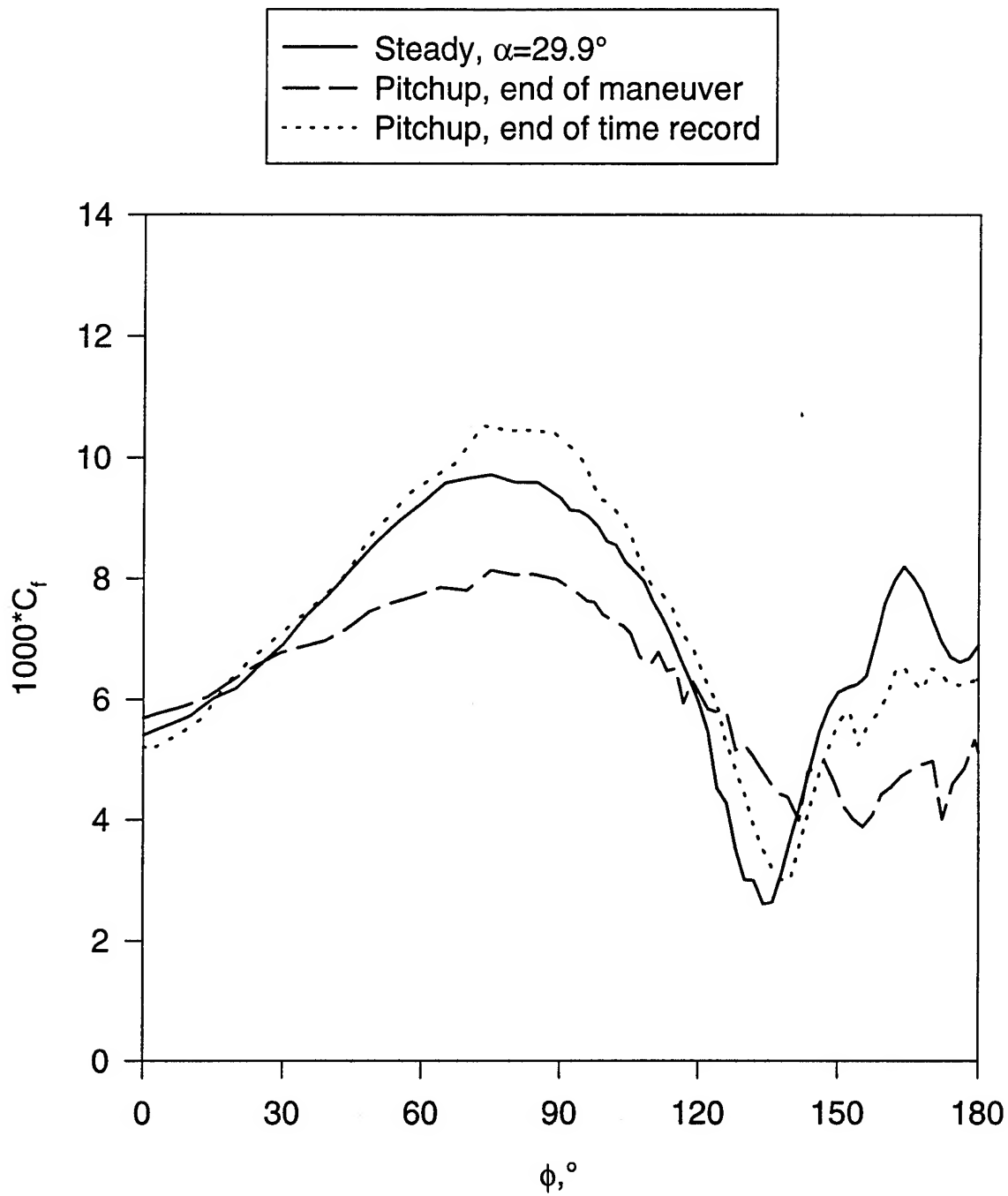


Figure 217. Comparison of wall shear distribution at  $x/L=0.347$  for steady data and pitchup maneuver at  $\alpha=29.9^\circ$ .

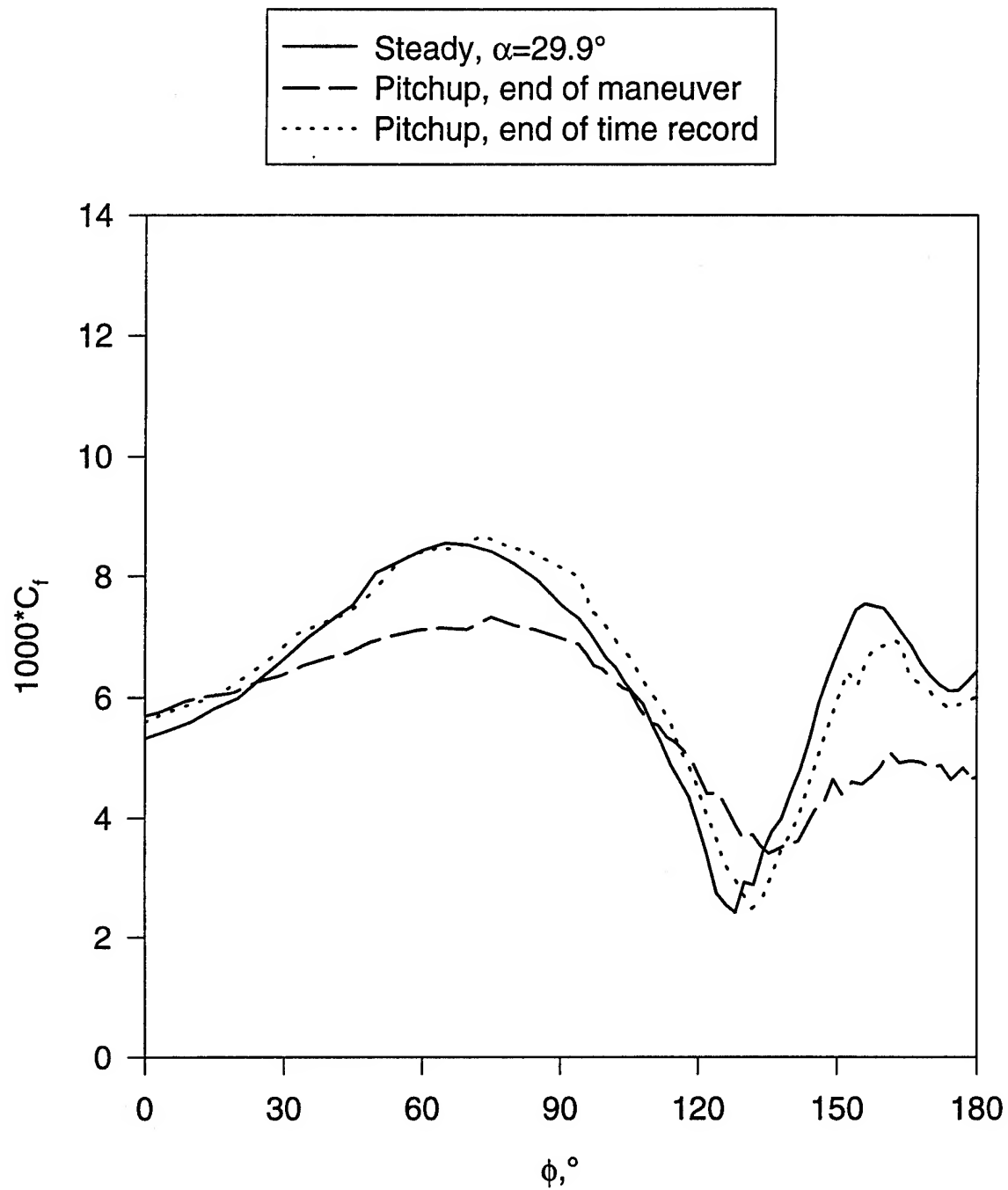


Figure 218. Comparison of wall shear distribution at  $x/L=0.424$  for steady data and pitchup maneuver at  $\alpha=29.9^\circ$ .

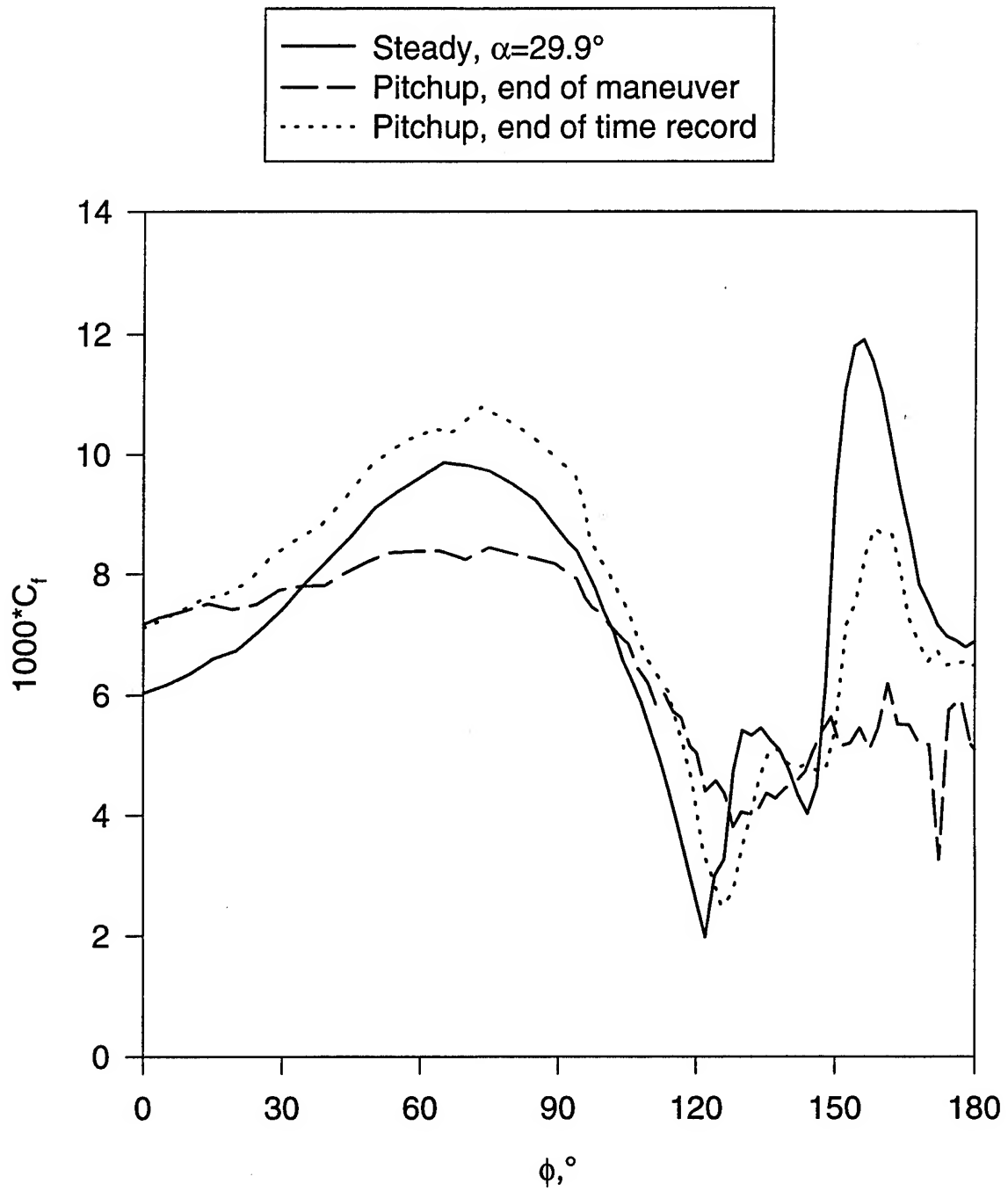


Figure 219. Comparison of wall shear distribution at  $x/L=0.500$  for steady data and pitchup maneuver at  $\alpha=29.9^\circ$ .

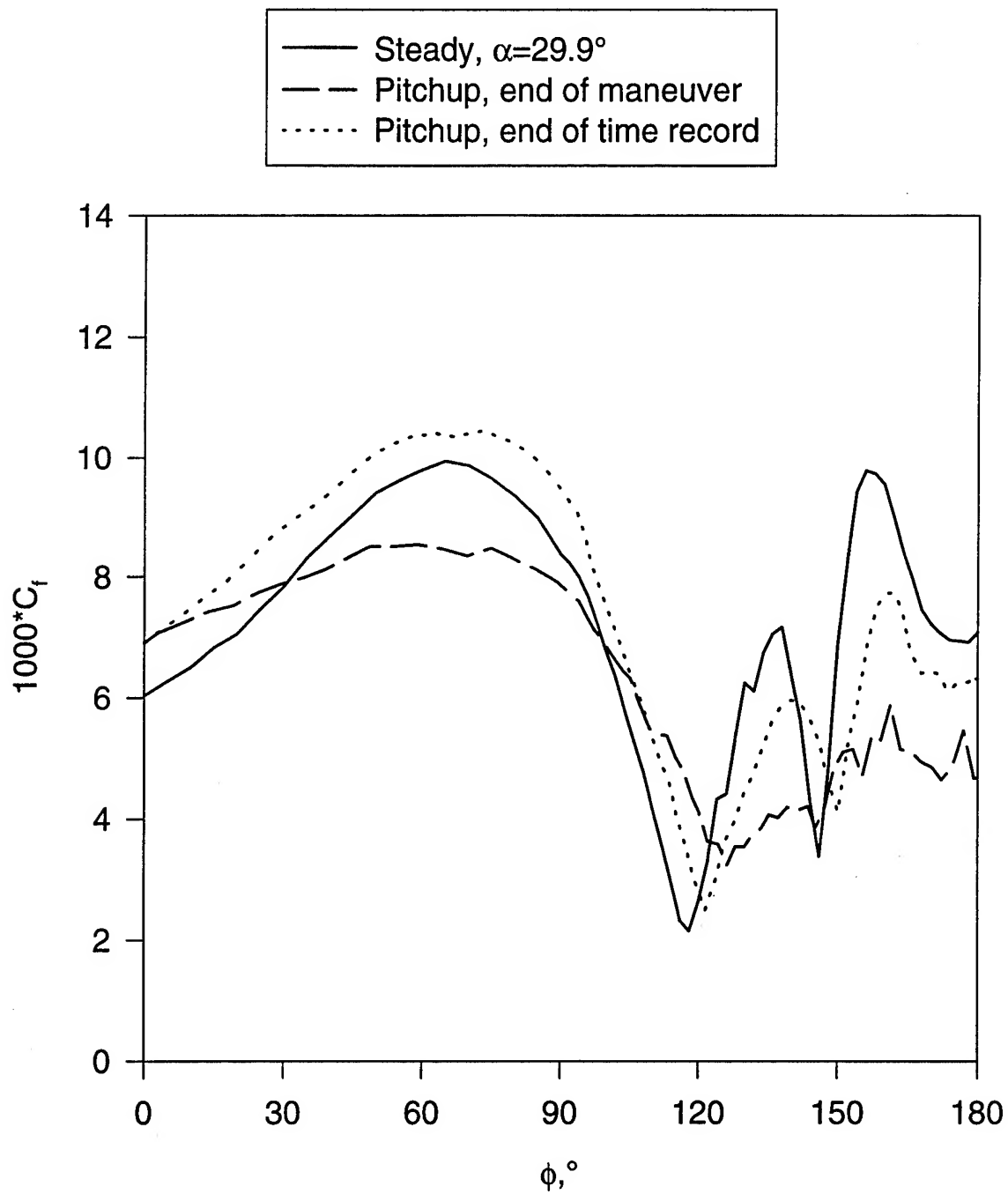


Figure 220. Comparison of wall shear distribution at  $x/L=0.576$  for steady data and pitchup maneuver at  $\alpha=29.9^\circ$ .

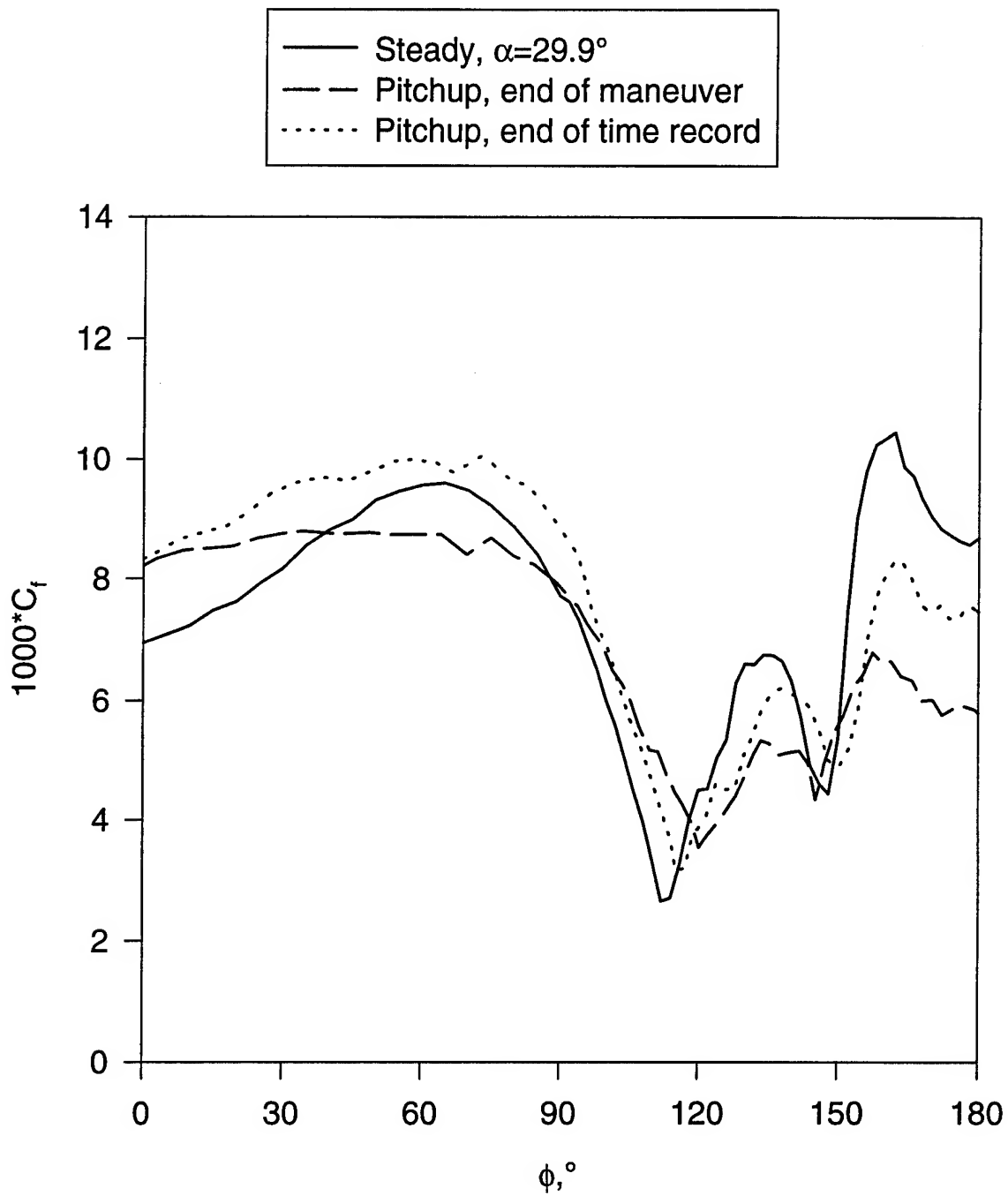


Figure 221. Comparison of wall shear distribution at  $x/L=0.653$  for steady data and pitchup maneuver at  $\alpha=29.9^\circ$ .



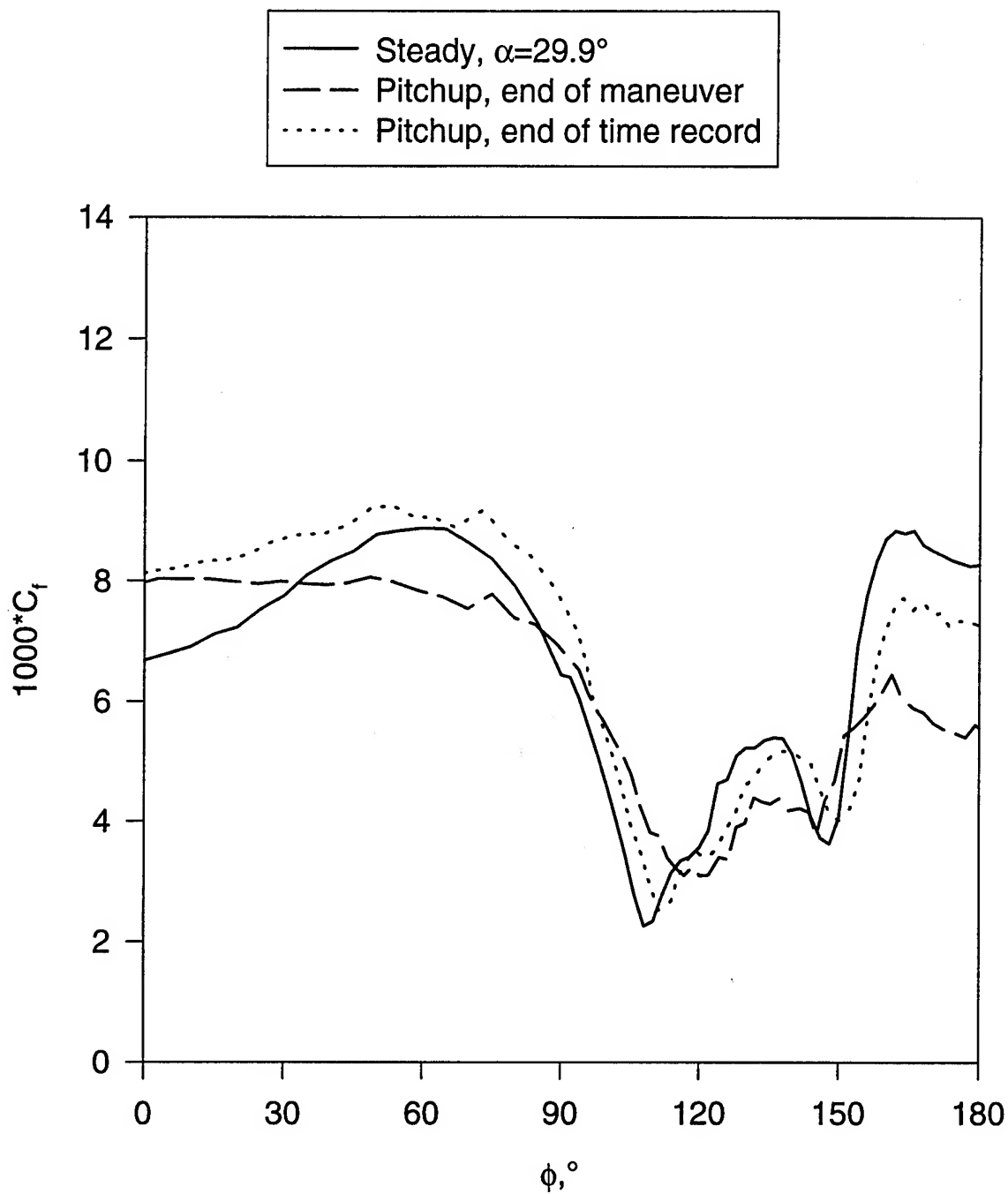


Figure 222. Comparison of wall shear distribution at  $x/L=0.729$  for steady data and pitchup maneuver at  $\alpha=29.9^\circ$ .

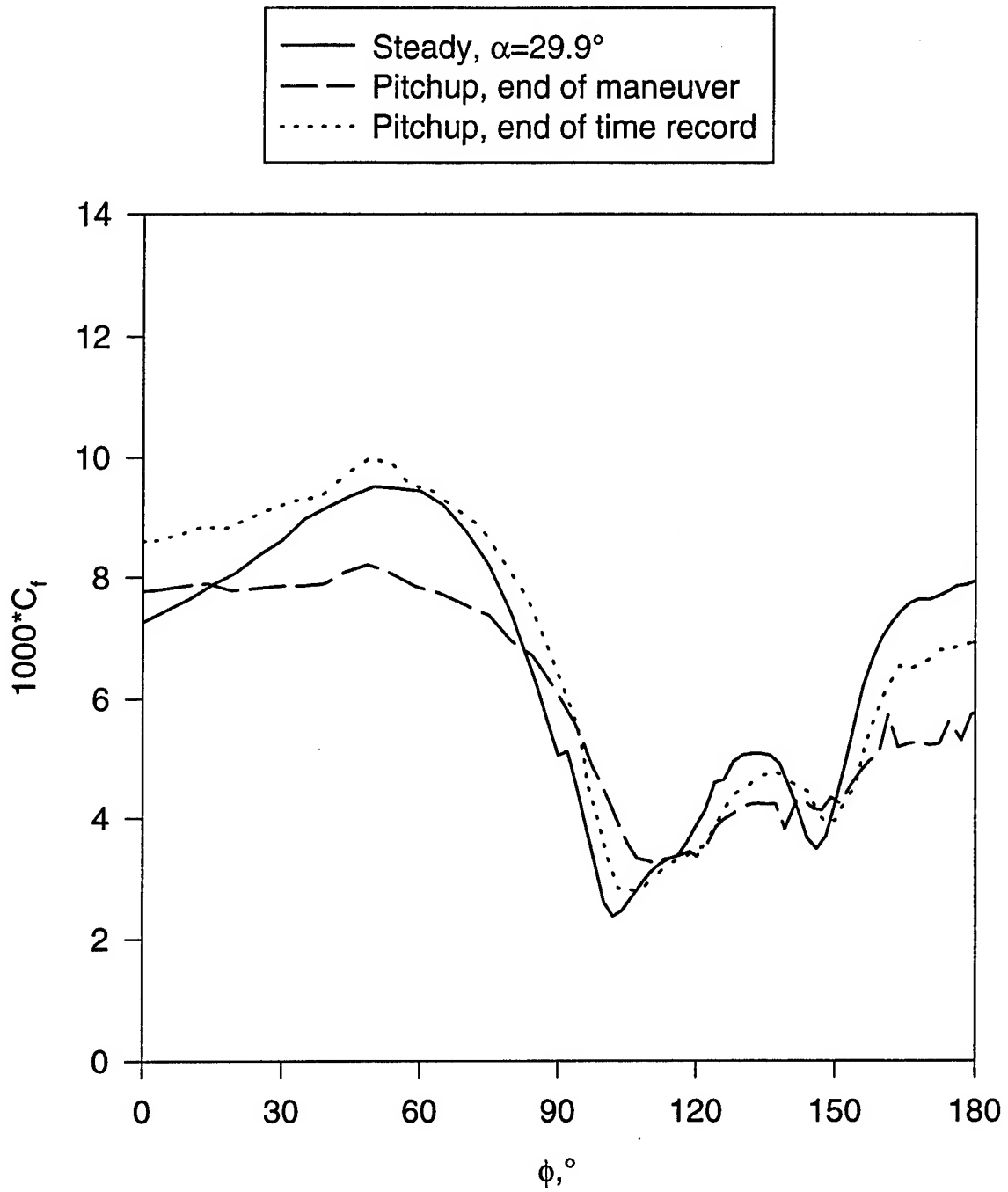


Figure 223. Comparison of wall shear distribution at  $x/L=0.831$  for steady data and pitchup maneuver at  $\alpha=29.9^\circ$ .

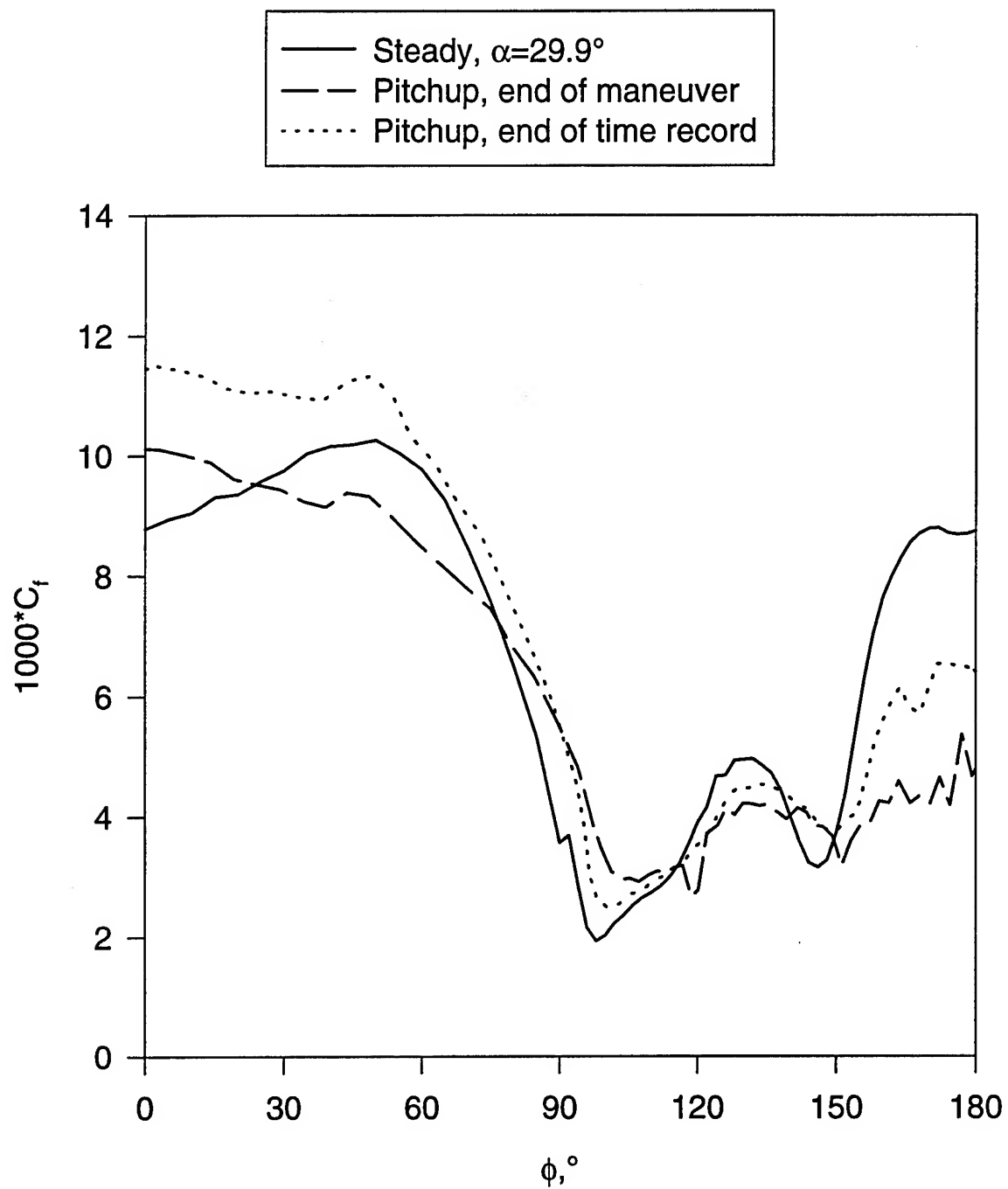


Figure 224. Comparison of wall shear distribution at  $x/L=0.882$  for steady data and pitchup maneuver at  $\alpha=29.9^\circ$ .

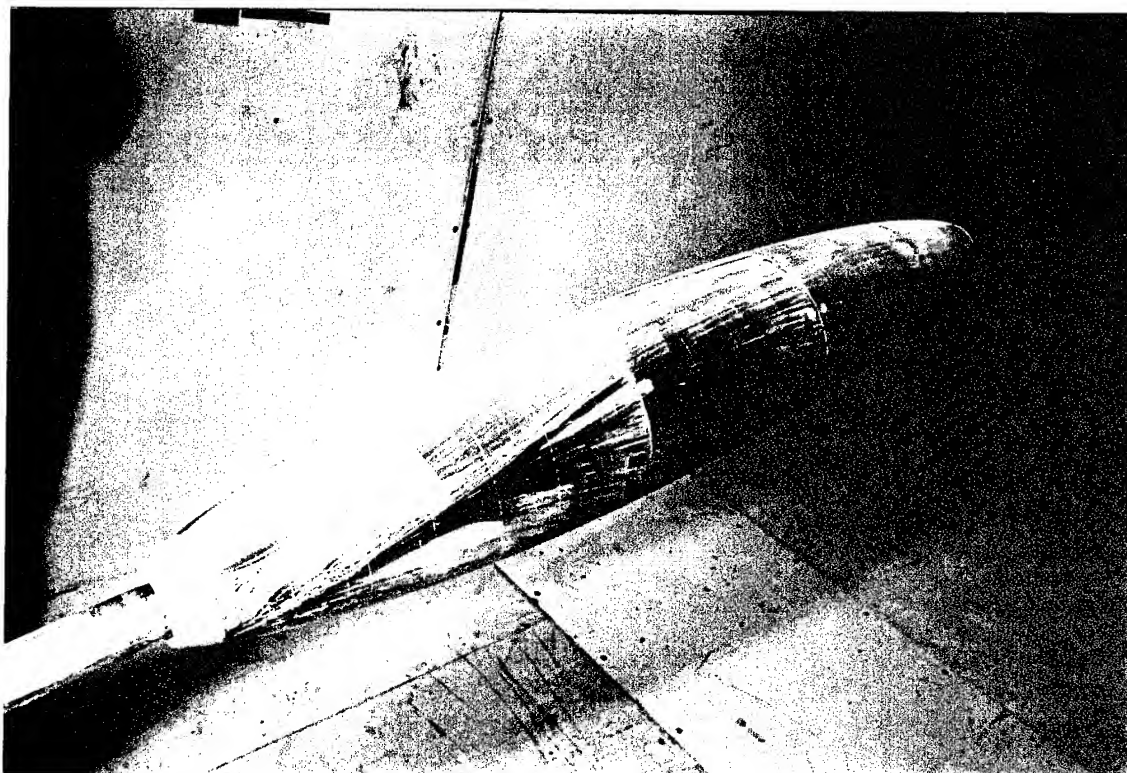


Figure 225. Oil flow visualization for  $\alpha = 10^\circ$ ,  $Re = 4.2$  million.

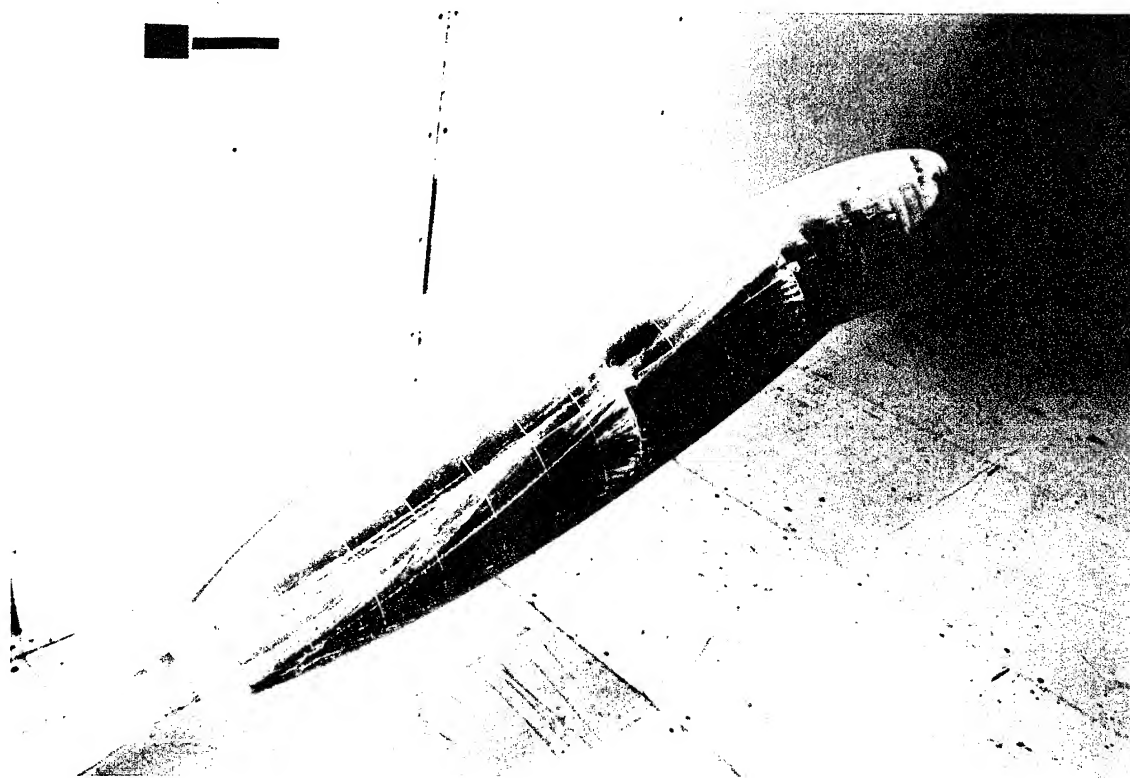


Figure 226. Oil flow visualization for  $\alpha = 15^\circ$ ,  $Re = 4.2$  million.

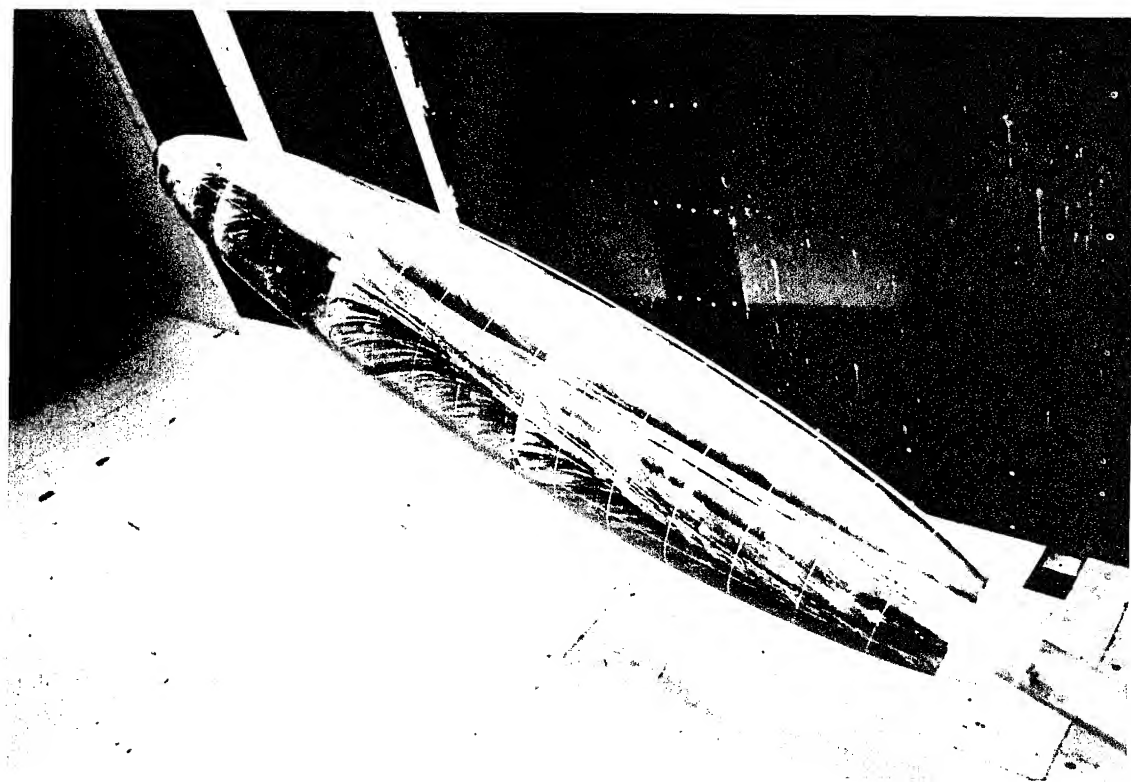


Figure 227. Oil flow visualization for  $\alpha = 20^\circ$ ,  $Re = 4.2$  million.

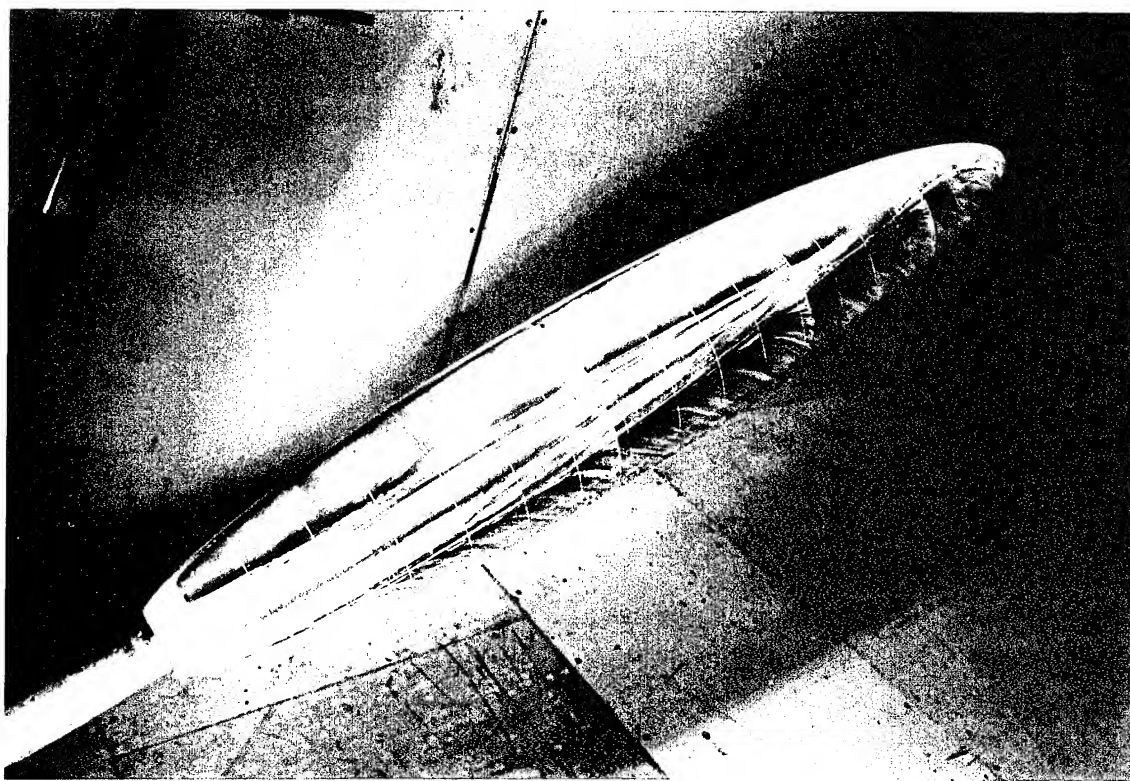


Figure 228. Oil flow visualization for  $\alpha = 25^\circ$ ,  $Re = 4.2$  million.



Figure 229. Oil flow visualization for  $\alpha = 30^\circ$ ,  $Re = 4.2$  million.



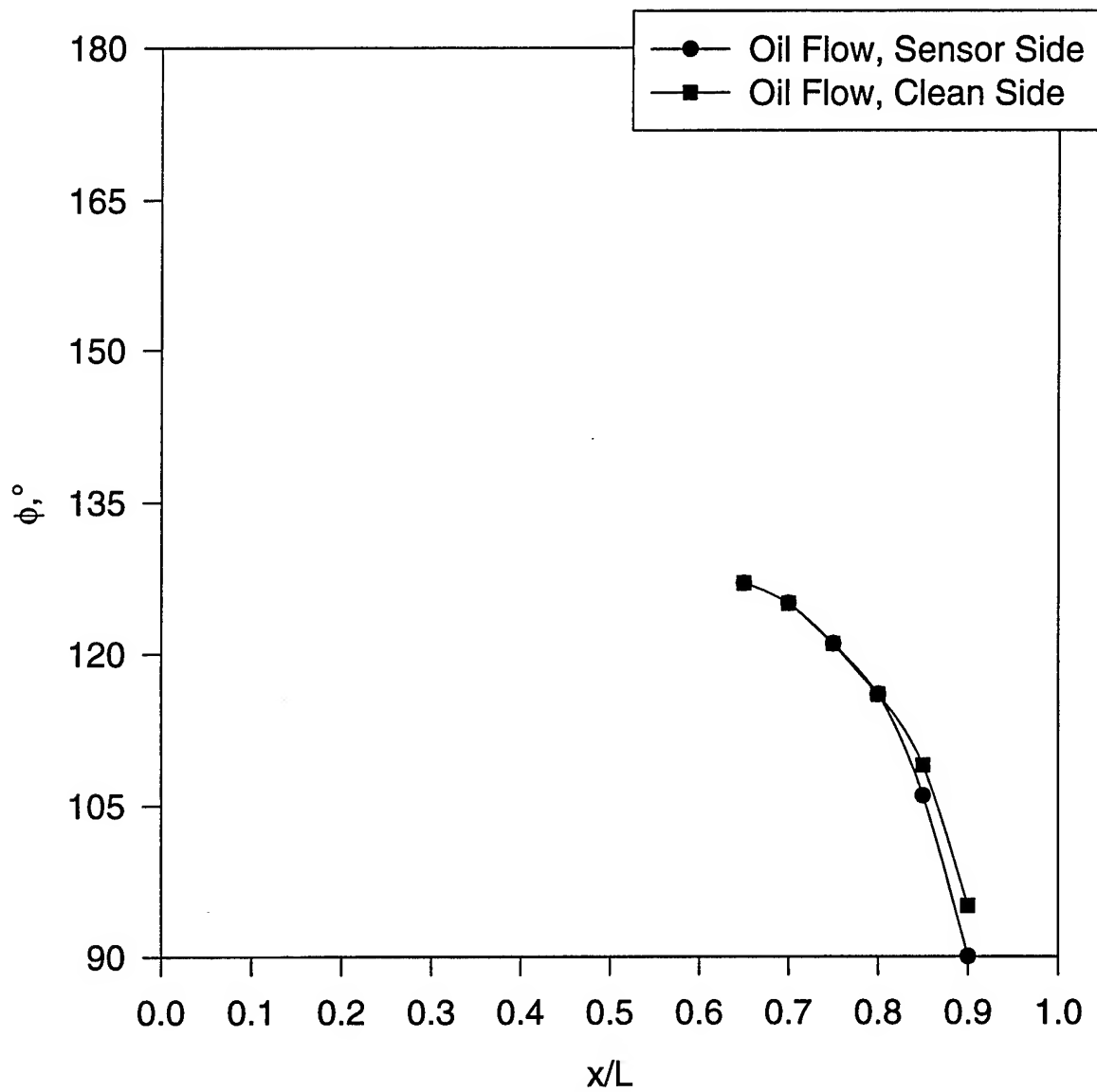


Figure 230. Primary and secondary separation lines for  $\alpha = 10^\circ$ ,  $Re = 4.2$  million.

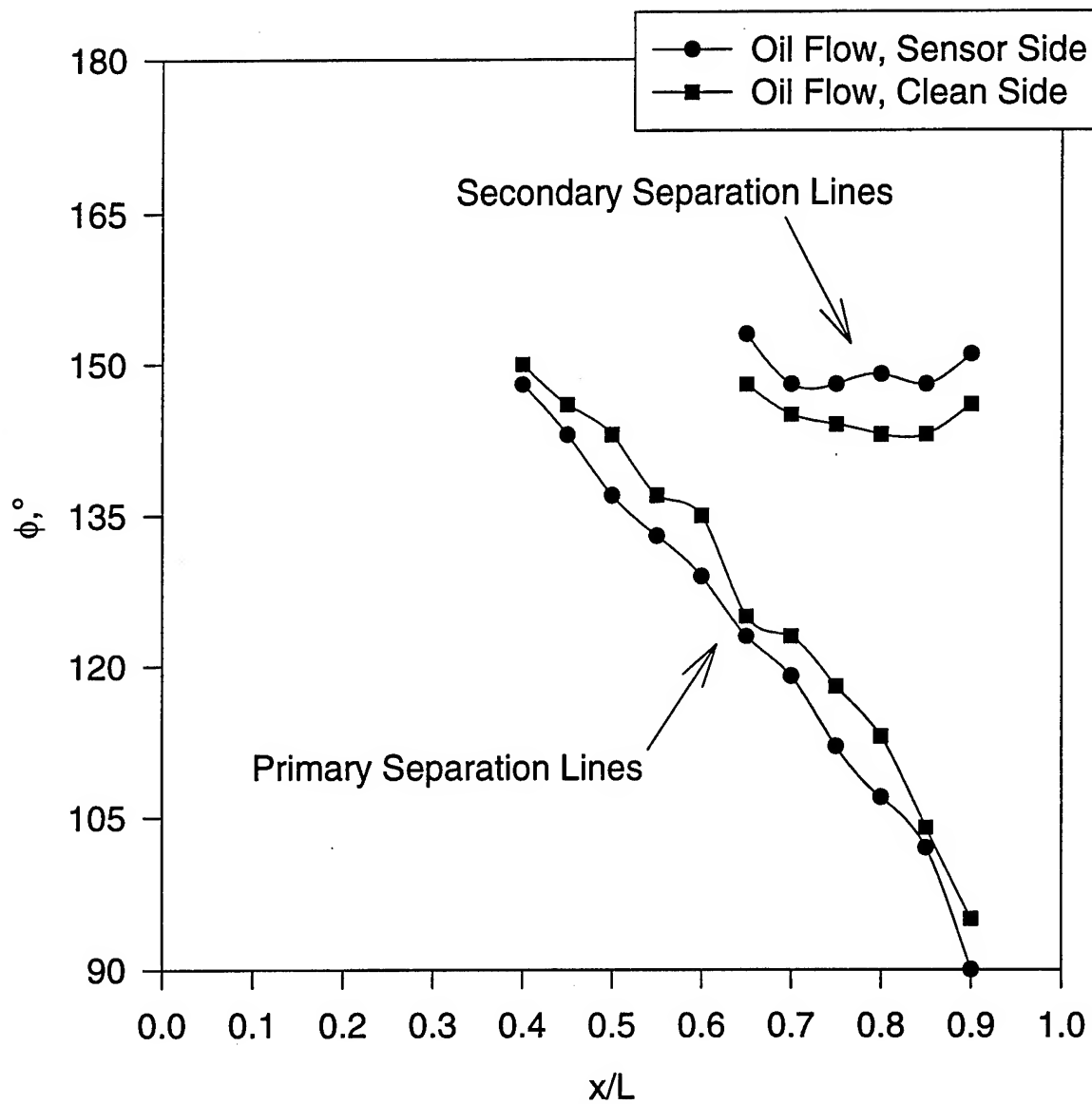


Figure 231. Primary and secondary separation lines for  $\alpha = 15^\circ$ ,  $Re = 4.2$  million.

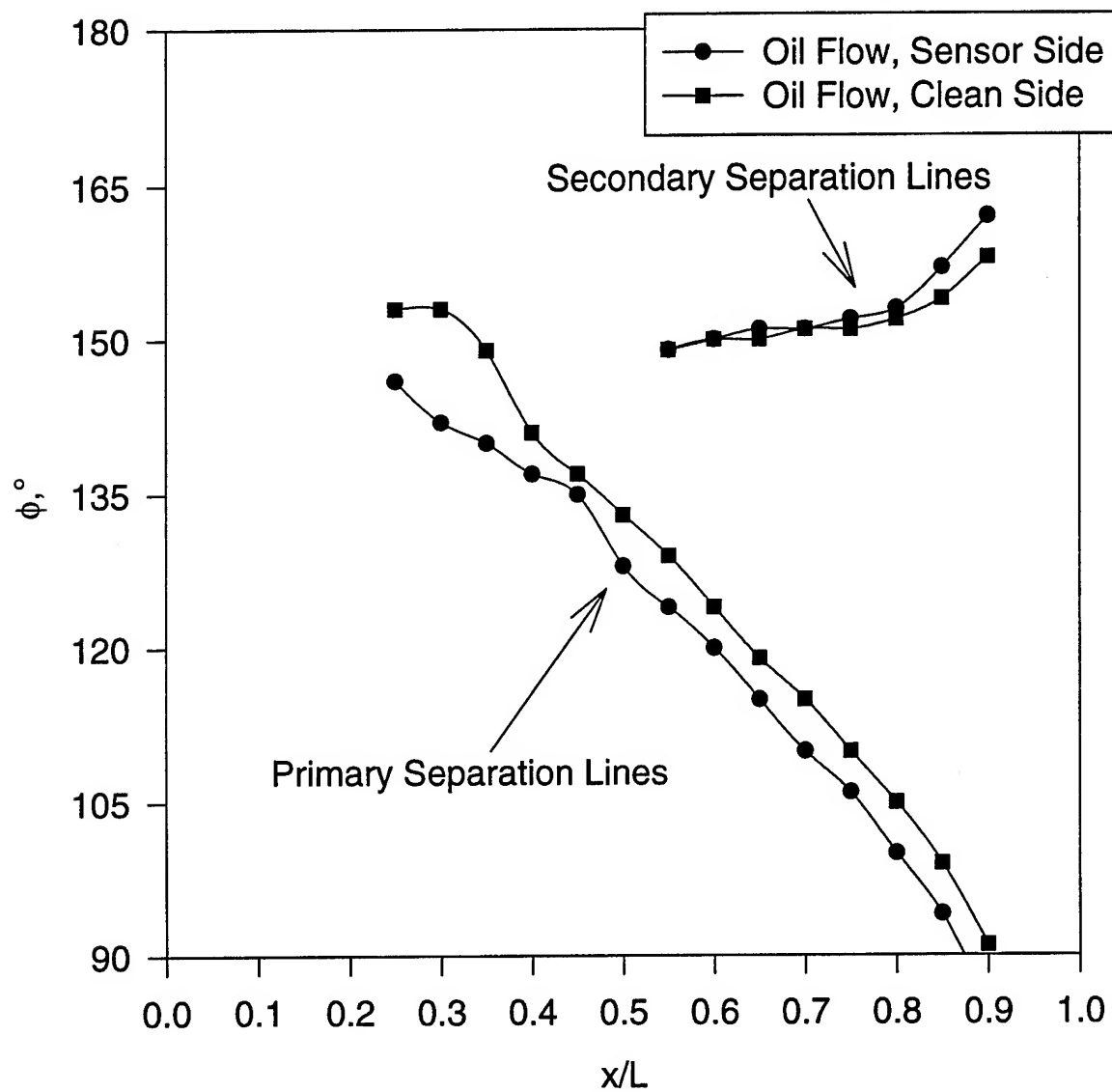


Figure 232. Primary and secondary separation lines for  $\alpha = 20^\circ$ ,  $Re = 4.2$  million.

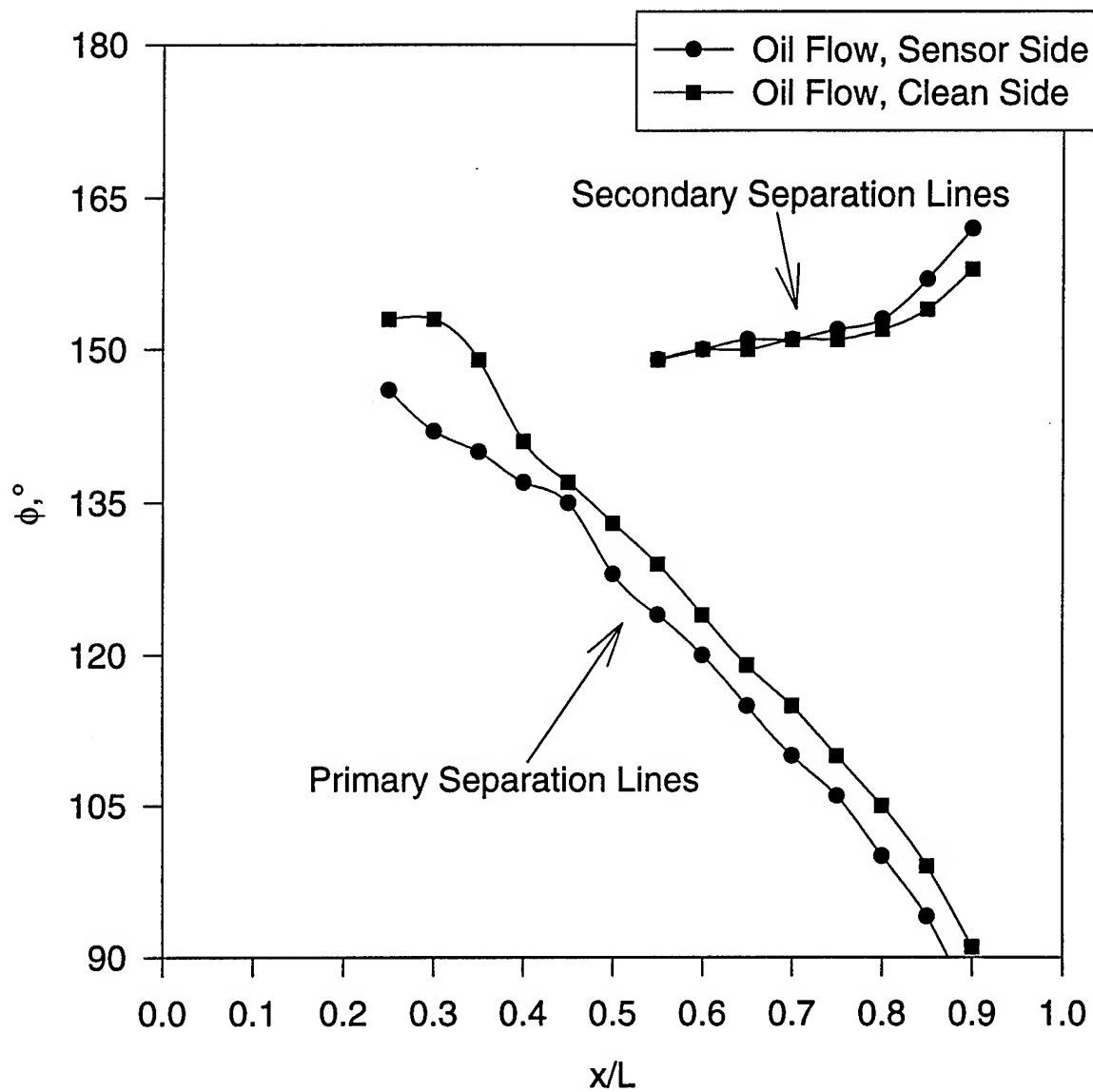


Figure 233. Primary and secondary separation lines for  $\alpha = 25^\circ$ ,  $Re = 4.2$  million.

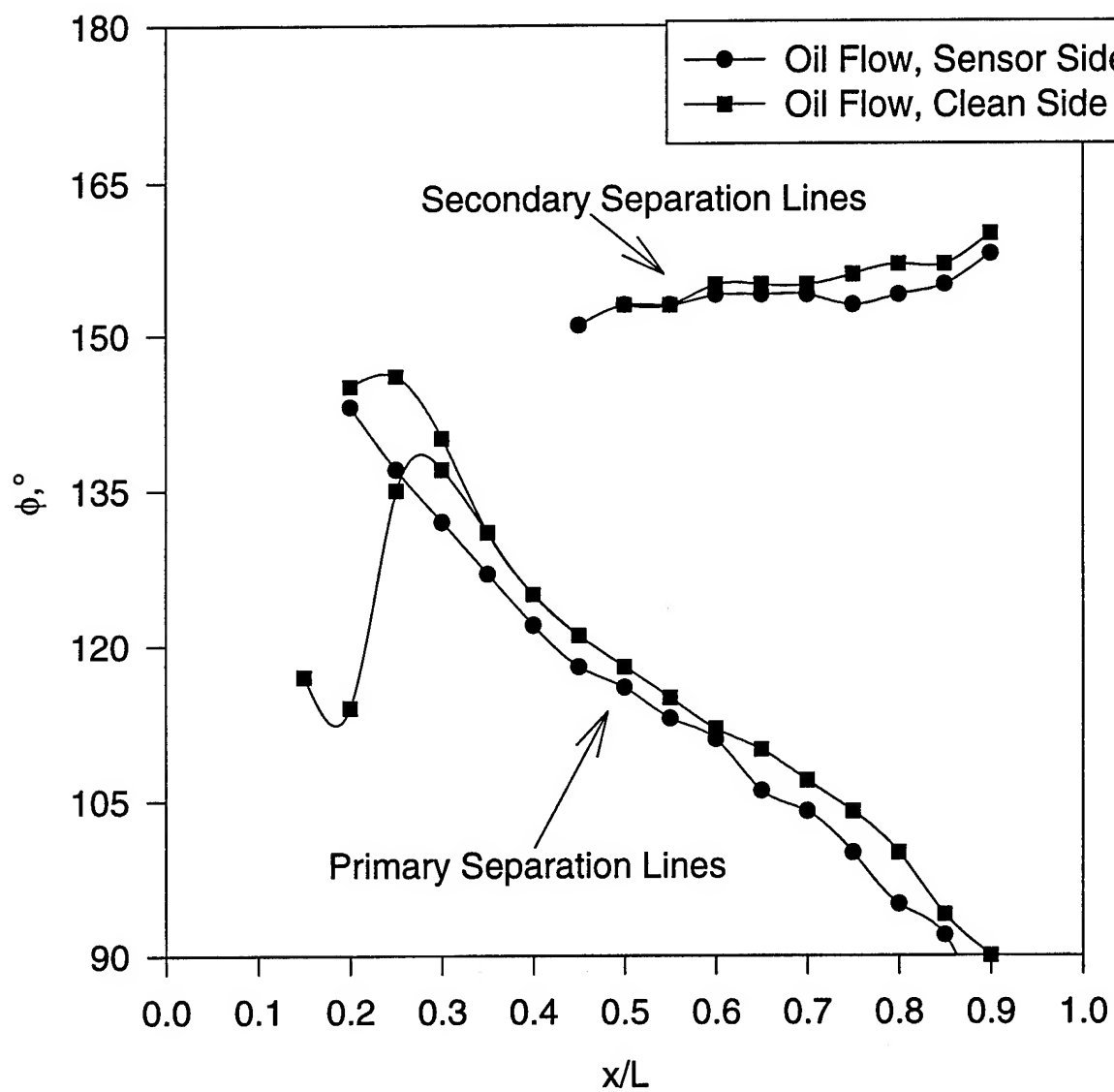


Figure 234. Primary and secondary separation lines for  $\alpha = 30^\circ$ ,  $Re = 4.2$  million.

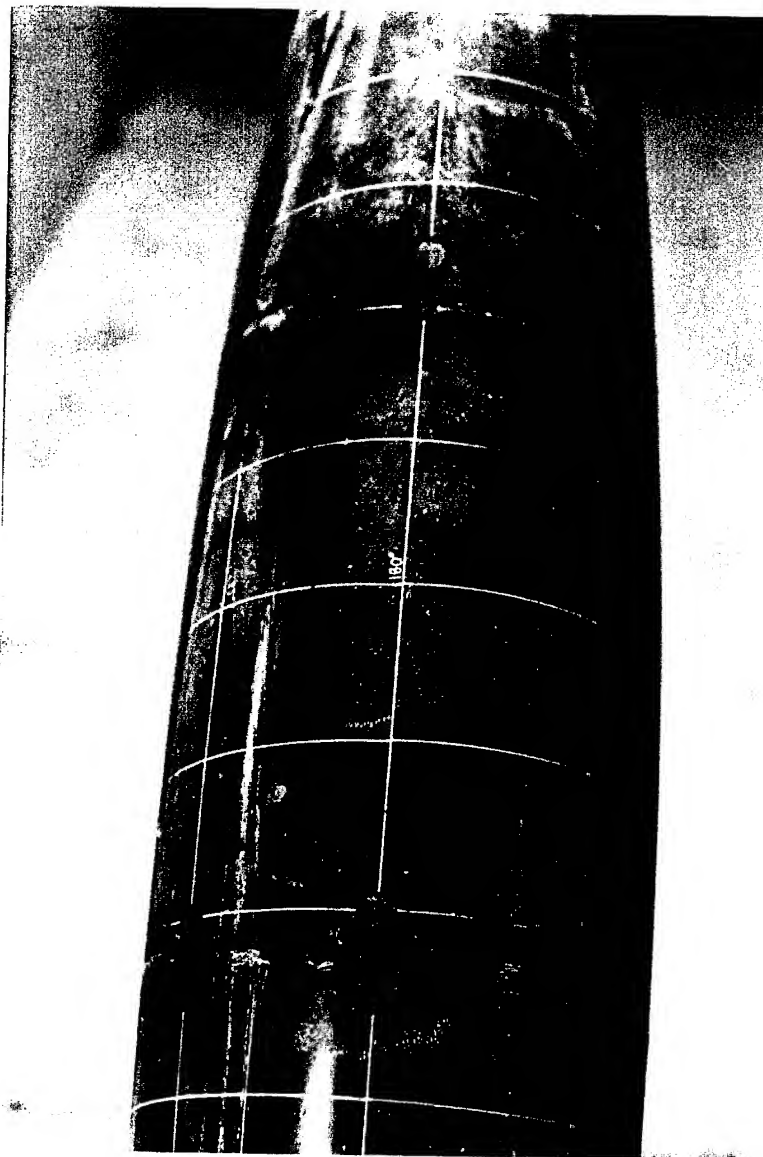


Figure 235. Asymmetry of secondary separation lines,  $\alpha=30^\circ$ .

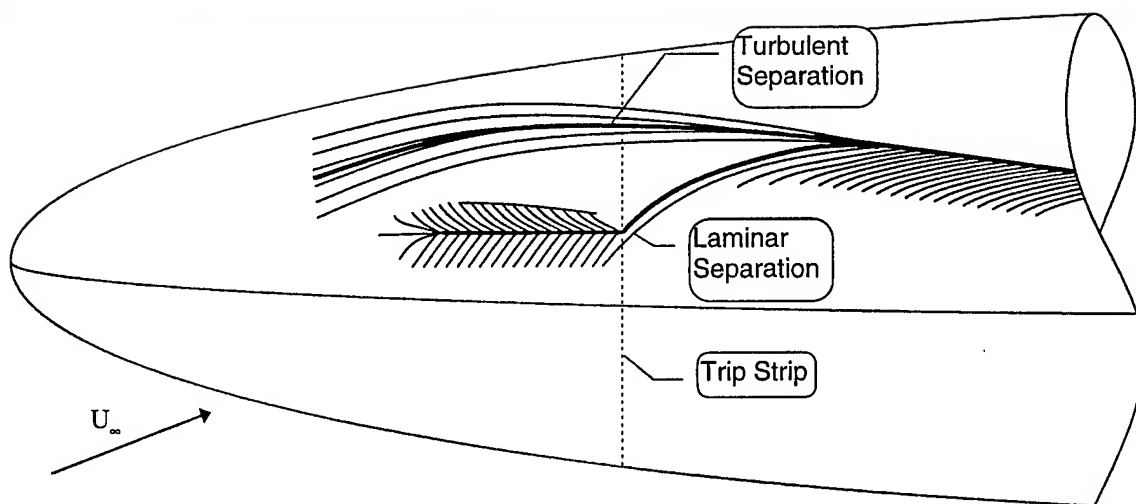
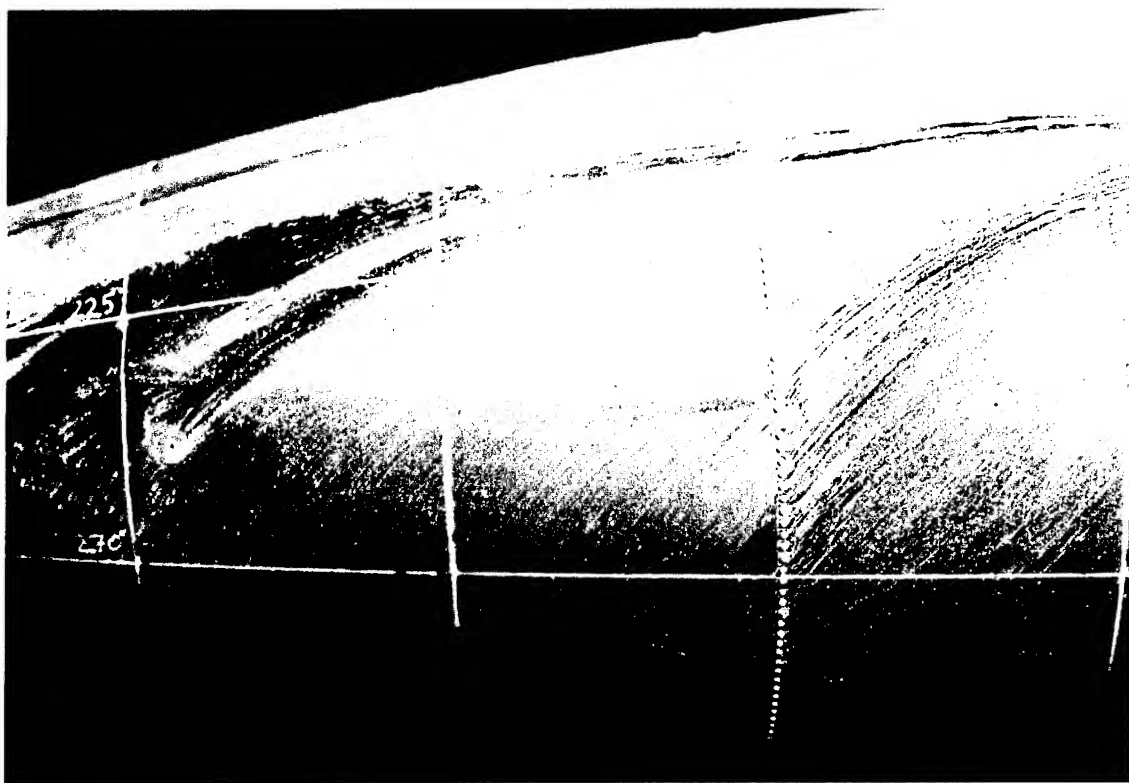


Figure 236. Laminar nose separation topology.

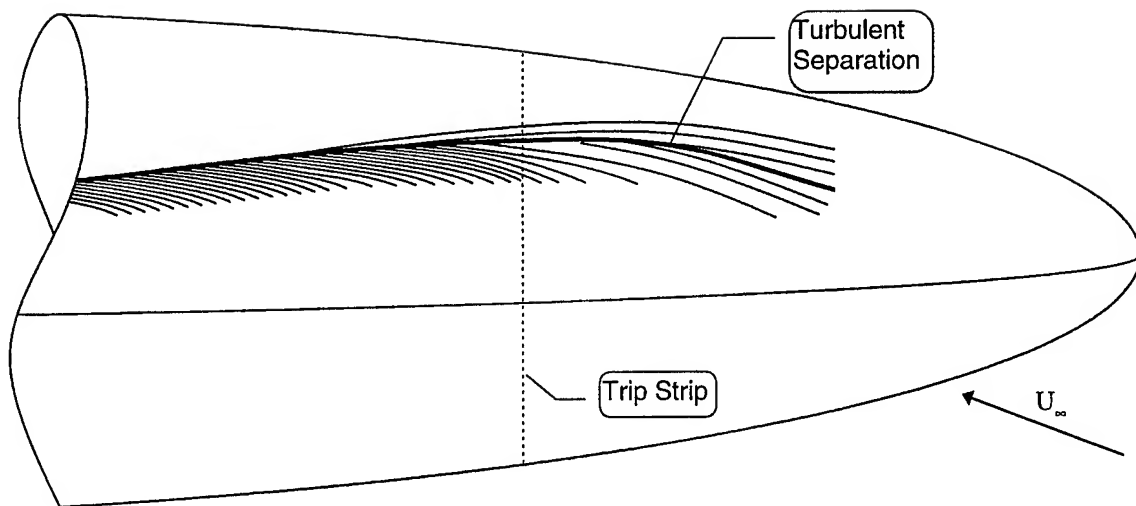
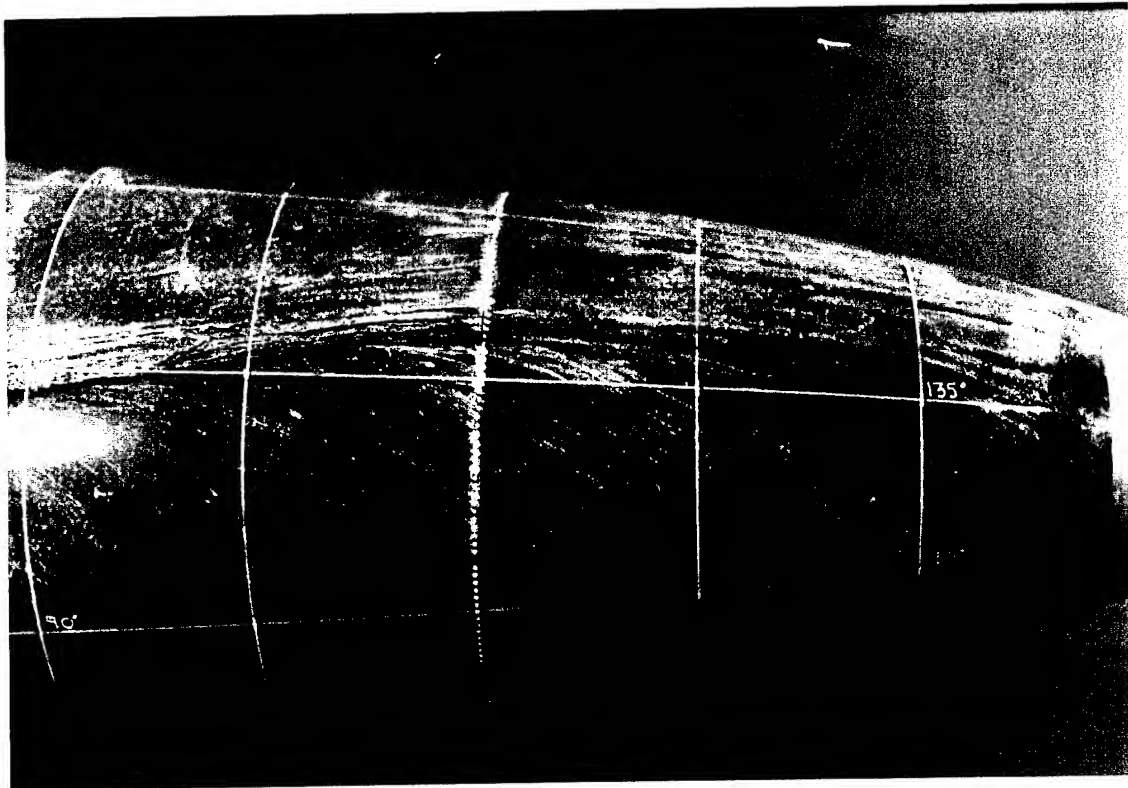


Figure 237. Turbulent nose separation topology.



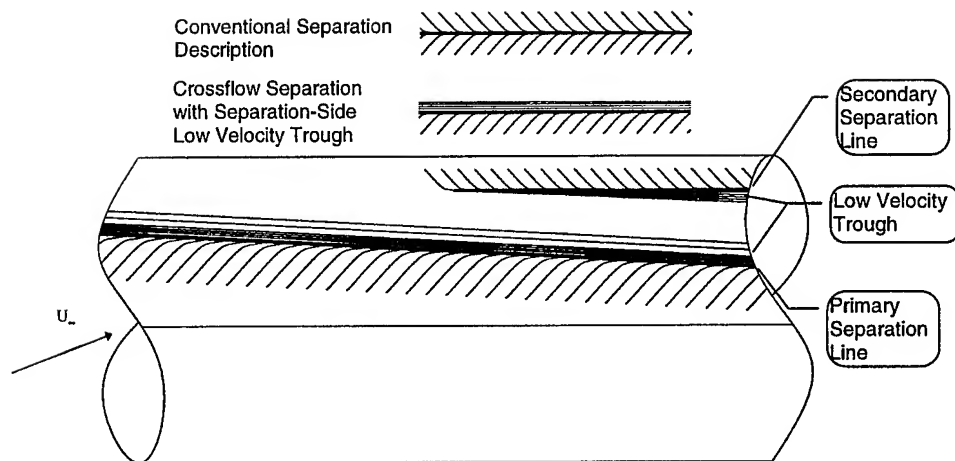
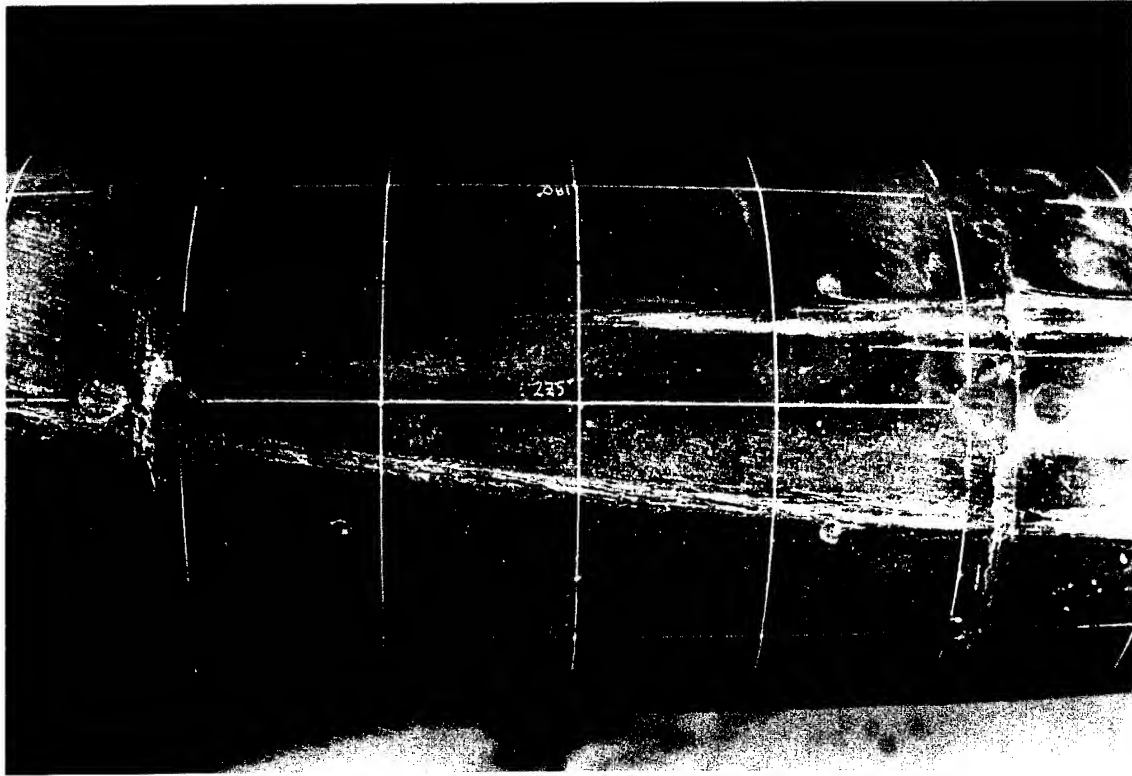


Figure 238. Crossflow separation/low-velocity trough topology.

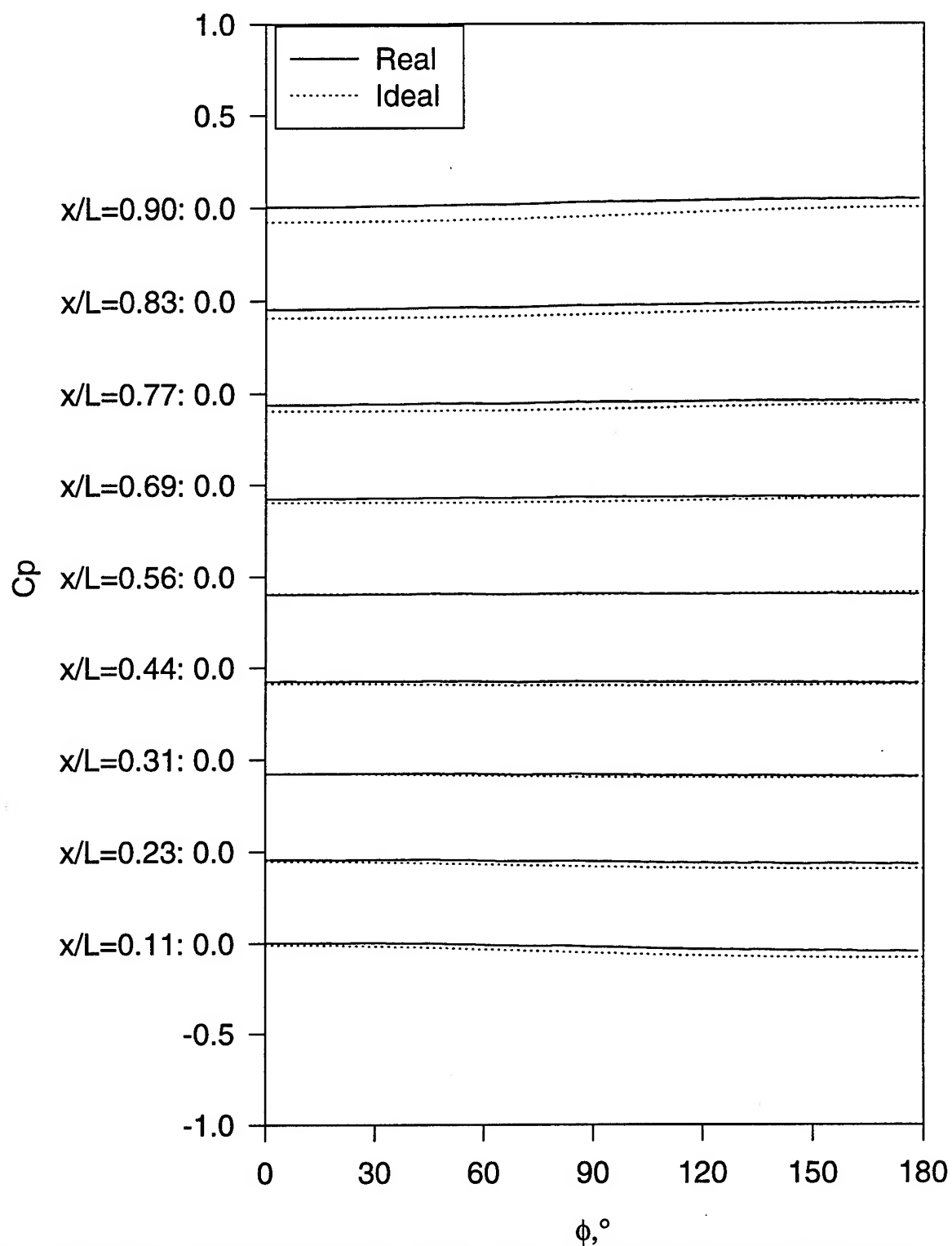


Figure 239. Steady  $C_p$  vs.  $\phi$  for all  $x/L$ ,  $\alpha = 2.2^\circ$ . "Real" refers to the measured data while "Ideal" refers to potential flow solution.

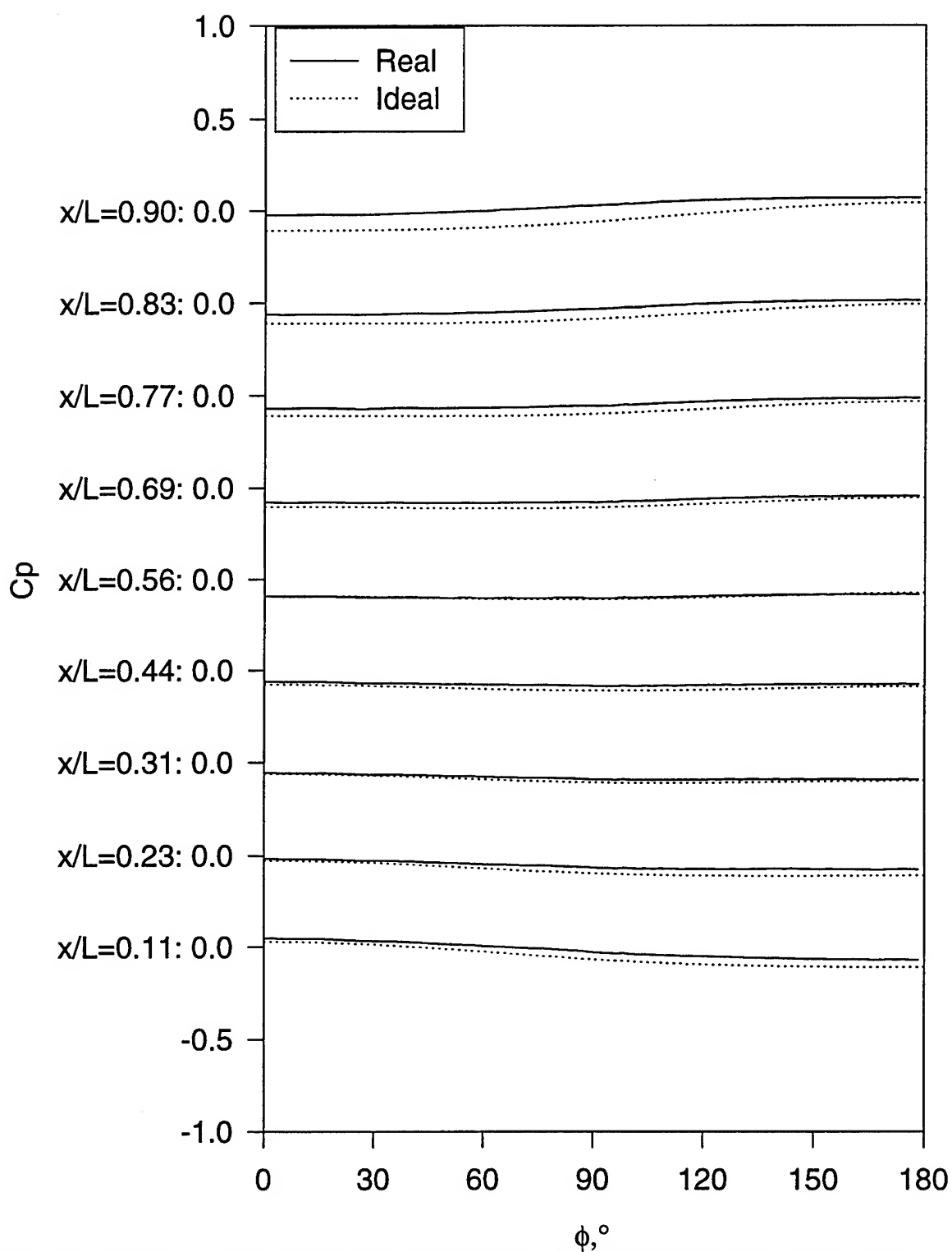


Figure 240. Steady  $C_p$  vs.  $\phi$  for all  $x/L$ ,  $\alpha=4.8^\circ$ . "Real" refers to the measured data while "Ideal" refers to potential flow solution.

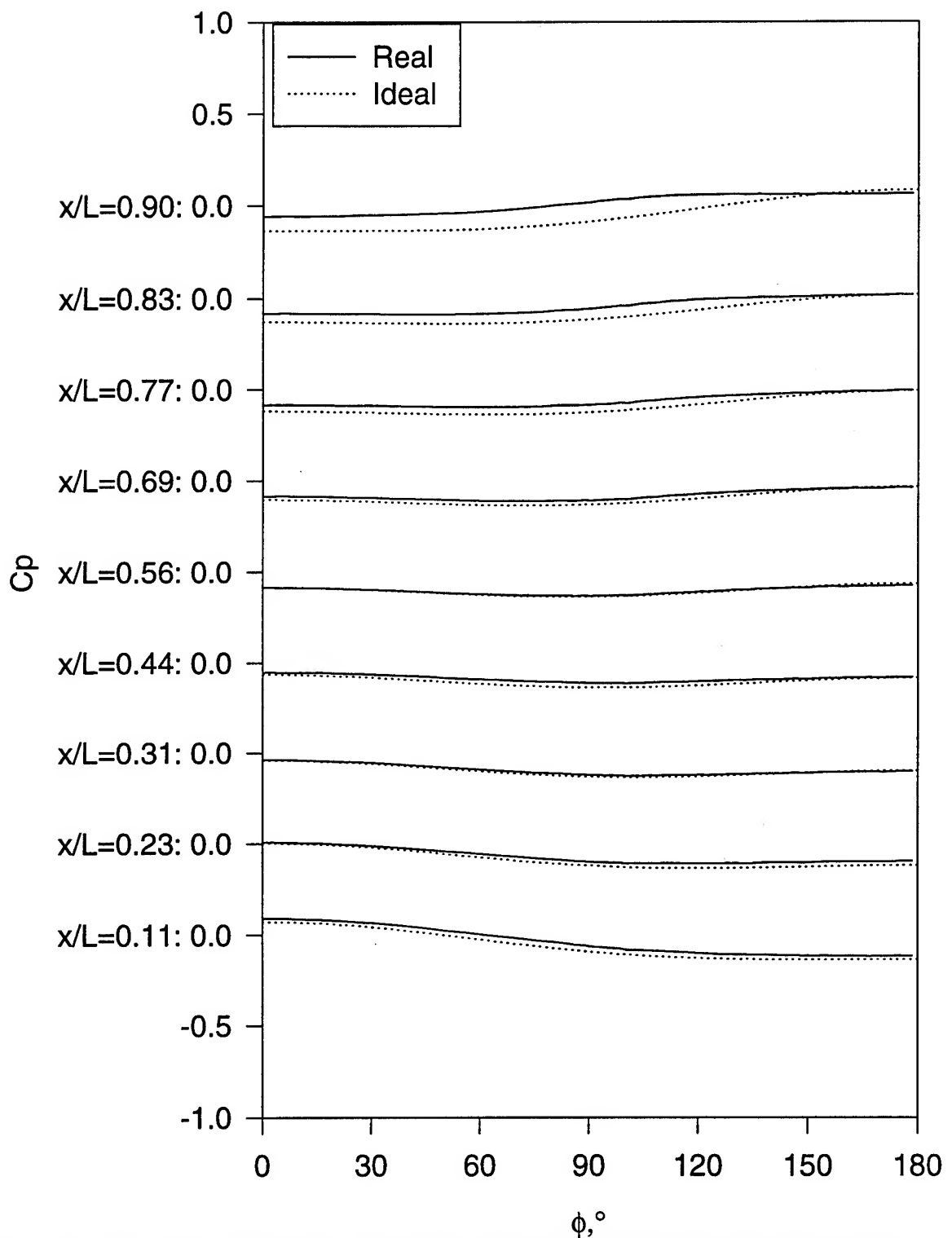


Figure 241. Steady  $C_p$  vs.  $\phi$  for all  $x/L$ ,  $\alpha=7.6^\circ$ . "Real" refers to the measured data while "Ideal" refers to potential flow solution.

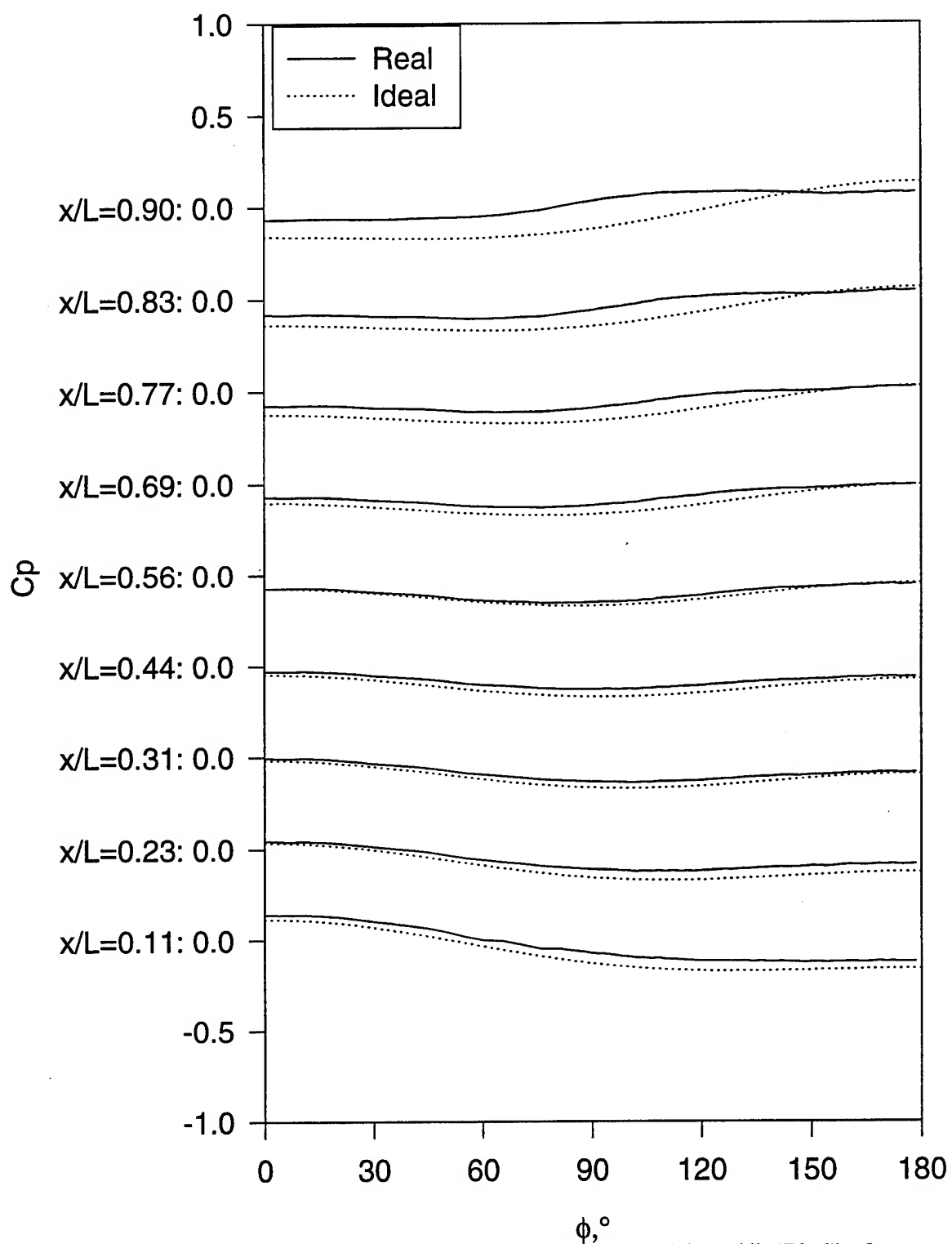


Figure 242. Steady  $C_p$  vs.  $\phi$  for all  $x/L$ ,  $\alpha=9.8^\circ$ . "Real" refers to the measured data while "Ideal" refers to potential flow solution.

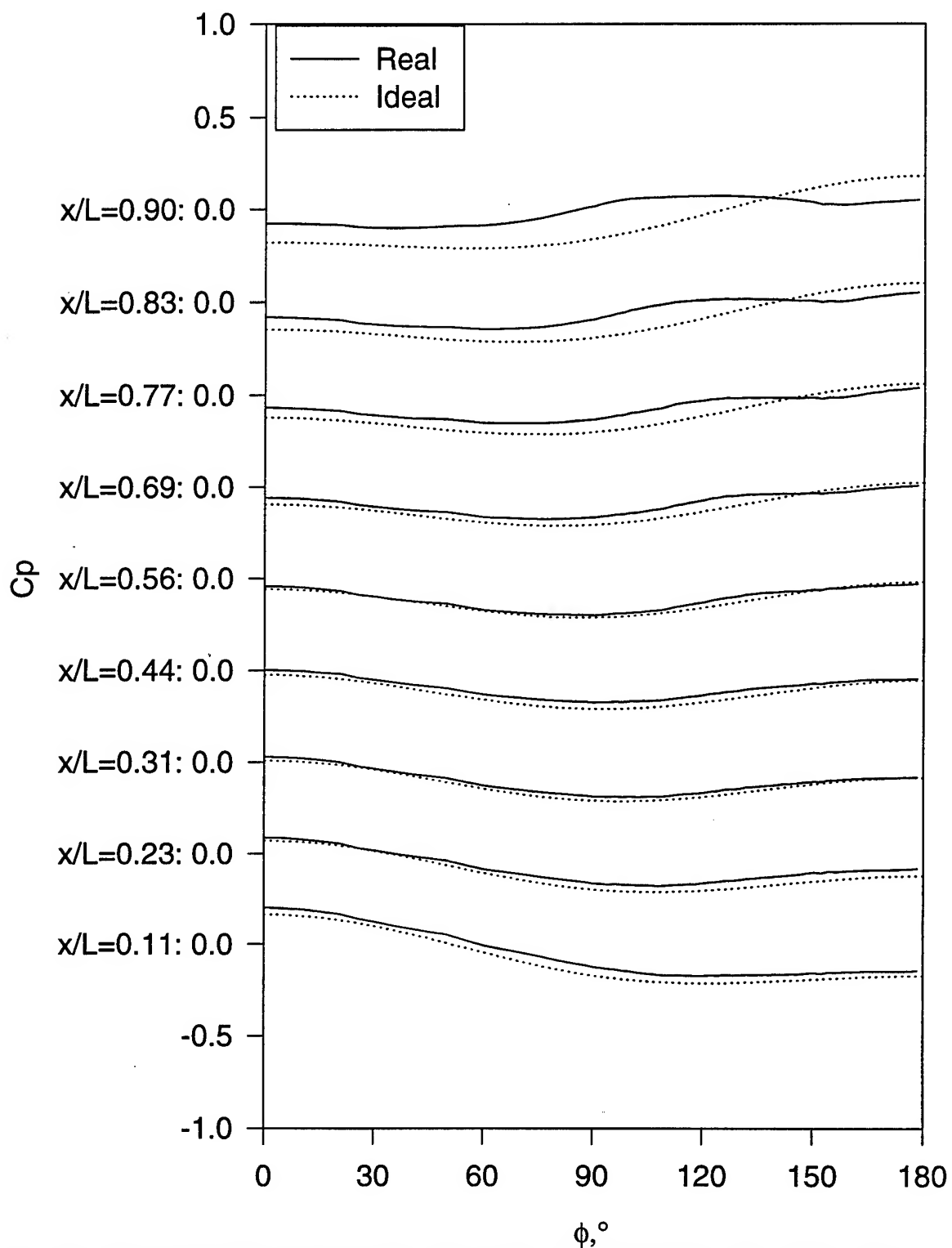


Figure 243. Steady  $C_p$  vs.  $\phi$  for all  $x/L$ ,  $\alpha=12.7^\circ$ . "Real" refers to the measured data while "Ideal" refers to potential flow solution.

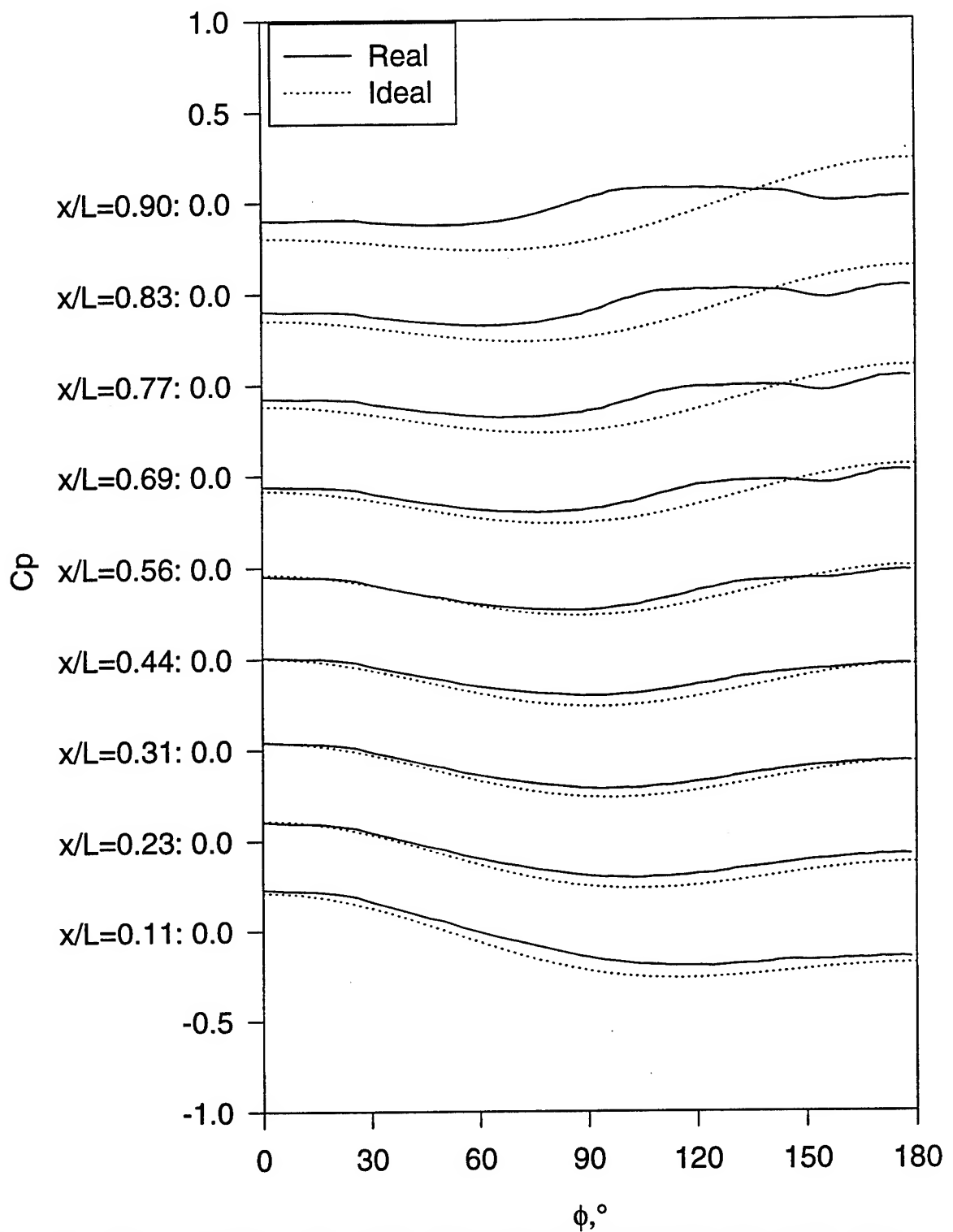


Figure 244. Steady  $C_p$  vs.  $\phi$  for all  $x/L$ ,  $\alpha=14.9^\circ$ . "Real" refers to the measured data while "Ideal" refers to potential flow solution.

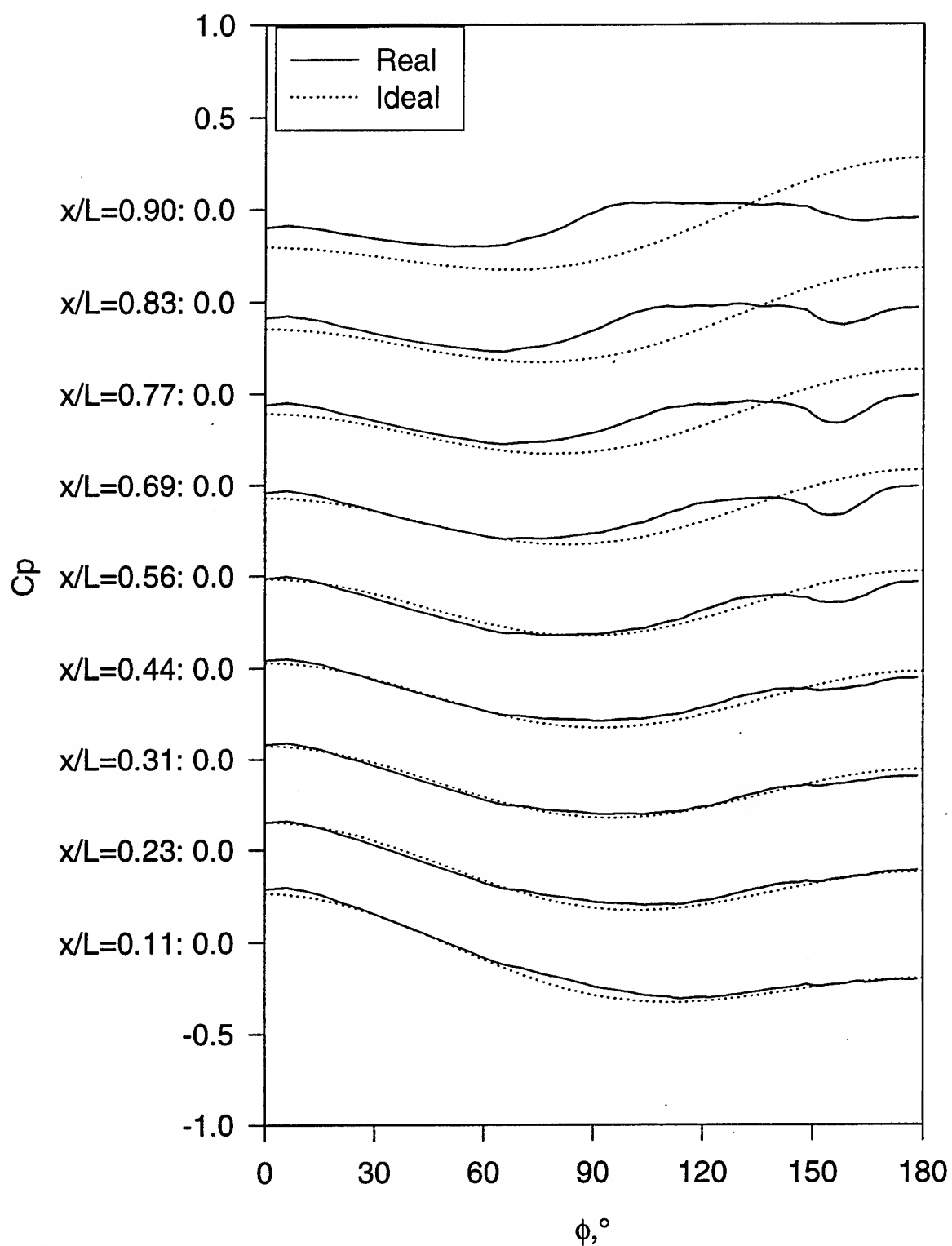


Figure 245. Steady  $C_p$  vs.  $\phi$  for all  $x/L$ ,  $\alpha=17.8^\circ$ . "Real" refers to the measured data while "Ideal" refers to potential flow solution.



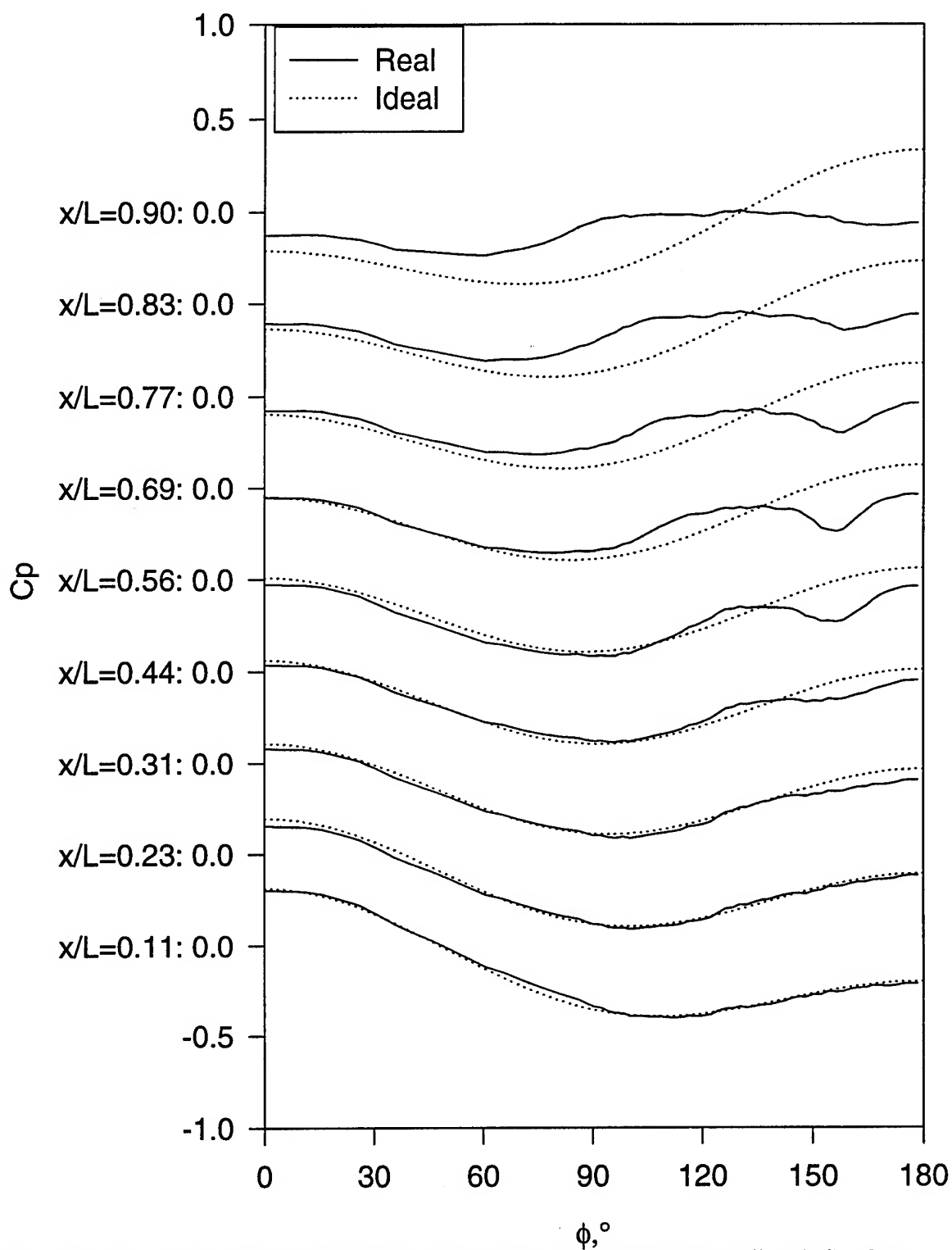


Figure 246. Steady  $C_p$  vs.  $\phi$  for all  $x/L$ ,  $\alpha=19.9^\circ$ . "Real" refers to the measured data while "Ideal" refers to potential flow solution.

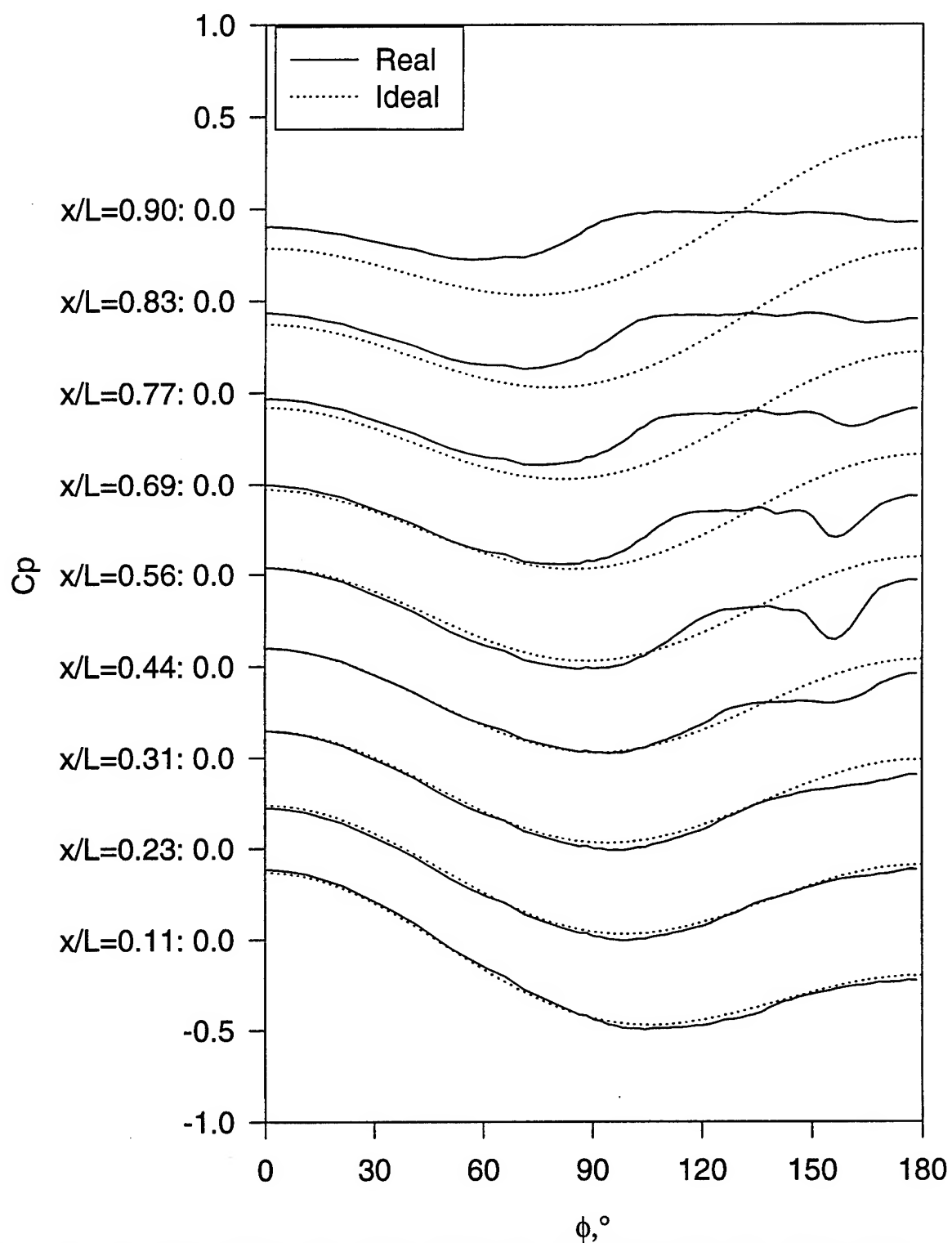


Figure 247. Steady  $C_p$  vs.  $\phi$  for all  $x/L$ ,  $\alpha=22.8^\circ$ . "Real" refers to the measured data while "Ideal" refers to potential flow solution.

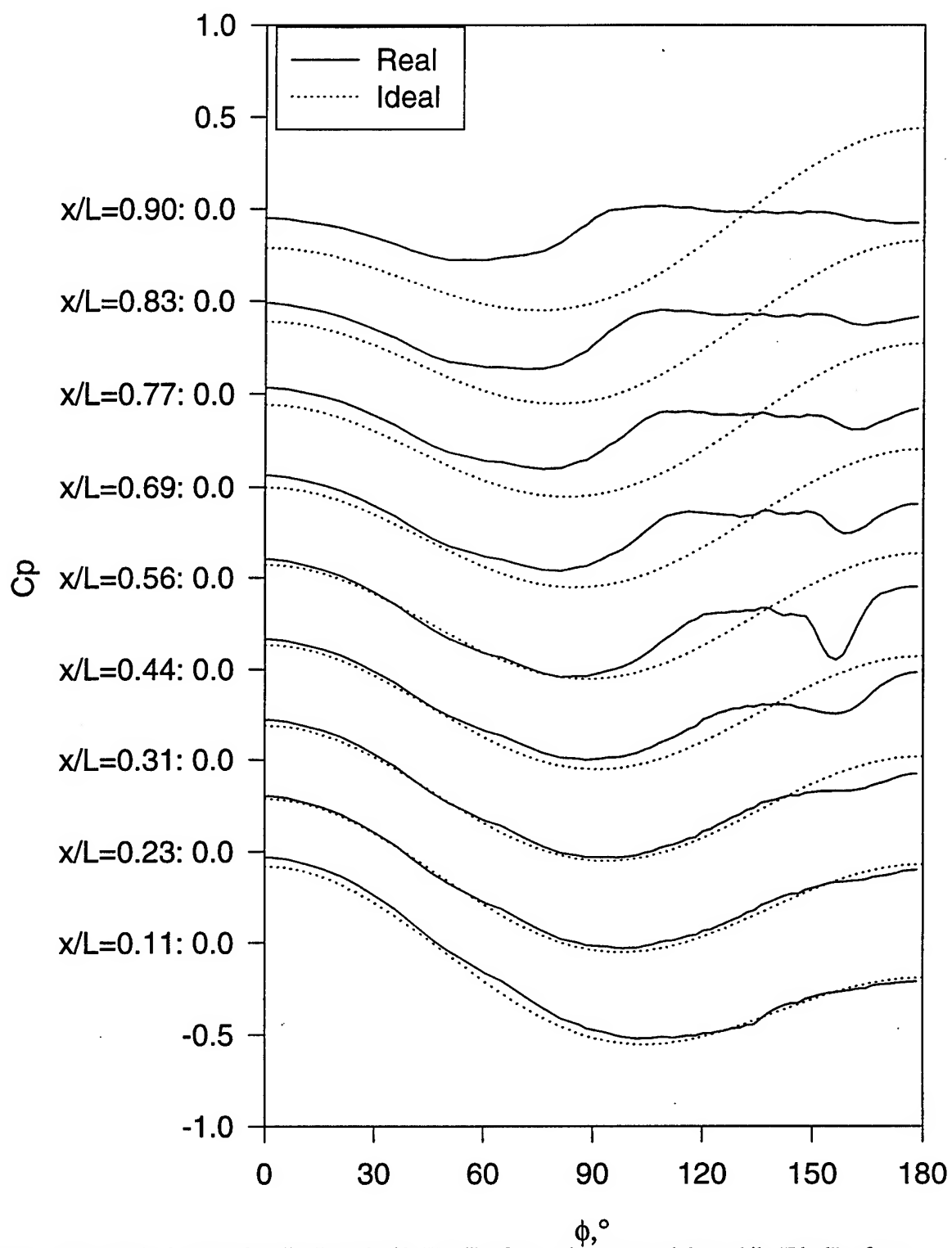


Figure 248. Steady  $C_p$  vs.  $\phi$  for all  $x/L$ ,  $\alpha=24.9^\circ$ . "Real" refers to the measured data while "Ideal" refers to potential flow solution.

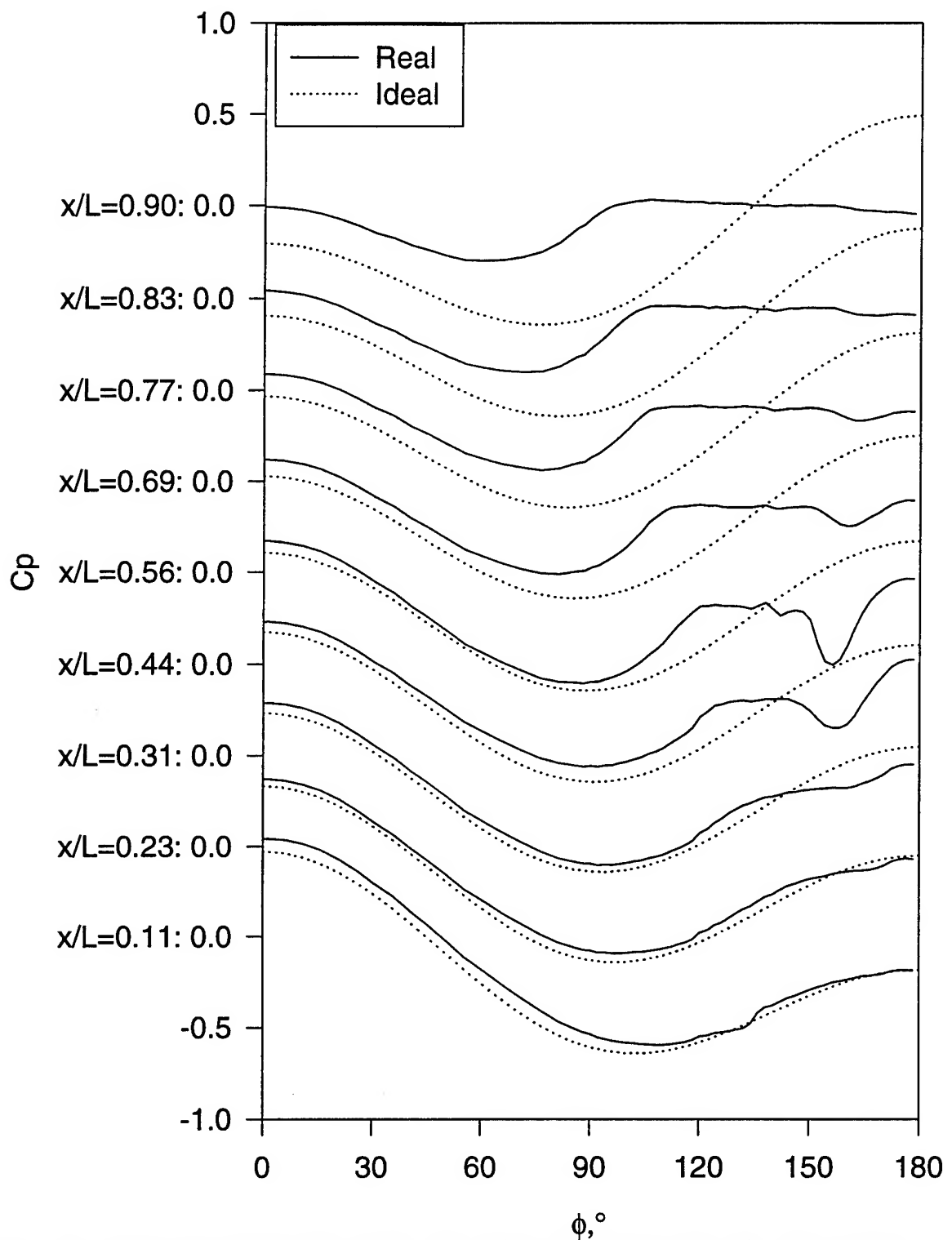


Figure 249. Steady  $C_p$  vs.  $\phi$  for all  $x/L$ ,  $\alpha=27.8^\circ$ . "Real" refers to the measured data while "Ideal" refers to potential flow solution.

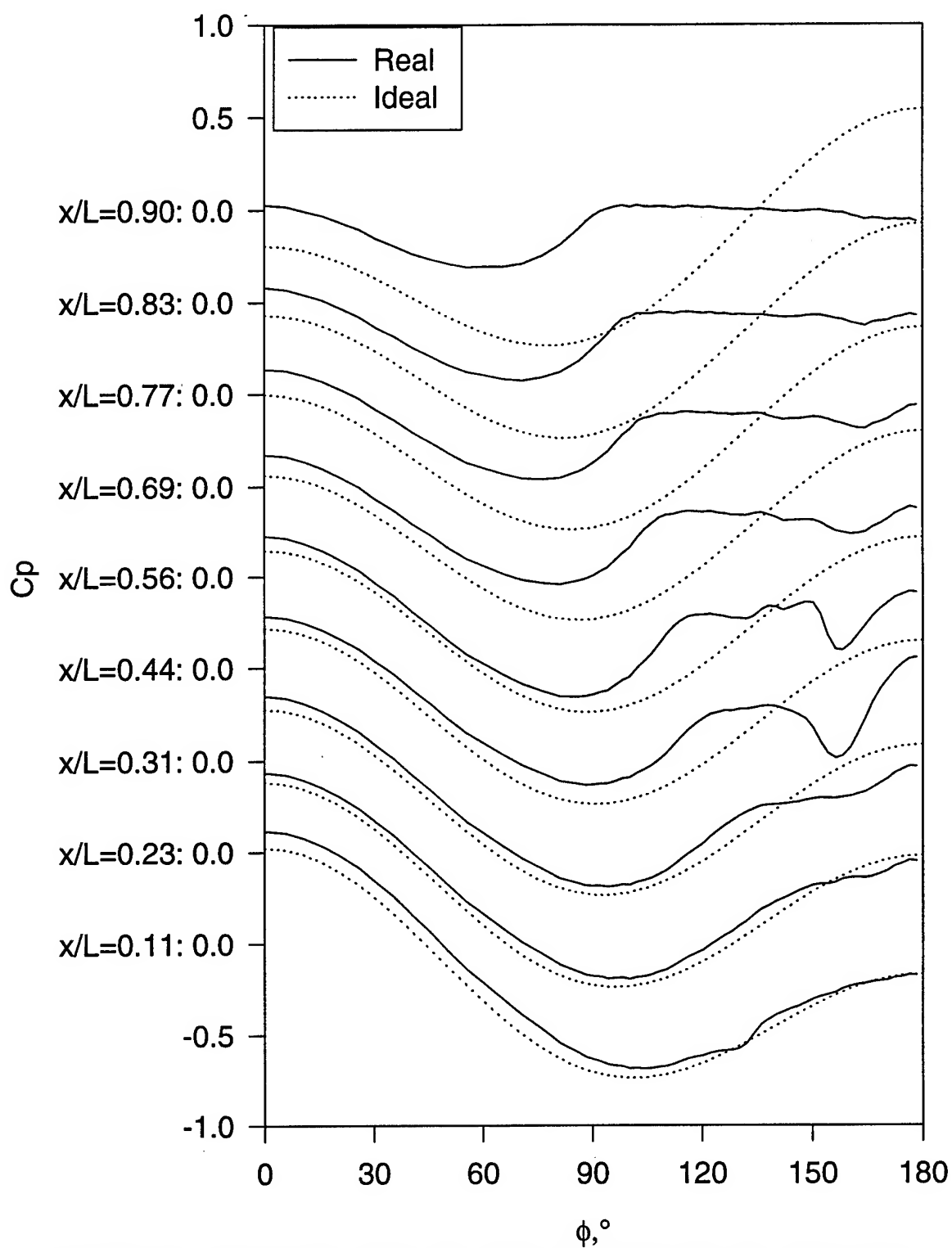


Figure 250. Steady  $C_p$  vs.  $\phi$  for all  $x/L$ ,  $\alpha=30.0^\circ$ . "Real" refers to the measured data while "Ideal" refers to potential flow solution.

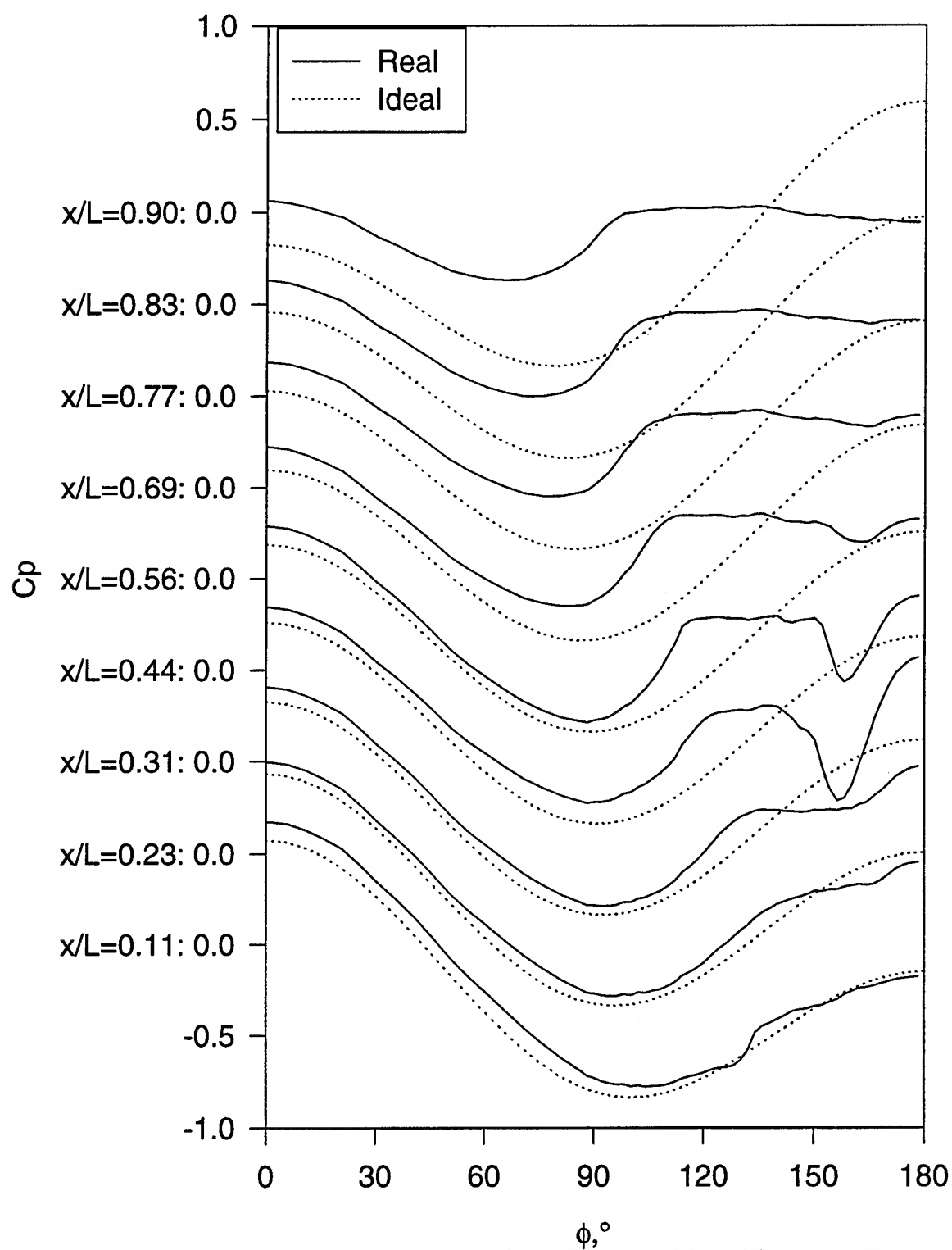


Figure 251. Steady  $C_p$  vs.  $\phi$  for all  $x/L$ ,  $\alpha=32.5^\circ$ . "Real" refers to the measured data while "Ideal" refers to potential flow solution.

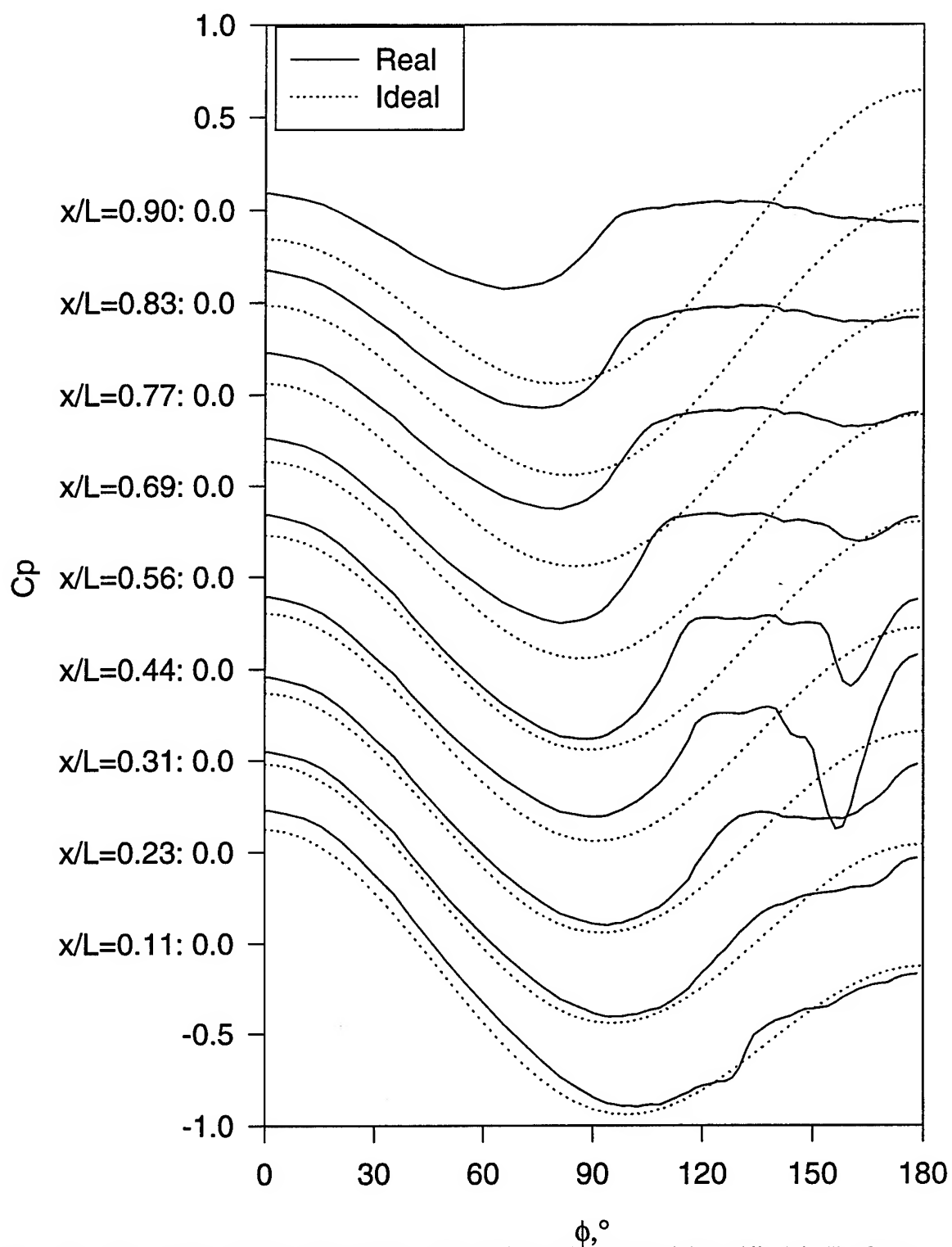


Figure 252. Steady  $C_p$  vs.  $\phi$  for all  $x/L$ ,  $\alpha=35.0^\circ$ . "Real" refers to the measured data while "Ideal" refers to potential flow solution.

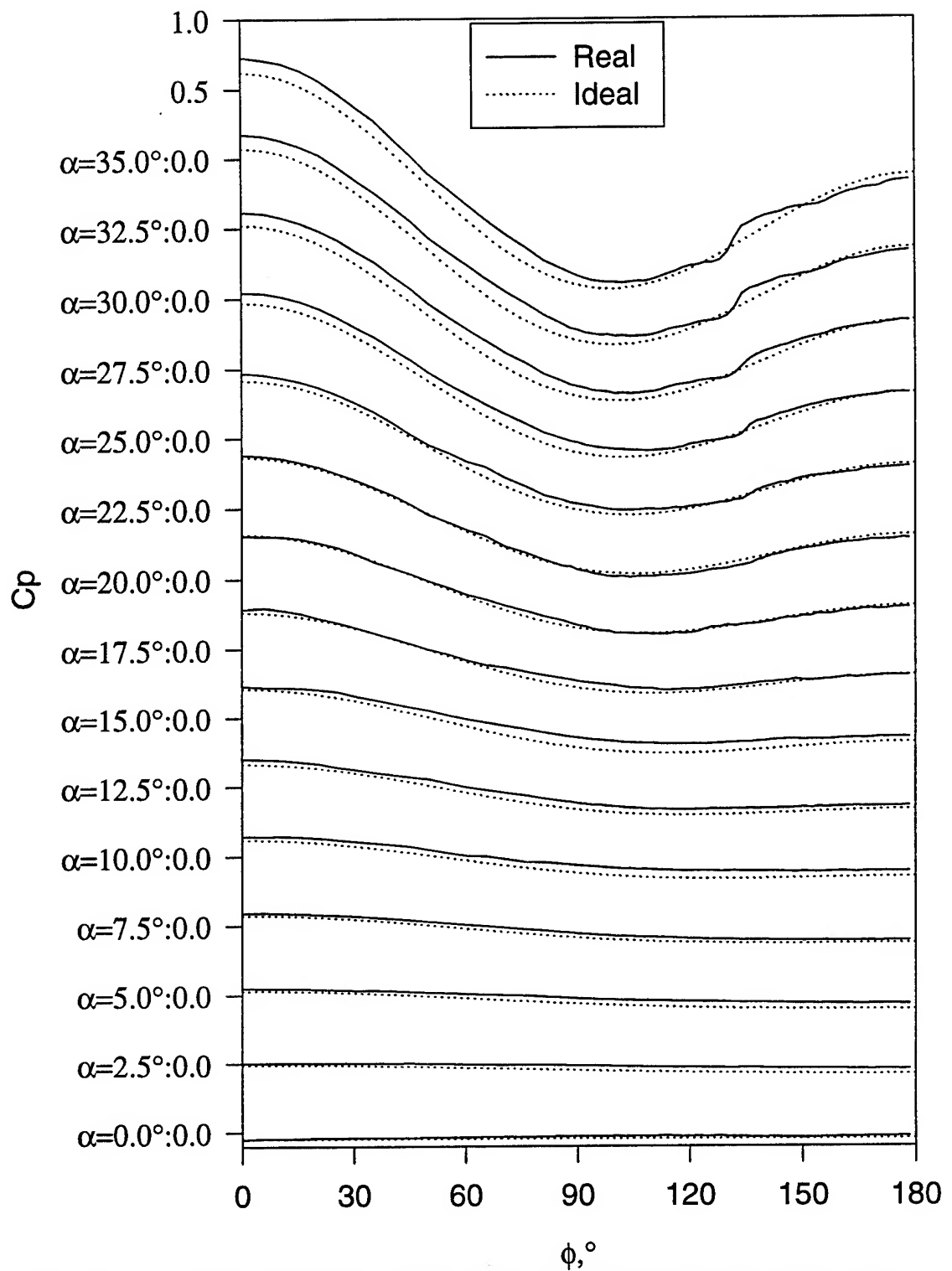


Figure 253. Steady  $C_p$  vs.  $\phi$  for all  $\alpha$ ,  $x/L=0.11$ . "Real" refers to the measured data while "Ideal" refers to potential flow solution.



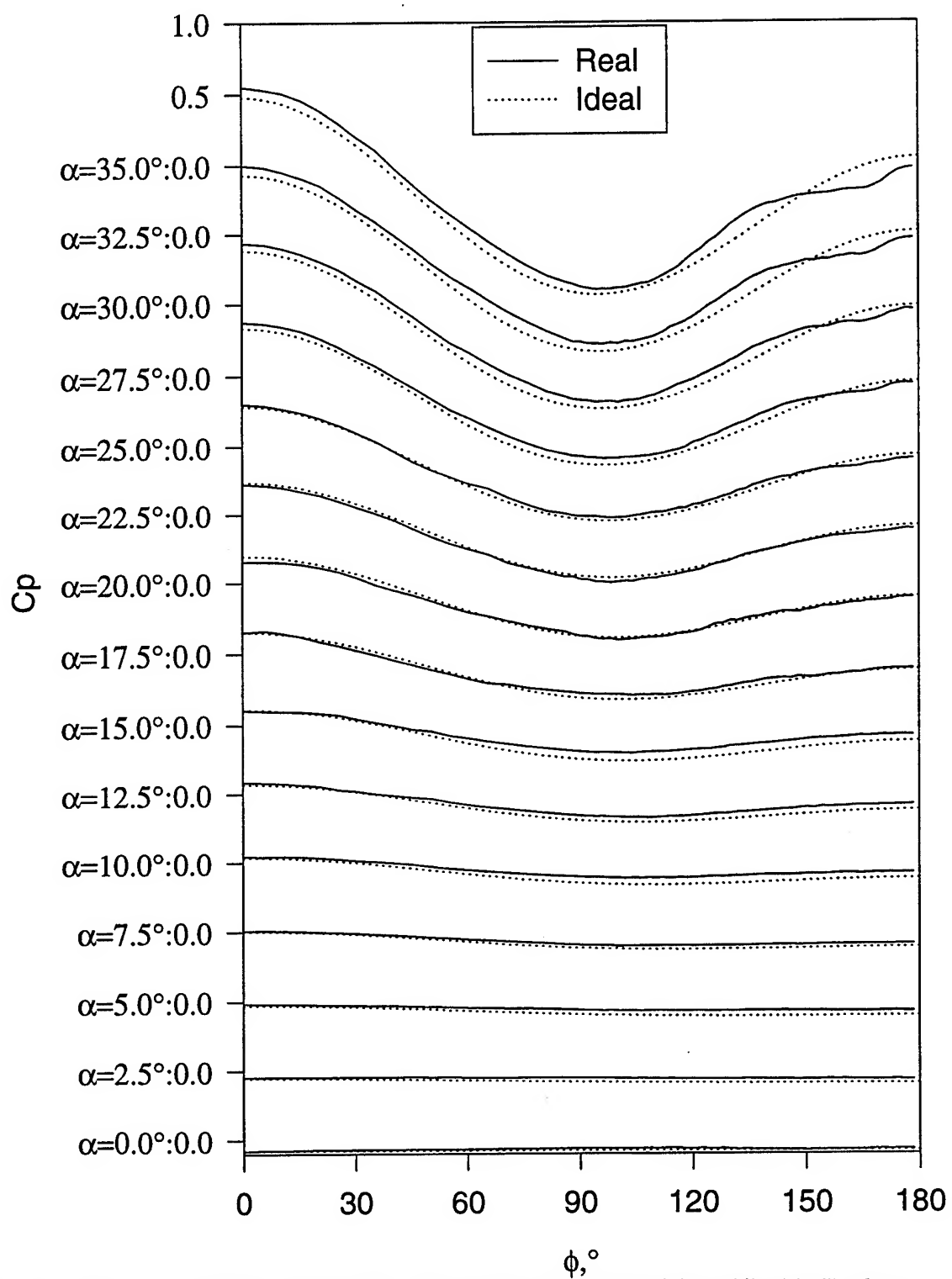


Figure 254. Steady  $C_p$  vs.  $\phi$  for all  $\alpha$ ,  $x/L=0.23$ . "Real" refers to the measured data while "Ideal" refers to potential flow solution.

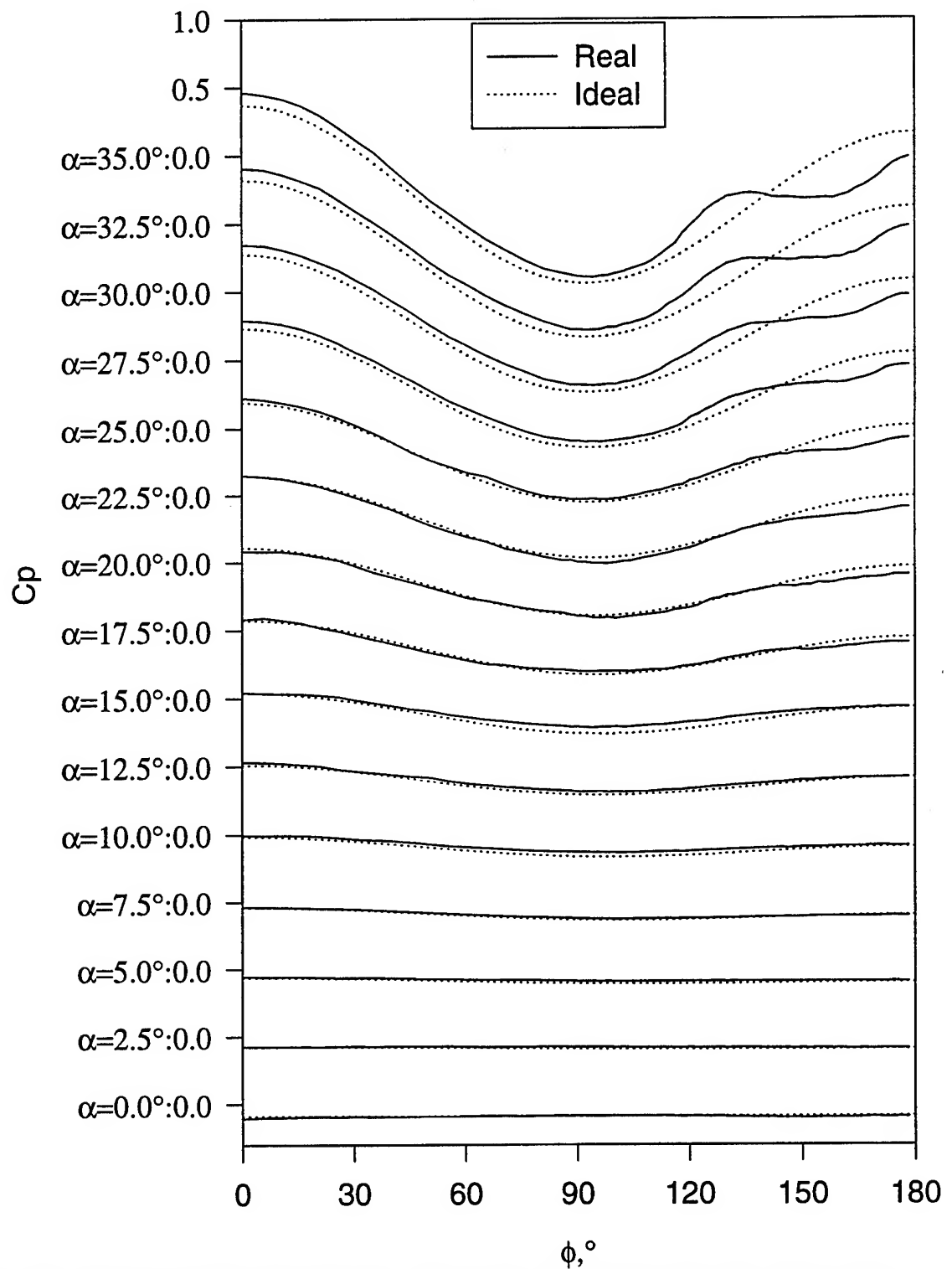


Figure 255. Steady  $C_p$  vs.  $\phi$  for all  $\alpha$ ,  $x/L=0.31$ . "Real" refers to the measured data while "Ideal" refers to potential flow solution.

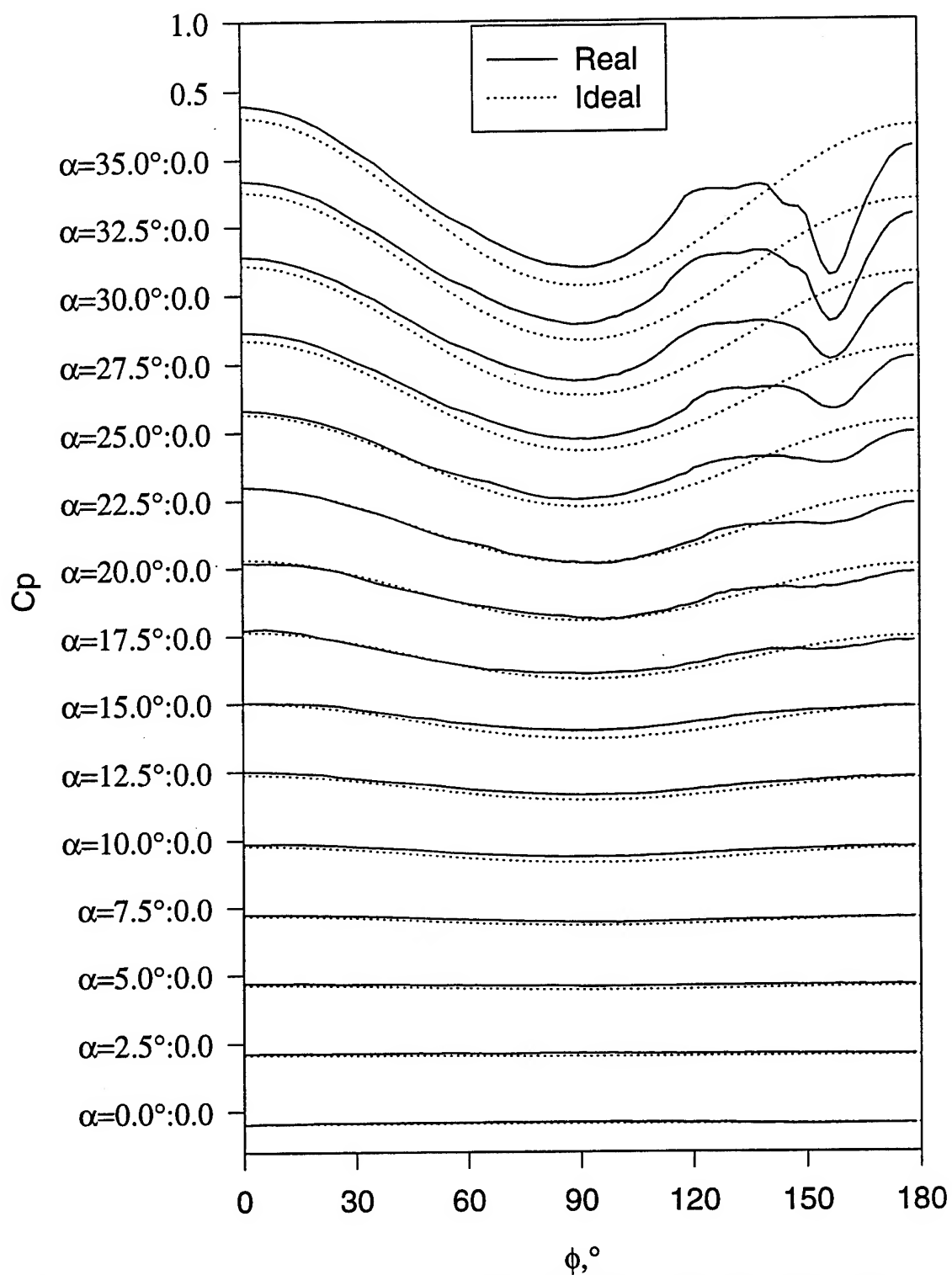


Figure 256. Steady  $C_p$  vs.  $\phi$  for all  $\alpha$ ,  $x/L=0.44$ . "Real" refers to the measured data while "Ideal" refers to potential flow solution.

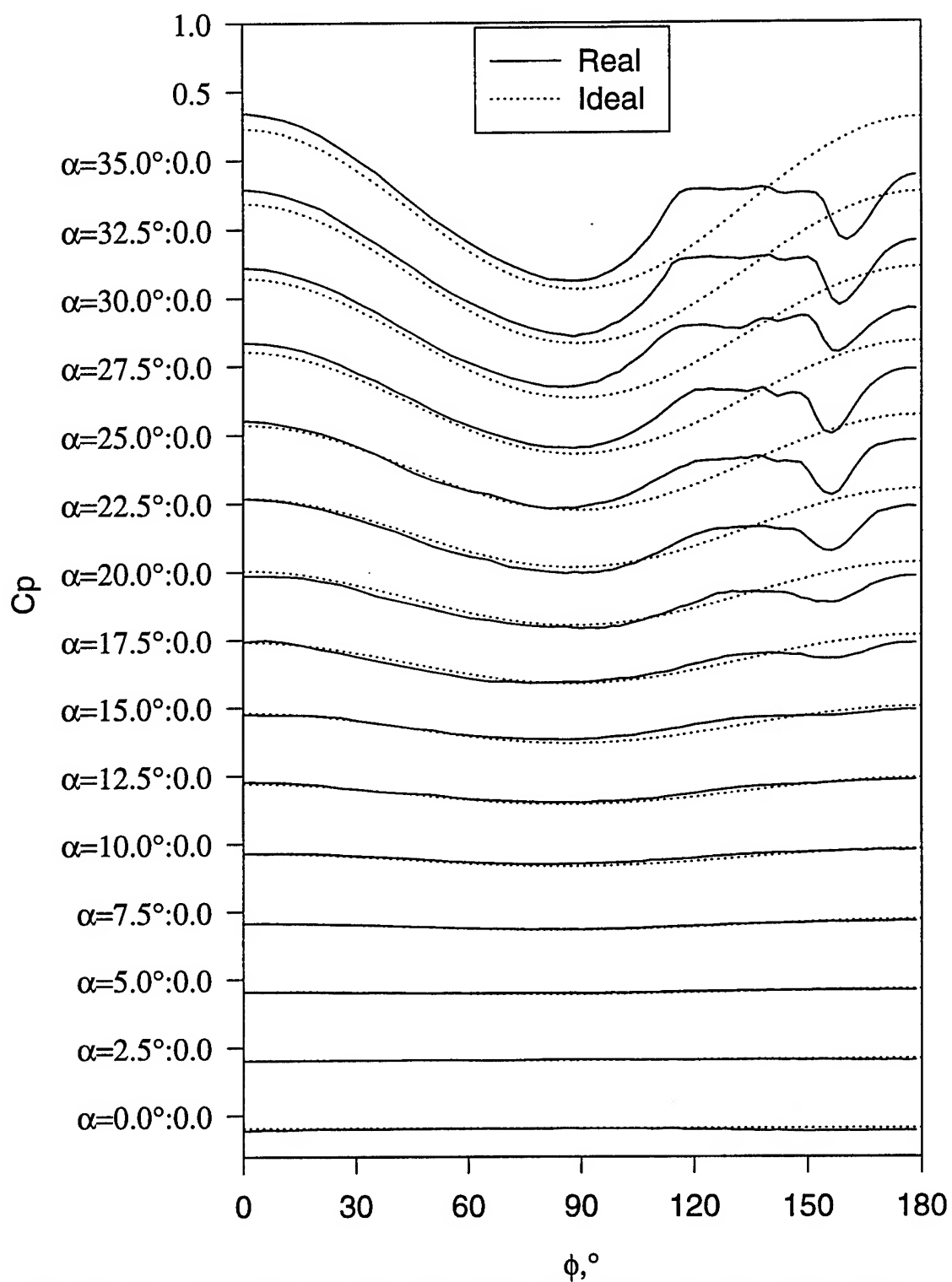


Figure 257. Steady  $C_p$  vs.  $\phi$  for all  $\alpha$ ,  $x/L=0.56$ . "Real" refers to the measured data while "Ideal" refers to potential flow solution.

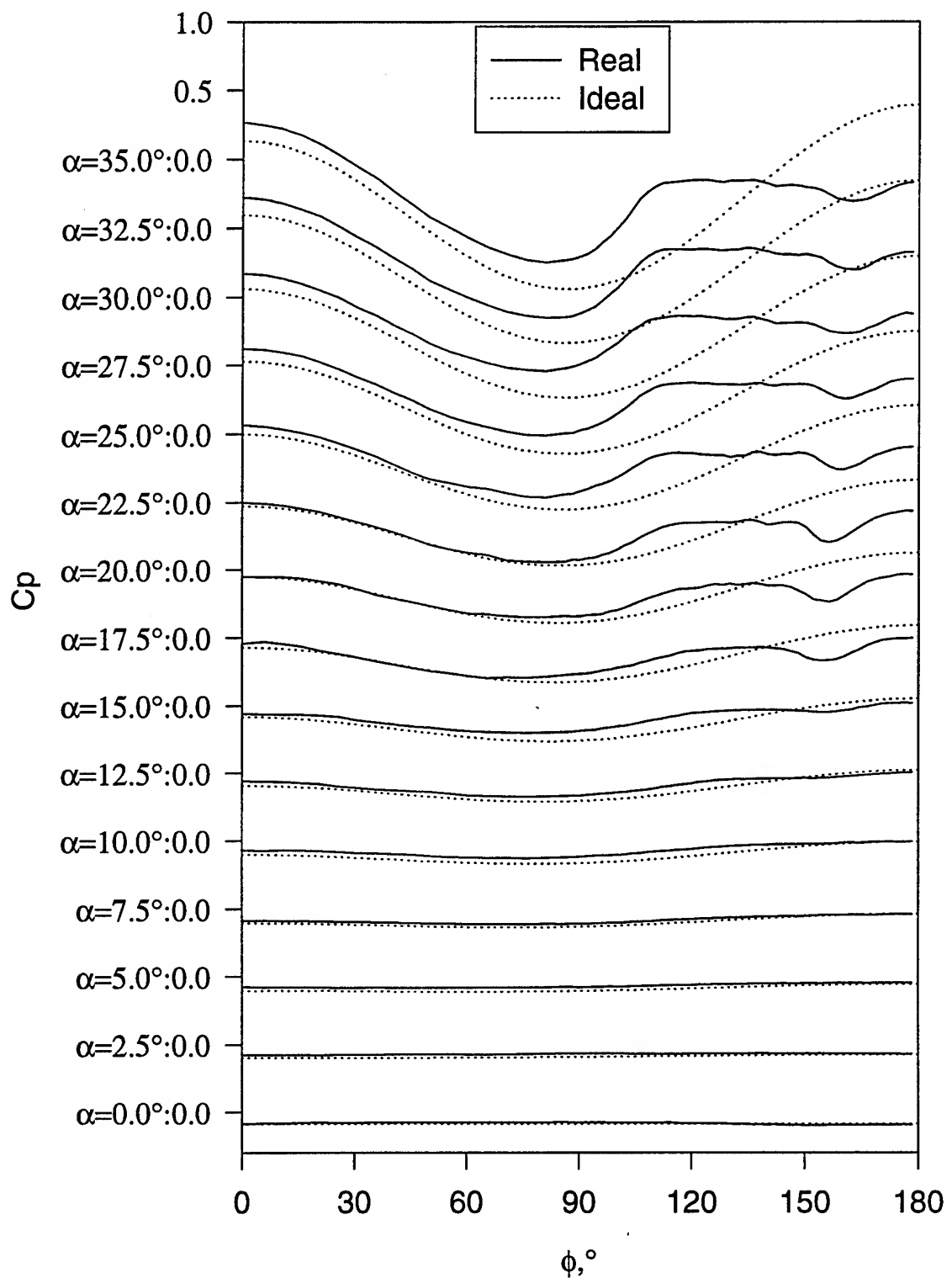


Figure 258. Steady  $C_p$  vs.  $\phi$  for all  $\alpha$ ,  $x/L=0.69$ . "Real" refers to the measured data while "Ideal" refers to potential flow solution.

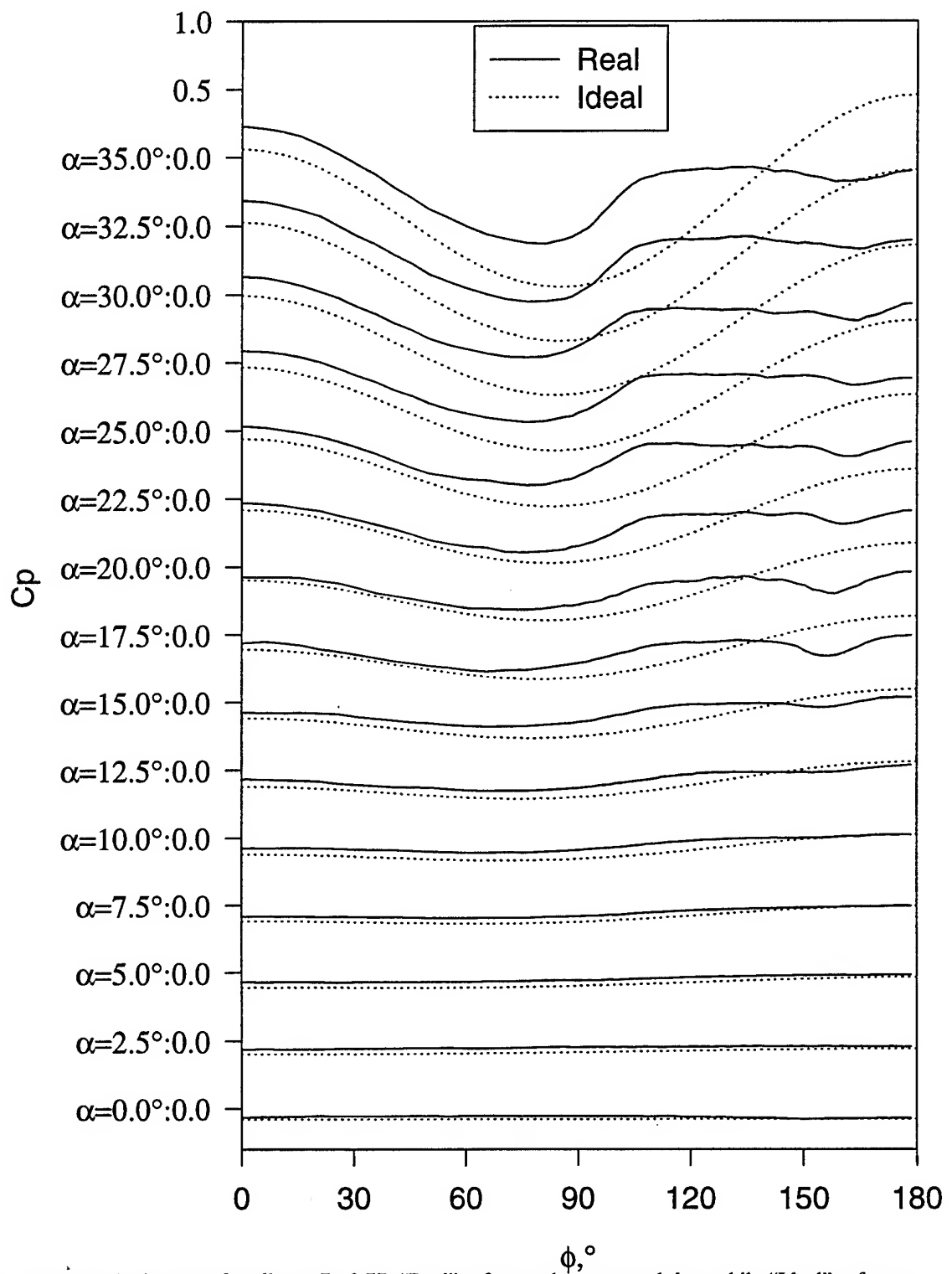


Figure 259. Steady  $C_p$  vs.  $\phi$  for all  $\alpha$ ,  $x/L=0.77$ . "Real" refers to the measured data while "Ideal" refers to potential flow solution.

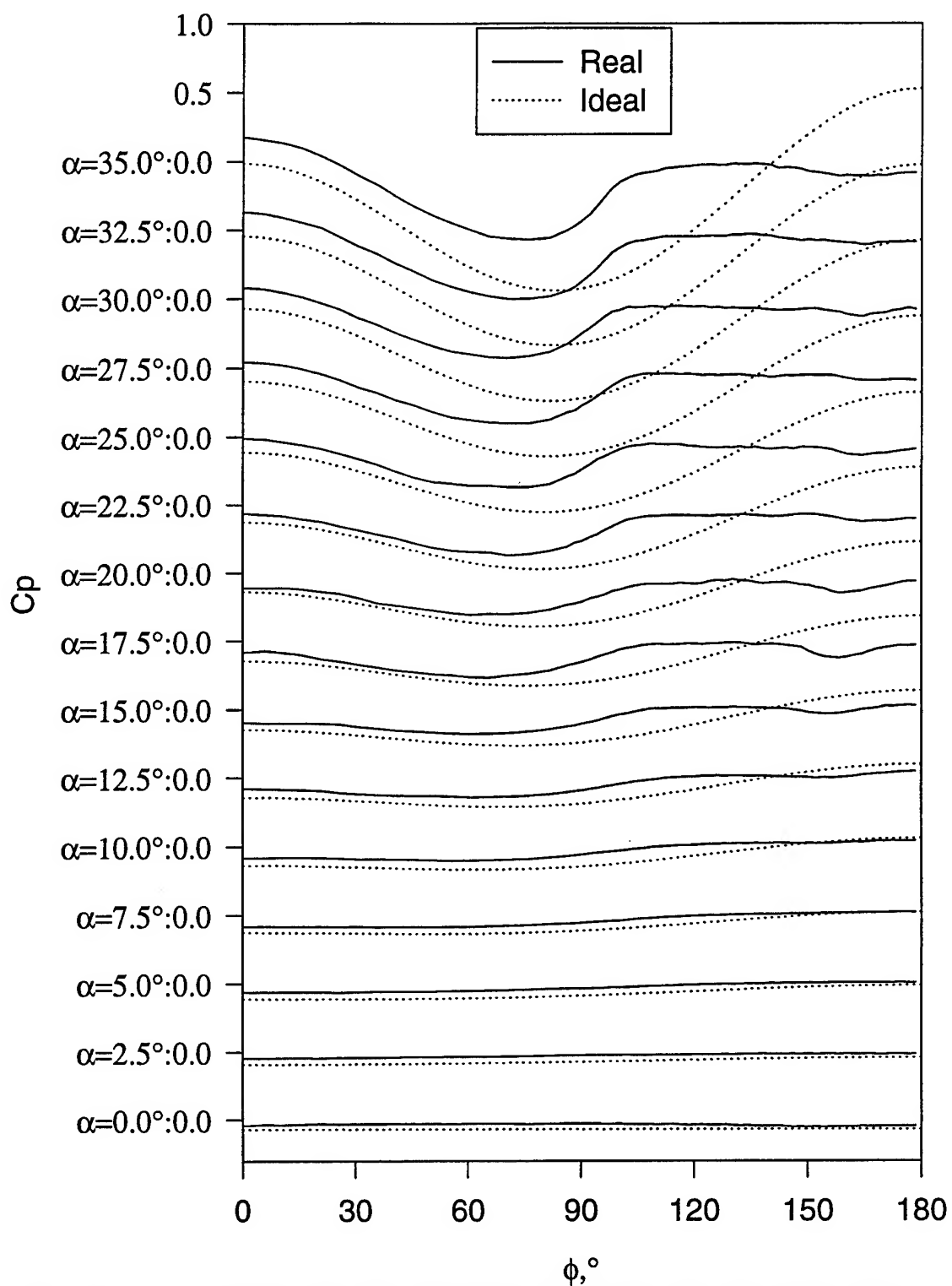


Figure 260. Steady  $C_p$  vs.  $\phi$  for all  $\alpha$ ,  $x/L=0.83$ . "Real" refers to the measured data while "Ideal" refers to potential flow solution.

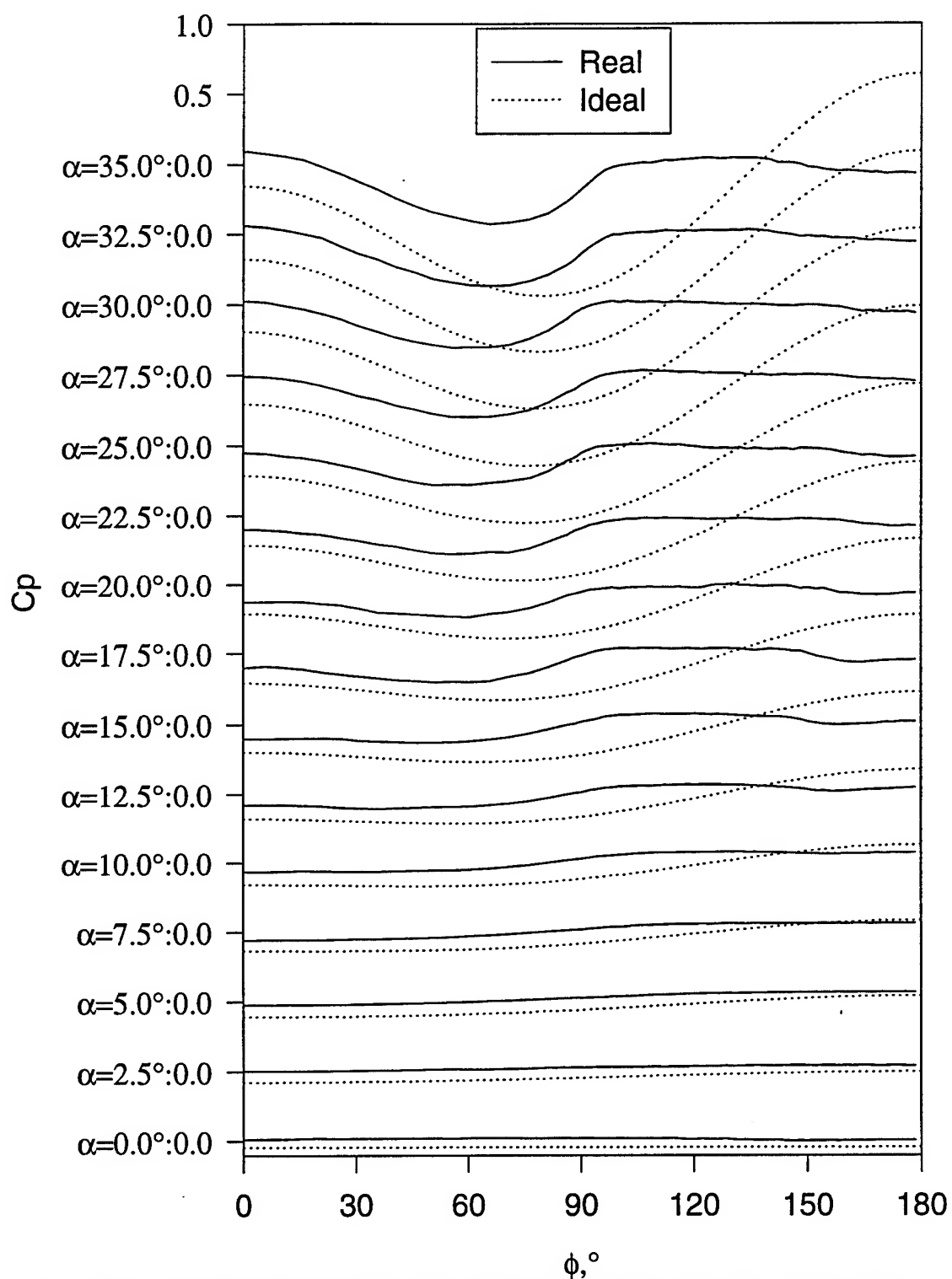


Figure 261. Steady  $C_p$  vs.  $\phi$  for all  $\alpha$ ,  $x/L=0.90$ . "Real" refers to the measured data while "Ideal" refers to potential flow solution.



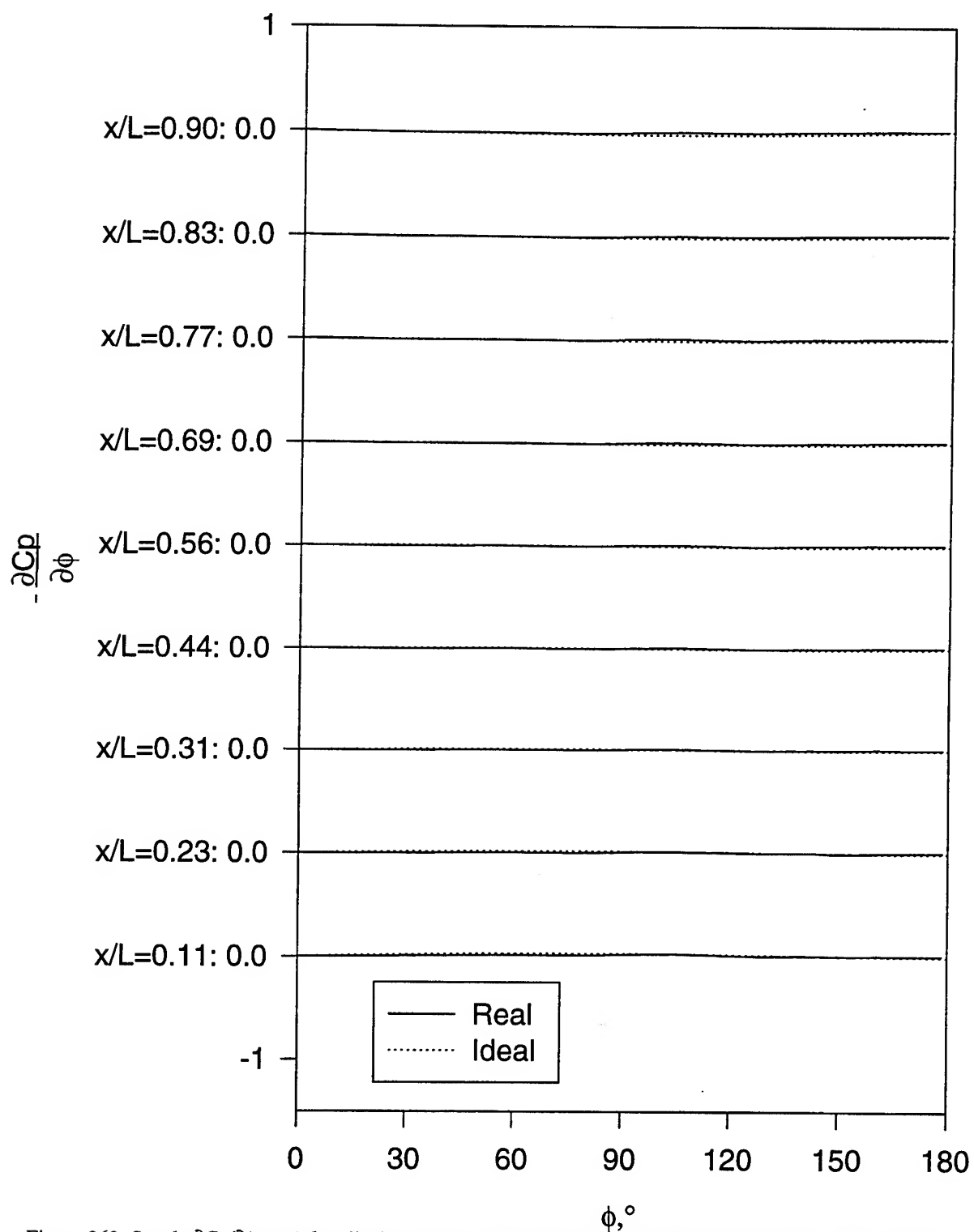


Figure 262. Steady  $\partial C_p / \partial \phi$  vs.  $\phi$  for all  $x/L$ ,  $\alpha=2.2^\circ$ . "Real" refers to the measured data while "Ideal" refers to potential flow solution.

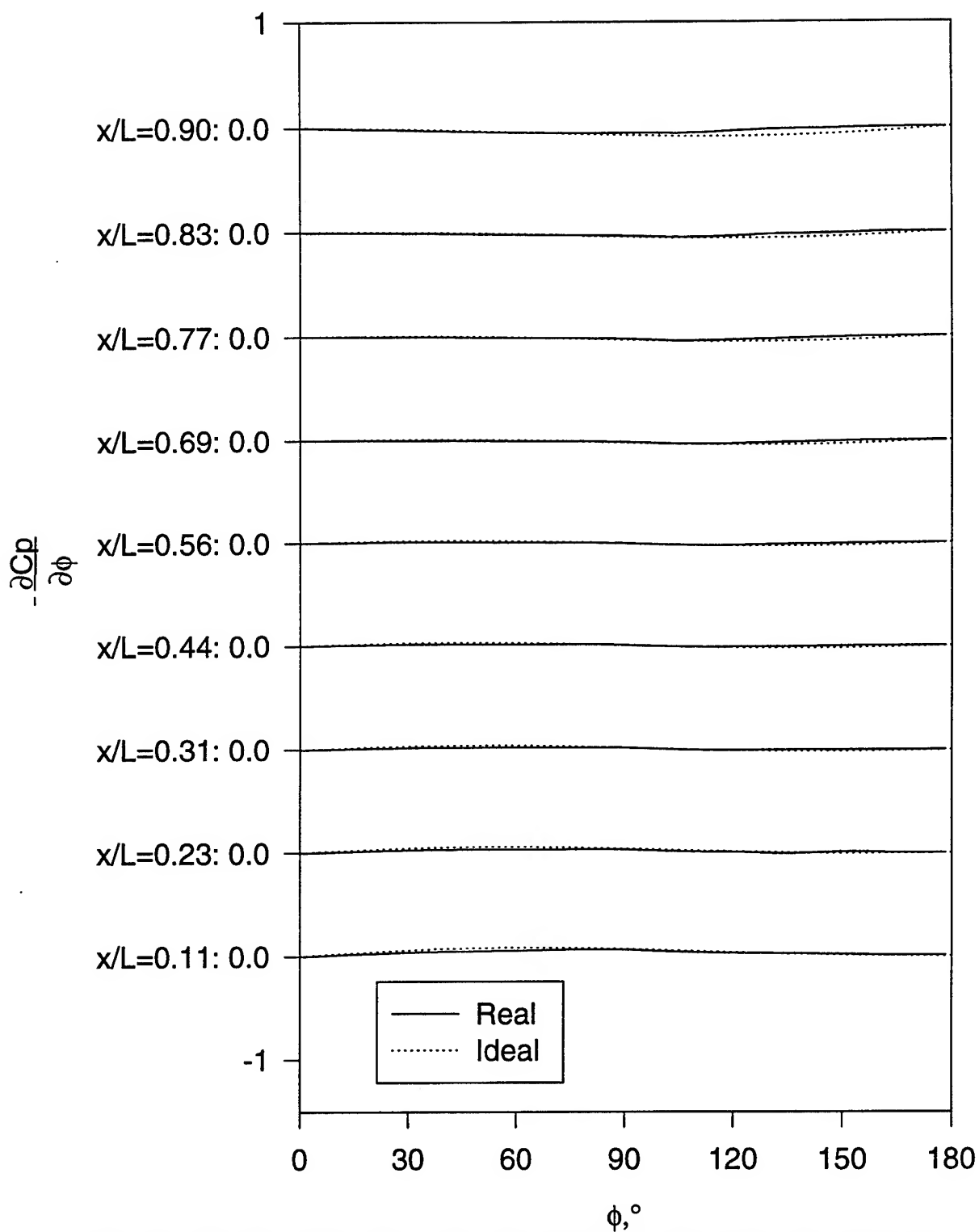


Figure 263. Steady  $\partial C_p / \partial \alpha$  vs.  $\phi$  for all  $x/L$ ,  $\alpha=4.8^\circ$ . "Real" refers to the measured data while "Ideal" refers to potential flow solution.

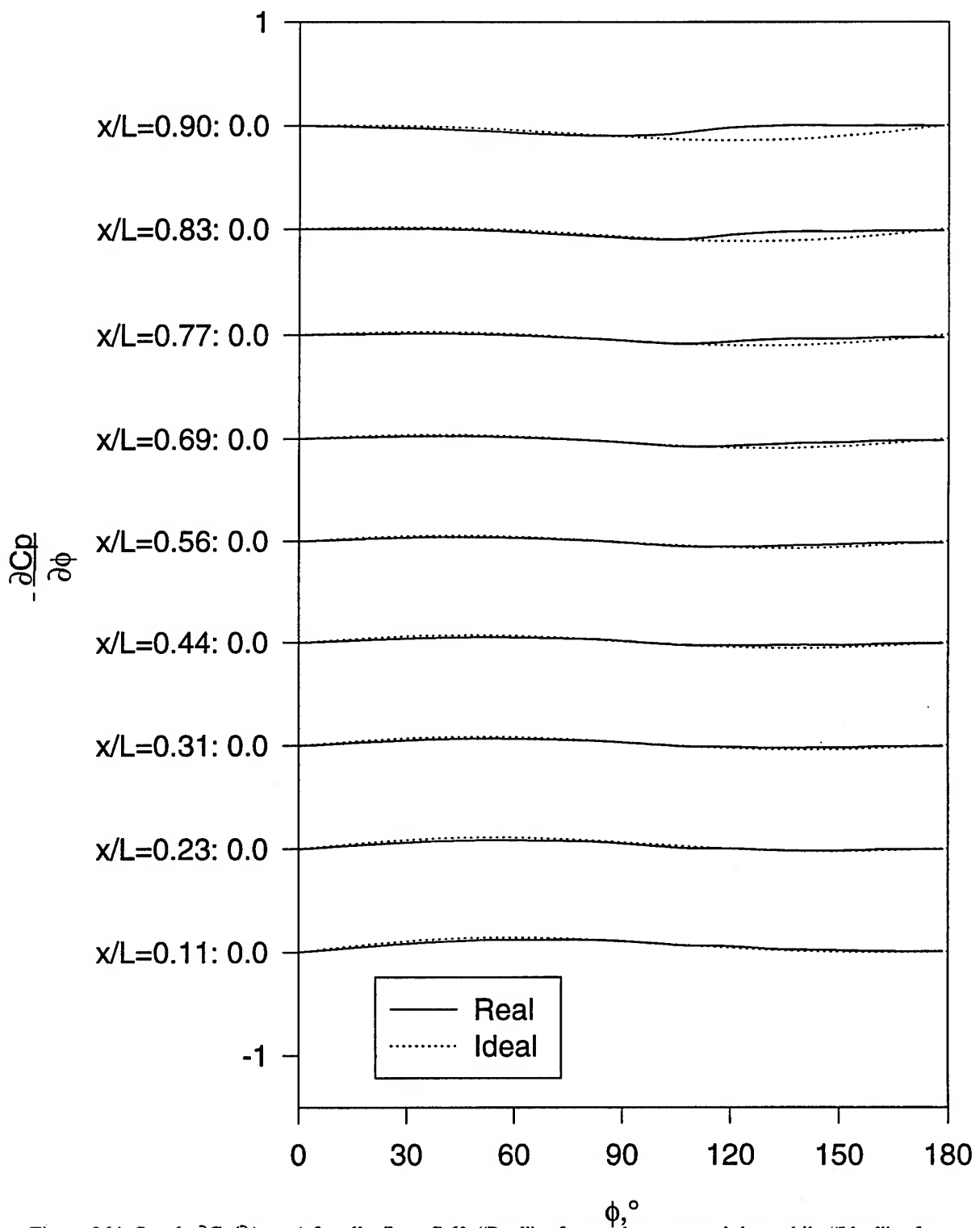


Figure 264. Steady  $\partial C_p / \partial \phi$  vs.  $\phi$  for all  $x/L$ ,  $\alpha = 7.6^\circ$ . "Real" refers to the measured data while "Ideal" refers to potential flow solution.

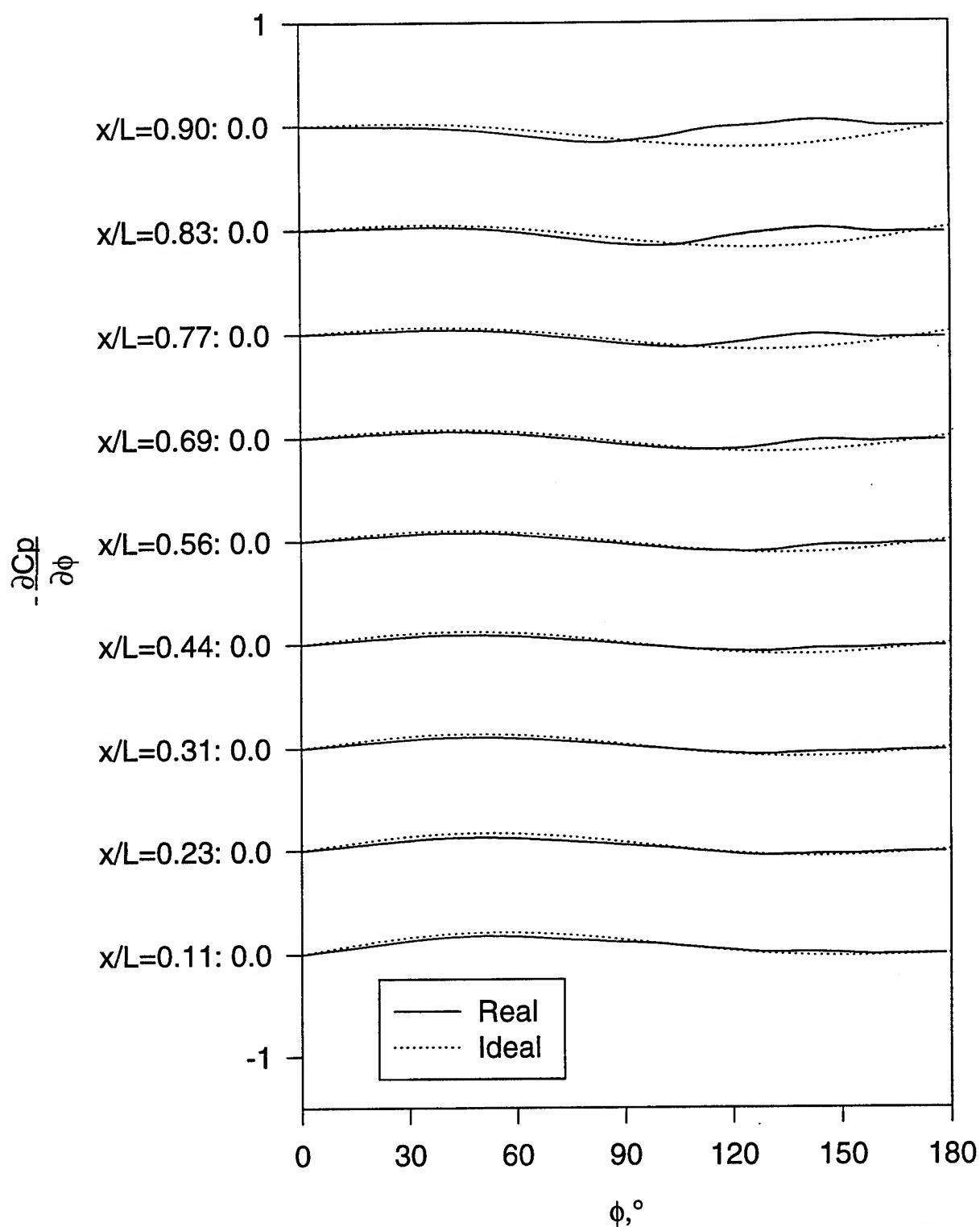


Figure 265. Steady  $\partial C_p / \partial \phi$  vs.  $\phi$  for all  $x/L$ ,  $\alpha=9.8^\circ$ . "Real" refers to the measured data while "Ideal" refers to potential flow solution.

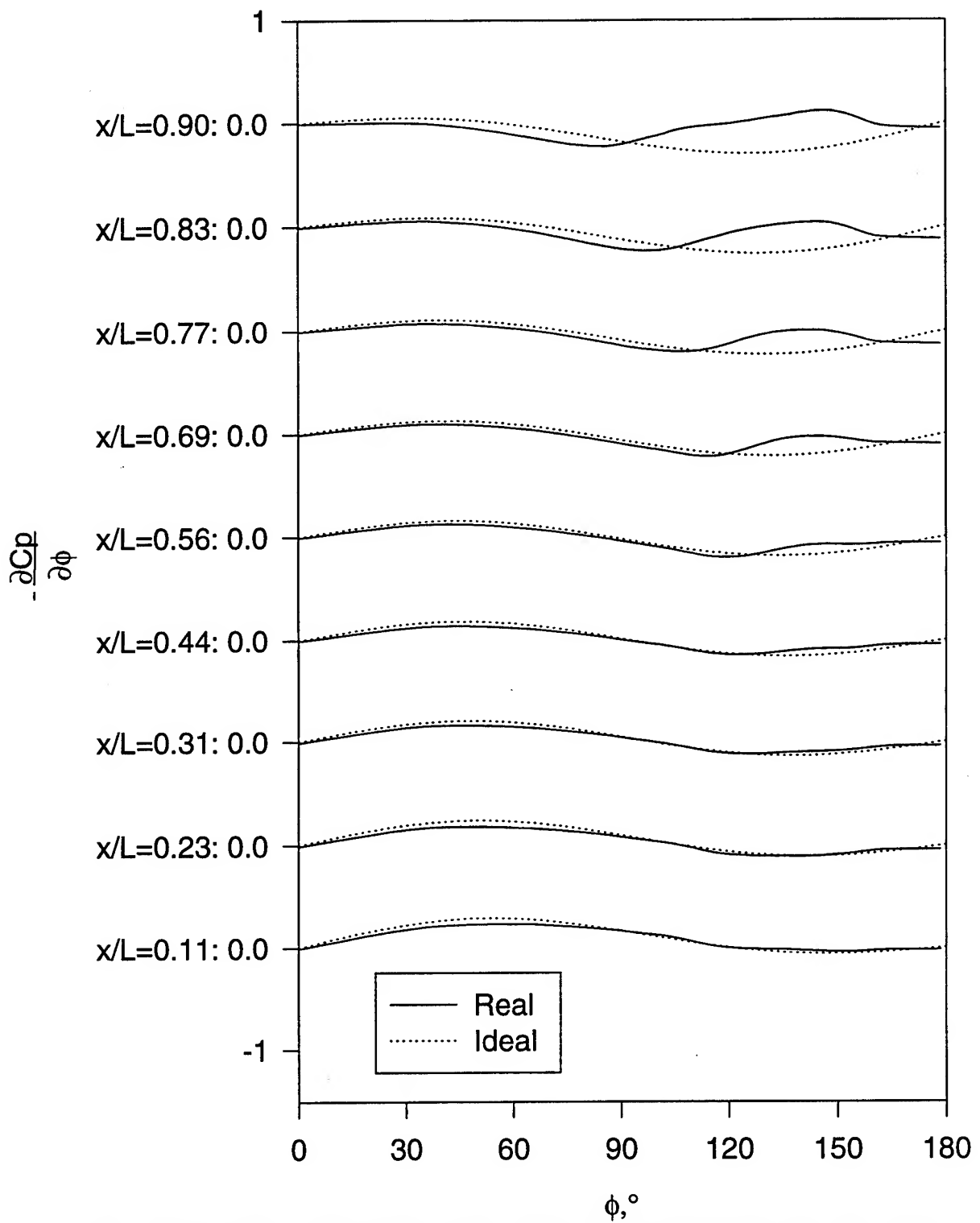
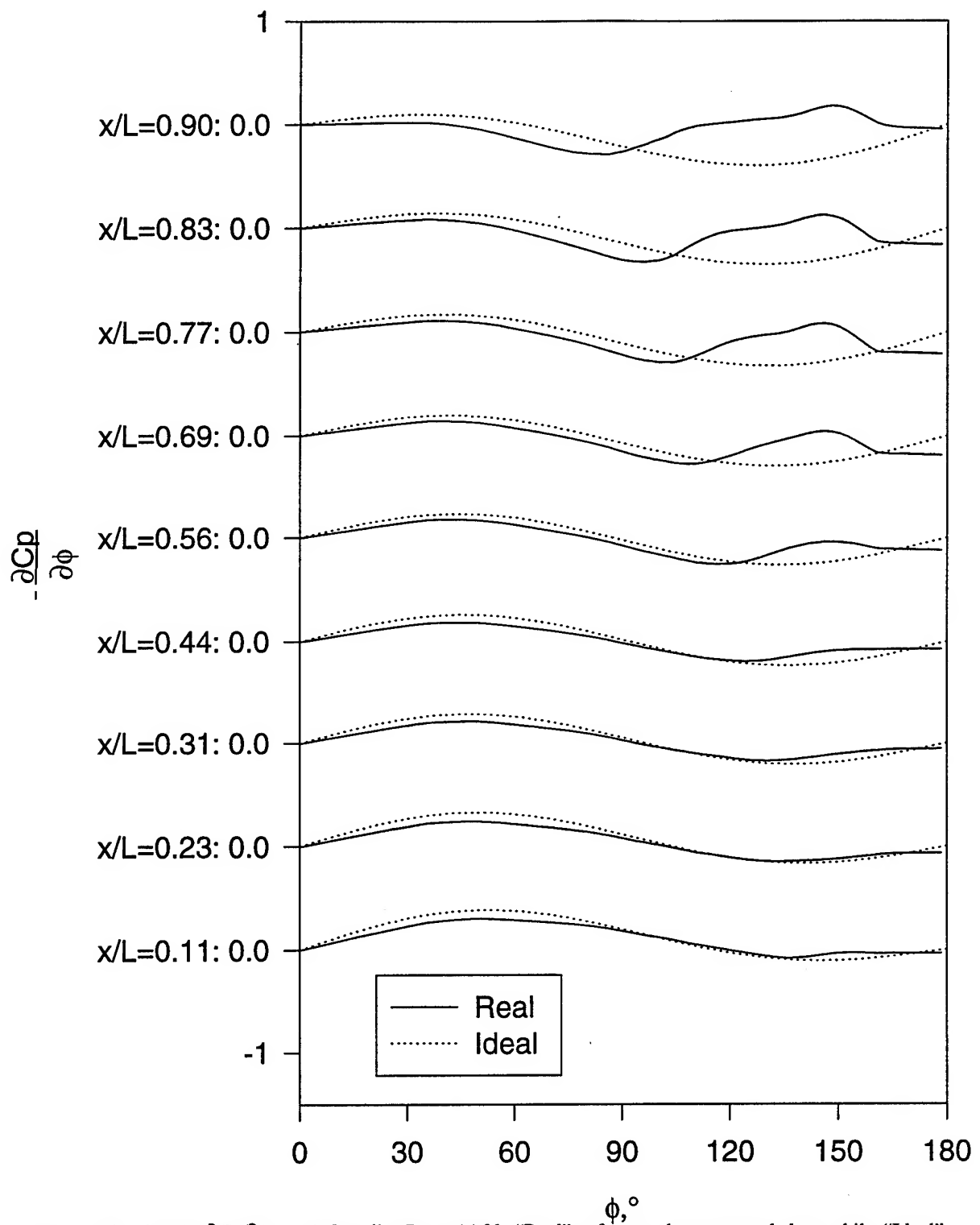


Figure 266. Steady  $\partial C_p / \partial \alpha$  vs.  $\phi$  for all  $x/L$ ,  $\alpha=12.7^\circ$ . "Real" refers to the measured data while "Ideal" refers to potential flow solution.



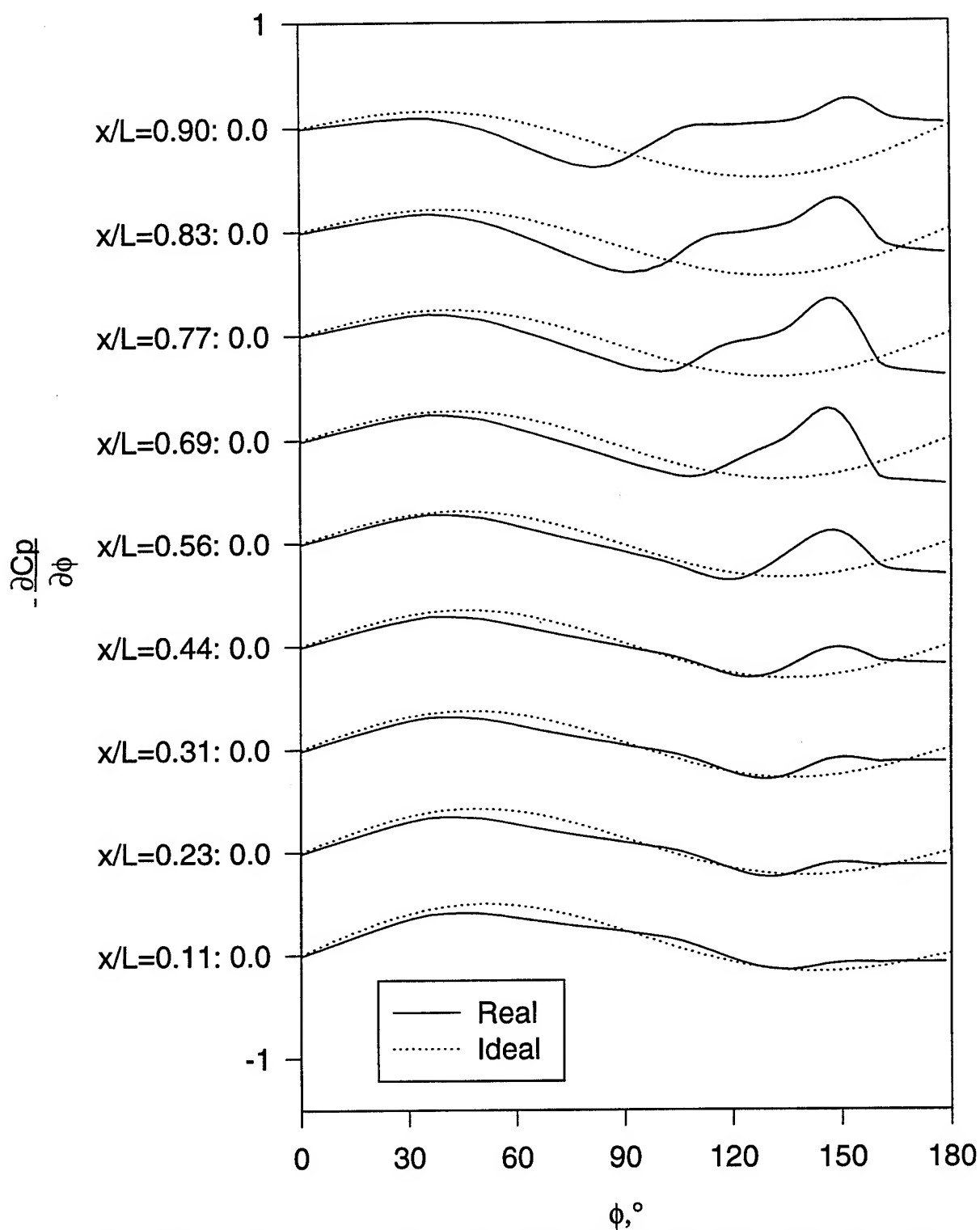


Figure 268. Steady  $\partial C_p / \partial \phi$  vs.  $\phi$  for all  $x/L$ ,  $\alpha = 17.8^\circ$ . "Real" refers to the measured data while "Ideal" refers to potential flow solution.

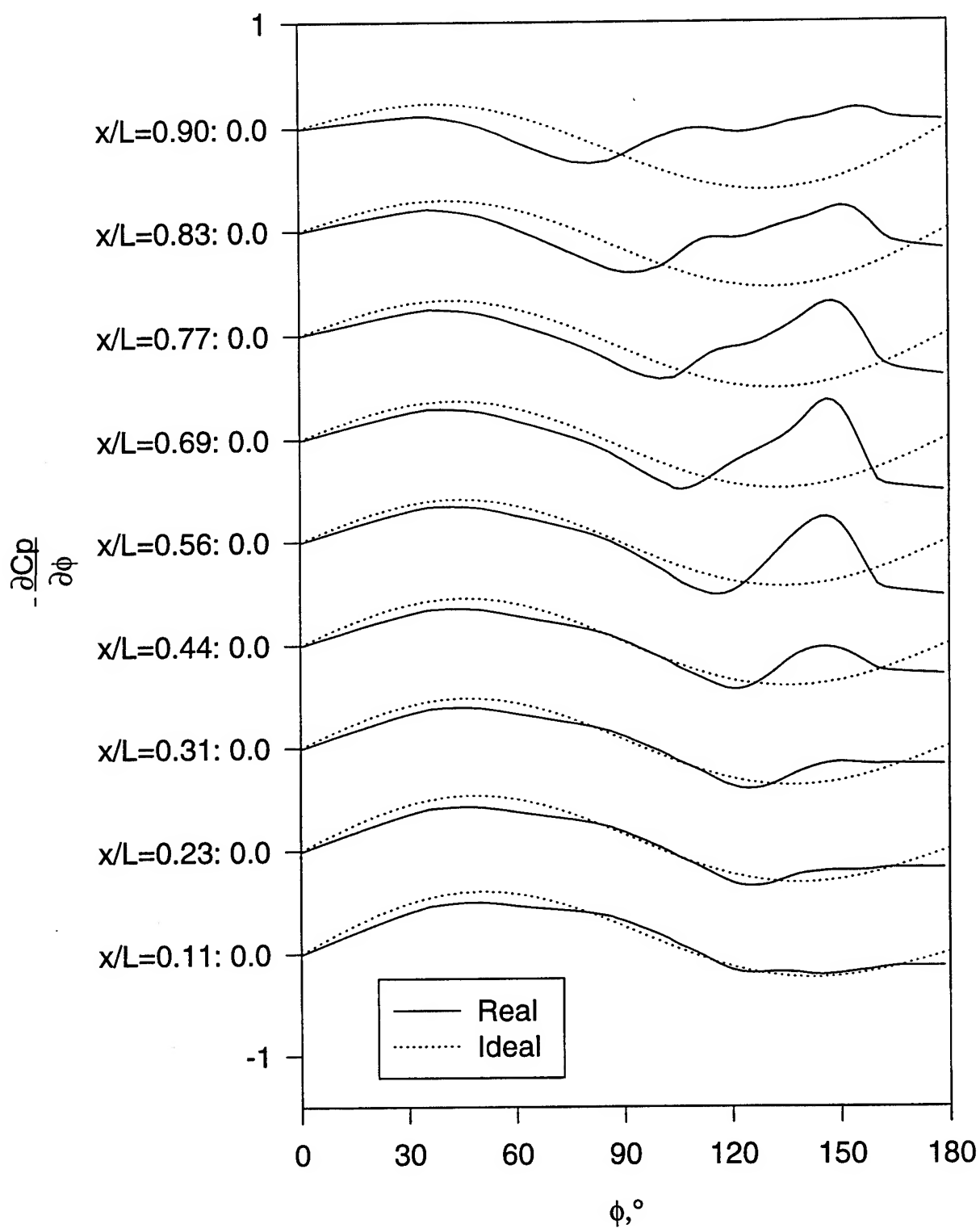


Figure 269. Steady  $\frac{\partial C_p}{\partial \alpha}$  vs.  $\phi$  for all  $x/L$ ,  $\alpha=19.9^\circ$ . "Real" refers to the measured data while "Ideal" refers to potential flow solution.



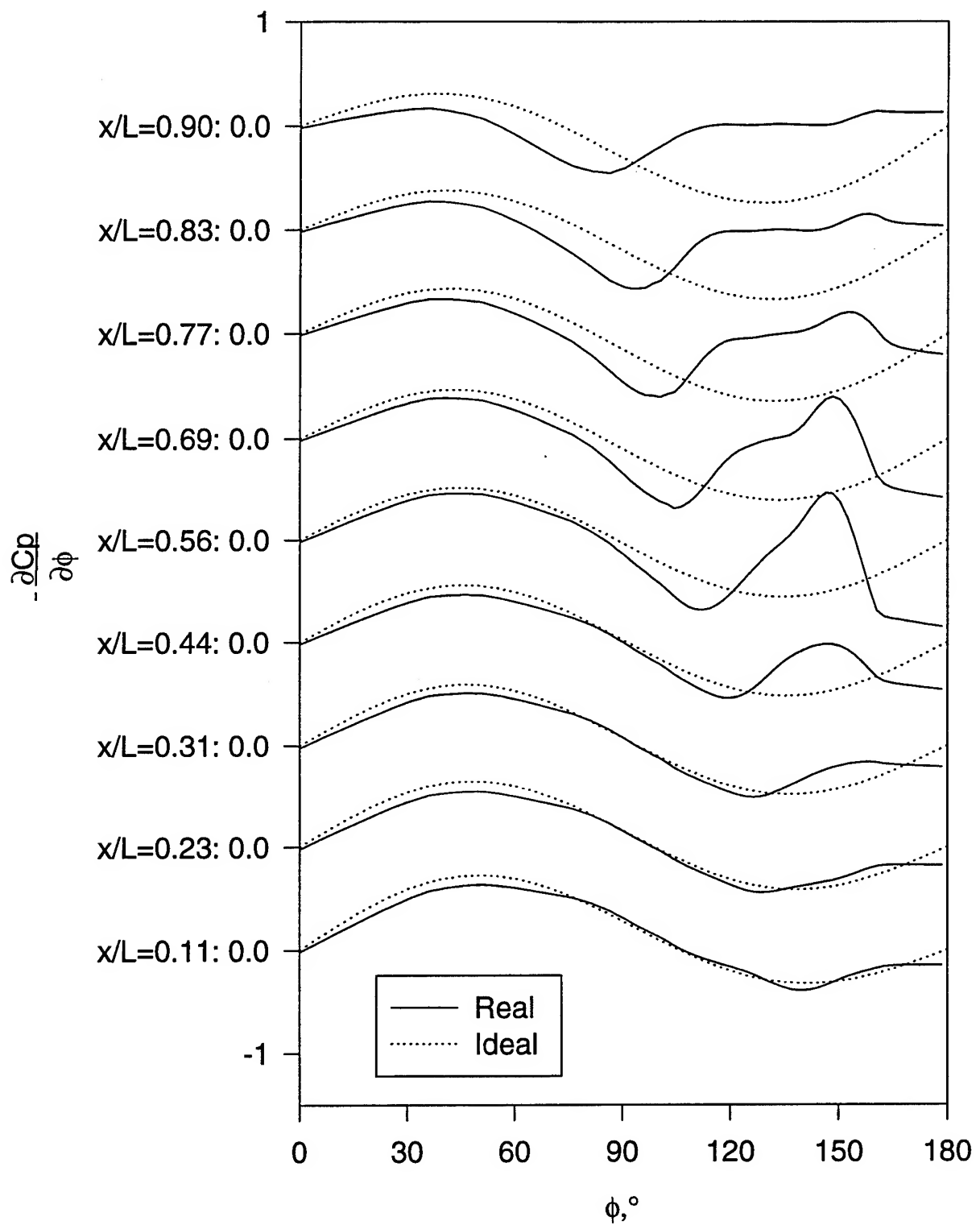


Figure 270. Steady  $\partial C_p/\partial \alpha$  vs.  $\phi$  for all  $x/L$ ,  $\alpha=22.8^\circ$ . "Real" refers to the measured data while "Ideal" refers to potential flow solution.

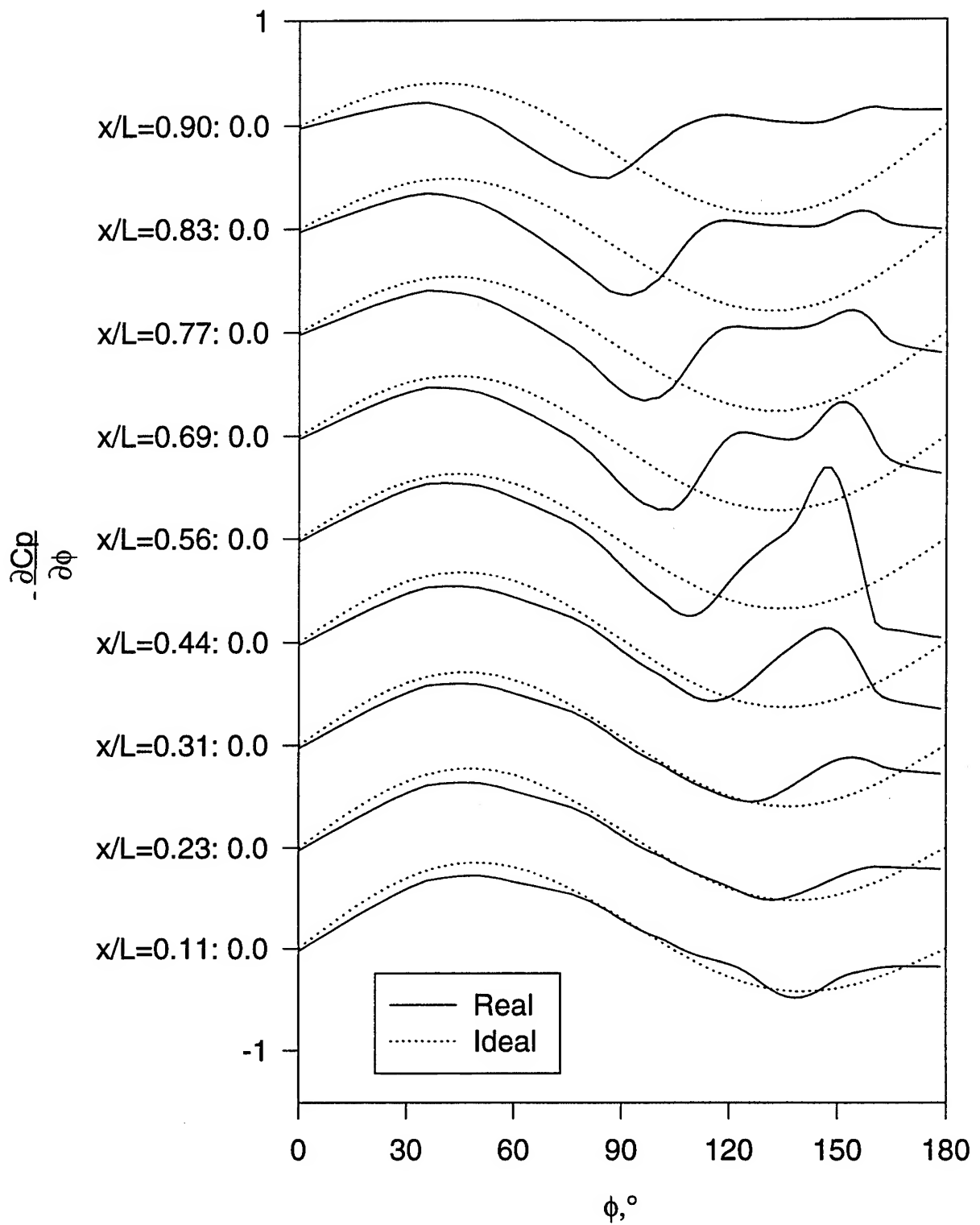


Figure 271. Steady  $\partial C_p / \partial \alpha$  vs.  $\phi$  for all  $x/L$ ,  $\alpha=24.9^\circ$ . "Real" refers to the measured data while "Ideal" refers to potential flow solution.

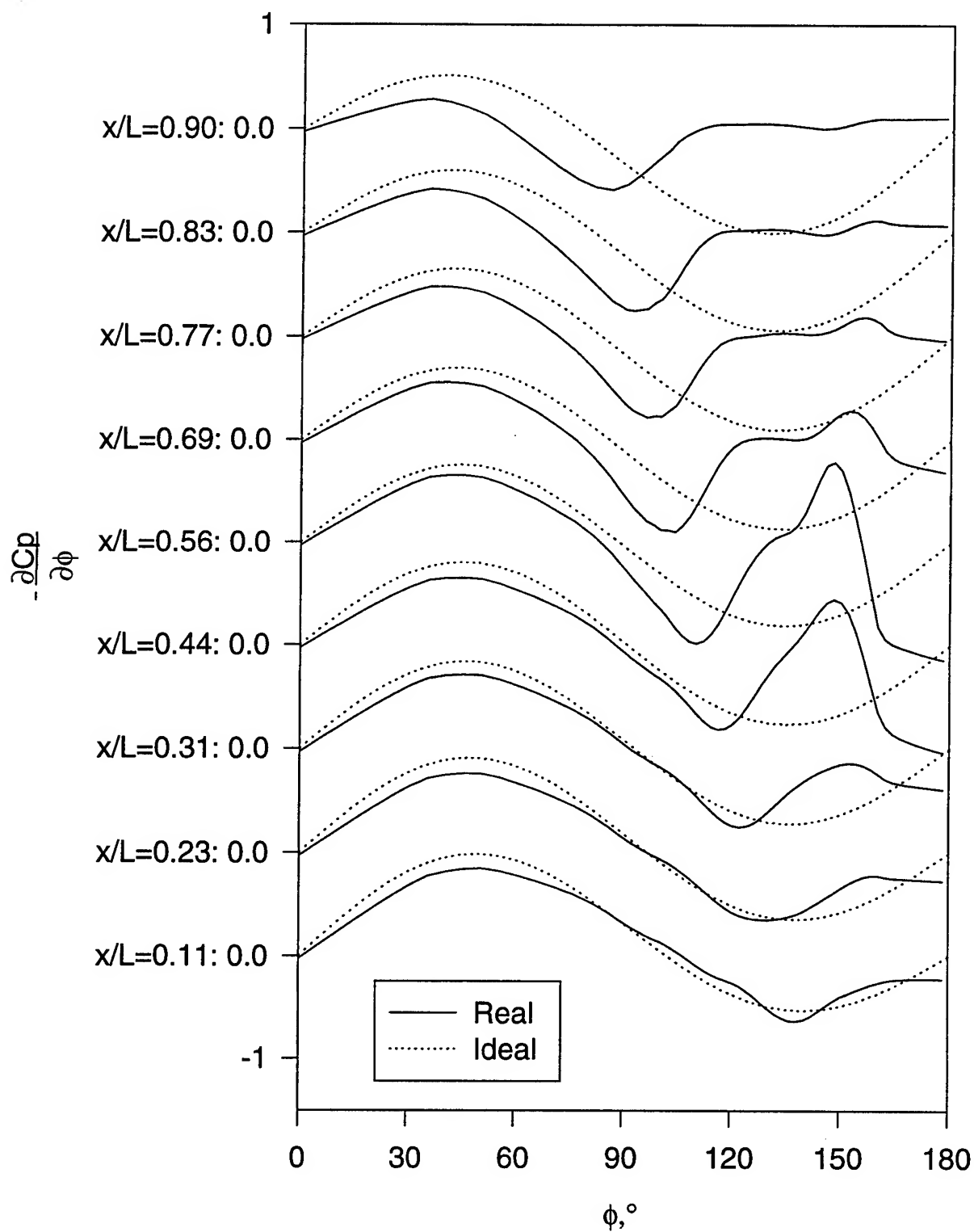


Figure 272. Steady  $\partial C_p / \partial \phi$  vs.  $\phi$  for all  $x/L$ ,  $\alpha = 27.8^\circ$ . "Real" refers to the measured data while "Ideal" refers to potential flow solution.

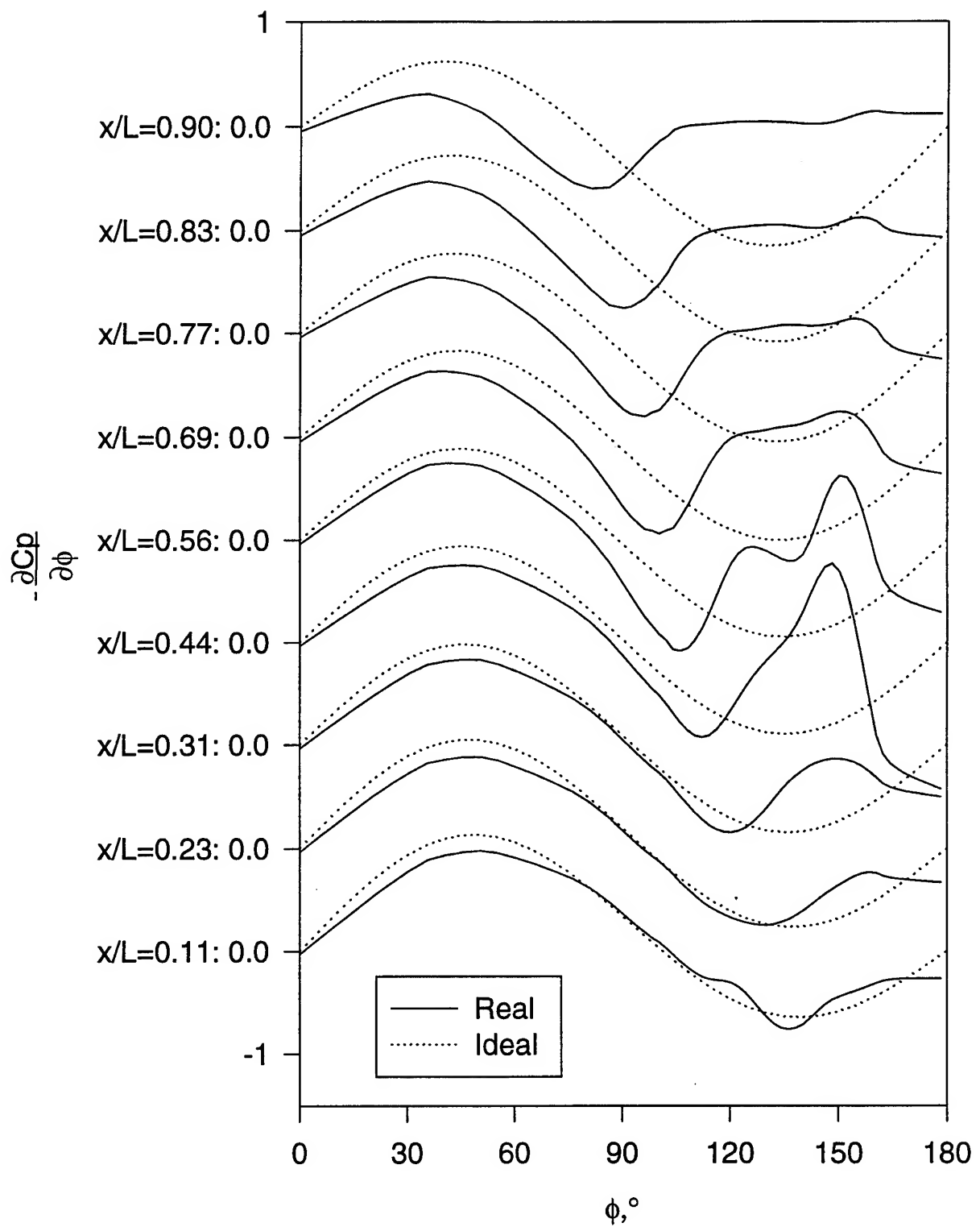


Figure 273. Steady  $\partial C_p / \partial \phi$  vs.  $\phi$  for all  $x/L$ ,  $\alpha = 30.0^\circ$ . "Real" refers to the measured data while "Ideal" refers to potential flow solution.

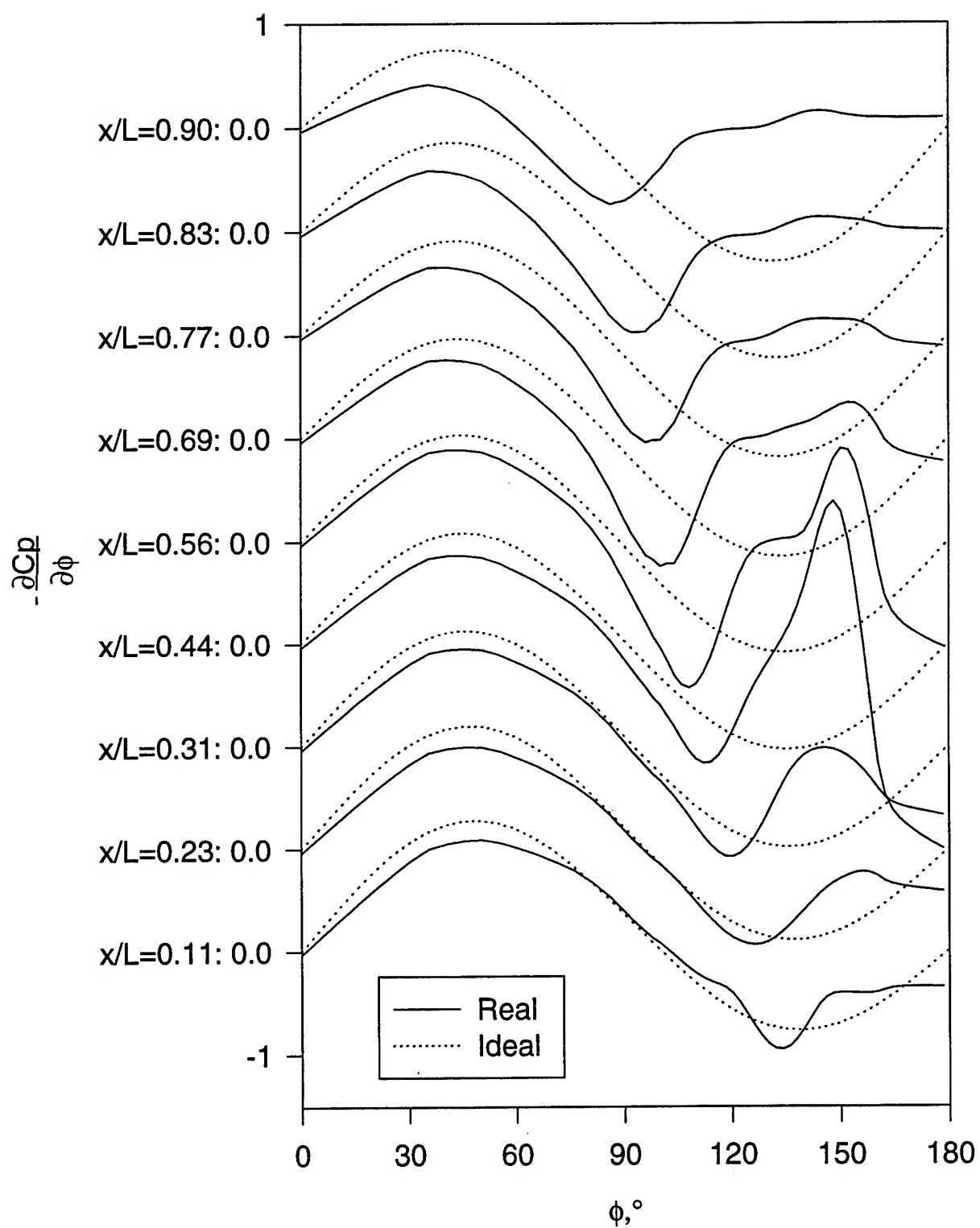


Figure 274. Steady  $\partial C_p / \partial \alpha$  vs.  $\phi$  for all  $x/L$ ,  $\alpha=32.5^\circ$ . "Real" refers to the measured data while "Ideal" refers to potential flow solution.

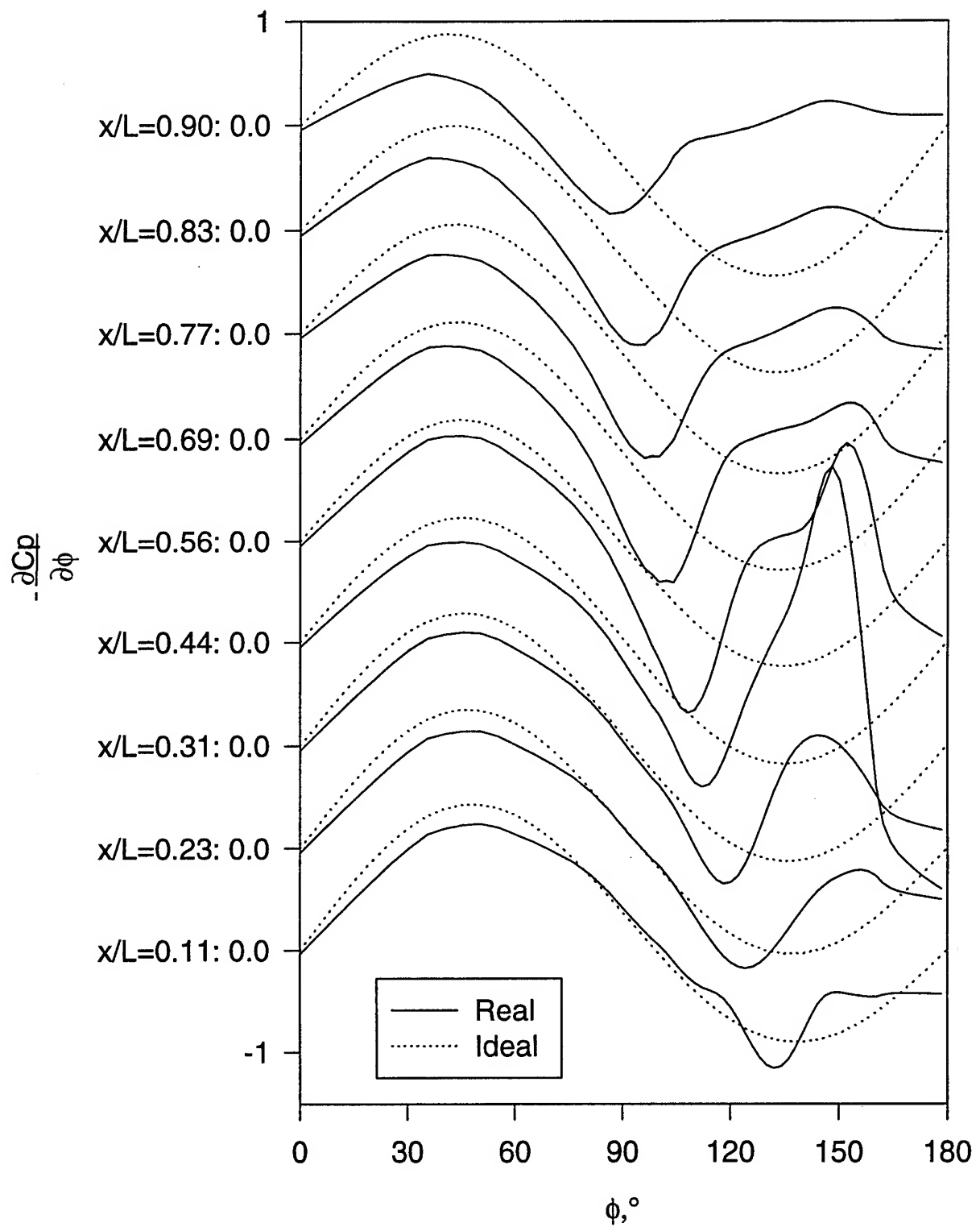


Figure 275. Steady  $\frac{\partial C_p}{\partial \alpha}$  vs.  $\phi$  for all  $x/L$ ,  $\alpha=35.0^\circ$ . "Real" refers to the measured data while "Ideal" refers to potential flow solution.

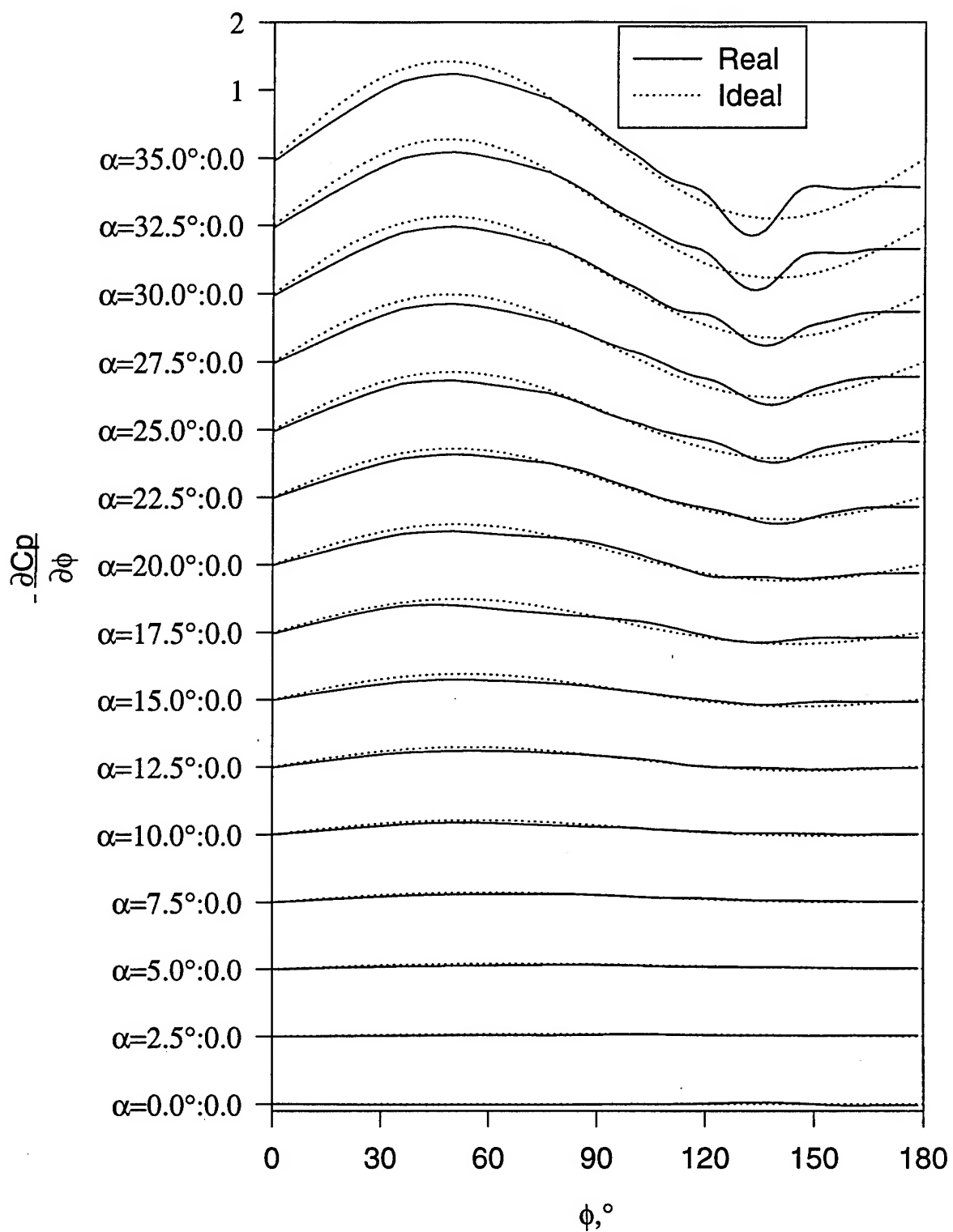


Figure 276. Steady  $\frac{\partial C_p}{\partial \alpha}$  vs.  $\alpha$  for all  $\alpha$ ,  $x/L=0.11$ . "Real" refers to the measured data while "Ideal" refers to potential flow solution.

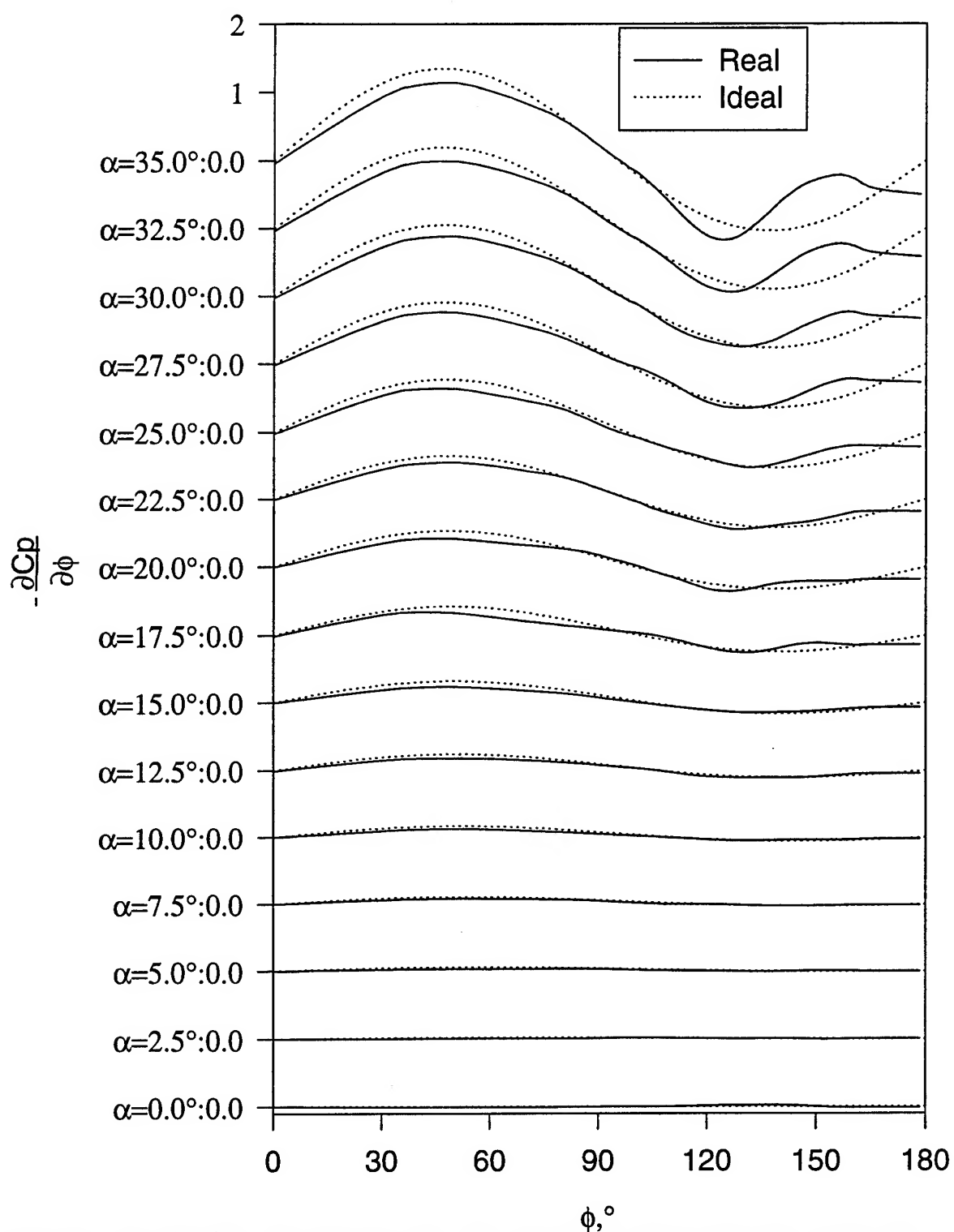


Figure 277. Steady  $\partial C_p / \partial \alpha$  vs.  $\alpha$  for all  $\alpha$ ,  $x/L=0.23$ . "Real" refers to the measured data while "Ideal" refers to potential flow solution.



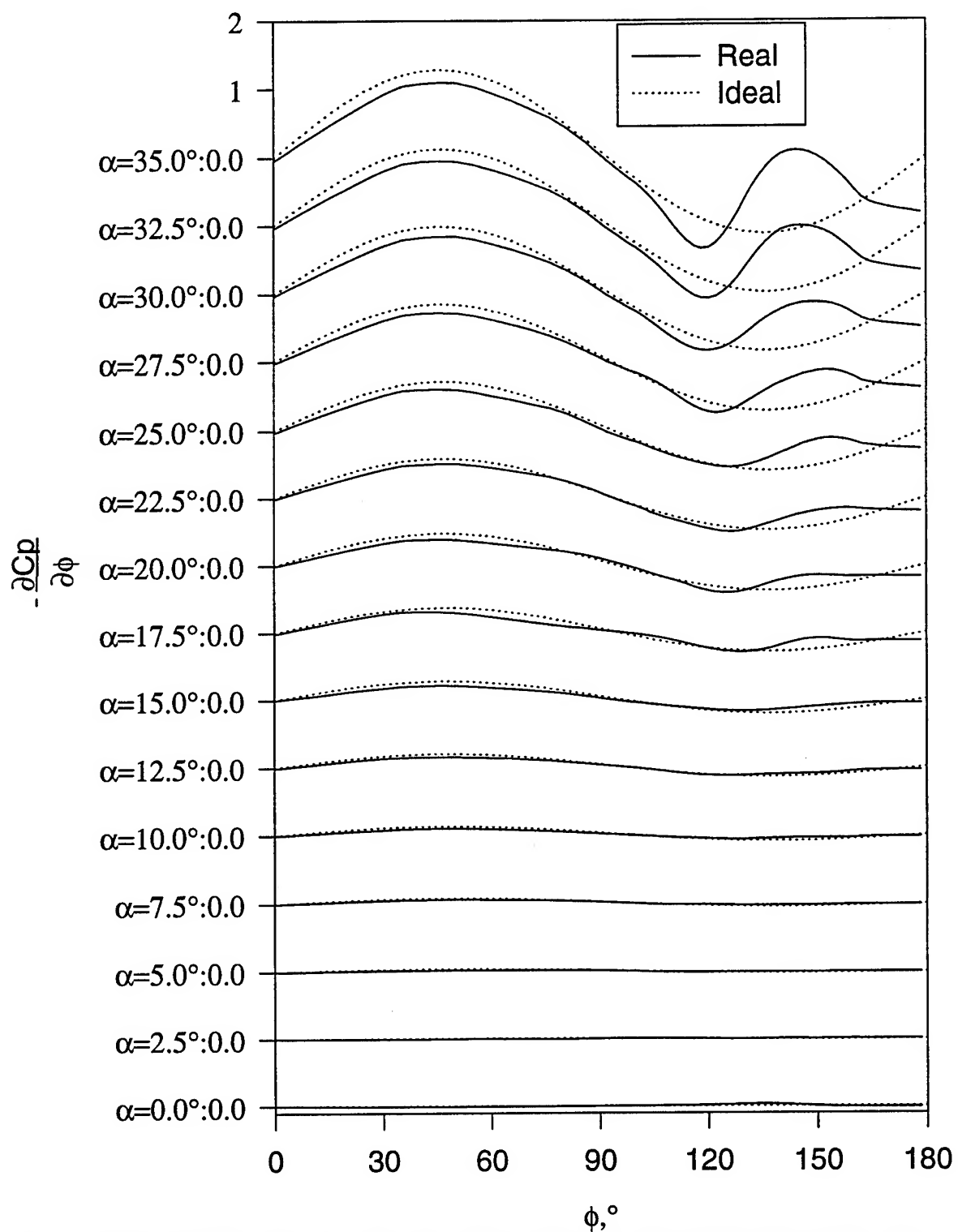


Figure 278. Steady  $\partial C_p / \partial \alpha$  vs.  $\alpha$  for all  $\alpha$ ,  $x/L=0.31$ . "Real" refers to the measured data while "Ideal" refers to potential flow solution.

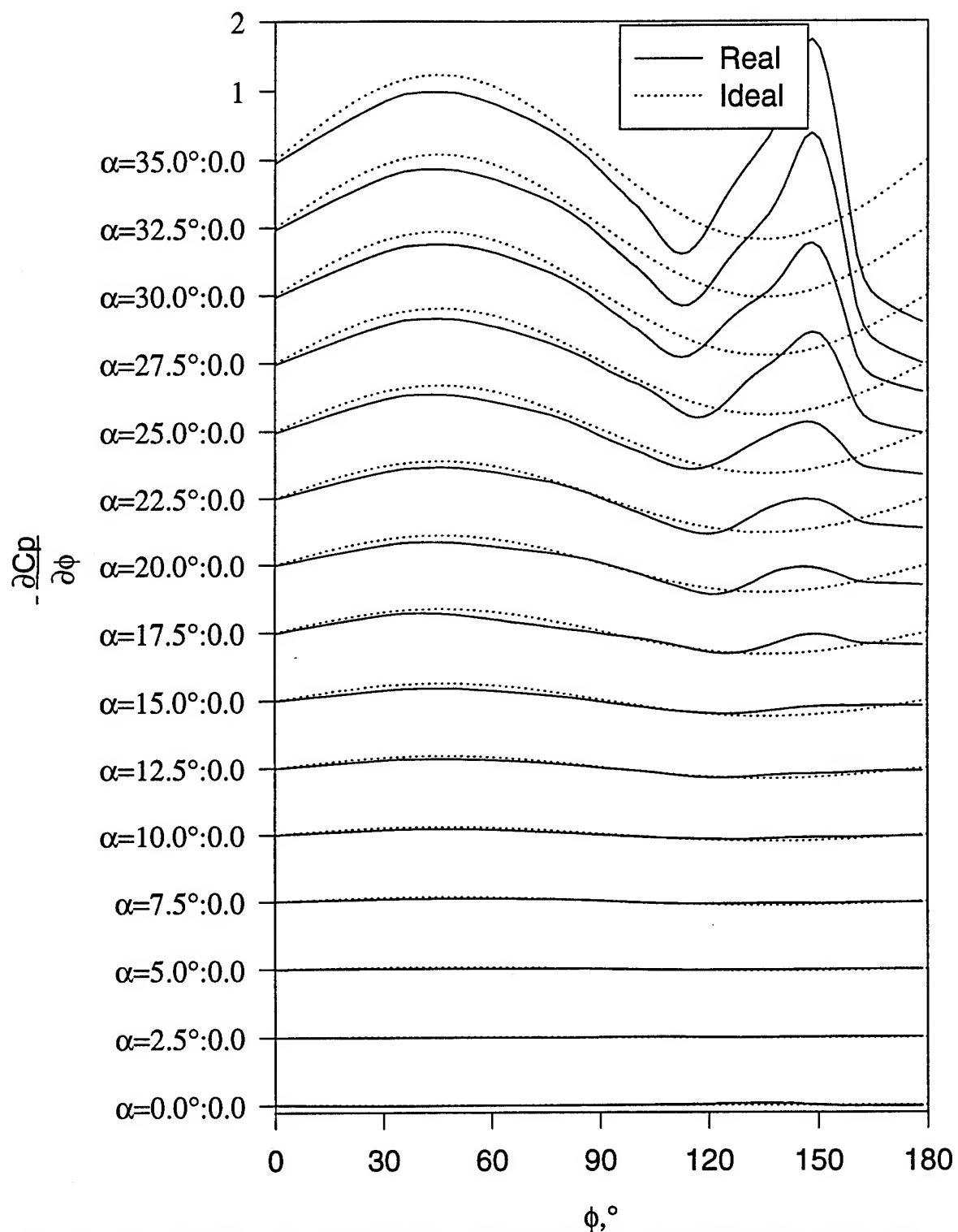


Figure 279. Steady  $\partial C_p / \partial \phi$  vs.  $\phi$  for all  $\alpha$ ,  $x/L=0.44$ . "Real" refers to the measured data while "Ideal" refers to potential flow solution.

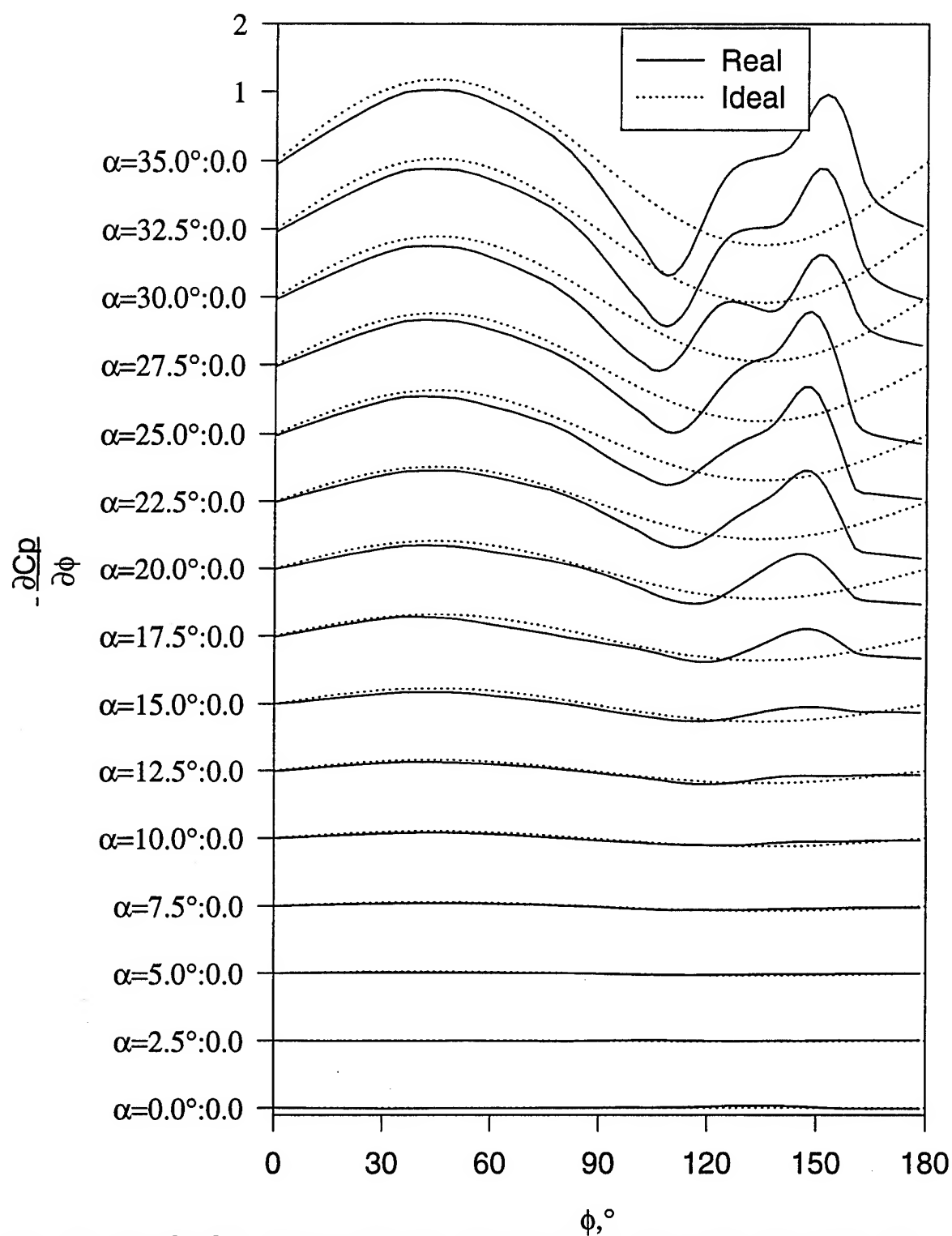


Figure 280. Steady  $\partial C_p / \partial \alpha$  vs.  $\alpha$  for all  $\alpha$ ,  $x/L=0.56$ . "Real" refers to the measured data while "Ideal" refers to potential flow solution.

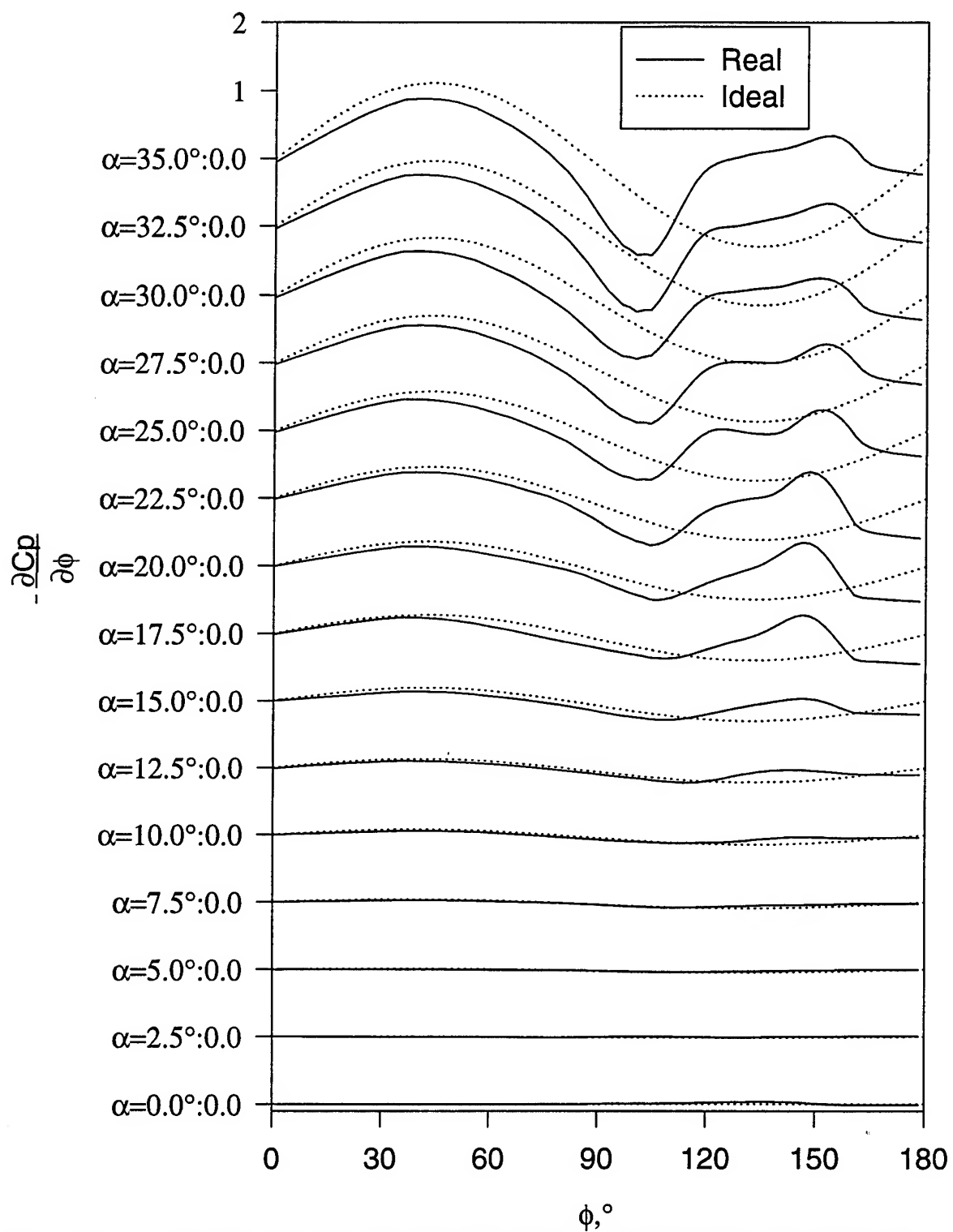


Figure 281. Steady  $\partial C_p / \partial \alpha$  vs.  $\alpha$  for all  $\alpha$ ,  $x/L=0.69$ . "Real" refers to the measured data while "Ideal" refers to potential flow solution.

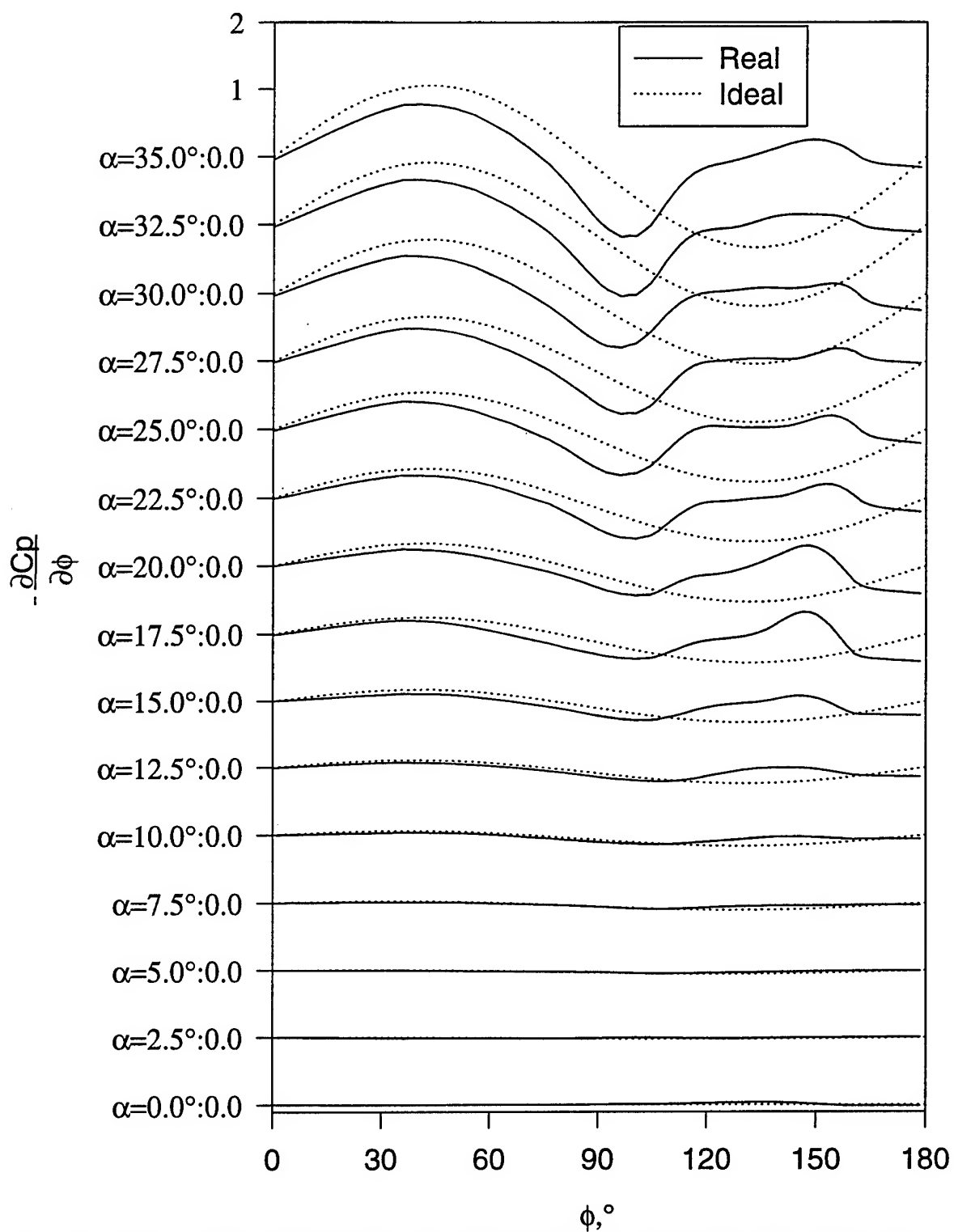


Figure 282. Steady  $\partial C_p / \partial \alpha$  vs.  $\phi$  for all  $\alpha$ ,  $x/L=0.77$ . "Real" refers to the measured data while "Ideal" refers to potential flow solution.

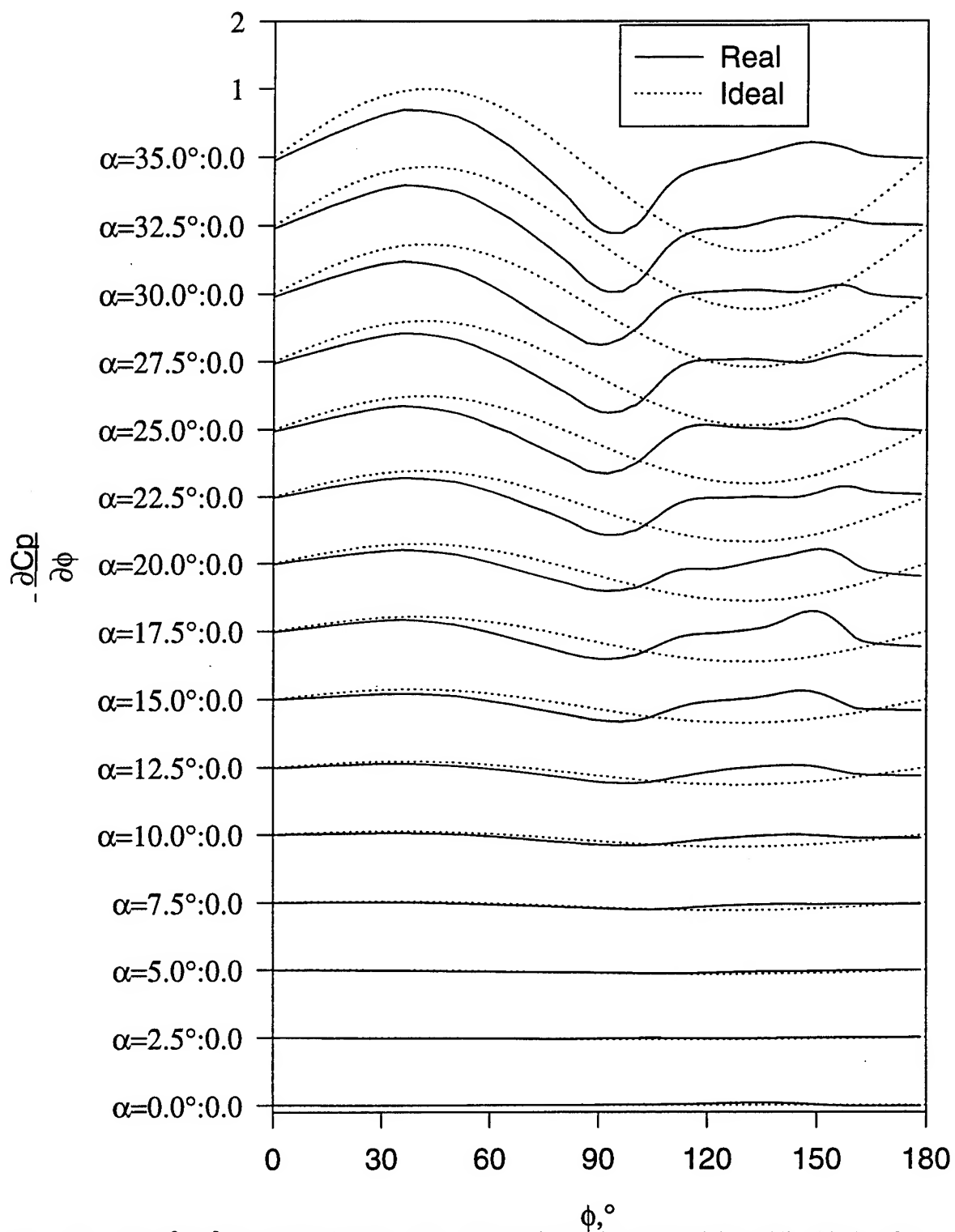


Figure 283. Steady  $\partial C_p / \partial \alpha$  vs.  $\alpha$  for all  $\alpha$ ,  $x/L=0.83$ . "Real" refers to the measured data while "Ideal" refers to potential flow solution.

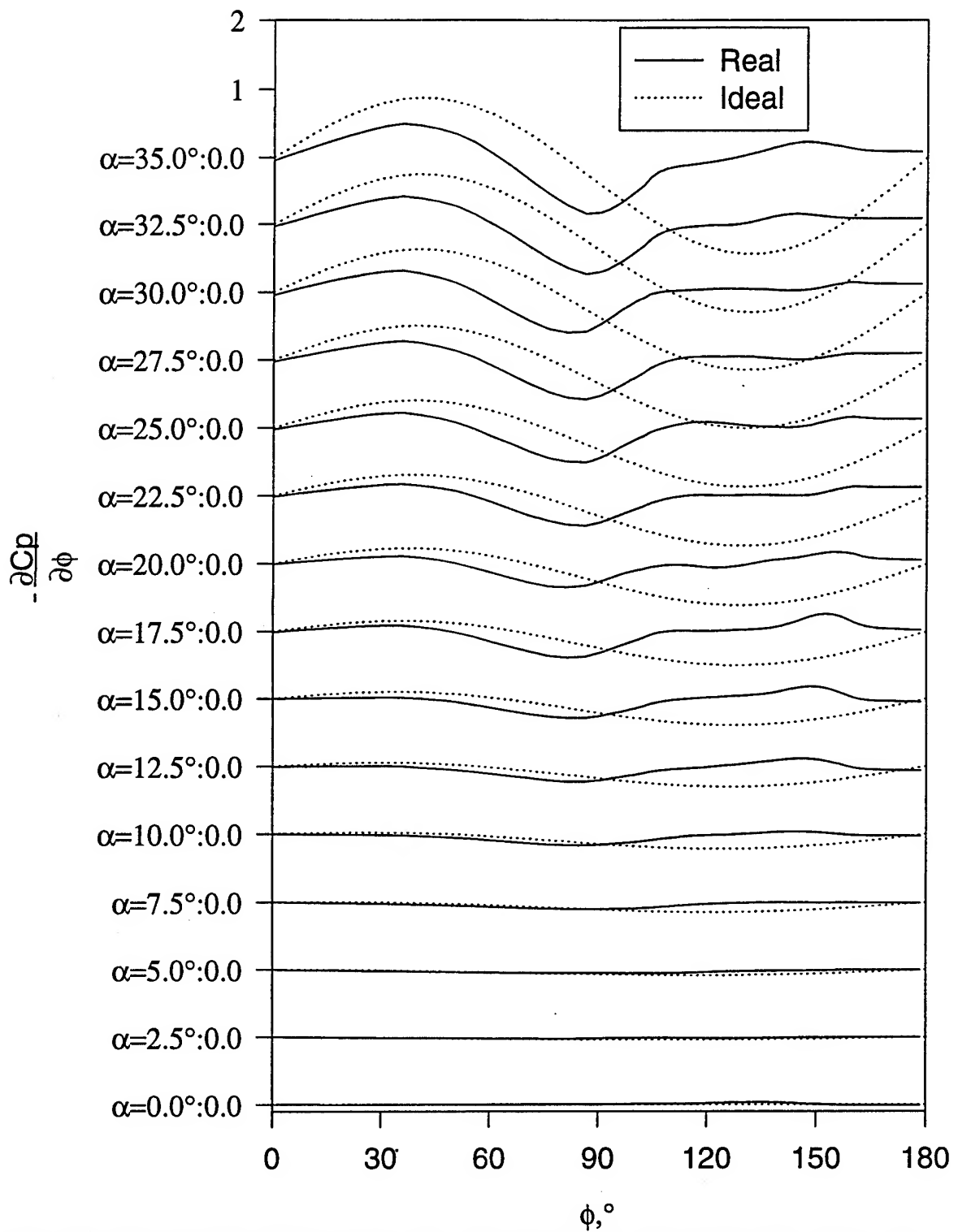


Figure 284. Steady  $\partial C_p / \partial \alpha$  vs.  $\alpha$  for all  $\alpha$ ,  $x/L=0.90$ . "Real" refers to the measured data while "Ideal" refers to potential flow solution.

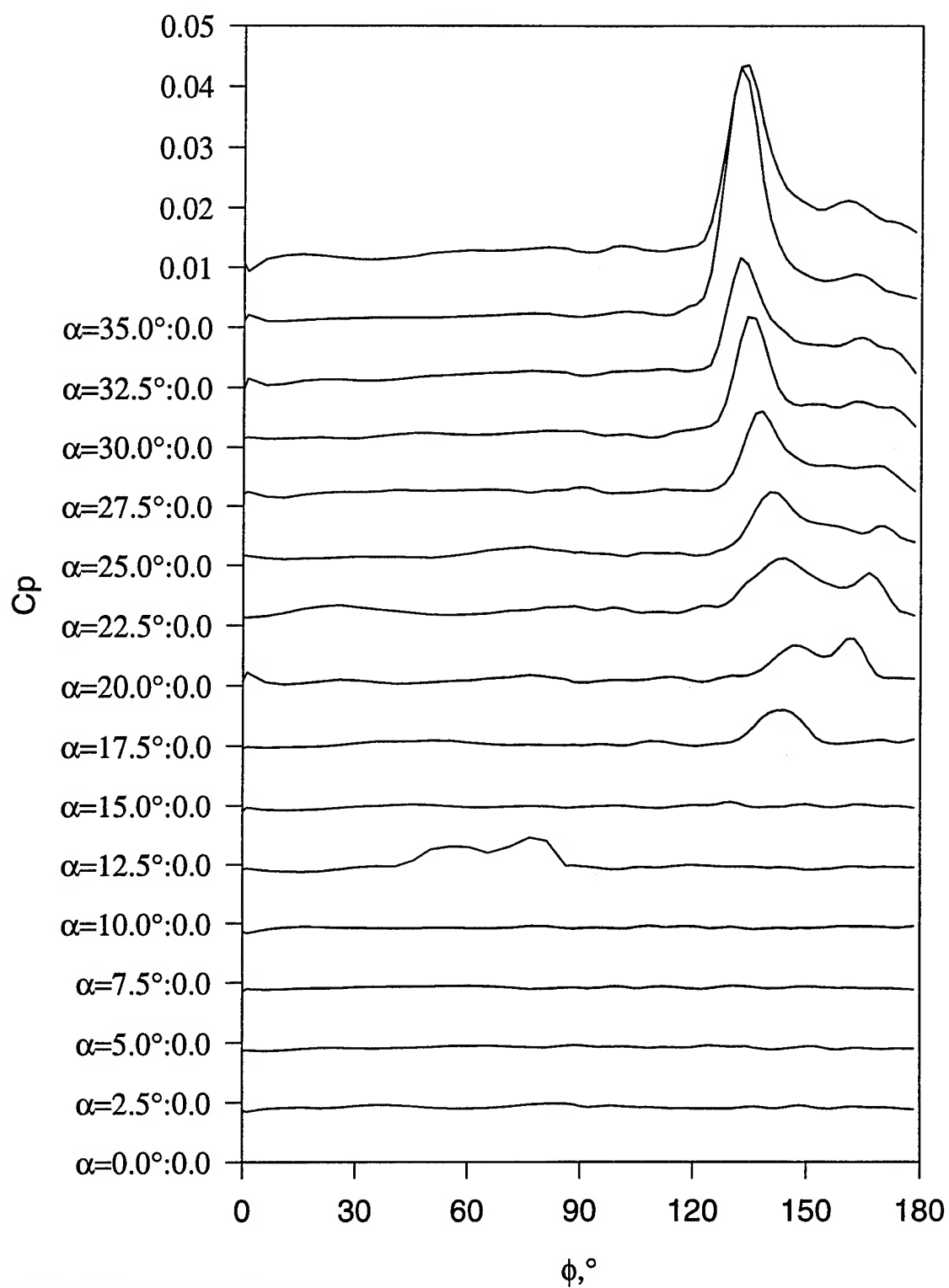


Figure 285. Steady  $C_{p_{RMS}}$  vs.  $\phi$  for all  $\alpha$ ,  $x/L=0.11$ .



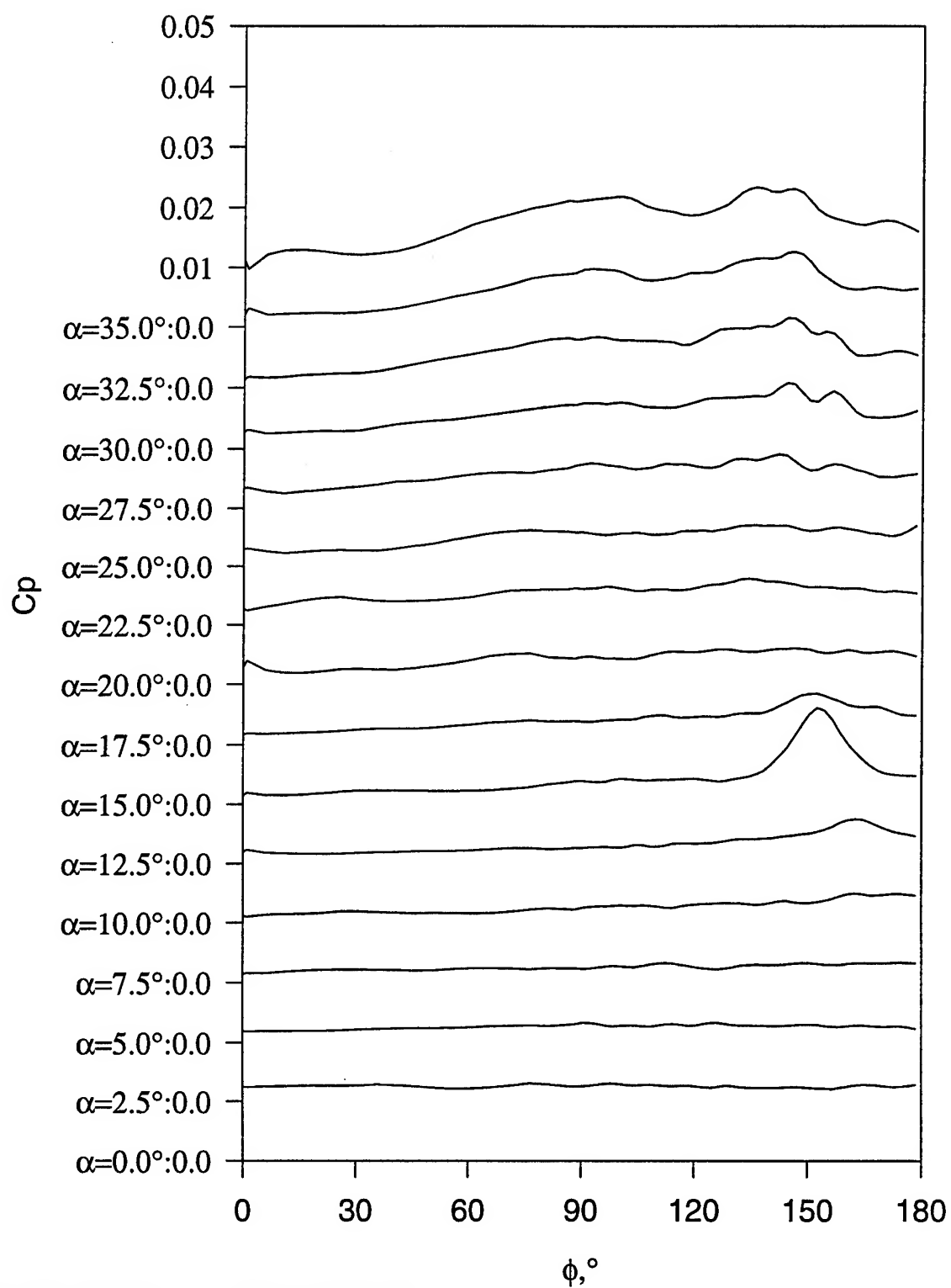


Figure 286. Steady  $C_{p_{RMS}}$  vs.  $\phi$  for all  $\alpha$ ,  $x/L=0.23$ .

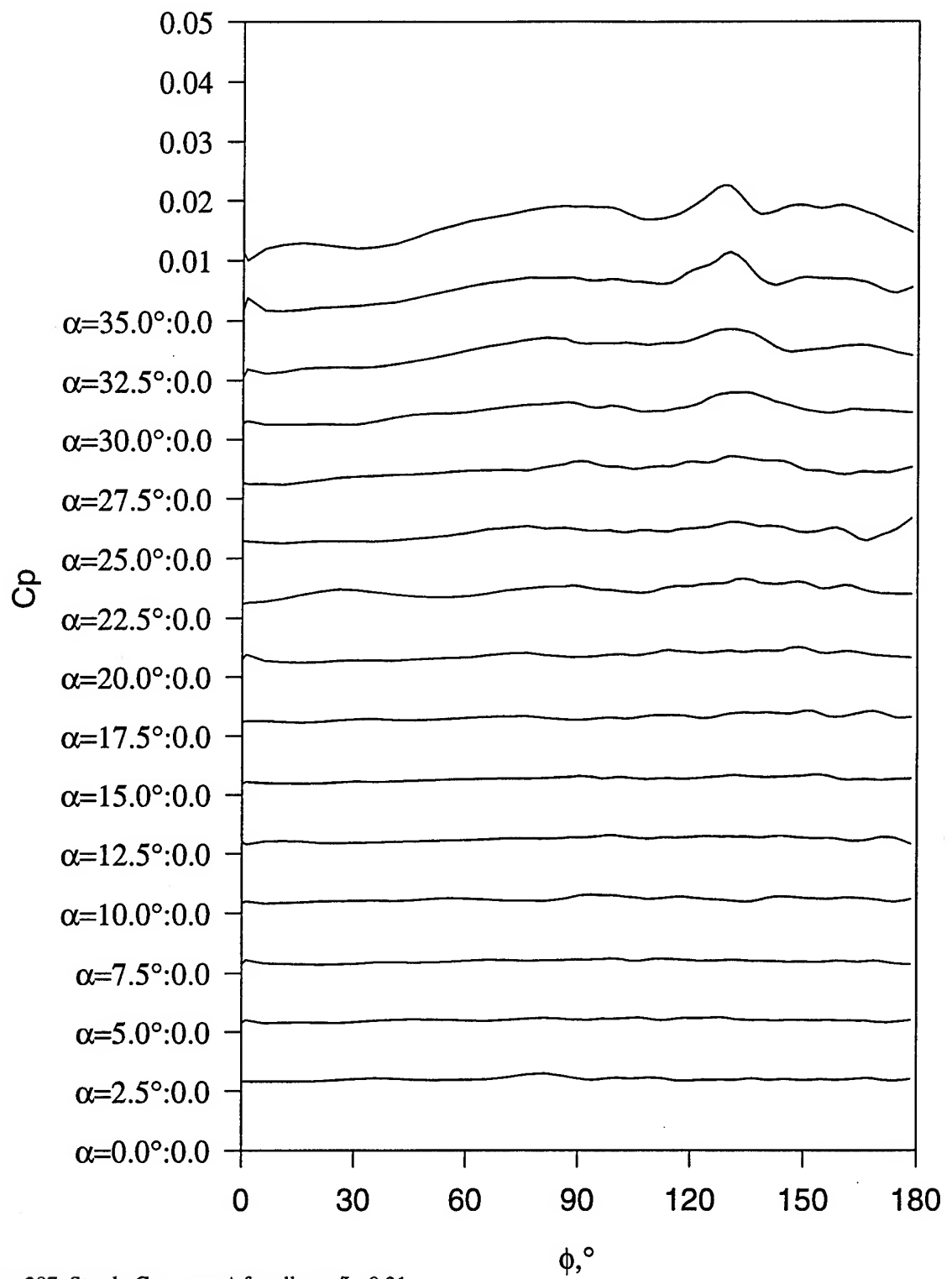


Figure 287. Steady  $C_{p_{RMS}}$  vs.  $\phi$  for all  $\alpha$ ,  $x/L=0.31$ .

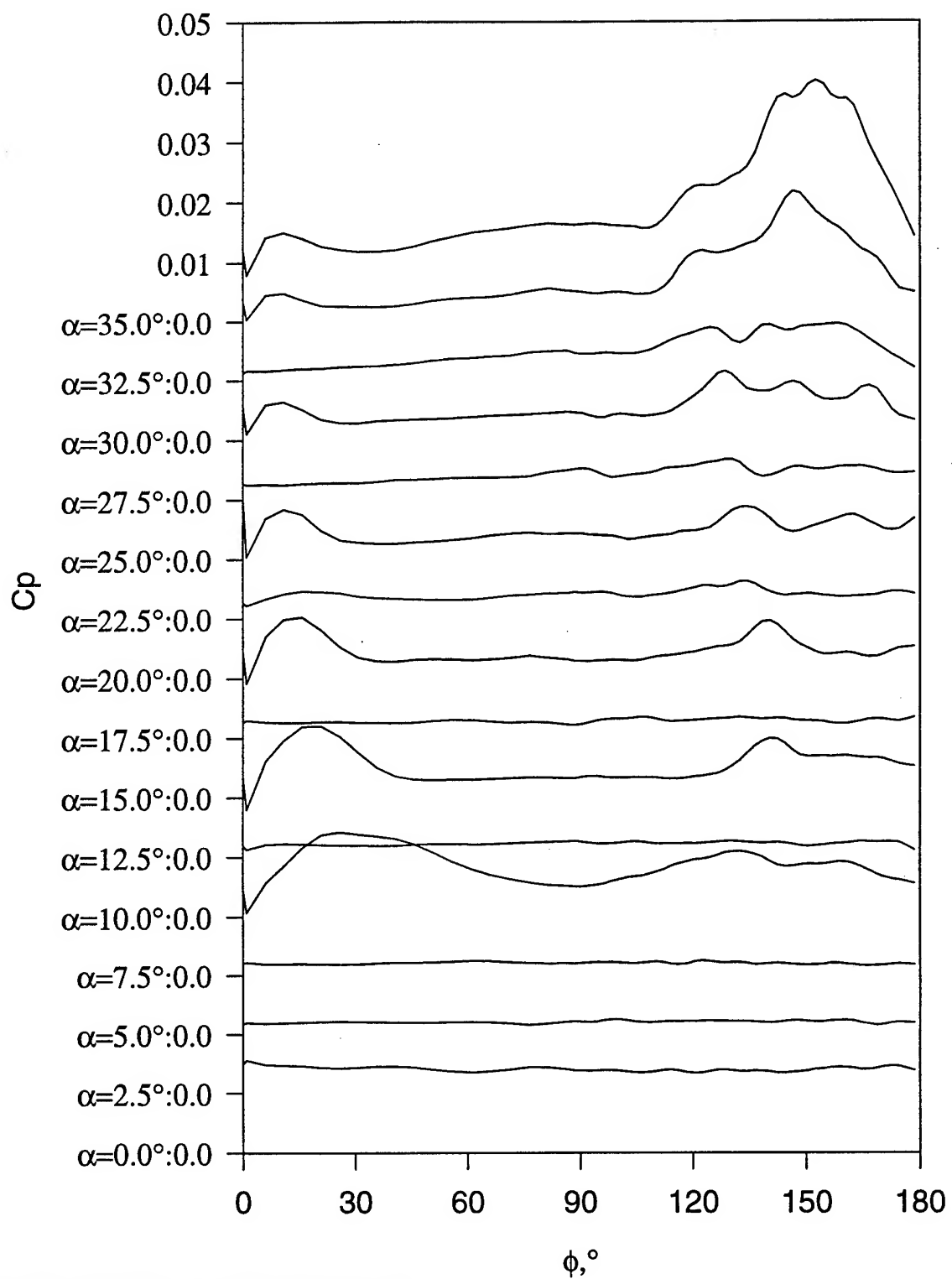


Figure 288. Steady  $C_{p_{RMS}}$  vs.  $\phi$  for all  $\alpha$ ,  $x/L=0.44$ .

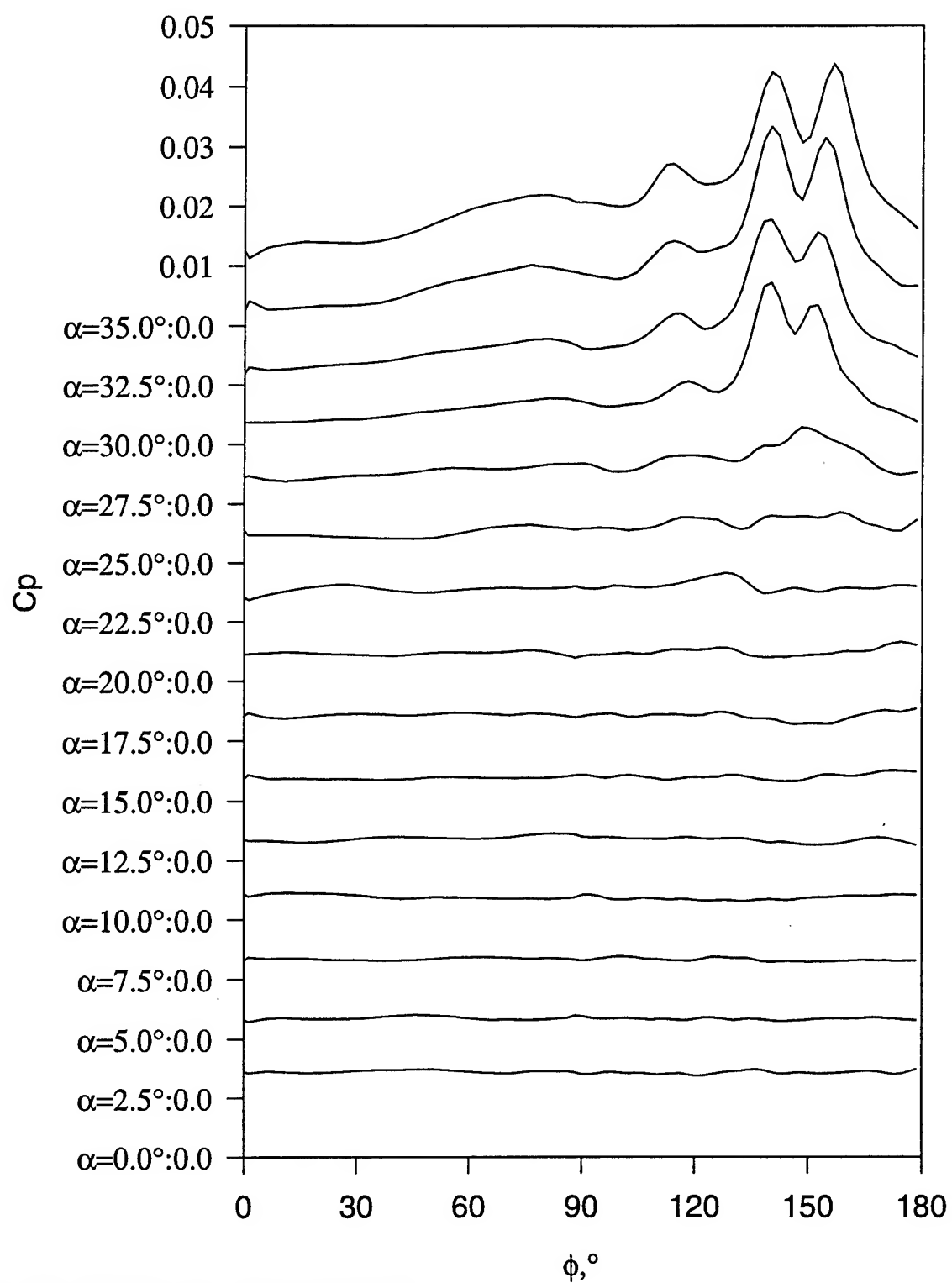


Figure 289. Steady  $C_{p_{RMS}}$  vs.  $\phi$  for all  $\alpha$ ,  $x/L=0.56$ .

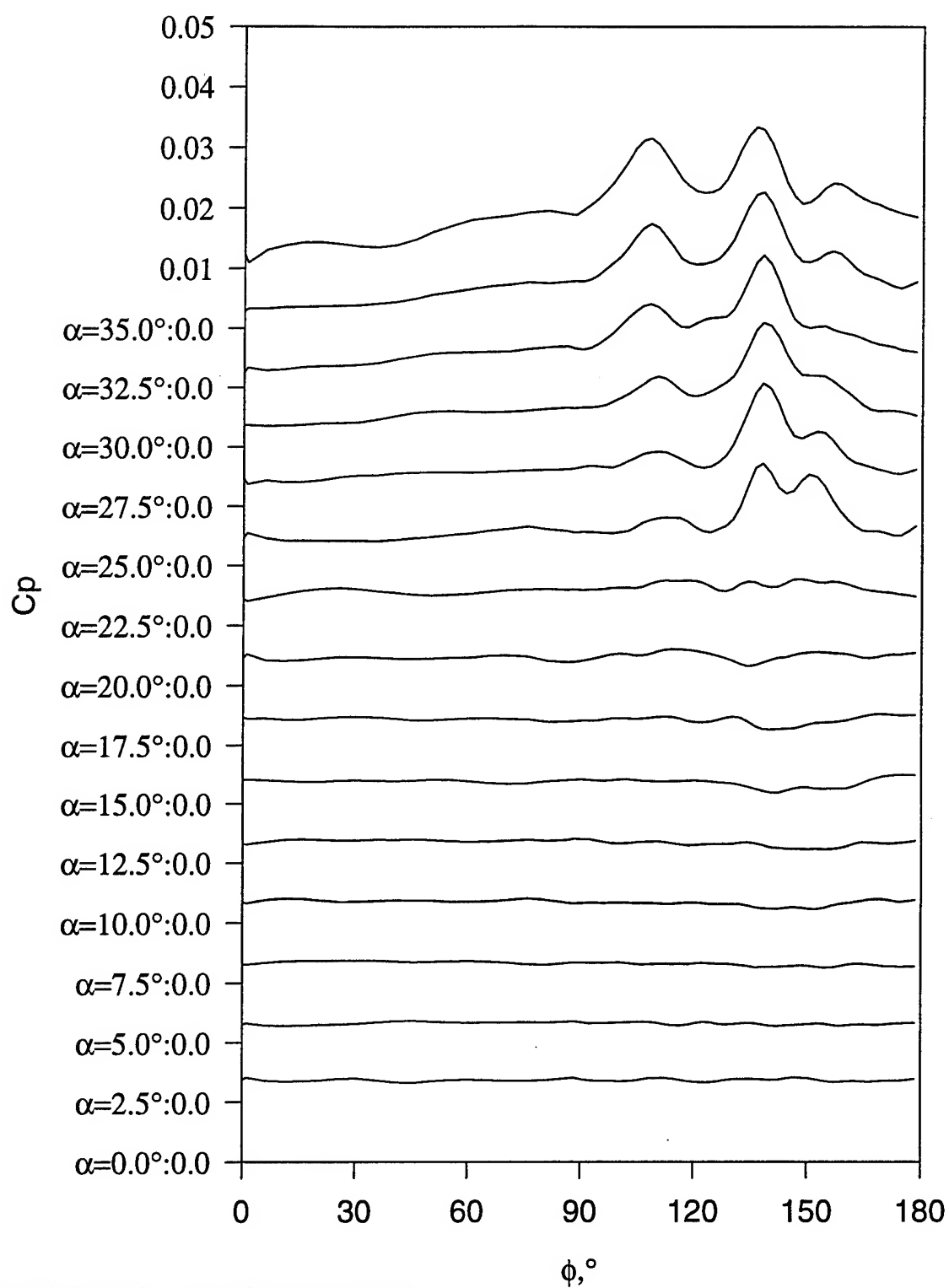


Figure 290. Steady  $C_{p_{RMS}}$  vs.  $\phi$  for all  $\alpha$ ,  $x/L=0.69$ .

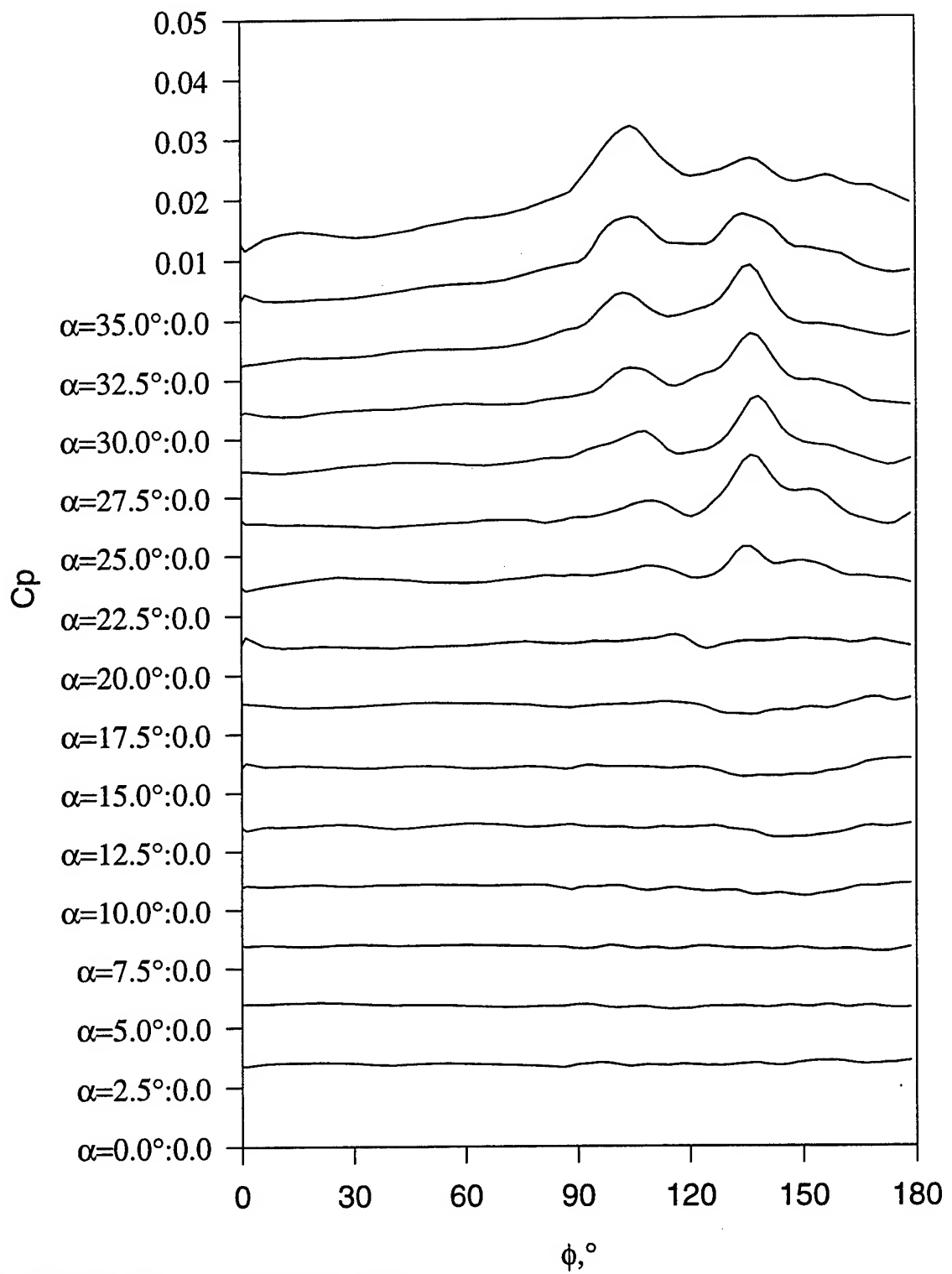


Figure 291. Steady  $C_{p_{RMS}}$  vs.  $\phi$  for all  $\alpha$ ,  $x/L=0.77$ .

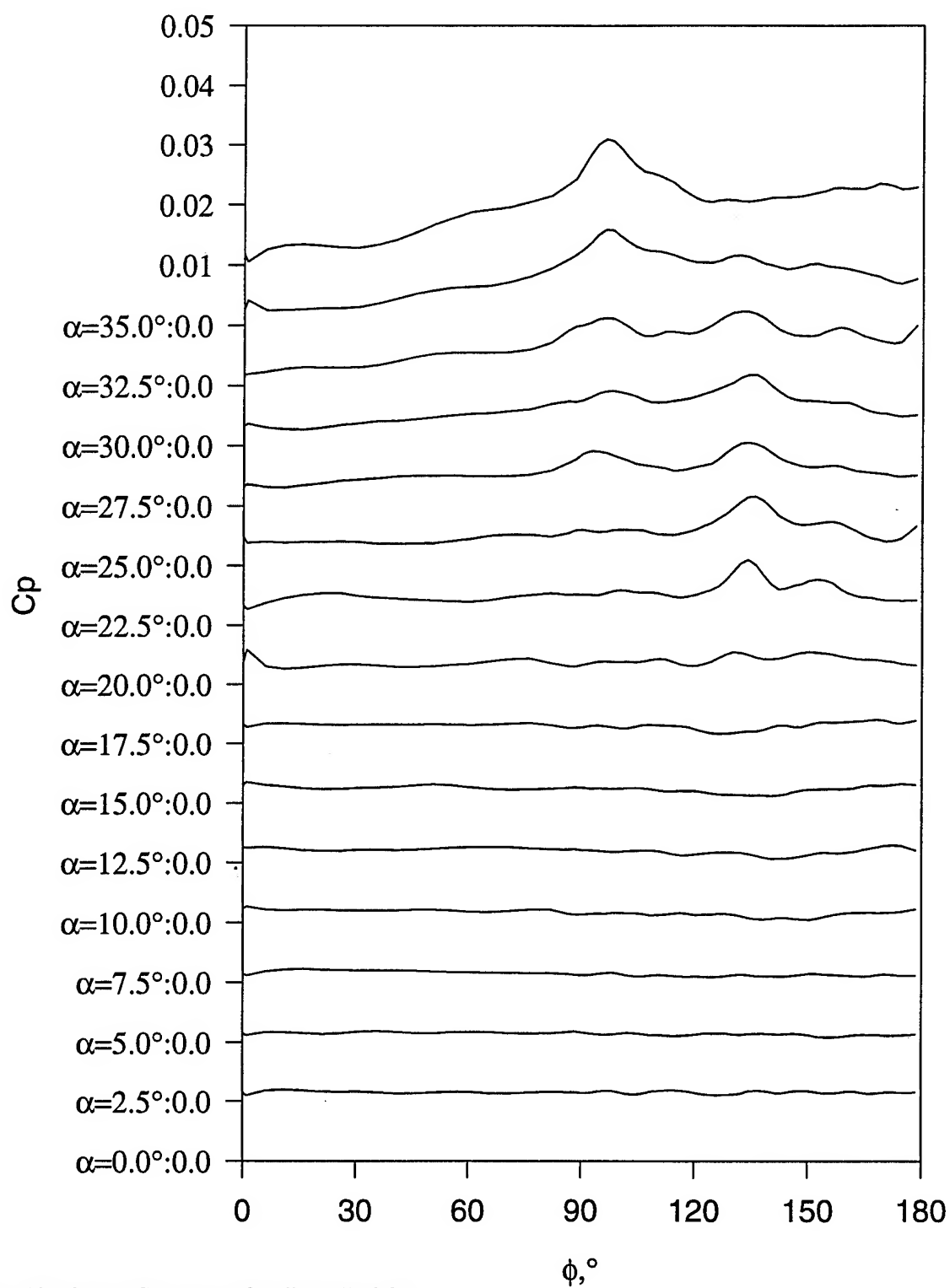


Figure 292. Steady  $C_{p_{RMS}}$  vs.  $\phi$  for all  $\alpha$ ,  $x/L=0.83$ .

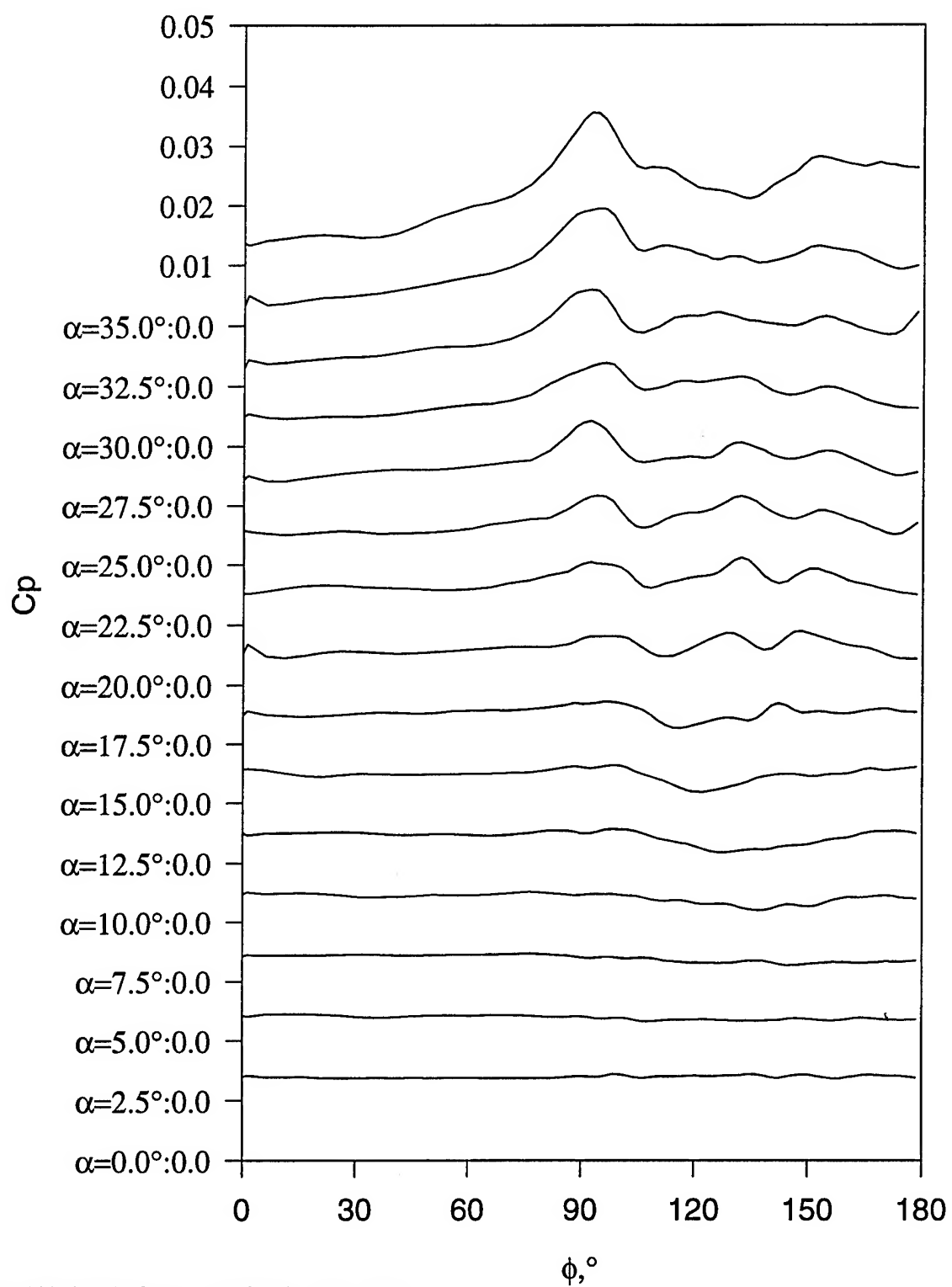


Figure 293. Steady  $C_{p_{RMS}}$  vs.  $\phi$  for all  $\alpha$ ,  $x/L=0.90$ .



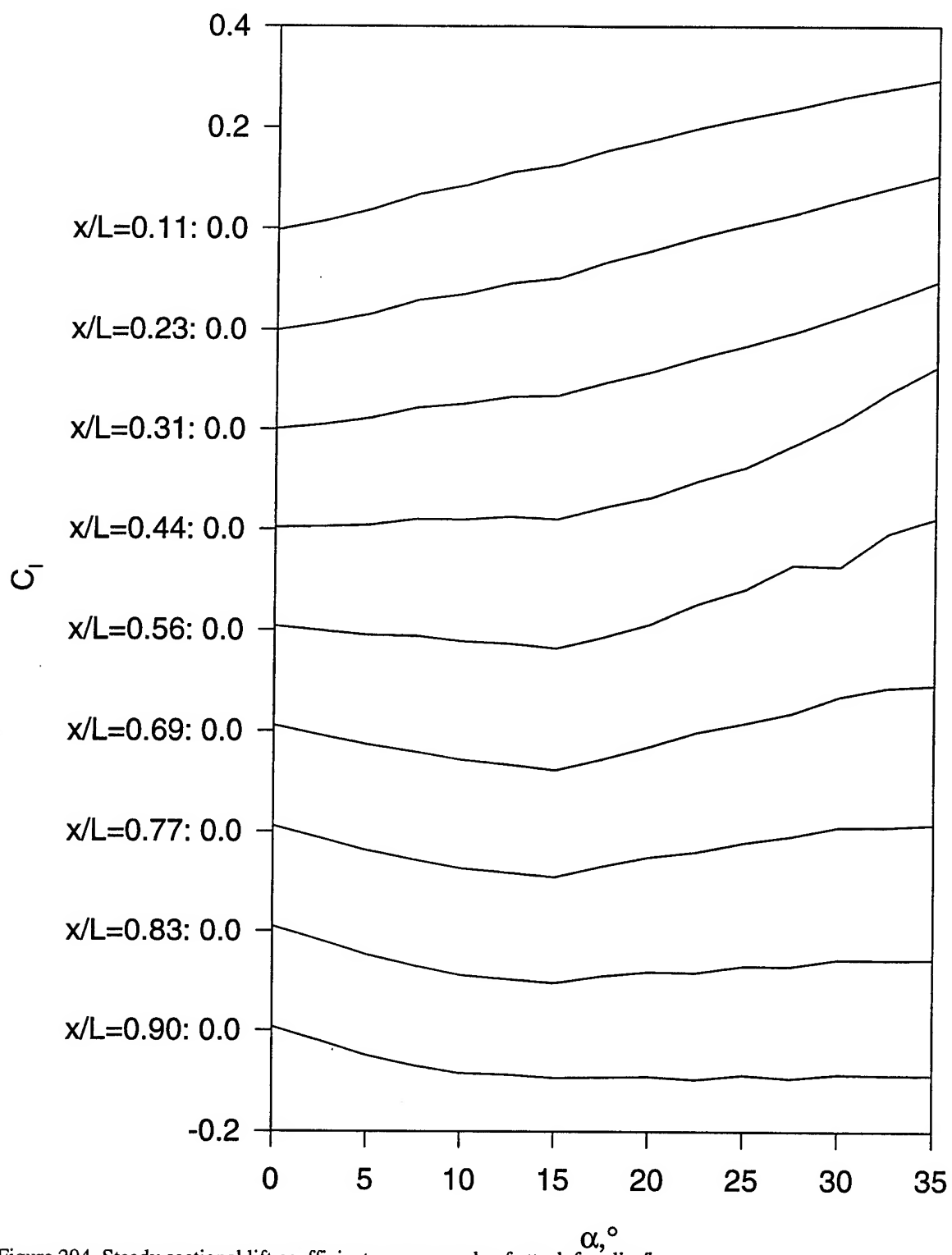


Figure 294. Steady sectional lift coefficients versus angle of attack for all  $x/l$ .

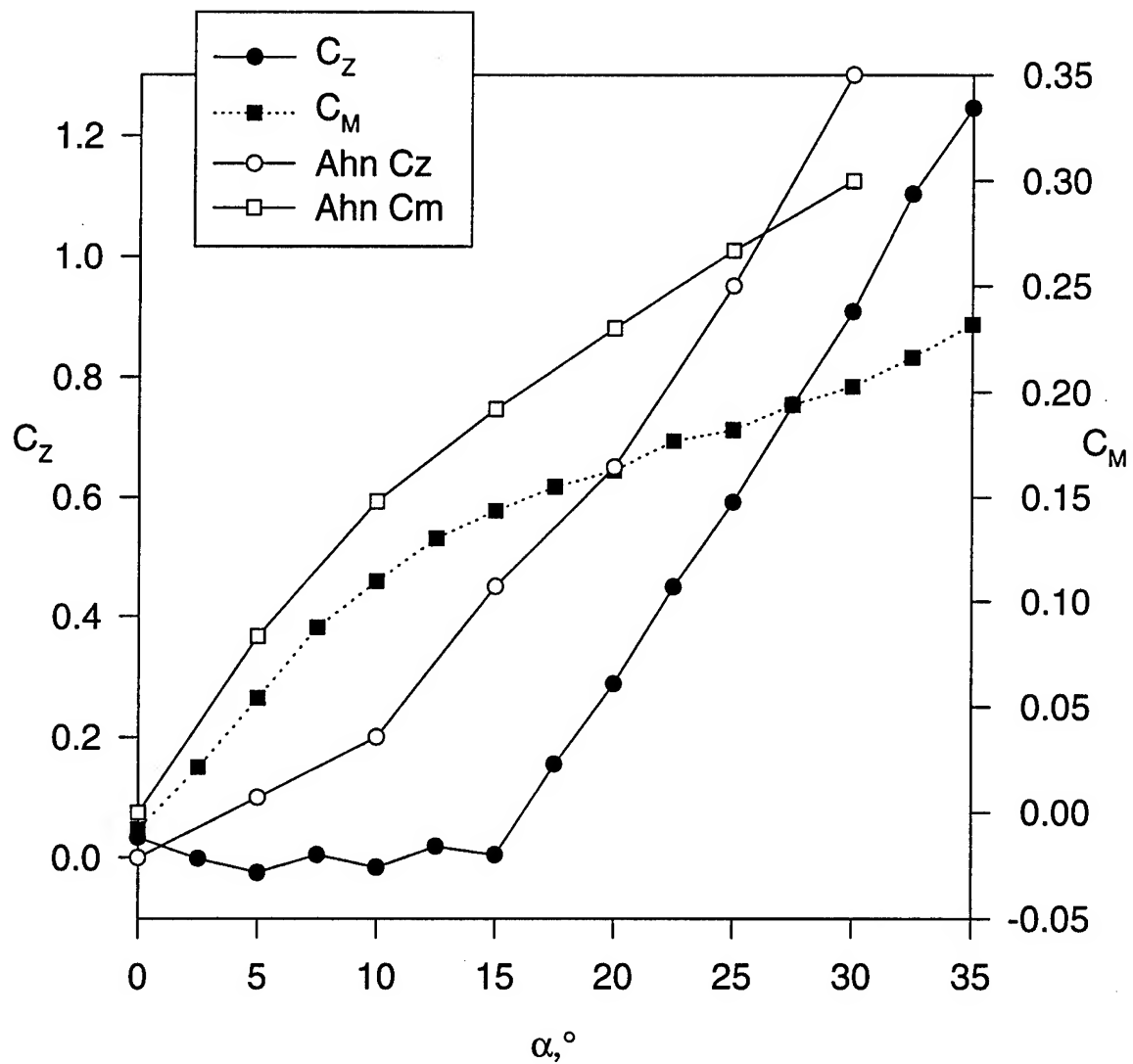


Figure 295. Steady normal force coefficient and pitch moment versus angle of attack computed from surface pressure data.

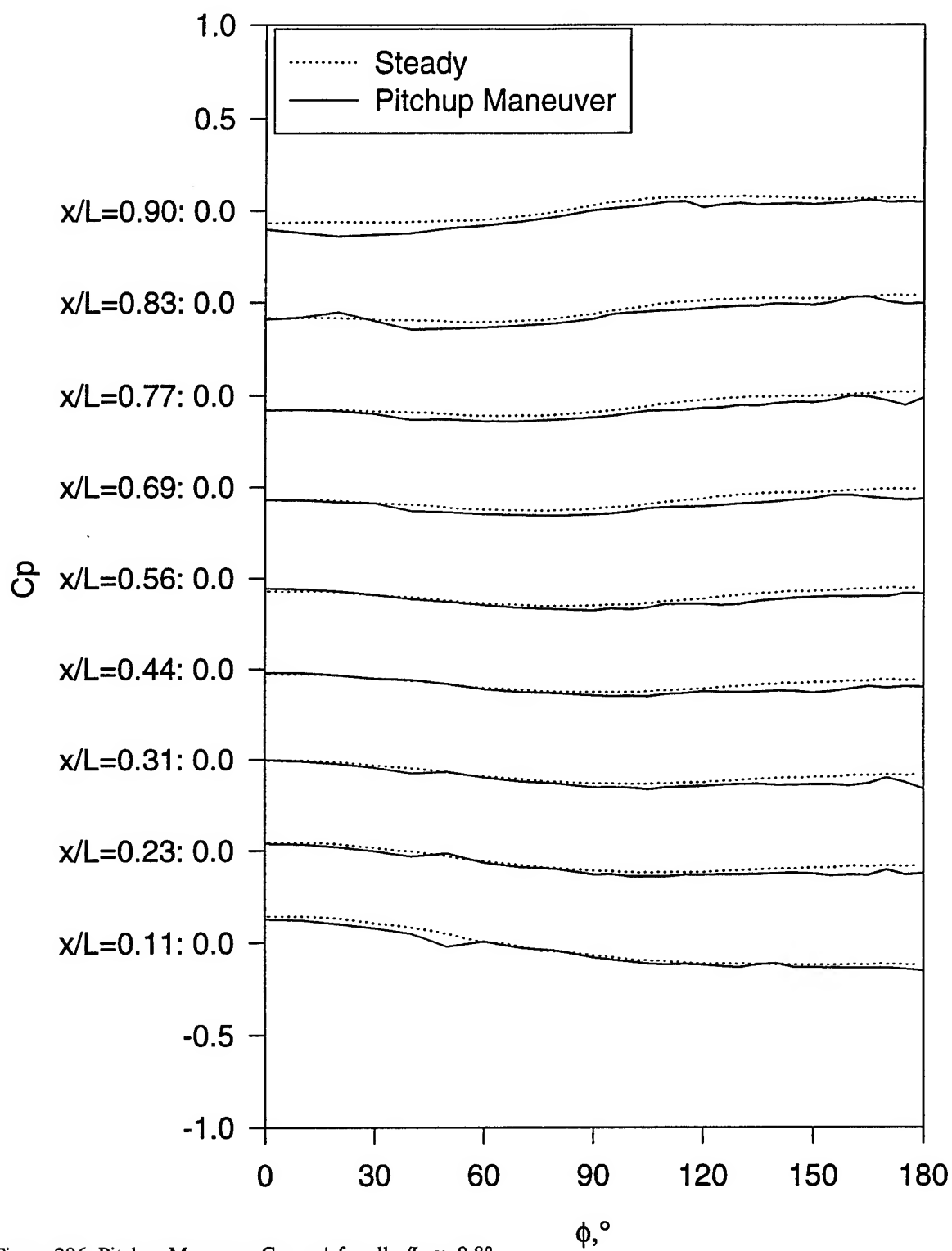


Figure 296. Pitchup Maneuver  $C_p$  vs.  $\phi$  for all  $x/L$ ,  $\alpha=9.8^\circ$ .

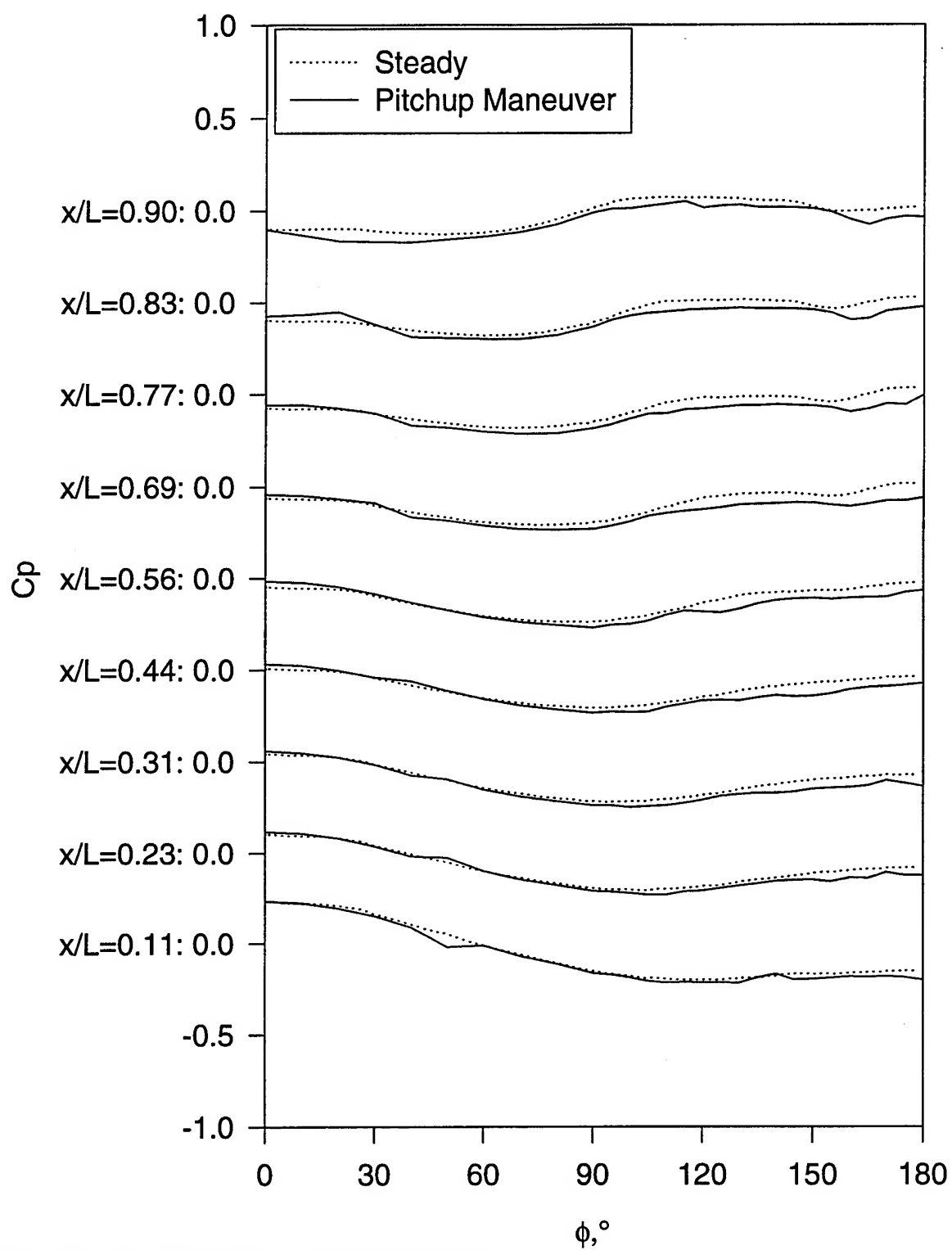


Figure 297. Pitchup Maneuver  $C_p$  vs.  $\phi$  for all  $x/L$ ,  $\alpha=14.9^\circ$ .

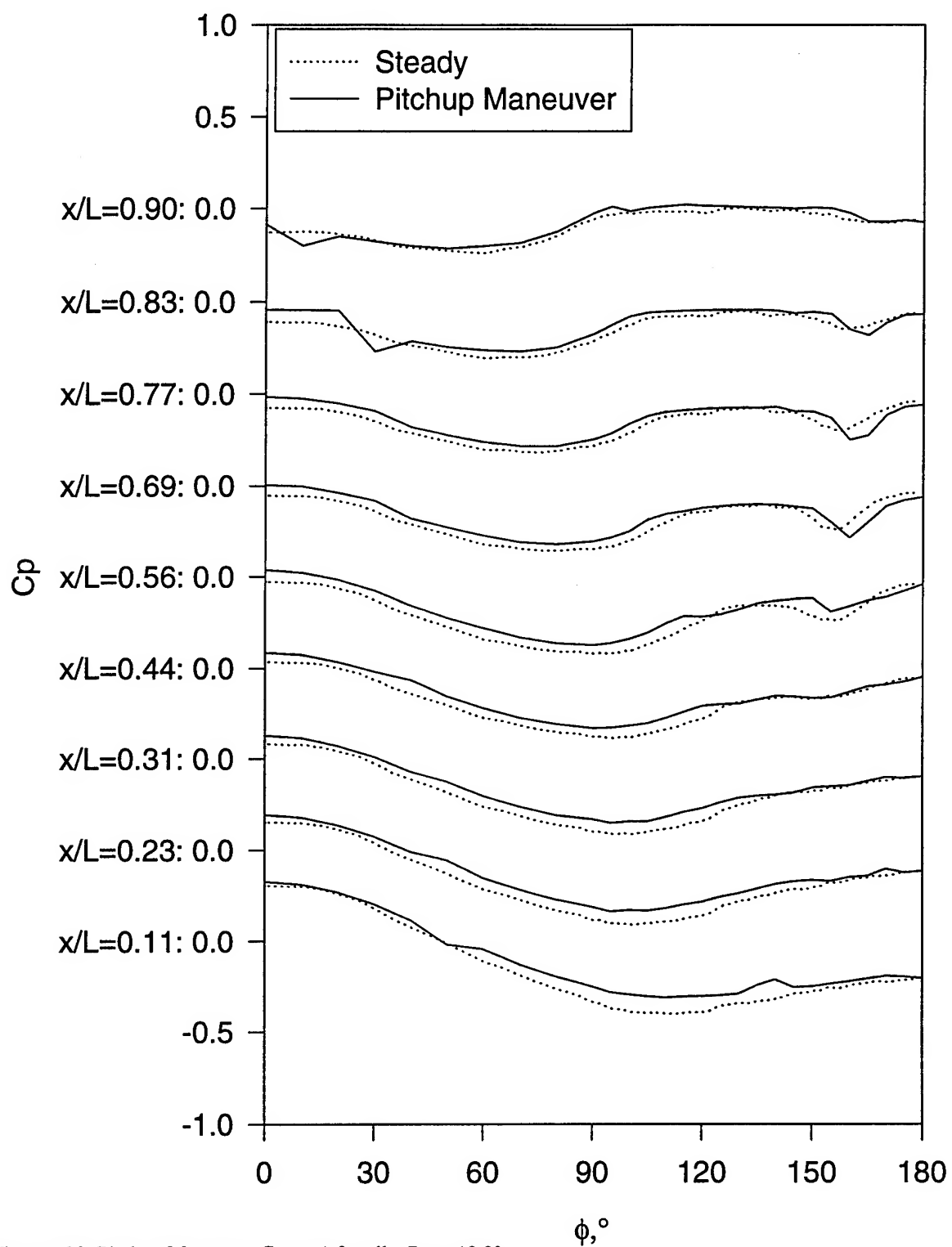


Figure 298. Pitchup Maneuver  $C_p$  vs.  $\phi$  for all  $x/L$ ,  $\alpha=19.9^\circ$ .

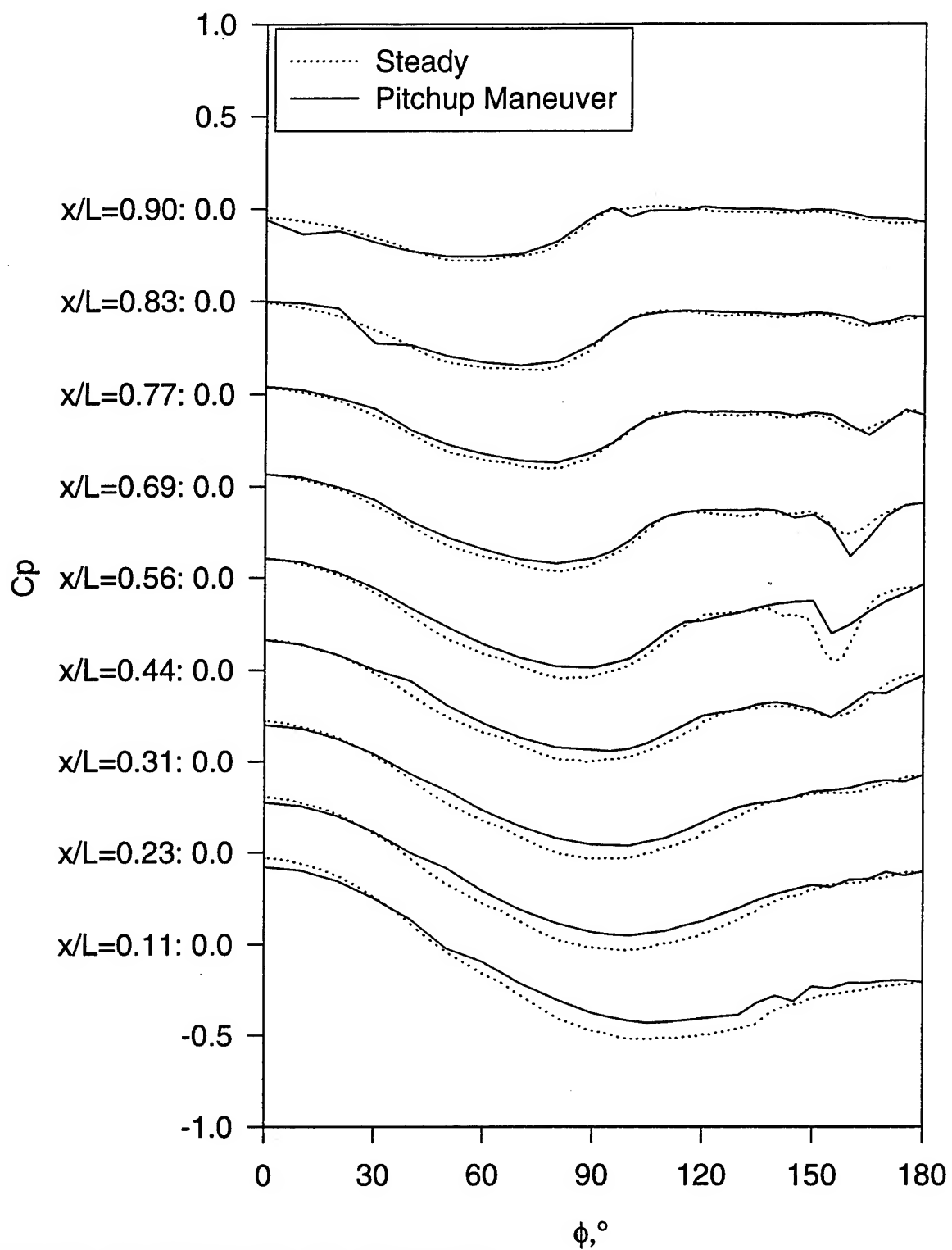


Figure 299. Pitchup Maneuver  $C_p$  vs.  $\phi$  for all  $x/L$ ,  $\alpha=24.9^\circ$ .

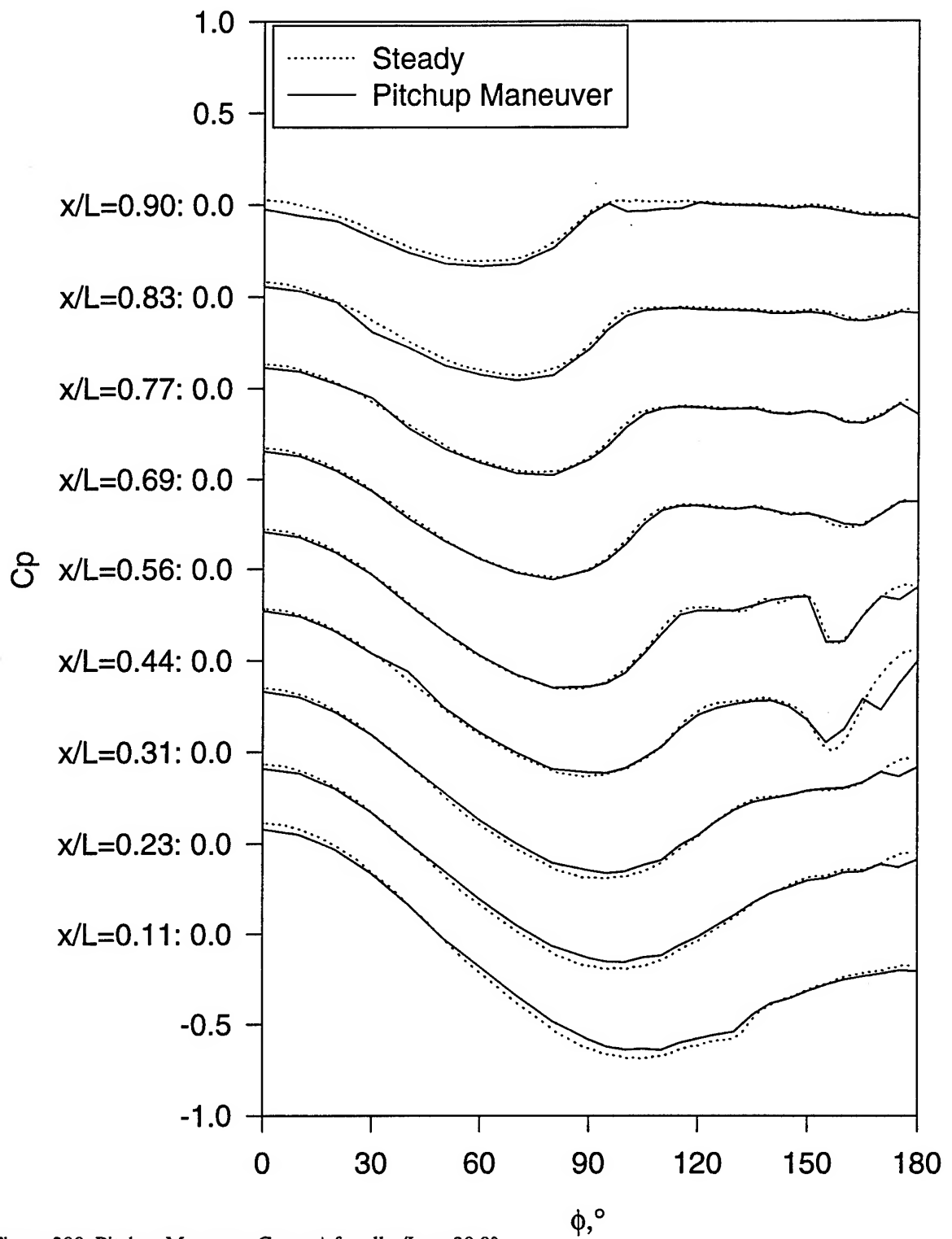


Figure 300. Pitchup Maneuver  $C_p$  vs.  $\phi$  for all  $x/L$ ,  $\alpha=30.0^\circ$ .

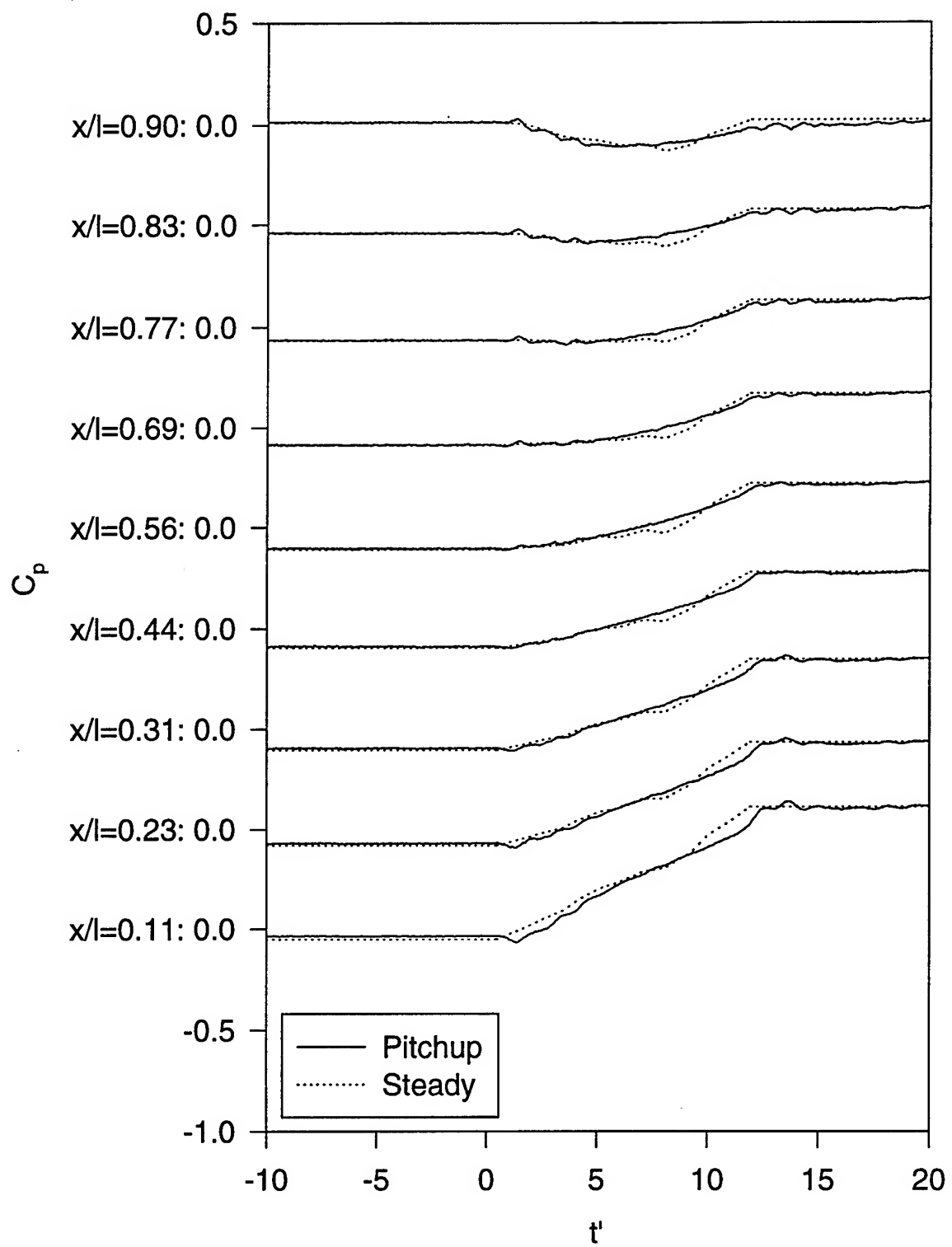


Figure 301. Pitchup Maneuver  $C_p$  vs. time for all  $x/L$ ,  $\phi=0^\circ$ .



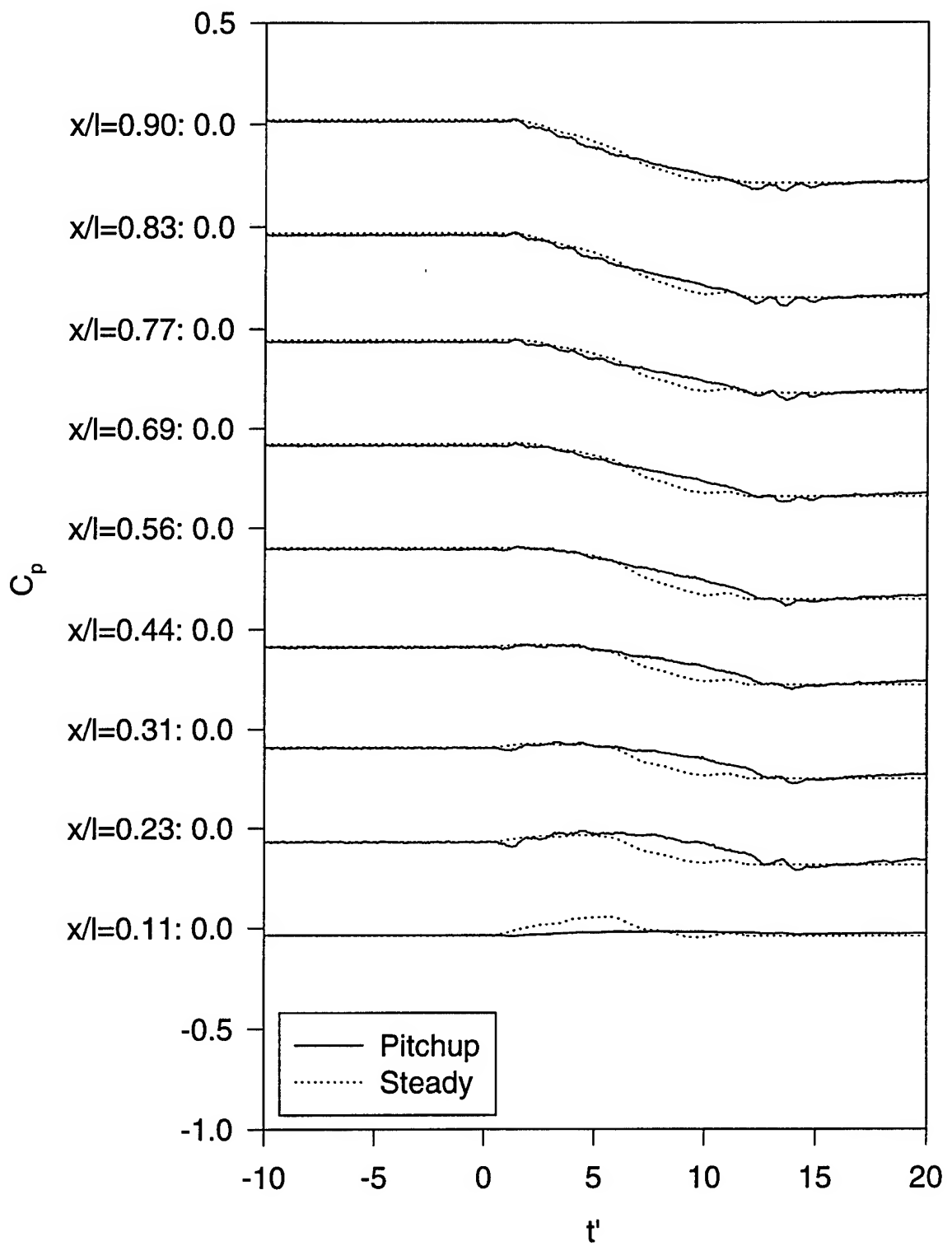


Figure 302. Pitchup Maneuver  $C_p$  vs. time for all  $x/L$ ,  $\phi=50^\circ$ .

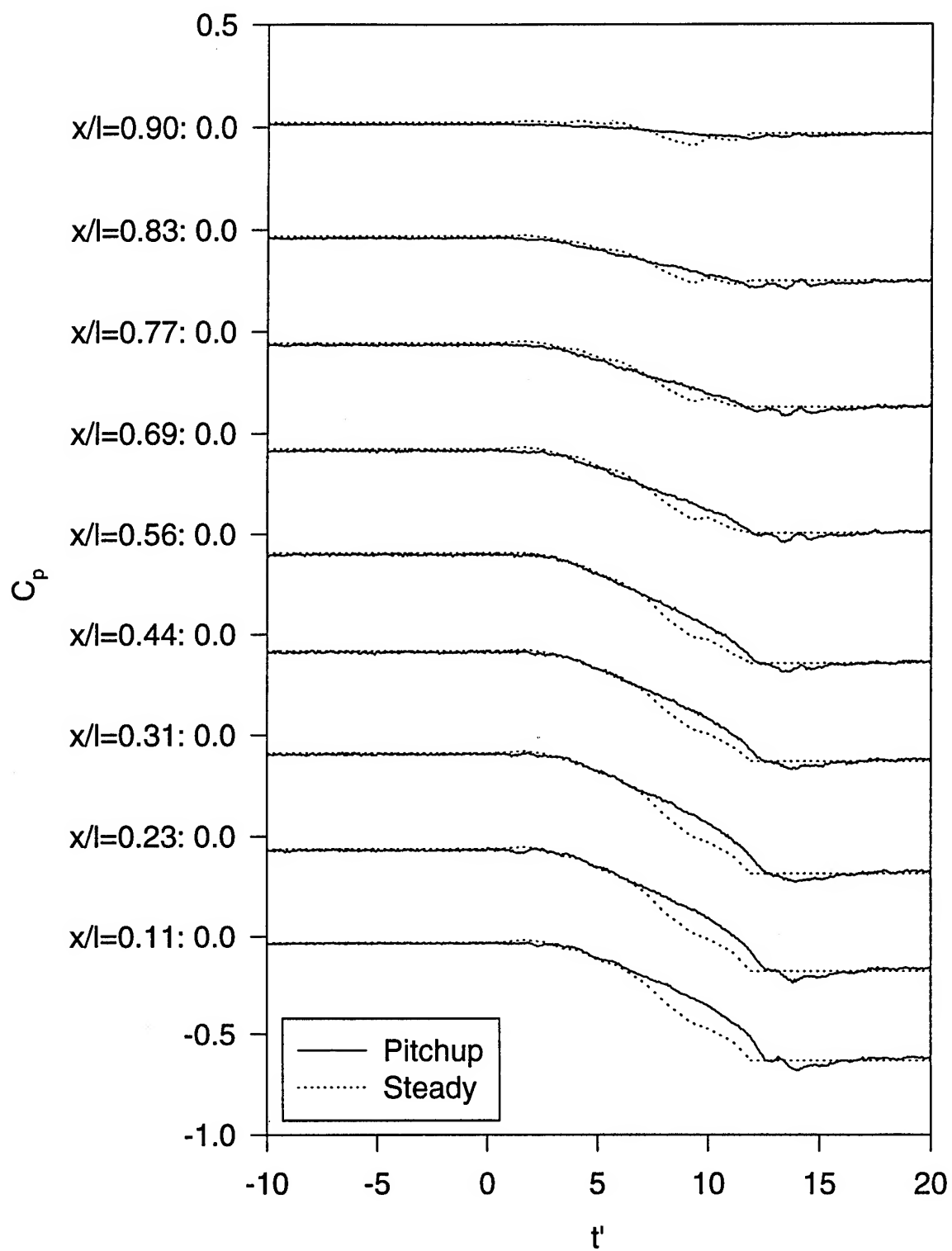


Figure 303. Pitchup Maneuver  $C_p$  vs. time for all  $x/L$ ,  $\phi=90^\circ$ .

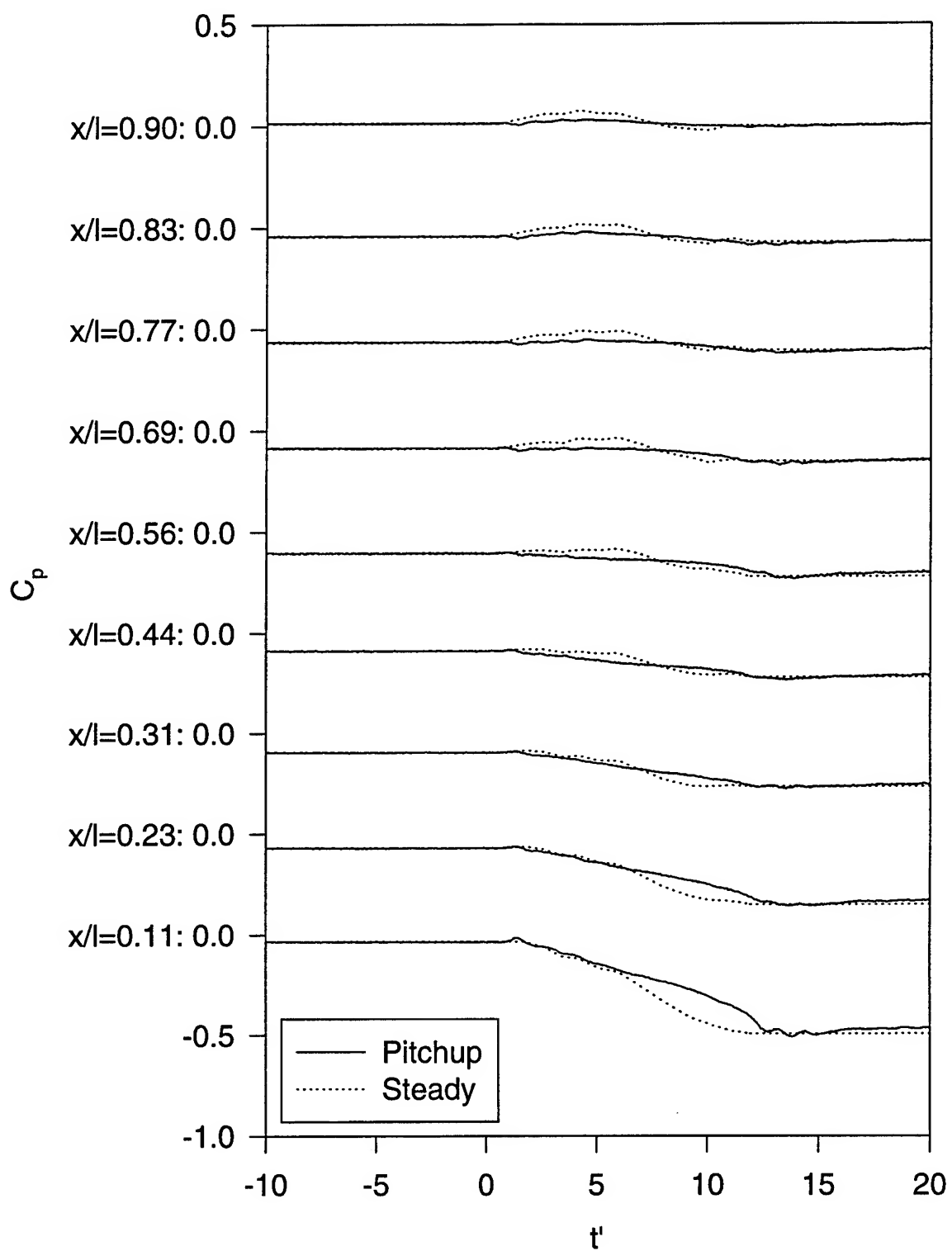


Figure 304. Pitchup Maneuver  $C_p$  vs. time for all  $x/L$ ,  $\phi=135^\circ$ .

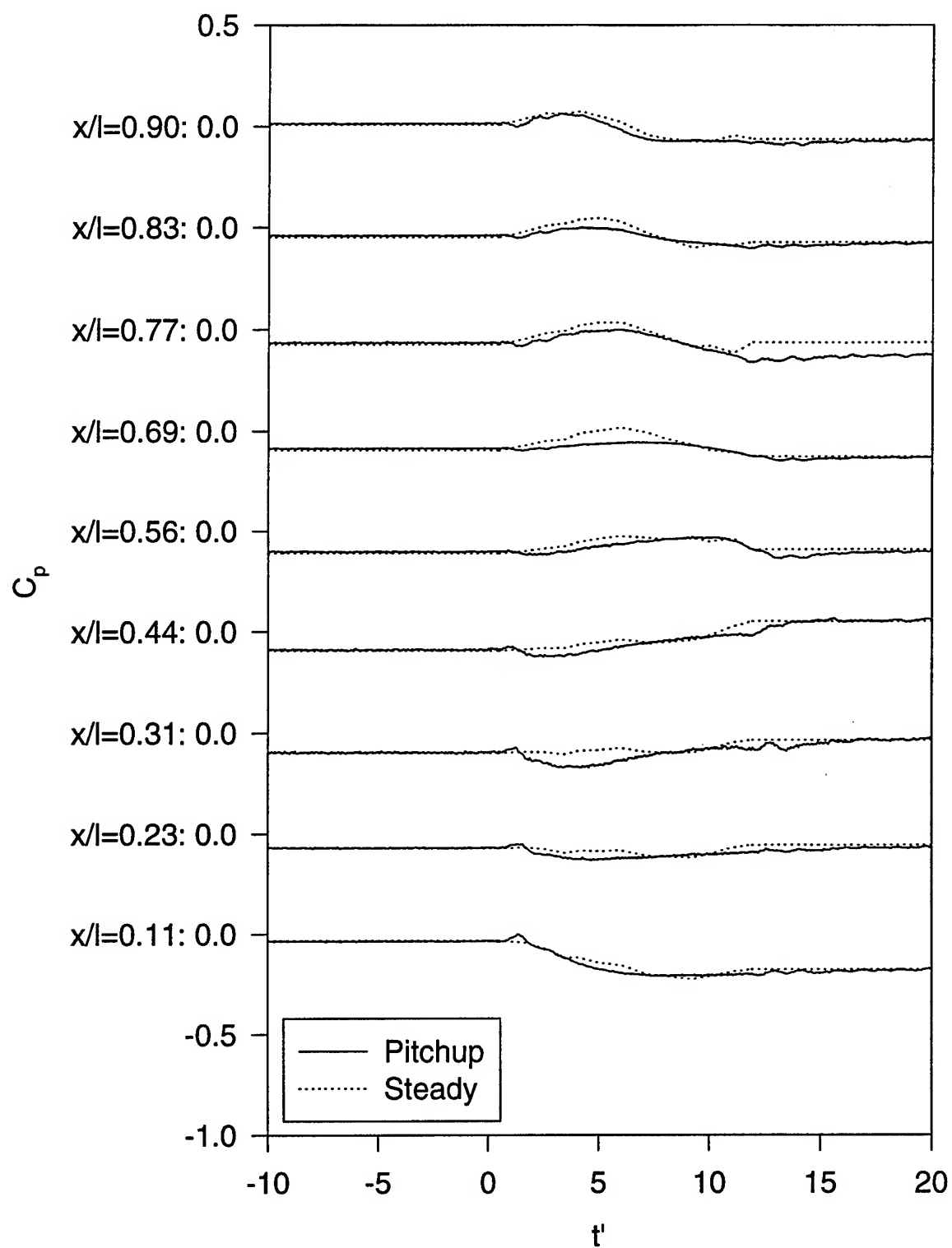


Figure 305. Pitchup Maneuver  $C_p$  vs. time for all  $x/L$ ,  $\phi=180^\circ$ .

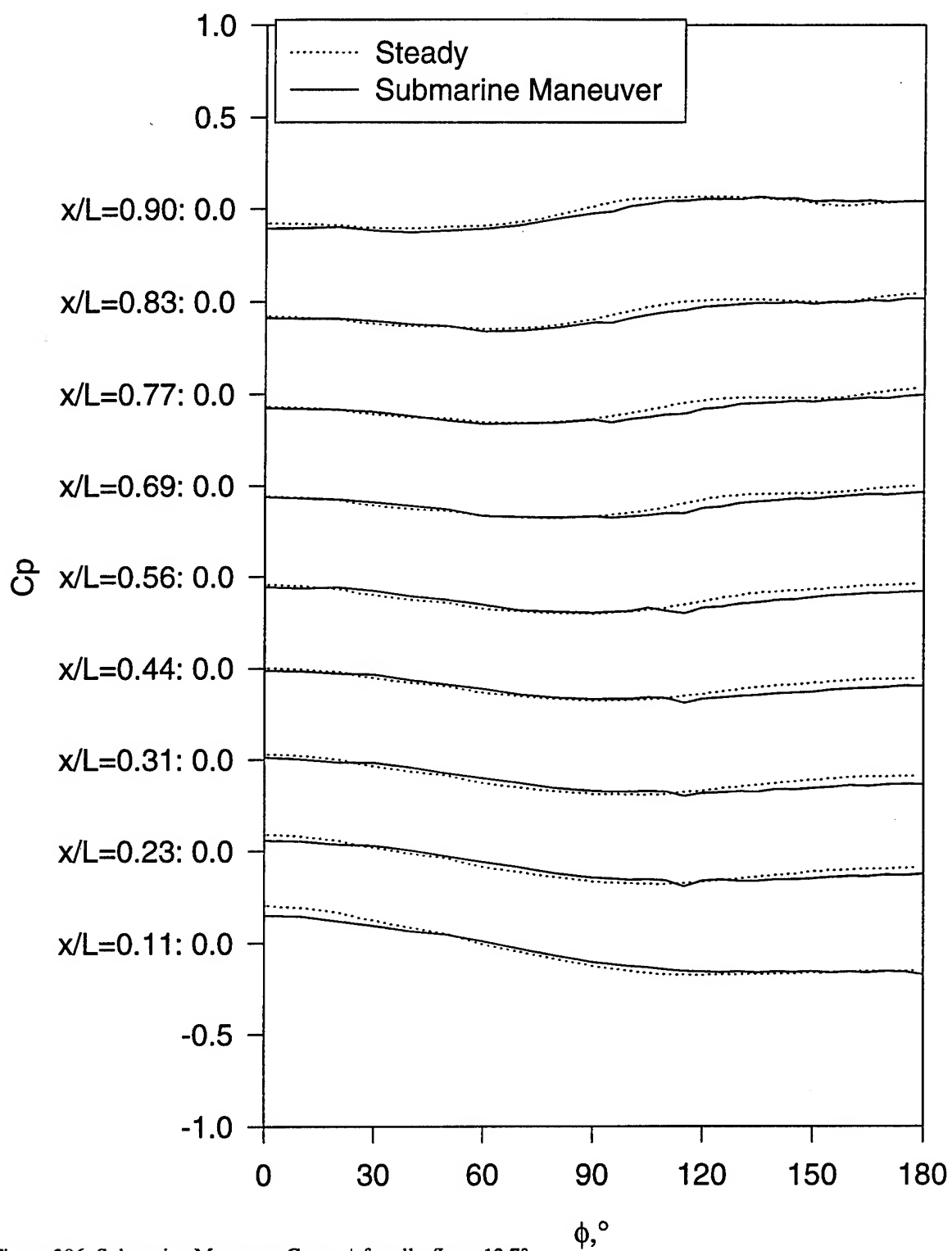


Figure 306. Submarine Maneuver  $C_p$  vs.  $\phi$  for all  $x/L$ ,  $\alpha=12.7^\circ$ .



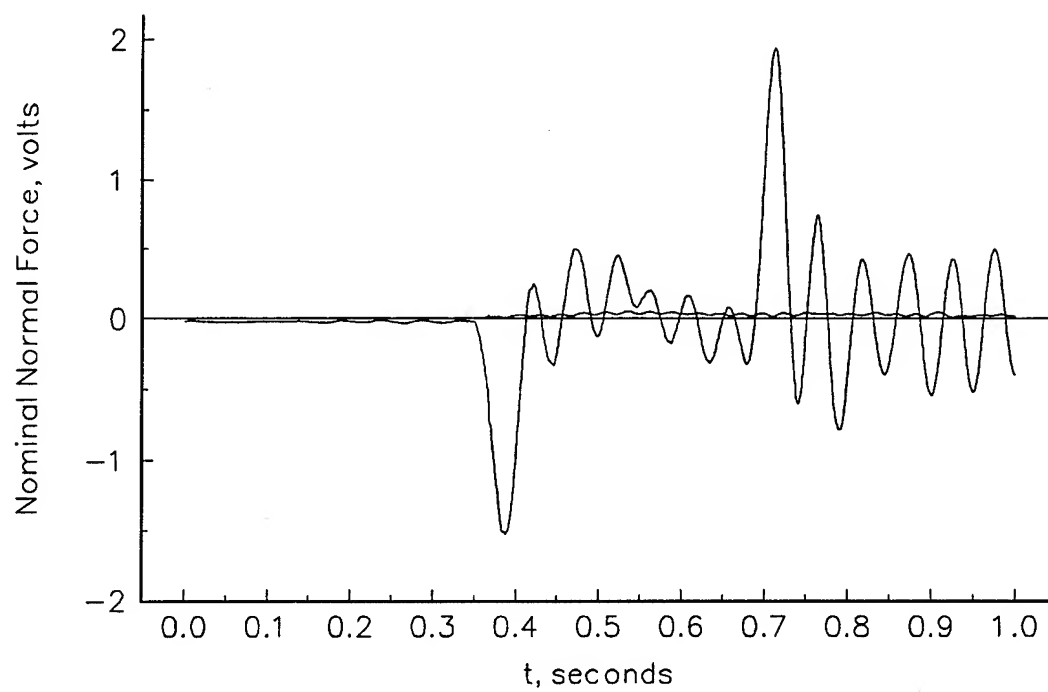


Figure 308. Typical dynamic response on original five-component balance.

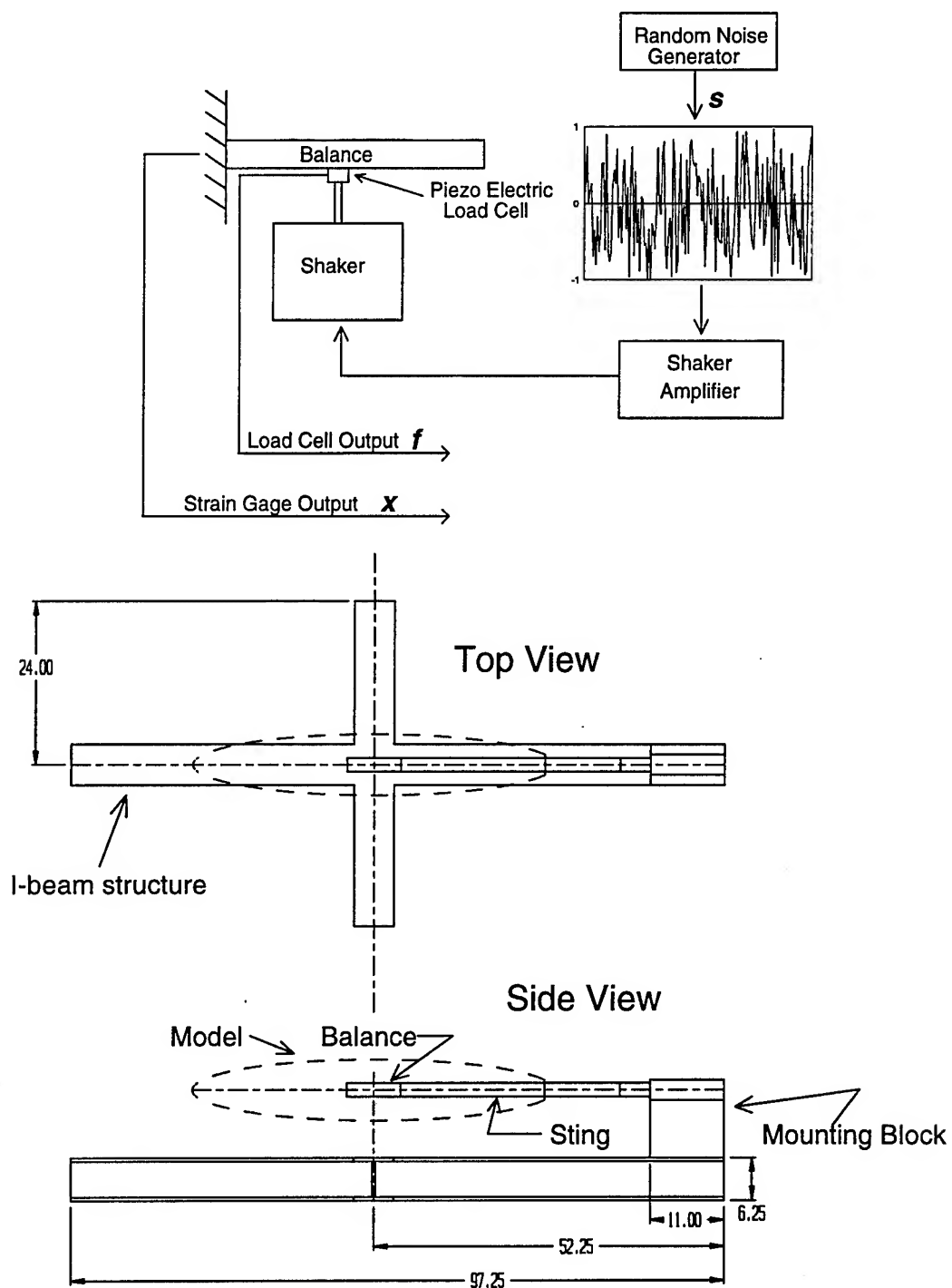


Figure 309. Dynamic calibration frame.



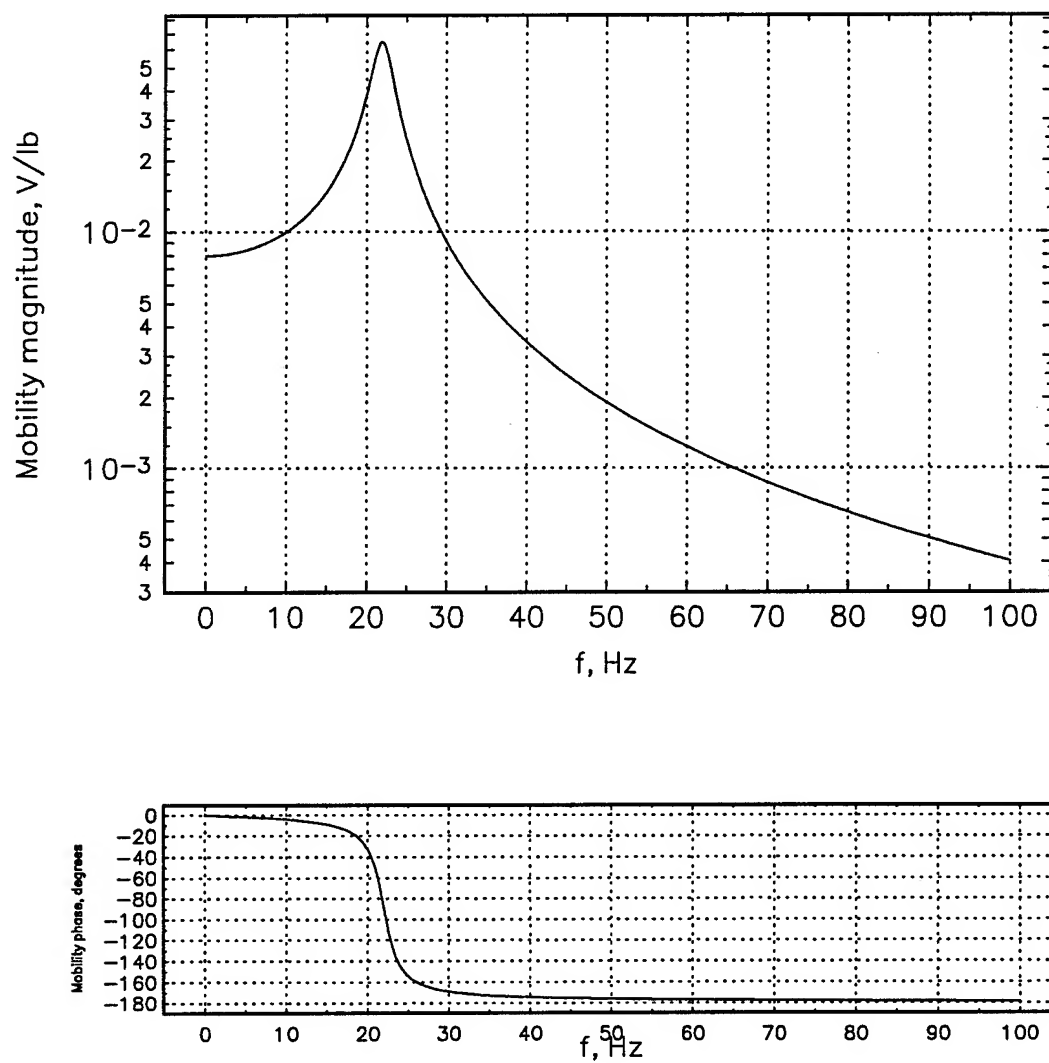


Figure 310. Typical second order transfer function.

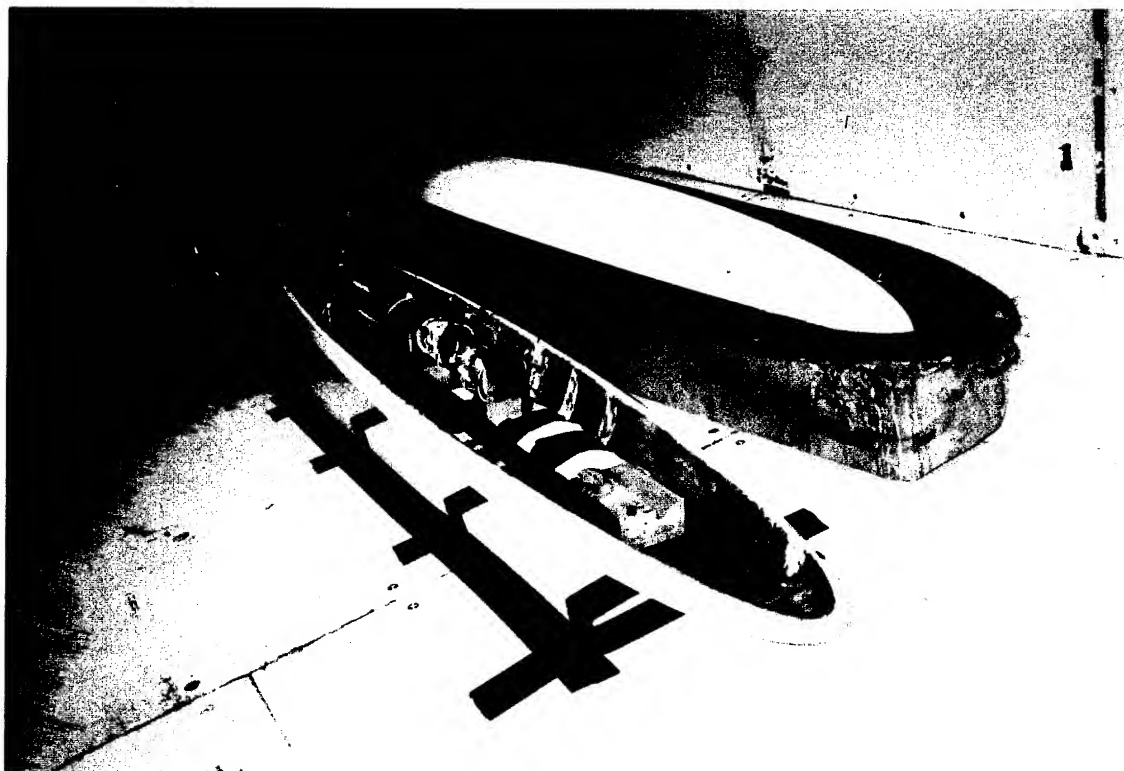


Figure 311. Light-weight model.

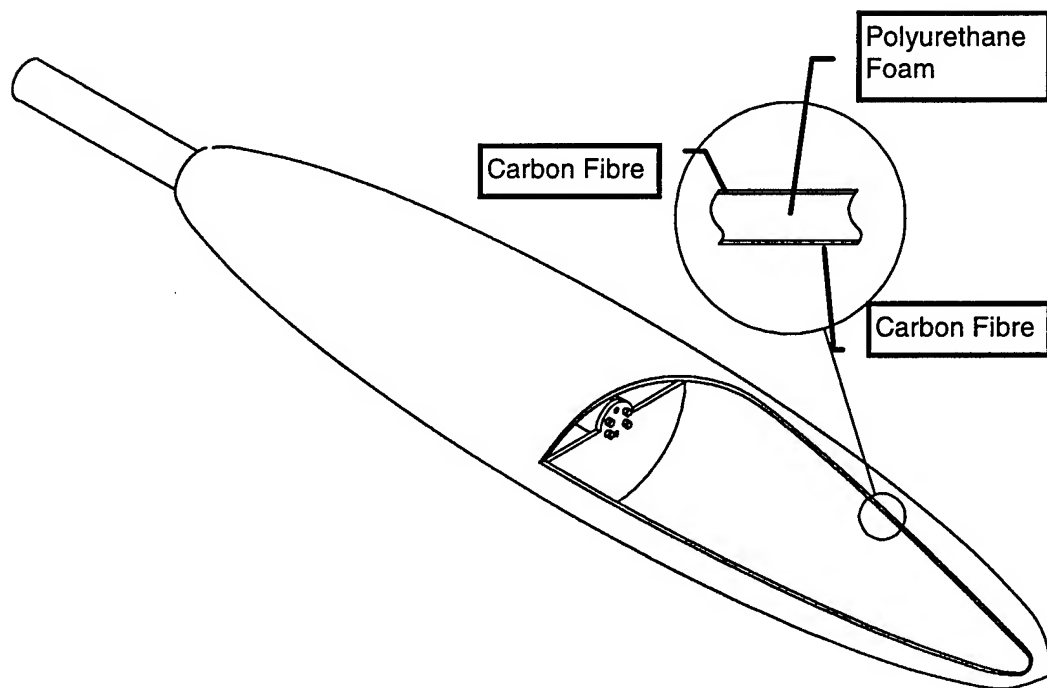


Figure 312. Lightweight model construction.

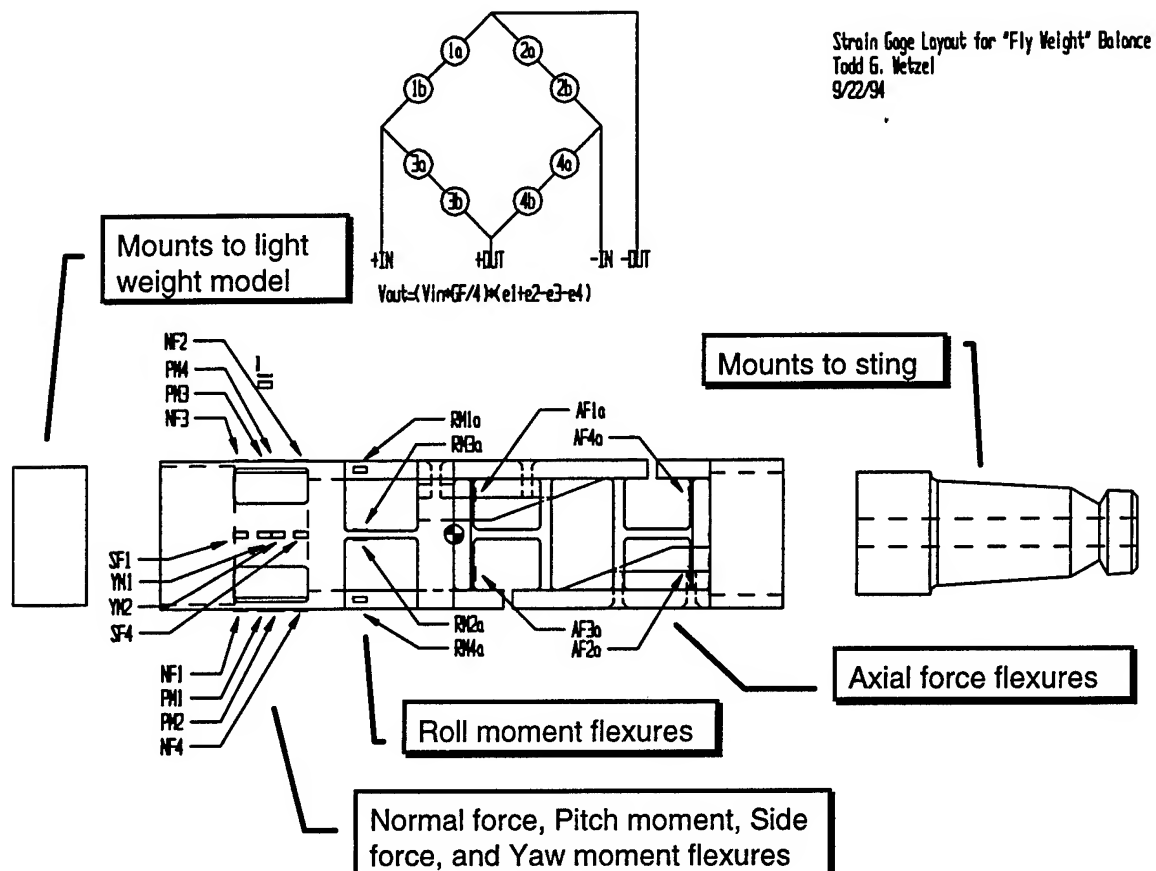


Figure 313(a). "Fly-weight" balance strain gage layout. NF = normal force, PM = pitch moment, SF = side force, YM = yaw moment, RM = roll moment, and AF = Axial force.

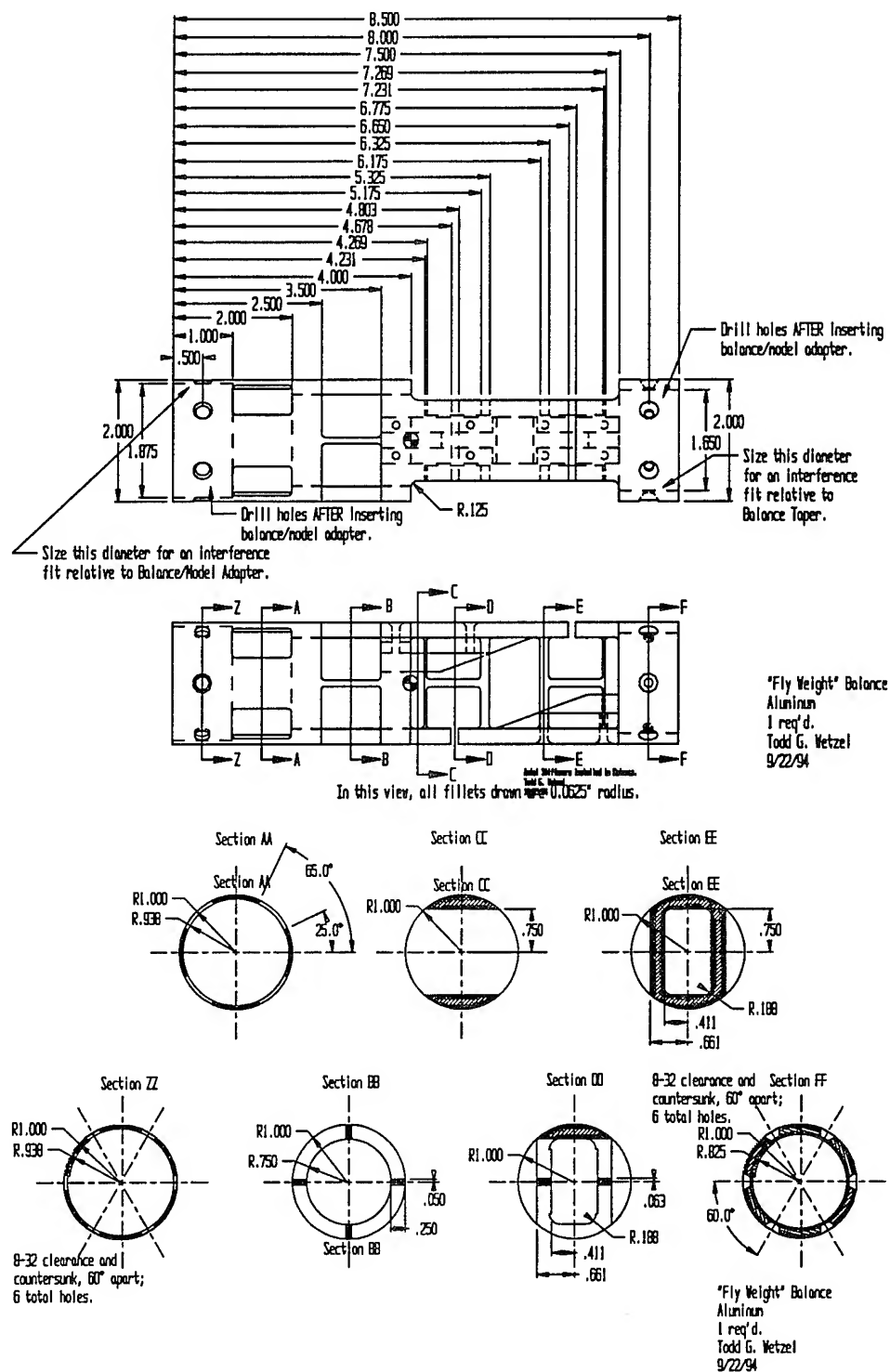


Figure 313(b). "Fly-Weight" Balance. Section geometry.

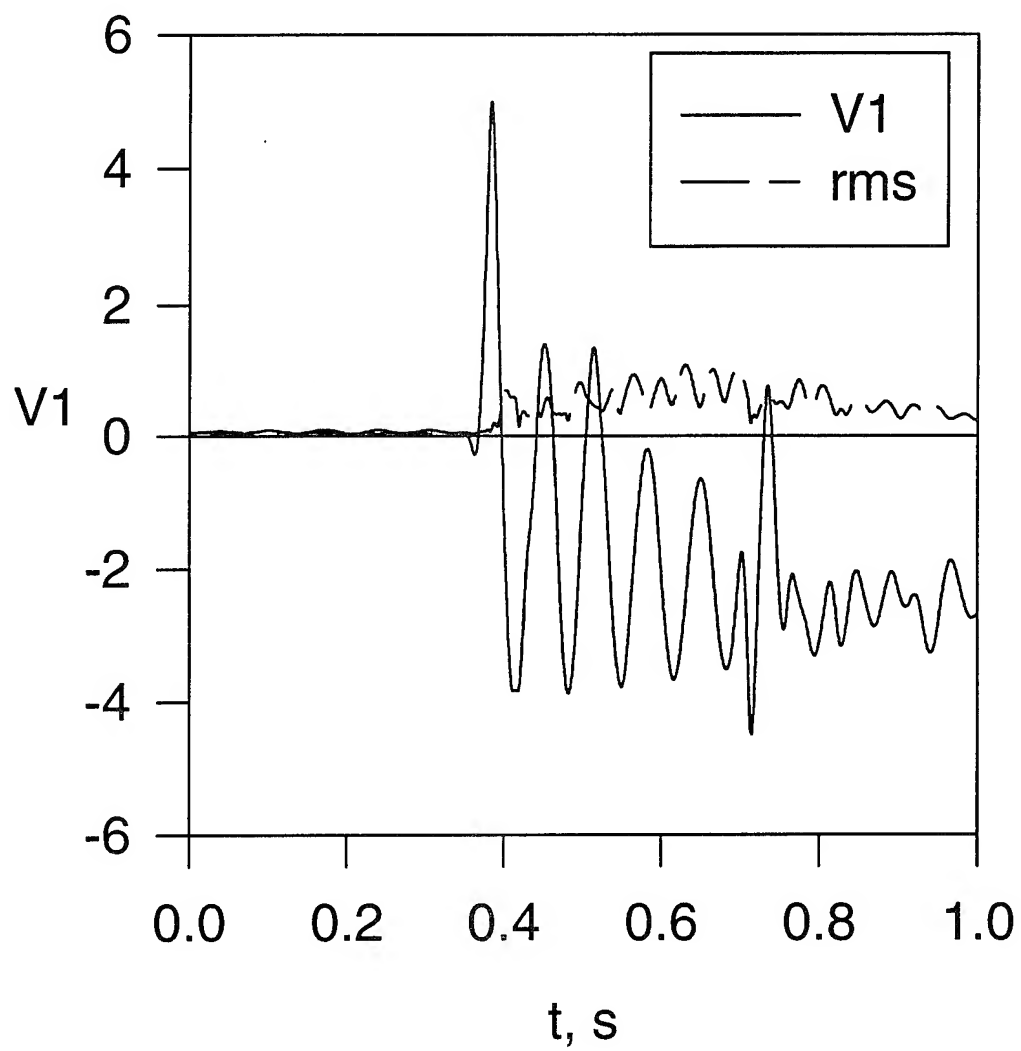


Figure 314. Typical dynamic response of "fly-weight" balance.

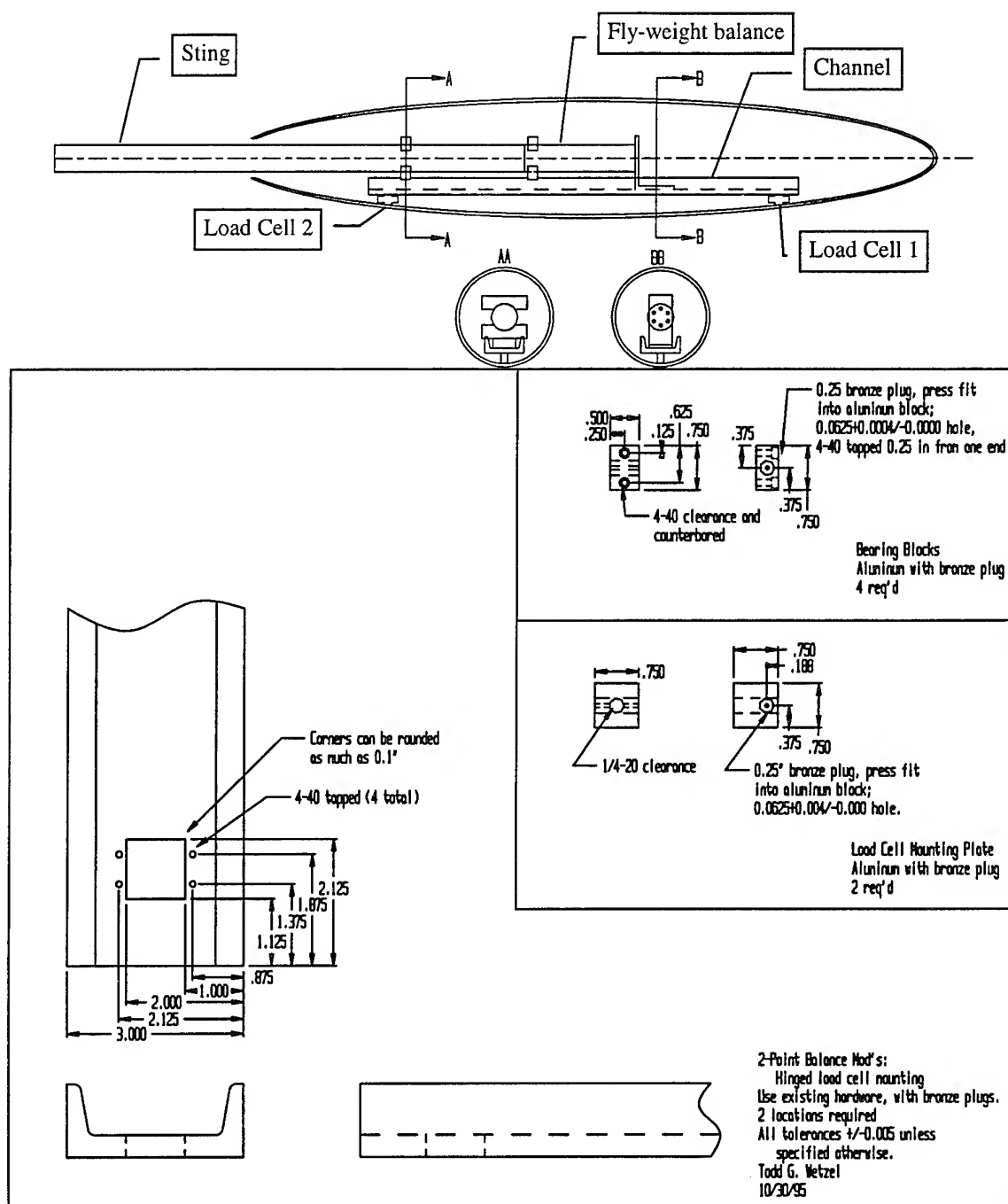


Figure 315. Two point balance.

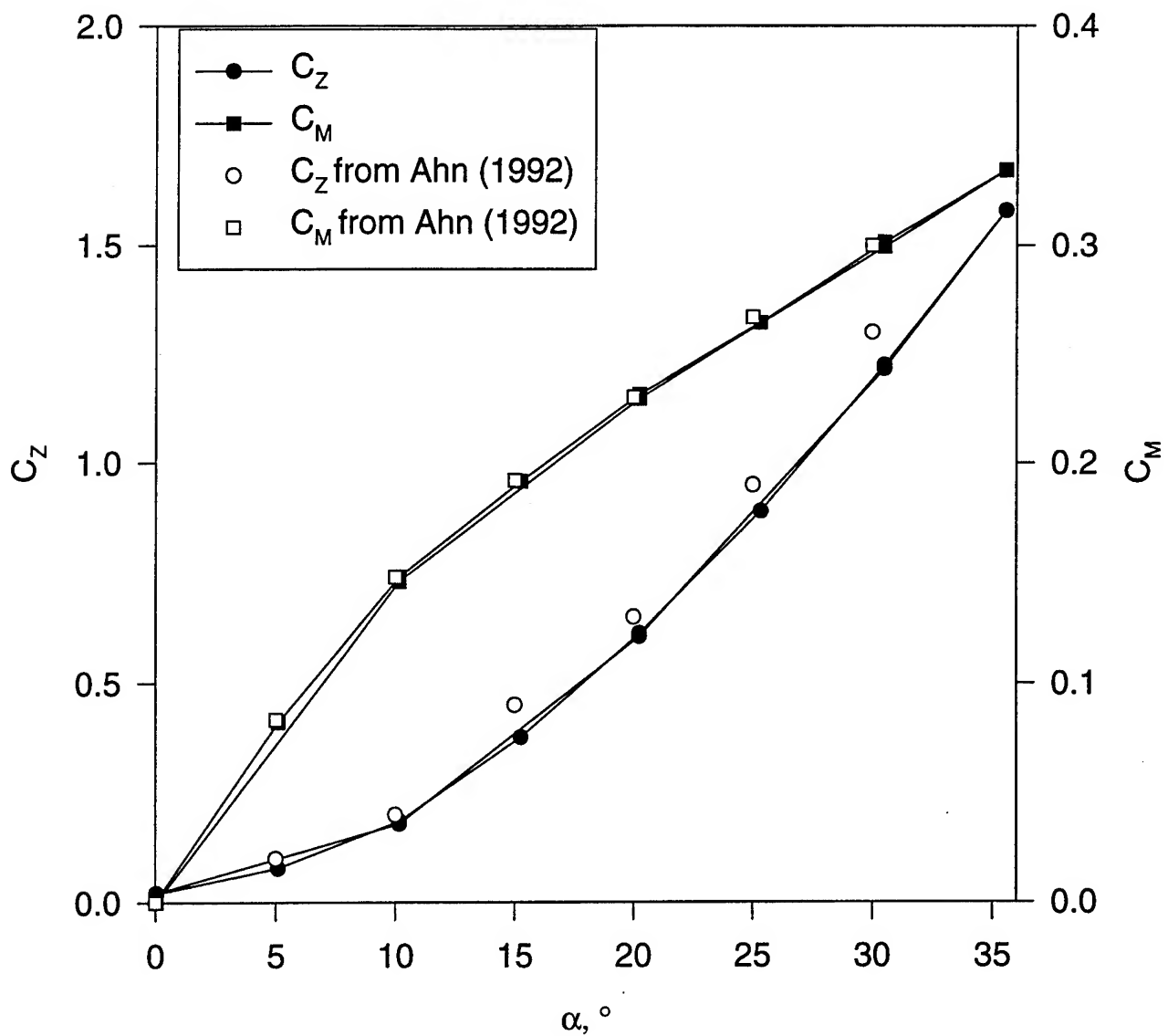


Figure 316. Steady normal force and pitch moment on prolate spheroid at  $Re = 4.2$  million for various angles of attack from balance data. Compared with data from Ahn (1992).



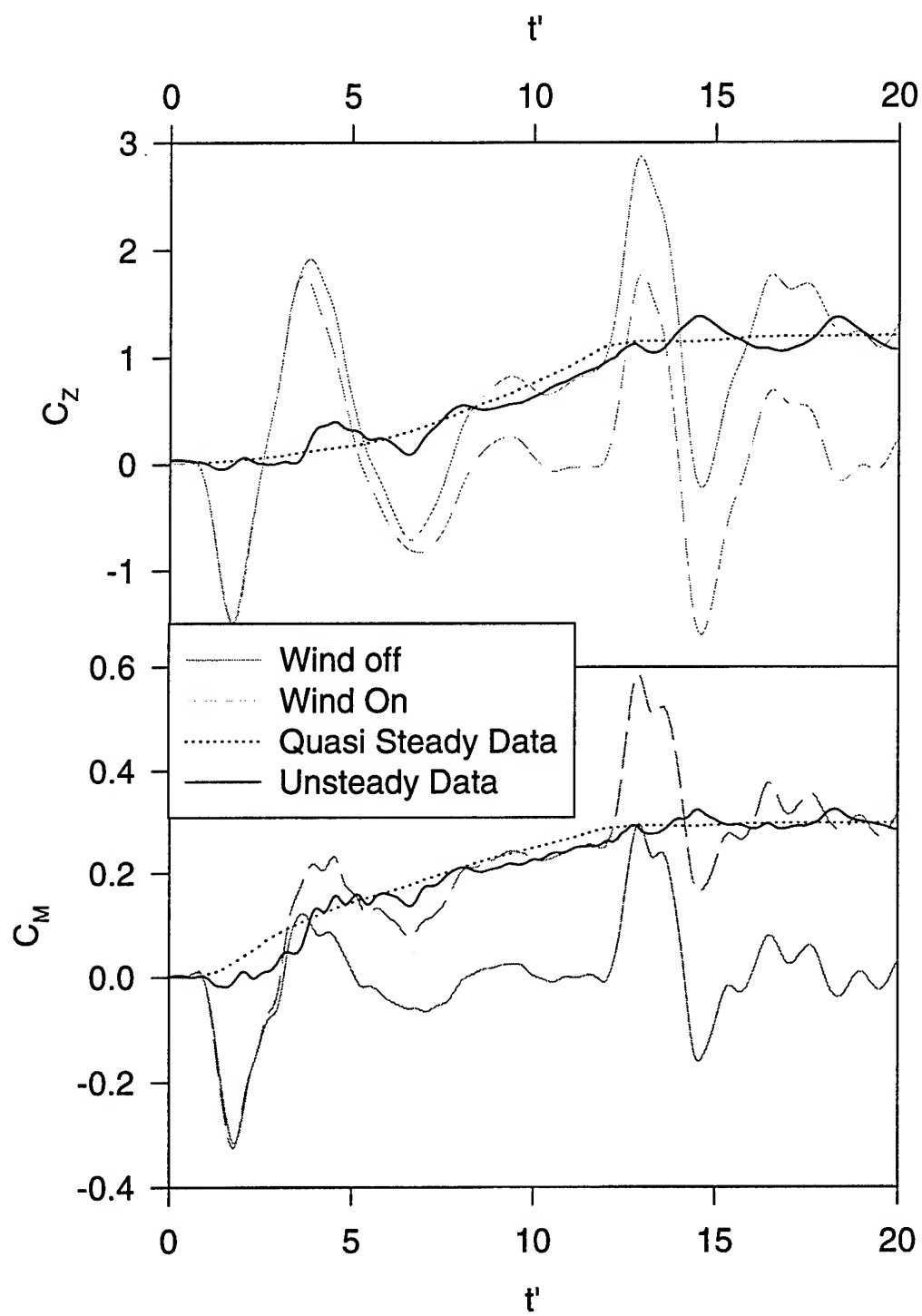


Figure 317. Unsteady normal force and pitch moment for pitchup maneuver.

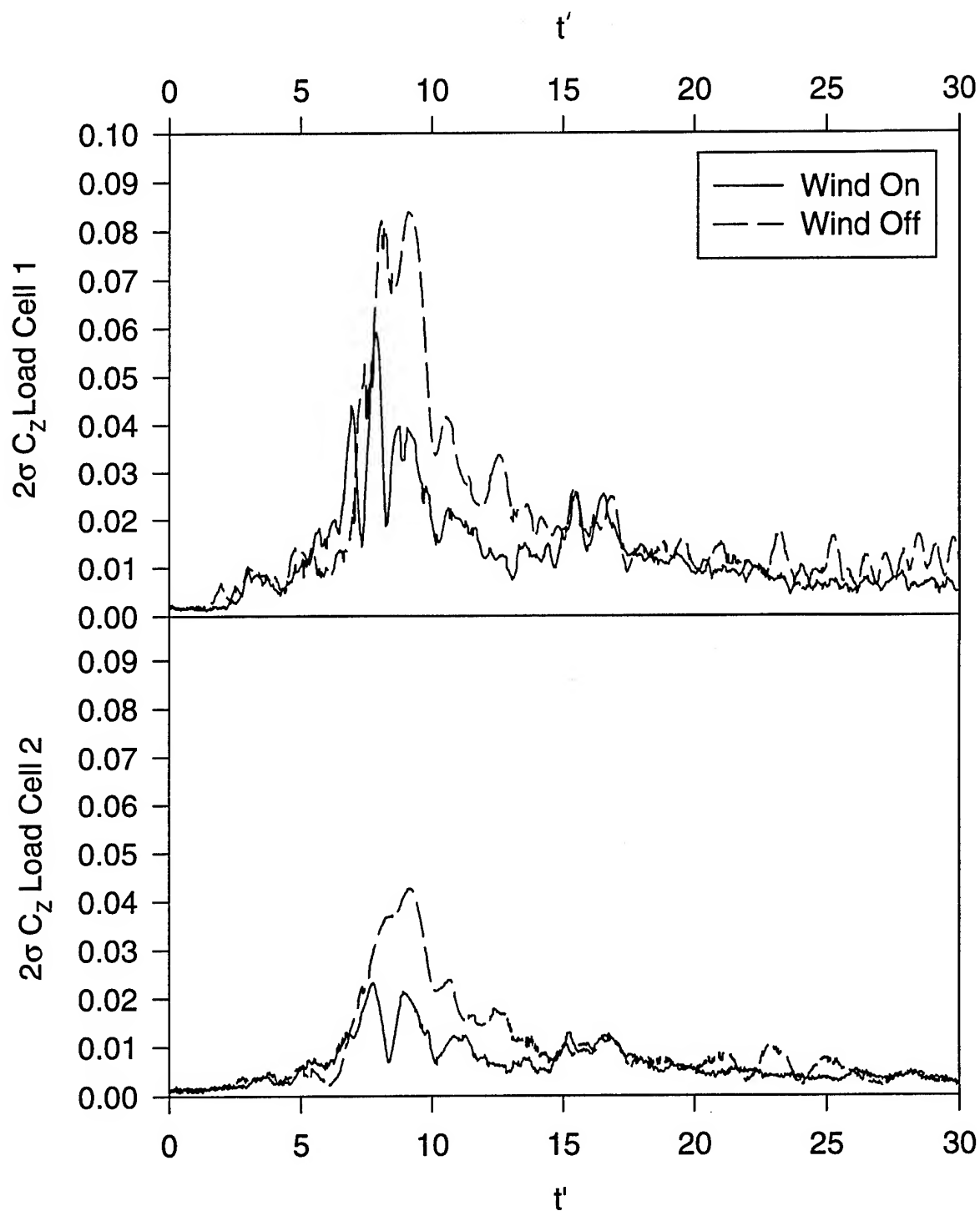


Figure 318. Repeatability for load cell 1 and 2 during pitchup maneuver. The “2σ” level on the y-axis of each plot represents the 20:1 odds repeatability for each instant in time.

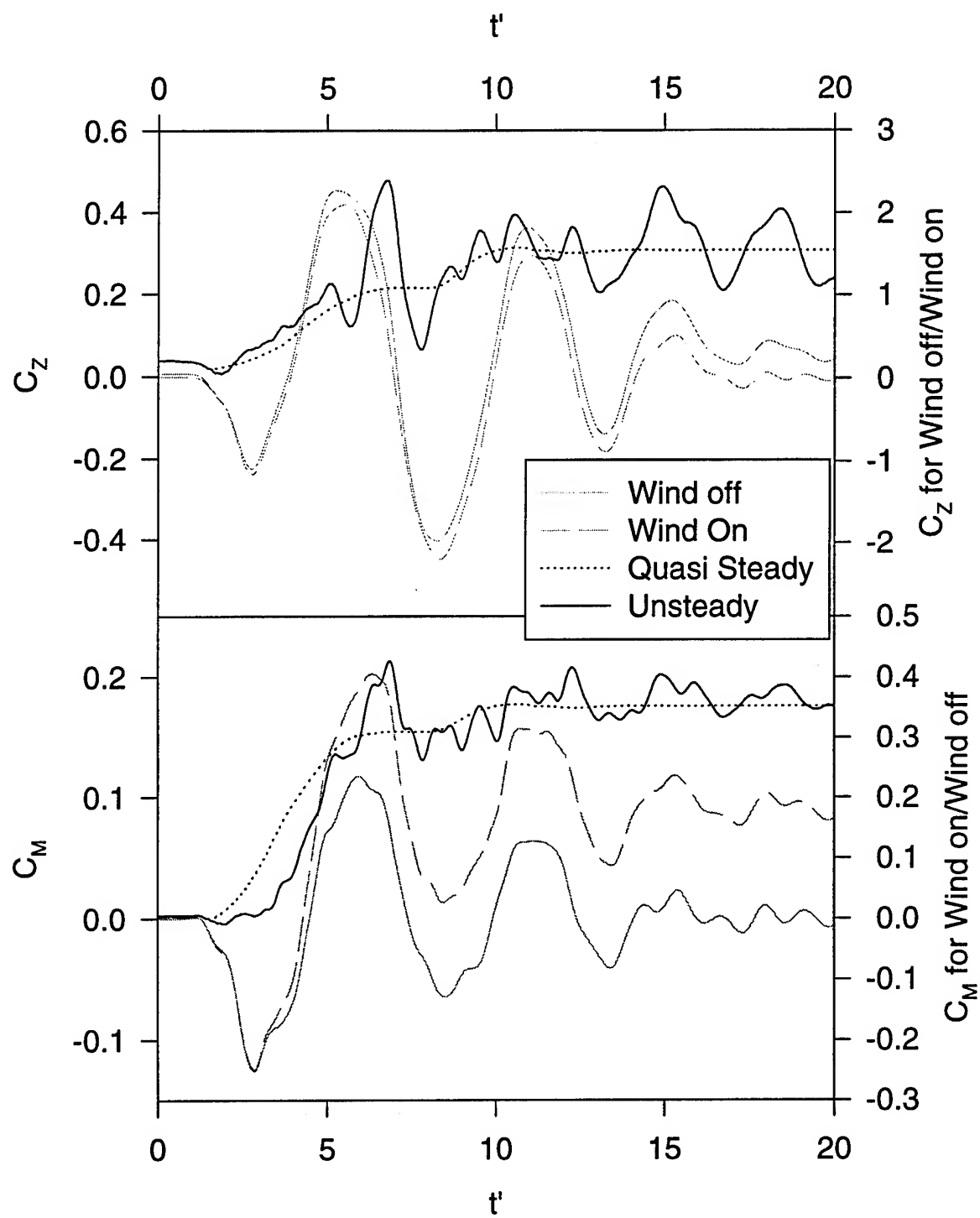


Figure 319. Unsteady normal force and pitch moment for submarine maneuver.

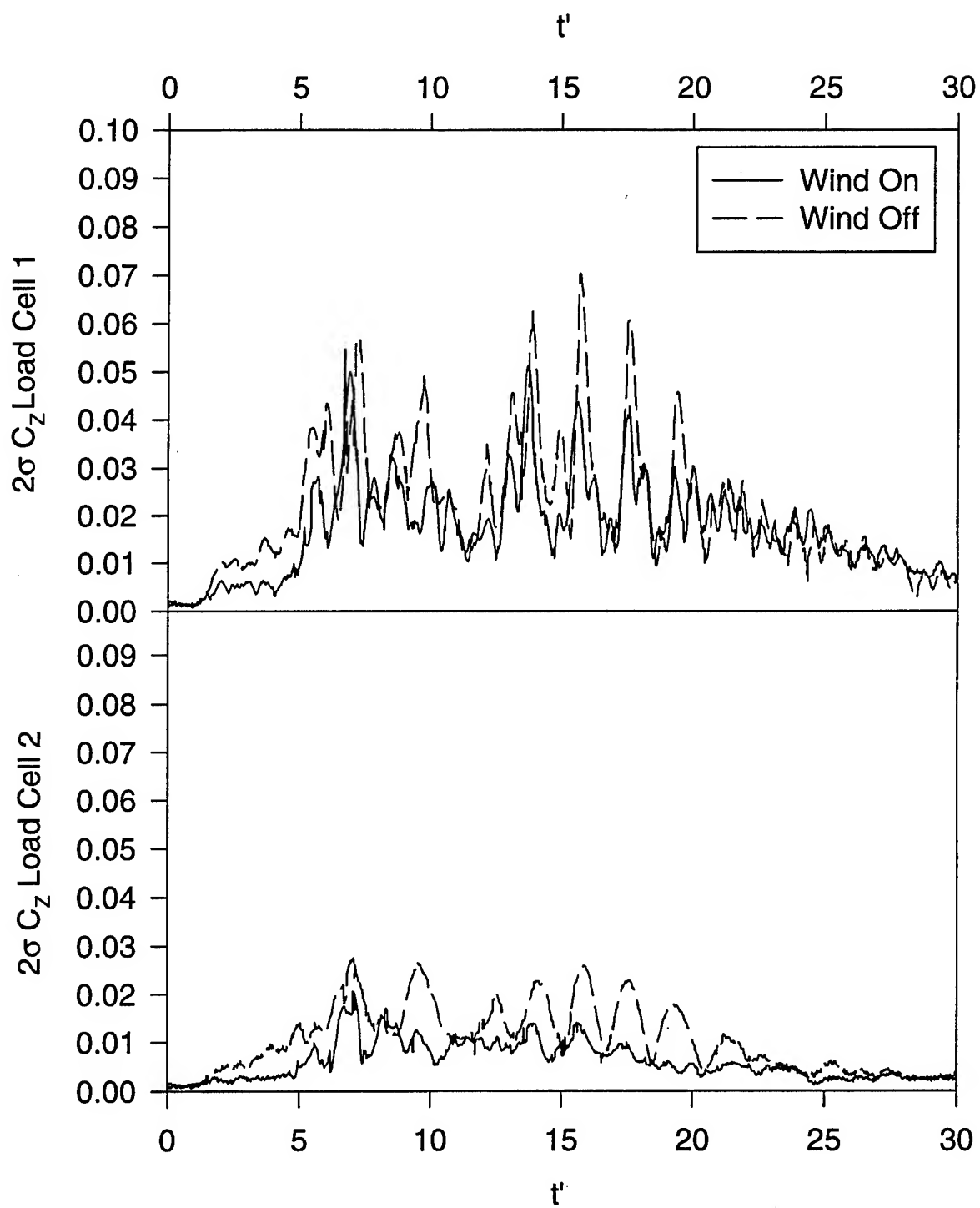


Figure 320. Repeatability for load cell 1 and 2 during the submarine maneuver. The “ $2\sigma$ ” level on the y-axis of each plot represents the 20:1 odds repeatability for each instant in time.

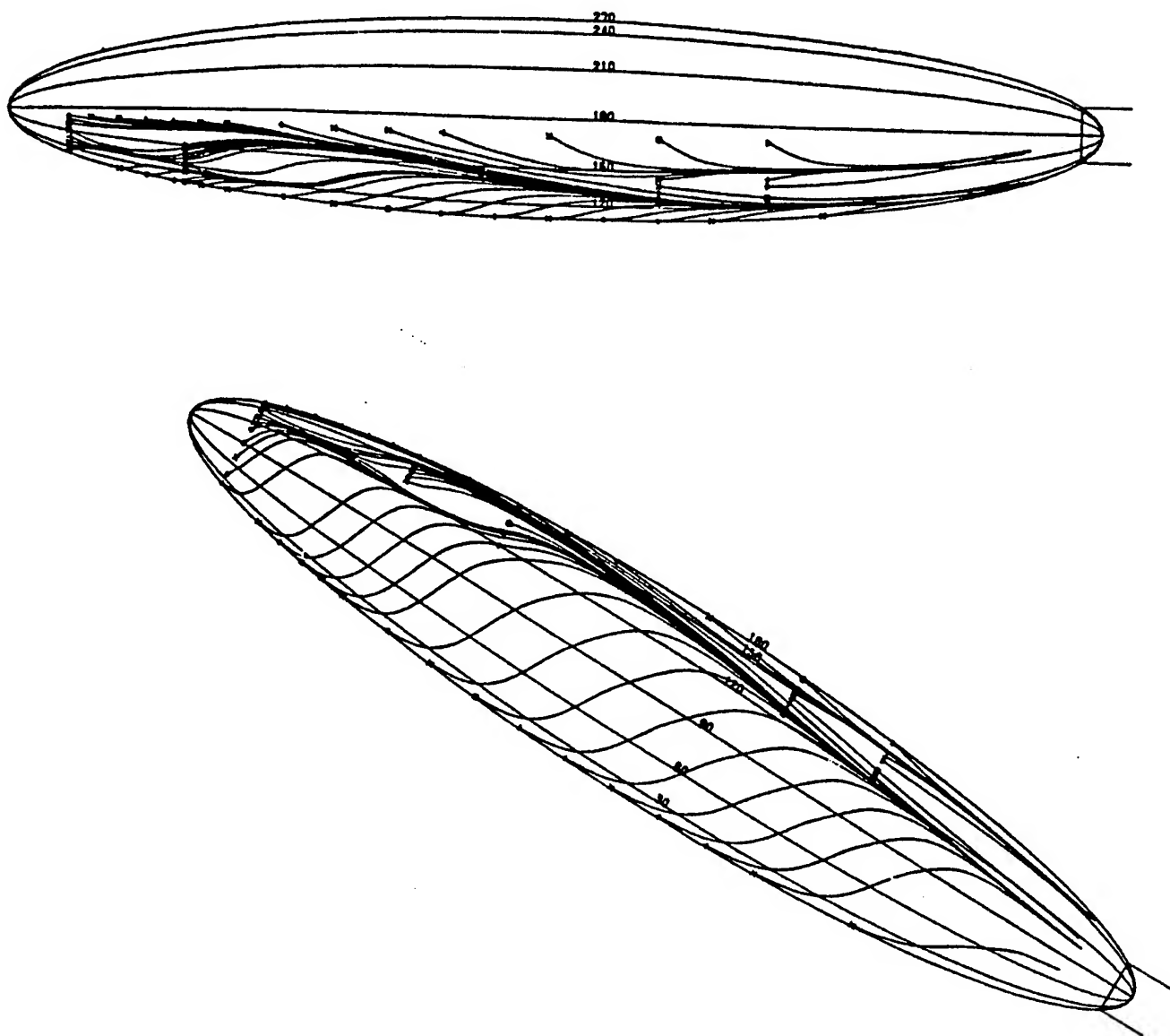


Figure 321. Typical skin friction streamline pattern obtained from directional hot-film skin friction gages (Kreplin et. al., 1985).

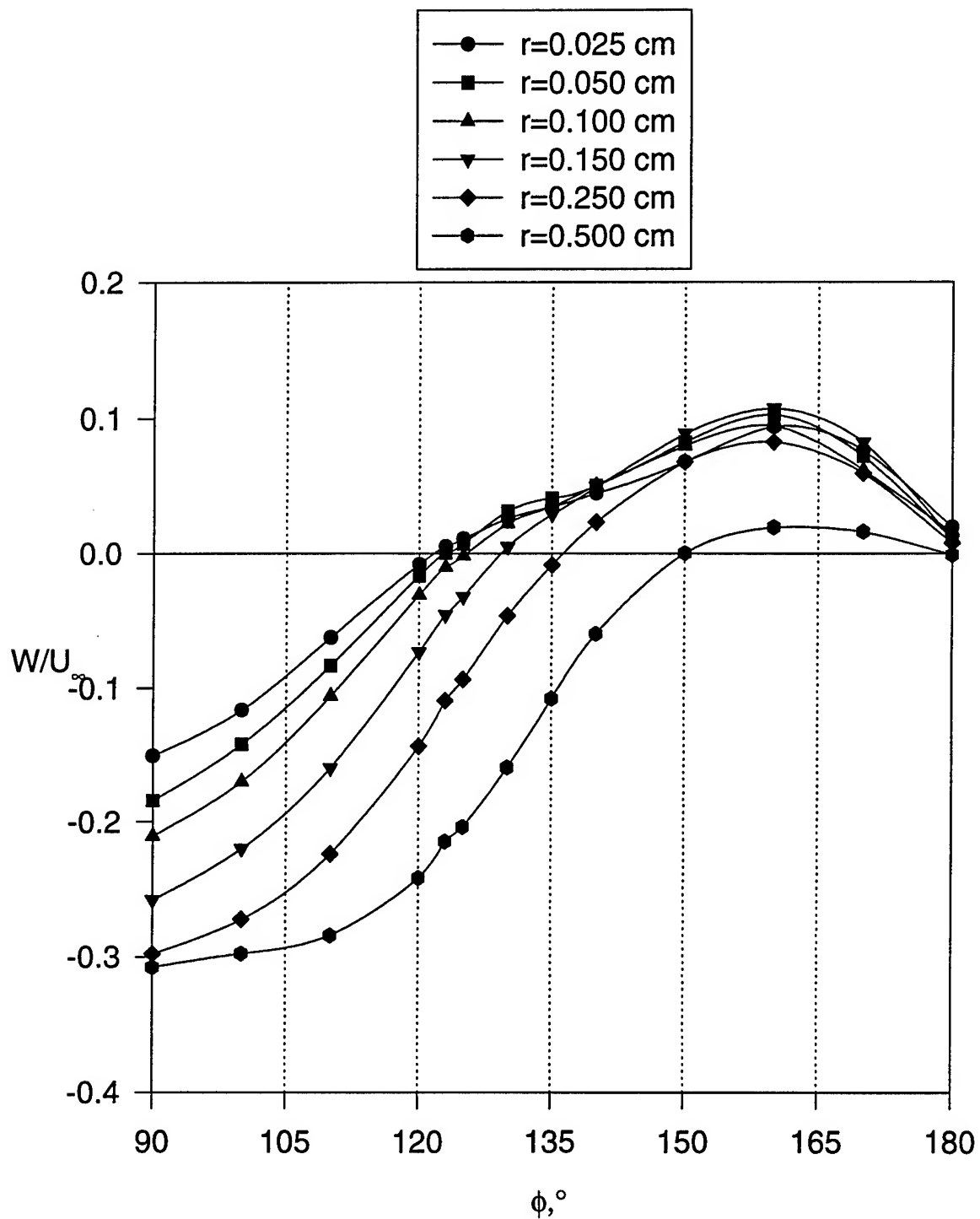


Figure 322. Circumferential distributions of crossflow velocity at fixed distances from model surface.  $\alpha=20^\circ$ ,  $x/L=0.77$ . Crossflow velocity in body coordinates (Chesnakas, 1996).

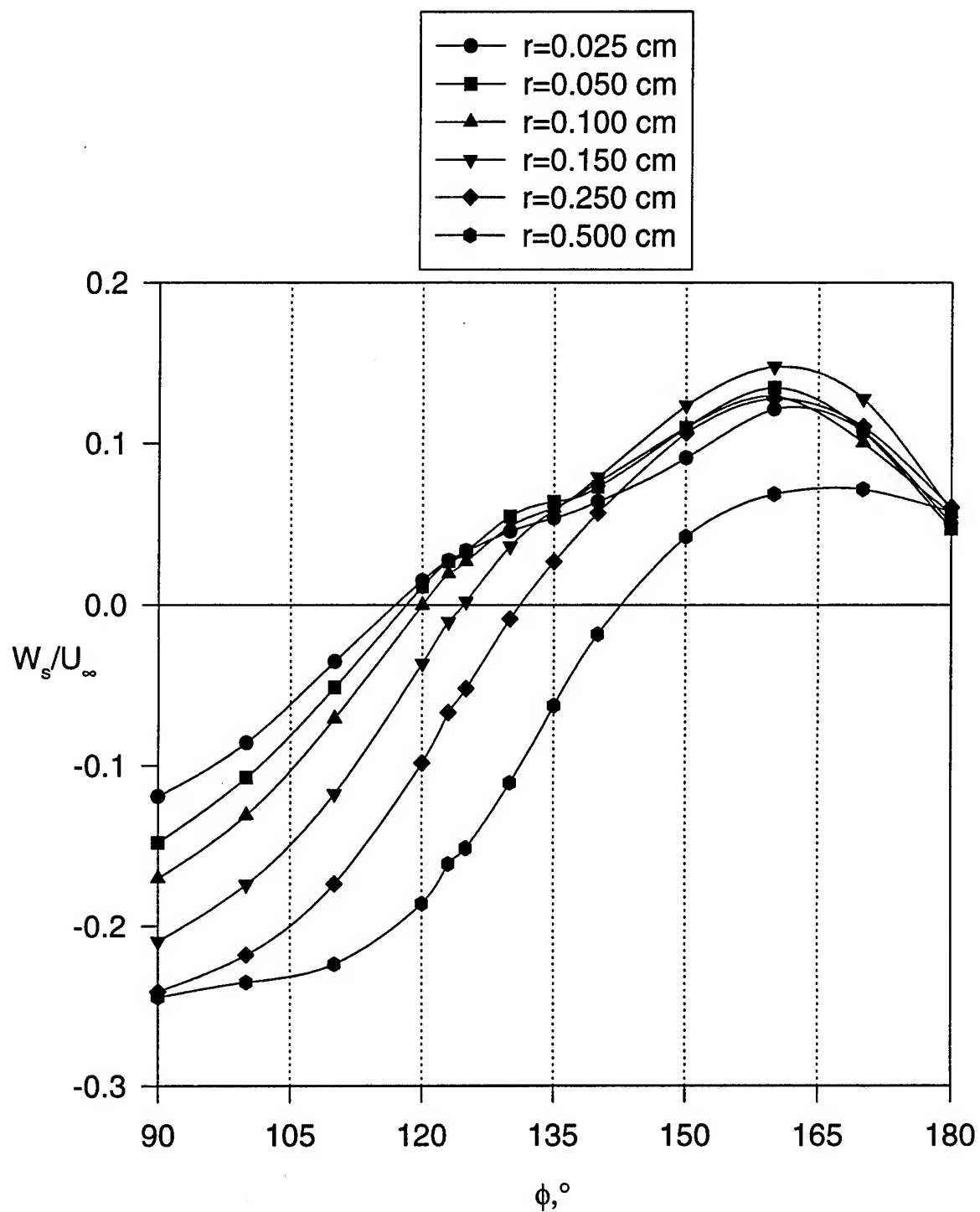


Figure 323. Circumferential distributions of crossflow velocity at fixed distances from model surface.  $\alpha=20^\circ$ ,  $x/L=0.77$ . Crossflow velocity in coordinate system perpendicular to local separation line. (Chesnakas, 1996).

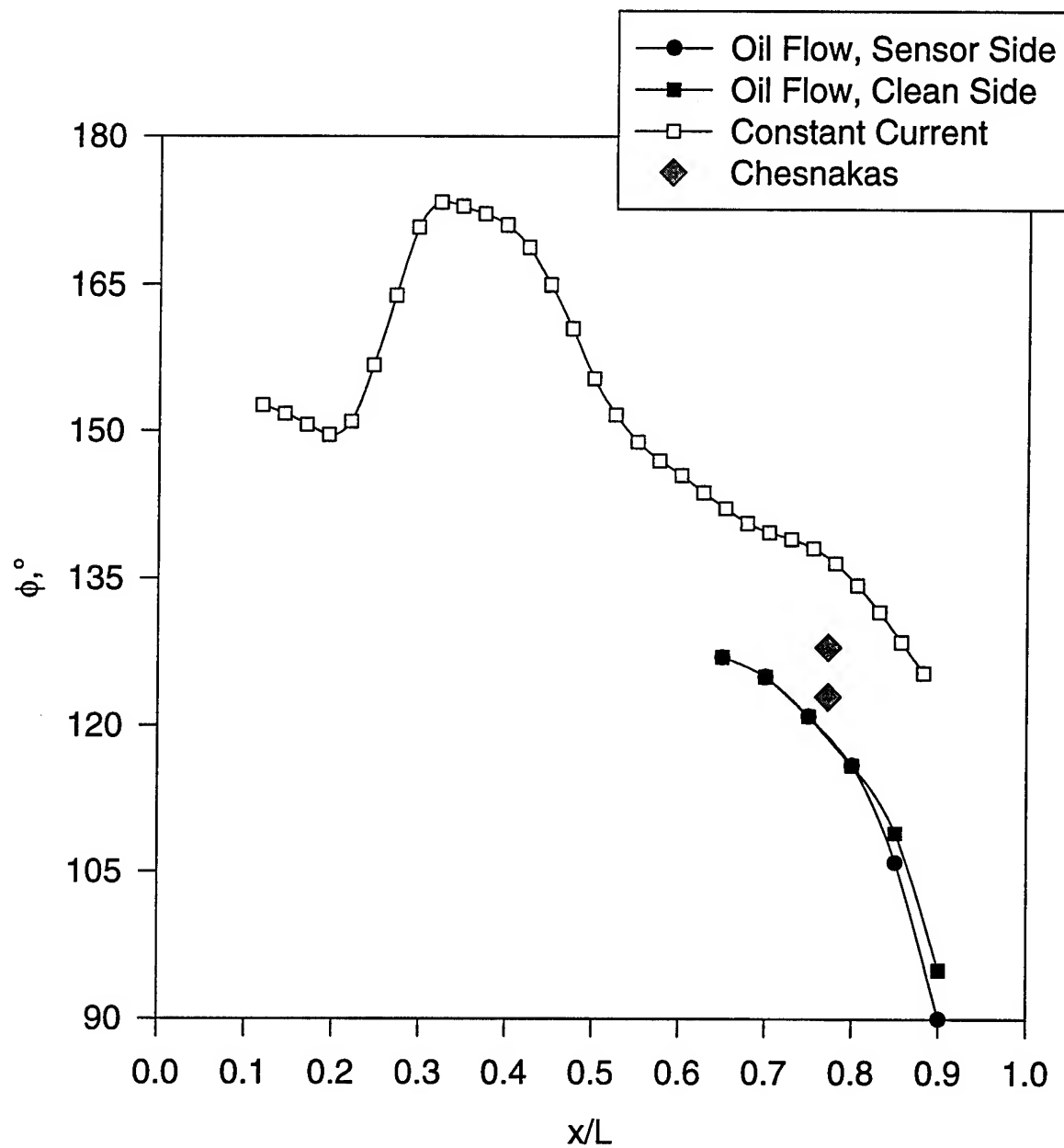


Figure 324. Various separation line comparisons for  $\alpha=10^\circ$ .



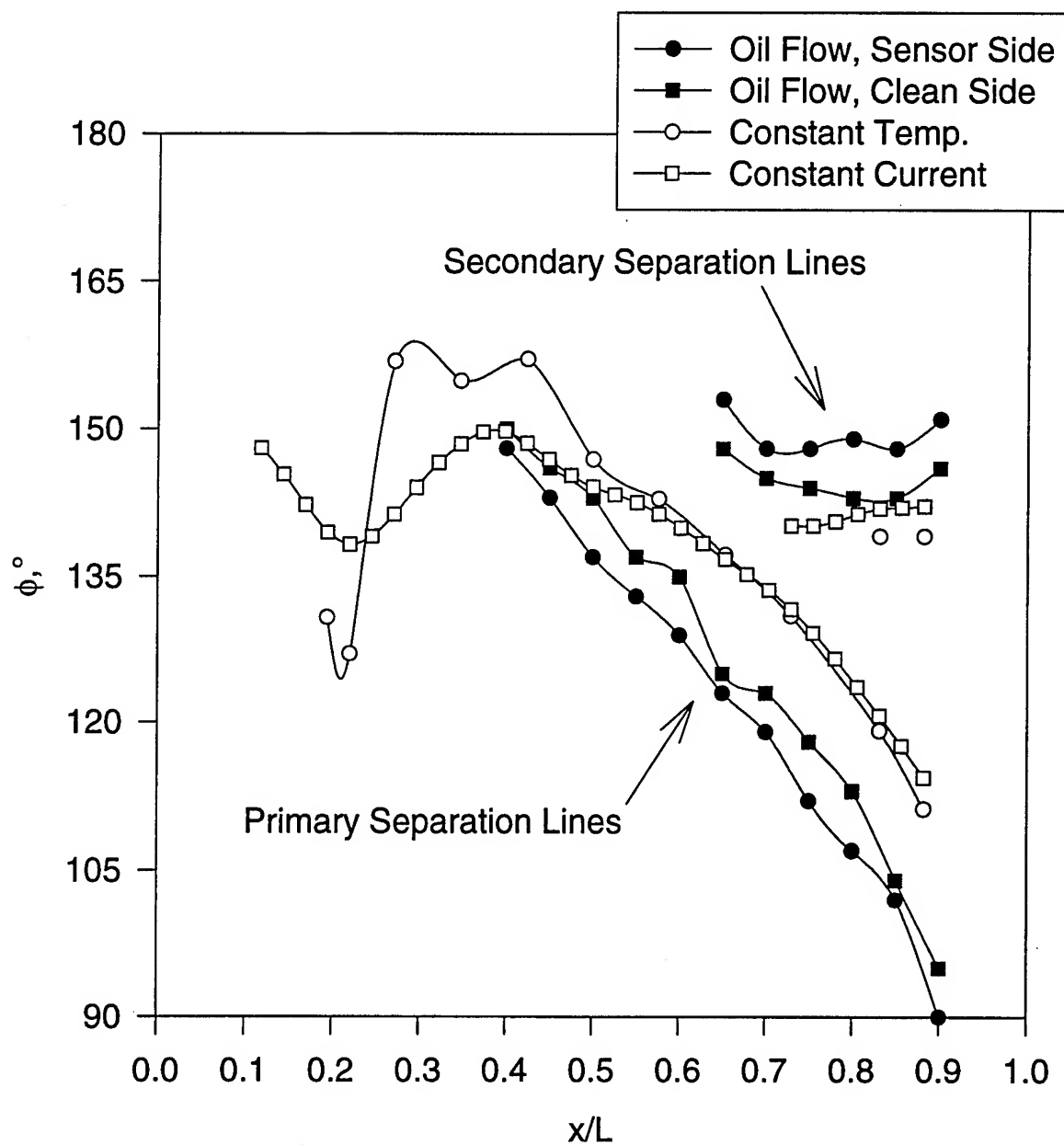


Figure 325. Various separation line comparisons for  $\alpha=15^\circ$ .

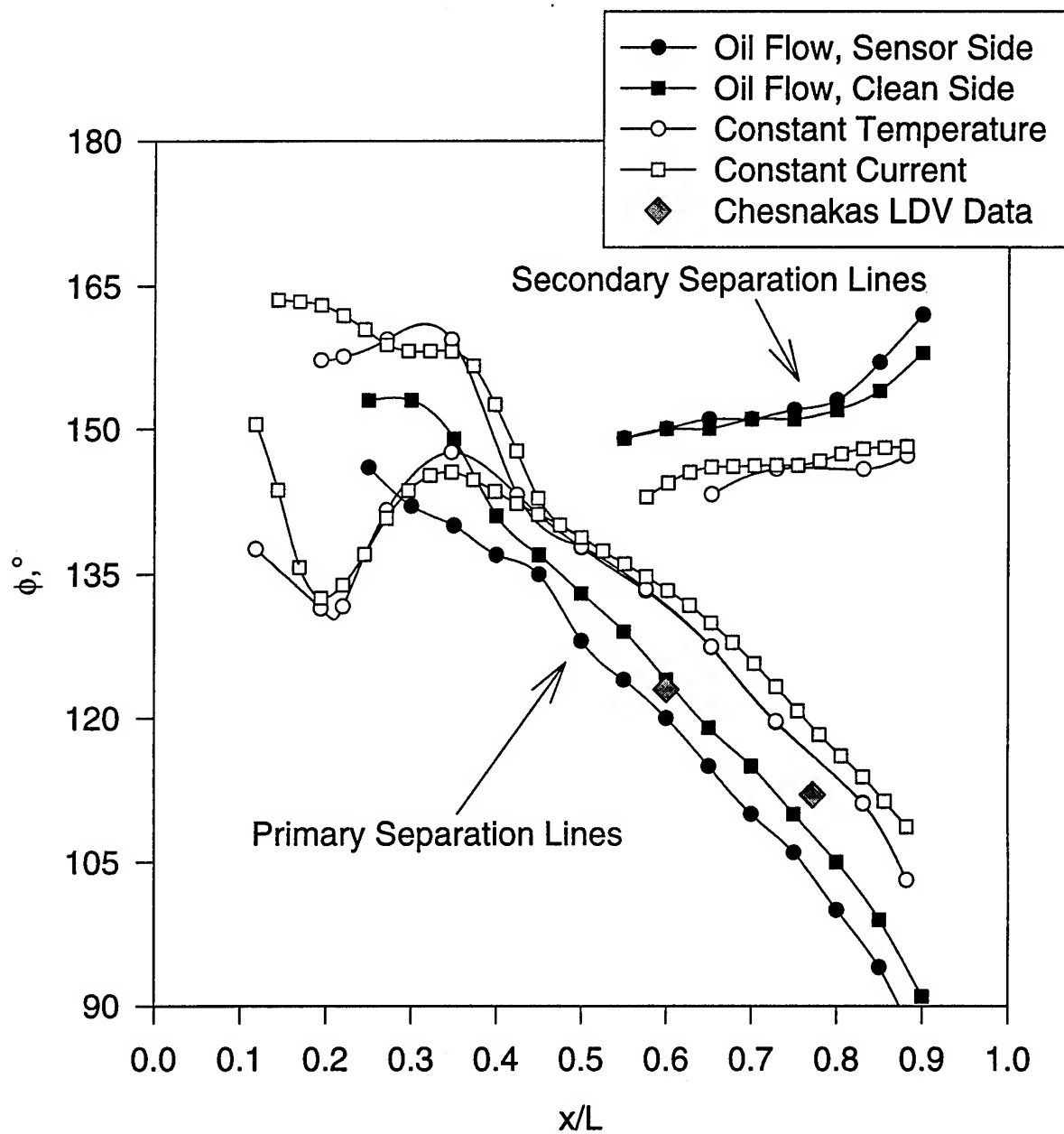


Figure 326. Various primary and secondary separation line comparisons for  $\alpha=20^\circ$ .

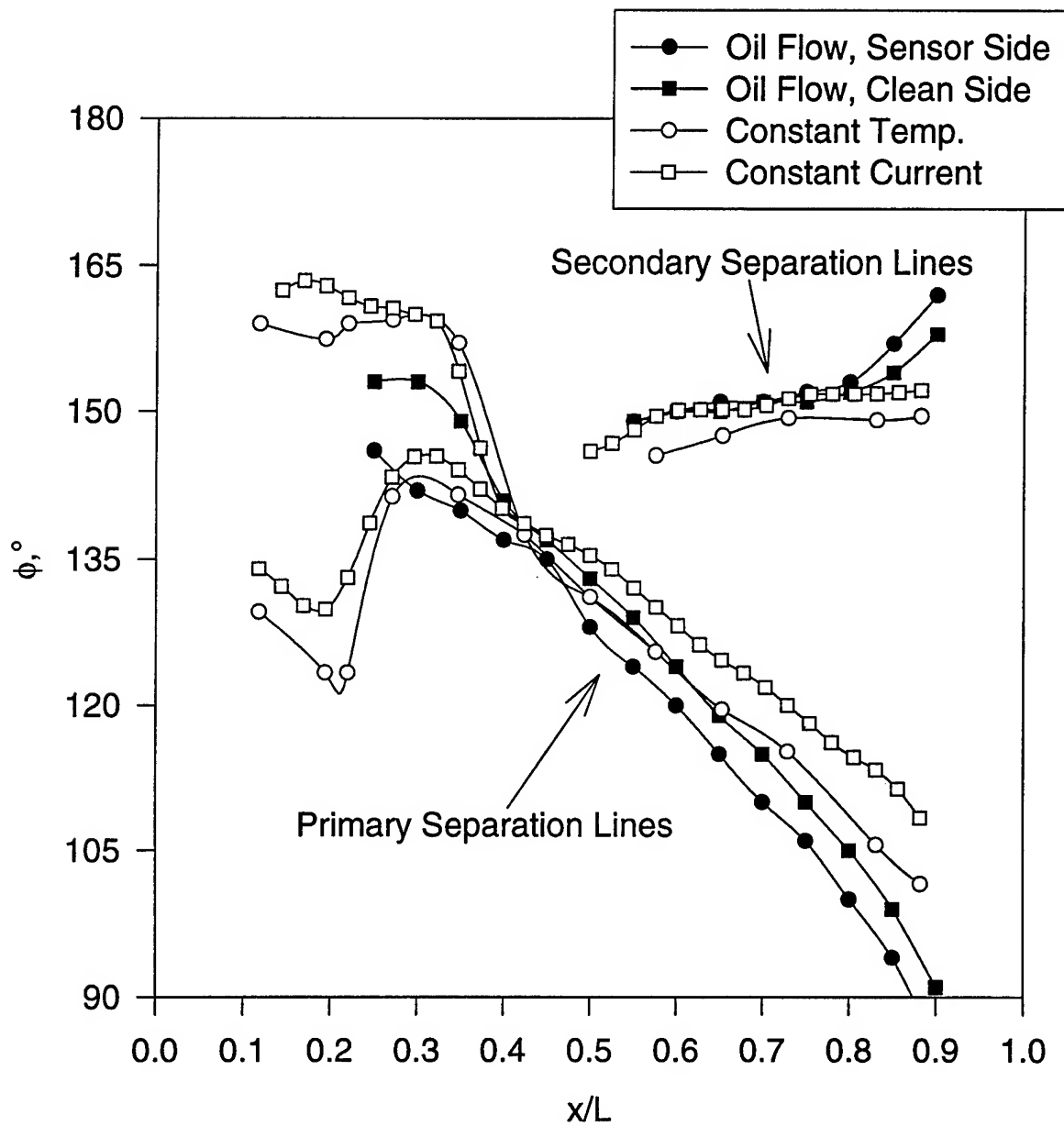


Figure 327. Various separation line comparisons for  $\alpha=25^\circ$ .

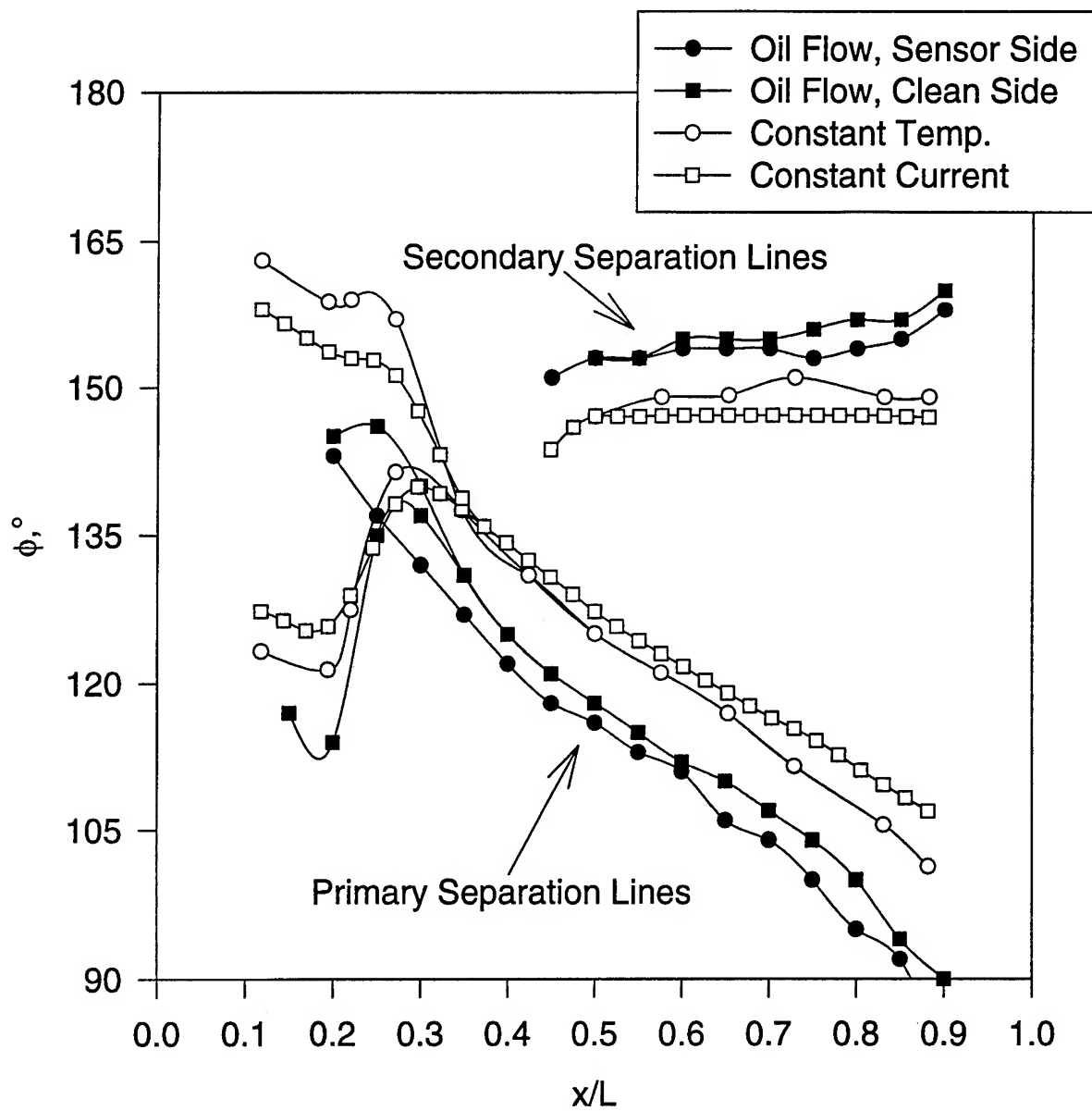


Figure 328. Various separation line comparisons for  $\alpha=30^\circ$ .

# Appendix A: Integral Momentum Boundary Layer Solution for a Line of Symmetry on a Body of Revolution

---

## A.1 Method Derivation

Many techniques have been utilized with relative success to calculate the boundary layer on a flat plate, and these have been extended to axisymmetric bodies. Often, the simplest integral techniques capture the flow physics to adequate precision (Schetz, 1993). The case of an axisymmetric body at angle of attack is a more difficult proposition due to flow three-dimensionality manifested in skewing in the boundary layer and complex separation phenomena (Simpson, 1995). However, the plane of symmetry on the windward side of such a body presents a flow environment that is more predictable. The favorable pressure gradient results in a very stable boundary layer with no flow separation. Also, this windward-side plane-of-symmetry boundary layer is quasi-two-dimensional in that there can be no boundary layer skewing due to the flow symmetry condition. Therefore, it is plausible that this line-of-symmetry windward-side flow can be computed with adequate precision to capture the most important flow physics.

A full derivation follows. First, a local coordinate system is chosen at a given longitudinal station  $x_0$  such that the radius of the model is  $r_0(x_0)$ . In this coordinate system,  $x$  points parallel to the body surface and the model axis,  $y$  points in the radial direction, and  $z$  completes the right-hand sense, indicating the crossflow direction. With  $r$  indicating a position in the flow in the  $y$  (radial) direction but measured from the model axis, the continuity equation for a differential control volume is:

$$\frac{\partial(Ur)}{\partial x} + \frac{\partial(Vr)}{\partial y} + \frac{\partial(Wr)}{\partial z} = 0$$

Similarly, the x-momentum equation is given by:

$$\frac{\partial(U^2r)}{\partial x} + \frac{\partial(UVr)}{\partial y} + \frac{\partial(UWr)}{\partial z} = -\frac{1}{\rho} \frac{\partial(Pr)}{\partial x} + \frac{1}{\rho} \frac{\partial(\tau r)}{\partial y}$$

In this equation,  $P$  is the pressure at the control volume, and  $\tau$  is the shear force in the x-direction at the control volume. It is important to note that as yet these equations are exact and fully applicable to any point in the flow, since no boundary layer or plane-of-symmetry assumptions have been applied. The x-momentum equation can be expanded and grouped to yield:

$$U \frac{\partial(Ur)}{\partial x} + Ur \frac{\partial U}{\partial x} + U \frac{\partial(Vr)}{\partial y} + Vr \frac{\partial U}{\partial y} + U \frac{\partial(Wr)}{\partial z} + Wr \frac{\partial U}{\partial z} = -\frac{r}{\rho} \frac{dP}{dx} + \frac{r}{\rho} \frac{\partial \tau}{\partial y} - \frac{P}{\rho} \frac{dr}{dx} + \frac{\tau}{\rho}$$

$$\frac{U}{r} \left( \frac{\partial(Ur)}{\partial x} + \frac{\partial(Vr)}{\partial y} + \frac{\partial(Wr)}{\partial z} \right) + U \frac{\partial U}{\partial x} + V \frac{\partial U}{\partial y} + W \frac{\partial U}{\partial z} = -\frac{1}{\rho} \frac{dP}{dx} + \frac{1}{\rho} \frac{\partial \tau}{\partial y} - \frac{P}{\rho r} \frac{dr}{dx} + \frac{\tau}{\rho r}$$

The first term drops out due to continuity. Also recognizing that  $W=0$  on a flow plane of symmetry, and noting that the last two terms are negligible because  $r$  is assumed to be much larger than the boundary layer thickness, the  $x$ -momentum equation becomes the more familiar:

$$U \frac{\partial U}{\partial x} + V \frac{\partial U}{\partial y} = -\frac{1}{\rho} \frac{dP}{dx} + \frac{1}{\rho} \frac{\partial \tau}{\partial y}$$

To formulate the integral method, the continuity equation is used to eliminate  $V$ :

$$V = -\frac{1}{r} \int_0^y \left[ \frac{\partial(Ur)}{\partial x} + \frac{\partial(Wr)}{\partial z} \right] dy$$

$$= -\frac{1}{r} \int_0^y \left[ U \frac{\partial r}{\partial x} + r \frac{\partial U}{\partial x} + W \frac{\partial r}{\partial z} + r \frac{\partial W}{\partial z} \right] dy$$

$$= -\frac{1}{r} \int_0^y \left[ U \frac{\partial r}{\partial x} + r \frac{\partial U}{\partial x} + r \frac{\partial W}{\partial z} \right] dy$$

Bernoulli's equation is also used:

$$-\frac{1}{\rho} \frac{dP}{dx} = U_{\infty} \frac{dU_{\infty}}{dx}$$

So replacing the expression for  $V$  from the continuity equation and using Bernoulli's equation, the following differential  $x$ -momentum equation is obtained:

$$U \frac{\partial U}{\partial x} - \frac{1}{r} \frac{\partial U}{\partial y} \int_0^y \left[ U \frac{\partial r}{\partial x} + r \frac{\partial U}{\partial x} + r \frac{\partial W}{\partial z} \right] dy = U_{\infty} \frac{dU_{\infty}}{dx} + \frac{1}{\rho} \frac{\partial \tau}{\partial y}$$

This equation is integrated over  $y$ , from the wall ( $y=0$ ) to some arbitrary height  $H$  outside the boundary layer to yield the following integral equation:

$$\int_0^H \left\{ U \frac{\partial U}{\partial x} - \frac{1}{r} \frac{\partial U}{\partial y} \int_0^y \left[ U \frac{\partial r}{\partial x} + r \frac{\partial U}{\partial x} + r \frac{\partial W}{\partial z} \right] dy - U_{\infty} \frac{dU_{\infty}}{dx} \right\} dy = \int_0^H \left( \frac{1}{\rho} \frac{\partial \tau}{\partial y} \right) dy$$

To evaluate these integrals, several steps are required. First, each component of the sub-integral within the main integral on the left hand side can be simplified using the chain rule:

$$\int_0^H \frac{\partial U}{\partial y} \left( \int_0^y * dy \right) dy = U_\infty \int_0^H * dy - \int_0^H U * dy$$

where \* represents some term within the inner integral. Using this chain rule to expand the x-momentum equation results in the following:

$$\int_0^H \left\{ U \frac{\partial U}{\partial x} - \frac{1}{r} \left[ U_\infty U \frac{\partial r}{\partial x} - U^2 \frac{\partial r}{\partial x} + U_\infty r \frac{\partial U}{\partial x} - U r \frac{\partial U}{\partial x} + U_\infty r \frac{\partial W}{\partial z} - U r \frac{\partial W}{\partial z} \right] - U_\infty \frac{dU_\infty}{dx} \right\} dy = -\frac{\tau_w}{\rho}$$

which can be further regrouped as:

$$\int_0^H \left\{ U \frac{\partial U}{\partial x} - U_\infty \frac{\partial U}{\partial x} + U \frac{\partial U}{\partial x} - U_\infty \frac{dU_\infty}{dx} \right\} dy - \int_0^H \frac{U}{r} (U_\infty - U) \frac{\partial r}{\partial x} dy - \int_0^H (U_\infty - U) \frac{\partial W}{\partial z} dy = -\frac{\tau_w}{\rho}$$

The three terms on the left hand side can then be evaluated. The first term is the term typically found in the flat plate formulation of the integral boundary layer equations, and reduces to an elegant and classical result:

$$\begin{aligned} \int_0^H \left\{ 2U \frac{\partial U}{\partial x} - U_\infty \frac{\partial U}{\partial x} - U_\infty \frac{dU_\infty}{dx} \right\} dy &= \int_0^H \left\{ \frac{\partial(U^2)}{\partial x} - \frac{\partial(UU_\infty)}{\partial x} + (U - U_\infty) \frac{dU_\infty}{dx} \right\} dy \\ &= \int_0^H \frac{\partial(U^2 - UU_\infty)}{\partial x} dy + \int_0^H (U - U_\infty) \frac{dU_\infty}{dx} dy \\ &= -\frac{d}{dx} \left( U_\infty^2 \int_0^H \frac{U}{U_\infty} \left( 1 - \frac{U}{U_\infty} \right) dy \right) - U_\infty \frac{dU_\infty}{dx} \int_0^H \left( 1 - \frac{U}{U_\infty} \right) dy \\ &= -\frac{d(U_\infty^2 \theta)}{dx} - U_\infty \frac{dU_\infty}{dx} \delta^* \\ &= -U_\infty^2 \frac{d\theta}{dx} - 2U_\infty \frac{dU_\infty}{dx} \theta - U_\infty \frac{dU_\infty}{dx} \delta^* \\ &= -U_\infty^2 \frac{d\theta}{dx} - \theta(2 + H)U_\infty \frac{dU_\infty}{dx} \end{aligned}$$

The second term incorporates the effects due to the curvature of the model radius, and thus the control volume, on the momentum transfer in the boundary layer. To reduce this term, it is assumed that  $1/r$  and  $\partial r/\partial x$  do not vary much over the integration and can be evaluated as the values at the model surface. This is a result of the assumption that the boundary layer is much thinner than the model radius.

$$\begin{aligned} -\int_0^H \frac{U}{r} (U_\infty - U) \frac{\partial r}{\partial x} dy &= -\frac{U_\infty^2}{r_0} \frac{dr_0}{dx} \int_0^H \frac{U}{U_\infty} \left(1 - \frac{U}{U_\infty}\right) dy \\ &= -\theta \frac{U_\infty^2}{r_0} \frac{dr_0}{dx} \end{aligned}$$

Evaluation of the third term requires some description about the three-dimensional nature of the boundary layer near the windward plane of symmetry on a body of revolution. For zero and slightly favorable pressure gradient turbulent boundary layers, the integral momentum equation is eventually solved by assuming a boundary layer profile shape, usually a  $1/7^{\text{th}}$  power law. Just off the line of symmetry on a body of revolution, the spanwise velocity is very small because it goes to zero exactly at the line of symmetry. In fact, very near the line of symmetry, the boundary layer profile is probably very nearly quasi-two-dimensional, pointing in a direction slightly off axis. In other words, within an infinitesimally small region surrounding the windward plane of symmetry the boundary layers are not yet significantly skewed. It is therefore a very reasonable assumption that the boundary layer profiles located slightly off the windward plane of symmetry are very collateral and can be represented as a locally two-dimensional boundary layer profile turned at some small angle off longitudinal that is coincident with the free-stream velocity direction. It follows that the spanwise velocity profile,  $W(y)$ , can be assumed to exhibit the same shape as the streamwise velocity profile:

$$U(y) = U_\infty f(y)$$

$$W(y) = W_e f(y)$$

$$\text{constraint: } f(0) = 0, f(\infty) = 1$$

Of course, the edge velocity does not vary with  $y$ . Then the spanwise velocity gradient term can be evaluated as:

$$\frac{\partial W}{\partial z} = \frac{dW_e}{dz} f(y) = \frac{dW_e}{dz} \frac{U}{U_\infty}$$

The spanwise edge velocity gradient is obtained from the potential flow solution. Using this assumption, the third term in the integral  $x$ -momentum equation above can be evaluated as:



$$\begin{aligned}
-\int_0^H (U_\infty - U) \frac{\partial W}{\partial z} dy &= -\int_0^H (U_\infty - U) \frac{\partial W_e}{\partial z} \frac{U}{U_\infty} dy \\
&= -U_\infty \frac{\partial W_e}{\partial z} \int_0^H \left(1 - \frac{U}{U_\infty}\right) \frac{U}{U_\infty} dy \\
&= -\theta U_\infty \frac{\partial W_e}{\partial z}
\end{aligned}$$

Integration of the right hand side results trivially in the wall shear. Substituting all of these evaluated integrals back into the  $x$ -momentum equation yields the following integral formulation:

$$\begin{aligned}
-U_\infty^2 \frac{d\theta}{dx} - U_\infty \theta (2 + H) \frac{dU_\infty}{dx} - U_\infty^2 \theta \frac{1}{r_0} \frac{dr_0}{dx} - U_\infty \theta \frac{\partial W_e}{\partial z} &= -\frac{\tau_w}{\rho} \\
\frac{d\theta}{dx} + \theta \left( \frac{2 + H}{U_\infty} \frac{dU_\infty}{dx} + \frac{1}{r_0} \frac{dr_0}{dx} + \frac{1}{U_\infty} \frac{\partial W_e}{\partial z} \right) &= \frac{C_f}{2}
\end{aligned}$$

where  $\theta$  is the momentum thickness;  $H$  is the shape factor  $\delta^*/\theta$ ; and  $C_f$  is the skin friction coefficient. This equation parallels the ones presented in Schlichting (1979) and Kays and Crawford (1980) for both two-dimensional boundary layers and boundary layers in axisymmetric flows. The term with the derivative of the model radius with respect to  $x$  (where  $x$  is specifically the coordinate in the direction locally parallel to the model surface and not a coordinate along the model axis) represents the affect of model radius, and is identical to the term found in the axisymmetric equations in Kays and Crawford (1980). It is the term with the edge crossflow velocity gradient that allows the computation of the windward boundary layer for a model at angle of attack.

The problem is classically solved by assuming the shape factor is constant, which is the case if one assumes a given boundary layer profile shape. The classical treatment of this problem for a turbulent boundary layer also assumes a skin friction law to get the equation in terms of the momentum thickness.

For the problem at hand, the calculation must start in a laminar boundary layer and proceed through fixed transition. There are techniques for computing the laminar boundary layer in a pressure driven flow such as the Polhausen method and the Thwaites-Walz method (Schetz, 1993), but these do not include the spanwise velocity gradient term and thus are not easily ported over to this flow case. Therefore, for the sake of simplicity and consistency for these tests, the laminar portion of the boundary layer is calculated using a similar set of assumptions and exactly the same equation. The two pieces of information that must be supplied for both the laminar and turbulent portions of the calculation are a shape factor and a skin friction law. The shape factor for the two flow regimes is assumed to be  $H=2.6$  for laminar flow and  $H=1.3$

for turbulent flow (assuming a  $1/7^{\text{th}}$  law in this latter case) (Schetz, 1993). The skin friction law is assumed to take the form:

$$C_f = \beta \text{Re}_\delta^m$$

with the constants used being (Schetz, 1993):

	$\beta$	$m$
laminar	3.32	-1
turbulent	0.0456	-0.25

The final problem that needs to be addressed is the treatment of the transition strip. The transition strip in these tests is a row of posts 0.05" in diameter, 0.21" high and spaced 0.1" center to center. The trip posts were sized to be larger than the approach laminar boundary layer. The primary effect that the flow receives from the presence of the posts is a decrease in flow momentum due to the drag of the posts. Following Schlichting (1979), the drag on a given post in a boundary layer flow can be related to the change in momentum thickness by:

$$\frac{D}{\frac{1}{2}\rho U_e^2} = C_D A = \frac{1}{2} b(\theta_2 - \theta_1)$$

where  $D$  is the drag on the post,  $C_D$  is the post drag coefficient,  $A$  is the post frontal area, and  $b$  is the post width. Since the posts are spaced with a 50% blockage, the change in momentum over the entire trip width is 50% of this value. Using  $A=bh$ , the momentum thickness change is:

$$\theta_2 = \theta_1 + \frac{1}{4} C_D h$$

An appropriate value for  $C_D$  is 1.0 (Schlichting, 1979).

The calculation then proceeds as follows. First, flow velocity, temperature, and Reynolds number are specified to set the flow conditions, and angle of attack is specified to set the model orientation. The starting condition is supplied by using the Thwaites-Walz solution for an axisymmetric stagnation point as an approximation:

$$\theta(0) = \sqrt{\frac{0.563\nu}{(dU_\infty/dx)_0}}$$

$$\left(\frac{dU_\infty}{dx}\right)_0 = \frac{3}{2} \frac{U_\infty}{R_0}$$

where  $R_0$  is the radius of curvature of the nose. Euler's method is then used to integrate the momentum equation in terms of momentum thickness along the line of symmetry of the prolate spheroid. The analytical

potential flow solution for a prolate spheroid at incidence as presented by Band and Payne (1979) is used to obtain both the streamwise and spanwise velocity gradients, and laminar flow shape factors and skin friction laws are used. When the trips strips are reached, the momentum thickness is immediately increased proportional to the post drag, and the shape factors and skin friction law are changed to appropriate versions for turbulent flow. The integration is then carried over the rest of the length of the model. It is assumed that the pressure gradient is not strong enough to re-laminarize the line-of-symmetry flow. This is supported by the data of Meier and Kreplin (1985). Typical results of this calculation method are plotted in Figure 22. The calculations, performed for a Reynolds number of 4.2 million, are compared with the 6.4 million Reynolds number data of Meier and Kreplin. The effect of the Reynolds number discrepancy is discussed in Chapter 3, section 3.7.

To demonstrate the impact of the  $dr/dx$  and  $dW/dz$  terms on the solution, the skin friction distribution was computed for the  $30^\circ$  angle of attack case with these terms removed to compare to the full solution. Figure A1 shows the results. In this figure it is clear that the  $dr/dx$  term provides a relatively small correction except at the extreme tail, but the  $dW/dz$  term dramatically impacts the skin friction levels.

It was found that the solution technique was numerically robust downstream of  $x/L=0.05$  in that large changes in starting conditions and in trip transition conditions had only a very local influence on the solutions. The skin friction distribution is mostly determined by the pressure gradient, the assumed shape factors, and the skin friction laws. The initial momentum thickness and transition momentum thickness increment play minor, localized roles in the solution.

## A.2 The Code

The basic code for performing these calculations, bl.c, is listed below. The Borland C/C++ 4.0 compiler was used.

```
/* Calculate skin friction distribution on windward side of prolate */
/* spheroid using integral method. */

#include <stdio.h>
#include <math.h>
#include <time.h>
#include <alloc.h>
#include <string.h>
#include <stdlib.h>
#include <conio.h>

#define Pi 3.1415926539

#define numsteps 1000

/* Flow quantities. */
```

```

#define Uinf      50.0          /* m/s */
#define Tref      300.0        /* K */
#define rhoref    1.225        /* kg/m^3 */

#define untripped 0
#define tripped 1

#define Cd 1.0
#define htrip 5.3e-4           /* m */

#define H del_theta/del_dels

/* Geometry constants. */

#define a 0.6858               /* m */
#define b (a/6.0)             /* m */
#define L (2.0*a)             /* m */

/* Subroutine declarations. */

double nu(double T,double rho);
double Ue(double x,double alp);
double x_to_s(double x);
double dUeds(double x,double alp);
double R(double x);
double dRds(double x);
double dWedz(double x,double alp);

main(int argc,char *argv[])
{
    double theta,
           theta0,
           dtheta,
           x,
           dx,
           s,
           sold,
           del_dels,
           del_theta,
           nuref,
           Beta,
           m,
           G,
           G1,
           G2,
           G3,
           Cf,
           alpha;
    short flow;
    FILE *fout;
    char filename[20];

    /* Get command line parameters. */

    if (argc<2)

```

```

    {
        printf("USAGE: bl alpha\n");
        exit(-1);
    }

alpha=atof(argv[1])*Pi/180.0;

/* open output file. */

clrscr();

sprintf(filename,"blcf%d.new",(short) (atof(argv[1])));
fout=fopen(filename,"w");

/* Use Thwaites-Walz blunt nose axisymmetric solution for starting */
/* momentum thickness. */

nuref=nu(Tref,rhoref);

theta0=sqrt(0.0375*b*b/a*nuref/Uinf);
theta=theta0;

/* March through x. */

dx=L/((double) numsteps);
x=dx;
s=0.0;
del_dels=3.1;
del_theta=8.0;
Beta=3.32;
m=-1.0;
flow=untripped;

/* Find stagnation point. */

while(Ue(x,alpha)<=0.0)
    x+=dx;

Cf=Beta*pow(Ue(x+dx,alpha)*del_theta*theta/nuref,m);

fprintf(fout,"%7.4f %7.4f \n",x/L,Cf*1000.0);

for(;x<0.98*L;x+=dx)
{
    printf("%f\n",x/L);
    sold=s;
    s=x_to_s(x);
    if (x>L*0.2)
    {
        /* Now turbulent. */

        del_dels=3.1;
        del_theta=8.0;
        Beta=0.0456;
        m=-0.25;
    }
    /* In this program, x is the axial
    /* coordinate; s is the surface
    /* coord., corresponding to x in the
    /* derivation above.

```

```

    if((x>L*0.2)&&(flow==untripped))
    {
        flow=tripped;

        /* Increment theta according to the momentum drop from the */
        /* trips. */

        theta+=0.25*htrip*Cd;
    }

    G1=(2.0+H)/Ue(x,alpha)*dUeds(x,alpha);
    G2=dRds(x)/R(x);
    G3=1.0/Ue(x,alpha)*dWedz(x,alpha);
    G=G1+G2+G3;

    dtheta=(Cf/2.0-G*theta)*(s-sold);

    /* These next statements are to limit instabilities in the solution, */
    /* particularly near the nose where gradients are large. */

    if (-dtheta>theta)
        dtheta=0.0;

    theta+=dtheta;

    Cf=Beta*pow(Uinf*del_theta*theta/nuref,m);

    fprintf(fout,"%7.4f %7.4f \n",x/L,Cf*1000.0);
}

fclose(fout);

return 0;
}

/*****/
double nu(double T,double rho)
/* Returns knimetaic viscosity in m^2/s. */
{
    return 1.458e-6*pow(T,1.5)/(T+110.4)/rho;
}

/*****/
double Ue(double x,double alp)
/* This routine computes the non-dimensional Ue on a 6:1 prolate */
/* spheroid at angle of attack a. */
/* x is non-dimensionalized by the length L. */
/* a is in radians. */
/* Ue is non-dimensionalized by Uinf. */

```

```

{
    double zeta,
           cosbetahat,
           sinbetahat,
           V0,
           V90,
           t,
           term,
           betahat;

    zeta=2.0*(x/L)-1.0;
    t=1.0/6.0;
    term=1.0-t*t;

    if (R(x)!=0.0)
        betahat=atan(-(a-x)*b*b/a/a/R(x));
    else
        betahat=Pi/2.0;

    if (zeta>0.0)
        betahat=-fabs(betahat);
    else
        betahat=fabs(betahat);

    cosbetahat=cos(betahat);
    sinbetahat=sin(betahat);

    V0=pow(term,1.5)/
        ( sqrt(term) - 0.5*t*t*log( (1.0+sqrt(term))/(1.0-sqrt(term)) ) );
    V90=2.0*V0/(2.0*V0-1.0);

    return Uinf*(V0*cos(alp)*cosbetahat-V90*sin(alp)*sinbetahat);
}

/*****/

double x_to_s(double x)
/* Given x, compute s. */

{
#define steps 100

    double theta,
           dtheta,
           r,
           s=0.0;
    short i;

    r=R(x);

    if (x<a)
        theta=fabs(atan(r/(a-x)*a/b));
    else if (x==a)

```

```

        theta=Pi/2.0;
    else
        theta=Pi-fabs(atan(r/(a-x)*a/b));

    dtheta=theta/((double) steps);

    theta=0.0;

    for(i=0;i<steps;i++)
    {
        theta+=dtheta;
        s+=sqrt(pow(a*sin(theta),2)+pow(b*cos(theta),2))*dtheta;
    }

    return s;
}

/*****/

double dUeds(double x,double alp)
/* Given x/L, compute dUeds. */
{
    double Ue1,
           Ue2,
           s1,
           s2,
           fac;

    fac=10.0*((double) numsteps);

    s1=x_to_s(x-a/fac);
    s2=x_to_s(x+a/fac);

    Ue1=Ue(x-a/fac,alp);
    Ue2=Ue(x+a/fac,alp);

    return (Ue2-Ue1)/(s2-s1);
}

/*****/

double R(double x)
/* This function computes the prolate spheroid radius as a function */
/* of x. */
{
    return b*sqrt(1.0-(a-x)*(a-x)/a/a);
}

/*****/

double dRds(double x)
/* This function computes the prolate spheroid slope (over arc length */

```



```

/* s) at position x.                                     */
{
    double R1,
           R2,
           s1,
           s2,
           fac;

    fac=10.0*((double) numsteps);

    s1=x_to_s(x-a/fac);
    s2=x_to_s(x+a/fac);
    R1=R(x-a/fac);
    R2=R(x+a/fac);

    return (R2-R1)/(s2-s1);
}

/*****/

double dWedz(double x,double alp)

/* Compute the crossflow velocity gradient at x.          */
{
    double V0,
           V90,
           t=1.0/6.0,
           term=1.0-t*t;;

    V0=pow(term,1.5)/
        ( sqrt(term) - 0.5*t*t*log( (1.0+sqrt(term))/(1.0-sqrt(term)) ) );

    V90=2.0*V0/(2.0*V0-1.0);

    return Uinf*V90*sin(alp)/R(x);
}

```

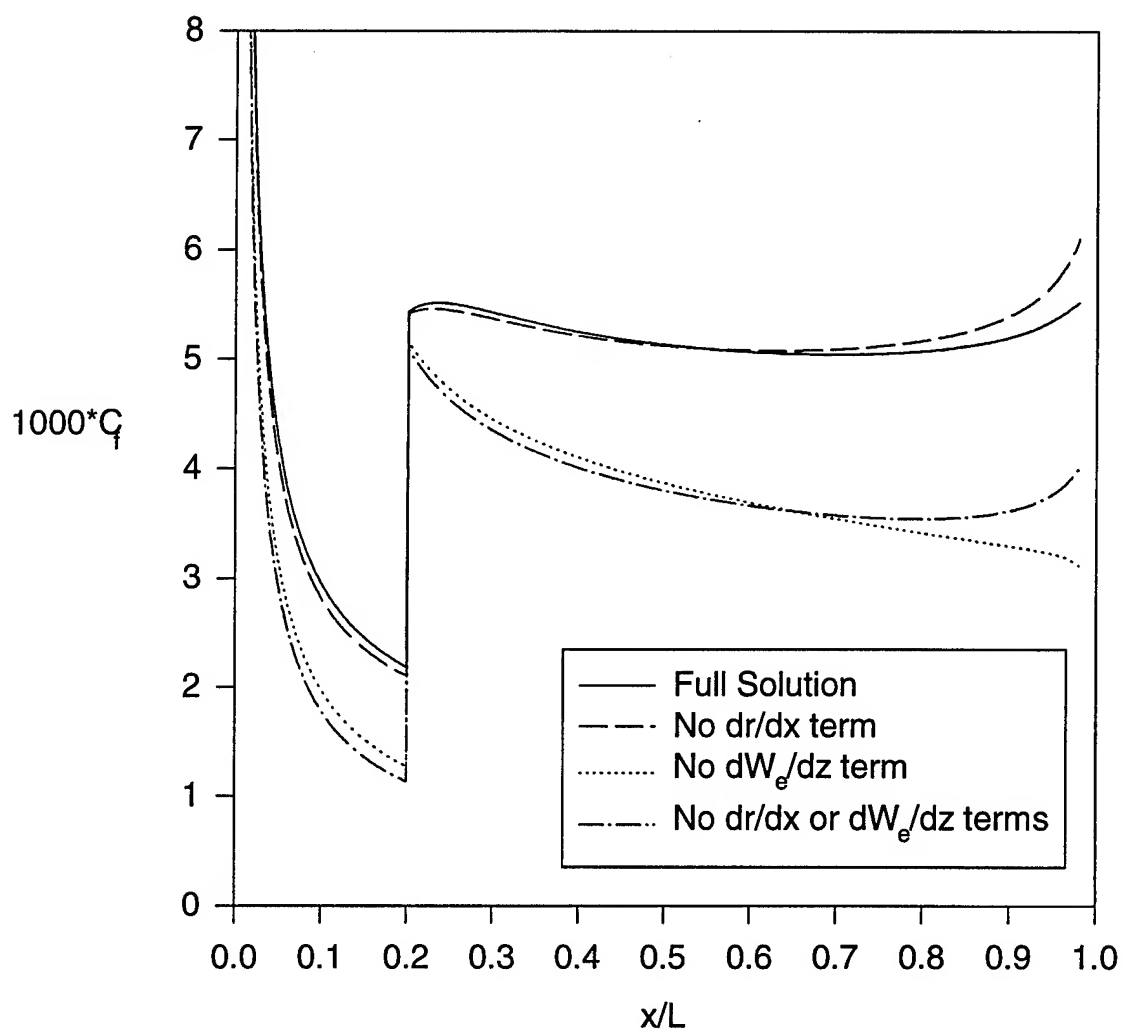


Figure 11. Line of symmetry  $C_f$  calculations at  $\alpha=30^\circ$  with specific terms from the integral momentum equation removed.

## Vita

---

The author was born on April 20, 1971, in Allentown, Pennsylvania. He grew up in Macungie, Pennsylvania, and graduated from Emmaus High School in June of 1989. Summers during high school were spent working on cars for his father who is a mechanic at Wetzel's Garage, Macungie, PA. The author then matriculated to Virginia Polytechnic Institute and State University, where he completed a Bachelors of Science in Aerospace Engineering in May of 1992 and a Masters of Science in Aerospace Engineering in July of 1993.